AFIT/DS/ENY/98M-02

The Influence of Surface Roughness on Supersonic High Reynolds Number Turbulent Boundary Layer Flow

DISSERTATION

Robert M. Latin, B.S., M.S.
Captain, USAF

AFIT/DS/ENY/98M-02

Disclaimer

The views expressed in this dissertation are those of the author and do not reflect the official policy or position of the United States Air Force, the Department of Defense, or the United States Government.

AFIT/DS/ENY/98M-02

The Influence of Surface Roughness on Supersonic High Reynolds Number Turbulent Boundary Layer Flow

DISSERTATION

Presented to the Faculty of the Graduate School of Engineering of the Air Force Institute of Technology Air University In Partial Fulfillment for the Degree of

Doctor of Philosophy

Robert M. Latin, B.S., M.S.

Captain, USAF

Air Force Institute of Technology

Wright-Patterson AFB, Ohio

March, 1998

Sponsored by Air Force Research Laboratory/PRSS and Air Force Office of Scientific Research/NA

AFIT/DS/ENY/98M-02

The Influence of Surface Roughness on Supersonic High Reynolds Number Turbulent Boundary Layer Flow

Robert M. Latin, B.S., M.S.

Captain, USAF

Approved:

Dr. Rodney D. W. Bowersox
Committee Chairman — Date: 2 Apr 98

Dr. Philip S. Beran
Committee member — Date: 2 Apr 98

Maj Jeffery K. Little
Committee member — Date: 14 Apr 98

Dr. David E. Weeks
Committee member — Date: 2 Apr 98

Dr. William M. Brown
Dean's Representative — Date: 2 Apr 98

Accepted:

Dr. Robert A. Calico
Dean, School of Engineering

Acknowledgments

I would like to take this opportunity to thank everyone who lent me support during the last three years. First, I would like to thank my advisor, Dr. Rodney Bowersox, for his encouragement, knowledge, and experience. Without his tireless efforts, this research would not have been possible. Thanks go to my committee members for their inputs and timely response, particularly during the last push to complete this effort. I would also like to thank Dr. Mark Glauser of the Air Force Office of Scientific Research (AFOSR/NA) and Drs. Mark Gruber and Diana Glawe of the Air Force Research Laboratory (AFRL/PRSS) who provided the funding for this research.

Second, I would like to thank the laboratory staff and the modeling shop for their efforts and support. Jay Anderson and the rest of the laboratory staff provided the equipment and facilities required in a cheerful and timely manner. I would especially like to thank Andy Pitts for sharing his knowledge and experience in the setup and use of the laboratory equipment; and for listening to my stories and providing many of his own. Though the last few years of the AFIT model shop have been trying, the efforts of Russel Hastings and Jan LeValley during this period is greatly appreciated. From them, I learned how fanciful drawings on paper become tangible objects in hand.

I would especially like to thank my wife. Though the last few years have been very difficult, Anita has provided support and encouragement throughout. Finally, I would like to thank my parents, John and Roselyn, for providing me the foundation and discipline required to reach so high. They have always believed in me.

Robert Michael Latin

Table Of Contents

Page

List of Figures

Page

Page

Page

Page

Page

Page

Page

Page

Page

List of Tables

Page

Page

List of Symbols

English Symbols

Symbol	Definition
A^+, A_o^+	Dimensionless damping constant
C_f	Skin Friction coefficient
C_D	Coefficient of Drag
C_p	Specific heat at constant pressure
d	Diameter
d_p	Mean particle size
E	Total Error
e	Specific internal energy
	Error
e_o	Specific total energy
f	Hot-wire effective Reynolds number sensitivity
	frequency
f_o	QLS-Method new loading factor constant
$\overrightarrow{\mathbf{F}}$	Inviscid flux vector in the x coordinate direction
$\overrightarrow{\mathbf{F}}_v$	Viscous flux vector in the x coordinate direction
g	Hot-wire total temperature sensitivity
g_o	QLS-Method new loading factor slope
$\mathbf{g}$	Inviscid flux vector in the y coordinate direction
$\mathbf{g}_v$	Viscous flux vector in the y coordinate direction
h_o	Specific total enthalpy

h	Specific internal enthalpy
	inviscid flux vector in the y coordinate direction
$\hat{i}, \hat{j}, \hat{k}$	Unit vectors in the x, y, and z directions
k	Thermal conductivity
k_t	Wire Thermal conductivity
k_s	Equivalent Sand-grain roughness height
k^+	Roughness Reynolds Number
k_s^+	Equivalent Sand-grain Roughness Reynolds Number
L	Length
l_m	Mixing length
M	Mach number
N	Number of overheat ratios
Nu	Nusselt number
n	Thermal property power law powers
	Normal vector
Pr	Prandtl number
P, p	Pressure
P_{o_2}	Total pressure behind a normal shock
Q	Vector of conserved quantities
	Velocity Magnitude
q_j	Heat transfer rate per unit area in index notation
q_i^T	Reynolds-averaged, incompressible turbulence heat transfer rate
	per unit area in index notation
q_i^R	Reynolds-averaged, compressible turbulence heat transfer rate

	per unit area in index notation
q_i^F	Favre-averaged, turbulence heat transfer rate per unit area in index notation, W/m^2
q_w	Wire heat transfer
R	Resistance
	Length
	Residual vector
R_E	Correlation Function
Re	Reynolds number
Re_e	Effective cooling Reynolds number
Re_{oe}	Effective Reynolds number with $\mu = \mu_o$
Re_l	Reynolds number, with reference length l
R, r	Pipe Radius
r	Recovery Factor
St	Stanton number
S	Turbulent Schmidt number
	Single overheat matrix coefficients
T	Temperature
	Length of time
T_{aw}	Adiabatic Wall Temperature
T_e	Equilibrium temperature
T_{ref}	Reference temperature
T_w	Wire temperature
T_1	Time scale of fluctuating component

T_2	Time scale of mean flow variations
t	time
V, v	Voltage
u, v, w	Velocities in the x,y,z directions, respectively
u_i	Velocity in index notation
u_e	Boundary layer edge velocity
u^+	Dimensionless, boundary layer scaled velocity
u^*	Friction Velocity
x,y,z	Rectangular Cartesian coordinates
x_i	Position vector in tensor notation
y^+	Dimensionless, sublayer-scaled distance

Greek Symbols

Symbol	Definition
α, β	Hot-wire function of Mach number
β_x, β_y	Blockage Parameter
δ_{ij}	Kronecker delta
δ	Boundary layer height
δ^*	Displacement Thickness
Δ	Forward difference operator
∇	Backward difference operator
γ	Ratio of specific heats
κ	Thermal conductivity coefficient

	Spatial discretization parameter
λ	Second bulk viscosity coefficient
	Pipe friction factor
	Roughness Geometry/Spacing Parameter
	Wave Length
μ	First bulk viscosity coefficient, molecular viscosity
μ_t	Turbulent eddy viscosity
μ_t^S	Situ and Schetz,extended turbulent eddy viscosity, N·s/m^2,kg/(m·s)
ξ, η	Dimensionless coordinates
ξ_i, η_i	Transformation metrics
ρ	Density
σ_{ij}	Shear-stress tensor component
τ	Dummy variable of integration
	Temperature loading factor
τ^*	New wire temperature loading factor
τ_{ij}	Shear stress tensor component
τ_{ij}^T	Reynolds-averaged, incompressible turbulent shear-stress tensor component
τ_{ij}^R	Reynolds-averaged, compressible turbulent shear-stress tensor component
τ_{ij}^F	Favre-averaged, turbulent shear-stress tensor component
τ_w	Shear stress at the wall
Φ	Arbitrary flow variable
ϕ	Spatial discretization parameter
θ	Mass flux flow angle
	Momentum Thickness

ω	Turbulence specific dissipation rate
	Magnitude of the vorticity vector
	Vigneron factor

Subscripts

Symbol	Definition
i, j,k	tensor indices
i,o	Boundary layer inner and outer regions, respectively
i	Incompressible
k	Kinematic
ref	Reference Value
t	Total conditions
v	viscous quantity
	Cell volume
o	Stagnation value
	Reference value
∞	Freestream or undisturbed value

Superscripts

Symbol	Definition
F	Favre-averaged value
R	Reynolds-averaged value
T	Turbulent value
$*$	Non-dimensional value

$\tilde{*}$	Mean value of Favre-averaged variable
$*''$	Fluctuating value of Favre-averaged variable
$\overline{*}$	Mean value of Reynolds-averaged variable, time average of any variable or group of variables
$*'$	Fluctuating value of Reynolds-averaged variable
$\hat{*}$	Denotes unit vector or direction cosine

Abbreviations

Abbreviation	Definition
A/D	Analog-to-Digital
ADC	Amps, Direct Current
AFIT	Air Force Institute of Technology
BSA	Burst Spectrum Analyzer
CAMMLE	Compressible Apparent Mass Mixing Length Extension model
CCD	Charge Coupled Device
CFD	Computational Fluid Dynamics
CFM	Cubic Foot per Minute
CFVPNS	Cell centered, Finite Volume, Parabolized Navier-Stokes Solver
CTA	Constant Temperature Anemometry
DFT	Discrete Fourier Transform
DNS	Direct Numerical Simulation
FANS	Favre-Averaged Navier-Stokes
GLS	General Least Squares
HWA	Hot Wire Anemometry

LDV	Laser Doppler Velocimetry
LES	Large Eddy Simulation
LHS	Left Hand Side
LSM	Laser Scan Microscope
LVDT	Linear Variable Displacement Transducer
MOH	Multiple Over-Heat
N-S	Navier-Stokes
PC	Personal Computer
PM	Photomultiplier
QLS	Quadratic Least Squares
RAM	Random Access Memory
RANS	Reynolds-Averaged Navier-Stokes
RHS	Right Hand Side
rms	Root-Mean-Square
SOH	Single Over-Heat
S/N	Signal-to-Noise
TKE	Turbulent Kinetic Energy
TKE_c	Compressible Turbulent Kinetic Energy

Abstract

A comprehensive study of rough-wall high-speed (M=2.9) high Reynolds number (Re/m = $1.9{\cdot}10^7$) turbulent boundary layer flow was performed consisting of experimental, analytical, and numerical methods. Six wall topologies consisting of a smooth and five rough surfaces (two- and three-dimensional machined roughness plates; and 80, 36, and 20 grit sand-grain roughened plates) were studied. A confocal laser scan microscope was used to measure the topography of the sand-grain roughnesses. The experimental measurement techniques included a convention Pitot pressure probe, laser Doppler velocimetry, hot-wire anemometry, color schlieren and laser sheet Mie scattering images. Mean measurements included velocity, Mach number, density, and mass flux. Turbulent measurements included velocity and mass flux turbulence intensities, kinematic Reynolds shear stress, compressible Reynolds shear stress in two planes, and the traverse apparent mass flux. Kinematic turbulent flow statistical properties were found to scale by local mean quantities and displayed a weak dependence on surface roughness. Turbulent flow statistical properties with the explicit appearance of density did not scale by local mean quantities, and had a strong linear dependence on roughness. Surface roughness also had a significant effect on the flow structure size, angles, and energy spectra. A theoretical analysis was performed and a new integral method for the estimation of skin friction was developed. The skin friction estimates were within 4% of compressible semi-empirical relations. A numerical study was performed which used a parabolized Navier-Stokes solver with two algebraic turbulence models and the Rotta model for surface roughness. A new method for the estimation of momentum loss improved the numerical flow predictability. The algebraic turbulence models predicted qualitatively correct profile shapes and accurately predicted the kinematic and compressible Reynolds shear stress levels for all but the near wall region ($y/\delta < 0.4$).

The Influence of Surface Roughness on Supersonic High Reynolds Number Turbulent Boundary Layer Flow

Chapter 1 - Introduction

1.1 Motivation

The understanding of supersonic boundary layer flow is of great importance to many fields in science and engineering. Supersonic viscous boundary layers are responsible for skin friction drag, convective heat transfer, and mass transfer over high-speed aircraft; missiles; re-entry vehicles; and propulsion systems. Surface roughness has a significant effect on supersonic viscous boundary layers and may occur in hypersonic engine inlets, combustors, and diffuser sections, turbine blade film cooling, and possible surface radiation signature reduction. Since all manufactured components of these systems have some inherent surface roughness or through operation roughness is generated, it is important to understand how surface roughness affects supersonic boundary layers in both a qualitative and quantitative manner to enable better systems designs for high performance applications.

Since the 1960's, hypersonic aircraft with scramjet propulsion have been proposed, but until recently, not a reality. The Hyper-X hypersonic flight test program has been initiated by NASA and is set to fly in 1999 in the Mach 5 to 10 range. According to NASA, the scramjet engine is the key enabling technology for hypersonic flight [2]. The ability of the scramjet to use atmospheric air as an oxidizer gives it a significant cargo/payload advantage over rocket propulsion. However, difficulties in the design of scramjet engines with regard to fuel mixing and combustion, low thrust-to-drag ratio, and limited ground test facilities, make numerical analysis and flight test essential. Current design analyses indicate that scramjet propulsion systems will operate very near the thrust

margin (i.e., the thrust will just exceed the drag) [30]. Hence, the increased drag due to roughness can potentially have a very serious impact on hypersonic vehicles.

The above listed modern technologies currently under development underscore the timeliness of the present research program. The current research program is focused on improving the flowfield understanding and predictability for supersonic flow over rough surfaces.

1.2 Current Flowfield Understanding and Prediction Limitations

Semi-empirical relations or Computational Fluid Dynamics (CFD) are used to estimate pragmatic engineering quantities (e.g., skin friction, C_f and heat flux, St). For high-speed flow, the semi-empirical techniques are based on "reasonable" extrapolations from the incompressible data base, i.e., most of the available data has been acquired for low-speed flow (see Chapter 2). Further, the extrapolation to high-speed flow usually entails invoking a compressibility transformation (e.g., Van Driest [62]), which are only valid for "smooth" flat plates. Hence, the utilization of semi-empirical methods yield qualitative or unproven information at best.

Computational techniques suffer a similar dilemma, where the extreme dearth of high-speed turbulence data, even for simple smooth wall flows (Bradshaw [15] and Spina et al. [56]), have severely limited the development and validation of turbulence models. It is also important to point out that **all** current high-speed turbulence models, with the exceptions of Large Eddy Simulation (LES) or Direct Numerical Simulation (DNS), were developed by "extending" existing low-speed formulations. Based on Morkovin's [43] observation ".. the essential dynamics supersonic boundary layers follow the incompressible pattern" along with the similarity of the compressible Farve-averaged Navier-Stokes equations (see Chapter 2) to the incompressible equations, has lead researchers to use incompressible turbulence models for flows up to Mach 5. Recent research by Bowersox and Buter [9], Smits et al. [54] and Spina [57] has indicated that the realm of applica-

bility of Morkovin's hypothesis is more restrictive then originally believed, and has suggested the need for further research into high-speed compressible boundary layer flows.

Numerical techniques are more useful for complex geometries as compared to classical flat plate semi-empirical methods; however, the lack of experimental data, complexity of turbulent boundary layers, and the state of current models are key limitations to prediction accuracy. The design of high speed vehicles requires an integrated approach to balance the subsystems of propulsion, payload, airframe structure, controls, and surface shape (both for aerodynamics and radiation signature). Since the building and testing of each design can be quite costly, computational modeling plays a key role in the design of each of the subsystems and the total system as a whole. While most areas of CFD are well advanced, the area of turbulent modeling requires further refinement. This is particularly true for high-speed turbulent boundary layers with surface roughness, where studies aimed at understanding the processes involved and developing better prediction methods are clearly lacking.

To improve flowfield understanding and prediction capability for high-speed boundary layers with surface roughness, detailed information is required in the areas of mean and turbulence data and surface roughness statistics. Mean flow information, such as, velocity, density, mass flux, and Mach number data is required. From this mean data, integral quantities such as, displacement and momentum thicknesses, can be estimated and, when combined with surface roughness statistics allow the verification and/or development of new semi-empirical relations.

Turbulence data and detailed surface roughness statics allow for the development and validation of turbulence models that include the underlying physics involved with rough surface high-speed turbulent boundary layer flow. For high-speed flow turbulence measurements must provide both velocity fluctuating and density fluctuating quantities to assess the effects of surface roughness on a compressible turbulent boundary layer.

In the past, sand-grain rough surface heights were provided by sand-grain size measurements prior to application on an arbitrary surface or by profilometer measurements. This type of roughness height measurement provides mean height and standard deviation information, but does not provide topographical information over the surface roughness area. Topographical surface roughness information will be beneficial in three-dimensional turbulence modeling and DNS.

1.3 Research Challenges and Recent Developments That Allow for the Present Research

High-Reynolds number turbulent boundary layers are characterized by a large range of spatial and temporal scales. To directly simulate turbulence with the time-dependent form of the governing equations requires a prohibitively large number of grid points for spatial and temporal resolution [67]. For this reason, intensive research is on going in the area of turbulence modeling through the use of the approximate time-averaged and mass-weighted time-averaged forms of the governing equations (see Chapter 2) in which the flow variables are assumed to be "decomposable" into a mean and a fluctuating component. This process results in second order moments, which translates into additional unknowns. The closure problem of turbulence hinges on developing models for these unknowns.

Empirical evidence is the cornerstone element of turbulence modeling. Detailed experimental studies focused on supersonic boundary layer flow with surface roughness are exceedingly scarce and studies that include turbulence are virtually nonexistent. Hence a major "first-step" challenge is to design an experiment aimed at producing a detailed and accurate database from which improved flowfield understanding and prediction capability will follow. The measurements must provide information suitable for the development of advanced turbulence models and improve the database for engineering design.

Measurement advances in the past 30 years, such as Laser diagnostics, high-frequency response Hot-Wire Anemometry (HWA), data reduction routines, and surface measurement equipment allow for a more complete description of high-speed turbulence. Large bandwidth frequency analyzers ($\sim$ 100 Mhz) yield Laser Doppler Velocimetry (LDV) suitable for supersonic flow. Though HWA has been used in the past for high-speed flow, combining LDV and HWA data with recently developed data reduction routines (Bowersox [12] and Bowersox and Buter [9]) has allowed for the direct measurement of the apparent mass flux components such as, $\overline{\rho' v'}$, providing quantitative information on the compressible turbulence terms in high speed flows.

The advances in numerical processing power has allowed DNS of the Navier-Stokes equations for low Reynolds number flows [67]. However, DNS still can not resolve the high-speed high Reynolds number flowfield around individual roughness elements (whether intentionally created or naturally generated), so turbulence modeling is still required. For this reason, better insight into the physics of high-speed rough surface boundary layer flow is required. This includes information on the flowfield itself and boundary conditions such as surface roughness. Surface roughness measurement, using a confocal Laser Scanning Microscope (LSM), provides a topographical map of surface roughness and provides statistical information, such as, mean height, maximum height, and standard deviation, all of which will be useful for defining appropriate boundary conditions for numerical analysis.

1.4 Research Objectives

The overall objective of this research is to provide a complete characterization of high-speed high Reynolds number turbulent boundary layer flow over flat plates of various surface roughness. The turbulent characterization will be used to better understand the physics of the flowfield (in-

cluding compressibility effects) and provide better flowfield predictability for both classical and numerical methods. The specific objectives are

- Expand the experimental database for high-speed rough surface boundary layers for both sand-grain and machined uniformly distributed surface roughnesses. This database includes mean and turbulence data, as well as, topographical surface roughness information, all of which will be useful for the development and validation of new turbulence models.

- Use the above described database to enhance the understanding of the physics of high-speed rough surface boundary layers by investigating the effect of surface roughness on mean flow quantities (e.g., velocity, Mach number, mass flux, C_f, etc...), turbulence intensities, turbulent shear stresses, and flow structure size, angles, and energy spectra. The investigation includes evaluating the effects of increasing roughness height and blockage.

- Investigate compressibility effects that arise due to surface roughness. Specifically, to evaluate the effect of surface roughness on density variations at the smooth/rough surface interface and on turbulence terms containing density fluctuations (e.g., mass flux turbulence intensity, $\sqrt{\overline{(\rho u)'^2}}$ and the traverse apparent mass flux, $\overline{\rho' v'}$).

- Evaluate and further develop algebraic turbulence models [16] for rough-wall boundary layers. The algebraic models are the Prandtl mixing length and Compressible Apparent Mass Mixing Length Extension (CAMMLE) turbulence models [10]. These models will be evaluated based on their performance in predicting both mean flow quantities (e.g., velocity, density, etc...) and kinematic Reynolds shear stress. In addition, weaknesses will be identified and corrections will be made. The CAMMLE model will also be evaluated based on its performance in predicting compressible turbulence.

- Evaluate and further develop semi-empirical skin friction and integral methods for rough-wall boundary layers. Rough-wall incompressible skin friction relations developed by Schlichting [51] and White [66], as well as, a compressible relation by Goddard [28] are evaluated and a new integral method of predicting skin friction is developed and evaluated.

1.5 Overview of Research Method

Complimentary experimental measurements, in three key areas, were accomplished to meet the research objectives outlined above. The three areas are flow visualization, mean flow quantities, and turbulent quantities. Color schlieren and Laser Sheet Imaging (LSI) provide averaged and instantaneous flow visualization, respectively. The color schlieren photographs clearly show the nozzle exit/surface roughness interface with compression and expansion waves generated by individual roughness elements (see Figures 23 through 28). LSI provides an instantaneous boundary layer image providing qualitative information of boundary layer structures.

Mean flow quantities are provided by Pitot, LDV, and HWA. The Pitot probe measurements give velocity, density, mass flux, and Mach boundary layer profiles and can be used to determine the effects of surface roughness on velocity defect, wall shear stress, and skin friction. LDV measurements can also provide velocity, density, mass flux, and Mach profiles, while for compressible flows, HWA provides mean mass flux. Favorable comparisons between Pitot and LDV measurements enhances the confidence in validity of turbulence data collected using LDV. The density was also found by combining LDV and HWA data.

Turbulent flow quantities are provided by LDV, cross-film HWA, and frequency resolved HWA. Each measurement technique provides an important piece in the physical puzzle of rough surface boundary layer flow. LDV provides velocity turbulence intensities and kinematic Reynolds shear stress, while cross-film HWA provides mass flux turbulence intensities and compressible Reynolds

shear stress. Combining LDV and cross-film HWA will give a measure of the apparent mass flux and an indication of how surface roughness affects the compressible terms of the Reynolds shear stress. Boundary layer flow structure was determined using high-frequency HWA with normal- and parallel-film probes. From these measurements micro and integral length scales, energy spectra, and flow structure angle were determined for each smooth and rough surface boundary layer.

Six models were chosen for this research, consisting of a smooth flat plate, two uniformly distributed rough surfaces, and three sand-grain rough surfaces. The smooth flat plate was used to compare with the rough surfaces and with previous smooth plate data collected by other researchers. The uniformly distributed and sand-grain rough surfaces are in the fully rough flow regime, and were chosen to provide a range of roughness elements comparable to that in literature [28,44–46,51]. The two uniformly distributed rough surfaces had roughness elements consisting of two-dimensional lateral grooves and three-dimensional elements. The two uniformly distributed roughness surfaces were designed specifically to investigate the "effects of roughness blockage." In addition, the uniform roughness distributions are attractive for future LES calculations. The sand-grain rough surfaces were created using 80, 36, and 20 grit sandpaper spanning a large range of roughness heights. The three sand-grain roughness plates were chosen to examine the "effects of roughness height." [The criteria established by Settles and Dodson [52] guided the experimental procedure to insure the usefulness of the data to other researchers (see Table 1)].

In addition to the experimental portion of this research, theoretical and numerical analyses were performed. The theoretical analysis consisted of evaluating the experimental data by classical methods and developing a new integral method for the estimation of skin friction. The numerical study consisted of using a parabolized Navier-Stokes solver, which used two algebraic turbulence models and the Rotta model for surface roughness described in Cebeci and Chang [16], to assess a current turbulence models for suitability.

1.6 Research Contribution

The first contribution of this research is a more complete experimental description of high-speed rough-wall turbulent boundary layer flow. This study provides detailed information on mean flow quantities, turbulence quantities, flow structure size and angles, and energy spectra, with the goal of investigating the influence of roughness height and blockage. More specifically:

- The acquired mean flow and turbulence data allowed for an assessment of the effects of compressibility and the development (or validation) of scaling laws. For example, kinematic turbulent flow statistical properties (e.g., kinematic Reynolds shear stress and turbulence kinetic energy) were found to scale by local mean quantities. These quantities also displayed a weak dependence on surface roughness height and blockage and are proportional to $\ln(k_s^+)$. Conversely, compressible turbulent flow statistical properties (e.g., compressible Reynolds shear stress and traverse apparent mass flux) did not scale by local mean quantities, and had a strong linear dependence on roughness height and blockage. The streamwise mass flux turbulence intensity and shear stress scale reasonably well with the wall density and friction velocity.

- The flow visualization images acquired through this study allowed the qualitative analysis of the rough surface high-speed high Reynolds number boundary layer. The evaluation revealed that surface roughness had a visible effect on the boundary layer and freestream. Compression and expansion waves were visible and their magnitude and rate of occurrence were directly related to roughness height and blockage.

- The frequency resolved HWA data allowed a detailed assessment of the influence of surface roughness on boundary layer flow structures. From the frequency and correlation data, surface roughness was found to have a significant effect on the flow structure size, angles and energy

spectra. Surface roughness increases the size of the small scale structures and decreases the size of the large scale structures. Increasing surface roughness height increases the flow structure angle, with the largest effect occurring in the upper boundary layer region. In the near wall region, surface roughness shifts the mass flux turbulent power to larger, lower frequencies structures.

The second contribution of this research is improved prediction methodologies for high-speed rough-wall turbulent boundary layers. This study focused on developing and validating new integral methods for analytical predictions, and improving and validating algebraic turbulence models for numerical predictions. More specifically:

- With the present empirical data available, a new integral prediction method was developed and validated for the estimation of rough surface skin friction. The method utilizes the momentum thickness at two streamwise boundary layer locations and accurately predicted the skin friction for a range of surface roughness heights and geometries. In addition, various existing correlations are evaluated with this present data.

- The Rotta surface roughness model, which was incorporated into a parabolized Navier-Stokes code, was evaluated. A key weakness was identified relating to the way in which the momentum losses were estimated. This was corrected and improved results were obtained. Overall, the Prandtl and CAMMLE turbulence models with the modified Rotta model for surface roughness were found to produce reasonably accurate predictions of the mean flow quantities for simple flat plate flow. Both the Prandtl and CAMMLE models accurately predict the kinematic Reynolds shear stress across the boundary layer except in the near wall region for rough surfaces. The CAMMLE model did a reasonable job of predicting the compressible Reynolds shear stress across the boundary layer for smooth and rough surfaces.

1.7 Overview of Dissertation

This chapter has provided motivation, objectives and methodology for this research. Chapters 2 through 5 provide more detail into the state of classical and numerical surface roughness theory (Chapter 4 describes the new integral method developed as part of this study), the facilities and apparatus, data reduction methods, and numerical methods used for this research. Chapter 6 presents the experimental results and Chapter 7 presents the integral and numerical results of this study. Finally, Chapter 8 provides conclusions and recommends for follow on research.

Chapter 2 - Background

As briefly discussed in Chapter 1, most engineering predictions of velocity profiles and skin-friction use Computational Fluid Dynamics (CFD) or semi-empirical relations (classical analysis), respectively. This chapter provides a more detailed description of classical flat plate boundary layer analysis and numerical analysis used to obtain engineering quantities of interest. The classical analysis section covers boundary layer flow and turbulence, scaling laws, compressibility extensions to incompressible relations, and surface roughness. The numerical analysis section covers the averaged forms of the Navier-Stokes (N-S) equations, turbulence modeling, surface roughness modeling, and turbulence measurements.

2.1 Classical Analysis

2.1.1 Boundary Layers

The thin flow region between the surface and the freestream of a wall bounded flow is where the velocity gradient varies very quickly, and hence, has large shear stresses. This thin layer, termed the boundary layer, as first suggested by Prandtl, is the region of the flow where all viscous effects take place. Two distinct types of boundary layer flows have been observed, they are laminar and turbulent. Laminar flows are characterized by smoothly varying streamlines, parallel (hence laminar) to each other and the surface boundary. Unlike smoothly varying laminar flow, turbulent flows are highly irregular. The two most popular definitions of turbulence are

> "Turbulence is an irregular motion which in general makes its appearance in fluids, gaseous or liquid, when they flow past solid surfaces or even when neighboring streams of the same fluid flow past or over one another." *G. I. Taylor and T. Von Karman* [31]

> "Turbulent fluid motion is an irregular condition of flow in which the various quantities show a random variation with time and space coordinates, so that statistically distinct average values can be discerned." *Hinze* [31]

Along with being highly irregular, turbulent flows are dissipative, diffusive, rotational, three-dimensional, and have a wide range of spatial and temporal scales. Turbulent kinetic energy is trans-

ferred from the largest eddies and swirls down to the smallest in a cascading fashion. The smallest eddies and swirls dissipate the turbulent kinetic energy into heat. The diffusivity of turbulence plays a key part in mixing rates, momentum transfer, and heat transfer. All of which are important in engineering applications.

2.1.2 Scaling Laws

For laminar flows, when scaling the transverse (or y) distance and velocity by the boundary layer length, δ, and the edge velocity, u_e, all data collapse to one curve. Similar correlations have been sought for turbulent flows. The turbulent boundary layer was found to have three distinct regions of flow. They are the laminar sublayer, the inner region, and the outer region. Each region requires different turbulent length and velocity scales, Table 2 summaries the scales for the three regions.

The inner region velocity scale is defined as the friction velocity, $u^* = \sqrt{\frac{\tau_w}{\rho_w}}$, where τ_w is the wall shear stress and ρ_w is the fluid density at the wall. When normalizing the boundary layer velocity defect $(u - u_e)$ by the friction velocity, all profiles collapse onto a single curve for the outer region of the boundary layer. So the outer region **defect law** is defined as

$$\frac{u - u_e}{u^*} = f\left(\frac{y}{\delta}\right) \tag{1}$$

In the inner region, the normalized variables are

$$u^+ = \frac{u}{u^*} \quad \text{and} \quad y^+ = \frac{yu^*}{\upsilon} \tag{2}$$

and the **law of the wall** is

$$u^+ = g\left(y^+\right) \tag{3}$$

and in the laminar sublayer,

$$u^+ = y^+ \tag{4}$$

For flat plate turbulent boundary layer flow, the logarithmic region of the law of the wall can be written as

$$u^+ = \frac{1}{\kappa}\ln(y^+) + B \tag{5}$$

where $\kappa = 0.41$ and $B = 5.5$. In 1956, Coles [19] introduced the law of the wake to account for the boundary layer flow in the outer region. Using Cole's law of the wake, the law of the wall becomes

$$u^+ = \frac{1}{\kappa}\ln(y^+) + B + \frac{\Pi}{\kappa}W\left(\frac{y}{\delta}\right) \tag{6}$$

with $\Pi = 0.51$ and

$$W\left(\frac{y}{\delta}\right) = 2\sin^2\left(\frac{\pi}{2}\frac{y}{\delta}\right)$$

For compressible flow, Van Driest [62] introduced an effective velocity

$$u_{eff} = \frac{U_e}{B_1}\left[\sin^{-1}\left(\frac{2B_1^2\frac{\bar{u}}{U_e} - B_2}{\sqrt{B_2^2+4B_1^2}}\right) + \sin^{-1}\left(\frac{B_2}{\sqrt{B_2^2+4B_1^2}}\right)\right] \tag{7}$$

with

$$B_1 = \sqrt{\frac{\gamma-1}{2}rM_e^2\frac{T_e}{T_w}} \qquad B_2 = \frac{T_{aw}}{T_w} - 1$$

where the recovery factor is given by, $r = (\mathrm{Pr})^{\frac{1}{3}}$ for turbulent flow and U_e is the boundary layer edge velocity. The above equation essentially maps the mean velocity, $\bar{u}$, from the compressible flow regime into the incompressible regime where the law of the wall becomes

$$u^+_{eff} = \frac{u_{eff}}{u^*} = \frac{1}{\kappa}\ln(y^+) + B + \frac{\Pi}{\kappa}W\left(\frac{y}{\delta}\right) \tag{8}$$

To determine the compressible flat plate skin friction, Van Driest [62] used the velocity profile given in Equation (8) and the Crocco-Busemann density profile (see Chapter 4) along with the zero pressure gradient momentum integral equation given by

$$\frac{C_f}{2} = \frac{d\theta}{dx} \tag{9}$$

to obtain

$$\frac{1}{\sqrt{C_f\left(\frac{T_{aw}}{T_e}-1\right)}}\left[\sin^{-1}\left(\frac{2B_1^2-B_2}{\sqrt{B_2^2+4B_1^2}}\right) + \sin^{-1}\left(\frac{B_2}{\sqrt{B_2^2+4B_1^2}}\right)\right] \approx 4.15\log\left(Re_xC_f\frac{\mu_e}{\mu_w}\right) + 1.7 \tag{10}$$

which is known as the Van Driest II theory for compressible flat plate skin friction. The effective velocity concept and Equations (8) and (10) are logical extensions of incompressible flat plate theory. For incompressible flow ($M_e \approx 0$), B_1 and B_2 equal zero, so Equation (8) reduces to the incompressible law of the wall and Equation (10) reduces to the Karman-Schoenherr incompressible relation [66] given by

$$\frac{1}{\sqrt{C_f}} \approx 4.15 \log\left(Re_x C_f\right) + 1.7 \tag{11}$$

2.1.3 Surface Roughness

Surface roughness increases skin friction, convective heat transfer, and mass transfer; and greatly speeds up the transition from laminar to turbulent flow. Surface roughness has a direct affect on the inner region and is typically described by a single parameter

$$k^+ = \frac{ku^*}{\upsilon} \tag{12}$$

where k is the roughness height. A study of sand-grain roughness effects on water flow through pipes was undertaken by Nikuradse [44]. Sand-grain particles of various sizes were glued with maximum density to the inside of pipes to measure the effects of roughness on the coefficient of resistance, λ. The sand-grain roughness increased the velocity defect and skin friction, increasing the friction velocity, u^*, and shifting Equation (5) downward giving

$$u^+ = \frac{1}{\kappa}\ln(y^+) + B - \frac{\Delta U}{u^*}\left(\frac{ku^*}{\upsilon}\right) \tag{13}$$

where $\frac{\Delta U}{u^*}$ is the amount of downward shift and is a function of the roughness Reynolds number, k^+. Through experimentation, three regimes of roughness have been identified for low-speed flows and are given by

$$\begin{aligned} \text{Aerodynamically smooth regime:} \quad & k^+ < 4, \\ \text{Transitional-roughness regime:} \quad & 4 < k^+ < 60, \\ \text{Fully-rough regime:} \quad & k^+ > 60. \end{aligned}$$

For the aerodynamically smooth regime, all of the roughness elements are contained in the laminar sublayer and do not affect the boundary layer flow. As the roughness height increases, the

boundary layer is increasingly influenced until the roughness height reaches the fully-rough regime which was the focus of this research. Subsequent work was performed by Schlichting [51] on fully-developed channel flow with uniformly distributed roughness elements consisting of spheres, spherical segments,cones, and "short" angles. To relate his work to Nikuradse's extensive sand-grain roughness data, Schlichting introduced the concept of equivalent sand-grain roughness, k_s. The equivalent sand-grain roughness is defined to correlate any surface roughness to the equivalent Nikuradse sand-grain roughness for comparison. For fully rough flow $\frac{\Delta U}{u^*}$ has the form

$$\frac{\Delta U}{u^*} = \frac{1}{\kappa} \ln\left(\frac{ku^*}{\nu}\right) + C \tag{14}$$

Combining Equations (13) and (14) gives the fully rough law of the wall as

$$u^+ = \frac{1}{\kappa} \ln(\frac{y}{k}) + D \tag{15}$$

Nikuradse found

$$u^+ = \frac{1}{\kappa} \ln(\frac{y}{k_s}) + 8.5 \tag{16}$$

Combining the above two equations gives

$$\frac{1}{\kappa} \ln(\frac{k_s}{k}) = 8.5 - D \tag{17}$$

By determining the intercept, D, from experimental data and using the above equation, any roughness can be correlated to an equivalent sand-grain roughness.

For incompressible fully-rough, flow Schlichting [51] provides the following relation for skin friction with roughness based on the equivalent sand-grain roughness

$$C_f = \left[2.87 + 1.58 \log\left(\frac{x}{k_s}\right)\right]^{-2.5} \tag{18}$$

and White [66] provides

$$C_f = \left[1.4 + 3.7 \log\left(\frac{x}{k_s}\right)\right]^{-2} \tag{19}$$

for $\frac{k}{x} > \frac{Re_x}{1000}$.

The equivalent sand-grain roughness concept has two main areas of concern. The first is the need for experimental measurements to determine k_s for each unique distribution of roughness. The second is that the singular k_s roughness height value does not include roughness geometry or spacing. Several researchers have presented correlations to include roughness geometry and spacing into velocity profile and skin friction predictions.

Bettermann and Dvorak (extracted from [53]) introduced a roughness density parameter, $\lambda = \frac{L}{S}$, for two-dimensional roughness elements where L is the spacing between the elements and S is the length of the elements. The rough wall skin friction relation can be found using the relation developed by Clauser [18]

$$\sqrt{\frac{2}{C_f}} = A \log\left(\frac{u\delta^*}{\nu}\right) + B - \frac{\Delta U}{u^*} \tag{20}$$

with

$$\frac{\Delta U}{u^*} = A \log\left(\frac{ku^*}{\nu}\right) + C \tag{21}$$

C is a function of the density parameter and is given by

$$C(\lambda) = \begin{cases} 17.35\,(1.625 \log \lambda - 1) & \lambda < 4.68 \\ -5.95\,(1.103 \log \lambda - 1) & \lambda > 4.68 \end{cases}$$

Dirling [23] has also developed an equivalent roughness correlation for computing rough wall heat transfer rates on reentry nosetips based on a roughness geometry/spacing parameter and is given by

$$\lambda = \frac{d}{k}\left(\frac{A_{ws}}{A_p}\right)^{4/3} \tag{23}$$

where d is the spacing between roughness elements; k is the roughness height; A_{ws} is the total windward surface area of the elements, and A_p is the projected windward surface area of the elements. The correlation between k_s and λ is given by

$$\frac{k_s}{k} = \begin{cases} 0.0164\lambda^{3.78} & \lambda < 4.93 \\ 139\lambda^{-1.9} & \lambda > 4.93 \end{cases}$$

Goddard [28] investigated the influence of compressibility on the effects of sand-grain surface roughness boundary layer flows over a body of revolution. Goddard measured skin friction drag for a range of Mach numbers from 1.98 to 4.54 and sand-grain rms roughness heights of 0 to 0.0390 inch. Goddard [28] found "... that the entire compressibility effect is a reduction of the fluid density at the surface as the Mach Number increases" and that the shift in the velocity profile, $\frac{\Delta U}{u^*}$, is a function of the roughness Reynolds number, $k^+ = \frac{ku^*}{\upsilon}$, and follows the same law as the incompressible case when using the Van Driest [61] compressibility transformation. In addition, Goddard found the incompressible - compressible skin friction ratio to be equal to the adiabatic wall density relation, that is

$$\frac{C_f}{C_{f_i}} \doteq \frac{\rho_w}{\rho} = \frac{1}{1 + r\frac{\gamma-1}{2}M^2} \tag{25}$$

The skin friction for compressible flow over rough surfaces can be estimated using Equation (18) or (19) along with the above equation if the equivalent sand-grain roughness is known.

2.2 Numerical Methods

The governing equations for Newtonian fluid flow are derived (for derivations see White [66]) from three laws of conservation: continuity, Newton's second law (momentum), and the 1^{st} law of thermodynamics (energy). For a Newtonian fluid, with Stokes hypothesis ($\lambda + \frac{2}{3}\mu = 0$), the three momentum equations (one for each independent coordinate) are termed the Navier-Stokes (N-S) equations (shown in integral form in Chapter 5). However, it is common practice, when referring to the "Navier-Stokes equations", to include the continuity and energy equations as well. For the remainder of this study, the meaning of "Navier-Stokes equations" will follow convention.

The N-S equations have been around a very long time (1845) and because of their nonlinear nature, are exceedingly difficult to solve (analytically or numerically). Various simplifying assumptions for specific flow fields have been developed (e.g., inviscid, adiabatic, laminar, boundary layer

flow) to provide more tractable analytical and numerical solutions. Recently, full N-S CFD solutions became possible with the advent of vector and parallel processing supercomputers. However, as discussed in Chapter 1, the required temporal and spatial grid resolution prohibit the simulation of turbulent flows, hence scientists and engineers are forced to rely on approximate statistically averaged forms of the N-S equations.

2.2.1 Reynolds-Averaged Navier-Stokes Equations

The Reynolds-Averaged N-S (RANS) equations are derived (Reference [17]) by replacing the turbulent, random, three-dimensional, unsteady flow variables (e.g., u, v, ρ) by a mean plus a fluctuating component, such as

$$\Phi_i = \overline{\Phi}_i + \Phi_i' \tag{26}$$

where the arbitrary mean flow variable, $\overline{\Phi}_i$, is defined as

$$\overline{\Phi}_i = \frac{1}{T}\int_t^{t+T} \Phi_i\left(x_j, \tau\right) d\tau \tag{27}$$

and

$$T_1 \ll T \ll T_2$$

with T_1 as the time scale of the fluctuating component and T_2 as the time scale of the mean flow variations. Using $\Phi_i' = \Phi_i - \overline{\Phi}_i$, it is easily shown that the time-average of the fluctuating term is zero (note: averaged 2^{nd} order fluctuating terms are not identically zero, $\overline{\Phi_i'\Phi_i'} \neq 0$). The compressible RANS equations, as given in Bowersox [14], are

$$\frac{\partial \bar{\rho}}{\partial t} + \frac{\partial\left(\bar{\rho}\bar{u}_j + \overline{\rho' u_j'}\right)}{\partial x_j} = 0 \tag{28}$$

$$\frac{\partial\left(\bar{\rho}\bar{u}_i + \overline{\rho' u_i'}\right)}{\partial t} + \frac{\partial\left(\bar{\rho}\bar{u}_i\bar{u}_j\right)}{\partial x_j} = -\frac{\partial \overline{p}}{\partial x_i} + \frac{\partial\left(\overline{\tau}_{ij} + \tau_{ij}^R\right)}{\partial x_j} \tag{29}$$

$$\frac{\partial\left(\overline{\rho e_o}+\overline{\rho' h_o'}\right)}{\partial t}+\frac{\partial\left(\overline{\rho}\overline{u}_j\overline{h_o}\right)}{\partial x_j}=\frac{\partial\left(\overline{u}_i\overline{\tau}_{ij}+\overline{u_i'\tau_{ij}'}-\overline{q}_j-q_j^R\right)}{\partial x_j} \tag{30}$$

where e_o is the stagnation (or total energy) and

$$\overline{\tau}_{ij}=\mu\left[\left(\frac{\partial\overline{u}_i}{\partial x_j}+\frac{\partial\overline{u}_j}{\partial x_i}\right)-\frac{2}{3}\delta_{ij}\frac{\partial\overline{u}_k}{\partial x_k}\right] \tag{31}$$

$$\tau_{ij}'=\mu\left[\left(\frac{\partial u_i'}{\partial x_j}+\frac{\partial u_j'}{\partial x_i}\right)-\frac{2}{3}\delta_{ij}\frac{\partial u_k'}{\partial x_k}\right] \tag{32}$$

$$\overline{q}_i=-\kappa\frac{\partial\overline{T}}{\partial x_i} \tag{33}$$

$$\tau_{ij}^R=-\overline{\rho}\overline{u_i'u_j'}-\overline{u_i}\overline{\rho' u_j'}-\overline{u_j}\overline{\rho' u_i'}-\overline{\rho' u_i'u_j'} \tag{34}$$

$$q_i^R=\overline{\rho}\overline{u_i'h_o'}+\overline{h_o}\overline{\rho' u_i'}+\overline{u_i}\overline{\rho' h_o'}+\overline{\rho' u_i'h_o'} \tag{35}$$

In Equation (28), $\overline{\rho' u_i'}$ is referred to as the apparent, or compressible, mass. The components of the compressible Reynolds shear stress tensor, τ_{ij}^R, are given by Equation (34). In this expression, the first term is referred to as the kinematic turbulent shear stress ($\tau_{ij}^T=-\overline{\rho}\overline{u_i'u_j'}$) and the other three terms arise due to density fluctuations. The components of the compressible turbulence heat transfer, q_i^R, are given by Equation (35). Again, the first term in the expression is the kinematic turbulence heat transfer ($q_i^T=\overline{\rho}\overline{u_i'h_o'}$) and the other three terms are the compressible turbulence heat transfer. Also appearing in the Reynolds-averaged energy equation is an apparent unsteady term, $\frac{\partial\left(\overline{\rho' h_o'}\right)}{\partial t}$.

2.2.2 Favre-Averaged Navier-Stokes Equations

The Favre-Averaged N-S (FANS) equations are derived (Reference [17] or [67]) by replacing some of the turbulent, random, three-dimensional, unsteady flow variables by a mass-averaged mean plus a fluctuating component.

$$\Phi_i = \widetilde{\Phi}_i + \Phi_i'' \tag{36}$$

In this decomposition the mean flow is defined as

$$\widetilde{\Phi}_i = \frac{\int_t^{t+T} \rho(x_j,\tau)\,\Phi_i(x_j,\tau)\,d\tau}{\int_t^{t+T} \rho(x_j,\tau)\,d\tau} \tag{37}$$

or

$$\widetilde{\Phi}_i = \frac{\overline{\rho\Phi}}{\overline{\rho}} \tag{38}$$

and

$$T_1 \ll T \ll T_2$$

with T_1 as the time scale of the fluctuating component and T_2 as the time scale of the mean flow variations. It is important to note, for Favre-averaging, $\overline{\Phi''} \neq 0$.

The compressible N-S equations are averaged using a combination of Favre and Reynolds-averaged flow properties, which are decomposed as follows:

$$u_i = \tilde{u}_i + u_i'' \qquad e = \tilde{e} + e''$$

$$\rho = \bar{\rho} + \rho' \qquad p = \bar{p} + p'$$

$$\tau_{ij} = \overline{\tau}_{ij} + \tau_{ij}' \qquad q_i = \bar{q}_i + q_i'$$

$$h = \tilde{h} + h''$$

The compressible FANS equations, as given in Bowersox [14], are

$$\frac{\partial \bar{\rho}}{\partial t} + \frac{\partial(\bar{\rho}\tilde{u}_j)}{\partial x_j} = 0 \tag{39}$$

$$\frac{\partial(\bar{\rho}\tilde{u}_i)}{\partial t} + \frac{\partial(\bar{\rho}\tilde{u}_i\tilde{u}_j)}{\partial x_j} = -\frac{\partial \overline{p}}{\partial x_i} + \frac{\partial\left(\overline{\tau}_{ij} + \tau_{ij}^F\right)}{\partial x_j} \tag{40}$$

$$\frac{\partial\left(\bar{\rho}\widetilde{e}_o\right)}{\partial t}+\frac{\partial\left(\bar{\rho}\tilde{u}_j\widetilde{h}_o\right)}{\partial x_j}-\frac{\partial\left(\tilde{u}_i\overline{\tau}_{ij}+\overline{u_i''\tau_{ij}}-\overline{q}_j+q_j^F\right)}{\partial x_j}=0 \tag{41}$$

where

$$\overline{\tau}_{ij}=\mu\left[\left(\frac{\partial\widetilde{u}_i}{\partial x_j}+\frac{\partial\widetilde{u}_j}{\partial x_i}\right)-\frac{2}{3}\delta_{ij}\frac{\partial\widetilde{u}_k}{\partial x_k}\right]+\mu\left[\left(\frac{\partial\overline{u_i''}}{\partial x_j}+\frac{\partial\overline{u_j''}}{\partial x_i}\right)-\frac{2}{3}\delta_{ij}\frac{\partial\overline{u_k''}}{\partial x_k}\right] \tag{42}$$

$$\tau_{ij}^F\equiv-\overline{\rho u_i''u_j''} \tag{43}$$

$$q_{ij}^F\equiv\overline{\rho u_j''h_o''} \tag{44}$$

In Equation (42), τ_{ij}^F is the Favre-averaged Reynolds shear stress, but is usually referred to as the Reynolds shear stress tensor. In Equation (41), $\widetilde{e}_o$ is the Favre-averaged total energy and $\widetilde{h}_o$ is the Favre-averaged specific total enthalpy.

Favre-averaging transforms the compressible N-S equations into a form similar to the incompressible N-S equations. The apparent mass term is no longer present in the continuity equation and both the turbulent shear stress and heat transfer terms have only one component. For these reasons, most compressible computational models are based on Favre-averaged extensions of previously developed incompressible codes.

2.2.3 Relating Reynolds and Favre Averaged Equations

Setting Equations (26) and (36) equal to each other, the Reynolds-averaged fluctuating term can be expressed as

$$\Phi'=\widetilde{\Phi}+\Phi''-\overline{\Phi} \tag{45}$$

then time-averaging the above equation gives

$$\widetilde{\Phi}=-\overline{\Phi''}+\overline{\Phi} \tag{46}$$

and finally the Reynolds-averaged fluctuating component can be expressed as

$$\Phi'=\Phi''-\overline{\Phi''} \tag{47}$$

Similarly, 2^{nd} order fluctuating components can be related by

$$\overline{u'v'} = \overline{u''v''} - \overline{u''}\,\overline{v''} - \overline{v''}\,\overline{u''} + \overline{u''}\,\overline{v''} = \overline{u''v''} - \overline{u''}\,\overline{v''} \tag{48}$$

It was previously stated that the Favre fluctuation term, $\overline{\Phi''}$, is not equal to zero, this can be shown by starting with Equation (46)

$$\overline{\Phi''} = \overline{\Phi} - \widetilde{\Phi} \tag{49}$$

and substituting in Equation (38) to give

$$\overline{\Phi''} = \overline{\Phi} - \frac{\overline{\rho\Phi}}{\bar{\rho}} = \overline{\Phi} - \frac{\overline{\left(\overline{\rho} + \rho'\right)\left(\overline{\Phi} + \Phi'\right)}}{\bar{\rho}} \tag{50}$$

after expanding and time-averaging

$$\overline{\Phi''} = \overline{\Phi} - \frac{\overline{\overline{\rho}\overline{\Phi} + +\overline{\rho}\Phi' + \rho'\overline{\Phi} + \rho'\Phi'}}{\bar{\rho}} = \overline{\Phi} - \overline{\Phi} - \frac{\overline{\rho'\Phi'}}{\bar{\rho}} \tag{51}$$

finally

$$\overline{\Phi_i''} = -\frac{\overline{\rho'\Phi_i'}}{\bar{\rho}} \neq 0 \tag{52}$$

To relate the Favre-averaged turbulent shear stress in Reynolds fluctuating components, start with Equation (48)

$$\overline{\rho}\overline{u'v'} = \overline{\rho}\overline{u''v''} - \overline{\rho}\overline{u''}\,\overline{v''} \tag{53}$$

or

$$\tau_{ij}^{F} = -\overline{\rho}\overline{u''v''} = -\overline{\rho}\overline{u'v'} - \overline{\rho}\overline{u''}\,\overline{v''} \tag{54}$$

and substitute in Equation (52) to give

$$\tau_{ij}^{F} = -\overline{\rho}\overline{u''v''} = \tau_{ij}^{T} - \overline{\rho}\frac{\overline{\rho'u_i'}}{\bar{\rho}}\frac{\overline{\rho'v_i'}}{\bar{\rho}} \tag{55}$$

assuming the fourth-order fluctuating term, $\overline{\rho}\frac{\overline{\rho'u_i'}}{\bar{\rho}}\frac{\overline{\rho'v_i'}}{\bar{\rho}}$, is negligible gives

$$\tau_{ij}^{F} = -\overline{\rho}\overline{u''v''} \approx -\overline{\rho}\overline{u'v'} = \tau_{ij}^{T} \tag{56}$$

so, to 3^{rd} order, the Favre-averaged turbulent shear stress is equal to the kinematic Reynolds shear stress.

2.2.4 Turbulence Modeling and Closure

Due to the nonlinearity of the N-S equations, the use of Reynolds or Favre-averaging introduces additional unknowns into the problem as seen by the apparent mass flux, Reynolds shear stress, and turbulent heat flux in Equations (28), (34), and (35), respectively. Transport equations for these additional terms can be generated by taking moments of the N-S equations, generating additional higher order unknowns. Additional equations have to be developed to provide closure of the problem. Turbulence modeling provides equations for the unknown correlations; hopefully, by using insight into the underlying physics.

Two of the most common algebraic turbulence models are the eddy viscosity and mixing-length models. The eddy viscosity model uses the Boussinesq approximation and makes the kinematic Reynolds shear stress analogous to molecular shear, i.e.

$$\tau_{ij}^{T} = -\overline{\rho}\overline{u'v'} = \mu_T \frac{\partial \overline{u}}{\partial y} \tag{57}$$

where μ_t is the eddy viscosity and has the same dimensions as μ , but is not a fluid property and varies with geometry and flow conditions. The Prandtl mixing-length model, as presented in White [66], relates turbulent shear to a length scale and velocity gradient,

$$-\overline{u'v'} \approx (const)\sqrt{\overline{u'^2}}\sqrt{\overline{v'^2}} \approx (const)\left(l_1\frac{\partial \overline{u}}{\partial y}\right)\left(l_2\frac{\partial \overline{u}}{\partial y}\right) \approx l_m^2\left(\frac{\partial \overline{u}}{\partial y}\right)\left(\frac{\partial \overline{u}}{\partial y}\right) \tag{58}$$

where l_m is called the mixing length. The two models become equivalent if the eddy viscosity is

$$\mu_T = \rho l_m^2 \left|\frac{\partial \overline{u}}{\partial y}\right| \tag{59}$$

The formulations for the mixing length across the boundary layer are given by [66]

$$l_m = \begin{cases} \kappa y\left[1 - e^{\frac{y^+}{A^+}}\right] & l_m \leq 0.09\delta \\ 0.09\delta & l_m > 0.09\delta \end{cases} \tag{60}$$

where $\kappa \approx 0.4 - 0.41$.

Bowersox and Schetz [13] have extended the mixing length formulation to account for compressibility for the Reynolds-averaged N-S equations, giving

$$m_j^T = \left|\frac{\partial \overline{\rho}}{\partial y}\right| \frac{\partial \overline{u}}{\partial y} \frac{l_m^2}{S}$$

$$\tau_{ij}^T = \mu_T \frac{\partial \overline{u}}{\partial y} + \overline{u} m_j^T \tag{61}$$

$$q_j^T = -k_T \frac{\partial \overline{T}}{\partial y} - \overline{u} \mu_T \frac{\partial \overline{u}}{\partial y} \overline{h_o} m_j^T$$

with $k_T = \mu_T c_p / \mathrm{Pr}_T$. For adiabatic wall boundary layers, the Situ number, $S = 1.0$ (Bowersox [12]).

2.2.5 Surface Roughness Modeling

Three methods of adding surface roughness to current numerical methods are covered in this section. The three methods are a velocity shift parameter, the discrete element approach, and the specific dissipation rate surface boundary condition for the $K - \omega$ turbulence models. The first method (and the method used in this research) involves a roughness model first suggested by Rotta [16]. Rotta noted the velocity profiles of smooth and rough wall boundary layer flows were similar if the coordinates of the rough walls were displaced. Adding an additional Δy to the mixing length inner region term is a simple way to account for the velocity profile displacement. Using Rotta's model the new inner region mixing length becomes

$$l_m = \kappa (y + \Delta y) \left[1 - e^{\frac{(y+\Delta y)^+}{A^+}}\right] \tag{62}$$

with Δy given by

$$\Delta y = 0.9 \left(\frac{\nu}{u^*}\right) \left[\sqrt{k_s^+} - k_s^+ e^{\frac{-k_s^+}{6}}\right] \tag{63}$$

which is valid for an equivalent sand-grain roughness range from $4.535 < k_s^+ < 2000$.

The discrete element approach as used by Taylor, Coleman and Hodge [59] consists of adding a blockage and drag term to the momentum equation. The momentum equation with uniform roughness elements consisting of distributed hemispheres and cones is given as

$$0 = \frac{\mu}{R-y}\frac{d}{dy}\left(\left(R-y\right)\beta_y\left(1+\frac{\mu_T}{\mu}\right)\frac{du}{dy}\right) - \beta_x\frac{dP}{dx} - \frac{1}{2}\rho C_D\frac{u^2 d\left(y\right)}{\left(R-y\right)L^2/R} \tag{64}$$

where the blockage, $\beta_x = \beta_y = 1 - \frac{\pi d^2(y)}{4(R-y)L^2/R}$ and $d\left(y\right)$ are determined from roughness element geometry. The coefficient of drag, C_D, is found by the correlation (based on corrected Schlichting data)

$$\begin{aligned} \log C_D &= -0.125\log\left(Re_d\right) + 0.375, \qquad && Re_d \leq 6\cdot 10^4 \\ C_D &= 0.6, && Re_d \geq 6\cdot 10^4 \end{aligned} \tag{65}$$

where $Re_d = \frac{u(y)d(y)}{\nu}$. For the details of this numerical method see Taylor, Coleman and Hodge [59].

The third method of including surface roughness into turbulent models involves arbitrarily selecting the specific dissipation rate, ω, surface boundary condition using

$$\omega = \frac{u^{*2}}{v}S_R \text{ at } y = 0 \tag{66}$$

based on the correlation from Wilcox [67]

$$S_R = \begin{cases} \left(50/k_R^+\right)^2, & k_R^+ < 25 \\ 100/k_R^+, & k_R^+ \geq 25 \text{ to } 400 \end{cases}$$

where k_R^+ is the average height of sand-grain roughness elements based on data by Nikuradse [44].

All three methods outlined above were developed for incompressible flow and require some information from experimentation, either in determining the roughness Reynolds number, k_s^+ and k_R^+, or in the coefficient of drag. Of the three methods, only the discrete element approach attempts to incorporate explicit blockage and drag effects.

2.3 Experimental Turbulence Measurements

Turbulence quantities can be measured using LDV and HWA. LDV provides the mean velocities, $\overline{u_i}$, the velocity turbulence intensity $\sqrt{\overline{u_j'^2}}$, and the velocity cross-correlation, $\overline{u_i'u_j'}$, which are Reynolds-averaged quantities. LDV also provides the third and fourth order velocity moments given by

$$S_{unweighted} = \overline{u_j'^3} = \frac{\sum_i (u_i - \overline{u})^3}{\sigma^3 N} \tag{68}$$

and

$$F_{unweighted} = \overline{u_j'^4} = \frac{\sum_i (u_i - \overline{u})^4}{\sigma^4 N} \tag{69}$$

where S is the skewness, F is the flatness, N is the number of samples, and $\sigma = \sqrt{\overline{u_j'^2}}$. Through the use of Equation (55), the Favre velocity fluctuation correlations can be found.

Hot-Wire Anemometry (HWA) provides mean mass flux, $\overline{\rho u_i}$, the mean total temperature, $\overline{T_t}$, the mass flux turbulence intensities, $\sqrt{\overline{(\rho u_i)'^2}}$, and the mass flux shear stress $\overline{(\rho u_i)'(\rho u_j)'}$ correlations. Bowersox [12] has shown that a combined analysis using LDV and cross-wire data can provide direct measurement of the compressible Reynolds shear stress (Equation (34)), the mean transverse Favre velocity fluctuation, the Reynolds and Favre-averaged turbulent heat flux, and the mean density. The compressible Reynolds shear stress can be related to cross-wire measurements using

$$\tau_{ij}^R = -\frac{(\rho u_i)'(\rho u_j)'}{\overline{\rho}} + \overline{\rho u_i u_i}\left(\frac{\rho'}{\overline{\rho}}\right)^2 \tag{70}$$

The first term on the right-hand side of the above equation is directly measurable by cross-wire anemometry and for thin boundary layer flows the second term is usually much smaller than the first, so the compressible Reynolds shear stress can be directly measured. The mean transverse

Favre velocity fluctuation can be measured using

$$\frac{\overline{v''}}{U} = \frac{\overline{\rho' v'}}{\overline{\rho u}} = \frac{\overline{u'v'}}{\overline{u}^2} - \frac{\overline{(\rho u)'(\rho v)'}}{(\overline{\rho u})^2} \tag{71}$$

2.4 Summary of Chapter

In summary, classical analysis, numerical methods, and experimental turbulence measurements were reviewed. From classical analysis, the turbulent boundary layer has three distinct regions; the inner and outer regions, and the laminar sublayer, each with appropriate scaling lengths and velocities. The inner and outer regions are characterized by the law of the wall and defect law, respectively. Surface roughness has a direct affect on the laminar sublayer and inner region and is characterized by three roughness regimes. They are the aerodynamically smooth, transitional-roughness, and fully-rough regimes. For fully-rough surfaces the law of the wall is shifted downward and is a function of y/k only. Traditionally, the roughness is described by a single parameter, k. To compare sand-grain surface roughness with uniformly distributed roughness elements, Schlichting defined the equivalent sand-grain roughness, k_s.

Numerical methods are based on the N-S equations, derived from the conservation of continuity, momentum, and energy. The N-S equations govern all Newtonian fluid flows, including turbulent boundary layers. The non-linearity of the N-S equations combined with the nature of turbulent flows, leads to the statistical averaging of the N-S equations to provide useful solutions. Two forms of averaging are the time-averaged RANS equations and the mass-weighted, time-averaged FANS equations. By averaging the N-S equations, the RANS and FANS introduce additional cross-correlation terms which must be modeled. Algebraic models are the easiest to implement and numerically process. The algebraic models were originally developed for incompressible flow and have only recently been extended for compressible flows.

Finally, measurement techniques such as, LDV and HWA, provide direct measurement of turbulent quantities. LDV provides fluctuating velocity quantities and HWA provides fluctuation mass flux quantities. Through the combined use of LDV and MOH-HWA measurements, all turbulence terms appearing in either the Reynolds- or Favre-averaged N-S equations can be measured.

Chapter 3 - Facilities and Apparatus

This chapter discusses the facilities and equipment used to complete this research. It covers three main areas, the Mach 2.9 wind tunnel, measurement equipment, and computational facilities. Included in the Mach 2.9 wind tunnel section are descriptions of the high-pressure air supply, vacuum system, plenum, nozzle, and test sections. The measurement equipment section presents the flow visualization, pressure, Laser Doppler Velocimetry (LDV), and Hot-Wire Anemometry (HWA) apparatus. Finally, the computational facilities section covers the computer hardware and software used to process this research.

3.1 Wind Tunnel Facilities

The experiments were performed in the Air Force Institute of Technology Mach 2.9 wind tunnel. The Mach 2.9 wind tunnel was an intermittent blowdown/evacuation tunnel with a run time of approximately 25 seconds and an evacuation time of six minutes. A schematic of the upstream high-pressure air supply, valving, plenum chamber, test section, and downstream evacuation system are shown in Figure 1.

3.1.1 High-Pressure Air Supply

The high-pressure air supply used by the Mach 2.9 wind tunnel consists of two Atlas Copoco GAU 807 air compressor with a nominal pressure of 0.69 MPa and a flow rate of 0.5 kg/sec. The high-pressure air was dried by two Pioneer, Model R500A Refrigerant Air Dryers before entering the air-supply system. Two air filtering systems were used prior to the high-pressure air reaching the plenum chamber. The first filter consisted of a centrifugal moisture and particle separator. The second filter was a Pneumatic Products Corp., PCC 1200AF, 0.9 micron particulate filter.

3.1.2 Vacuum System

The downstream evacuation system for the Mach 2.9 wind tunnel consisted of a 16.0 cubic meter vacuum tank farm and a Stokes Model 412 MBX two stage mechanical vacuum pump. The vacuum pump consisted of a 412-11 microvac pump in series with a dry lobe blower rated at 189 and 91 cubic meters per minute, respectively. The vacuum pump evacuated the tank farm to a pressure of 5 mm Hg in approximately six minutes.

3.1.3 Plenum Chamber

The plenum chamber total conditions were monitored by an Endevco Model 8510C-100, 0.69 MPa (0-100 psi $\pm 0.5\%$) pressure transducer connected to an ENDEVCO Model 4428A Conditioner and an Omega Engineering type K thermocouple connected to an Omega DP41-TC High Performance Temperature Indicator. The pressure transducer/conditioner had a gain error of $\pm 0.5\%$ and a gain stability of $\pm 0.2\%$. The type K themocouple/indicator had an accuracy of ± 1K. The Pitot (total) pressure and total temperature conditions were measured downstream of the flow straighteners and upstream of the convergent-divergent nozzle. The operating conditions for each measurement are shown in Table 5. The plenum chamber stagnation pressure was manually controlled by a Leslie brand dome regulator.

3.1.4 Mach 2.9 Nozzle

The plenum chamber high-pressure air was accelerated by a convergent-divergent half nozzle with a length of 27 cm and an exit cross-section of 6.35 by 6.35 cm. The nozzle exit Mach number and freestream turbulence were measured by Huffman [32]. The Mach number was found to be Mach 2.9 $\pm 1.8\%$ with a freestream turbulence of 0.8% and a standard deviation of 0.2%.

3.1.5 Wind Tunnel Operation

Once the dome regulator was adjusted for a given plenum stagnation pressure, the vacuum tank farm was evacuated. A Kinney Corporation GP-8 gate value was actuated, which opened the vacuum tank farm to the test section. After the test section evacuation, a E1-O-Matic ball value was opened which provided high-pressure air to the plenum chamber. The tunnel flow required approximately 5 seconds to stabilize and provided a run time of 25 seconds. To shut down the wind tunnel, the reverse order of the above process was followed. First, the high-pressure air was closed and then the vacuum tank farm was shut. A blowoff value was provided to vent high-pressure air to the atmosphere if the air was inadvertently supplied without the evacuation system being open.

3.1.6 Test Section

The tunnel test section had a constant cross-section of 6.35 by 6.35 cm and consisted of interchangeable modular test sections of 33.02 or 66.04 cm in length. For this research, the test section length was 66.04 cm with the measurement location at 53.98 cm downstream of the nozzle exit. Color schlieren photographs were also taken 5.035 cm from the nozzle exit to provide qualitative information on the nozzle exit/rough surface interface.

For measurements requiring optical quality tunnel access (i.e., color schlieren, laser sheet imaging, and LDV), two piece modular side walls with one section consisting of plexiglass and the other of aluminum with two 7.62 cm diameter, 1.27 cm thick optical quality glass widows from Oriel Corporation were used. A schematic of the aluminum side wall with the placement of the optical widows is shown in Figure 2. For other measurements, the side walls consisted of a single piece of plexiglass 62.23 cm in length.

Six different floor sections were used during testing with each section having a different surface roughness (a photograph of the six floor sections is shown in Figure 3). The six floor sections were

66.04 by 6.35 by 1.91 cm and consisted of a smooth plate, two-dimensional and three-dimensional machined roughnesses, and sandpaper roughnesses of 20, 36, and 80 grit. The aluminum plates were machined on a Bridgeport EZ TRACK SX Computer Numerical Control (CNC) milling machine with an accuracy of $\pm 0.0254\ mm$ $\left(\pm\frac{1}{1000}\text{ inch}\right)$ over a 304.8 mm (12 inch) movement. Each plate was aligned so the tops of the roughness elements were level with the nozzle exit. The following section provides more detailed information on the surface roughnesses.

3.1.7 Surface Roughness

3.1.7.1 Machined Surfaces

The three machined surfaces were the smooth plate and the two-dimensional and three-dimensional roughness plates. The smooth plate was not polished to represent typical surface roughness tolerance for machined aluminum. The topography of the smooth plate is shown in Figure 4. The two-dimensional (2D) roughness plate was machined using a 1.626 mm $\left(\frac{64}{1000}\text{ inch}\right)$ end mill, cutting lateral grooves to a width and depth of 0.559 mm $\left(\frac{22}{1000}\text{ inch}\right)$ and a wavelength, λ, of 2.184 mm $\left(\frac{86}{1000}\text{ inch}\right)$. The three-dimensional (3D) roughness plate was machined identically to the 2D plate, but with grooves cut in the longitudinal direction as well. Schematics of the 2D and 3D plates are shown in Figures 5 and 6, respectively.

3.1.7.2 Sandpaper Surfaces

The three sand-grain roughnesses were generated by gluing Varathane Brand 80, 36, and 20 grit flooring sandpaper to the top surface of three aluminum flat plates. Representative topography for each sandpaper surface is shown in Figures 7, 8, and 9. The heights of the sand-grains were not measured prior to being glued to the sandpaper surface and may not be assumed to be of maximum density. For this reason, the roughness heights of the sandpaper used here should not be expected to

correspond directly to Nikuradse sand-grain roughness. Instead, direct measurements of the roughness topology were made as described in the next section.

3.1.7.3 Surface Roughness Measurement

The six floor section roughnesses were measured using a Carl Zeiss LSM 320 Confocal Laser Scan Microscope (LSM) with a 5 mW, 633 nm Helium-Neon laser. The system consisted of a LSM base system with laser, a 14 inch control monitor, 16 inch picture monitor, an electronics cabinet and a control PC. The control PC ran the LSM 3 Software and Microsoft Windows 3.1 operating system. Each plate was scanned at three locations and the LSM was used to determine the mean, maximum and standard deviation of the surface roughness. Table 3 lists each plate and its associated roughness statistics.

3.2 Measurement Apparatus

3.2.1 Laser Doppler Velocimetry

A DANTEC brand 57N Enhanced BSA three component laser Doppler anemometer system consisting of Laser optics, data acquisition equipment, a traverse, and seeding apparatus is described in detail in the following subsections.

3.2.1.1 Laser Optics

The Laser optic system consists of an Argon-Ion Laser, a transmitter, the transmitting optics, the receiving optics, and the photomultiplier (PM) tubes. Below is a description of each component.

The Laser was a Model 5500A-00 Argon-ion laser from Ion Laser Technology and was powered by a Ion Technology Model 5405A power supply. The Laser had a maximum (rated) output of 300 mW and was designed to operate in TEM_{oo} with a beam centered around the optical axis and maximum power at the center. The $\frac{1}{e^2}$ beam diameter was 0.82 mm and the three beams have wavelengths of 514.5 nm (green), 488 nm (blue) and 476.5 nm (violet). Only the two highest pow-

ered beams were used for the two axis measurements. The green and blue laser beams were used to measure flow along the x-y plane at the downstream test location. The Laser power was sent to the transmitting optics through a FiberFlow 60X41 transmitter.

The DANTEC FiberFlow 60X41 transmitter split the Laser into three wavelengths: green, blue, and violet, each of these beams were then split for a total of six beams. One beam of each of the three wavelengths was frequency shifted 40 Mhz by a Bragg cell to provide a shifting optical fringe pattern when the two beams from each wavelength were crossed at the measurement point. This removes the directional ambiguity associated with a stationary fringe pattern. Six DANTEC 60X24 fiber manipulators were used to connect the fiber optic cables to the transmitter. The fiber manipulators allow the fiber optical cables to be aligned precisely with the transmitting optics to obtain the maximum Laser efficiency.

The transmitting optics consisted of two probes: a DANTEC 60X61 and 60X60 optic probe. Each of the two probes contained an optic transducer, a distributor unit, and transmitting and receiving fibers. The DANTEC 60X60 optic probe transmitted one wave length (violet) and received the other two wavelengths (green and blue). Conversely, the DANTEC 60X61 optic probe transmitted both the green and blue wave lengths and received only the violet wavelength. In this manner, one probe was placed on each side of the test section windows and Doppler bursts from a particle passing through the measurement volume were received by the optic probes by forward scattering of light, improving the signal-to-noise ratio. On the front of both probes was a 600 mm focal-length lens. Figure 10 shows the position and spacing of the green and blue laser beams on the face of the DANTEC 60X61 optic probe transmitter. The DANTEC 60X60 optic probe was mounted to the traversing mechanism using a DANTEC 60X3631 probe support which used micrometers for precise alignment in three dimensions. The DANTEC 60X61 optic probe used a DANTEC 60X3611 probe support which provides angular adjustment in two dimensions.

Each optical probe received light through a beam expander and transmitted the signal through the fiber optic cables to a DANTEC 55X35 color separator where the received signal was split. If the signal was from the DANTEC 60X60 the signal was split into 514.4 (green) and 488.0 nm (blue) wavelengths. Each of the received signals were then transferred to a DANTEC 55X35 photomultiplier tube where the signals of light were converted into electrical signals associated with each wavelength received.

3.2.1.2 Data Acquisition Equipment

The Doppler signals received by the optic probes and converted to electrical signals by the photomultiplier tubes were sent to two BSAs for processing. The processing equipment consisted of a DANTEC 57N20 BSA Enhanced and a DANTEC 57N35 BSA Enhanced Model S processors. The 57N20 BSA was used as the master BSA for calculating coincidence filtering and had an interior clock of 1 Mhz. A Gateway 2000 486 DX/33 personal computer running DANTEC Burstware 2.0 software was used to run the DANTEC LDV system and to collect data.

3.2.1.3 Traverse

To control the position of the LDV measurement volume and collect data over a wide spacial range while maintaining optical probe alignment, a DANTEC 3-D Traverse System was used. The traverse was powered by three Cleveland Machine Controls stepper motors regulated by a Dynapar Model M20100003331 encoder. One thousand pulses from the encoder translated into one revolution of the traverse positioning screw and a 2 mm displacement. The traverse had an accuracy of $\pm$ 80 μm over a 600 mm range (or 0.13 $\mu m/mm$) with a maximum loading of 445 N.

3.2.1.4 Seeding Apparatus

Though the LDV measurement was non-intrusive in the sense that the measurement equipment was external to the flow field, particles must be introduced into the flow that reflect light in sufficient

quantities and were small enough to follow the smallest flow structures to be measured. A TSI Inc. six-jet atomizer was attached to an injector mounted in the Mach 2.9 settling chamber. The atomizer was connected to the injector using a Tyson brand plastic tube (type R-3603) with an inner diameter of 1.27 cm. Bertoli Brand extra light olive oil was used as the flow following particles and had a mean particle size of $d_p \leq 1\ \mu m$ [12]. The density of the olive oil particles in the flow was controlled by two methods. The first was to use the pressure control valve to regulate the pressure difference in the atomizer. The second method of controlling the particle density was to increase or decrease the number of jets used to inject the olive oil particles into the wind tunnel settling chamber. The injector consisted of a copper pipe pressed into a streamline shape and mounted just ahead of the flow straightener. Slots were cut along the trailing edge of the copper pipe for injection of the olive oil particles. Figure 11 shows a schematic of the injector with its location in the Mach 2.9 stagnation chamber.

Detailed information for the processing of the scattered laser light can be found in the DANTEC BURSTware Installation and User's Guide [20] and DANTEC BSA Enhanced User's Guide [22]. Appendix B also provides information on the LDV system settings used for these experiments.

3.2.2 Hot-Wire Anemometry

3.2.2.1 Hot-Wire Equipment

Hot-Wire anemometry was performed on a DANTEC StreamLine Constant Temperature Anemometry (CTA) System which consisted of a StreamLine Frame, three CTA Modules, and a Personal Computer (PC) with the DANTEC StreamWare software. The PC communicated with the DANTEC Frame using a National Instruments Model AT-MIO-16E-1 interface card and the COM1 serial port.

The frame contained a power supply, a controller, and an ambient temperature probe. It held three CTA or Calibration Modules and provided analog outputs for each of the modules and the tem-

perature probe. To electrically isolate each Module, the frame provided six galvanically separated power supplies. The frame controller provided three functions: 1) transfer and storage of setup parameters for the CTA Modules, 2) DC voltage measurements for probe resistance, bridge balance, and ambient temperature from the temperature transducer, and 3) to record CTA square wave response data.

Two of the three CTA Modules were used to collect data for normal, parallel, and cross-film probes in the boundary layer above the roughened flat plate surfaces. The Modules contained a CTA and a Signal Conditioner in one box. The anemometry provided two internal Wheatstone bridge configurations (1:20 and 1:10), as well as, an external bridge (1:1) which allowed for a higher frequency response of the hot-film to flow conditions. The external bridge configuration was used in this setup using non-wire wound ceramic potentiometers (20 ohms maximum) connected to DANTEC microdot cable and BNC cables of the same length as the cables connected to the probe holder. The signal conditioner provided in each CTA Module was used to match the CTA bridge output to the input range of an Analog-to-Digital (A/D) converter and provide filtering of the bridge signal.

The StreamWare software ran on an Acer 100 Mhz Pentium PC and controlled the StreamLine Hardware System for acquiring, processing, and presenting hot-film data. The PC controlled the frame by the use of the COM1 serial port and collected data using the National Instruments Model AT-MIO-16E-1 A/D converter. The A/D converter was a 16 channel, 12 ADC bit resolution board with a voltage range of either ± 5 or 0-10 volts. The StreamWare software was used to control the StreamLine Frame and to collect hot-film data. The processing and presenting of results were done on a Hewlett Packard Pavilion Model 7320 PC described below. This was done since the DANTEC Calibration System was usable only in the air flow range of a few *cm*/sec up to Mach 1. All information for the description of the DANTEC Streamline CTA System was found in the

DANTEC StreamLine Installation & User's Guide [21]. The hardware and software settings used for each hot-film experiment are presented in Appendix A.

3.2.2.2 Traverse

The normal, parallel, and cross-film probes were positioned in the roughened flat plate turbulent boundary layer using a three-axis UniSlide traverse by Velmex, Inc., controlled by a Velmex, Inc. 8300 Series Stepping Motor Controller/Driver. Figure 12 shows the UniSlide traverse and tunnel setup for cross-film measurements. Each traverse axis had a travel length of 600 mm with an error of $\pm$ 80 μm over a 600 mm range (or 0.13 $\mu m/mm$). The 8300 Series controller was a microcomputer controller which ran the three stepper motors from a host PC connected by a RS-232C interface cable.

3.2.2.3 Hot-Film Probes

In general, two probe types are commonly used for turbulence measurements. They are hot-wire and hot-film probes. The hot-wire probes are exactly that, wire stretched across two leads. Because wires can be made extremely thin, the thermal inertia of the sensor gives a higher frequency response to flow fluctuations. The wires small size also makes the probes very fragile and so a trade-off between response and robustness must be made. Hot-Film probes are typically made of a cylindrical quartz substrate with a thin-film of platinum deposited on the outer surface. The cylindrical quartz substrate and platinum film are larger and more robust than the wire sensors but have a slower frequency response. For this dissertation, the term "hot-wire" is used as a generic term identifying both hot-wire and hot-film measurement techniques, though only hot-film probes were used in this research.

Three hot-film probe types were used in these experiments: normal, parallel, and cross-film probes. The normal-film probe was a TSI Model 1218-20 probe with Platinum sensors mounted to a

TSI Model 1150 Single Sensor Probe Support. The parallel-film probe was a TSI Model 1246AD-20 probe consisting of two hot-film sensors positioned normal to the x-y plane, parallel to each other, and spaced 1.085 mm apart in the y-axis direction. Two cross-film probes were used in these experiments. They were the TSI Model 1243-20 x-array probe which measured mean and turbulent information in the x-y plane and the TSI Model 1243AN-20 which measured information in the x-z plane. Both cross-film probes provided mean and turbulent information in the streamwise or x-axis direction. The two sensor probes (TSI 1246AD-20, 1243-20, and 1243AN-20) were mounted to a TSI Model 1155 Dual Sensor Probe Support. All of the probes were TSI "-20" hot-film probes with sensor diameters of 50.8 μm, sensor lengths of 1.02 mm, distance between supports of 1.65 mm, and temperature coefficients of 0.0024 $\frac{1}{^oC}$. Figures 13, 14, 15, and 16 provide drawings of the normal, parallel, and both cross-film probes, respectively [60].

The normal-film and parallel-film probes were used to collect high-frequency information in the boundary layer. The normal-film probe measured energy spectra and autocorrelation information and the parallel-film probe measured boundary flow structure angles using the cross-correlation between the two film sensors. For these probes, the DANTEC system was used to tune and maintain the bridge during the tunnel runs. The DANTEC system and external resistors provided a nominal frequency response of 130 kHz using the square wave technique in the Mach 2.9 freestream. A Nicolet Multipro data acquisition system was used to collect hot-film voltage data. The Nicolet Multipro system consisted of a chassis unit with four A/D acquisition boards, each with four input channels. The Multipro system acquired each channel at a 1Mhz rate (non-interlaced) with a maximum of 256k samples per board.

3.2.3 Pressure Measurement

A Pitot pressure probe was used to measure pressures through the boundary layer of each of the six models. The Pitot probe had an inner tube height of 0.762 mm (0.030 in.) and outer tube height of 1.168 mm (0.046 in.). A picture of the Pitot probe is shown in Figure 17. The position and deflection of the Pitot probe and hot-film probes was measured using a Gaertner travelling telemicroscope with a digital readout. The telemicroscope used a M-303 micrometer slide with a length of 100 mm and an accuracy to ± 0.0005 mm.

3.2.4 Flow Visualization

Two flow visualization methods were used in this research. The first method used color schlieren photographs to provide mean flow information. While the second method used Laser Sheet Mie Scattering Imaging (LSI) to provide instantaneous boundary layer flow information.

3.2.4.1 Color Schlieren

The color schlieren flow visualization equipment consisted of a mercury light source, two 15.24 cm (6 in) mirrors, a color slide, and a Nikon/Kodak Digital CCD camera. Figure 18 is a photograph of the equipment setup while Figure 19 is a schematic showing the positioning of the light source, mirrors, slide, and camera. The color schlieren slide used as the knife edge had blue and red regions separated by a thin green band. As light traverses through the test section, density gradients deflect the light up or down into the red and blue regions of the slide. Therefore, regions with no density gradients appeared green and regions with density gradients appeared red or blue, depending on the gradient direction. For this setup a horizontal knife edge provided $\frac{\partial \rho}{\partial y}$ information and a vertical knife edge provided $\frac{\partial \rho}{\partial x}$ information. From these photographs, the mean boundary layer height could be seen along with any compression or expansion waves. The color contrast

information for each photograph was modified, by the same contrast curve, using Adobe Photoshop Version 4.0.

3.2.4.2 Laser Sheet Imaging

The LSI system consisted of a Surelite I10 Laser, Surelite I10 Power Cooling Group, Surelite, Separation Package, three flat mirrors, two cylindrical lenses, and a focal spherical lens. A photograph and schematic of the LSI setup is shown in Figures 20 and 21, respectively. The Surelite I10 laser was a 4.0 Watt YAG laser with two primary wavelengths of $1.06\mu m$ and $532nm$. The $532nm$ wave length beam was used for the imaging with a Q-switch setting of $300\mu s$. The same Nikon/Kodak camera used for the color schlieren photographs was used for the laser sheet images. The camera had a resolution of 1524 by 1012, pixel depth of 12 bits per color (RGB), and a hard disk capacity of 260 Mbytes (approximately 55 photographs). The flow imaging particulates were provided by a Rosco Model 1600 Fogger using Rosco Fog Fluid. The fogger was placed in a pressurized PVC container to provide positive pressure from the fogger into the tunnel stagnation chamber.

3.3 Computational Facilities

The following computational hardware and software was used to complete this research.

3.3.1 Hardware

The data reduction and processing was completed on two classes of computer hardware, a Digital Workstation and IBM compatible PCs. The workstation was a Digital Alpha Station model $200^{4/233}$ running Digital Unix, Fortran 90 and connected to the Aeronautical and Astronautical Engineering Department workstation network using DEC Tulip Ethernet. The system had a single Alpha processor running at 233 Mhz with 128 Mbytes of dynamic RAM and one 4 Gbyte local hard disk drive. The Alpha station provided a 1280 by 1024 display resolution with a pixel depth of 8

bits to a 17 inch monitor. The PC was a Hewlett Packard 166 Mhz Pentium MMX computer with 80 Mbytes of dynamic RAM and 2.5 Gbytes of local hard disk space.

3.3.2 Software

The software for this research consisted of in-house data reduction routines and over-the-counter software packages. The in-house programs were WinMShear, discrete Fourier transformation (DFT), correlation, and the computational fluid dynamics programs. The WinMShear program used the raw mean and rms voltage information from the DANTEC Streamline system and calculated the mean and turbulent flow quantities (see: Chapter 4 Data Reduction). WinMShear was based on MShear written by Bowersox [7] and modified to run as a Microsoft Windows 95 program. The DFT and correlation (cross and auto) routines reduced the Nicolet high-frequency data into energy spectra, microscale, integral scale, and structure angle information. The CFD code know as CFVPNS [6] (Cell-centered, Finite Volume, Parabolized N-S) is more fully described in Chapter 5. The CFVPNS was run on the Digital Alpha Workstation, while the other programs were run on a PC. The over-the-counter software used for this research included Scientific WorkPlace Version 2.5, Adobe Photoshop Version 4.0, Visio Sampler, Microsoft PowerStation Fortran Version 4.0, and Microsoft Office97.

Chapter 4 - Experimental Data Reduction Techniques

This chapter describes the data reduction techniques used in this research. Four areas of data reduction covering Pitot, Hot-Wire Anemometry (HWA), Laser Doppler Velocimetry (LDV), and high-frequency normal-film data are discussed. The mean flow Mach number was calculated using the Rayleigh-Pitot tube formula and normal shock relationships. Following the Pitot data reduction, techniques for reducing HWA turbulent and mean flow quantities using the effective Reynolds number concept are covered. After the HWA data reduction, LDV output by the DANTEC BSA will be discussed along with the quantities directly measured by LDV techniques. Following the hot-film and LDV sections is a combined analysis developed by Bowersox [12] which uses both HWA and LDV data. Finally, the energy spectra, autocorrelation, and cross-correlation methods will be covered.

4.1 Mean Flow and Integral Analysis

4.1.1 Mean Flow

Tunnel stagnation chamber total conditions, P_{o_∞} and T_{o_∞}, and test section Pitot pressure, P_{o_2}, were measured. In the freestream, the Mach number was found using the total pressure ratio across a normal shock given by

$$\frac{P_{o_2}}{P_{o_1}} = \left(\frac{\left(\frac{\gamma+1}{2}\right) M_1^2}{1 + \frac{\gamma+1}{2} M_1^2} \right)^{\frac{\gamma}{\gamma-1}} \left(\frac{2\gamma M_1^2}{\gamma+1} - \frac{\gamma-1}{\gamma+1} \right)^{-\left(\frac{1}{\gamma-1}\right)} \tag{72}$$

From the isentropic pressure relationship, the freestream static pressure was found. Finally, assuming the static pressure is constant across the boundary layer, the Rayleigh-Pitot tube formula [34]

$$\frac{P_{o_2}}{P_1} = \left(\frac{(\gamma+1)^2 M_1^2}{4\gamma M_1^2 - 2(\gamma-1)} \right)^{\frac{\gamma}{\gamma-1}} \frac{1 - \gamma + 2\gamma M_1^2}{\gamma+1} \tag{73}$$

was used to calculate the boundary layer Mach number profile. In the above equation, M_1 is the mean Mach number, P_{o_2} is the total pressure behind the normal shock in front of the probe, and P_1 is the freestream static pressure.

The temperature and density boundary layer profiles for the six floor sections were determined using two methods, the Crocco-Busemann approximation and isentropic flow relations. The Crocco-Busemann approximation [61] is given by

$$\frac{\rho_w}{\bar{\rho}} = \frac{\bar{T}}{T_w} = 1 + B' \left(\frac{\bar{u}}{u_\infty}\right) - \left(A'\right)^2 \left(\frac{\bar{u}}{u_\infty}\right)^2 \tag{74}$$

where ρ_w and T_w are the wall density and temperature, respectively, with

$$\left(A'\right)^2 = \frac{\left(\frac{\gamma-1}{2}\right) r M_\infty^2}{\frac{T_w}{T_\infty}} \quad \text{and} \quad B' = \frac{1+\left(\frac{\gamma-1}{2}\right) r M_\infty^2}{\frac{T_w}{T_\infty}} - 1 \tag{75}$$

The recovery factor, r, is given by $r = (\mathrm{Pr})^{\frac{1}{3}}$ for turbulent boundary layer flow. The temperature at the wall was assumed to be the adiabatic wall temperature, T_{aw}, calculated using

$$\frac{T_{aw}}{T_\infty} = 1 + \left(\frac{\gamma-1}{2}\right) r M_\infty^2 \tag{76}$$

with the wall density found using the perfect gas relation

$$\rho_w = \frac{p_w}{R T_w} \tag{77}$$

The second method of calculating the density uses the local Mach number and tunnel stagnation temperature. With the Mach number and stagnation temperature the local flow density can be determined assuming the static pressure is constant.

4.1.2 Integral Analysis for a Smooth Flat Plate Boundary Layer

Also from the Pitot data, the boundary layer, displacement and momentum thicknesses were calculated. Two boundary layer heights, δ and δ_M, were calculated based on the velocity and Mach profiles, respectively. They are the y-axis location at which $\frac{u}{u_\infty} = 0.99$ and $\frac{M}{M_\infty} = 0.99$, respec-

tively. The displacement and momentum thicknesses are given by

$$\delta^* = \int_0^\infty \left(1 - \frac{\overline{\rho}\bar{u}}{\rho_\infty u_\infty}\right) dy \tag{78}$$

and

$$\theta = \int_0^\infty \frac{\overline{\rho}\bar{u}}{\rho_\infty u_\infty}\left(1 - \frac{\bar{u}}{u_\infty}\right) dy \tag{79}$$

While the kinematic displacement and momentum thickness are given by

$$\delta_k^* = \int_0^\infty \left(1 - \frac{\bar{u}}{u_\infty}\right) dy \tag{80}$$

and

$$\theta_k = \int_0^\infty \frac{\bar{u}}{u_\infty}\left(1 - \frac{\bar{u}}{u_\infty}\right) dy \tag{81}$$

The skin friction was calculated using the Van Driest II equation for the smooth plate. The Van Driest II [66] equation is given by

$$\frac{\sin^{-1}\left(\frac{2B_1^2 - B_2}{\sqrt{B_2^2 + 4B_1^2}}\right) + \sin^{-1}\left(\frac{B_2}{\sqrt{B_2^2+4B_1^2}}\right)}{\sqrt{C_f\left(\frac{T_{aw}}{T_e} - 1\right)}} \approx 4.15 \log\left(Re_x C_f \frac{\mu_e}{\mu_w}\right) + 1.7 \tag{82}$$

with

$$B_1 = \sqrt{\frac{\gamma - 1}{2} r M_e^2 \frac{T_e}{T_w}} \qquad B_2 = \frac{T_{aw}}{T_w} - 1 \tag{83}$$

the skin friction, C_f, was found using an iterative approach.

4.1.3 New Integral Method for a Rough-Wall Boundary Layer

For the rough plates, the skin friction value was calculated based on the fully rough "Law of the Wall" written as [50]

$$\sqrt{\frac{2}{C_f}} = \frac{1}{\kappa} \ln\left(\frac{\delta}{k}\right) + B \tag{84}$$

where k is the roughness height, $\kappa = 0.41$, and B is a constant. Rewriting the above equation using the momentum thickness gives

$$\sqrt{\frac{2}{C_f}} = \frac{1}{\kappa} \ln\left(\frac{\theta}{k}\right) + B' \tag{85}$$

Combining Equation (85) with the zero pressure gradient momentum integral equation given by

$$\frac{C_f}{2} = \frac{d\theta}{dx} \tag{86}$$

and integrating gives

$$\frac{\theta}{k}\left[5.95\left(\ln^2\frac{\theta}{k}-2\left[\ln\frac{\theta}{k}-1\right]\right)+4.88B'\left(\ln\frac{\theta}{k}-1\right)+B'^2\right]\Big|_{\theta_i}^{\theta_f}=\frac{\Delta x}{k} \tag{87}$$

For known θ_i, θ_f, k, and Δx, the constant, B', can be calculated for each plate and the skin friction found from Equation (85).

4.2 Turbulent Flow

This section contains the data reduction of hot-film and LDV data beginning with general theory and overheat (multiple and single) analysis for hot-film data. Followed by a section on LDV data reduction, combined analysis for both hot-film and LDV data, and finally, energy spectra and correlation data reduction.

4.2.1 Hot-Wire Anemometry

4.2.1.1 General Theory

The multiple overheat cross-wire (or film) data reduction techniques used and presented in this section were developed by Bowersox [14]. First, general theory is presented for flow over hot-wires, followed by the development of cross-wire and normal-wire data reduction equations. For turbulent compressible flow over a cylinder, the non-dimensional heat transfer or Nusselt number has the following functional form [36].

$$Nu = Nu(\frac{L}{d}, M, \mathrm{Pr}, Re_e, \tau) \tag{88}$$

where L/d is the wire aspect ratio, M is the Mach number, Pr is the Prandtl number, Re_e is the effective cooling Reynolds number based on wire diameter, and τ is the temperature loading factor $[\tau = (T_w - T_e)/T_t]$. T_w is the wire temperature and T_e is the equilibrium temperature an unheated

wire would reach if placed in the flow. Equation (88) simplifies to

$$Nu = Nu(Re_e, \tau) \tag{89}$$

under the following assumptions: the aspect ratio is much greater than one, the Mach number is greater than 1.2 or $M \sin\phi$ is greater than one, the Prandtl number is constant, and for Reynolds numbers greater than 20, T_e is about 97% of T_t. For wires normal to the flow, the experimental data has been found to collapse onto the following curve

$$Nu = aRe_e^n + b \tag{90}$$

where a and b are found from calibration.

The Nusselt number is also proportional to the power supplied to the wire

$$Nu = \frac{q_w}{\pi k_t L(T_w - T_e)} \tag{91}$$

where q_w is the wire heat transfer and k_t is the thermal conductivity of the wire. Assuming the power supplied to the wire is equal to the heat transfer away from the wire, q_w is given by

$$q_w = i_w^2 R_w \tag{92}$$

where R_w is the wire resistance and i_w is the wire current given by [1]

$$i_w = \frac{V_w}{R_w + R_s + R_L} \tag{93}$$

Assuming $T_e \approx T_t$ Equations (91), (92), and (93) can be combined to give

$$Nu = \frac{V_w^2 R_w}{(R_w + R_s + R_L)^2} \frac{1}{\pi k_t L(T_w - T_t)} \tag{94}$$

Using the turbulent power laws for thermal conductivity and viscosity given by

$$k_t = k_o \left(\frac{T_t}{T_o}\right)^{n_k} \quad \text{and} \quad \mu_t = \mu_o \left(\frac{T_t}{T_o}\right)^{n_\mu}$$

with $n_k = 0.89$ and $n_\mu = 0.77$ and combining Equations (94) and (90) gives

$$\frac{v_w^2}{C_o} = \left(\frac{T_t}{T_o}\right)^{-n_k} \left[a\sqrt{Re_{oe}} \left(\frac{T_t}{T_o}\right)^{-\frac{n_\mu}{2}} + b\right] (T_w - T_t) \tag{95}$$

where

$$C_o = (R_w + R_s + R_L)^2 \frac{\pi k_o L}{R_w}$$

and Re_{oe} is the effective Reynolds number with $\mu = \mu_o$. Replacing v_w, Re_{oe}, and T_t by the mean plus the fluctuating component, using the Binomial Theorem, retaining only the first order terms and solving for $v_w'/\overline{V}_w$ gives the hot-film fluctuation equation

$$\frac{v_w'}{\overline{V}_w} = f\frac{Re_{oe}'}{\overline{Re}_{oe}} + g\frac{T_t'}{T_t} \tag{96}$$

where the hot-film sensitivities are given by

$$f = \frac{1}{4}\left(1 + \frac{b}{a\sqrt{\overline{Re}_e}}\right) \quad \text{and} \quad g = -\frac{\overline{T}_t}{2(T_w - \overline{T}_t)} + \frac{n_k}{2} - fn_\mu \tag{97}$$

Equation (96) can be rewritten using the mean quantities $\sqrt{\overline{Re}_e}$ and $\overline{T}_t$.

$$\sqrt{\overline{Re}_e} + \chi_i \overline{T}_t \sqrt{\overline{Re}_e} + \psi_i \overline{T}_t = \xi_i \tag{98}$$

where $\chi_i = -1/T_{wi}$, $\psi_i = -b_i/(a_i T_{wi})$, and $\xi_i = \overline{V}_{wi}^2/(C_i a_i T_{wi}) - b_i/a_i$. The subscript i indexes the overheat ratio. At a minimum, two overheat ratios are required to solve for the two unknowns, $\sqrt{\overline{Re}_e}$ and $\overline{T}_t$. If more overheat ratios are used, then a least squares analysis is used:

$$\begin{aligned} &N\sqrt{\overline{Re}_e} + \overline{T}_t\left(\sum \chi_i - \sum \psi_i \xi_i\right) + 2\overline{T}_t\sqrt{\overline{Re}_e}\sum \chi_i \\ &+\overline{T}_t^2 \sum \chi_i \psi_i + \overline{T}_t^2 \sqrt{\overline{Re}_e}\sum \chi_i^2 = \sum \xi_i \end{aligned} \tag{99}$$

$$\begin{aligned}\sqrt{\overline{Re_e}}\left(\sum\psi_i-\sum\chi_i\xi_i\right)+\overline{T_t}\sum\psi_i^2+2\overline{T_t}\sqrt{\overline{Re_e}}\sum\chi_i\psi_i\\ +\sqrt{\overline{Re_e^2}}\sum\chi_i+\overline{T_t}\sqrt{\overline{Re_e^2}}\sum\chi_i^2=\sum\psi_i\xi_i\end{aligned}\tag{100}$$

where N is the number of overheats and the summations are over i which goes from 1 to N. The solution of the above two nonlinear equations was found using the iterative secant method.

Equation (96) was squared and averaged yielding the turbulent result

$$f_i^2\overline{\left(\frac{\mathrm{Re}'_{oe}}{\overline{\mathrm{Re}}_{oe}}\right)^2}+2f_ig_i\overline{\left(\frac{\mathrm{Re}'_{oe}}{\overline{\mathrm{Re}}_{oe}}\frac{T'_t}{T_t}\right)}+g_i^2\overline{\left(\frac{T'_t}{T_t}\right)^2}=\overline{\left(\frac{v'_w}{\overline{v}_w}\right)^2}_i\tag{101}$$

To solve for the three turbulent terms, $\overline{\left(\frac{\mathrm{Re}'_{oe}}{\overline{\mathrm{Re}}_{oe}}\right)^2}$, $\overline{\left(\frac{\mathrm{Re}'_{oe}}{\overline{\mathrm{Re}}_{oe}}\frac{T'_t}{T_t}\right)}$, and $\overline{\left(\frac{T'_t}{T_t}\right)^2}$, three overheat ratios are required. Again, if more than three overheats are used, a General Least Squares (GLS) analysis can be applied to Equation (101) yielding

$$\begin{aligned}&\begin{bmatrix}\sum f_i^4 & 2\sum f_i^3g_i & \sum f_i^2g_i^2\\ \sum f_i^3g_i & 2\sum f_i^2g_i^2 & \sum f_ig_i^3\\ \sum f_i^2g_i^2 & 2\sum f_ig_i^3 & \sum g_i^4\end{bmatrix}\begin{pmatrix}\overline{\left(\frac{\mathrm{Re}'_{oe}}{\overline{\mathrm{Re}}_{oe}}\right)^2}\\ \overline{\left(\frac{\mathrm{Re}'_{oe}}{\overline{\mathrm{Re}}_{oe}}\frac{T'_t}{T_t}\right)}\\ \overline{\left(\frac{T'_t}{T_t}\right)^2}\end{pmatrix}\\ &=\begin{pmatrix}\sum f_i^2\overline{\left(\frac{v'_w}{\overline{v}_w}\right)^2}_i\\ \sum f_ig_i\overline{\left(\frac{v'_w}{\overline{v}_w}\right)^2}_i\\ \sum g_i^2\overline{\left(\frac{v'_w}{\overline{v}_w}\right)^2}_i\end{pmatrix}\end{aligned}\tag{102}$$

the GLS analysis of turbulent terms does have one deficiency; any errors introduced in the experiment are amplified by a power of four. For this reason a new method, the Quadratic Least Squares (QLS) method (Bowersox [14]), has been developed.

The QLS method assumes errors in the hot-films are purely random and all bias errors are contained in f and g. In addition, the only variable in Equation (101) that is not constant for a given flow location is the wire temperature. By defining a new wire temperature loading function as

$$\tau^* = \frac{(T_w - \overline{T}_t)}{\overline{T}_t} \tag{103}$$

and rewriting the sensitivities as

$$f = f_o + m_f \frac{1}{\tau^*} \quad \text{and} \quad g = g_o + m_g \frac{1}{\tau^*} \tag{104}$$

where f_o and m_f are determined from wire calibration and

$$g_o = \frac{n_k}{2} - f_o n_\mu \quad \text{and} \quad m_g = -\left(\frac{1}{2} + n_\mu m_f\right) \tag{105}$$

Rewriting Equation (101) using Equation (104) gives

$$\overline{\left(\frac{v'_w}{\overline{v}_w}\right)^2} = a_o + a_1\left(\frac{1}{\tau^*}\right) + a_2\left(\frac{1}{\tau^*}\right)^2 \tag{106a}$$

where

$$\begin{bmatrix} f_o^2 & 2f_o g_o & g_o^2 \\ 2f_o m_f & 2\left(f_o m_g + g_o m_f\right) & 2g_o m_g \\ m_f^2 & 2m_f m_g & m_g^2 \end{bmatrix} \begin{pmatrix} \overline{\left(\frac{\mathrm{Re}'_{oe}}{\overline{\mathrm{Re}}_{oe}}\right)^2} \\ \overline{\left(\frac{\mathrm{Re}'_{oe}}{\overline{\mathrm{Re}}_{oe}}\frac{T'_t}{\overline{T}_t}\right)} \\ \left(\frac{T'_t}{\overline{T}_t}\right)^2 \end{pmatrix} = \begin{pmatrix} a_o \\ a_1 \\ a_2 \end{pmatrix} \tag{107}$$

Equation (107) requires a minimum of three overheat ratios to solve. If more overheat ratios are used, then Equation (106a) can be evaluated using the QLS analysis to obtain the a_j terms and then Equation (107) can be used to compute the turbulent quantities. The QLS method developed in Equation (107) was used to reduce the effect of bias errors on the hot-film sensitivities, f and g.

The wire temperature, T_w, was calculated (in Kelvin) using [1]

$$T_w = T_{ref} + \frac{100}{\gamma_{ref} R_{ref}} (R_w - R_{ref})$$

with T_{ref} equal to 293.15 K (20^oC) and γ_{ref} is the temperature coefficient of resistance (sensor dependent).

4.2.1.2 Normal-Wire

For a normal-wire probe, the effective Reynolds number, Re_e is the x-component of the Reynolds number in the flow (or wind) direction, given by Re_{wx}. So, the normal-wire response equation is obtained by replacing Re_{oe} by Re_{wx} in Equation (95) and using the two non-linear Equations (99) and (100).

4.2.1.3 Cross-Wire

Early work has shown that the response of cross wires (swept wires) is independent of Mach number if $M \sin\phi \geq 1$ [55], but they are still dependent on the normal Reynolds number component. The following analysis uses oblique shock theory to relate the effective Reynolds number to the x-y coordinate system and was developed by Bowersox [14]. Using a coordinate transformation, the effective Reynolds number can be shown to be

$$Re_{ej}^2 = A_{1j} Re_x^2 + 2A_{2j} Re_x Re_y + A_{3j} Re_y^2 \tag{108}$$

with

$$A_{1j} = \cos^2\phi_j + k_c^2 \sin^2\phi_j \quad A_{2j} = (1 - k_c)\cos\phi_j \sin\phi_j \quad A_{1j} = k_c^2 \cos^2\phi_j + \sin^2\phi_j$$

and j indexing one of the two wires for a cross-wire probe and ϕ_j is the hot wire incidence angle. Using first order assumptions, k_c can be shown to be

$$k_c = \frac{\overline{\rho_1}}{\overline{\rho_2}} k \tag{109}$$

Replacing Re_{oe}, Re_{ox}, and Re_{oy} by their mean and fluctuating components, applying the binomial theorem, and the following definitions

$$\begin{aligned} R_o &= \frac{\overline{Re_{oy}}}{\overline{Re_{ox}}} = \frac{\overline{\rho v}}{\overline{\rho u}} \\ B_1 &= \frac{A_1}{B_3} \\ B_2 &= \frac{A_2}{B_3} \\ B_3 &= A_1 + 2A_2R_o \end{aligned} \tag{110}$$

it can be shown that

$$\overline{Re_{oe_j}} = \overline{Re_{ox}}\sqrt{B_{3j}} \tag{111}$$

and

$$\left(\frac{Re'_{oe}}{\overline{Re}_{oe}}\right)_j = B_{1j}\left(\frac{Re'_{ox}}{\overline{Re}_{ox}}\right) + B_{2j}\left(\frac{Re'_{oy}}{\overline{Re}_{ox}}\right) \tag{112}$$

assuming $R_o^2 \ll 1$. Solving this set of equations and decomposing into x and y components of Re gives

$$\overline{Re}_{ox} = \frac{\overline{\rho u} d_w}{\mu_o} = \sqrt{\frac{\overline{Re}_{oe1}^2/A_{21} - \overline{Re}_{oe2}^2/A_{22}}{A_{11}/A_{21} - A_{12}/A_{22}}} \tag{113}$$

$$\overline{Re}_{oy} = \frac{\overline{\rho v} d_w}{\mu_o} = \frac{1}{2\overline{Re}_x}\frac{\overline{Re}_{oe1}^2/A_{11} - \overline{Re}_{oe2}^2/A_{12}}{A_{21}/A_{11} - A_{22}/A_{12}} \tag{114}$$

Decomposing the fluctuation Equation (112) into x and y components gives the turbulent results

$$\overline{\left(\frac{Re'_{ox}}{\overline{Re}_{ox}}\right)^2} = \frac{1}{D_2^2}\left[\begin{array}{c} \frac{1}{B_{21}^2}\overline{\left(\frac{Re'_{oe}}{\overline{Re}_{oe}}\right)_1^2} - \\ \frac{2}{B_{21}B_{22}}\overline{\left(\frac{Re'_{oe}}{\overline{Re}_{oe}}\right)_1\left(\frac{Re'_{oe}}{\overline{Re}_{oe}}\right)_2} + \frac{1}{B_{22}^2}\overline{\left(\frac{Re'_{oe}}{\overline{Re}_{oe}}\right)_2^2} \end{array}\right]$$

$$\overline{\left(\frac{Re'_{oy}}{\overline{Re}_{ox}}\right)^2} = \frac{1}{D_1^2}\left[\begin{array}{c} \frac{1}{B_{11}^2}\overline{\left(\frac{Re'_{oe}}{\overline{Re}_{oe}}\right)_1^2} - \\ \frac{2}{B_{11}B_{12}}\overline{\left(\frac{Re'_{oe}}{\overline{Re}_{oe}}\right)_1\left(\frac{Re'_{oe}}{\overline{Re}_{oe}}\right)_2} + \frac{1}{B_{12}^2}\overline{\left(\frac{Re'_{oe}}{\overline{Re}_{oe}}\right)_2^2} \end{array}\right] \tag{115}$$

$$\overline{\frac{Re'_{ox}}{\overline{Re}_{ox}}\frac{Re'_{oy}}{\overline{Re}_{ox}}} = \frac{1}{2B_{11}B_{21}}\left[\begin{array}{c} \overline{\left(\frac{Re'_{oe}}{\overline{Re}_{oe}}\right)_1^2} - B_{11}^2\overline{\left(\frac{Re'_{ox}}{\overline{Re}_{ox}}\right)^2} \\ -B_{21}^2\overline{\left(\frac{Re'_{oy}}{\overline{Re}_{ox}}\right)^2} \end{array}\right]$$

where $D_1 = \left(\frac{B_{21}}{B_{11}} - \frac{B_{22}}{B_{12}}\right)$ and $D_2 = \left(\frac{B_{11}}{B_{21}} - \frac{B_{12}}{B_{22}}\right)$. Either the GLS or QLS method can be used to solve for all terms on the right-hand-side of the above equations except for the middle correlation term between wire 1 and 2. This term can be found using the covariance between the two wires of the cross-wire probe. The covariance relationship can expressed as

$$\begin{aligned} &\overline{\left(\frac{Re'_{oe}}{\overline{Re}_{oe}}\right)_1\left(\frac{Re'_{oe}}{\overline{Re}_{oe}}\right)_2}\sum f_{1i}f_{2i} \\ &= \sum\overline{\left(\frac{v'_w}{\overline{v}_w}\right)_1\left(\frac{v'_w}{\overline{v}_w}\right)_2} - \overline{\left(\frac{T'_t}{\overline{T}_t}\right)^2}\sum g_{1i}g_{2i} \\ &-\overline{\left(\frac{Re'_{oe}}{\overline{Re}_{oe}}\frac{T'_t}{\overline{T}_t}\right)_1}\sum f_{1i}g_{2i} - \overline{\left(\frac{Re'_{oe}}{\overline{Re}_{oe}}\frac{T'_t}{\overline{T}_t}\right)_2}\sum f_{2i}g_{1i} \end{aligned} \tag{116}$$

where the summations are over N overheat ratios. Finally, the Reynolds number total temperature correlations can be shown to be

$$\begin{aligned} \overline{\frac{Re'_{ox}T'_t}{\overline{Re}_{ox}\overline{T}_t}} &= \frac{1}{D_2}\left[\frac{1}{B_{21}}\overline{\left(\frac{Re'_{oe}T'_t}{\overline{Re}_{oe}\overline{T}_t}\right)_1} - \frac{1}{B_{22}}\overline{\left(\frac{Re'_{oe}T'_t}{\overline{Re}_{oe}\overline{T}_t}\right)_2}\right] \\ \overline{\frac{Re'_{oy}T'_t}{\overline{Re}_{ox}\overline{T}_t}} &= \frac{1}{D_1}\left[\frac{1}{B_{11}}\overline{\left(\frac{Re'_{oe}T'_t}{\overline{Re}_{oe}\overline{T}_t}\right)_1} - \frac{1}{B_{12}}\overline{\left(\frac{Re'_{oe}T'_t}{\overline{Re}_{oe}\overline{T}_t}\right)_2}\right] \end{aligned} \tag{117}$$

For the x-z plane, cross-film probes, the data reduction routines are identical to those above with the y and v terms replaced with z and w, respectively.

4.2.1.4 *Separation of Turbulence Variables*

The formulas for separation of mass flux and total temperature terms into non-conservative velocity and density fluctuations are

$$\begin{aligned} \frac{u'}{\overline{u}} &= \frac{(\rho u)'}{\overline{\rho u}} - \frac{\rho'}{\overline{\rho}} \\ \frac{v'}{\overline{u}} &= \frac{(\rho v)'}{\overline{\rho u}} - R_o \frac{\rho'}{\overline{\rho}} \\ \frac{\rho'}{\overline{\rho}} &= \frac{1}{\alpha+\beta}\left[\beta\left(\frac{(\rho u)'}{\overline{\rho u}} + R_o\frac{(\rho v)'}{\overline{\rho u}}\right) - \frac{T_t'}{\overline{T_t}} + \alpha\frac{p'}{\overline{p}}\right] \end{aligned} \tag{118}$$

where

$$\alpha = \frac{1}{1+\frac{\gamma-1}{2}M^2} \quad \text{and} \quad \beta = \alpha\left(\gamma-1\right)M^2$$

Typically, the pressure fluctuation term is assumed to be zero ($p' \approx 0$) [14]. Thus all of the turbulent shear terms in the RANS equations can be found using Equation (118) and $p' \approx 0$.

$$\begin{bmatrix} 1 & 0 & 1 & 2 & 0 & 0 \\ 0 & 1 & R_o^2 & 0 & 2R_o & 0 \\ \beta^2 & \beta^2 R_o^2 & \alpha^2 & -2\alpha\beta & -2\alpha\beta R_o & 2\beta^2 R_o \\ 0 & 0 & R_o & R_o & 1 & 1 \\ \beta & 0 & -\alpha & \beta-\alpha & \beta R_o & \beta R_o \\ 0 & \beta R_o & -\alpha R_o & \beta R_o & \beta R_o^2 - \alpha & \beta \end{bmatrix} \begin{pmatrix} \overline{\left(\frac{u'}{\overline{u}}\right)^2} \\ \overline{\left(\frac{v'}{\overline{u}}\right)^2} \\ \overline{\left(\frac{\rho'}{\overline{\rho}}\right)^2} \\ \overline{\frac{\rho' u'}{\overline{\rho u}}} \\ \overline{\frac{\rho' v'}{\overline{\rho u}}} \\ \overline{\frac{u'v'}{\overline{u}\overline{u}}} \end{pmatrix} = \begin{pmatrix} \overline{\left(\frac{(\rho u)'}{\overline{\rho u}}\right)^2} \\ \overline{\left(\frac{(\rho v)'}{\overline{\rho u}}\right)^2} \\ \left(\frac{T_t'}{\overline{T_t}}\right)^2 \\ \overline{\frac{(\rho u)'(\rho v)'}{(\overline{\rho u})^2}} \\ \overline{\frac{(\rho u)' T_t'}{\overline{\rho u}\,\overline{T_t}}} \\ \overline{\frac{(\rho v)' T_t'}{\overline{\rho u}\,\overline{T_t}}} \end{pmatrix} \tag{119}$$

For use in the FANS equations the following transformations can be used

$$\frac{\overline{u''}}{U} = \frac{-\overline{\rho' u'}}{\overline{\rho u}}$$

$$\frac{\overline{v''}}{U} = \frac{-\overline{\rho' v'}}{\overline{\rho u}} \tag{120}$$

$$\overline{u''v''} = \overline{u'v'}$$

$$U = \frac{\overline{\rho u}}{\overline{\rho}}$$

4.2.1.5 Single Overheat Analysis

To minimize the sensitivity to the total temperature fluctuations, the hot-film is often operated at the largest possible overheat. For small total temperature fluctuations, the single overheat (SOH) technique can obtain accurate mass flux results. For negligible total temperature fluctuations, $T_t' \approx 0$ [42]. With this assumption, the cross-wire equations can be approximated by

$$[S_{ij}] \begin{pmatrix} \overline{\left(\frac{Re'_{ox}}{\overline{Re_{ox}}}\right)^2} \\ \overline{\frac{Re'_{ox}}{\overline{Re_{ox}}} \frac{Re'_{oy}}{\overline{Re_{ox}}}} \\ \overline{\left(\frac{Re'_{oy}}{\overline{Re_{ox}}}\right)^2} \end{pmatrix} = \begin{pmatrix} \overline{\left(\frac{v'_w}{\overline{V_w}}\right)_1^2} \\ \overline{\left(\frac{v'_w}{\overline{V_w}}\right)_2^2} \\ \overline{\left(\frac{v'_w}{\overline{V_w}}\right)_1 \left(\frac{v'_w}{\overline{V_w}}\right)_2} \end{pmatrix} \tag{121}$$

with the coefficients of the $[S_{ij}]$ matrix as

$$
\begin{aligned}
S_{11} &= f_1^2 B_{11}^2 \\
S_{12} &= 2 f_1^2 B_{11} B_{21} \\
S_{13} &= f_1^2 B_{21}^2 \\
S_{21} &= f_2^2 B_{12}^2 \\
S_{22} &= 2 f_2^2 B_{12} B_{22} \\
S_{23} &= f_2^2 B_{22}^2 \\
S_{31} &= f_1 f_2 B_{11} B_{12} \\
S_{32} &= f_1 f_2 \left(B_{11} B_{22} + B_{12} B_{21} \right) \\
S_{33} &= f_1 f_2 B_{21} B_{22}
\end{aligned}
\tag{122}
$$

4.2.2 Laser Doppler Velocimetry

Laser Doppler Velocimetry has been used in many fluid flow problems and a complete description including areas of concern such as particle seeding, seeding density and size, directional ambiguity, particle correlation, and angular bias can be found in the DANTEC Enhanced BSA User's Guide [22]. When a seed particle passes through the laser measurement volume, the DANTEC BSA receives a Doppler burst signal. From the burst signal the BSA calculates the corresponding Doppler frequency, f_d (if the signal meets the required Signal-to-Noise (S/N) ratio and particle validation steps). The velocity of the seed particle is related to the geometry and Doppler frequency by the following equation

$$
u = \frac{x_f}{T_d} = f_d x_f = f_d \frac{\left(\frac{\lambda}{2}\right)}{\sin\frac{\theta}{2}} \tag{123}
$$

where x_f is the distance between two successive fringes of the Laser interference pattern, T_d is the time taken for the seed particle to cover the distance between the fringes, and $\left(\frac{\lambda}{2}\right) / \left[\sin\frac{\theta}{2}\right]$ is the calibration factor denoted by C_{fv} and is found from the optical setup. From the Doppler frequency

the particle velocity can be determined and with a large number of samples the mean velocity ($\overline{u}$ for one Laser), turbulence intensity (u' for one Laser), and the first term of the kinematic Reynolds shear stress

$$\frac{\tau_{xy}^{T}}{\overline{\rho}\overline{u}^{2}} = -\frac{\overline{u'v'}}{\overline{u}^{2}} \tag{124}$$

which is related to the Favre shear stress by the following identity (see Section 2.2.3)

$$\overline{\rho}\widetilde{u''v''} \equiv \overline{\rho}\overline{u'v'} + \overline{\rho}\widetilde{u''}\,\widetilde{v''} \tag{125}$$

where $\widetilde{u_i''} = -\frac{\overline{\rho' u_i'}}{\overline{\rho}}$.

The turbulent kinetic energy is defined as

$$TKE = \frac{(u')^2 + (v')^2 + (w')^2}{2} \tag{126}$$

Assuming the w-component turbulence intensity is the same order as the v-component, the above equation can found using

$$TKE = \frac{(u')^2}{2} + (v')^2 \tag{127}$$

[39] where u' and v' are found using a two component LDV system. The compressible turbulent kinetic energy is defined as [14]

$$TKE = \frac{(\rho u)'^2 + (\rho v)'^2 + (\rho w)'^2}{2} \tag{128}$$

The mean and fluctuating Mach numbers can be found using

$$\overline{M} = \left[\frac{2\overline{Q}^2}{2\gamma R\overline{T_o} - \overline{Q}^2(\gamma - 1)}\right]^{\frac{1}{2}} \tag{129}$$

and

$$\overline{(M')^2} = \overline{M}\frac{\overline{(Q')}^2}{\overline{Q}}\left[1 + \frac{\gamma - 1}{2}\overline{M}^2\right] \tag{130}$$

respectively [39], where $\overline{Q} \equiv \sqrt{\overline{u}^2 + \overline{v}^2 + \overline{(v')^2}}$ and $\overline{(Q')}^2 \approx (u')^2$.

4.2.3 Combined Analysis

The LDV and cross-wire data can be combined to give direct measurement of the mean Favre velocity fluctuations for thin-layer flow ($\overline{v}/\overline{u} \ll 1.0$) [12]. Combining Equation (34) from Chapter 2 and Equations (90) and (96) gives

$$\frac{\overline{\rho' v'}}{\overline{\rho u}} = -\frac{\overline{v''}}{U} = \frac{\overline{u'v'}}{\overline{u}^2} - \frac{\overline{(\rho u)'(\rho v)'}}{(\overline{\rho u})^2} \tag{131}$$

So, the mean traverse Favre velocity fluctuation can be found indicating the magnitude of the compressibility terms found in the Reynolds shear stress. Additionally, the LDV and cross-wire mean flow data can be combined to estimate the mean density:

$$\overline{\rho} = \frac{\overline{\rho u}}{\overline{u}} - \frac{\overline{\rho' u'}}{\overline{u}} \tag{132}$$

The second-order turbulence correlation terms on the right-hand side of the above equation have been neglected.

4.2.4 High-Frequency Hot-Film Analysis

The high-frequency data collected by the DANTEC Streamline and Nicolet systems was reduced using both discrete Fourier transform and correlation analysis

4.2.4.1 Energy Spectra Analysis

The TSI 1218-20 normal-film probe was used to collect high-frequency boundary layer data. The hot-film probe was run by the DANTEC Streamline system while the hot-film voltage data was recorded by the Nicolet Multipro system. The Nicolet collected 250,000 samples at a frequency of 1Mhz for 0.25 seconds. The data was broken into 23 blocks and reduced using the discrete Fourier transform (DFT) [48] given by

$$V(f) = \frac{1}{N} \sum_{N} V(t)\, e^{-\frac{2\pi i f t}{N}} \tag{133}$$

where N is the 10,869 samples. The results of the DFT process for each of the 23 blocks was averaged with the final results given in the following form

$$\left[\frac{(\rho u)'(f)}{(\rho u)'_{rms}}\right]^2 = \left[\frac{V'(f)}{V'_{rms}}\right]^2 \tag{134}$$

4.2.4.2 Correlation Analysis

The normal-film probe voltage data from above was also autocorrelated using

$$R_E(\tau) = \frac{\rho u'(t)\rho u'(t+\tau)}{\overline{(\rho u)'^2}} \tag{135}$$

[17]. The microscale (λ) and integral scale (Λ) were found using the normalized autocorrelated normal-film data. The microscale was found by fitting the first few points of the autocorrelation function with an "osculating" parabola and locating the parabola's positive y-intercept. The integral scale was found by integrating the area under the autocorrelation function from $\tau = 0$ to ∞.

The parallel-film probe was also connected to the DANTEC and Nicolet systems and used to collect high-frequency boundary layer information. The Nicolet collected 128k samples from each of the two, parallel, hot-film sensors at a 1Mhz rate. The data from the two sensors were cross-correlated using

$$R_E(\tau) = \frac{[\rho u'(t)]_1 [\rho u'(t+\tau)]_2}{\overline{(\rho u)'^2}} \tag{136}$$

The structure angle associated with a large-scale motion can be determined from the time delay between signals (τ), the mean streamwise velocity ($\bar{u}$), and the wire separation distance (w) using the following equation.

$$\theta = \tan^{-1}\left(\frac{w}{\bar{u}\tau}\right) \tag{137}$$

with θ being the structure angle.

Chapter 5 - Numerical Methods

This chapter outlines the details of the CFD code used in this study. The first section presents the details of the code including the equations solved and the solution method. Following the details of the CFD code, the algebraic turbulence models are discussed. Finally, a description of turbulence model enhancements to include surface roughness is covered.

5.1 Computational Fluid Dynamics Code

The code used to predict the smooth plate boundary layer profile was a two-dimensional, Cell centered, Finite Volume, Parabolized, Navier-Stokes Solver (or CFVPNS) written by Bowersox [6] and modified for this application. The code uses a space marching scheme to solve the Navier-Stokes equations in parabolic form and reaches a steady state solution on a plane by driving the residuals to zero using a four stage Runge-Kutta time integration technique. In the marching direction a full flux algorithm is used and in the transverse plane, a Roe's flux differencing scheme is used

5.1.1 Navier-Stokes Equations

The CFVPNS code solves a simplified version of the Navier-Stokes equations using finite volume discretization. The first section of Chapter 2 gives the conservative, differential form of the Navier-Stokes equations, which are shown here in integral form

$$\frac{d}{dt}\int_{Vol} Q dVol + \int_{Surf}\left(\overrightarrow{F} - \overrightarrow{F}_v\right)\cdot\hat{n}dSurf = 0 \tag{138}$$

where

$$Q = \begin{pmatrix} \rho \\ \rho u \\ \rho v \\ \rho e_o \end{pmatrix} \quad \overrightarrow{F} = \begin{pmatrix} \rho u \\ \rho u^2 + p \\ \rho uv \\ \rho u h_o \end{pmatrix}\hat{j} + \begin{pmatrix} \rho v \\ \rho uv \\ \rho v^2 + p \\ \rho v h_o \end{pmatrix}\hat{k}$$

$$\overrightarrow{F}_v = \begin{pmatrix} 0 \\ \tau_{xx} \\ \tau_{xy} \\ u\tau_{xx} + v\tau_{xy} - \dot{q}_x \end{pmatrix} \widehat{j} + \begin{pmatrix} 0 \\ \tau_{xy} \\ \tau_{yy} \\ u\tau_{xy} + v\tau_{yy} - \dot{q}_y \end{pmatrix} \widehat{k} \tag{139}$$

The laminar shear stresses and heat fluxes are given as

$$\begin{aligned} \tau_{xx} &= \tfrac{2}{3}\mu\left(2\tfrac{\partial u}{\partial x} - \tfrac{\partial v}{\partial y}\right) \\ \tau_{yy} &= \tfrac{2}{3}\mu\left(2\tfrac{\partial v}{\partial y} - \tfrac{\partial u}{\partial x}\right) \\ \tau_{xy} &= \mu\left(\tfrac{\partial u}{\partial y} + \tfrac{\partial v}{\partial x}\right) \\ \dot{q}_x &= -k\tfrac{\partial T}{\partial x} \\ \dot{q}_y &= -k\tfrac{\partial T}{\partial y} \end{aligned} \tag{140}$$

Sutherland's formula is used for the laminar coefficient of viscosity, given by

$$\mu = C_1 \frac{T^{\frac{2}{3}}}{T + C_2} \tag{141}$$

where the coefficients are $C_1 = 1.458 \cdot 10^{-6}\ kg/msK^{\frac{1}{2}}$ and $C_2 = 110.4$ K. The thermal conductivity, k, is calculated assuming the Prandtl number is equal to 0.72 for air.

5.1.2 Non-Dimensionalization

The use of dimensional analysis has long been a useful tool in understanding the dominant terms in a system of equations and identifying useful simplifying assumptions. The governing equations shown in (138) and (139) are non-dimensionalized using the following scales

$$\begin{aligned} t^* &= \tfrac{t}{L_{ref}/V_{ref}} & (x^*, y^*, z^*) &= \tfrac{(x,y,z)}{L_{ref}} & u^* &= \tfrac{u}{V_{ref}} \\ p^* &= \tfrac{p}{\rho_{ref} V_{ref}^2} & T &= \tfrac{T}{T_{ref}} & \rho^* &= \tfrac{\rho}{\rho_{ref}} \\ e_o^* &= \tfrac{e_o}{V_{ref}^2} & h_o^* &= \tfrac{h_o}{V_{ref}^2} \end{aligned} \tag{142}$$

The reference values for density, ρ_{ref}, temperature, T_{ref}, velocity, V_{ref}, and length, L_{ref} are inputs to the CFVPNS program. If the following choices

$$R_{ref} = \frac{V_{ref}^2}{T_{ref}} \qquad \mu_{ref} = \rho_{ref} L_{ref} V_{ref} \qquad k_{ref} = \mu_{ref} R_{ref} \tag{143}$$

are made then the non-dimensional form of the equations have the same form as equation (138) and the calculations are dimensional if $\rho_{ref} = T_{ref} = V_{ref} = L_{ref} = 1$ (e.g., the reference Reynolds number is one).

5.1.3 Finite Volume Discretization and Generalized Coordinates

The CFD code was written to solve a system of equations in a generalized or computational coordinate system. The physical coordinate system of the problem (often Cartesian or spherical coordinates) is mapped into the computational coordinate system, the solution found and mapped back into the physical system. In this way the CFD code can be written and optimized for one coordinate system and used for a wide range of real world problems. For the CFVPNS code, the physical domain is discretized as shown in Figure 22, (x, y) are Cartesian coordinates and (ξ, η) are the generalized coordinates.

Now that the equations are non-dimensionalized the volume averaged state or $\overline{Q}$ vector is given as

$$\overline{Q} = \frac{1}{Vol} \int_{Vol} Q dVol \tag{144}$$

where the cell volume is found using a two-dimensional quadrilateral (times one for the third dimension)

$$\begin{aligned} vol(j,k) &= SurfaceArea \cdot 1 = \tfrac{1}{2} \left| \overrightarrow{a}_1 \times \overrightarrow{a}_2 \right| \\ &= \tfrac{1}{2} \left[(x_{j+1,k+1} - x_{j,k}) (y_{j,k+1} - y_{j+1,k}) - (x_{j,k+1} - x_{j+1,k}) (y_{j+1,k+1} - y_{j,k}) \right] \end{aligned} \tag{145}$$

Thus equation (138) for the (j, k) control volume becomes

$$\frac{\overline{dQ_{j,k}}}{dt_v} + \int_{j-\frac{1}{2}} \left(\overrightarrow{F} - \overrightarrow{F}_v\right) \cdot \hat{n}_{j-\frac{1}{2}} ds_{j-\frac{1}{2}} + \int_{j+\frac{1}{2}} \left(\overrightarrow{F} - \overrightarrow{F}_v\right) \cdot \hat{n}_{j+\frac{1}{2}} ds_{j+\frac{1}{2}}$$

$$+ \int_{k-\frac{1}{2}} \left(\overrightarrow{F} - \overrightarrow{F}_v\right) \cdot \hat{n}_{k-\frac{1}{2}} ds_{k-\frac{1}{2}} + \int_{k+\frac{1}{2}} \left(\overrightarrow{F} - \overrightarrow{F}_v\right) \cdot \hat{n}_{k+\frac{1}{2}} ds_{k+\frac{1}{2}} = 0 \tag{146}$$

where $t_v = \frac{t}{\text{Cell Volume}}$ and $\hat{n}_{\#-\frac{1}{2}}$ is the normal vector to the $\# - \frac{1}{2}$ surface. Rewriting the flux integrals (assuming the flux surface is a line in the (x, y) plane) gives

$$\frac{\overline{dQ_{j,k}}}{dt_v} + \left(\hat{f} - \hat{f}_v\right)_{j+\frac{1}{2}} \Delta s_{j+\frac{1}{2}} + \left(\hat{f} - \hat{f}_v\right)_{j-\frac{1}{2}} \Delta s_{j-\frac{1}{2}}$$

$$+ \left(\hat{g} - \hat{g}_v\right)_{k+\frac{1}{2}} \Delta s_{k+\frac{1}{2}} + \left(\hat{g} - \hat{g}_v\right)_{k-\frac{1}{2}} \Delta s_{k-\frac{1}{2}} = 0 \tag{147}$$

where

$$\begin{aligned} \hat{f} &= \hat{\xi}_x f + \hat{\xi}_y g \\ \hat{f}_v &= \hat{\xi}_x f_v + \hat{\xi}_y g_v \\ g &= \eta_x f + \eta_y g \\ \hat{g}_v &= \hat{\eta}_x f_v + \hat{\eta}_y g_v \end{aligned} \tag{148}$$

Note: f and g are the $\hat{j}$ and $\hat{k}$ components of the flux vector $\overrightarrow{F}$, respectively and f_v and g_v are the $\hat{j}$ and $\hat{k}$ components of the viscous flux vector $\overrightarrow{F_v}$, respectively.

Solving for equations (147) and (148) can be computationally expensive. For many problems, the viscous terms in the streamwise direction are negligible compared to those terms in the transverse plane. For this case, we can drop the streamwise viscous terms, $\hat{f}_v$, and neglect the streamwise gradient terms in the evaluation of the heat fluxes and shear stresses in the $\hat{g}_v$ formulation. Now, if the flow is steady and supersonic, the solution can be marched in the streamwise direction. The space marching of the solution works for a hyperbolic system of equations. For this reason a modification to the equations must be made to account for elliptic effects caused by subsonic portions of the

boundary layer (this code uses the Vigneron technique [3]). For the above simplifying assumptions, equation (147) becomes

$$\frac{d\overline{Q_{j,k}}}{dt_v} = -R_{j,k} \tag{149}$$

where $R_{j,k}$ is called the residual, and for the present discretization is given by

$$R_{j,k} = \hat{f}_{j+\frac{1}{2}}\Delta s_{j+\frac{1}{2}} + \hat{f}_{j-\frac{1}{2}}\Delta s_{j-\frac{1}{2}} + \hat{g}_{k+\frac{1}{2}}\Delta s_{k+\frac{1}{2}} - \hat{g}_{v_{k+\frac{1}{2}}}\Delta s_{k+\frac{1}{2}} + \hat{g}_{k-\frac{1}{2}}\Delta s_{k-\frac{1}{2}} - \hat{g}_{v_{k-\frac{1}{2}}}\Delta s_{k-\frac{1}{2}} \tag{150}$$

where the flux vector is given in equation (139), the pressure term in f and g; however, is multiplied by the Vigneron factor, ω, given by

$$\omega = \frac{\sigma\gamma M_\xi^2}{1 + (\gamma - 1) M_\xi^2} \tag{151}$$

The safety factor, σ, is hard coded to 0.95.

By discretizing the right-hand-side of equation (149), the system reduces to a first order ODE in time. To time integrate the semi-discrete equation, the CFVPNS code uses a four stage Runge-Kutta technique until a steady-state solution is achieved by driving the L_2 norm of the residual down to a specified tolerance (usually 10^{-3}). Since CFVPNS is a space marching code, a fully upwind flux evaluation algorithm is used to evaluated the streamwise flux vectors (f), i.e.,

$$\hat{f}_{j+\frac{1}{2}} = \hat{f}\left(q_{j+\frac{1}{2}}\right) \tag{152}$$

where q is the state vector converted to primitive variables. The full flux interpolation is given by

$$q_{j+\frac{1}{2}} = q_{j,k} + \frac{\phi}{2}\left(q_{j,k} - q_{j-1,k}\right) \tag{153}$$

The algorithm is first order if ϕ is equal to zero and second order if ϕ is equal to one.

To compute the $\hat{g}$ flux components, a Roe flux difference splitting scheme is used. The interpolated q vectors are found using an upwind biased $\phi - \kappa$ formulation given by

$$\begin{aligned} q^-_{k\pm\frac{1}{2}} &= \left[I + \tfrac{\phi}{4}\left[(\kappa+1)\Delta + (1-\kappa)\nabla\right]\right] q_{\substack{k \\ k-1}} \\ q^+_{k\pm\frac{1}{2}} &= \left[I - \tfrac{\phi}{4}\left[(1-\kappa)\Delta + (\kappa+1)\nabla\right]\right] q_{\substack{k+1 \\ k}} \end{aligned} \tag{154}$$

where

$$\Delta q_k = q_{k+1} - q_k \quad \text{and} \quad \nabla q_k = q_k - q_{k-1} \tag{155}$$

and the state vector $q_{k\pm\frac{1}{2}}$ is found using

$$q_{k+\frac{1}{2}} = \frac{1}{2}\left[q^-_{k+\frac{1}{2}} + q^+_{k+\frac{1}{2}} - ([[q]]_1 + [[q]]_2 + [[q]]_3)\right] \tag{156}$$

with $[[q]]_1$, $[[q]]_2$, and $[[q]]_3$ found from the characteristic waves (see Reference [64])

To compute the transverse gradients required to represent $\hat{g}_v$, a second order central difference is used. The q vector is geometrically averaged to the cell faces by linear interpolation, in order to evaluate the central differences. The interpolation for the q vector at the cell face is given by

$$q_{face} = \frac{\Delta y_a}{\Delta y_a + \Delta y_b} q_b + \frac{\Delta y_a}{\Delta y_a + \Delta y_b} q_a \tag{157}$$

or rewritten in terms of the grid shown in Figure (22)

$$q_{j,k+\frac{1}{2}} = \frac{\overline{\Delta y_{j,k-1}}}{\Delta y_{j,k-1} + \Delta y_{j,k}} q_{j,k+1} + \frac{\overline{\Delta y_{j,k}}}{\Delta y_{j,k-1} + \Delta y_{j,k}} q_{j,k} \tag{158}$$

where the over bars indicate averaging of the $j - \frac{1}{2}$ and $j + \frac{1}{2}$ Δy's. To allow the grid to be nonuniform, the second order central difference algorithm is actually coded as

$$\frac{\partial q}{\partial y}\Big|_{j,k-\frac{1}{2}} = \frac{q_{j,k+\frac{1}{2}} - q_{j,k-\frac{1}{2}}}{\Delta y_{j,k}} - \left[\frac{\theta q_{j,k-\frac{1}{2}} - (1-\theta)\, q_{j,k+\frac{1}{2}} + q_{j,k+\frac{3}{2}}}{\theta\,(1+\theta)\,\Delta y_{j,k}}\right] \tag{159}$$

where the θ term accounts for variable grid spacing ($\theta \equiv \frac{\Delta y_{k+1}}{\Delta y_k}$). Finally, the x gradients are evaluated using a first order upwind scheme given by

$$\frac{\partial q}{\partial x} = \frac{q_j - q_{j-1}}{\Delta x} \tag{160}$$

5.1.4 Current Turbulence Model

The CFVPNS code currently uses two algebraic turbulence models to compute the turbulent transport parameters. They are the Prandtl mixing-length and CAMMLE turbulence models. Both the Prandtl mixing-length and CAMMLE models use a mixing length term described in the inner

region as

$$l_m = \kappa y \left[1 - e^{\frac{y^+}{A^+}}\right] \tag{161}$$

where $A^+ = 26$, $\kappa = 0.4$, and $\left[1 - e^{\frac{y^+}{A^+}}\right]$ is the Van Driest damping factor. The inner region normalized y variable is

$$y^+ = \frac{yu^*}{\upsilon} \tag{162}$$

where u^* is the friction velocity.

Rotta (extracted from [16]) noted the velocity profiles of smooth and rough wall boundary layer flows were similar if the coordinates of the rough walls were displaced. Adding an additional Δy to the mixing length inner region term is a simple way to account for the velocity profile displacement. Using Rotta's model the new inner region mixing length becomes

$$l_m = \kappa (y + \Delta y) \left[1 - e^{\frac{(y+\Delta y)^+}{A^+}}\right] \tag{163}$$

with Δy given by

$$\Delta y = 0.9 \left(\frac{\nu}{u^*}\right) \left[\sqrt{k_s^+} - k_s^+ e^{\frac{-k_s^+}{6}}\right] \tag{164}$$

which is valid for an equivalent sand-grain roughness range from $4.535 < k_s^+ < 2000$ (extracted from [16]).

As discussed in the next section, the CFD code was started at the nozzle throat and marched to the test location, 81.785 cm from the nozzle throat and 53.975 cm from the nozzle exit. For the smooth plate, Δy was set to zero. For the five rough plates, the first thirty-three x-axis, wall bounded stations, Δy was set to zero, corresponding with the smooth nozzle floor. After the thirty-third station, Δy was calculated based on Equation (164). To fully simulate the flow, k_s was set to a constant, with k_s^+ calculated for each station. Because the boundary layer height grows and the friction velocity changes as the solution is marched downstream, k_s^+ decreases along the plate in the flow direction.

Another concern regarding the roughness modification to the inner region mixing length is the proper calculation of the friction velocity. The traditional wall shear stress is calculated using

$$\tau_w = \mu \frac{\partial u}{\partial y} |_{y=0} \tag{165}$$

for smooth plate flow. For the rough wall case this equation no longer holds, because the shear stress at the wall is composed of two components, the shear at the wall and the form drag due to the roughness elements protruding into the boundary layer flow. In addition, the "true" location of the wall (i.e., where $y = 0$) may not be exact. Some rough surface turbulence models calculate the wall shear stress based on flow conditions a distance away from the wall [16]. For this study, the rough surface wall shear stress was calculated from the momentum integral equation.

For the rough wall case, the wall shear stress and friction velocity were calculated based on the zero pressure gradient momentum integral equation given by

$$\frac{C_f}{2} = \frac{d\theta}{dx} \tag{166}$$

and the definition of the skin friction coefficient

$$C_f \equiv \frac{\tau_w}{\frac{1}{2}\rho_\infty u_\infty^2} \tag{167}$$

Using the above two equations, the wall shear stress and friction velocity become

$$\tau_w = \rho_\infty u_\infty^2 \frac{d\theta}{dx} \tag{168}$$

and

$$u^* = \sqrt{\frac{\tau_w}{\rho_w}} = \sqrt{\frac{\rho_\infty u_\infty^2}{\rho_w} \frac{d\theta}{dx}} \tag{169}$$

respectively. The momentum thickness gradient, $\frac{d\theta}{dx}$, was calculated using

$$\left(\frac{d\theta}{dx}\right)_j = \frac{\theta_j - \theta_{j-1}}{\Delta x} \tag{170}$$

Since the solution to the $j^{th} - 1$ station was used for the initial j^{th} solution, the momentum thickness gradient was set to the $j^{th} - 1$ value until more than 200 iterations of the new station velocity profile had been calculated along with the corresponding momentum thickness.

5.2 Grid Convergence, Initial Conditions, and Boundary Conditions

5.2.1 Grid Convergence

To simulate the conditions over smooth versus rough plates, a grid, consisting of 101 by 201 points, was generated using GridGen. Along the downstream or x-axis, 101 points were evenly spaced from 0.000 to 81.785 cm with the measurement test location at station 100. The CFD grid includes the nozzle and test section length with station 100 located 80.975 cm from the nozzle throat and the nozzle length being 27.000 cm. Along the y-axis, the grid consisted of 201 points distributed using a hyperbolic tangent function to provide tighter grid spacing near the wall boundary where the boundary layer gradients were the largest. The first y-axis grid point was set at the wall (i.e., $y = 0$) with the second grid point at $y = 5.0 \cdot 10^{-6}$ m corresponding to a y^+ value of between 0.8 and 1.5 depending on the surface roughness. The final y-axis grid spacing was at 10.000 cm above the tunnel floor. A discussion on grid convergence and flat plate turbulence model validation can be found in Appendix D. *Numerical Validation Methods*.

5.2.2 Initial Conditions

The initial conditions for the CFD code consisted of two parts, the code variables values and the flow input conditions. The code variables were made up of the Courant, Fredrichs, and Lewy (CFL) number, the full flux algorithm order, the Roe flux ϕ and κ, and the Situ number (see Section 2.2.4). For the Prandtl mixing-length and CAMMLE models the CFL number was initially set to 0.3. The second order full flux algorithm was used with ϕ being set to 1.0 and κ being set to $\frac{1}{3}$. The Situ number was set to $1 \cdot 10^{10}$ for the standard Prandtl model and 1 for the CAMMLE model. Two code modifications were made to improve the CFD code robustness and shorten the run times. The two modifications made were to make the CFL number adaptable and to fix the boundary layer edge location after the residual had been decreased to an acceptable level. The first modification checked

the residual every fifty iterations. If the residual increased over the fifty iterations, the CFL number was decreased by 20% with a minimum possible CFL of 0.05. The second modification was to stop the boundary layer edge hunting between two adjacent grid points. Essentially, the boundary layer edge was fixed once the residual was driven below $1 \cdot 10^{-2}$.

The initial CFD flow conditions consisted of the Mach number, reference density, reference temperature, wall temperature, and equivalent sand-grain roughness (if applicable). The freestream flow conditions measured using the Pitot pressure probe were used for the initial flow conditions. Table 4 gives each of the above values for each of the six tunnel floor plates.

5.2.3 Boundary Conditions

Since this flow was supersonic, three boundary conditions have to be specified, they are the 0^{th} station inflow conditions, the upper grid location, and the wall boundary. The inflow boundary conditions in nondimensional form are

$$\begin{aligned} \rho &= \frac{\rho}{\rho_{ref}} = 1 & p &= \frac{p}{\rho_{ref} u_{ref}^2} = \frac{1}{\gamma} \\ u &= \frac{u}{u_{ref}} = Mach & v &= \frac{v}{u_{ref}} = 0 \end{aligned} \tag{171}$$

where ρ_{ref}, u_{ref}, and $Mach$ are provided from the initial conditions. The upper-wall boundary conditions were extrapolated using

$$\Phi_{j,k\,\mathrm{dim}+1} = \Phi_{j,k\,\mathrm{dim}} + \frac{\Phi_{j,k\,\mathrm{dim}-1} - \Phi_{j,k\,\mathrm{dim}}}{2} \tag{172}$$

where Φ is an arbitrary mean flow variable. Finally, the wall boundary condition used was a no slip, adiabatic wall. For the no slip (and impermeable) condition, $u = 0$ and $v = 0$ and for the adiabatic wall, $\frac{\partial T}{\partial n} = 0$.

Chapter 6 - Experimental Results

Recall that the main objective of this study is to provide insight into the physics of high-speed rough wall turbulent boundary layer flow. To this end, a large and varied array of carefully selected experimental measurements have been made. The first two sections in this chapter present the results and detailed analyses for each of the individual measurement techniques. The *Mean Flow Data* section presents the mean data acquired from the color schlieren images, Pitot, Laser Doppler Velocimetry (LDV), and Hot-Wire Anemometry (HWA) measurements. While the *Turbulent Flow Data* section presents the turbulent data acquired from the Laser Sheet Images (LSI), LDV and HWA measurements. Finally, the last section (*Empirical Flowfield Description*) presents a brief overview of the overall influence of surface roughness on the turbulent boundary layer flowfield and their implications. The purpose of the last section is to assimilate the empirical information in Sections 6.1 and 6.2 into a manageable description of the salient flow properties. The implications towards modeling are also highlighted.

The flow conditions for each experiment are briefly discussed below and tabulated in Table 5. The detailed error analysis associated for each measurement is given in Appendix C.

6.1 Mean Flow Data

This section presents the color schlieren flow visualizations, and mean flow Pitot pressure, velocity, Mach, density, and mass flux profiles for each of the six models at $x = 53.975\ cm$. Where appropriate, duplicate information from separate experiments has been grouped together for comparison.

6.1.1 Flow Visualization

Schlieren photographs provide qualitative information regarding flow structures and allow a visual comparison of the flow field between each of the six surface models. The information pro-

vided by visualization techniques (e.g., color schlieren) when combined with quantitative experimental data gives a more complete picture of the flow field characteristics. For this study, color schlieren photographs were taken at two locations in the test section. The first or upstream location was 4.285 cm downstream of the nozzle exit near the beginning of the rough floor, and the second was at the test location, 53.975 cm downstream of the nozzle exit. For all color schlieren photographs, the tunnel was operated at a stagnation pressure of $2.17 \cdot 10^5 \pm 0.4\%$ Pa and a stagnation temperature of 296 ± 1.0 K (see Table 5).

At the nozzle exit, both horizontal and vertical knife edge color schlieren photographs were taken. The horizontal knife edge photographs for the six models are shown in Figures 23 through 28. While the vertical knife edge photographs are shown in Figures 29 through 34. For this setup, a horizontal knife edge responds to $\frac{\partial \rho}{\partial y}$ and a vertical knife edge responds to $\frac{\partial \rho}{\partial x}$.

The flow features noticeable in the nozzle exit horizontal knife edge schlieren images (Figures 23 through 28) include wall surface boundary layers (both lower and upper surfaces), nozzle/test section seam generated waves, surface roughness generated waves, a mirror aberration, and nozzle characteristic waves. All horizontal knife edge images show a red lower wall boundary layer and a blue upper wall boundary layer with the flow moving from right to left. With the vertical direction being specified by the y-axis and the origin located at the lower surface, the lower wall boundary layer has increasing density in the positive y direction. So a positive density gradient, $\frac{\partial \rho}{\partial y}$, in this photograph appears red and a negative density gradient appears blue. As a check, the upper surface has increasing density going from the wall surface to the freestream, which is in the negative y direction giving a negative density gradient.

Also seen in the nozzle exit horizontal knife edge images is the nozzle/test section seam interface which generated two weak waves that propagate downstream. Depending on the seam alignment the wave could have been a compression or expansion. If the seam had the downstream edge

protruding into the flow, the wave would have been a compression. Conversely, if the seam had the downstream edge below the upstream edge, the wave would have been an expansion wave. The seam wave angle measured between 20.0^o and 22.0^o in all of the nozzle exit photographs, with an average of 21.3^o. The Mach angle for the $M = 2.88$ nozzle is 20.3^o; thus, these waves were very weak (almost infinitesimal).

For all rough surface models, except for the 2D plate, waves were generated due to individual roughness elements protruding into the supersonic portion of the boundary layer. The cause of the roughness generated waves were attributed to two aspects of the surface roughness geometry; the maximum and mean roughness height. For example, consider the 20 grit sandpaper model. Since the tops of the surface roughness models were aligned with the nozzle exit floor, the bottom of the 20 grit sandpaper model was 1.65 mm below the nozzle exit floor (see Table 3). Assuming the frontal area of the protruding roughness elements to be equal to the mean roughness height times the test section width, the flow exiting the nozzle experienced an effective area increase of 0.827 mm (per unit width). The flow leaving the nozzle exit expanded into this region, and compression waves were generated when the flow met a roughness element protruding into the supersonic portion of the boundary layer. How high the roughness element protruded into the flow is a function of the maximum roughness height. As indicated in Figures 23 through 28, these waves appeared for all of the sandpaper generated surface roughnesses with increasing intensity as the surface roughness increased (both mean and maximum height). All of the waves generated by the sandpaper models had an impact on the boundary layer and freestream since they distorted the boundary layer edge and were clearly visible in the freestream.

For the uniformly distributed 3D roughness model, weak surface roughness waves were generated by the 3D roughness elements (see Figure 25). Though both machined roughness element models had the identical maximum roughness height of 559 μm, the 2D roughness elements spanned

the entire test section width, while the 3D roughness elements were spaced with a wave length of $\lambda = 2.18\ mm$ (see Figure 6) in the traverse direction. Here, the flow exiting the nozzle experienced an effective area increase of $0.416\ mm$ (per unit width) in which the flow expanded after the nozzle exit. The effective area increase of the 3D plate, and the 80 and 36 grit plates were similar (see Table 3); however, the 3D plates maximum roughness was 53% of the 80 grit plate height and 40% of the 36 grit plate height. Thus, waves generated by the 3D plate surface roughness elements were considerably weaker and had a smaller effect on the freestream flow.

The 2D machined roughness plate did not create an effective area increase at the nozzle exit/test section interface. As indicated in Figure 24, the 2D plate roughness elements did not appear to generate compression or expansion waves. One reason for this is that the roughness elements did not protrude into the supersonic portion of the boundary layer. Furthermore, the spacing of the 2D plate roughness elements (see Figure 5) may have been too close for supersonic flow to "dip" into the cavity, and thus create a noticeable wave structure. The 2D plate has a λ/k ratio of 3.9 which is referred to as a "d-type" roughness, rather than a "k-type" roughness as described in references [4, 37, 46]. Perry et al. [46] remark that, for a "d-type" rough-wall, "the outer flow rides relatively undisturbed over the crests of the elements." With the transition between "d-type" and "k-type" roughness at around $\lambda/k \sim 4$, the 2D plate exhibited flow characteristics of both types of roughness elements.

Two nonuniformities could also be seen in the color schlieren photographs. The first was a circular mirror aberration which appeared in all photographs, and the second was the nozzle characteristics that appeared in the nozzle exit photographs. The wave coming from the nozzle exit upper surface consisted of a red-than-blue-than-red region (going from right to left). These, again, very weak waves were the result of imperfect cancellation of the nozzle characteristics. As with the seam

waves, the influence of these waves on the present study was infinitesimal. In fact, these waves were so weak that present modern instrumentation (e.g., LDV) could not detect their disturbances.

The significant flow features (e.g., the boundary layer and impact of surface roughness generated waves) identified in the horizontal knife edge, nozzle exit schlieren photographs could also be seen in the vertical knife edge photographs shown in Figures 29 through 34. The boundary layer/freestream edge appeared as a dark red horizontal line for each of the six models. This was due to the mixing of swirls or eddies of various densities in the boundary layer/freestream edge. The vertical knife edge, nozzle exit schlieren photographs also showed the surface roughness generated waves. The 3D plate surface generated waves were more easily identified in Figure 31 than the horizontal knife edge image.

The test location, color schlieren, horizontal knife edge images are shown in Figures 35 through 40. Roughness generated waves were no longer visible. This is due to the growth of the boundary layer, where at this station the roughness elements no longer protruded into the supersonic region of the boundary layer. The boundary layer edge determination was complicated by the size of the boundary layer itself. The density change from the tunnel wall (governed by the wall temperature) and the freestream (governed by the freestream temperature) had remained relatively constant and the boundary layer height had increased. Thus, the density change had been spread out over a larger distance. For this reason, the density gradient in the vertical direction had been greatly reduced from the nozzle exit levels, and the color changes from the boundary layer to the freestream were not as intense. Despite these difficulties, the estimated boundary layer heights for each of the six models based on the color schlieren test location photographs are shown in Table 6 along with the heights calculated from the Pitot probe and LDV experiments. With the static pressure assumed to be constant across the boundary layer, a schlieren photograph shows essentially the thermal boundary layer height, δ_T. The thermal boundary layer height is slightly larger than the velocity boundary

layer. This can be seen by the nondimensional Prandtl number given by

$$\mathrm{Pr} = \frac{c_p \mu}{k} = \frac{\nu}{\alpha} \tag{173}$$

which is a ratio of the momentum and thermal diffusivities in a fluid [33] and is approximately 0.7 for air. For laminar flow, $\frac{\delta_T}{\delta} = \frac{1}{1.03\,\mathrm{Pr}^{1/3}} \simeq 1.09$ [50].

As expected, the boundary layer height was largest for the roughest surface, the 20 grit sandpaper, with the boundary layer height decreasing as the roughness decreases. As indicated in Table 6, as the sandpaper roughness height increased, the boundary layer thickness increased. However, the machined rough plates exemplify the importance of blockage. Both the 2D and 3D surface roughness elements have the same height, but the roughness density or blockage was 3.9 times larger in the 2D plate case, which produced a thicker turbulent boundary layer.

6.1.2 Velocity Profiles

The velocity profiles for each of the six models were measured using Pitot and Laser Doppler Velocimetry (LDV) at the test location with the flow conditions shown in Table 5. The Pitot probe measures the total mean pressure behind a normal shock and is used to provide total pressure information and indirectly, the streamwise Mach number, velocity, density, and mass flux boundary layer profiles. LDV measures (for this case) two components of the mean velocity and indirectly, the streamwise Mach number, density, and mass flux boundary layer profiles. The Pitot and LDV measurement techniques compliment each other providing verification of the mean data, with LDV providing additional turbulence data.

The velocity profiles for the six models are shown in Figures 41 through 43. All velocity profiles are presented with the local velocity and boundary layer height nondimensionalized by the model specific freestream velocity ($\overline{u_e}$) and boundary layer thickness (δ), respectively. Table 6 shows the references velocities, Mach numbers, and boundary layer thicknesses (both δ and δ_M)

for the Pitot and LDV measurements. The freestream velocities measured using the Pitot and LDV methods give identical results with a difference of less than 1% between the two methods.

The velocity profiles estimated from the Pitot data are presented in Figure 41. Also, the data from Goddard [28] for smooth and rough plates at Mach 2.6 and from Fiore [27] for rough plates in hypersonic flow at Mach 5.54 are included for comparison (these velocity data were also estimated using Pitot pressure profiles). The velocity profile results show the expected, based on the incompressible database, smooth versus rough plate differences, with the fully rough profiles collapsing on to a singular curve with a larger velocity defect relative to the smooth plate. The data from Goddard and Fiore agree very well with the present experiments, the slight differences are primarily attributed to reading data from Goddard's figures. The 80 grit Pitot data indicates a slightly smaller defect than the other rough plates. The slightly smaller defect relative to the other rough plates may be a function of the boundary layer height uncertainty and/or the surface roughness height. The 80 grit plate surface roughness Reynolds number was found to be $k_s^+ = 103.9$ which is marginally in the fully-rough regime ($k_s^+ > 70$). Thus, factoring in the aforementioned uncertainties, it is possible that the 80 grit roughness elements are actually transitional.

The LDV velocity profiles are shown in Figure 42. The trend noticed for the Pitot probe data are confirmed by the LDV velocity profiles. Also included in Figure 42 are the smooth wall LDV data from Luker *et al.* [38]. The agreement between this experiment's LDV data and Luker *et al.* smooth plate data is excellent. This agreement shows the consistency of the Mach 2.9 tunnel and LDV equipment, since Luker's data was taken more than two years earlier and at a different downstream location (44.5 *cm* downstream of the nozzle exit versus 53.98 *cm* for this study).

The present Pitot and LDV data are combined in Figure 43, excellent agreement is noted between the two methods, though considerably more scatter was present with the Pitot probe. Since the LDV velocity measurement for the 80 grit plate shows essentially the same velocity defect as the

other rough plates, the above mentioned smaller defect indicated by the Pitot probe measurement is attributed to boundary layer height uncertainty. The nonintrusive nature of the LDV measurement techniques provide very consistent data without the problems associated with Pitot measurements (i.e., Pitot/Wall interference effects, probe vibration, probe cavity response damping, and pressure probe flexing). Though LDV does have challenges with regard to seeding difficulties and density bias. The agreement between the two measurement techniques implies that both techniques are suitable as applied.

To better assess any systematic affects of surface roughness on velocity profiles, a new relative velocity defect profile is defined as

$$\nabla_u \equiv \left(\frac{\overline{u}}{\overline{u_e}}\right)_{smooth} - \left(\frac{\overline{u}}{\overline{u_e}}\right)_{rough} \tag{174}$$

The primary purpose of this parameter is to help identify mean flow quantity differences between the rough surface models; specifically, the effect of surface roughness height and blockage. The new relative velocity defect profiles are shown in Figures 44 and 45. The Pitot relative velocity defect profiles (Figure 44) show considerable scatter with the 80 grit profile showing a smaller relative defect as indicated above. The other roughness model data show no significant trends between surface roughness and the relative velocity defect. The LDV profiles (Figure 45) confirm the absence of a systematic roughness effect. Comparing the Pitot and LDV profiles indicates that any variance in the relative velocity defect profiles can be attributed to scatter and the difficulty in accurately determining the boundary layer height.

6.1.3 Mach Profiles

The Mach profiles for each of the six models were measured using Pitot and LDV techniques at the test location with the flow conditions shown in Table 5. The Mach profiles for the six models are shown in Figure 46. All Mach profiles are presented with the local Mach number and boundary

layer height nondimensionalized by the model specific freestream Mach number ($\overline{M_e}$) and Mach number boundary layer thickness (δ_M), respectively (see Table 6). The freestream Mach number measured using the Pitot probe was $\overline{M_e} = 2.75$ for smooth plate with a decreasing freestream Mach number as surface roughness increases (Table 6 lists the freestream Mach numbers for each plate). The decrease in the freestream Mach number with surface roughness is attributed to the increased boundary layer height for the rough surface models. The freestream Mach number measured using LDV was $\overline{M_e} = 2.80$ for the smooth plate. Again, showing a decrease in freestream Mach number with increasing surface roughness. The freestream Mach number values had a difference of less than 3% between the two measurement techniques, validating the assumptions made in reducing the LDV data to give Mach number.

Since the velocity profiles discussed above are based on the Mach number calculated using the Rayleigh-Pitot formula shown in Equation (73) of Chapter 4, the same trends identified for the Pitot velocity profiles appear in the Mach profiles. The Mach profile results show the smooth versus rough plate differences, with the fully rough profiles collapsing on to a singular curve with a larger Mach defect relative to the smooth plate. Again, the 80 grit Pitot data indicates a slightly smaller Mach number defect than the other rough plates attributed to boundary layer height uncertainties. The LDV Mach profiles are based on the velocity values directly measured by the LDV process and follow the same trends as identified in the velocity profiles. Finally, Figure 46 shows that Pitot and LDV measurement methods provide excellent agreement for the Mach profiles. As with the velocity profiles, the relative Mach number plots (Figures 47 and 48) do not elucidate any systematic roughness effects.

6.1.4 Mass Flux Profiles

The mean mass flux profiles were directly measured using x-y plane and x-z plane cross-film measurements, and estimated with Pitot and LDV measurements. Hot-Wire Anemometry (HWA) is used to relate film sensor voltage to mean and fluctuating mass flux (for compressible flow) over the sensor. Using two types of cross-film probes, the mean mass flux for each flow axis (x, y, and z) was determined. As discussed in Section 3.2.2.3, each of the x-y and x-z probes provide axial (x-direction) data. Hence, direct comparison between the two probe types are possible. The streamwise mass flux for the Pitot and LDV measurements were also estimated by multiplying the density (see Section 6.1.5) and velocity values, and were used to compare with the streamwise mass flux found using hot-film probes. For the x-y plane cross-film probe, the tunnel was operated at a stagnation pressure of $2.17 \cdot 10^5 \pm 0.4\%\ Pa$ and a stagnation temperature of $296 \pm 1.0\ K$ and for the x-z plane cross-film probe, the tunnel was operated at a stagnation pressure of $2.39 \cdot 10^5 \pm 0.3\%$ Pa and a stagnation temperature of $296 \pm 1.0\ K$ (see Table 5).

The streamwise mean mass flux profiles found using the x-y plane cross-film probe are presented in Figure 49. All mean mass flux profiles are presented with the local mass flux and boundary layer height nondimensionalized by the model specific freestream mean mass flux $\left[\overline{(\rho u)_e}\right]$ and boundary layer thickness (δ), respectively. The streamwise mean mass flux profile for each of the five rough plates are virtually identical in the boundary layer with a slight difference in the freestream. The streamwise mean mass flux profile for the smooth plate has a smaller defect in the boundary layer and a slightly larger defect just above the boundary layer. The difference between the smooth plate and rough surface plates are more clear in the relative mass flux defect profiles shown in Figure 50 with the relative mass flux defined as

$$\nabla_{\rho u} = \left(\frac{\overline{\rho u}}{\overline{\rho u_e}}\right)_{smooth} - \left(\frac{\overline{\rho u}}{\overline{\rho u_e}}\right)_{rough} \tag{175}$$

Figure 50 shows that the streamwise mass flux defect for the rough surface models were $4-8\%$ for $y/\delta \leq 0.5$, and decreased toward the boundary layer edge. The 36 grit plate and 20 grit plates bound the streamwise mass flux defect values for all models in the boundary layer indicating surface roughness size variation (assuming all models are fully-rough) does not affect the boundary layer streamwise mean mass flux.

The streamwise mean mass flux profiles found using the x-z plane cross-film probe are presented in Figure 51. The streamwise mean mass flux profiles found using the x-z plane probe show excellent agreement with the x-y plane probe data (as shown in Figure 52) and follow the observations made using the x-y plane probe with a slightly larger degree of scatter. The larger scatter is attributed to the probe geometry in which one film sensor was positioned lower in the boundary layer than the other. The relative mass flux defect profiles shown in Figure 53 again show the same trends as that with the x-z plane probe, with the streamwise mass flux defect to be $2-6\%$ larger than the smooth plate model. With the relative mass flux profiles decreasing and crossing zero in the boundary layer height range of $0.5 < y/\delta < 1.0$. The relative mass flux defect profiles show no discernible trends due to surface roughness size variation.

The mean traverse and span mass flux profiles were also estimated from the two cross-film probes. The cross film mean flow angles given by

$$\theta_{xy} = \tan^{-1}\left(\frac{\overline{\rho v}}{\overline{\rho u}}\right) \quad \text{and} \quad \theta_{xz} = \tan^{-1}\left(\frac{\overline{\rho w}}{\overline{\rho u}}\right)$$

are the for the x-y plane and x-z plane, respectively and are shown in Figures 54 and 55 . The vertical axis of both figures are left nondimensionalized to provide information relative to the tunnel. The x-y plane flow angle profiles for each of the six models appear to have the same general shape. Since the angles are small, relative to the freestream, the mass flux angles are attributed to slight miss-alignment between the probe in the tunnel and possible film angle miss-alignment on the probe itself. This is also true of the x-z plane mean mass flux angle profiles.

6.1.5 Density Profiles

Mean density profiles were estimated using Pitot, LDV, and combined LDV and HWA. The Pitot mean density profiles were estimated using the Crocco-Busemann relation and by the isentropic temperature - Mach relationship combined with the prefect gas relation. The LDV density data was estimated from the Crocco-Busemann relation. Finally, the LDV and HWA data were combined to provide an estimate of the Pitot mean density based on the HWA mean streamwise mass flux and the LDV mean velocity values.

The Pitot mean density profiles for the six models estimated using the Crocco-Busemann relation are shown in Figure 56 and using the isentropic relation, in Figure 57. Since both reduction methods use either the mean velocity or Mach number values to estimate the mean density, the trends identified for the mean velocity and Mach number profiles appear in the two figures. Figure 58 combines the two reduction methods for the Pitot data showing a clear trend. The Crocco-Busemann method gives a slightly higher density ($\sim 3\%$) values near the wall than the isentropic method. While both methods agree extremely well near the freestream. This difference can be attributed to the assumptions made in using the Crocco-Busemann and isentropic methods. With the assumption of an adiabatic wall, the second term on the RHS of Equation (74) becomes zero. For a non-adiabatic wall, the second term is positive giving a larger $\frac{\rho_w}{\overline{\rho}}$ ratio, and hence a smaller $\overline{\rho}$ value as compared to an adiabatic wall. For the isentropic method, the local mean density was determined using the isentropic temperature - Mach relationship and the perfect gas equation, so an adiabatic wall assumption was not necessary.

The mean density profiles estimated using the combined HWA streamwise mean mass flux and LDV mean velocity is shown in Figure 59 along with the Pitot Crocco-Busemann density estimates. The combined HWA and LDV density profiles showed larger density defect throughout the boundary layer with respect to the Pitot profiles with a downward turn in the density defect slope in the

boundary layer height range of approximately $0.2 < y/\delta < 0.7$. The differences between the two methods are within the expected uncertainties listed in Appendix C.

6.1.6 Mean Flow Statistics Summary

Based on the mean flow data collected using color Schlieren, Pitot, LDV and HWA measurement techniques, surfaces roughness has two significant effects on the turbulent boundary layer. First, surface roughness height and blockage had a significant influence on density gradients in the smooth nozzle/rough wall interface region, as evidenced by the compression and expansion waves visible in the nozzle exit horizontal knife edge color schlieren photographs. The compression and expansion waves appeared for all three sand-grain roughened surfaces and for the 3D machined roughness plate. The 2D plate, which had four times the blockage of the 3D plate, showed no visible waves. Second, surface roughness increased the velocity, Mach, mass flux, and density defect profiles with a corresponding increase in the momentum loss across the boundary layer. For all of the rough surface plates (all in the fully rough regime), the defect increase was identical (within experimental scatter) with no discernible influence due to increasing roughness height and blockage.

6.2 Turbulent Flow Data

The turbulent flow data in this section was acquired by Laser Sheet Imaging (LSI), LDV, and Hot-Film anemometry, and is presented in four subsections. The first subsection provides qualitative flow information based on the LSI measurements. The second section contains the first and second order turbulent quantities obtained from LDV and HWA experiments. The third section presents the frequency resolved spectra data collected using the normal-film probe. Finally, the fourth section reviews the correlation data collected from the normal-film and parallel-film measurements.

6.2.1 Visualization

Laser sheet images for the six models are shown in Figures 60 through 65 with the flow moving from right to left and the test location marked. Though statistical values are not obtainable for single images, each image is evaluated for the location of the lowest inviscid penetration and highest turbulent structure with the values shown in Table 7. Also listed in Table 7 is the location of the lowest intermittent structures relative to the highest, showing the region of boundary layer intermittence. The images show the relative heights and turbulence of the boundary layer for each model, with the smooth plate having the smallest boundary layer followed by the 80 grit, 3D, 2D, 36 grit, and 20 grit plates. The boundary layer heights appear consistent with the Pitot and LDV data. For all models, the lowest visible structures begin at approximately 60% of the boundary layer height, except for the 36 grit plate. The 36 grit plate was difficult to interpret because of a low density of seed.

6.2.2 Turbulence Intensities

Velocity and mass flux turbulence intensities were measured using LDV and cross-film measurements. The velocity turbulence intensities were measured using LDV and give an indication of the magnitude of the velocity fluctuations about the mean flow velocity. The velocity turbulence intensities for all six models are shown in Figures 66, 67, and 68. Included in Figures 67 and 68 are smooth plate velocity turbulence intensities profiles from Luker [39]. The agreement between the present smooth plate results and Luker's study was considered excellent ($< 1\%$ difference); with both sets of data showing a freestream turbulence intensity of less than 1%. In addition, the values matched the trend shown by Klebanoff [35], where the v-component turbulence intensity was smaller than the u-component as a result of wall damping.

A significant result of Figures 67 and 68, as indicated by the rough surface turbulence intensity profiles, was that the u- and v-component turbulence intensities generated over rough plates scale by the local u-component mean velocity and boundary layer height. The rough plate velocity intensities were approximately twice the smooth plate rate (beginning from the freestream and moving downward) with the largest u-component velocity turbulence intensities close to 18% versus 9% for the smooth plate case. For the v-component turbulence intensity, the largest rough plate values were approximately 9% versus 4% for the smooth place case.

Even though the rough plate data scaled well with outer flow properties. Some differences in the profiles did exist, to better assess any systematic affects of surface roughness on turbulent quantities, a new relative difference variable was defined as

$$\Delta_\phi \equiv \phi_{rough} - \phi_{smooth} \tag{176}$$

where ϕ is an arbitrary nondimensionalized flow variable. Two types of plots for each flow variable of interest are shown. The first is the relative difference variable profile and the second is the peak relative difference variable plotted versus the roughness Reynolds number (k_s^+). To evaluate terms, such as, velocity turbulence intensities and kinematic Reynolds shear stress, where no identifiable peak value exists (other than at the lowest boundary layer position), the flow variable at $y/\delta = 0.4$ was plotted versus roughness Reynolds number.

The u-component turbulence intensity difference, $\Delta_{u'}$, (scaled by the local mean streamwise velocity) for the five rough surface models is shown in Figure 69. In the near wall region, the turbulence intensity difference increased with increasing surface roughness height shown by the 36 and 20 grit turbulence intensity differences versus the 80 grit value. The 36 and 20 grit sandpaper models gave almost identical values throughout the boundary layer. Increasing surface roughness blockage also increased the turbulence intensity difference as indicated by the larger difference values for the 2D machined plate relative to the 3D plate.

In the outer boundary layer region, the smallest surface roughness models (80 grit and 3D plates) showed a turbulence intensity difference increase, while the large roughness models (36 grit, 20 grit, and 2D plates) showed a decrease. The outer region boundary layer values were very sensitive to the boundary layer height value. If the smooth plate boundary layer height increases slightly, the smooth plate turbulence intensity profile shifts downward and all roughness models will show a positive turbulence intensity difference through out the boundary layer.

As mentioned earlier, the sand-grain roughness models give an indication of how roughness height affects flow variables, and the uniformly distributed surface roughness elements give an indication of how roughness blockage affects flow variables. Figure 71 shows the u- and v-component turbulence intensity difference versus roughness Reynolds number at a boundary layer location of $y/\delta = 0.4$. The sand-grain roughness turbulence intensity difference data points were fit with a logarithmic curve indicating that an increasing roughness height increased the turbulence intensity, though only slightly. The slope of the sand-grain curve fits are shown in Table 8 indicating the rate at which roughness Reynolds number increases turbulence intensity. The rate of increase of turbulence intensity is higher for the v-component rather than the u-component. Comparison of the 3D and 2D roughness model results also show that increasing blockage, increases the turbulence intensity.

The mass flux turbulence intensities measured with cross-film HWA are shown in Figures 72 through 74. Recall, hot-film measurements are based upon the Nusselt number - Reynolds number relationship outlined in Chapter 4. Assuming the heat flux from the wire to the freestream air flow is in equilibrium, the film sensor voltage can be related to the film diameter effective Reynolds number. For incompressible flow, HWA gives velocity information and for compressible flow, mass flux (ρu) information.

The ρu-component of the mass flux turbulence intensity measured by the x-y plane cross-film probe is shown in Figure 72. From the cross-film data, it is apparent that the mass flux turbulence

intensity did not scale by the local mean quantity as was the case for the u- and v-component turbulence intensities measured by LDV. Based on the x-y plane cross-film probe, the mass flux turbulence intensities for each of the six models reach a maximum value at approximately $y/\delta = 0.6-0.8$. The smooth plate ρu-turbulence intensity maximum is approximately 0.12, with the 80 grit plate at 0.15 (a 21% increase), the 3D plate at 0.16 (a 29% increase), the 2D at 0.165 (a 35% increase), the 36 grit at 0.175 (a 43% increase), and the 20 grit at 0.18 (a 49% increase). Unlike the velocity turbulence intensities, the mass flux intensities (including ρu-, ρv-, and ρw-components) do not reach the freestream value near $y/\delta = 1.0$. This is an indication that the thermal boundary layer is thicker than the velocity boundary, since the density fluctuations captured by HWA mass flux turbulence intensities extend beyond the velocity boundary layer thickness given by δ. The cross-film measurements have a freestream ρu-turbulence intensity of approximately $3 - 4\%$ with the freestream value increasing slightly with increasing roughness height and roughness blockage. The higher freestream turbulence intensity values could be the result of the compression and expansion wave effects on the freestream or due to probe resolution.

The ρv-component of the mass flux turbulence intensity measured by the x-y plane cross-film probe is shown in Figure 73. The ρv-turbulence intensity also does not scale by the local mean quantity. The ρv-turbulence intensities for each of the six models reach a maximum value at the lowest probe position in the boundary layer, though the largest roughness height and blockage models (the 20 grit and 2D plates, respectively) begin to show a down turn in the turbulence intensity values near the wall. The smooth plate ρv-turbulence intensity maximum is approximately 0.083, with the 80 grit plate at 0.107 (a 29% increase), the 3D plate at 0.114 (a 37% increase), the 2D at 0.115 (a 39% increase), the 36 grit at 0.132 (a 59% increase), and the 20 grit at 0.132 (a 59% increase).

The ρw-component of the mass flux turbulence intensity measured by the x-z plane cross-film probe is shown in Figure 74. The ρw-turbulence intensity also does not scale by the local mean quantity. The ρw-turbulence intensities for each of the six models reach a maximum value at the lowest probe position, but unlike the ρv-turbulence intensity, the largest roughness height and blockage models (the 20 grit and 2D plates, respectively) do not show a down turn in the turbulence intensity values near the wall. The smooth plate ρw-turbulence intensity maximum is approximately 0.092, with the 80 grit plate at 0.127 (a 39% increase), the 3D plate at 0.144 (a 57% increase), the 2D at 0.155 (a 69% increase), the 36 grit at 0.162 (a 77% increase), and the 20 grit at 0.182 (a 100% increase).

The mass flux turbulence intensity (including ρu-, ρv-, and ρw-components) was scaled by inner variables (wall density and friction velocity) and the results are shown in Figure 75, 76, and 77. As compared to the local quantity scaling, the inner or wall scaling does a better job collapsing the rough surface plate ρu-component results with the mid to lower boundary layer region ($y/\delta > 0.8$) values within 5% of each other. Though the data scales well with the wall density and friction velocity, some systematic differences do occur, which should be expected since the friction velocity represents a momentum loss and not a mass flux loss. Both increasing roughness height and blockage results in increasing ρu-component mass flux intensities scaled by wall quantities. The wall scaling does not collapse the ρv- and ρw-components of the mass flux turbulence intensity.

The ρu-, ρv-, and ρw-component turbulence intensity differences, $\Delta_{(\rho *)'}$, (scaled by the local mean streamwise mass flux) for the five rough surface models are shown in Figures 78, 79, and 80, respectively. All three profiles show increasing mass flux turbulence intensity as a result of surface roughness. The peak mass flux turbulence intensity differences versus roughness Reynolds number are shown in Figure 81. The sand-grain roughness mass flux turbulence intensity difference data points were fit with a line indicating that increasing roughness height, increased the mass flux

turbulence intensity linearly. The 3D and 2D roughness models also show that increasing blockage, increases the turbulence intensity. The largest affect of roughness height and blockage is in the ρw-component, then the ρu-component, and finally, the ρv-component. The ρw-turbulence intensity difference had the largest rate of increase with regard to the roughness Reynolds number with $\frac{d\Delta_{(\rho w)'}}{dk_s^+} = 0.00011$ or $\frac{\%\text{ increase}}{k_s^+} = 0.013$ over the smooth plate case. This may appear as a small slope, however, for the largest roughness height (the 20 grit plate) this is a 100% increase over the smooth plate value. The $\frac{d\Delta_{(\rho w)'}}{dk_s^+}$, $\frac{\%\text{ increase}}{k_s^+}$, and percent increase values for each plate and mass flux turbulence intensity are presented in Table 8. The ρu-turbulence intensity difference is the second largest with a rate of increase of $\frac{d\Delta_{(\rho w)'}}{dk_s^+} = 0.000073$ or $\frac{\%\text{ increase}}{k_s^+} = 0.006$ over the smooth plate case. The ρv-turbulence intensity difference rate of increase is $\frac{\Delta_{(\rho v)'}}{k_s^+} = 0.000056$ or $\frac{\%\text{ increase}}{k_s^+} = 0.003$ over the smooth plate case. The large increase of the ρw-component over the ρv-component is attributed to the wall damping effect for the traverse component not "felt" by the lateral component mass flux turbulence intensity.

6.2.3 Fluctuating Mach Number

The fluctuating Mach number for each of the six models was estimated based on LDV data (see Chapter 4) and shown in Figure 82 along with smooth plate fluctuating Mach data by Luker [39]. The smooth plate fluctuating Mach number measured by Luker is slightly higher than that measured in this experiment by approximately 4% in the boundary layer. As seen in the figure, the fluctuating Mach number for each of the plates was well below one, confirming the lack of turbulence generated local "shocklets." The freestream fluctuating Mach number was $M' \approx 0.06$ with the fluctuating Mach number increasing in the region from $y/\delta = 1.4$ down to 0.6. Below $y/\delta = 0.6$, the fluctuating Mach number remains relatively constant with the magnitude dependent on the roughness height and blockage.

The effect of roughness height and blockage is more clearly seen in Figure 83 which shows the fluctuating Mach number difference, $\Delta_{M'}$, for each of the six models and Figure 84 which shows the fluctuating Mach number difference versus the roughness Reynolds number at $y/\delta = 0.4$. The sand-grain roughness models showed a logarithmic relationship between the fluctuating Mach number difference and roughness Reynolds number (i.e., $\Delta_{M'} \sim A\ln(k_s^+)$ with $A \approx 0.0106$). The 80, 36, and 20 grit plates showed increases of 0.022, 0.036, and 0.040 or 8.2%, 13.3%, and 14.8%, respectively. An increase in roughness blockage or density also increased the fluctuating Mach number. The 3D and 2D roughness plates showed increases of 0.023 and 0.027 or 8.5%, and 10.0%, respectively. The fluctuating Mach number decreased near the beginning of the intermittency region until a freestream fluctuating Mach number of $M' \approx 0.06$ was reached. This general shape is consistent for all models with the exception of the 3D and 80 grit models which have a slightly raised profile attributed to the slightly higher M/M_e values.

6.2.4 Shear Stress

The kinematic Reynolds shear stresses and mass flux shear stresses were found from LDV and cross-film measurements. The kinematic Reynolds shear stress scaled by the square of the local mean streamwise velocity measured using LDV is shown in Figure 85. Flat plate LDA measurements from Luker [39] and cross-wire measurements from Miller [41] are included for comparison. The present smooth plate LDV results overlap with the data collected by Luker and Miller. The smooth plate kinematic Reynolds shear stress reaches a maximum value of approximately 0.002, while the rough surface plates each reach 0.0077, an increase of 285%. As was the case for the velocity turbulence intensities, the kinematic Reynolds shear stress for each roughness model scales by the local mean streamwise velocity. Some scatter occurs among the rough model incompressible Reynolds shear stress profiles. This is attributed to the second order nature of the shear stress

term and the associated larger errors relative to first order turbulent quantities (see Appendix C for uncertainty analysis).

Figure 86 shows the kinematic Reynolds shear stress difference, $\Delta_{u'v'}$, profile for each of the six models, and Figure 87 shows the kinematic Reynolds shear stress difference versus the roughness Reynolds number at $y/\delta = 0.4$. As with the velocity turbulence intensities, also measured using LDV, for fully rough flow, the kinematic Reynolds shear stress remained fairly constant across a large range of roughness Reynolds numbers. The sand-grain roughness models (indicating sensitivity to roughness height) show a logarithmic relationship between the kinematic Reynolds shear stress difference and roughness Reynolds number with a proportion of $\Delta_{u'v'} \sim A\ln(k_s^+)$ with a very small slope of $A \approx 4.8 \cdot 10^{-5}$ (see Table 8). The 2D and 3D roughness followed the trend of the sand-grain roughness models.

The kinematic Reynolds shear stress was also scaled by the wall shear stress and is shown in Figure 88 along with smooth plate LDV measurements from Luker [39] and cross-wire measurements from Miller [41]. The agreement between the three sets of data (present LDV, Luker, and Miller) is consider good with the smooth plate data reaching near 1.0 if extrapolated to the wall. In the outer boundary layer region, the smooth plate data from this study gives slightly higher values for the kinematic Reynolds shear stress than does data from Luker; again the likely cause is boundary layer height uncertainties.

The incompressible Reynolds shear stress measurements for this study were scaled by the wall shear stress found in *Flowfield Analysis* section of this chapter. All profiles tend toward the wall shear stress as expected based on the smooth flat plate relationship [8]

$$\tau_w = \tau_{xy}^T + \mu\frac{\partial \overline{u}}{\partial y} \tag{177}$$

but do not fully reach the expected value of 1.0 at the wall (except the smooth plate case). In the logarithmic region of the boundary layer, $\tau_{xy}^T \gg \mu\frac{\partial \overline{u}}{\partial y}$, so $\tau_{xy}^T \simeq \tau_w$. Typically, the Favre-averaged

shear stress, $-\overline{\rho u'' v''}$, is assumed to be equal to the kinematic Reynolds shear stress term [12]; thus, $\tau_w \simeq -\overline{\rho u' v'}$. The compressibility effects due to roughness may cause the density fluctuation terms of the compressible Reynolds shear stress to be larger. In addition, the wall shear stress found using the momentum loss over the boundary layer length takes into account the form drag of the protruding roughness elements, where the measured $\overline{u'v'}$ term does not. Based on the velocity defect profiles shown in Figures 160 and 162, the wall shear stress values calculated using the integral analysis were deemed accurate. So the difference between τ_w and $\overline{\rho u' v'}\,|_{near\ wall}$ gives an indication of the magnitude of the form drag. The relatively large amount of scatter in a plot such as Figure 88 makes quantifying the form drag very difficult. However, as expected, the two uniformly distributed rough surface plate data indicates that the higher blockage of the 2D plate produced significantly more form drag (50% of τ_w) as compared to the 3D plate (26%). No discernible trend was noticed in the sand-grain roughness plate results.

The kinematic Reynolds shear stress difference, $\Delta_{\rho u' v'}$, (nondimensionalized by the wall shear stress) is shown in Figure 89, and the difference versus the roughness Reynolds number at $y/\delta = 0.4$ is shown in Figure 90. The sand-grain roughness models (indicating sensitivity to roughness height) show a decreasing logarithmic relationship between the kinematic shear stress difference and roughness Reynolds number with a proportion of $\Delta_{\overline{\rho u' v'}} \sim A \ln(k_s^+)$ with $A \approx -0.091 \cdot 10^{-5}$. Indicating that increasing roughness height increases the wall shear stress at a greater rate than the kinematic Reynolds shear stress ($\overline{\rho u' v'}$), since $\overline{u'v'}$ has been shown to be fairly constant over a large range of roughness Reynolds numbers. At $y/\delta = 0.4$, effects of blockage appear to be the opposite of roughness height; however, at $y/\delta = 0.4$, the 2D and 3D plate, $\overline{\rho u' v'}$ values are very close with the 2D plate having a considerably decreased value near the wall (as indicated in Figure 76). So increasing blockage also increases the wall shear stress at a greater rate than the kinematic Reynolds shear stress.

The x-y plane turbulent mass flux shear stress measured by the x-y plane cross-film probe is shown in Figure 91. Like the mass flux turbulence intensity, the mass flux shear stress did not scale by the local mean quantity as was the case for the kinematic Reynolds shear stress measured using LDV. The x-y plane mass flux shear stress for each of the six models reached a maximum value between $y/\delta = 0.3 - 0.7$. The smooth plate x-y plane shear stress maximum was 0.0043, with the 80 grit plate at 0.0068 (a 59% increase), the 3D plate at 0.0066 (a 55% increase), the 2D plate at 0.0071 (a 66% increase), the 36 grit plate at 0.0085 (a 99% increase), and the 20 grit plate at 0.009 (a 111% increase). The 20 grit and 2D plate x-y plane mass flux shear stress values decrease after reaching their peak values. Again the x-y plane mass flux shear stress, does not reach the freestream value near $y/\delta = 1.0$ indicating that the thermal boundary layer is thicker than the velocity boundary. The cross-film measurements have a freestream x-y plane mass flux shear stress of ~ 0.001; this value represents the probe resolution limit.

The x-z plane mass flux shear stress measured by the x-z plane cross-film probe is shown in Figure 92. Again the mass flux shear stress did not scale by the local mean quantity. Unlike the x-y plane mass flux shear stress, the x-z plane values did not reach a peak, but increased continuously with decreasing boundary layer height. In the near wall region, the smooth plate x-z plane shear stress maximum was 0.0038, with the 80 grit plate at 0.009 (a 141% increase), the 3D plate at 0.0015 (a 300% increase), the 2D plate at 0.00.19 (a 399% increase), the 36 grit plate at 0.020 (a 433% increase), and the 20 grit plate at 0.0274 (a 631% increase). Unlike the x-y plane mass flux shear stress, the x-z plane mass flux shear stress does reach the freestream value near $y/\delta = 1.0$. The cross-film measurements have a freestream x-z plane shear stress of ~ 0.001.

The x-y plane and x-z plane turbulent mass flux shear stress scaled by the wall density and wall shear stress are shown in Figures 93 and 94, respectively. Again, the inner or wall scaling does a better job at collapsing the rough surface plate x-y plane turbulent mass flux shear stress

as compared to the local quantity scaling. However, the results do show that increasing roughness height and blockage increased the x-y plane peak turbulent mass flux shear stress. For the x-y plane turbulent mass flux shear stress, when scaled by local quantities, the 2D machined and 20 grit plates reach peak values near $y/\delta \simeq 0.7$. When scaled by wall density and wall shear stress, the x-y plane turbulent mass flux shear stress, for all plates, reaches a peak value near $y/\delta = 0.6 - 0.8$. The wall scaling does not collapse the x-z plane turbulent mass flux shear stress.

The x–y and x-z plane mass flux shear stress differences, $\Delta_{(\rho*)'(\rho*)'}$, (scaled by the local mean streamwise mass flux) for the five rough surface models are shown in Figures 95 and 96, respectively. Both figures show increasing mass flux shear stress as a result of surface roughness. The peak mass flux shear stress differences versus roughness Reynolds number are shown in Figure 97. The sand-grain roughness mass flux shear stress difference data points were fit with a line indicating that increasing roughness height, increased the mass flux shear stress linearly. The 3D and 2D roughness models also showed that increasing blockage, increased the mass flux shear stress. The effect of surface roughness height and blockage had a significantly larger effect on the x-z plane mass flux shear stress compared to the x-y plane values with a rate of increase of $\frac{d\Delta_{(\rho v)'(\rho w)'}}{dk_s^+} = 3.7 \cdot 10^{-5}$ compared to $\frac{d\Delta_{(\rho u)'(\rho v)'}}{dk_s^+} = 5.6 \cdot 10^{-6}$ for the x-y plane case (see Table 8). This result is reasonable, since the ρw-component turbulence intensity was shown to increase significantly with increased roughness height and blockage (see the *Turbulence Intensities* subsection above or Figure 81) as compared to the ρu- and ρv-component turbulence intensities.

Combining HWA and LDV measurements allows the estimation of the second term of the compressible Reynolds shear stress, $\frac{\overline{\rho' v'}}{\overline{\rho u}}$ (density-transverse velocity correlation), which is equal to the negative of the Favre averaged velocity fluctuation, $\frac{\overline{v''}}{U}$ and is shown in Figure 101. Since the density-transverse velocity correlation is a combination of the kinematic Reynolds and x-y plane turbulent mass flux shear stresses and the kinematic Reynolds shear stress has a relatively constant

profile for fully rough surfaces, the density-traverse velocity correlation exhibits all of the traits of the turbulent mass flux shear stress. The density-traverse velocity correlation for each of the six models reaches a maximum value between $y/\delta = 0.4 - 0.7$. The smooth plate density-traverse velocity correlation maximum is -0.0034, with the 80 grit plate at -0.0044 (a 29% increase), the 3D plate at -0.0044 (a 29% increase), the 2D plate at -0.006 (a 76% increase), the 36 grit plate at -0.006 (a 76% increase), and the 20 grit plate at -0.0081 (a 138% increase). Like the x-y plane turbulent mass flux shear stress, the 20 grit and 2D plate density-traverse velocity correlation values decrease after reaching their peak values.

The density-traverse velocity correlation difference, $\Delta_{\rho' v'}$, (scaled by the local mean streamwise mass flux) for the five rough surface models are shown in Figure 102. The peak density-traverse velocity correlation differences versus roughness Reynolds number are shown in Figure 103. The sand-grain roughness density-traverse velocity correlation difference data points were fit with a line indicating that increasing roughness height increased the correlation linearly. The 3D and 2D roughness models also show that increasing blockage, increased the turbulence intensity. The rate of increase for the difference is $\frac{d\Delta_{\rho' v'}}{dk_s^+} = 8.1 \cdot 10^{-6}$ (see Table 8).

6.2.5 Turbulent Kinetic Energy

Figure 104 shows the turbulent kinetic energy scaled by the square of the local downstream mean velocity. The turbulent kinetic energy for the smooth plate case agrees with data collected by Luker [39]. The rough plate turbulent kinetic energies were significantly larger than the smooth plate case by as much as six times in magnitude near the wall boundary. The turbulent kinetic energy for the rough plates scales with the local mean quantities. To identify any differences in the fully rough flow turbulent kinetic energy with regard to roughness height and blockage, the turbulent kinetic energy difference, Δ_{TKE}, was calculated with the results shown in Figure 105. The

turbulent kinetic energy difference versus roughness Reynolds number for each of the rough surface models at $y/\delta = 0.4$ is shown in Figure 106. As with the velocity turbulence intensities, for fully rough flow, the turbulent kinetic energy remained fairly constant across a large range of roughness Reynolds numbers; indicating that the roughness height and blockage (once the surface is fully rough) have only a small affect on the turbulent kinetic energy. The sand-grain roughness models show a logarithmic relationship between the turbulent kinetic energy difference and roughness Reynolds number with a proportion of $\Delta_{TKE} \sim A\ln(k_s^+)$ with a slope of $A \approx 0.00076$.

Figure 107 shows the compressible turbulent kinetic energy scaled by the square of the local mean streamwise mass flux. As was the case for the mass flux turbulence intensities, the compressible turbulent kinetic energy does not scale by the local mean quantity. The compressible turbulent kinetic energy for each of the six models reaches a maximum value at the lowest probe position in the boundary layer. The smooth plate compressible turbulent kinetic energy maximum is approximately 0.013, with the 80 grit plate at 0.023 (a 73% increase), the 3D plate at 0.027 (a 103% increase), the 2D plate at 0.029 (a 121% increase), the 36 grit plate at 0.035 (a 164% increase), and the 20 grit plate at 0.041 (a 207% increase).

The compressible turbulent kinetic energy difference, Δ_{TKEc}, (scaled by the local mean streamwise mass flux) for the five rough surface models are shown in Figure 108. The peak turbulent kinetic energy differences versus roughness Reynolds number are shown in Figure 109. The sand-grain roughness compressible turbulent kinetic energy difference values were fit with a line indicating an increasing roughness height, increases the compressible turbulent kinetic energy linearly. The 3D and 2D roughness models also show increasing blockage, increases the compressible turbulent kinetic energy. The compressible turbulent kinetic energy difference rate of increase with respect to roughness Reynolds number is $\frac{\Delta_{TKEc}}{k_s^+} = 0.000037$ (see Table 8).

6.2.6 Intermittency

Figure 98 shows the intermittency function, γ_u, profiles for each of the six models estimated from the LDV flatness (third order velocity correlation). The intermittency function for the smooth plate case by Luker [39] is included in the figure. The agreement of this studies smooth plate intermittency with Luker's data is consider good with the present study giving slightly larger values in the mid-boundary layer region. To identify any differences in the fully rough flow intermittency function with regard to roughness height and blockage, the intermittency difference, Δ_{γ_u}, profiles are shown in Figure 99. The intermittency difference versus roughness Reynolds number for each of the rough surface models at $y/\delta = 0.4$ is shown in 100. Based on the intermittency difference, the surface roughness only has an effect in the near wall region ($y/\delta < 0.4$) with a slightly increasing intermittency function (γ) for increasing roughness height and blockage.

6.2.7 Turbulent Statistical Quantities Summary

Based on the LDV and HWA turbulence measurements, three overriding trends regarding turbulence data are apparent. First, the fluctuation quantities that do not include density fluctuations (i.e., velocity turbulence intensities, fluctuating Mach number, kinematic Reynolds shear stress, turbulent kinetic energy, and intermittency) scale with the local mean flow quantities. The fluctuating quantities have a weak dependence on roughness height and blockage for fully rough surfaces and are proportional to $\ln(k_s^+)$. Second, terms including density fluctuations do not scale with the local mean flow quantities and are significantly affected by roughness height and blockage. For fully rough surfaces, the roughness height and blockage directly affect density fluctuations appearing in the mass flux turbulence intensities, mass flux shear stresses, density-traverse velocity correlation, and the compressible turbulent kinetic energy. For the sand-grain roughnesses, a linear dependence was found (over the present range of roughness Reynolds numbers, k_s^+). Third, the streamwise mass

flux turbulence intensity and shear stress scale reasonably well with the wall density, friction velocity, and wall shear stress. The implications of this are that rough surface turbulence models used for compressible flows need to include a compressibility correction if the Reynolds-averaged approach is used. In addition, even though the Farve-averaged form of the Navier-Stokes equation does not explicitly include the density-traverse velocity correlation, the correlation, in the form of the traverse velocity fluctuation, $\overline{v''}$, enters the Favre-averaged turbulent shear stress transport equation through the pressure work production term, $-\overline{v_i''}\frac{\partial \overline{p}}{\partial x_i}$.

6.2.8 Power Spectra

A normal-film probe was used to collect the frequency resolved spectra at three locations over each of the six models, $y/\delta_M = 0.25$, 0.50, and 0.75 (designated lower, middle, and upper). The frequency resolved measurements provide information on the distribution of turbulent mass flux power over a range of frequencies from 1 kHz to the normal-film frequency response of 130 kHz. For all frequency resolved spectra measurements, the tunnel was operated at a stagnation pressure of $2.41 \cdot 10^5 \pm 0.2\%$ Pa and a stagnation temperature of 296 ± 1.0 K (see Table 5). The frequency spectra data is presented in four formats.

The first format is the dimensional power spectra given by $\overline{(\rho u)'^2} = \overline{(\rho u)'^2}(freq)$ with units of $\left(\frac{kg}{m^2 s}\right)^2$, which gives an indication of the overall turbulent power spectra distribution across the boundary layer for each of the six models. To identify trends in the dimensional power spectra, the second format presents the difference with respect to the outer boundary layer position as given by

$$\Delta_{\frac{y}{\delta}=0.75-(*)} = \left(\overline{(\rho u)'^2}(freq)\right)_{y/\delta=0.75} - \left(\overline{(\rho u)'^2}(freq)\right)_{y/\delta=(*)} \tag{178}$$

for $y/\delta = 0.25$ and 0.50. The third format is the power spectra data normalized by the mass flux variance, which gives a % indication of the how the available turbulent mass flux power is frequency distributed (with lower frequencies associated with larger flow structures and vice-versa). Finally,

the fourth format is the square root of the power spectra difference normalized by the mass flux standard deviation given by

$$\Delta_{\rho u(f)_{rms}} = \left(\sqrt{\frac{\overline{(\rho u)'^2}(freq)}{\overline{(\rho u)'^2}}} \right)_{rough} - \left(\sqrt{\frac{\overline{(\rho u)'^2}(freq)}{\overline{(\rho u)'^2}}} \right)_{smooth} \tag{179}$$

This format gives an indication of the affect of roughness height and blockage on the distribution of turbulence intensity power over a range of frequencies and boundary layer locations.

Figures 110 through 115 show the dimensional power spectra at the lower, middle, and upper boundary layer regions for each of the six models, and Figures 116 through 118 show the dimensional power spectra for each of the six models at the three boundary layer regions. From the dimensional power spectra data three features can be distinguished between the models. The first is the magnitude of the power contained in each region of the boundary layer; the second is the rate of power roll-off as frequency increases, and the third is how the difference between each boundary layer region is affected by surface roughness height and blockage.

For all models, except the smooth plate, the outer boundary layer region has the largest power spectra, followed by the middle region, and then the lower region. For the smooth plate, the magnitude of the power spectra for all regions are approximately equal with the middle region being only slightly larger, followed by the outer region, and than the lower region. To evaluate the difference between the three boundary layer regions over a frequency range of 1 kHz to 10 kHz, Figures 119 and 120 show the dimensional power spectra difference for the lower and middle regions relative to the outer boundary layer region. In this format, the magnitude of the power spectra between each boundary layer region and the rate at which the power spectra decreases with increasing frequency can be assessed. Since both middle and lower boundary layer regions are referenced from the upper region, when the upper region power rolls-off faster than the other two regions, the slope of the difference is negative. When the middle and lower region power rolls-off faster than the outer region the slope of the difference is positive.

For each of the rough surface models, the power spectra difference for the middle and lower regions decrease in the frequency range of 1 kHz to 2 kHz, indicating a larger power spectra decrease in the outer boundary layer region than for the lower and middle regions. After this initial outer region drop-off, the lower and middle regions begin to roll-off at a greater rate than the outer region, as indicated by the increasing power spectra difference in the frequency range of 2 kHz to 6 kHz. Beyond 6 kHz, the outer boundary layer region begins to roll-off at a larger rate than the other regions and the power spectra difference decreases. The trend in which the low frequency (1 kHz to 2 kHz) power spectra difference decreases, followed by an increase in the middle frequency range (approximately 2 kHz to 6 kHz), and finally, a decrease in the upper frequency range (beyond 6 kHz) occurs for all rough surface plates except the 2D machined plate.

For the smooth plate, there is an initial power spectra difference drop in the same frequency range as the rough surface models. At higher frequencies the difference value increases only slightly and the power spectra for each of the three boundary layer regions remain flat indicating all three regions have an almost even distribution of power in the 1 kHz to 10 kHz frequency range. Based on the dimensional power spectra difference values, increasing roughness height increased the power spectra difference between the boundary layer regions and increased the roll-off rate trend identified above. Increasing the roughness blockage increased the power spectra difference between the boundary layer regions but had a smaller affect on the roll-off trend than the surface roughness height.

Figures 121 through 126 show the power spectra normalized by the mass flux variance at the lower, middle, and upper boundary layer regions for each of the six models. Figures 127 through 129 show the power spectra normalized by the mass flux variance for each of the six models at the three boundary layer regions. From the nondimensional power spectra data two features can be distinguished. The first is the distribution of mass flux turbulent power across the frequency range,

and the second is the effect of surface roughness height and blockage. The data in Figures 121 through 126 show the lower boundary layer region mass flux power spectra crosses the middle and upper region spectra indicating that in the lower region, most of the power is contained in large, low-frequency flow structures. The frequency at which the inner region power spectra crosses the outer region power spectra is 17 kHz for the smooth plate, 8 kHz, 7 kHz, 4 kHz and for the 80, 36, and 20 grit sandpaper plates,respectively, and 9 kHz and 7 kHz for the 3D and 2D plates, respectively. This indicates that increasing surface roughness height and blockage leads to a larger proportion of low frequency structures in the near wall region. For the middle and upper regions, the power is spread across a wider range of frequencies (from 1 kHz to about 10 kHz) and flow structure sizes.

To provide more detail into the effects of surface roughness height and blockage on power spectra, Figure 130, 131, and 132 show the square root of the power spectra difference normalized by the mass flux standard deviation (i.e., $\Delta_{\rho u(f)_{rms}}$) for the lower, middle, and upper boundary layer regions, respectively. The sand-grain roughness models were fit with a logarithmic curve fit for the lower region and a linear curve fit for the middle and upper boundary layer regions. The slope for each model and boundary layer region are shown in Table 9. The data indicates that increasing surface roughness height and blockage increases the power spectra difference with the largest effect at the lowest frequencies in the lower region near the wall. Further away from the wall, the effect of increasing roughness height and blockage is spread over a larger range of frequencies. This is indicated by Figures 131 and 132 which shows nearly identical power spectra difference values over the frequencies ranges of $977 - 1955$ Hz and 977-5860 Hz, respectively.

Based on the spectra data, the largest energy (except for the smooth plate) is contained in the outer region, which is fed from the freestream and is fairly evenly distributed across a wide range of frequencies (approximately 1 kHz to 20 kHz). The lower region has the least overall power, which is contained in large low frequency structures. The middle region is a blending of the two upper and

lower regions, containing more overall energy than the lower region, spread over a larger range of frequencies. Overall, increasing surface roughness and blockage height increased the power spectra and the power spectra difference between the three boundary layer regions, and shifted the mass flux turbulent power to lower frequencies in the near wall region. Peaks were observed in the power spectra data (see Figures 110 through 115, Figures 116 through 118, Figures 121 through 126, and Figures 127 through 129) above 10 kHz and may be a result of probe/holder vibration, but were not completely understood.

6.2.9 Autocorrelation

Autocorrelation information was calculated from the normal-film probe measurements using the same data collected for the power spectra. Using the normal-film voltage, the autocorrelation indicates how the flow structure or mass flux fluctuations occurring at one time instant are related to fluctuations occurring at an earlier time instant. The autocorrelation for a given time offset, τ, is nondimensionalized by the mass flux variance, $\overline{(\rho u)'^2}$ giving the Eulerian time-correlation coefficient, $R_E(\tau)$ [17]. For $\tau = 0$, the autocorrelation, $\overline{(\rho u(t))'(\rho u(t+\tau))'} = \overline{(\rho u)'^2}$ which gives $R_E(0) = 1$, and as τ increases $R_E(\tau)$ decreases. Since turbulent flow is characterized by a large range of spatial scales, the rate at which the Eulerian time-correlation coefficient drops as τ increases from zero gives an indication of the size of the smallest flow structures. The length of time it takes for $R_E(0)$ to reach zero (though it may not do so) is an indication of the size of the largest flow structures.

The autocorrelation information is presented in three formats. The first is the Eulerian time-correlation coefficient time trace for mass flux showing all three boundary layer regions (lower, middle, and upper) for each of the six models. The second format is the Eulerian time-correlation coefficient showing all of the six models for each boundary layer region. The third format is the

microscale and integral length scale versus roughness Reynolds number which gives an estimate of the smallest and largest flow structures and how surface roughness height and blockage affect them.

Figures 133 through 138 show the autocorrelation time traces with all boundary layer locations ($y/\delta_M = 0.25, 0.50$, and 0.75, designated lower, middle, and upper) for each of the six models. Figures 139, 140, and 141, show all six model autocorrelation time traces for each of the three boundary layer locations. A trend noticed from these figures is that the lower boundary layer region had the smallest rate of time-correlation decrease for all models, indicating that the small scale structures were largest in the near wall region. This is echoed by the power spectra data which showed, for the lower region, the power was distributed toward large, low frequency structures. For the smooth plate, the middle and upper boundary layer regions had nearly the same autocorrelation time trace with differences only appearing at larger time offsets (τ), which is also shown by the power spectra curves. This indicates that the small scale structures for the two regions were approximately the same; however, the large scale structures were larger for the outer region of the boundary layer. For the rough surface models, the lower region also had the smallest rate of time-correlation decrease; however, the middle region had a smaller rate of decrease than the upper region. The autocorrelation time trace at larger time offsets were also different for each boundary layer region. For the rough surfaces, the small scale structure size was largest in the lower region with the size decreasing in the middle and outer regions. Conversely, the large scale structure size was largest in the outer region and decrease in the middle and lower regions.

To better quantify how surface roughness affects the flow structure sizes, the microscale and integral scale time values for each model were calculated and are shown in Table 10 and Figures 142 and 143, respectively. Typically Taylor's hypothesis, $\left(\frac{\partial}{\partial t} = -\overline{u}\frac{\partial}{\partial x}\right)$, which assumes that the turbulent structures are convected at the mean streamwise velocity, is used to present autocorrelation structure scales as lengths; however, this only works well for low turbulence levels ($< 1\%$) [17].

For this reason, the microscale and integral scale lengths are presented in time coordinates. The microscale values are determined by fitting an osculating parabola to the autocorrelation time trace and determining the parabola's x-axis intercept (see Figure 144). Trends regarding the boundary layer region and surface roughness are apparent. First, the lower region has the largest small scale structures, followed by the middle and upper regions. Second, increasing surface roughness height and blockage increased the size of the small scale structures. The smooth plate and sand-grain microscale values were fit with a line, with the slope indicating the rate at which surface roughness height affects the microscale. The rate, $\frac{d(microscale)}{dk_s^+}$, for each boundary layer region is shown in Table 8. The slopes are $5.3 \cdot 10^{-9}$ $\left(\frac{\text{sec}}{1}\right)$, $4.8 \cdot 10^{-9}$ $\left(\frac{\text{sec}}{1}\right)$, and $2.5 \cdot 10^{-9}$ $\left(\frac{\text{sec}}{1}\right)$, for the lower, middle, and upper boundary layer regions, respectively. The largest rate of increase was in the lower or near wall region with a decreasing rate toward the freestream. This indicates that the effect of surface roughness is to increase the size of the smallest flow structures (given by the microscale) with the largest increase occurring in the near wall region.

The integral length scale represents the magnitude of the largest structures in a turbulent flow. The data in Figure 143 indicates that the largest flow structures occur in the outer boundary layer region, followed by the middle, and then the lower region. This shows that the wall boundary dampens or limits the largest size structures. Surface roughness decreases the integral length scale in all three boundary layer regions. The rate at which increasing surface roughness height decreases the integral length scale is largest in the outer region, followed by the middle, and inner regions of the boundary layer. Increasing roughness blockage shows inconclusive results with respect to the integral length scale, though the roughness height of the 3D and 2D models does reduce the integral length scale throughout the boundary layer relative to the smooth plate values.

Overall, the effect of roughness is to move the structure sizes toward the middle, by increasing the size of the small scale structures and decreasing the large scale structures. The larger the

roughness height, the larger the effect, as evidenced in microscale and integral length scale figures. For the smooth plate, the power spectra indicates that the middle and outer region flow has an even distribution of small high-frequency and large low-frequency structures; this is shown in the auto-correlation data by the widest range between the microscale and integral length scales.

6.2.10 Cross-Correlation

A parallel-film probe was used to collect the flow structure angle measurements at three locations over each of the six models, $y/\delta_M = 0.25$, 0.50, and 0.75 (designated lower, middle, and upper). The cross-correlation of the two parallel-film sensor voltages give an indication of the flow structure angle. For a flow structure or eddy with an angle of 90 degrees to the streamwise direction, the eddy reaches both parallel-film sensors at the same instant giving a cross-correlation peak at $\tau = 0$. For an eddy with an angle less than 90 degrees, the eddy reaches one of the film sensors before the other, shifting the time correlation peak to a higher time offset (increasing τ). Estimates of the flow structure angle can be found based on the probe sensor separation distance and the local mean streamwise velocity. For all flow structure angle measurements, the tunnel was operated at a stagnation pressure of $2.33 \cdot 10^5 \pm 0.3\%\ Pa$ and a stagnation temperature of $296 \pm 1.0\ K$.

Figures 145 through 150 show the cross-correlation time traces with all three boundary layer locations for each of the six models. For all six models, the cross-correlation time trace peak drop-off rate is largest for the outer boundary layer region, followed by the middle, and then the lower region. As for the autocorrelation of a single film probe, the drop-off rate gives an indication of the small scale structure size. Assuming the eddies are circular or elliptic and that the mean streamwise velocity of the eddies is significantly faster than the eddy rotational velocity, the drop-off rate gives an indication of the eddy streamwise thickness for eddies with a height of at least the parallel-film sensor separation distance. The drop-off rate shows that the small scale eddy streamwise thickness

is largest near the wall boundary and decreases as you move toward the freestream. This result from the parallel-film cross-correlation agrees with the results found from the normal-film autocorrelation measurements.

Figures 151, 152, and 153, show all six model cross-correlation time traces for each of the three boundary layer locations. The drop-off rate for the smooth plate was larger than the rate for the rough surface models in each boundary layer region, indicating surface roughness increased the small scale streamwise thickness. Increasing surface roughness height and blockage increased the small scale streamwise thickness as shown by the lower drop-off rate for the 2D and 20 grit plates relative to the 3D and 80 and 36 grit plates, respectively. Again, these results matched the results from the normal-film autocorrelation measurements, which indicated that the effect of surface roughness was to increase the size of the smallest flow structures (given by the microscale) with the largest increase occurring in the near wall region.

The flow structure angles estimated from the cross-correlation traces are shown in Table 11 and Figure 154 along with error bars indicating sampling rate resolution. All structure angles were between approximately 30 and 60 degrees. The flow structure angles were smallest near the wall (lower region) and increased toward the boundary layer edge. The data in Figure 154 indicates that increasing surface roughness height, increased the flow structure angle, with the largest effect occurring in the outer boundary layer region. The 2D plate flow structure angles remained relatively constant across the boundary layer, whether this was a feature of the two-dimensional roughness elements and spacing or due to the sampling rate resolution was unknown.

6.2.11 Frequency Resolved Turbulence Summary

Surface roughness had a large effect on the power spectra, size, and angle of flow structures across the turbulent boundary layer. Increasing surface roughness height and blockage increased

the power spectra and the power spectra difference between the three boundary layer regions, and shifted the mass flux turbulent power to lower frequencies in the near wall region. Surface roughness increased the size of the small scale structures and decreased the size of the large scale structures. The larger the roughness height, the larger the effect, as evidenced in microscale and integral length scale values. For very large roughnesses ($k_s^+ \gtrsim 600$), the integral scale approached the same value across the entire boundary layer. The flow structure angles were smallest near the wall (lower region) and increased toward the boundary layer edge. Increasing surface roughness height, increased the flow structure angle, with the largest effect occurring in the outer boundary layer region.

6.3 Empirical Flowfield Description (A Synopsis)

Sections 6.1 and 6.2 presented a comprehensive and detailed analysis of each measurement technique. The influence of roughness on a long list of flow properties has been extensively covered. The results and discussions from those sections will not be repeated here. Instead, the purpose of this section is to assimilate that information into an overview description of the influence of surface roughness on the boundary layer flow, and where appropriate, implications towards modeling have been identified. This section starts by examining the effects of the surface roughness on the overall structure of the boundary layer. This analysis is then used to explain the observations noted in Sections 6.1 and 6.2 concerning the mean and turbulent flow properties.

Focusing first on the frequency resolved turbulence data, it was noticed that the presence of the roughness elements increased the overall energy levels, decreased the integral or larger scales, and increased the micro or smaller scales throughout the boundary layer. The roughness elements also redistributed the turbulent energy toward the lower frequencies (i.e., toward the larger flow structures) in the near wall region. These effects were found to have a strong dependence on the roughness height and geometry. These observations show that the roughness elements significantly

altered turbulence production mechanisms, which is not overly surprising since, for smooth plates, the near wall region ($y^+ < 30$) has been shown to be very important in determining the structure of the boundary layer [31]. In particular, as the roughness height and blockage were increased, the large scale structures (based on integral scale values) converged to a nominally constant size across the boundary layer, which indicated a possible integral length scale independence of boundary layer location for very large roughness Reynolds numbers (k_s^+). This result suggested that the roughness generated turbulence becomes the dominant term in the near wall production/dissipation balance and was consistent with the familiar logarithmic "law of the wall" for fully rough flow, where u^+ is proportional to the roughness Reynolds number and independent of the flow Reynolds number due to the disappearance of the laminar sublayer [50] for fully rough flow.

From the frequency resolved data, the rough surface turbulent boundary layer was characterized as having a higher population of higher energy eddies that were distributed over a narrower range of length and time scales. The instantaneous Mie scattering images qualitatively supported this description of the boundary layer structure. This qualitative view of the boundary layer structure was instrumental to understanding the mechanisms responsible for changes in the mean and turbulent flow properties that resulted from the presence of the roughness elements. For example, the increased turbulence and mixing in the boundary layer, that, as a consequence of the roughness, produced increased entrainment rates of freestream fluid into the boundary layer when compared to the smooth plate; thus, increasing the rate of the boundary layer growth. This was indicated by the larger rough surface boundary layer thicknesses, relative to the smooth plate value, measured using the Pitot probe, LDV, and flow visualization. This type of information is important for Reynolds-averaged turbulence models where a velocity and length scale are defined and for large eddy simulation validation and subgrid modeling. Specifically, the integral scale mean size at large roughness

Reynolds numbers may lead to adjustments in the outer region of the Prandtl mixing length turbulence model.

A second feature unique to compressible flows was density fluctuations. The turbulent Mach number was found to be on the order of 0.3 for all cases. Hence, the turbulence generated density fluctuations were expected to be on the order of 4.0% (a crude assessment assuming locally isentropic flow). However, a second mechanism for the production of density fluctuations was identified from the experimental measurements. That mechanism was the compression and expansion waves generated by the roughness elements protruding into the supersonic region of the boundary layer, which interacted with the turbulent flow structures to produce relatively large (comparable to the velocity fluctuations) density fluctuations. The magnitude and occurrence of these waves increased as the roughness height increased and the blockage area decreased, and was visibly evident in the color schlieren photography. These roughness generated density fluctuations also had a large influence on the turbulence quantities that included density fluctuations (described below).

The increased turbulent energy and mixing due to surface roughness (as described above) had an important impact on the mean velocity and density defects across the entire boundary layer, with the most noticeable effect in the near wall region. The increased velocity defect near the wall is attributed to both the increased near wall turbulent shear stresses (a direct result of the presence of larger higher energy eddies near the wall) and the form drag generated by the roughness elements protruding into the boundary layer. Both the velocity and density defects, when scaled by outer flow variables, were found to be virtually independent of the surface roughness height for the present fully rough cases. This finding has important implications in both the integral analysis and numerical modeling of this flow. However, as expected, the local wall shear stress (i.e., momentum losses) were not independent of surface roughness. As discussed in Chapter 7, these finding were used to improve the integral and numerical prediction methods.

The kinematic turbulence quantities (e.g., velocity turbulence intensity, kinematic Reynolds shear stress, etc...), when scaled by the local mean quantities (i.e., outer variables), were found to collapse onto a single curve for fully rough flow. Conversely, the measured turbulence quantities that included density fluctuations (e.g., mass flux turbulence intensity and traverse apparent mass flux) did not scale with the local mean flow quantities and were significantly affected by roughness height and blockage. The implications here are that for the Farve-averaged approach, though new turbulence models developed from compressible data is preferred, incompressible models with the appropriate compressible extensions should be reasonable for simple flat plate geometries. This assessment is founded in the present empirical data and the realization that the Farve-averaged approach works well for high-speed smooth wall turbulent boundary layers. However, for more complex flow geometries, the roughness/density fluctuation complications can feed into the Favre averaged shear stresses through the pressure-work terms present in the shear stress transport equations. On the other hand, for the Reynolds-averaged approach, the explicit appearance of fluctuating density correlations requires addition modeling for the compressible turbulence terms. For both averaging techniques, the assumption that the wall shear stress and turbulent shear stress are equivalent near the wall is no longer valid for fully rough flow. The form drag due to the surface roughness elements has to be taken into account when estimating the wall shear stress (and hence, skin friction and friction velocity). For this reason, a new more predictive method was used to calculate the wall shear stress for the rough surface numerical predictions (see Chapters 5 and 7). This finding also indicates that roughness models that include explicit formulations for the form drag in the governing momentum equations have some intrinsic merit.

Chapter 7 - Analysis and Prediction

Integral analyses and numerical predictions were performed on the six models based on information collected from the experiments described in Chapter 3 and the data shown in Chapter 6. The first section below presents the results of the integral analysis on the boundary layer data, while the second section presents the numerical predictions based on the parabolized Navier-Stokes solver described in detail in Chapter 5.

7.1 Integral Analysis

The Integral analysis consists of three sections: *Boundary Layer Quantities*, *Defect and Van Driest Velocity Profiles*, and *Equivalent Sand-Grain Roughness*.

7.1.1 Boundary Layer Quantities

Based on the Pitot probe measurements, the following quantities: δ, δ_M, δ_k^*, δ^*, θ_k, θ, C_f, τ_w, and u^* were calculated for each of the six models. The quantities, δ and δ_M, are the boundary layer heights based on the location were the boundary layer velocity and Mach number reach 99% of the freestream value. The kinematic displacement and momentum thicknesses are given by δ_k^* and θ_k, respectively, with the displacement and momentum thicknesses given by δ^* and θ, respectively (see definitions in Chapter 4). The skin fiction coefficient, C_f, for the smooth plate was calculated using the Van Driest skin friction relationship [61] and was used to determine the wall shear stress, τ_w, and friction velocity, u^*. For the rough plate models, the Van Driest skin friction relationship is not valid. Hence, a new relationship based on the logarithmic form of the momentum thickness/roughness height ratio and skin friction, combined with the zero pressure gradient integral momentum equation was developed (see Chapter 4 for details) to determine the skin friction over the rough plate models. From these skin friction values, the wall shear stress and friction velocity were calculated.

Table 12 presents the results of the above quantities for each of the six models. As indicated in Table 12, as the sandpaper roughness height increases, the boundary layer thickness increased. For the Pitot measurements, the boundary layer thickness for the 20 grit plate was 1.6% less than the 36 grit plate which has maximum roughness height of 18.0 mm versus 17.7 mm for the 20 grit plate. The slight apparent decrease in the boundary layer thickness for the 20 grit plate was attributed to uncertainties in boundary layer thickness (see Appendix C). The LDV and color schlieren boundary layer thicknesses listed in Table 6 showed the 20 grit plate value to be larger than the 36 grit plate. The machined rough plates also indicated as roughness density or blockage increases, the boundary layer thickness increased. The Mach number boundary layer was directly related to the thermal boundary layer and, as such, was larger than the velocity boundary layer height for each of the six models. Figure 155 shows velocity, Mach, and thermal boundary layers versus roughness Reynolds number as measured by the Pitot, LDV, and color schlieren techniques. The data in Figure 155 shows the trend of increasing δ versus k_s. The large amount of scatter in Figure 155 is typical; it is this scatter that has forced researchers to use integrated length scales (e.g., δ^* and θ) and abandon turbulent models based on δ.

To better assess the affects of surface roughness on integral quantities, Figures 156 and 157 show the displacement and momentum thicknesses for each of the six models versus roughness Reynolds number. The displacement and momentum thicknesses are often used to describe a boundary layer in place of the boundary layer thickness since, by integrating across the entire boundary layer, uncertainties involving the boundary layer edge are eliminated (see Equations (78) through (81)). The Pitot displacement and momentum thicknesses showed considerably less scatter than the boundary layer thickness and indicated clear trends with regard to surface roughness height and blockage. The surface roughness height and blockage showed a logarithmic relationship for the displacement and momentum thicknesses versus roughness Reynolds number. Unlike turbulence

data, surface roughness blockage showed the same relationship as surface roughness height. For the kinematic displacement thickness and momentum thickness the logarithmic relation was given by $\delta_k^* = 0.55\ln(k_s^+) - 0.41$ and $\theta_k = 0.35\ln(k_s^+) + 0.027$, respectively. For the displacement and momentum thicknesses, the logarithmic relation was given by $\delta^* = 0.93\ln(k_s^+) + 0.53$ and $\theta = 0.21\ln(k_s^+) + 0.16$, respectively.

Figures 158 and 159 show the skin friction coefficient and friction velocity for each of the six models versus roughness Reynolds number. As with the displacement and momentum thicknesses, the surface roughness height and blockage show a logarithmic relationship for skin friction and friction velocity versus roughness Reynolds number. The skin friction logarithmic relation is given by $C_f = 6.5 \cdot 10^{-4}\ln(k_s^+) + 7.8 \cdot 10^{-5}$. While the friction velocity logarithmic relation is given by $u^* = 3.2\ln(k_s^+) + 20.9$.

7.1.2 Defect and Van Driest Velocity Profiles

Based on the integral analysis information, the velocity defect and Van Driest velocity profiles were found for each of the six plates. Figures 160 and 161 show the velocity defect profiles for both the smooth plate and rough plates. Figure 160 is the velocity defect scaled by the friction velocity and Figure 161 is the Van Driest effective velocity defect scaled by the friction velocity (see Chapter 2, Equation (7)). By scaling the velocity defect with the friction velocity, all of the models collapse into a single curve. This result has been shown before for incompressible smooth and rough walls [17,50,66], and the results shown in Figures 160 and 161 give confidence in the method developed to calculate the rough wall skin friction. Both the velocity and effective velocity defect profiles were plotted on a logarithmic scale and shown in Figures 162 and 163, respectively. These figures show that the velocity defect scaled directly with the friction velocity and boundary layer height in

the outer region. However, these scalings are somewhat inadequate in the inner region near the wall (this is also consistent with the incompressible database [17, 50, 66]).

Figures 164 and 165 present the Van Driest velocity profiles for the Pitot and LDV data, respectively. Near the wall, the velocity is scaled by the friction velocity (i.e., inner scaling) and the boundary layer height position is scaled by friction velocity and kinematic viscosity. The match between the smooth plate Pitot and the logarithmic "law of the wall" (including Cole's "law of the wake" [50]) is considered excellent. The LDV data is slightly higher than flat plate theory (see Figure 166). The difference is attributed to the use of the friction velocity calculated using Pitot data. The number of LDV measurements for each plate did not allow an accurate calculation of the momentum thickness (and hence, the friction velocity) so the Pitot data friction velocity was used. The friction velocities required for the LDV Van Driest Profiles to collapse with the Pitot data are shown in Table 14. For all models, the friction velocity difference between the adjusted LDV and Pitot values is less than 4 %. Hence, the level of disagreement between the LDV and the Pitot data shown in Figure 166 is within the measurement uncertainties.

The rough surface Van Driest velocity data show a downward shift that is in proportion to the surface roughness, and is consistent with the incompressible results in the literature [17, 50, 66]. The 80 grit plate showed the least amount of shift, followed by the 3D, 2D, 36 grit, and 20 grit plates. Figure 167 presents the Van Driest velocity profiles using the effective velocity, which is more appropriate for comparison to incompressible measurements. The Van Driest compressibility transformation (Chapter 2, Equation (7)) is used to determine the equivalent sand-grain roughness values in the next section.

7.1.3 Equivalent Sand-Grain Roughness

The equivalent sand-grain roughness, k_s, for each of the five rough models was calculated based on the method outlined in Section 2.1.3. Figure 168 shows the Van Driest velocity profile plot using the effective y origin as outlined in references [4, 45–47]. Along with the Pitot data, each profile is curve fit (in the logarithmic region) with a straight line of slope $\frac{1}{\kappa}$. Based on the equivalent sand-grain roughness equation presented by Schlichting [51], the k_s values are shown in Table 4 along with the nondimensional roughness Reynolds number, k_s^+. All of the rough model plates have a roughness Reynolds number greater than 70 and are in the completely rough regime. Figure 169 shows the Van Driest effective velocity profile for each of the five rough models versus $\frac{(y+\varepsilon)}{k_s}$. Based on the equivalent sand-grain roughness, each of the velocity profiles collapse in the lower region showing this region is no longer scaled by the kinematic viscosity, but instead by the roughness height. Finally, Figure 170 shows the Van Driest velocity profile downward shift as a function of the roughness Reynolds number, which matches the shift predicted by the sand-grain theory (with the understanding that this is a result of the method of calculating k_s).

7.1.4 Skin Friction Prediction

Most initial engineering calculations use semi-empirical relations to estimate the quantities of interest. For fluid dynamics, the estimation of skin friction is vitally important with little data available for use in high-speed compressible flows. For uniformly distributed rough surfaces or when the equivalent sand-grain roughness is unknown either, an effective roughness correlation based on the roughness geometry/spacing, such as that developed by Bettermann and Dvorak (extracted from [53]) for square rods or Dirling [23], must be used or experimental measurements performed in order to estimate C_f. For experimental measurements, either a drag balance or skin friction estimates based on momentum loss are required.

The experimental skin friction measurements from this study were compared to three semi-empirical methods. Two of the three compressible skin friction estimates were calculated by applying the density - skin friction relation by Goddard [28] (Equation (25)) with the incompressible relations by Schlichting [51] and White [66] (Equations (18) and (19), respectively). The third compressible method uses the rough wall skin friction ratio correlation by Goddard [28], given as

$$\frac{C_f}{C_{f_0}} = 0.39\left(\ln k_s^+ - 2.3\right) + 1.0 \tag{180}$$

where C_{f_0} is the compressible smooth plate skin friction. For this analysis, C_{f_0} is found using the Van Driest II [62] smooth flat plate relation (Equation (10)). Figure 171 shows the three relations along with the integral analysis data from this study. The agreement between the experimentally estimated skin friction using the integral method developed in Chapter 4 and the correlation by Goddard is considered excellent with a difference of less than 3% for all models. Both the Schlichting and White relations underestimate the skin friction for compressible flows by as much as 30%. Included in Figure 171 is an estimate for 2D machined roughness plate skin friction based on the roughness geometry/spacing correlation of Bettermann and Dvorak with $\lambda = 3.9$. The skin friction estimate for the 2D machined roughness plate also used the compressible density - skin friction relation by Goddard. The 2D machined roughness plate skin friction estimate was underestimated by 8% relative to the measured value.

Based on these results, the integration method using the boundary layer momentum thickness at two locations and the sand-grain roughness correlation developed by Schlichting [51] (see Equation (17)) provide excellent estimates of the skin friction and equivalent sand-grain roughness. When the equivalent sand-grain roughness is known, the skin friction for compressible high-speed flows can be found by using Equation (180).

7.2 Numerical Predictions

A parabolized Navier-Stokes solver was used to numerically calculate the flow over the smooth and rough plates using two algebraic turbulence models: Prandtl mixing length and the Compressible Apparent Mass Mixing Length Extension (CAMMLE) models. The algebraic models were extended using Rotta's model for roughness (see Chapter 5 for details). The results of the two models are presented and compared to the experimental data below. Though more complicated higher-order models exist, these two models are still commonly used throughout industry and will be used to assess the Rotta roughness model.

The numerical predictions were evaluated with the experimental data from this study in three subsections: *Mean Flow Data*, *Turbulent Flow Data*, and *Integral Analysis*. The *Mean Flow Data* subsection compares the numerical predictions from the two models with the Pitot and LDV experimental velocity and density profiles. The *Turbulent Flow Data* subsection compares the numerical predictions of the kinematic Reynolds shear stress, compressible Reynolds shear stress, and the second order density-traverse velocity correlation with LDV and HWA experimental data. Finally, the *Integral Analysis* subsection compares integral quantities (e.g., δ, δ^*, θ_k, etc...) and Van Driest velocity profiles to estimates from Pitot measurements.

7.2.1 Mean Flow Data

The velocity profile numerical predictions for each turbulence model are shown with Pitot and LDV experimental data in Figures 172 through 177. The calculations were converged to the point where the normalized residual was reduced by three orders of magnitude. The minor fluctuations in the profiles reflect this level of convergence (see Appendix D for further details on the CFD grid and model validation studies). The turbulence models did a credible job for both the smooth and rough plates, with the Prandtl and CAMMLE models predicting almost identical velocity profiles.

Both turbulence models over predicted the smooth plate velocity defect (which may be attributed to boundary layer thickness uncertainty in the experimental or numerical data), but did an excellent job for the rough surface plates as evidenced by the velocity defect plots.

The density profile numerical predictions for each model are shown with Pitot and LDV experimental data in Figures 178 through 183. The Prandtl and CAMMLE turbulence models predicted the rough-wall experimental Pitot density profiles and under predicted the smooth plate profile. Near the freestream each turbulence model slightly over predicted the freestream density ratio, $\frac{\overline{\rho}}{\rho_e}$, by 1.0%.

The velocity defect plots based on the velocity profiles and friction velocity from the Prandtl and CAMMLE models are shown in Figures 184 and 185, respectively. The Prandtl and CAMMLE turbulence models predicted almost identical velocity defect profiles with the only differences attributed to slight friction velocity value differences. For all six plates, the friction velocity difference between the two turbulence models was less than 2%. The velocity defect profiles from the Prandtl and CAMMLE turbulence models match the Pitot data found experimentally.

Figures 186 through 191 show the numerically predicted Van Driest velocity profiles for the six plate models using both the Prandtl and CAMMLE turbulence models. Both turbulence models provide nearly identical profiles with only slight exceptions (notably: the sand-grain roughened surfaces) attributed to friction velocity differences. The match between the smooth plate Pitot, the logarithmic "law of the wall" (including Cole's "law of the wake" [50]), and the model predictions is considered excellent.

For the rough surface plates, the turbulence models over predict the downward velocity shift, $\frac{\Delta u}{u*}$ attributed to the numerically predicted friction velocity values. The numerically predicted friction velocity values were over predicted by as much as 20%. To estimate the difference between the Pitot and numerical Van Driest velocity profiles, the friction velocity from the numerical predictions

was adjusted to match the experimental data. Table 14 gives the original numerical predictions for the friction velocity, the adjusted values, and the percent difference from the numerical predictions and the experimentally estimated values. All rough plate Van Driest velocity profiles match the experimental profiles for friction velocity values of 38.0 and 37.2 for the 2D and 3D machined plates, respectively, and 34.0, 38.8, and 38.8 for the 80, 36, and 20 grit plates, respectively. These adjusted values were within 4% of the experimentally determined friction velocities, indicating the method used to numerically determine the skin friction and friction velocity for the turbulence models may require slight refinement.

7.2.2 Turbulent Flow Data

Since the Prandtl model is based on Favre-averaging, $\tau_{xy}^{T} = -\overline{\rho u'' v''}$. Bowersox [12] has shown that $\overline{\rho u'' v''} = \overline{\rho u' v'}$ (to third order). Hence, the Prandtl model shear stress predictions can be compared to the LDV data. The CAMMLE model is based on Reynolds-averaging of thin layer type flows,

$$\tau_{xy}^{T} \simeq -\overline{\rho u' v'} - \overline{u \rho' v'} \tag{181}$$

Thus, from the above equation, comparisons with the cross-film and combined cross-film/LDV data are appropriate.

The kinematic Reynolds shear stress numerical predictions for each turbulence model is shown with LDV experimental data in Figures 192 through 197. For the smooth plate, the Prandtl and CAMMLE models accurately predicted the incompressible Reynolds shear stress in the region from approximately $y/\delta = 0.4$ to the freestream. Below $y/\delta \approx 0.4$, the turbulence models under predicted the incompressible Reynolds shear stress.

For the rough surface plates, the models again accurately predicted the incompressible Reynolds shear stress from $y/\delta = 0.4$ to the freestream. Below $y/\delta \approx 0.4$, neither model matched the in-

crease in shear stress as a result of the surface roughness. The maximum incompressible Reynolds shear stress measured using LDV was as much as 133% larger than that predicted by the turbulence models. In addition, the rough surface model predictions, when scaled by the local quantities did not collapse into a single curve as was the case for the LDV experimental data, but showed an increase in the incompressible Reynolds shear stress with increasing surface roughness height and blockage.

The mass flux shear stress numerical predictions (i.e., the compressible Reynolds shear stress) from the CAMMLE model are shown with x-y plane, cross-film experimental data in Figures 198 through 203. The cross-film mass flux shear stress presented in the *Experimental Information* section has been shifted left by the freestream mass flux shear stress value attributed to freestream turbulence and film sensor resolution. Based on the experimental and numerical data, the CAMMLE model slightly under predicts the mass flux shear stress in the outer boundary layer region ($y/\delta \leq 0.4$), while over predicting the mass flux shear stress near the wall. As mentioned in the *Turbulence Intensity* subsection, the cross-film sensor is sensitive to mass flux and, thus, the thermal boundary layer, accounting for the slight difference between the CAMMLE model and the experimental data in the outer boundary layer region ($y/\delta > 1.0$)

The maximum experimental mass flux shear stress (Figures 198 through 203) is -0.0037 for the smooth plate,-0.0065 and -0.0060 for the machined 2D and 3D plates, respectively, and -0.0061, -0.0079, -0.0084 for the 80, 36, and 20 grit plates, respectively (note: the cross-film measurements have been shifted by freestream x-y plane shear stress of -0.0006). The CAMMLE model maximum mass flux shear stress was 15% larger than the experimental data for the smooth plate, 40% and 46% larger for the machined 2D and 3D plates, respectively, and 23%, 18%, and 20% larger for the 80, 36, and 20 grit plates, respectively.

The CAMMLE compressible extension $\left(\frac{\overline{u}}{S}\frac{\partial\overline{\rho}}{\partial y}\frac{\partial\overline{u}}{\partial y}\right)$ provides an estimate of the compressible components of the Reynolds shear stress and is compared to the density-transverse velocity correla-

tion $(\overline{\rho' v'})$ obtained from combined LDV and HWA analysis in Figure 204. The density-transverse velocity correlation has been shifted by the freestream value. The CAMMLE model predicts qualitatively correct profile shapes. The CAMMLE model also predicts the increasing compressible component of the Reynolds shear stress with increasing roughness Reynolds number.

7.2.3 Integral Analysis

The following quantities: δ, δ_k^*, θ_k, θ, H, $\frac{d\theta}{dx}$, C_f, u^*, and k_s^+ were calculated for each of the six models based on numerical predictions by the CFD code and turbulence models. Table 15 shows the numerical estimates for these quantities. The numerical predictions show that increasing roughness height and blockage increases boundary layer thickness as was the case for the experimentally collected data. The numerical predictions for the boundary layer thickness were as much as $\pm 20\%$ off compared to the Pitot data.

To better assess the affects of surface roughness on integral quantities, Figures 205 and 206 show the displacement and momentum thicknesses for each of the six models versus roughness Reynolds number. The logarithmic relationship for the displacement and momentum thicknesses versus roughness Reynolds number found in the experimental data is also shown in the numerical data. The Prandtl and CAMMLE models; both over predict the kinematic displacement thickness and provide almost identical values with slight variations due to roughness Reynolds number differences. The numerical predication for the kinematic displacement thickness over the smooth plate was 9% larger than the experimental data, and between 16% and 25% larger for the rough surface plates. For the momentum thickness, the difference between the numerical and experimental values was less than 7% for all plates and for the kinematic momentum thickness, the difference was less than 1% for the smooth plate and less than 11% for the rough surface plates.

The skin friction and friction velocity numerical predictions are shown in Figures 207 and 208. For the smooth plate, the skin friction and friction velocity are accurately predicted with differences of less than 4% and 2% from the experimental values, respectively. For the rough surface plates, the numerical data follows the trend exhibited by the experimental data, with increasing roughness height and blockage increasing skin friction and friction velocity; however, the method of determining the rough wall skin friction over predicts the value by as much as 40% relative to the experimental values. The same results occur for the friction velocity with an over prediction as much as a 20%.

Overall the turbulence models did a credible job of predicting the mean and turbulent flow quantities for the simple smooth plate geometries. Though the two algebraic turbulence models match the velocity and density profiles fairly well for the smooth and rough surface models, they are less accurate in predicting the Reynolds shear stress in the near wall region for the rough surface models. The CAMMLE model did a reasonable job predicting the full Reynolds shear stress across the boundary layer for the smooth and rough surfaces.

Chapter 8 - Discussion

8.1 Dissertation Summary

As discussed in Chapter 1, the understanding of rough surface supersonic boundary layer flow is of great importance in the development of scramjet engines, turbine blade film cooling, and possible radiation reflection reduction. Two methods are currently used to provide engineering estimates for the design of aircraft and engines with surface roughness; they are semi-empirical relations and numerical methods. Both methods have limitations with regard to high-speed rough surface boundary layers. The semi-empirical relations are based on incompressible rough surface relations and compressibility transformations developed for smooth flat plates. As such, these relations yield qualitative information at best. Numerical methods are also limited by the available compressible turbulence database and the use of compressibility extensions to existing low-speed formulations for all but Large Eddy Simulation (LES) and Direct Numerical Simulation (DNS). For these reasons, research into the effects of surface roughness in a high-speed boundary layer, specifically including turbulence measurements, is of timely importance.

The overall objective of this research was to provide a complete characterization of rough surface high-speed high Reynolds number boundary layer flow. The extensive experimental techniques and rough surface models for this research were carefully selected to enhance the understanding of the physics of high-speed rough surface boundary layers, including the investigation of increasing roughness height and blockage in fully rough flow. The experimental data was also used to evaluate two algebraic turbulence models along with the Rotta surface roughness model. Three semi-empirical skin friction coefficient relations and a new integral method of predicting skin friction (developed as part of this study) were evaluated. Finally, this research was designed to expand the

high-speed experimental database both for pragmatic engineering concerns and to provide mean and turbulent data for use in developing future turbulence models.

Three basic types of experimental information were obtained, flow visualization, mean flow quantity measurements, and turbulent quantity measurements. Visualization, consisted of color schlieren and Laser Sheet Imaging (LSI) which provided averaged and instantaneous flow visualization, respectively. Mean flow quantities were measured by Pitot, Laser Doppler Velocimetry (LDV), and Hot-Wire Anemometry (HWA). These measurements provided boundary layer velocity, density, Mach number, and mass flux data across the rough surface turbulent boundary layer. This mean information was also used to determine integral quantities and assess the suitability of current semi-empirical relations for skin friction estimation.

Besides mean flow data, LDV and HWA also provided turbulence information; including velocity and mass flux turbulence intensity and shear stress, fluctuating Mach number, Turbulent Kinetic Energy (TKE) and compressible TKE. Combining LDV and HWA (see 4.2.3) provided estimations of the density-traverse velocity correlations or apparent traverse mass flux which gives a direct indication of compressibility in high-speed flows. Additional HWA measurements using normal and parallel-film probes gave energy spectra, micro and integral length scales, and flow structure angles.

To further enhance this research, six flat plate models were chosen consisting of a smooth flat plate, two uniformly distributed rough surfaces, and three sand-grain rough surfaces. The smooth plate was used to compare with the rough surfaces and with previous smooth flat plate data collected by other researchers. The rough surface plates were all in the fully rough regime and specifically chosen to investigate the effects of surface roughness height and blockage on a high-speed turbulent boundary layer.

8.2 Conclusions

8.2.1 Experimental Data

The present experiments demonstrated that for fully rough surface high-speed boundary layer flow, roughness height and blockage had a strong impact on compressible turbulence terms (i.e., terms with ρ;). Kinematic turbulent quantities (e.g., velocity turbulence intensity, kinematic Reynolds shear stress, etc...) were less influenced by increasing surface roughness height and blockage. These conclusions were indicated by the color schlieren flow visualization and experimentally measured mean and turbulent flow quantities discussed below.

The initial onset of surface roughness had a visible effect on the boundary layer and freestream flow due to compressibility - surface roughness interactions. Color schlieren photography identified significant differences between smooth flat plate and rough surface boundary layers in the region where roughness elements protruded into the supersonic portion of the boundary layer. Compression and expansion waves were visible over machined 3D and sand-grain roughness plates at the nozzle exit/rough surface interface which would not occur over low-speed rough surfaces. This effect is related to both the surface roughness height and blockage. The magnitude and occurrence of waves over sand-grain roughness models increased with increasing roughness height. The blockage effect is illustrated by the lack of visible waves over the 2D machined rough surface, which had considerably larger blockage (3.9 times higher in the streamwise direction) than the 3D rough surface.

Mean and turbulent quantities that did not include density fluctuations (i.e., velocity turbulence intensities, fluctuating Mach number, kinematic Reynolds shear stress, turbulent kinetic energy, and intermittency) scaled with the local mean flow quantities. The fluctuating quantities had a weak dependence on roughness height and blockage for fully rough surfaces and were proportional to $\ln(k_s^+)$.

Conversely, mean and turbulent quantities that included density fluctuations did not scale with the local mean flow quantities and were significantly affected by roughness height and blockage. For fully rough surfaces, the roughness height and blockage directly affected density fluctuations appearing in the mass flux turbulence intensities, mass flux shear stresses, density-traverse velocity correlation, and the compressible turbulent kinetic energy, and for the sand-grain roughnesses, in a linear manner. The streamwise mass flux turbulence intensity and shear stress scaled reasonably well with inner variables (wall density, friction velocity, and wall shear stress). These results have important implications for numerical modeling of both Favre- and Reynolds-averaged equations. Though fluctuating density terms do not explicitly appear in the Favre-averaged Navier-Stokes equations (Section 2.2.2), they are present in the form of the mean traverse Favre fluctuation velocity ($\overline{v''}$) (see 4.2.3) in the Favre-averaged turbulent shear stress transport equation. The compressible Reynolds-averaged Navier-Stokes equations (Section 2.2.1) must account for density fluctuations in the apparent mass flux, Reynolds shear stress, and turbulent heat flux.

Surface roughness had a large effect on the power spectra, size, and angle of flow structures across the turbulent boundary layer. Increasing surface roughness height and blockage increased the power spectra and the power spectra difference between the three boundary layer regions, and shifted the mass flux turbulent power to lower frequencies in the near wall region. The effect of surface roughness on structure size was to move the sizes toward the middle, by increasing the size of the small scale structures and decreasing the size of the large scale structures. The larger the roughness height, the larger the effect, as evidenced in microscale and integral length scale values. The flow structures angles were smallest near the wall (lower region) and increased toward the boundary layer edge. Increasing surface roughness height, increased the flow structure angle, with the largest effect occurring in the outer boundary layer region. These results will be useful in the development of turbulence models, including Large Eddy Simulation (LES).

8.2.2 Integral Methods

When experimental data is available, the integration method (using the boundary layer momentum thickness at two locations) developed here (see Chapter 4) and the sand-grain roughness correlation developed by Schlichting [51] provided excellent estimates of the skin friction and the equivalent sand-grain roughness, respectively. When experimental data is unavailable and the equivalent sand-grain roughness is known (or can be found based on an effective roughness correlation), the compressible rough/smooth wall skin friction ratio correlation by Goddard provides a very good estimate (within 4% of present data) of the skin friction over rough surfaces.

8.2.3 Numerical Methods

The Prandtl mixing length and CAMMLE turbulence models with the Rotta surface roughness model did a credible job at predicting the mean and turbulent profiles (qualitatively correct profile shapes) for simple flat plate geometries. The two algebraic turbulence models matched the velocity and density profiles well for the flat plate and rough surface models. Both models accurately predicted the kinematic Reynolds shear stress across the boundary layer except in the near wall region for the rough surface models. The CAMMLE model also provided estimates of the compressible Reynolds shear stress and the density-traverse velocity correlation. The CAMMLE model did a reasonable job predicting the mass flux shear stress across the boundary layer for smooth and rough surfaces. The CAMMLE turbulence model did match experimental data in that increasing roughness Reynolds number, increased the compressible Reynolds shear stress and density-velocity correlation.

For the rough surface plates, the numerical data followed the trend exhibited by the experimental data, with increasing roughness height and blockage, increasing skin friction and friction velocity; however, the method of determining the rough wall skin friction over predicted the value

by as much as 40% relative to the experimental values. The same results occurred for the friction velocity with an over prediction up to 20%. Adjusted skin friction values that matched the numerically predicted Van Driest velocity profiles with the experimental data were calculated and found to be within 4% of the experimentally determined friction velocities.

8.3 Recommendations

The information and improved understanding gathered from this research provided a detailed characterization of the influence of surface roughness on supersonic turbulent boundary layer flow. This study will be a valuable aid to researchers and engineers in the development of semi-empirical relations (such as those in Chapter 4) and turbulence models (such as those in Chapter 5). However, three areas of further research are recommended.

The first recommendation is for the accurate measurement of the local wall shear stress over rough surfaces using a rough surface skin friction gauge small enough to capture the local skin friction. A skin friction gauge similar to those used by Hazelton [29] modified to include appropriate surface roughness elements would provide local skin friction estimates. Most shear stress estimates are based on drag balance measurements over the entire rough surface length or on momentum integral relations and/or pressure gradient. For flat plate boundary layer flows, the kinematic Reynolds shear stress near the wall is approximately equal to the wall shear stress. For rough surfaces this is not necessarily the case due to surface roughness elements protruding into the boundary layer. For compressible flows, the difference between the kinematic Reynolds shear stress provided by two component LDV measurements and the wall shear stress found using a local skin friction gauge can provide information on the magnitude of the form drag due to surface roughness.

The second recommendation is to extend the scope of the machined roughness spacing portion of this study for both 2D and 3D distributions of roughness elements, on high-speed turbulent bound-

ary layer flows. As discussed above the effect of surface roughness blockage follows the trends of surface roughness height; however, the limited quantity of machined models precludes a more detailed examination. A systematic study varying the 2D and 3D element spacing for high-speed turbulent flows would provide insight into the effect of compressibility and roughness blockage. The importance of which can be seen in the nozzle exit/rough surface interface where compression and expansion waves were visible over the 3D machined roughness elements and not the 2D elements, even though both models had the same roughness height. The 2D and 3D element spacing should span a range of "wavelengths", λ, corresponding to λ/k values covering both "d-type" and "k-type" [4,37,46] roughnesses discussed in Section 6.1.1. The study should include measurement techniques which provide kinematic and mass flux or density fluctuations based on the findings of this study.

The third recommendation is to evaluate higher order turbulence models, such as the $K-\omega$ turbulence model using the boundary condition roughness model outlined in Wilcox [68] and the Reynolds Shear Stress model. Though algebraic turbulence models are still in general use throughout industry, the availability of faster computational resources and more complicated flow field geometries has lead to the use of higher order turbulence models to more accurately predict turbulent flow fields. The turbulent quantities measured in this study provide valuable information for the development of more predictive higher order turbulence models.

APPENDIX A - Hot-Film Equipment Setup, Calibration, and Multiple Overheat

This appendix covers the equipment hardware and software settings along with the hot-film calibration and data reduction information for each of the four hot-film measurement methods used in the present study. The four hot-film measurement techniques are x-y plane cross-film, x-z plane cross-film, normal-film, and parallel-film probes.

A.1 X-Y Plane Probe

A.1.1 Single Overheat

A.1.1.1 Equipment Setup

The hardware was connected to the DANTEC system and a project file was created. The project file contains information regarding the hardware setup, experiments, and any acquired data files. After the project was created, a hardware and experimental setup file were completed. The hardware setup file allows the setting of wire/film resistance, tuning, and conditioning information, while the experimental setup describes the data acquisition and triggering information. The hardware used to measure the x-y plane cross-film data consisted of the DANTEC Streamline system and a TSI 1243-20 cross-film probe. The hardware setup file consisted of a schematic with probe, holder, and DANTEC connections; probe resistance and overheat settings; bridge tuning information; and signal conditioning information. The settings for the x-y axis cross-film measurements are shown in Table 16

Once the hardware file was properly setup, an experiment file was created which outlines the specific data to be collected, the acquisition rate, the number of data points to be collected, and a trigger (if any). Table 17 shows the specific experiment information used to collected data for the

x-y plane cross-film measurements. Table 17 also includes traverse rate information which is not part of the StreamLine system in the current configuration.

A.1.1.2 Calibration and Data Reduction

The calibration of the TSI 1243-20 x-y plane cross-film probe was done by positioning the probe at 3.175 cm from the top of the lower surface plates (i.e., from the top of the smooth plate or the top of the roughness elements, as required) using the travelling telemicroscope. Figure 209 is a plot of the Mach 2.9 tunnel averaged stagnation pressure and cross-film voltages collected during a calibration run. Five points from the cross-film calibration data were selected and placed in a file for each wire for use in the WinMShear hot-film data reduction software. The voltage and flow variable data points are processed into Nusselt and Reynolds values, respectively, for the determination of the calibration constants, a and b. As an example, the five calibration points, and calibration constants are shown in Table 18. A plot of the Nusselt and Reynolds values along with the line fit is shown in Figure 210. The data reduction consists of measuring the probe deflection, processing the cross-film data, and putting the data into files usable by WinMShear.

For the TSI 1243-20 probe, the deflection was measured at two locations. A total of three measurements were taken at each location measuring the amount of downward probe deflection. The average for each location was calculated along with the equation of a line through the two location points. The line equation was used in the data reduction routine to properly locate the y-axis position of the probe at it was traversed through the boundary layer.

The cross-film data processing consisted of averaging the voltage data and calculating rms value for each film sensor, along with the two sensor cross-correlation voltage data. The average, rms, and cross-correlation data files, combined with a calibration file for each sensor (and each

overheat ratio) and mean flow Pitot information were used by the WinMShear program to calculate mean and turbulent flow information over the smooth and rough plates.

A.1.2 Multiple Overheat

Seven calibration and experimental measurements corresponding to different film temperatures were completed for the 2D plate boundary layer flow for analysis using the Multiple Overheat Hot-Wire Anemometry (MOH-HWA) technique developed by Bowersox [14].

A.1.2.1 Equipment Setup

The DANTEC hardware and software setup for the x-y plane multiple overheat measurements are shown in Table 19 and 17, respectively. The hardware setup was identical to the single overheat measurements with the only exception being the external resistance values. Table 20 gives the external resistance values and corresponding overheat ratios for each of the seven measurements.

A.1.2.2 Calibration and Data Reduction

The calibration of the TSI 1243-20 x-y plane cross-film probe was done in the same manner as the single overheat measurements with a calibration required for each of the seven external resistance values (corresponding to seven overheat ratios). Again, the voltage and flow variable data points are processed into Nusselt and Reynolds values, respectively, for the determination of the calibration constants, a and b. A calibration file containing the calibration constants were created for each film sensor (two for an x-array probe) at each overheat ratio.

The cross-film data processing consisted of averaging the voltage data and calculating rms values for each film sensor, along with the two sensor cross-correlation voltage data at each overheat ratio. The average, rms, and cross-correlation data files, combined with a calibration file for each sensor (and each overheat ratio) and mean flow Pitot information were used by the WinMShear program to calculate mean and turbulent flow information over the smooth and rough plates.

A.1.2.3 Results

The ρu- and ρv-components of the mass flux turbulence intensity measured using the x-y plane cross-film probe are shown in Figure 211. The figure shows the experimental data reduced using Single Overheat (SOH) and Quadratic Least Squares (QLS) MOH reduction techniques. The QLS MOH method matches the results of the SOH with slight differences in the lower boundary layer region and near the boundary layer edge. The differences between the QLS MOH and the SOH data reduction techniques is attributed to errors introduced in the hot-film sensitivities and with the numerical difficulty in calculating very small total temperature fluctuations. The total temperature profile and total temperature turbulence intensity are shown in Figures 212 and 213. Figure 212 shows the total temperature remains approximately constant with less than 3% variation over the entire boundary layer. Figure 213 shows a total temperature turbulence intensity of between 1% and 2% in the freestream and less than 4% across the boundary layer with the largest intensity in the boundary layer edge region. The ρu- and ρv- components of the mass flux - total temperature correlation are shown in Figure 214 for the QLS MOH data reduction technique.

A.2 X-Z Plane Probe Equipment Setup, Calibration, and Reduction

The hardware file for the x-z plane cross-film probe was identical to the x-y plane probe with the exception of the probe itself (a TSI 1243AN-20) and sensor resistances. Table 21 shows the settings for the x-z plane cross-film measurements. The experiment file was setup identically to the x-y plane cross-film measurements. The probe calibration and data reduction were also preformed in the same manner as described above in Section A.1.2.2.

A.3 Normal-Wire Probe Equipment Setup

The TSI 1218-20 normal-film probe was used to collect frequency resolved boundary layer data. The normal-film probe was run by the DANTEC Streamline system with the film voltage data

collected by the Nicolet data acquisition system set for 250,000 samples at a frequency of 1 Mhz. The normal-film probe DANTEC hardware setup file settings are shown in Table 22. An experiment file was not required for this experiment. The data were reduced using discrete Fourier transform and autocorrelation routines discussed in Sections 4.2.4.1 and 4.2.4.2, respectively.

A.4 Parallel-Wire Probe Equipment Setup

The TSI 1246AD-20 parallel-film probe was used to collect boundary layer flow structure angularity information. Similar to the normal-film probe the parallel-film probe was run by the DANTEC Streamline system with the film voltage data collected by the Nicolet data acquisition system set for 125,000 samples at a frequency of 1 Mhz for each sensor. The parallel-film probe DANTEC hardware setup file settings are shown in Table 23. An experiment file was not required for this experiment.

APPENDIX B - LDV General Theory and Equipment Setup

The hardware used to acquire Laser Doppler Velocimetry (LDV) data is described in Section 3.2.1. This appendix presents a brief description of the LDV general theory and the system settings used to acquire this data.

B.1 General Theory

Laser Doppler velocimetry uses the wave-like properties of light to measure the velocity of tracer particles suspended in a fluid (or gas) of interest. When two laser beams of identical wavelength cross, an interference pattern is formed. For laser beams with gaussian distributions, the intersection of the beams forms a ellipsoid measurement volume with fringe pattern spacing dependent on the beam intersection angle, θ, and the wavelength of the beams, λ, and is given by

$$x_f = \frac{\lambda/2}{\sin(\theta/2)} \tag{182}$$

As seed (tracer) particles pass through the measurement volume and pass across the alternating dark and light fringe patterns, burst of scattered light is created and is called a Doppler burst. To eliminate directional ambiguity for a given Doppler burst, one laser beam is phase shifted 40 Mhz from the other using a Bragg cell. The receiving optics of the DANTEC LDV system collect and multiply this Doppler burst for processing in one of two Burst Spectrum Analyzers (BSAs) available in the DANTEC LDV system. The BSAs process each Doppler burst and based on the frequency, determine the individual seed particle velocities. The BSAs are also used to validate Doppler bursts to insure that the burst consists of only a single particle that has passed through the control volume near the center. When sufficient, valid particle velocities have been measured, statical properties, such as, the turbulence intensity, flatness, and skewness can be determined. For a two component LDV system the turbulent velocity cross-correlation (turbulent shear stress) can also be determined.

A more thorough discussion on the theory and processing of Doppler bursts can be found in the DANTEC BURSTware Installation and User's Guide [20], DANTEC BSA Enhanced User's Guide [22], or in *Principles and Practice of Laser-Doppler Anemometry* by Durst, Melling and Whitelaw [24].

B.2 System Settings

The DANTEC BURSTware system settings consisted of three menu settings. The three menus were the "Quick", "Soft", and "BSA Program" menus with the values shown in Tables 24, 25, and 26, respectively. Under the "Valid" menu, the collection method was set to "Valid Data". For data acquisition, the BSA buffers were set to First In, First Out (FIFO) with a record length 16 samples. For all measurements, the u-component burst validity rate was $10 - 23\%$ with no less than 4000 valid Doppler bursts per data point and the v-component validity rate was $4 - 9\%$ with no less than 2000 valid Doppler bursts.

APPENDIX C - Uncertainty Analysis

Error and uncertainty are inherent in any experimental research. This section attempts to identify sources of error and estimate their effects on the present data. Based on the analysis presented in Bowersox [14] this study uses the Euclidean (L_2) norm as the measure of error. The L_2 norm is defined as [58]

$$\|x_i\|_2 = \|x_1, x_2, ..., x_n\|_2 = \left[\sum_{i=1}^{n} x_i^2\right]^{1/2} \tag{183}$$

for a given set of data, x_i. The total dimensional error is defined as

$$E_f \equiv \|E_{x_i}\|_2 = \left[\sum_{i=1}^{n} \left(\frac{\partial f}{\partial x_i} E_{x_i}\right)^2\right]^{1/2} \tag{184}$$

where f is a function dependent on x_i and E_{x_i} is the error associated over the various applicable measurements. The percent or nondimensional error is given by

$$\varepsilon_f = \frac{E_f}{f} \tag{185}$$

which is the total error nondimensionalized by the mean value. The reduced data error bounds are estimated based on the linearized reduction equations and include the propagation of measurement errors. The subsections below examine the measurement and propagation errors for each experimental technique with the assumption that all errors are random and have a Gaussian distribution.

C.1 Measurement Errors

Seven separate measurement techniques were used to collect data for this study. They are Pitot, cross-film, parallel-film, and normal-film Hot-Wire Anemometry (HWA), Laser Doppler Velocimetry (LDV), color schlieren, and Laser Sheet Imaging (LSI) measurements. Typical freestream conditions and HWA parameters are shown in Tables 27 and 28, respectively, and were used in this analysis.

Plenum and Pitot pressure was measured using Endevco pressure transducers which measured gauge pressure. The Endevco pressure transducers had accuracies of $\pm 0.5\%$ [25], while the Endevco

conditioner had a maximum gain error of $\pm 0.5\%$ and a gain stability of $\pm 0.2\%$ [26]. The ambient air pressure was measured using a Druck DPI 141 Resonant Sensor Barometer with an accuracy of ± 0.0001 atm. The error introduced by any ambient air pressure inaccuracy was consider negligible compared to the pressure transducer and conditioner errors. As found by Volluz [63], turbulence induces approximately $\pm 0.0068\%$ atm error for Pitot probe measurements.

The calculation of boundary layer heights has large errors associated with the geometry of the problem. For boundary layers near the freestream, large changes in y give small changes in velocity and since every measurement has some associated scatter, the error in boundary layer edge placement can be large. The Pitot probe boundary layer height error consisted of both velocity uncertainty and vertical probe position uncertainty. The velocity uncertainty was determined graphically as in Luker [39] and found to be 20%. The vertical probe position uncertainty was as large as 5% giving a boundary layer height uncertainty of 21%. Boundary layer height error estimates based on LDV, color schlieren and laser sheet images were extremely difficult to ascertain and were estimated to be at least as large as the Pitot measurement method. Table 31 gives the boundary layer height uncertainty.

Multiple overheat (MOH) measurements by Miller [41] and McCann [40] in the AFIT Mach 2.9 wind tunnel has shown boundary layer total temperature rms fluctuations of 2.0%. The total temperature rms fluctuations give an error bound on total temperature measurements. The plenum total temperature thermocouple and conditioner had an accuracy of $\pm 1\ K$ with the total temperature varying not more than $\pm 1\ K$ during a tunnel run.

The position of each measurement probe also has associated uncertainties based on the measured position relative to the tunnel test location origin and probe flexing during tunnel operation. The travelling telemicroscope provided a position accuracy of ± 0.0005 mm for the scope cross-hairs and was used to determine the probe initial position relative to the tops of the surface roughness el-

ements and to determine the amount of probe flex during a tunnel run. For each probe, the amount of downward deflection at two points in the flowfield (near the wall and in the center of the tunnel) was measured three times and averaged to determine a linear equation giving the probes deflected y-axis position using LVDT position data. For each probe, the variation of the three measurements was not more than ± 0.05 mm; however, each probe vibrated during a tunnel run leading to additional uncertainty. The x and y position accuracy was estimated at ± 0.5 mm with probe flex giving an additional 1.1 mm error in the x-axis position and an additional uncertainty for the y position based on the A/D conversion of the LVDT voltage output. For a 12 bit A/D convertor measuring a voltage range of ± 5.0 volts, the voltage uncertainty was ± 0.0024 V with a position uncertainty of ± 0.015 mm. The z-axis position error was estimated to be twice the x- and y-axis position error (± 1.0 mm).

Based on the hot-wire measurements, the freestream film sensor voltage fluctuation rms value was found to be less than 1.0%. Two types of sensor angular alignment errors exist. The first is the angular probe alignment error relative to the tunnel coordinates and the second is the film sensor angular error relative to the probe leads and body. The probe was calibrated with the identical angular position relative to the tunnel coordinates before each experimental run greatly decreasing this source of angular error. The second error due to hot-film sensor misalignment is estimated at less than 1% based on freestream cross-film mean flow angle measurements. An additional error of ± 0.0024 V was included for the hot-wire voltage error based on A/D conversion.

The hardware and software setup, laser alignment, and experimental procedures for the LDV measurements follow the methods outlined in Luker [39] for turbulence measurements in the AFIT Mach 2.9 wind tunnel. An excellent discussion and analysis of LDV measurement uncertainties can be found in Appendix B of Luker [39]. Based on identical equipment setup and similar flow

conditions, the uncertainty analysis by Luker is deemed to provide an accurate assessment of LDV measurement uncertainty and is used for this study.

The pressure, temperature, position and film voltage measurement errors are shown in Table 29. While the LDV measurement errors are shown in Table 30.

C.2 Error Propagation

The measurement errors listed in Tables 29 and 30 influence all subsequent data reduction. The subsections below cover the propagated error for each measurement technique.

C.2.1 Properties Determined with Pitot Probes

The Pitot probe mean flow estimations are based primarily on the local Mach number, with the Mach Number calculated using the Rayleigh-Pitot tube formula given in Equation (73). The static pressure is determined from the freestream Mach number found using Equation (72). As an example of error propagation, applying Equations (184) and (185) to Equation (72) gives the percent error in M_∞ as

$$\varepsilon_{M\infty} = \frac{E_{M\infty}}{M_\infty} = \sqrt{\left(\frac{\partial M_\infty}{\partial P_{o1}}\frac{E_{P_{o1}}}{M_\infty}\right)^2 + \left(\frac{\partial M_\infty}{\partial P_{o2}}\frac{E_{P_{o2}}}{M_\infty}\right)^2} \tag{186}$$

Which gives

$$\varepsilon_{M\infty} = \frac{E_{M\infty}}{M_\infty} = \sqrt{\left(\frac{-P_{o2}}{P_{o1}^2}\frac{E_{P_{o1}}}{M_\infty}\right)^2 + \left(\frac{1}{P_{o1}}\frac{E_{P_{o2}}}{M_\infty}\right)^2} \tag{187}$$

The static pressure, P_1, percent error is defined as

$$\varepsilon_{P1} = \frac{E_{P1}}{P_1} = \sqrt{\left(\frac{\partial P_1}{\partial P_{o1}}\frac{E_{P_{o1}}}{P_1}\right)^2 + \left(\frac{\partial P_1}{\partial M_\infty}\frac{E_{M\infty}}{P_1}\right)^2} \tag{188}$$

using the isentropic relationship for the pressure ratio, P_{o1}/P_1, the static pressure percent error becomes

$$\varepsilon_{P1} = \frac{E_{P1}}{P_1} = \sqrt{\left(\frac{E_{P_{o1}}}{P_{o1}}\right)^2 + \left(-\gamma M^2\left[1+\frac{\gamma-1}{2}M^2\right]^{-1}\frac{E_{M\infty}}{P_1}\right)^2} \tag{189}$$

Finally, assuming the static pressure is constant across the boundary layer, the Mach number percent error is found by applying Equations (184) and (185) to the Rayleigh-Pitot tube formula which gives

$$\varepsilon_M = \frac{E_M}{M} = \sqrt{\left(\frac{\partial M}{\partial P_1}\frac{E_{P_1}}{M}\right)^2 + \left(\frac{\partial M}{\partial P_{o2}}\frac{E_{P_{o2}}}{M}\right)^2} \tag{190}$$

and

$$\varepsilon_M = \frac{E_M}{M} = \sqrt{\left(\frac{-P_{o2}}{P_1^2}\frac{E_{P_1}}{M}\right)^2 + \left(\frac{1}{P_1}\frac{E_{P_{o2}}}{M}\right)^2} \tag{191}$$

The Mach number and total temperature measured in the tunnel plenum was used to calculate the mean local tunnel static temperature, T_1, assuming isentropic flow. The equation of state and ideal gas laws were used to calculate mean density, speed, and mass flux. Table 32 presents the propagation errors of the Pitot pressure measurements. Propagated error estimates for Van Driest parameters were calculated as in Luker [39] and are also given in Table 32. The error in the wall shear stress for the smooth plate has been documented as approximately 10% [11] and was used for the rough surface wall shear stress error estimate.

C.2.2 Properties Determined with HWA

C.2.2.1 Cross-Film Probes

Single overheat (SOH) and Multiple Overheat (MOH) (see Appendix A) HWA was used to measure mass flux mean and fluctuating quantities over the six surfaces. For SOH analysis the total temperature fluctuations are assumed to be negligible which has been shown to be less than 2% [41] for the smooth wall boundary and less than 4% for the 2D rough surface plate (see Appendix A). For HWA, the relationship between the Nusselt number and Reynolds number [Equation (90)] is used to determine the mass flux over a hot-wire sensor based on the amount of voltage required to maintain the sensor at a constant temperature in a turbulent flowfield. The error in the Nusselt number is a function of the measured voltage and total temperature error, while the error in the effective Reynolds number, Re_e, is based on Equation (95). A logarithmic/derivative analysis was

performed on the hot-wire data reduction equations shown in Chapter 4 [49]. The error in the v- and w-components of mass flux were assumed to be the same as the streamwise or u-component. Table 33 summaries the propagation errors for hot-film probe measurements.

C.2.2.2 Normal-Film Probe

The normal-film probe was used to collect frequency resolved power spectra, microscale,and integral scale values for each of the six surface plates. The maximum power spectra normalized standard error is given by $\varepsilon_{ps} = \sqrt{\frac{1}{N}}$ [5], where N is the number of data blocks. The microscale values were determined by fitting an "osculating " parabola to the first few points of the normal-film autocorrelation function with errors introduced due to film voltage fluctuations and the data acquisition rate (1 Mhz). For each hot-film voltage measurement, 128 ksamples (131,072) were acquired, which were processed in 1024 blocks giving a film voltage error of less than 1% (based on a Chi-Square distribution). Hence, the primary error component of the microscale value (and integral scale to a lessor degree) is the data acquisition rate. This leads to a microscale error bound of $\pm 0.5\mu$sec. For a microscale estimate of $\sim 20\mu$sec, the percent error is $\pm 2.5\%$. Since the integral scale estimate is found by integrating the autocorrelation function from $\tau = 0$ to ∞, the integral scale is considerably less affected by the data acquisition rate; however, for this study, the integral scale is assumed to have an error equal to the microscale. Table 34 includes the propagation errors for normal-film measurements.

C.2.2.3 Parallel-Film Probes

The parallel-film probe was used to collect film voltage cross-correlation data, which, in turn, was used to determine the flow structure angle (see Equation (137)). The flow structure angle error is dependent upon the wire separation distance error, mean local velocity error, and the cross-correlation peak time lag error. For a wire separation of 1.85 mm, the travelling telemicroscope

gave an error of $\varepsilon_w \ll 1\%$ and is considered negligible. Assuming a mean local velocity error of 10 m/s in a 590 m/s streamwise flow, the mean local velocity error is approximately 2%. Finally, for the six plates the cross-correlation peak time lag ranged from 1 to 3 μsec. Figure 215 shows a typical flow structure angle versus the cross-correlation peak time lag. Assuming an error of one half the distance from a given time lag to an adjacent value (an interval of 1μsec for the 1Mhz data acquisition rate) the maximum error occurs between a peak lag of 0 - 1μsec leading to a maximum angular error of $\pm$14.4% (see Table 34). For this study, the flow structure angle error is dominated by the data acquisition rate, with both the mean local velocity and wire separation distance errors assumed to be negligible.

C.2.3 Properties Determined with LDV

The propagation errors based on LDV measurements are shown in Table 35 and are based on the uncertainty analysis by Luker [39].

C.2.4 Properties Determined with Combined HWA and LDV

Using the uncertainty analysis shown above, the estimated errors for the traverse apparent mass flux and mean density were determined and are also shown in Table 35. The traverse apparent mass flux error is dependent upon the kinematic Reynolds shear stress and the mass-flux turbulent shear stress errors, while the mean density is dependent upon the mean mass flux and mean velocity errors.

APPENDIX D - Numerical Validation Methods

Prior to numerically predicting the boundary layer flowfield over smooth and rough surface flat plates using the parabolized Navier-Stokes solver discussed in Chapter 5, a grid study and turbulence model validation were performed. The two sections below briefly discuss the results of the grid resolution study and turbulence model validation.

D.1 Grid Resolution

A grid resolution study was performed prior to numerically predicting the boundary layer flowfield for this study. The purpose of the grid resolution study was to determine the lowest resolution grid which gave computed results identical to higher resolution grids. The lowest resolution grid required the least computation time and was used to compute the results found in Chapter 7.

Three grid resolutions are presented in this section. They are 101 x 201, 101 x 251, and 201 x 251, with the first number representing the x-axis or streamwise stations and the second number representing the y-axis or traverse nodes. The grid resolutions are tabulated in Table 36 along with the streamwise grid spacing and the first traverse spacing value. Lower resolutions were also tried but were found to be inadequate and are not presented here.

Figures 216, 217, and 218 show the velocity, density, and kinematic shear stress profiles, respectively, for each of the three grid resolutions using the inflow conditions shown in Table 4 for the smooth plate. The numerical data show that the results are identical for each of the three grid resolutions with very slight variations for the kinematic Reynolds shear stress values. Only the Prandtl mixing length results are shown in this analysis, since the Compressible Apparent Mass Mixing Length Extension (CAMMLE) model gave identical results.

D.2 Turbulence Model Validation

The Prandtl and CAMMLE turbulence models were validated using the compressible Van Driest velocity profile correlation found in White [66] (after White and Christoph [65]). For zero pressure gradient and heat flux, compressible boundary layer flow; the Van Driest velocity profile is given by

$$u^+\left(y^+,\gamma\right) = \frac{1}{\sqrt{\gamma}}\sin\left(\frac{\sqrt{\gamma}}{\kappa}\ln\left(\frac{y^+}{y_o^+}\right)\right) \tag{192}$$

with

$$y_o^+ = e^{-\kappa B} \quad \text{and} \quad \gamma = \frac{ru^{*2}}{2c_pT_w}$$

where κ and B are given by the low-speed logarithmic correlation, r is the recovery factor, u^* is the friction velocity, c_p is the specific heat at constant pressure, and T_w is the wall boundary temperature. Figure 219 shows the Van Driest velocity profiles for the Prandtl mixing length model for each grid resolution versus the theory outlined above (again only the Prandtl model is shown since the CAMMLE model gave identical results). The agreement between the theory and turbulence models is considered excellent, validating the Prandtl and CAMMLE models as implemented in the parabolized Navier-Stokes solver used in this study.

APPENDIX E - Supplemental Data

This appendix presents supplemental measurement data covering experimental repeatability and tunnel flowfield characteristics, as well as, additional mean and turbulence data.

E.1 Repeatability and Two-Dimensionality

Additional Pitot and Hot-Wire Anemometry (HWA) measurements were performed to assess the repeatability of each measurement method. The repeatability of Laser Doppler Velocimetry (LDV) method has been shown by Luker [39] for the Mach 2.9 tunnel and DANTEC LDV equipment. Figures 220 and 221 show the velocity and Pitot probe total pressure profiles, respectively, for the 2D rough surface plate. Both figures include two separate experimental runs and show outstanding Pitot probe repeatability (within experimental scatter).

For the HWA system, two experimental measurements were completed for each plate using both the x-y and x-z plane, cross-film probes. The x-y plane, cross-film probe results are shown in Figures 222 through 225. Figure 222 shows the x-y plane, cross-film, ρu-component of the mean mass flux. The ρu- and ρv-turbulence intensities are shown in Figures 223 and 224, respectively. Finally, the x-y plane, cross-film, mass flux shear stress is shown in Figure 225. The repeatability of HWA is within the uncertainty eluded to in Appendix C and is considered excellent.

The flowfield two-dimensionality was checked by making three Pitot pressure measurement profiles at the test location for the smooth plate (i.e., z =0, $\pm$1.27 cm). The velocity profiles calculated from the Pitot probe total pressure are shown in Figure 226 and indicate the flowfield was two-dimensional.

E.2 Supplemental Data

The information in Chapter 6 was presented in a manner to facilitate the comparison of experimental results for each of the six plates. To this end, experimental values for all six plates are

combined on single plots. This section presents data from different sources (i.e., Pitot, LDV, et...) for each individual plate allowing a less cluttered format, as well as, additional results not presented in Chapter 6.

Mean flow results, including mean velocity, Mach, density, and mass flux profiles are shown in Figures 227 through 250. Figures 227 through 232 show the velocity profiles from Pitot and LDV measurements for each of the six models, respectively. Figures 233 through 238 show the Mach profiles and Figures 239 through 244 show the density profiles for Pitot and LDV measurements. The mean mass flux profiles measured using Pitot, LDV, and HWA are shown in Figures 245 through 250.

Additional turbulence measurement results are shown in Figures 251 through 257. Figure 251 shows the x-z plane, cross-film, mass flux turbulence intensity profiles. The data agrees with the x-y plane, cross-film, mass flux turbulence intensity profiles with the exception of the near wall region. The near wall region differences are attributed to the probe geometry in which one film sensor is below the other.

As a comparison, the incompressible Reynolds shear stress from the LDV measurements and the separated cross-film data are shown in Figures 252 through 257 for each of the six models. The separated cross-film data has been shifted left a value of 0.03, representing the difference in freestream measurements between the LDV and cross-film values. That is, the cross-film measurements typically have a larger freestream turbulence intensity than corresponding LDV measurements. All values agree exceptionally well in terms of magnitude and slope with the exception of the 2D and 20 grit plates.

APPENDIX F - Data Tables

This appendix presents the experimental data from the Pitot, Hot-Wire Anemometry (HWA) and Laser Doppler Velocimetry (LDV) measurement techniques. Tables 37 through 42 show the tabulated Pitot reduced data. Tables 43 through 48 show the tabulated x-y plane cross-film probe reduced data. Tables 49 through 54 show the tabulated x-z plane cross-film probe reduced data. Finally, Tables 55 through 60 show the tabulated LDV reduced data.

BIBLIOGRAPHY

[1] *Probe Catalog*. Denmark: Dantec Electronik, 1982.

[2] *NASA Hyper-X Hypersonic Aircraft Program*. Technical Report, www.dfrc.nasa.gov/-Projects/HyperX/index.html: NASA Langley Research Center, 1998.

[3] Anderson, Dale A., et al. *Computational Fluid Mechanics and Heat Transfer*. Hemisphere Publishing Corporation, 1984.

[4] Antonia, R. A. and D. H. Wood. "Calculation of a Turbulent Boundary Layer Downstream of a Small Step Change in Surface Roughness," *Aeronautical Quarterly*, August 202–210 1975.

[5] Bendat, J. S. and A. G. Piersol. *Random Data: Analysis and Measurement Procedures*. New York: John Wiley and Sons, Inc., 1971.

[6] Bowersox, R. D. W. *Cell-Centered, Finite Volume, Parabolized Navier-Stokes Solver*, 1994.

[7] Bowersox, R. D. W. *MShear Hot-Wire Data Reduction Program*, 1994.

[8] Bowersox, R. D. W., "AERO 827 Class Notes," 1996.

[9] Bowersox, R. D. W. and T. A. Buter. "Turbulence Measurements in a Mach 2.9 Boundary Layer Including Mild Pressure Gradients," *AIAA Journal*, Vol. 34 No. 12, 2479 – 2483 1996.

[10] Bowersox, R. D. W. and J. A. Schetz. "Model for Compressible Turbulence in Hypersonic Wall Boundary and High-Speed Mixing Layers," *AIAA Journal*, Vol. 32 No. 7, 1531–1533 1993.

[11] Bowersox, R. D. W., et al. "Technique For Direct Measurement of Skin Friction in High-Enthalpy Scramjet Flowfields," *AIAA Journal*, Vol. 33 No. 7, 1286–1291 July 1995.

[12] Bowersox, Rodney D. W. "Combined Laser Doppler Velocimetry and Cross-Wire Anemometry Analysis," *AIAA Journal*, Vol. 34 2269 – 2275 1996.

[13] Bowersox, Rodney D. W. and Joseph A. Schetz. "Compressible Turbulence Measurements in a High-Speed High-Reynolds-Number Mixing Layer," *AIAA Journal*, Vol. 32 No. 4, 758–764 April, 1994.

[14] Bowersox, Rodney Dale Welch. *Compressible Turbulence in a High-Speed High Reynolds Number Mixing Layer*. PhD dissertation, Virginia Polytechnic Institute and State University, 1992.

[15] Bradshaw, P. "The effect of Mean Compression or Dilatation on the Turbulence Structure of Supersonic Boundary Layers," *Journal of Fluid Mechanics*, Vol. 63 Part 3, 449–464 1974.

[16] Cebeci, Tuncer and K. C. Chang. "Calculation of Incompressible Rough-Wall Boundary-Layer Flows," *AIAA Journal*, Vol. 16 No. 7, 730–735 July, 1978.

[17] Cebeci, Tuncer and A. M. O. Smith. *Analysis of Turbulent Boundary Layers*. Applied Mathematics and Mechanics, Academic Press, 1974.

[18] Clauser, F. "The Turbulent Boundary Layer," *Advances in Applied Mechanics*, Vol. 4 1956.

[19] Coles, D. "The Law of the Wake in the Turbulent Boundary Layer," *J. Fluid Mechanics*,

Vol. 1 191–226 1956.

[20] DANTEC Measurement Technology. *BURSTware Installation and User's Guide*, 1995.

[21] DANTEC Measurement Technology A/S, Skovlunde, Denmark: DANTEC, Inc. *StreamLine Installation And User's Guide*.

[22] DANTEC Measurement Technology A/S, Skovlunde, Denmark: DANTEC, Inc. *User's Guide: 57N20/57N35 BSA Enhanced*.

[23] Dirling, R. B. "A Method for Computing Rough Wall Heat Transfer Rates on Reentry Nosetips," *AIAA Paper* 1973.

[24] Durst, F., et al. *Principles and Practice of Laser-Doppler Anemometry, Second Edition*. London: Academic Press, 1981.

[25] Endevco Corporation, San Juan Capistrano, California. *General Catalog Binder*, 1992.

[26] Endevco Corporation, San Juan Capistrano, California. *Model 4428A Pressure Indicator Instruction Manual*, 1994.

[27] Fiore, A. W. "Experimental Data for Compressible Turbulent Flow Over Rough Flat-Plate," *Air Force Wright Aeronautical Laboratories, WPAFB, OH* June, 1983.

[28] Goddard, Frank E. "Effect of Uniformly Distributed Roughness on Turbulent Skin-Friction Drag at Supersonic Speeds," *Journal of the Aero/Space Sciences*, Vol. 26 No. 1, 1–24 January, 1959.

[29] Hazelton, David M. *Direct Measurement of Skin Friction in High Temperature and Impulsively Started Supersonic Flowfields*. PhD dissertation, Air Force Institute of Technology, 1996.

[30] Heiser, W. H. and D. T. Pratt. *Hypersonic Airbreathing Propulsion, AIAA Education Series*. Washington DC: AIAA, 1994.

[31] Hinze, O. J. *Turbulence*. New York: McGraw-Hill, 1975.

[32] Huffman, R. *AFIT Mach 2.9 Lab Manual*, undated.

[33] Incropera, Frank P. and David P. DeWitt. *Fundamentals of Heat and Mass Transfer* (third Edition). John Wiley & Sons, 1990.

[34] John D. Anderson, Jr. *Introduction to Flight*. New York: McGraw-Hill Book Company, 1985.

[35] Klebanoff, P. S. *Characteristics of Turbulence in a Boundary Layer with Zero Pressure Gradient*. Technical Report TR-1247, NACA, 1953.

[36] Kovaszney, L. S. G. "The Hot-Wire Anemometer in Supersonic Flow," *Journal of Aeronautical Sciences*, Vol. 17 565–584 1950.

[37] Liu, C. K., et al. "An Experimental Study of Turbulent Boundary Layers on Rough Walls," Report MD-15 1966.

[38] Luker, J. J., et al. "Experimental Analysis of the Turbulent Shear Stresses for Distorted Supersonic Boundary Layers," *Journal of Propulsion and Power*, Vol. 14 No. 1, 110 – 118 January - February, 1998.

[39] Luker, Joel J. *Experimental Investigation of a Supersonic Boundary Layer Including Favorable Pressure Gradient Effects*. MS thesis, Air Force Institute of Technology, 1995.

[40] McCann, G. *Compressible Turbulence Measurements in Low-Angle Injection Into a Supersonic Flow*. MS thesis, MS Thesis, School of Engineering, Air Force Institute of Technology (AU), Wright-Patterson AFB OH, 1995.

[41] Miller, R. *Compressible Turbulence Measurements in a Supersonic Boundary Layer Including Favorable Pressure Gradient Effects*. MS thesis, MS Thesis, School of Engineering, Air Force Institute of Technology (AU), Wright-Patterson Air Force Base, OH, 1994.

[42] Morkovin, M. "Fluctuations and Hot-Wire Anemometry in Compressible Flow," *AGARDOGRAPH*, 24 1956.

[43] Morkovin, Mark V. "Effects of Compressiblity on Turbulent Flows." *The Mechanics of Turbulence* edited by A. Favre, 368–380, New York: Gordon and Breach, 1961.

[44] Nikuradse, J. "Stromungsgesetze in Rauhen Rohren," *Forschg.-Arb. Ing.-Wesen* 1933.

[45] Perry, A. E. and P. N. Joubert. "Rough-Wall Boundary Layers in Adverse Pressure Gradients," *Journal of Fluid Mechanics*, Vol. 17 193 – 211 1963.

[46] Perry, A. E., et al. "Rough Wall Turbulent Boundary Layers," *Journal of Fluid Mechanics*, Vol. 37 383–413 1969.

[47] Reda, Daniel C., et al. "Compressible Turbulent Skin Friction on Rough and Rough/Wavy Walls in Adiabatic Flow," *AIAA 7^{th} Fluid and Plasma Dynamics Conference* June 17-19, 1974.

[48] Reid, G. J. *Linear Systems Fundamentals: Continuous and Discrete, Classic and Modern*. New York: McGraw-Hill, 1983.

[49] Richard E. Huffman, Jr. *Mach 2.9 Investigation Into the Flow Structure in the Vicinity of a Wrap-Around Fin*. MS thesis, MS Thesis, School of Engineering, Air Force Institute of Technology (AU), Wright-Patterson AFB OH, 1995.

[50] Schetz, Joseph A. *Boundary Layer Analysis*. Prentice Hall, 1993.

[51] Schlichting, Hermann. *Boundary Layer Theory*. Mechanical Engineering, McGraw-Hill Book Co. Inc., 1955.

[52] Settles, Gary S. and Lori J. Dodson. "Supersonic and Hypersonic Shock/Boundary-Layer Interaction Database," *AIAA Journal*, Vol. 32 No. 7, July, 1994.

[53] Simpson, Roger L. "A Generalized Correlation of Roughness Density Effects on the Turbulent Boundary Layer," *AIAA Journal*, Vol. 11 No. 2, 242–244 February, 1973.

[54] Smits, A. J., et al. "A Comparison of the Turbulence Structure of Subsonic and Supersonic Boundary Layers," *Physics of Fluids*, A 1 11, 1865 – 1875 1989.

[55] Spagenberg, W. G. *Heat-Loss Characteristics of Hot-Wire Anemometers at Various Densities in Transonic and Supersonic Flow*. Technical Report NACA TN 3381, 1955.

[56] Spina, E., et al. "The Physics of Supersonic Turbulent Boundary Layers," *Annual Review of Fluid Mechanics*, Vol. 26 287–319 1994.

[57] Spina, E. F. *Organized Structures in a Supersonic Turbulent Boundary Layer*. PhD dissertation, Princeton University, 1988.

[58] Stoer, J. and R. Bulirsch. *Introduction to Numerical Analysis, Second Edition*. Springer-Verlag, 1993.

[59] Taylor, R. P., et al. *A Discrete Element Prediction Approach for Turbulent Flow Over Rough Surfaces*. Technical Report Report TFD-84-1, Mechanical and Nuclear Engineering Department, Mississippi State University, 1984.

[60] TSI Incorporated. *Innovation in Thermal Anemometry*.

[61] VanDriest, E. R. "Turbulent Boundary Layers in Compressible Fluids," *Journal of the Aeronautical Sciences*, 26 287–319 1951.

[62] VanDriest, E. R. "The Problem of Aerodynamic Heating," *Aero. Engrg. Rev.*, Vol. 15 No. 10, 26–41 1956.

[63] Volluz, R. *Handbook of Supersonic Aerodynamics*. Technical Report Report 1988, NAVORD, 1961.

[64] Walters, R. W., et al. "Characteristic-Based Algorithms for Flows in Thermochemical Nonequilibrium," *AIAA Journal*, Vol. 30 No. 5, 1304–1313 May, 1992.

[65] White, F. M. and G. H. Christoph. "A Simple Theory for the Two-Dimensional Compressible Turbulent Boundary Layer," *Journal of Basic Engineering*, Vol. 94 636–642 1972.

[66] White, Frank M. *Viscous Fluid Flow* (second Edition). McGraw-Hill, Inc., 1991.

[67] Wilcox, David C. *Turbulence Modeling for CFD*. DCW Industries, Inc., 1993.

[68] Wilcox, David C. "Simulation of Transition with a Two-Equation Turbulence Model," *AIAA Journal*, Vol. 32 No. 2, 247–255 February, 1994.

Tables

Table 1. Settles and Dodson Criteria for Useful Turbulence Data.

Settles and Dodson Criteria
1. Baseline applicability
2. Simplicity
3. Specific applicability
4. Well-defined experimental boundary conditons
5. Well-defined experimental error bounds
6. Adequate documentation of data
7. Adequate spatial resolution of data

Table 2. Length and Velocity Scales

Turbulence Region	**Scale**
Laminar Sublayer	Length: $\frac{\nu}{u^*}$
	Velocity: u^*
Inner Region	Length: y
	Velocity: u^*
Outer Region	Length: δ
	Velocity: u_e

Table 3. Surface Roughness Statistics

	Surface Roughness				
Model	**Mean** (μm)	**Max.** (μm)	**Std. Dev.** (μm)	**Area Increase** ($\frac{mm^2}{1mm}$)	**Blockage** ($\frac{mm^2}{1mm}$)
Flat Plate	6.7	20.3	5.4	N/A	N/A
2D Plate	559	N/A	24.2	0	0.559
3D Plate	559	N/A	24.2	0.416	0.143
80 Grit Plate	529.9	1045	172.7	0.515	0.530
36 Grit Plate	902.3	1411	342.2	0.509	0.902
20 Grit Plate	824.6	1651	496.0	0.827	0.824

Table 4. CFD Inflow Flow Conditions

Model	**Mach**	$\rho_{ref}\left(\frac{kg}{m^3}\right)$	$\mathbf{T}_{ref}\,(K)$	$\mathbf{T}_{wall}\,(K)$	$\mathbf{k}_s\,(mm)$	$\mathbf{k}_s^+$
Flat Plate	2.75	0.2611	117.5	276.2	N/A	N/A
2D Plate	2.73	0.2705	118.0	274.1	1.09	289
3D Plate	2.73	0.2725	117.6	273.2	0.91	241
80 Grit Plate	2.73	0.2697	117.1	273.1	0.44	104
36 Grit Plate	2.72	0.2743	117.6	272.7	1.42	395
20 Grit Plate	2.70	0.2805	118.5	272.5	1.98	571

Table 5. Measurement Flow Conditions

Measurement	P_t (Pa)	T_t (K)
Pitot	$2.17 \cdot 10^5 \pm 0.4\%$	296 ± 1.0
Cross-Film (x-y Plane)	$2.22 \cdot 10^5 \pm 0.3\%$	293 ± 1.0
Cross-Film (x-z Plane)	$2.39 \cdot 10^5 \pm 0.3\%$	296 ± 1.0
Laser Doppler Velocimetry	$2.41 \cdot 10^5 \pm 0.5\%$	294 ± 1.0
High-Frequency Normal-Film	$2.41 \cdot 10^5 \pm 0.2\%$	296 ± 1.0
High-Frequency Parallel-Film	$2.33 \cdot 10^5 \pm 0.3\%$	296 ± 1.0
Color Schlieren	$2.17 \cdot 10^5 \pm 0.4\%$	296 ± 1.0
Laser Sheet Imaging	$2.17 \cdot 10^5 \pm 0.4\%$	296 ± 1.0

Table 6. Reference Values

	Pitot				LDV				Schlieren
Model	δ (mm)	δ_M (mm)	u_∞ (m/s)	M_∞	δ (mm)	δ_M (mm)	u_∞ (m/s)	M_∞	δ_T (mm)
Flat Plate	12.4	15.4	598.3	2.75	10.2	11.1	602.6	2.80	13.8
2D Plate	16.8	18.1	593.4	2.73	19.2	21.9	590.5	2.68	16.0
3D Plate	15.8	17.3	592.3	2.73	15.3	17.0	593.1	2.69	15.1
80 Grit Plate	14.7	16.3	593.0	2.73	14.1	15.9	592.5	2.68	15.3
36 Grit Plate	18.0	19.2	591.5	2.72	19.7	21.5	590.5	2.65	17.3
20 Grit Plate	17.7	18.2	589.3	2.70	21.1	24.3	591.3	2.66	18.3

Table 7. Laser Sheet Image Data

	Boundary Layer Structure		
Model	High (mm)	Low (mm)	Ratio
Flat Plate	11.2	6.9	0.62
2D Plate	15.8	9.9	0.63
3D Plate	15.8	9.9	0.63
80 Grit Plate	14.3	8.4	0.59
36 Grit Plate	15.4	11.7	0.76
20 Grit Plate	17.1	11.1	0.65

Table 8. Turbulent Quantity, Roughness Reynolds Number Slopes

$\frac{d\Delta_{u'}}{d(\ln k_s^+)}$	$\frac{d\Delta_{v'}}{d(\ln k_s^+)}$	$\frac{d\Delta_{M'}}{d(\ln k_s^+)}$	$\frac{d\Delta_{(\rho u)'}}{dk_s^+}$	$\frac{d\Delta_{(\rho v)'}}{dk_s^+}$	$\frac{d\Delta_{(\rho w)'}}{dk_s^+}$	
0.0025	0.0044	0.0106	$7.25{\cdot}10^{-5}$	$5.64{\cdot}10^{-5}$	$1.14{\cdot}10^{-5}$	
$\frac{d\Delta_{u'v'}}{d(\ln k_s^+)}$	$\frac{d\Delta_{\rho u'v'}}{d(\ln k_s^+)}$	$\frac{d\Delta_{\rho' v'}}{dk_s^+}$	$\frac{d\Delta_{(\rho u)'(\rho v)'}}{dk_s^+}$	$\frac{d\Delta_{(\rho u)'(\rho w)'}}{dk_s^+}$	$\frac{d\Delta_{TKE}}{d(\ln k_s^+)}$	$\frac{d\Delta_{TKEc}}{dk_s^+}$
$4.83{\cdot}10^{-5}$	-0.097	$8.06{\cdot}10^{-6}$	$5.62{\cdot}10^{-6}$	$3.73{\cdot}10^{-5}$	$7.59{\cdot}10^{-4}$	$3.74{\cdot}10^{-5}$
$\frac{d(microscale)}{dk_s^+}\Big\vert_{y/\delta=0.25}$		$\frac{d(microscale)}{dk_s^+}\Big\vert_{y/\delta=0.50}$		$\frac{d(microscale)}{dk_s^+}\Big\vert_{y/\delta=0.75}$		
$5.29{\cdot}10^{-9}$		$4.81{\cdot}10^{-9}$		$2.48{\cdot}10^{-9}$		

Table 9. Power Spectra Difference, Roughness Reynolds Number Slopes

Frequency (Hz)	$\frac{d\Delta_{\rho u(f)_{rms}}}{d(\ln k_s^+)}$	$\frac{d\Delta_{\rho u(f)_{rms}}}{dk_s^+}$	$\frac{d\Delta_{\rho u(f)_{rms}}}{dk_s^+}$
977	$6.6{\cdot}10^{-3}$	$1.9{\cdot}10^{-5}$	$1.7{\cdot}10^{-5}$
1955	$5.5{\cdot}10^{-3}$	$2.2{\cdot}10^{-5}$	$1.7{\cdot}10^{-5}$
3910	$4.1{\cdot}10^{-3}$	$2.0{\cdot}10^{-5}$	$1.8{\cdot}10^{-5}$
5860	$3.2{\cdot}10^{-3}$	$1.4{\cdot}10^{-5}$	$1.9{\cdot}10^{-5}$
7810	$2.6{\cdot}10^{-3}$	$0.98{\cdot}10^{-5}$	$1.3{\cdot}10^{-5}$
9770	$2.0{\cdot}10^{-3}$	$0.99{\cdot}10^{-5}$	$1.3{\cdot}10^{-5}$

Table 10. Turbulent Length Scales

	Microscale (μ sec)			**Integral Length Scale** (μ sec)		
Model	$y/\delta\vert_{0.25}$	$y/\delta\vert_{0.50}$	$y/\delta\vert_{0.75}$	$y/\delta\vert_{0.25}$	$y/\delta\vert_{0.50}$	$y/\delta\vert_{0.75}$
Flat Plate	20.1	17.8	17.4	117	144	203
2D Plate	23.2	20.6	18.3	77.6	97.7	79.8
3D Plate	21.8	19.2	17.3	68.6	96.4	88.6
80 Grit Plate	21.4	19.3	18.3	80.0	106	150
36 Grit Plate	22.5	19.6	18.0	66.6	80.5	65.1
20 Grit Plate	23.4	21.2	19.3	59.2	59.6	70.0

Table 11. Flow Structure Angle

Model	Flow Structure Angle (deg)		
	$y/\delta\|_{0.25}$	$y/\delta\|_{0.50}$	$y/\delta\|_{0.75}$
Flat Plate	35	44	61
2D Plate	40	35	37
3D Plate	40	46	52
80 Grit Plate	37	46	43
36 Grit Plate	50	46	62
20 Grit Plate	51	47	52

Table 12. Integral Analysis

Model	δ (mm)	δ_M (mm)	δ_k^* (mm)	δ^* (mm)	θ_k (mm)	θ (mm)	C_f	τ_w (Pa)	u^* (m/s)
Flat Plate	12.4	15.4	1.30	3.32	1.09	0.80	0.00159	74.2	25.8
2D Plate	16.8	18.1	2.70	5.82	1.99	1.32	0.00375	178.7	39.2
3D Plate	15.8	17.3	2.64	5.67	1.92	1.29	0.00365	175.1	38.5
80 Grit Plate	14.7	16.3	2.09	4.77	1.62	1.11	0.00304	144.2	35.3
36 Grit Plate	18.0	19.2	2.89	6.24	2.14	1.43	0.00400	191.9	40.3
20 Grit Plate	17.7	18.2	3.00	6.26	2.18	1.45	0.00410	199.8	40.4

Table 13. Integral Quantity, Roughness Reynolds Number Slopes

$\frac{d\delta_k^*}{d(\ln k_s^+)}$	$\frac{d\theta_k}{d(\ln k_s^+)}$	$\frac{dC_f}{d(\ln k_s^+)}$
0.55	0.35	$6.5 \cdot 10^{-4}$
$\frac{d\delta^*}{d(\ln k_s^+)}$	$\frac{d\theta}{d(\ln k_s^+)}$	$\frac{d(u^*)}{d(\ln k_s^+)}$
0.93	0.21	3.2

Table 14. Adjusted Friction Velocity Values

Model	Pitot u^* (m/s)	LDV Adjusted u^* (m/s)	LDV % Diff.	Prandtl Turb. Model Adjusted u^* (m/s)	Prandtl Turb. Model % Diff.	CAMMLE Turb. Model Adjusted u^* (m/s)	CAMMLE Turb. Model % Diff.
Flat Plate	25.8	26.8	+3.5	N/A	N/A	N/A	N/A
2D Plate	39.2	38.2	-2.5	38.0	-3.0	38.0	-3.0
3D Plate	38.5	38.8	+0.7	37.2	-3.5	37.6	-2.4
80 Grit Plate	35.3	34.9	-1.1	34.0	-3.7	34.0	-3.7
36 Grit Plate	40.3	39.8	-1.2	38.8	-3.7	38.8	-3.7
20 Grit Plate	40.4	40.1	-0.8	38.8	-4.0	38.8	-4.0

Table 15. CFD Integral Analysis

Model		δ (mm)	δ^* (mm)	θ_k (mm)	θ (mm)	H	$\frac{d\theta}{dx}$	C_f	u^* (m/s)	k_s^+
Flat Plate:	Prandtl	10.1	1.42	1.09	0.75	1.31	0.00109	0.00153	25.4	N/A
	CAMMLE	10.1	1.42	1.09	0.75	1.31	0.00109	0.00153	25.4	N/A
2D Plate:	Prandtl	16.2	3.22	2.16	1.37	1.49	0.00213	0.00427	42.2	304
	CAMMLE	16.2	3.22	2.16	1.37	1.49	0.00212	0.00424	41.9	302
3D Plate:	Prandtl	15.6	3.08	2.08	1.33	1.48	0.00205	0.00410	41.3	251
	CAMMLE	15.6	3.07	2.08	1.33	1.48	0.00198	0.00396	40.6	247
80 Grit Plate:	Prandtl	13.5	2.51	1.76	1.16	1.42	0.00192	0.00384	40.0	115
	CAMMLE	13.5	2.49	1.75	1.15	1.42	0.00211	0.00423	41.9	121
36 Grit Plate:	Prandtl	16.8	3.45	2.28	1.44	1.52	0.00248	0.00497	45.2	436
	CAMMLE	16.8	3.45	2.28	1.44	1.52	0.00246	0.00493	45.0	434
20 Grit Plate:	Prandtl	17.4	3.73	2.42	1.53	1.54	0.00286	0.00572	48.0	667
	CAMMLE	17.4	3.73	2.42	1.53	1.54	0.00277	0.00555	47.2	657

Table 16. x-y Plane Cross-Film Measurement Hardware Setup

Hardware Setup	**Settings**	
Probe	TSI 1243-20	
Probe Holder	TSI 1155-18	
Cabling	4 m Coaxial Cable	
Overheat Section	**Film 1** (Ω)	**Film 2** (Ω)
R_{total}	5.856	5.897
$R_{cable+support}$	0.650	0.653
R_{leads}	0.15	0.14
R_{sensor}	5.056	5.104
$R_{external}$	10.407	10.490
Overheat Ratio	1.90	1.90
T_{ref} (^oC)	25.7	
Tuning Section	**Film 1**	**Film 2**
Filter	1	2
Gain	11	11
Cable	-1	-2
Sample Freq. (Hz)	1000	1000
Square Wave Freq. (Hz)	5000	5000
Traces	5	5
Response, $\frac{1}{1.3\Delta t}$ (kHz)	93	93
Conditioning Section	**Film 1**	**Film 2**
Offset $(Volt)$	1.0	1.0
Conditioning	*input*	*input*
High-Pass Filter	*none*	*none*
Low-Pass Filter	*none*	*none*

Table 17. Cross-Film Measurement Experiment Setup

Experiment Setup	**Settings**
Data Collected	*all*
Acquistion Rate	30 (kHz)
Data Points	135,000
Gain	$0 - 10\,V$
Clock	Internal
Trigger	External
Trigger Level	3.0 V
Trigger Channel	0
Polarity	Positive
Sensitivity	Edge
Traverse Rate	0.762 $\left(\frac{cm}{sec}\right)$

Table 18. x-y Plane Cross-Film Calibration Data

Film 1 (V)	P_t **(Psia)**	P_{t2}/P_{t1}	**Mach**	$T_t\ (K)$	$\rho u\ (kg/m2s)$	**Re**	**Nu**	**a**
4.183	14.2	0.403	2.758	294.05	68.71	136.31	6.15	0.5867
4.655	21.6	0.403	2.758	297.15	103.93	204.53	7.16	**b**
5.006	28.2	0.403	2.758	297.26	135.38	266.35	8.80	-0.7350
5.316	34.9	0.403	2.758	297.95	167.69	329.32	9.93	
5.534	40.5	0.403	2.758	297.86	194.55	382.16	10.76	
Film 2 (V)	P_t **(Psia)**	P_{t2}/P_{t1}	**Mach**	$T_t\ (K)$	$\rho u\ (kg/m2s)$	**Re**	**Nu**	**a**
4.206	14.2	0.403	2.758	294.05	68.71	136.31	6.29	0.6233
4.714	21.6	0.403	2.758	297.15	103.93	204.53	7.89	**b**
5.069	28.2	0.403	2.758	297.26	135.38	266.35	9.12	-1.015
5.379	34.9	0.403	2.758	297.95	167.69	329.32	10.27	
5.621	40.5	0.403	2.758	297.86	194.55	382.16	11.21	

Table 19. x-y Plane Cross-Film MOH Measurement Hardware Setup

Hardware Setup	**Settings**	
Probe	TSI 1243-20	
Probe Holder	TSI 1155-18	
Cabling	4 m Coaxial Cable	
Overheat Section	**Film 1** (Ω)	**Film 2** (Ω)
R_{total}	5.856	5.897
$R_{cable+support}$	0.650	0.653
R_{leads}	0.15	0.14
R_{sensor}	5.056	5.104
$R_{external}$ (see Table 20)		
Overheat Ratio (see Table 20)		
$T_{ref}\ (^oC)$	25.7	
Tuning Section	**Film 1**	**Film 2**
Filter	1	2
Gain	11	11
Cable	-1	-2
Sample Freq. (Hz)	1000	1000
Square Wave Freq. (Hz)	5000	5000
Traces	5	5
Response, $\frac{1}{1.3\Delta t}\ (kHz)$	93	93
Conditioning Section	**Film 1**	**Film 2**
Offset $(Volt)$	1.0	1.0
Conditioning	*input*	*input*
High-Pass Filter	*none*	*none*
Low-Pass Filter	*none*	*none*

Table 20. x-y Plane Cross-Film MOH External Resistance and Overheat Ratios

Film 1 (Ω)	**Film 2** (Ω)	**Overheat Ratio**
10.409	10.490	1.9
9.909	10.001	1.8
9.394	9.464	1.7
8.909	8.956	1.6
8.383	8.447	1.5
7.873	7.936	1.4
7.372	7.427	1.3

Table 21. x-z Plane Cross-Film Measurement Hardware Setup

Hardware Setup	**Settings**	
Probe	TSI 1243AN-20	
Probe Holder	TSI 1155-18	
Cabling	4 m Coaxial Cable	
Overheat Section	**Film 1** (Ω)	**Film 2** (Ω)
R_{total}	7.081	7.086
$R_{cable+support}$	0.644	0.665
R_{leads}	0.2	0.2
R_{sensor}	6.237	6.221
$R_{external}$	12.692	12.684
Overheat Ratio	1.90	1.90
T_{ref} (^oC)	22.4	
Tuning Section	**Film 1**	**Film 2**
Filter	4	4
Gain	11	12
Cable	0	0
Sample Freq. (Hz)	1000	1000
Square Wave Freq. (Hz)	5000	5000
Traces	5	5
Response, $\frac{1}{1.3\Delta t}$ (kHz)	93	93
Conditioning Section	**Film 1**	**Film 2**
Offset ($Volt$)	1.0	1.0
Conditioning	*input*	*input*
High-Pass Filter	*none*	*none*
Low-Pass Filter	*none*	*none*

Table 22. Normal-Film Measurement Hardware Setup

Hardware Setup	**Settings**
Probe	TSI 1218-20
Probe Holder	TSI 1150-6
Cabling	4 m Coaxial Cable
Overheat Section	**Film** (Ω)
R_{total}	6.611
$R_{cable+support}$	0.312
R_{leads}	0.2
R_{sensor}	6.099
$R_{external}$	12.109
Overheat Ratio	1.90
T_{ref} (^oC)	22.2
Tuning Section	**Film**
Filter	3
Gain	3
Cable	0
Sample Freq. (Hz)	1000
Square Wave Freq. (Hz)	5000
Traces	5
Response, $\frac{1}{1.3\Delta t}$ (kHz)	93
Conditioning Section	**Film**
Offset ($Volt$)	2.0
Conditioning	*input*
High-Pass Filter	*none*
Low-Pass Filter	*none*

Table 23. Parallel-Film Measurement Hardware Setup

Hardware Setup	**Settings**	
Probe	TSI 1246AD-20	
Probe Holder	TSI 1155-18	
Cabling	4 m Coaxial Cable	
Overheat Section	**Film 1** (Ω)	**Film 2** (Ω)
R_{total}	5.810	5.852
$R_{cable+support}$	0.643	0.656
R_{leads}	0.31	0.31
R_{sensor}	4.857	4.886
$R_{external}$	10.180	10.250
Overheat Ratio	1.90	1.90
T_{ref} (^oC)	20.8	
Tuning Section	**Film 1**	**Film 2**
Filter	4	4
Gain	10	11
Cable	0	0
Sample Freq. (Hz)	1000	1000
Square Wave Freq. (Hz)	5000	5000
Traces	5	5
Response, $\frac{1}{1.3\Delta t}$ (kHz)	110	101
Conditioning Section	**Film 1**	**Film 2**
Offset ($Volt$)	3.0	3.0
Conditioning	*input*	*input*
High-Pass Filter	*none*	*none*
Low-Pass Filter	*none*	*none*

Table 24. "Quick" Menu Software Settings

Category	**BSA 1 Setting**	**BSA 2 Setting**
Bandwidth	325.12	246.7
Shifter Mode	Norm	Norm
Signal Gain (dB)	42	42
High Voltage (V)	1504	1608
Max. Anode Current (mA)	1.6	1.6
Pedestal Attenuation (dB)	6	6
Duty Cycle (%)	100	100
Dead Time	0	0

Table 25. "Soft" Menu Software Settings

Category	BSA 1 Setting	BSA 2 Setting
Timer Clock	Master	Slave
Coincidence Mode	Master	Slave
Arrival Time Base	Internal	Internal
Burst Detection	Both	Both
Oversize Rejection	1	1
Buffer Mode	FIFO	FIFO
Max. Anode Current (mA)	1.6	1.6
Quality Factor (%)	50	50
Collection Mode	Burst	Burst

Table 26. "BSA Program" Menu Software Settings

Category	BSA 1 Setting	BSA 2 Setting
Timeout	12	12
Number of Burst	150000	150000
Velocity	Yes	Yes
Transit Time	Yes	Yes
Arrival Time	Yes	Yes

Table 27. Typical Freestream Conditions Used for Error Analysis

Condition	Value
T_{o1}	296 K
P_{o1}	2.188 atm
P_{o2}	0.884 atm
M_∞	2.75
R_{air}	287 m^2/s^2K
T	117.6 K
a_∞	217.4 m/s
P_1	0.0866 atm
ρ_1	0.259 kg/m^3
u	598.3 m/s
$\rho_1 u$	155.0 kg/m^2s
Re_∞	$1.9 \cdot 10^7$ 1/m

Table 28. Typical Freestream HWA Parameters

Condition	Value
E_f	5.0 V
T_f	700.0 K
T_e	297 K
R_f	10.0 Ω
R_s	50.0 Ω
R_L	0.3 Ω
a_k	0.587
b_k	-0.735
d	$5.1 \cdot 10^{-5}$ m
L	0.001 m
Re_e	300
Nu(wire)	9.42

Table 29. Elementary Measurement Errors

Measurement	Error
x	1.2 mm
y	0.5 mm
z	1.0 mm
T_{t1}	2.3%
P_{t1}	0.8%
P_{t2}	0.9%
E_f	1.0%

Table 30. LDV Measurement Errors

Measurement	Error
u	2.0%
v	2.0%
u'	1.7%
v'	7.9%
$u'v'$	2.8%
Sk_u	7.2%
Sk_v	33.5%
Fl_u	9.6%
Fl_v	44.7%

Table 31. Boundary Layer Height Error

Variable	Error
δ	21%
δ_M	11%

Table 32. Pitot Error Summary

Variable	Equation	Error
M	$\|0.371\varepsilon_{p_1}, 0.371\varepsilon_{p_{t2}}\|_2$	0.5%
T_1	$\|\varepsilon_{p_{t1}}, 1.204\varepsilon_{p_{t2}}\|_2$	2.3%
a	$0.5\varepsilon_{T1}$	1.2%
P_1	$\|\varepsilon_{p_{t1}}, 4.214\varepsilon_{p_{t2}}\|_2$	1.1%
u	$\|\varepsilon_M, \varepsilon_a\|_2$	1.3%
ρ_1	$\|\varepsilon_{T_1}, \varepsilon_{P_1}\|_2$	2.6%
$\rho_1 u$	$\|\varepsilon_{\rho_1}, \varepsilon_u\|_2$	2.9%
μ	$\|Sutherland's\ Law\|_2$	2.0%
u_{eff}	$\|0.5\varepsilon_{\rho e}, 0.5\varepsilon_{\rho w}, 2.0\varepsilon_u\|_2$	3.2%
τ_w	Bowersox et. al. [11]	10%
u^+	$\|0.5\varepsilon_{\tau w}, 0.5\varepsilon_{\rho w}\|_2$	5.2%
y^+	$\|\varepsilon_y, \varepsilon_{u^*}, \varepsilon_\mu, \varepsilon_{\rho w}\|_2$	7.9%
u^+_{eff}	$\|0.5\varepsilon_{\tau w}, 0.5\varepsilon_{ueff}\|_2$	5.2%

Table 33. HWA Error Summary

Variable	Equation	Error	Variable	Equation	Error
Nu	$\|\varepsilon_{Ef}, \varepsilon_{Tt1}\|_2$	3.0%	(ρu)	$\varepsilon_{\mathrm{Re}_x}$	10.6%
Re_e	$\|2.0\varepsilon_{Nu}, \varepsilon_{Ef}\|_2$	6.2%	(ρv)	$\varepsilon_{\mathrm{Re}_y}$	10.6%
f	$0.5\varepsilon_{\mathrm{Re}_e}$	3.1%	(ρw)	$\varepsilon_{\mathrm{Re}_z}$	10.6%
g	$\|\varepsilon_{T_{t1}}, \varepsilon_{E_f}\|_2$	2.5%	$(\rho u)'$	$\varepsilon_{\mathrm{Re}_x}$	10.6%
Re_e^2	$2.0\varepsilon_{\mathrm{Re}_e}$	12.2%	$(\rho v)'$	$\varepsilon_{\mathrm{Re}_y}$	10.6%
Re_x^2	$\|\varepsilon_{\mathrm{Re}_{e1}^2}, \varepsilon_{\mathrm{Re}_{e1}\,\mathrm{Re}_{e2}}, \varepsilon_{\mathrm{Re}_{e2}^2}\|_2$	21.2%	$(\rho w)'$	$\varepsilon_{\mathrm{Re}_z}$	10.6%
$\mathrm{Re}_x\mathrm{Re}_y$	$\varepsilon_{\mathrm{Re}_x^2}$	21.2%	$(\rho u)'(\rho v)'$	$\varepsilon_{\mathrm{Re}_x\,\mathrm{Re}_y}$	21.2%
$\mathrm{Re}_x\mathrm{Re}_z$	$\varepsilon_{\mathrm{Re}_x^2}$	21.2%	$(\rho u)'(\rho w)'$	$\varepsilon_{\mathrm{Re}_x\,\mathrm{Re}_w}$	21.2%
Re_x	$0.5\varepsilon_{\mathrm{Re}_x^2}$	10.6%			
Re_x	$\varepsilon_{\mathrm{Re}_x}$	10.6%			
Re_z	$\varepsilon_{\mathrm{Re}_x}$	10.6%			

Table 34. Frequency Resolved Error

Variable	Error
Power Spectra	21%
Microscale	2.5%
Integral Scale	2.5%
θ	14.4%

Table 35. LDV Error Summary

Variable	Error	Variable	Error
$\overline{Q}$	2.0%	p_w	0.6%
$\overline{M}$	9.0%	ρ_w	0.6%
u_e	1.3%	T	11.7%
Q_e	1.5%	p	6.6%
T_e	1.8%	ρ	13.5%
p_e	6.4%	γ_u	9.6%
ρ_e	6.6%	$u'v'$	11.4%
T_w	0.1%	$\rho'v'$ (HWA + LDV)	23%
		$\overline{\rho}$ (HWA + LDV)	13.8%

Table 36. Grid Resolution

Grid	x stations	y nodes	Δx	Δy_{wall}
101 x 201	101	201	0.8179 cm	$5.0 \cdot 10^{-6}$ m
101 x 251	101	251	0.8179 cm	$5.0 \cdot 10^{-6}$ m
201 x 251	201	251	0.4089 cm	$5.0 \cdot 10^{-6}$ m

Table 37. Smooth Plate Pitot Data

y (in)	y (mm)	y/δ_u	y/δ_M	P_{t1} (psia)	P_{t2} (psia)	P_{t2}/P_{t1}	P_e/P_{t2}	Mach	M/M_e	u (m/s)	u/u_e	ρ/ρ_e	ρ_w/ρ	y^+	u_{eff}^+	u^+	$(u-ue)/u^*$
0.016	0.406	0.033	0.026	32.311	3.793	0.117	0.337	1.377	0.500	404.8	0.677	0.577	0.737	67.23	16.45	15.66	-7.488
0.016	0.417	0.034	0.027	32.309	3.809	0.118	0.335	1.380	0.501	405.6	0.678	0.578	0.736	69.09	16.48	15.69	-7.458
0.025	0.638	0.052	0.042	32.295	4.043	0.125	0.316	1.433	0.520	416.5	0.696	0.590	0.721	105.83	16.98	16.12	-7.034
0.039	0.993	0.080	0.065	32.291	4.698	0.146	0.272	1.569	0.570	443.3	0.741	0.621	0.684	164.66	18.22	17.16	-5.996
0.057	1.443	0.117	0.094	32.282	5.401	0.167	0.236	1.702	0.618	467.5	0.781	0.655	0.649	239.14	19.36	18.09	-5.062
0.078	1.978	0.160	0.129	32.282	5.711	0.177	0.224	1.757	0.638	476.9	0.797	0.670	0.635	327.84	19.81	18.45	-4.699
0.102	2.592	0.209	0.169	32.284	6.296	0.195	0.203	1.856	0.674	493.0	0.824	0.697	0.610	429.64	20.60	19.08	-4.076
0.128	3.264	0.264	0.213	32.282	6.788	0.210	0.188	1.936	0.703	505.0	0.844	0.720	0.591	541.05	21.21	19.54	-3.610
0.157	3.988	0.322	0.260	32.271	7.225	0.224	0.177	2.004	0.728	514.8	0.861	0.740	0.574	661.02	21.70	19.92	-3.230
0.187	4.752	0.384	0.309	32.275	7.705	0.239	0.166	2.076	0.754	524.7	0.877	0.762	0.558	787.75	22.21	20.30	-2.848
0.218	5.546	0.448	0.361	32.265	8.670	0.269	0.147	2.214	0.804	542.5	0.907	0.806	0.528	919.36	23.15	20.99	-2.159
0.251	6.371	0.515	0.415	32.262	9.187	0.285	0.139	2.284	0.829	551.0	0.921	0.830	0.513	1056.16	23.60	21.32	-1.830
0.284	7.210	0.582	0.470	32.254	9.885	0.306	0.129	2.376	0.863	561.5	0.939	0.861	0.494	1195.20	24.18	21.73	-1.423
0.317	8.061	0.651	0.525	32.254	10.469	0.325	0.122	2.450	0.890	569.5	0.952	0.887	0.479	1336.29	24.62	22.04	-1.114
0.352	8.933	0.722	0.582	32.247	11.397	0.353	0.112	2.563	0.931	581.0	0.971	0.928	0.458	1480.89	25.27	22.48	-0.671
0.386	9.805	0.792	0.639	32.245	11.170	0.346	0.114	2.536	0.921	578.3	0.967	0.918	0.463	1625.37	25.11	22.38	-0.775
0.421	10.698	0.864	0.697	32.252	11.853	0.368	0.108	2.617	0.950	586.1	0.980	0.948	0.449	1773.34	25.56	22.68	-0.472
0.456	11.587	0.936	0.755	32.242	12.247	0.380	0.104	2.663	0.967	590.4	0.987	0.966	0.440	1920.83	25.81	22.85	-0.306
0.492	12.489	1.009	0.813	32.247	12.461	0.386	0.102	2.687	0.976	592.6	0.990	0.975	0.436	2070.31	25.94	22.93	-0.221
0.527	13.396	1.082	0.872	32.246	12.678	0.393	0.101	2.711	0.985	594.8	0.994	0.984	0.432	2220.69	26.07	23.02	-0.136
0.563	14.303	1.155	0.931	32.240	12.702	0.394	0.100	2.714	0.986	595.0	0.995	0.986	0.432	2370.93	26.08	23.03	-0.126
0.599	15.215	1.229	0.991	32.229	12.793	0.397	0.100	2.725	0.990	596.0	0.996	0.990	0.430	2522.16	26.14	23.06	-0.089
0.635	16.121	1.302	1.050	32.233	12.870	0.399	0.099	2.733	0.993	596.7	0.997	0.993	0.428	2672.45	26.18	23.09	-0.061
0.670	17.020	1.375	1.108	32.222	12.922	0.401	0.099	2.740	0.995	597.3	0.998	0.995	0.427	2821.49	26.22	23.11	-0.040
0.706	17.924	1.448	1.167	32.219	12.932	0.401	0.099	2.741	0.995	597.4	0.998	0.996	0.427	2971.35	26.22	23.12	-0.035
0.741	18.824	1.521	1.226	32.214	12.958	0.402	0.098	2.744	0.996	597.7	0.999	0.997	0.427	3120.39	26.24	23.13	-0.025
0.777	19.732	1.594	1.285	32.209	12.983	0.403	0.098	2.747	0.998	597.9	0.999	0.998	0.426	3270.94	26.25	23.14	-0.015
0.812	20.630	1.666	1.344	32.204	12.988	0.403	0.098	2.748	0.998	598.0	0.999	0.999	0.426	3419.79	26.26	23.14	-0.012
0.848	21.529	1.739	1.402	32.194	12.956	0.402	0.098	2.745	0.997	597.7	0.999	0.997	0.426	3568.81	26.24	23.13	-0.022
0.883	22.426	1.812	1.461	32.196	12.941	0.402	0.098	2.743	0.996	597.6	0.999	0.997	0.427	3717.63	26.23	23.12	-0.028
0.918	23.322	1.884	1.519	32.192	12.924	0.401	0.099	2.741	0.995	597.4	0.999	0.996	0.427	3866.04	26.22	23.12	-0.034
0.954	24.224	1.957	1.578	32.190	12.912	0.401	0.099	2.740	0.995	597.3	0.998	0.995	0.427	4015.65	26.21	23.11	-0.040
0.989	25.121	2.029	1.636	32.182	12.891	0.401	0.099	2.738	0.994	597.0	0.998	0.994	0.428	4164.37	26.20	23.10	-0.050
1.025	26.024	2.102	1.695	32.179	12.914	0.401	0.099	2.741	0.995	597.2	0.998	0.995	0.428	4313.96	26.21	23.11	-0.044
1.060	26.928	2.175	1.754	32.182	12.941	0.402	0.098	2.744	0.996	597.4	0.999	0.996	0.427	4463.83	26.22	23.12	-0.034
1.096	27.829	2.248	1.812	32.174	12.961	0.403	0.098	2.746	0.997	597.6	0.999	0.997	0.427	4613.20	26.24	23.13	-0.026
1.131	28.739	2.322	1.872	32.178	12.967	0.403	0.098	2.747	0.997	597.7	0.999	0.997	0.427	4764.15	26.24	23.13	-0.024
1.167	29.645	2.395	1.931	32.165	12.997	0.404	0.098	2.751	0.999	598.0	1.000	0.999	0.426	4914.30	26.26	23.14	-0.011
1.203	30.553	2.468	1.990	32.162	13.018	0.405	0.098	2.753	1.000	598.2	1.000	1.000	0.425	5064.70	26.27	23.15	-0.002
1.239	31.461	2.541	2.049	32.157	13.036	0.405	0.098	2.755	1.001	598.4	1.000	1.001	0.425	5215.34	26.28	23.16	0.005
1.274	32.369	2.615	2.108	32.163	13.065	0.406	0.097	2.758	1.002	598.7	1.001	1.002	0.425	5365.87	26.30	23.17	0.015
1.307	33.197	2.682	2.162	32.156	13.052	0.406	0.097	2.757	1.001	598.6	1.000	1.001	0.425	5503.16	26.29	23.16	0.011
1.313	33.355	2.694	2.172	32.152	13.084	0.407	0.097	2.761	1.003	598.9	1.001	1.003	0.424	5529.23	26.31	23.18	0.023
1.313	33.355	2.694	2.172	32.149	13.076	0.407	0.097	2.760	1.002	598.8	1.001	1.003	0.424	5529.27	26.31	23.17	0.021
1.313	33.357	2.695	2.172	32.145	13.070	0.407	0.097	2.760	1.002	598.8	1.001	1.002	0.424	5529.56	26.31	23.17	0.019
1.313	33.356	2.694	2.172	32.135	13.072	0.407	0.097	2.760	1.002	598.8	1.001	1.003	0.424	5529.42	26.31	23.17	0.022
1.313	33.356	2.694	2.172	32.137	13.032	0.406	0.098	2.756	1.001	598.5	1.000	1.001	0.425	5529.47	26.29	23.16	0.007
1.313	33.357	2.695	2.172	32.120	13.050	0.406	0.097	2.758	1.002	598.7	1.001	1.002	0.425	5529.64	26.30	23.17	0.016

Table 38. 2D Plate Pitot Data

y (in)	y (mm)	y/δ_u	y/δ_M	P_{t1} (psia)	P_{t2} (psia)	P_{t2}/P_{t1}	P_s/P_{t2}	Mach	M/M_e	u (m/s)	u/u_e	ρ/ρ_e	ρ_w/ρ	y^+	u_{eff}^+	u^+	$(u-ue)/u^*$
0.016	0.397	0.024	0.022	32.150	2.498	0.078	0.532	0.994	0.365	312.5	0.527	0.511	0.842	105.20	8.20	7.98	-7.170
0.017	0.422	0.025	0.023	32.145	2.454	0.076	0.542	0.978	0.359	308.4	0.520	0.509	0.846	111.90	8.09	7.87	-7.275
0.027	0.677	0.040	0.037	32.135	2.445	0.076	0.544	0.975	0.358	307.5	0.518	0.508	0.847	179.45	8.07	7.85	-7.296
0.042	1.074	0.064	0.059	32.140	2.985	0.093	0.445	1.143	0.419	350.0	0.590	0.537	0.802	284.64	9.26	8.93	-6.212
0.061	1.557	0.093	0.086	32.143	3.328	0.104	0.399	1.233	0.452	371.2	0.626	0.554	0.777	412.62	9.87	9.48	-5.671
0.084	2.128	0.127	0.117	32.144	3.672	0.114	0.362	1.315	0.483	389.7	0.657	0.571	0.754	563.88	10.41	9.95	-5.198
0.109	2.762	0.165	0.152	32.131	4.130	0.129	0.322	1.417	0.520	411.4	0.693	0.593	0.726	731.93	11.05	10.50	-4.646
0.136	3.451	0.206	0.190	32.134	4.442	0.138	0.299	1.481	0.544	424.4	0.715	0.608	0.709	914.68	11.44	10.83	-4.313
0.165	4.190	0.250	0.231	32.123	4.826	0.150	0.275	1.557	0.571	439.1	0.740	0.626	0.688	1110.55	11.89	11.21	-3.937
0.195	4.957	0.296	0.273	32.125	5.321	0.166	0.250	1.649	0.605	456.0	0.769	0.649	0.664	1313.75	12.42	11.64	-3.506
0.227	5.757	0.343	0.317	32.134	6.136	0.191	0.217	1.789	0.656	479.9	0.809	0.686	0.627	1525.79	13.18	12.25	-2.895
0.259	6.580	0.392	0.363	32.120	6.552	0.204	0.203	1.856	0.681	490.8	0.827	0.705	0.610	1743.84	13.53	12.53	-2.618
0.292	7.416	0.442	0.409	32.114	6.840	0.213	0.194	1.902	0.698	497.8	0.839	0.719	0.599	1965.55	13.76	12.71	-2.439
0.326	8.270	0.493	0.456	32.112	7.446	0.232	0.178	1.994	0.732	511.3	0.862	0.746	0.577	2191.78	14.21	13.05	-2.094
0.359	9.129	0.545	0.503	32.122	8.066	0.251	0.165	2.083	0.764	523.7	0.883	0.774	0.556	2419.63	14.63	13.37	-1.779
0.394	10.001	0.597	0.551	32.103	8.379	0.261	0.158	2.127	0.781	529.6	0.892	0.788	0.546	2650.53	14.83	13.52	-1.629
0.428	10.882	0.649	0.600	32.094	9.328	0.291	0.142	2.255	0.828	545.6	0.919	0.830	0.519	2884.18	15.39	13.93	-1.220
0.463	11.764	0.702	0.649	32.108	9.585	0.299	0.139	2.287	0.839	549.4	0.926	0.841	0.512	3117.77	15.53	14.03	-1.121
0.498	12.658	0.755	0.698	32.109	10.763	0.335	0.123	2.434	0.893	565.8	0.954	0.893	0.482	3354.88	16.12	14.44	-0.703
0.534	13.557	0.809	0.747	32.100	11.609	0.362	0.114	2.534	0.930	576.0	0.971	0.929	0.463	3593.03	16.50	14.71	-0.442
0.569	14.453	0.862	0.797	32.100	11.839	0.369	0.112	2.560	0.940	578.6	0.975	0.939	0.458	3830.45	16.60	14.77	-0.376
0.604	15.348	0.916	0.846	32.079	12.020	0.375	0.110	2.582	0.948	580.6	0.979	0.947	0.455	4067.83	16.67	14.82	-0.325
0.639	16.242	0.969	0.896	32.076	12.370	0.386	0.107	2.621	0.962	584.3	0.985	0.962	0.448	4304.77	16.81	14.92	-0.231
0.675	17.138	1.022	0.945	32.079	12.902	0.402	0.103	2.680	0.984	589.7	0.994	0.984	0.438	4542.26	17.02	15.05	-0.094
0.710	18.028	1.075	0.994	32.078	13.036	0.406	0.102	2.695	0.989	590.8	0.996	0.989	0.435	4777.92	17.07	15.08	-0.065
0.745	18.916	1.128	1.043	32.069	13.218	0.412	0.100	2.715	0.996	592.6	0.999	0.997	0.432	5013.37	17.13	15.13	-0.019
0.780	19.813	1.182	1.092	32.061	13.331	0.416	0.099	2.728	1.001	593.7	1.001	1.002	0.430	5251.03	17.18	15.16	0.009
0.815	20.695	1.235	1.141	32.077	13.418	0.418	0.099	2.736	1.004	594.4	1.002	1.005	0.428	5485.00	17.21	15.17	0.028
0.850	21.585	1.288	1.190	32.061	13.405	0.418	0.099	2.736	1.004	594.4	1.002	1.005	0.429	5720.83	17.20	15.17	0.027
0.885	22.472	1.340	1.239	32.056	13.385	0.418	0.099	2.734	1.003	594.2	1.001	1.004	0.429	5955.73	17.20	15.17	0.022
0.920	23.357	1.393	1.288	32.055	13.374	0.417	0.099	2.732	1.003	594.1	1.001	1.003	0.429	6190.32	17.19	15.17	0.020
0.955	24.246	1.446	1.337	32.056	13.366	0.417	0.099	2.732	1.003	594.0	1.001	1.003	0.429	6426.15	17.19	15.16	0.018
0.990	25.135	1.499	1.386	32.046	13.338	0.416	0.099	2.729	1.002	593.8	1.001	1.002	0.430	6661.61	17.18	15.16	0.012
1.025	26.027	1.553	1.435	32.049	13.320	0.416	0.099	2.727	1.001	593.6	1.000	1.001	0.430	6898.16	17.17	15.15	0.007
1.060	26.922	1.606	1.484	32.046	13.265	0.414	0.100	2.721	0.999	593.1	1.000	0.999	0.431	7135.20	17.15	15.14	-0.006
1.095	27.814	1.659	1.533	32.040	13.274	0.414	0.100	2.722	0.999	593.2	1.000	0.999	0.431	7371.59	17.16	15.14	-0.005
1.130	28.709	1.713	1.583	32.031	13.265	0.414	0.100	2.722	0.999	593.1	1.000	0.999	0.431	7608.77	17.15	15.14	-0.007
1.166	29.605	1.766	1.632	32.024	13.272	0.414	0.100	2.723	0.999	593.2	1.000	0.999	0.431	7846.22	17.16	15.14	-0.004
1.201	30.504	1.820	1.682	32.029	13.270	0.414	0.100	2.723	0.999	593.1	1.000	0.999	0.431	8084.61	17.15	15.14	-0.005
1.236	31.399	1.873	1.731	32.024	13.305	0.415	0.100	2.726	1.001	593.5	1.000	1.001	0.430	8321.76	17.17	15.15	0.003
1.272	32.298	1.927	1.781	32.013	13.296	0.415	0.100	2.726	1.000	593.4	1.000	1.000	0.430	8560.04	17.17	15.15	0.002
1.304	33.118	1.976	1.826	32.007	13.289	0.415	0.100	2.726	1.000	593.4	1.000	1.000	0.430	8777.46	17.17	15.15	0.002
1.309	33.261	1.984	1.834	32.005	13.293	0.415	0.100	2.726	1.001	593.5	1.000	1.000	0.430	8815.31	17.17	15.15	0.003
1.310	33.262	1.984	1.834	32.000	13.290	0.415	0.100	2.726	1.000	593.4	1.000	1.000	0.430	8815.52	17.17	15.15	0.002
1.310	33.267	1.984	1.834	31.991	13.283	0.415	0.100	2.726	1.000	593.4	1.000	1.000	0.430	8816.83	17.17	15.15	0.002
1.310	33.265	1.984	1.834	31.985	13.284	0.415	0.100	2.726	1.000	593.4	1.000	1.000	0.430	8816.35	17.17	15.15	0.002
1.310	33.266	1.984	1.834	31.982	13.274	0.415	0.100	2.725	1.000	593.4	1.000	1.000	0.430	8816.56	17.16	15.15	0.000
1.310	33.267	1.984	1.834	31.961	13.272	0.415	0.100	2.726	1.000	593.4	1.000	1.000	0.430	8816.90	17.17	15.15	0.002

Table 39. 3D Plate Pitot Data

y (in)	y (mm)	y/δ_u	y/δ_M	P_{t1} (psia)	P_{t2} (psia)	P_{t2}/P_{t1}	P_s/P_{t2}	Mach	M/M_e	u (m/s)	u/u_e	ρ/ρ_e	ρ_w/ρ	y^+	u_{eff}^+	u^+	$(u-ue)/u^*$
0.016	0.396	0.025	0.023	32.444	2.170	0.067	0.618	0.858	0.315	275.1	0.464	0.491	0.877	104.86	7.29	7.14	-8.231
0.017	0.428	0.027	0.025	32.447	2.200	0.068	0.610	0.871	0.320	278.8	0.471	0.493	0.874	113.16	7.39	7.23	-8.137
0.032	0.814	0.052	0.047	32.424	2.603	0.080	0.515	1.021	0.375	319.0	0.539	0.516	0.835	215.54	8.52	8.28	-7.093
0.054	1.366	0.087	0.079	32.417	3.056	0.094	0.439	1.155	0.424	352.3	0.595	0.539	0.799	361.60	9.48	9.14	-6.229
0.078	1.982	0.126	0.114	32.414	3.773	0.116	0.355	1.331	0.489	392.5	0.663	0.574	0.750	524.59	10.67	10.18	-5.185
0.104	2.651	0.168	0.153	32.420	4.104	0.127	0.327	1.403	0.515	407.7	0.688	0.590	0.730	701.69	11.12	10.58	-4.790
0.132	3.357	0.213	0.194	32.406	4.555	0.141	0.294	1.496	0.549	426.5	0.720	0.611	0.705	888.37	11.70	11.07	-4.304
0.161	4.096	0.260	0.237	32.395	5.037	0.155	0.266	1.589	0.583	444.2	0.750	0.633	0.680	1084.07	12.25	11.53	-3.843
0.192	4.867	0.309	0.281	32.388	5.378	0.166	0.249	1.651	0.606	455.5	0.769	0.649	0.663	1288.15	12.61	11.82	-3.551
0.223	5.655	0.359	0.327	32.395	5.930	0.183	0.226	1.746	0.641	472.0	0.797	0.674	0.638	1496.53	13.14	12.25	-3.123
0.254	6.460	0.410	0.373	32.381	6.819	0.211	0.196	1.890	0.694	495.0	0.836	0.715	0.602	1709.70	13.90	12.84	-2.527
0.286	7.272	0.461	0.420	32.376	7.216	0.223	0.186	1.950	0.716	504.0	0.851	0.733	0.588	1924.65	14.20	13.08	-2.291
0.319	8.097	0.514	0.468	32.369	8.033	0.248	0.167	2.069	0.759	520.8	0.879	0.769	0.560	2143.03	14.78	13.51	-1.856
0.352	8.935	0.567	0.516	32.362	8.201	0.253	0.163	2.093	0.768	524.0	0.885	0.777	0.554	2364.65	14.89	13.60	-1.773
0.385	9.776	0.620	0.565	32.360	8.746	0.270	0.153	2.168	0.796	533.7	0.901	0.801	0.538	2587.17	15.23	13.85	-1.520
0.418	10.628	0.674	0.614	32.346	9.525	0.294	0.140	2.271	0.833	546.3	0.922	0.835	0.516	2812.69	15.68	14.18	-1.194
0.452	11.479	0.728	0.663	32.347	10.286	0.318	0.130	2.366	0.868	557.3	0.941	0.868	0.496	3038.08	16.08	14.46	-0.909
0.486	12.339	0.783	0.713	32.340	10.602	0.328	0.126	2.405	0.883	561.6	0.948	0.882	0.488	3265.71	16.24	14.57	-0.799
0.520	13.200	0.837	0.762	32.338	11.456	0.354	0.117	2.506	0.920	572.1	0.966	0.918	0.469	3493.47	16.63	14.84	-0.525
0.553	14.056	0.892	0.812	32.346	11.693	0.362	0.114	2.533	0.930	574.8	0.970	0.928	0.464	3719.95	16.73	14.91	-0.455
0.587	14.915	0.946	0.861	32.341	12.468	0.386	0.107	2.621	0.962	583.2	0.985	0.961	0.448	3947.49	17.06	15.13	-0.236
0.621	15.768	1.000	0.911	32.327	12.783	0.395	0.105	2.656	0.975	586.4	0.990	0.974	0.442	4173.11	17.18	15.22	-0.153
0.654	16.621	1.054	0.960	32.325	12.974	0.401	0.103	2.677	0.983	588.3	0.993	0.982	0.438	4398.86	17.26	15.26	-0.105
0.688	17.477	1.109	1.009	32.323	13.202	0.408	0.101	2.702	0.992	590.4	0.997	0.992	0.434	4625.53	17.34	15.32	-0.049
0.722	18.329	1.163	1.059	32.320	13.117	0.406	0.102	2.693	0.988	589.6	0.995	0.988	0.436	4850.99	17.31	15.30	-0.070
0.755	19.179	1.217	1.108	32.313	13.197	0.408	0.101	2.702	0.992	590.4	0.997	0.992	0.434	5075.98	17.34	15.32	-0.049
0.788	20.027	1.270	1.157	32.316	13.226	0.409	0.101	2.705	0.993	590.7	0.997	0.993	0.434	5300.34	17.35	15.33	-0.042
0.822	20.871	1.324	1.205	32.313	13.216	0.409	0.101	2.704	0.992	590.6	0.997	0.992	0.434	5523.75	17.35	15.33	-0.045
0.855	21.725	1.378	1.255	32.304	13.229	0.410	0.101	2.706	0.993	590.8	0.997	0.993	0.434	5749.66	17.35	15.33	-0.040
0.889	22.571	1.432	1.304	32.308	13.233	0.410	0.101	2.706	0.993	590.8	0.997	0.993	0.434	5973.60	17.35	15.33	-0.040
0.922	23.425	1.486	1.353	32.304	13.275	0.411	0.101	2.711	0.995	591.2	0.998	0.995	0.433	6199.68	17.37	15.34	-0.029
0.956	24.280	1.540	1.402	32.302	13.292	0.412	0.100	2.713	0.996	591.4	0.998	0.996	0.432	6425.86	17.38	15.35	-0.025
0.990	25.135	1.594	1.452	32.297	13.335	0.413	0.100	2.718	0.997	591.8	0.999	0.998	0.432	6652.07	17.39	15.36	-0.014
1.023	25.992	1.649	1.501	32.298	13.390	0.415	0.100	2.723	1.000	592.3	1.000	1.000	0.431	6878.95	17.42	15.37	0.000
1.057	26.847	1.703	1.551	32.298	13.433	0.416	0.099	2.728	1.001	592.6	1.000	1.001	0.430	7105.16	17.43	15.38	0.007
1.091	27.707	1.758	1.600	32.292	13.438	0.416	0.099	2.729	1.002	592.7	1.001	1.002	0.430	7332.89	17.43	15.38	0.009
1.125	28.563	1.812	1.650	32.290	13.454	0.417	0.099	2.731	1.002	592.8	1.001	1.002	0.430	7559.34	17.44	15.38	0.013
1.158	29.420	1.866	1.699	32.283	13.431	0.416	0.099	2.728	1.001	592.7	1.001	1.001	0.430	7786.24	17.43	15.38	0.008
1.192	30.284	1.921	1.749	32.291	13.431	0.416	0.099	2.728	1.001	592.6	1.000	1.001	0.430	8014.97	17.43	15.38	0.007
1.226	31.142	1.975	1.799	32.283	13.403	0.415	0.100	2.725	1.000	592.4	1.000	1.000	0.430	8241.91	17.42	15.37	0.002
1.260	32.000	2.030	1.848	32.283	13.380	0.414	0.100	2.723	0.999	592.2	1.000	0.999	0.431	8469.08	17.41	15.37	-0.004
1.291	32.792	2.080	1.894	32.284	13.371	0.414	0.100	2.722	0.999	592.1	1.000	0.999	0.431	8678.71	17.41	15.36	-0.006
1.297	32.955	2.090	1.903	32.281	13.367	0.414	0.100	2.722	0.999	592.1	1.000	0.999	0.431	8721.71	17.41	15.36	-0.007
1.297	32.956	2.091	1.903	32.277	13.350	0.414	0.100	2.720	0.998	591.9	0.999	0.998	0.431	8721.91	17.40	15.36	-0.010
1.298	32.957	2.091	1.903	32.265	13.370	0.414	0.100	2.723	0.999	592.2	1.000	0.999	0.431	8722.34	17.41	15.37	-0.005
1.297	32.955	2.091	1.903	32.266	13.365	0.414	0.100	2.722	0.999	592.1	1.000	0.999	0.431	8721.88	17.41	15.36	-0.006
1.297	32.956	2.091	1.903	32.271	13.355	0.414	0.100	2.721	0.999	592.0	0.999	0.998	0.431	8721.91	17.40	15.36	-0.009
1.298	32.958	2.091	1.903	32.270	13.392	0.415	0.100	2.725	1.000	592.3	1.000	1.000	0.431	8722.47	17.42	15.37	0.000

Table 40. 80 Grit Plate Pitot Data

y (in)	y (mm)	y/δ_u	y/δ_M	P_{t1} (psia)	P_{t2} (psia)	P_{t2}/P_{t1}	P_s/P_{t2}	Mach	M/M_e	u (m/s)	u/u_e	ρ/ρ_e	ρ_w/ρ	y^+	u_{eff}^+	u^+	$(u-ue)/u^*$
0.015	0.391	0.027	0.024	32.246	3.296	0.102	0.399	1.233	0.451	370.6	0.625	0.552	0.777	93.00	10.93	10.50	-6.301
0.016	0.412	0.028	0.025	32.253	3.283	0.102	0.401	1.229	0.450	369.7	0.623	0.551	0.778	98.08	10.90	10.47	-6.326
0.032	0.810	0.055	0.050	32.239	3.191	0.099	0.412	1.206	0.441	364.3	0.614	0.547	0.784	192.78	10.73	10.32	-6.478
0.055	1.396	0.095	0.085	32.236	3.889	0.121	0.338	1.373	0.502	401.5	0.677	0.581	0.738	332.43	11.94	11.37	-5.425
0.080	2.043	0.139	0.125	32.231	4.413	0.137	0.298	1.485	0.543	424.3	0.715	0.606	0.708	486.35	12.70	12.02	-4.780
0.107	2.727	0.186	0.167	32.223	4.737	0.147	0.278	1.549	0.567	436.8	0.737	0.622	0.690	649.28	13.12	12.37	-4.425
0.136	3.452	0.235	0.211	32.218	5.155	0.160	0.255	1.628	0.596	451.5	0.761	0.641	0.669	821.84	13.63	12.79	-4.009
0.166	4.205	0.286	0.257	32.215	5.783	0.180	0.227	1.740	0.637	471.0	0.794	0.671	0.640	1000.93	14.31	13.34	-3.456
0.196	4.978	0.339	0.305	32.201	6.262	0.194	0.210	1.821	0.666	484.2	0.817	0.693	0.619	1185.04	14.78	13.72	-3.082
0.227	5.770	0.393	0.353	32.198	6.785	0.211	0.194	1.905	0.697	497.2	0.838	0.717	0.599	1373.44	15.25	14.08	-2.713
0.259	6.574	0.448	0.402	32.203	7.162	0.222	0.183	1.962	0.718	505.8	0.853	0.734	0.585	1564.99	15.57	14.33	-2.470
0.291	7.387	0.503	0.452	32.196	8.316	0.258	0.158	2.130	0.779	528.9	0.892	0.786	0.546	1758.51	16.44	14.98	-1.815
0.323	8.214	0.560	0.503	32.191	8.224	0.255	0.160	2.118	0.775	527.3	0.889	0.782	0.549	1955.38	16.38	14.94	-1.862
0.356	9.040	0.616	0.553	32.180	9.462	0.294	0.139	2.285	0.836	548.0	0.924	0.837	0.512	2151.93	17.19	15.52	-1.273
0.389	9.879	0.673	0.605	32.172	9.772	0.304	0.134	2.325	0.851	552.7	0.932	0.851	0.504	2351.71	17.37	15.66	-1.141
0.422	10.723	0.731	0.656	32.175	10.305	0.320	0.127	2.392	0.875	560.2	0.945	0.875	0.490	2552.72	17.67	15.87	-0.929
0.456	11.572	0.788	0.708	32.172	11.139	0.346	0.118	2.494	0.912	570.9	0.963	0.911	0.471	2754.65	18.11	16.17	-0.626
0.489	12.421	0.846	0.760	32.164	11.549	0.359	0.114	2.542	0.930	575.7	0.971	0.929	0.462	2956.93	18.31	16.31	-0.491
0.522	13.271	0.904	0.812	32.157	12.070	0.375	0.109	2.603	0.952	581.5	0.981	0.951	0.451	3159.14	18.55	16.47	-0.325
0.556	14.120	0.962	0.864	32.153	11.998	0.373	0.109	2.595	0.949	580.7	0.979	0.948	0.452	3361.16	18.52	16.45	-0.348
0.589	14.966	1.020	0.916	32.148	12.935	0.402	0.101	2.700	0.988	590.3	0.996	0.988	0.434	3562.55	18.93	16.72	-0.075
0.622	15.809	1.077	0.968	32.144	12.894	0.401	0.102	2.695	0.986	589.9	0.995	0.986	0.435	3763.39	18.91	16.71	-0.089
0.656	16.656	1.135	1.019	32.136	13.045	0.406	0.101	2.712	0.992	591.3	0.997	0.993	0.432	3965.02	18.97	16.75	-0.047
0.689	17.500	1.192	1.071	32.132	13.189	0.410	0.099	2.728	0.998	592.6	0.999	0.998	0.430	4165.80	19.03	16.79	-0.010
0.722	18.345	1.250	1.123	32.126	13.210	0.411	0.099	2.731	0.999	592.9	1.000	0.999	0.429	4367.02	19.04	16.79	-0.004
0.755	19.181	1.307	1.174	32.115	13.280	0.414	0.099	2.739	1.002	593.5	1.001	1.002	0.428	4566.10	19.07	16.81	0.015
0.788	20.022	1.364	1.225	32.108	13.272	0.413	0.099	2.738	1.002	593.4	1.001	1.002	0.428	4766.14	19.06	16.81	0.012
0.821	20.860	1.421	1.277	32.086	13.291	0.414	0.099	2.741	1.003	593.7	1.001	1.003	0.428	4965.83	19.07	16.82	0.020
0.854	21.703	1.479	1.328	32.096	13.277	0.414	0.099	2.739	1.002	593.5	1.001	1.002	0.428	5166.29	19.07	16.81	0.015
0.887	22.541	1.536	1.380	32.087	13.259	0.413	0.099	2.738	1.002	593.4	1.001	1.002	0.428	5365.95	19.06	16.81	0.011
0.921	23.388	1.594	1.431	32.084	13.270	0.414	0.099	2.739	1.002	593.5	1.001	1.002	0.428	5567.58	19.06	16.81	0.014
0.954	24.234	1.651	1.483	32.080	13.276	0.414	0.099	2.740	1.002	593.5	1.001	1.003	0.428	5768.80	19.07	16.81	0.016
0.987	25.079	1.709	1.535	32.070	13.240	0.413	0.099	2.737	1.001	593.3	1.000	1.001	0.428	5970.08	19.05	16.81	0.008
1.021	25.928	1.767	1.587	32.064	13.215	0.412	0.099	2.734	1.000	593.0	1.000	1.000	0.429	6172.18	19.05	16.80	0.002
1.054	26.777	1.824	1.639	32.065	13.186	0.411	0.099	2.731	0.999	592.8	1.000	0.999	0.429	6374.19	19.03	16.79	-0.006
1.088	27.626	1.882	1.691	32.055	13.152	0.410	0.099	2.728	0.998	592.5	0.999	0.998	0.430	6576.47	19.02	16.78	-0.014
1.121	28.474	1.940	1.743	32.050	13.142	0.410	0.100	2.727	0.998	592.4	0.999	0.997	0.430	6778.19	19.02	16.78	-0.016
1.154	29.324	1.998	1.795	32.057	13.188	0.411	0.099	2.731	0.999	592.8	1.000	0.999	0.429	6980.62	19.04	16.79	-0.005
1.188	30.176	2.056	1.847	32.052	13.177	0.411	0.099	2.730	0.999	592.7	1.000	0.999	0.429	7183.48	19.03	16.79	-0.007
1.221	31.025	2.114	1.899	32.049	13.182	0.411	0.099	2.731	0.999	592.8	1.000	0.999	0.429	7385.61	19.03	16.79	-0.006
1.255	31.872	2.172	1.951	32.034	13.185	0.412	0.099	2.732	1.000	592.9	1.000	1.000	0.429	7587.10	19.04	16.79	-0.003
1.287	32.677	2.226	2.000	32.031	13.177	0.411	0.099	2.731	0.999	592.8	1.000	0.999	0.429	7778.79	19.04	16.79	-0.005
1.295	32.893	2.241	2.013	32.043	13.223	0.413	0.099	2.736	1.001	593.2	1.000	1.001	0.429	7830.26	19.05	16.80	0.006
1.295	32.896	2.241	2.013	32.032	13.237	0.413	0.099	2.738	1.002	593.4	1.001	1.002	0.428	7830.94	19.06	16.81	0.011
1.295	32.889	2.241	2.013	32.020	13.207	0.412	0.099	2.735	1.001	593.2	1.000	1.001	0.429	7829.35	19.05	16.80	0.005
1.295	32.884	2.241	2.013	32.010	13.247	0.414	0.099	2.740	1.002	593.6	1.001	1.003	0.428	7828.14	19.07	16.81	0.017
1.295	32.887	2.241	2.013	32.024	13.251	0.414	0.099	2.740	1.002	593.5	1.001	1.003	0.428	7828.82	19.07	16.81	0.016
1.294	32.878	2.240	2.012	32.009	13.208	0.413	0.099	2.736	1.001	593.2	1.000	1.001	0.429	7826.64	19.05	16.80	0.006

Table 41. 36 Grit Plate Pitot Data

y (in)	y (mm)	y/δ_u	y/δ_M	P_{t1} (psia)	P_{t2} (psia)	P_{t2}/P_{t1}	P_s/P_{t2}	Mach	M/M_e	u (m/s)	u/u_e	ρ/ρ_e	ρ_w/ρ	y^+	u_{eff}^+	u^+	$(u-ue)/u^*$
0.016	0.394	0.022	0.021	32.293	2.548	0.079	0.527	1.002	0.368	313.7	0.530	0.513	0.840	109.60	8.01	7.79	-6.897
0.017	0.444	0.025	0.023	32.292	2.559	0.079	0.525	1.005	0.369	314.6	0.532	0.514	0.839	123.41	8.04	7.81	-6.873
0.035	0.887	0.049	0.046	32.303	2.841	0.088	0.473	1.093	0.402	336.9	0.570	0.529	0.816	246.65	8.64	8.36	-6.321
0.058	1.472	0.082	0.077	32.297	3.116	0.096	0.431	1.169	0.430	355.5	0.601	0.543	0.794	409.02	9.16	8.83	-5.858
0.083	2.114	0.118	0.110	32.290	3.769	0.117	0.356	1.328	0.488	391.8	0.662	0.575	0.750	587.41	10.19	9.73	-4.957
0.110	2.800	0.156	0.146	32.285	4.102	0.127	0.327	1.402	0.515	407.4	0.689	0.591	0.730	778.12	10.63	10.11	-4.571
0.139	3.522	0.196	0.184	32.278	4.514	0.140	0.297	1.486	0.546	424.6	0.718	0.610	0.707	978.86	11.14	10.54	-4.143
0.168	4.276	0.238	0.223	32.275	4.754	0.147	0.282	1.533	0.564	433.7	0.733	0.621	0.694	1188.55	11.41	10.77	-3.917
0.199	5.051	0.281	0.264	32.266	5.511	0.171	0.244	1.673	0.615	459.2	0.776	0.656	0.657	1403.72	12.18	11.40	-3.284
0.230	5.845	0.326	0.305	32.259	5.680	0.176	0.236	1.702	0.626	464.2	0.785	0.664	0.650	1624.50	12.33	11.52	-3.160
0.262	6.646	0.370	0.347	32.252	5.944	0.184	0.226	1.747	0.642	471.8	0.798	0.676	0.638	1847.22	12.57	11.71	-2.972
0.294	7.464	0.416	0.390	32.255	6.466	0.200	0.207	1.832	0.673	485.7	0.821	0.699	0.617	2074.37	13.00	12.06	-2.627
0.326	8.290	0.462	0.433	32.252	7.197	0.223	0.186	1.945	0.715	502.9	0.850	0.732	0.589	2303.97	13.55	12.49	-2.200
0.359	9.121	0.508	0.476	32.256	7.834	0.243	0.171	2.038	0.749	516.1	0.873	0.761	0.567	2535.06	13.99	12.81	-1.871
0.392	9.961	0.555	0.520	32.243	8.103	0.251	0.166	2.077	0.763	521.4	0.882	0.773	0.558	2768.34	14.16	12.94	-1.740
0.425	10.806	0.602	0.564	32.245	8.654	0.268	0.155	2.153	0.791	531.3	0.898	0.797	0.541	3003.22	14.49	13.19	-1.493
0.459	11.659	0.650	0.608	32.231	9.306	0.289	0.144	2.239	0.823	542.1	0.917	0.826	0.522	3240.33	14.86	13.46	-1.225
0.493	12.513	0.697	0.653	32.237	10.016	0.311	0.134	2.330	0.856	552.7	0.934	0.857	0.503	3477.68	15.23	13.72	-0.963
0.526	13.367	0.745	0.698	32.231	10.763	0.334	0.125	2.421	0.890	562.8	0.952	0.889	0.485	3714.92	15.58	13.97	-0.712
0.560	14.220	0.792	0.742	32.232	11.002	0.341	0.122	2.450	0.900	565.8	0.957	0.899	0.479	3952.14	15.69	14.05	-0.637
0.593	15.070	0.840	0.786	32.230	11.772	0.365	0.114	2.539	0.933	575.0	0.972	0.932	0.463	4188.49	16.02	14.28	-0.409
0.627	15.914	0.887	0.830	32.222	12.219	0.379	0.110	2.590	0.952	579.9	0.980	0.951	0.453	4422.95	16.21	14.40	-0.287
0.660	16.766	0.934	0.875	32.214	12.523	0.389	0.107	2.624	0.965	583.2	0.986	0.964	0.447	4659.78	16.32	14.48	-0.206
0.693	17.610	0.981	0.919	32.212	12.602	0.391	0.106	2.633	0.968	584.0	0.987	0.968	0.446	4894.35	16.35	14.50	-0.187
0.727	18.458	1.028	0.963	32.209	12.999	0.404	0.103	2.677	0.984	588.0	0.994	0.985	0.438	5129.84	16.50	14.60	-0.087
0.760	19.302	1.075	1.007	32.200	13.182	0.409	0.102	2.697	0.991	589.8	0.997	0.992	0.434	5364.57	16.57	14.64	-0.042
0.793	20.142	1.122	1.051	32.196	13.371	0.415	0.100	2.717	0.999	591.6	1.000	1.001	0.431	5597.89	16.64	14.69	0.003
0.826	20.984	1.169	1.095	32.188	13.347	0.415	0.100	2.715	0.998	591.4	1.000	1.000	0.431	5832.00	16.63	14.68	-0.002
0.859	21.826	1.216	1.139	32.183	13.386	0.416	0.100	2.720	1.000	591.7	1.000	1.001	0.431	6066.02	16.64	14.69	0.005
0.893	22.673	1.263	1.183	32.181	13.398	0.416	0.100	2.721	1.000	591.8	1.001	1.001	0.431	6301.30	16.65	14.69	0.008
0.926	23.517	1.310	1.227	32.174	13.392	0.416	0.100	2.721	1.000	591.8	1.000	1.001	0.431	6535.96	16.65	14.69	0.007
0.959	24.367	1.358	1.272	32.186	13.393	0.416	0.100	2.720	1.000	591.6	1.000	1.001	0.431	6772.28	16.64	14.69	0.004
0.993	25.224	1.405	1.316	32.178	13.403	0.417	0.100	2.722	1.000	591.7	1.000	1.001	0.431	7010.53	16.64	14.69	0.004
1.026	26.070	1.452	1.361	32.167	13.390	0.416	0.100	2.721	1.000	591.5	1.000	1.000	0.431	7245.64	16.64	14.68	0.000
1.060	26.921	1.500	1.405	32.173	13.364	0.415	0.100	2.718	0.999	591.2	1.000	0.999	0.432	7482.03	16.63	14.68	-0.007
1.094	27.778	1.548	1.450	32.164	13.360	0.415	0.100	2.718	0.999	591.2	1.000	0.999	0.432	7720.31	16.63	14.68	-0.007
1.127	28.624	1.595	1.494	32.162	13.324	0.414	0.100	2.714	0.997	590.9	0.999	0.997	0.432	7955.46	16.61	14.67	-0.015
1.161	29.479	1.642	1.538	32.147	13.312	0.414	0.100	2.713	0.997	590.8	0.999	0.997	0.433	8193.12	16.61	14.67	-0.017
1.194	30.334	1.690	1.583	32.152	13.317	0.414	0.100	2.714	0.997	590.8	0.999	0.997	0.432	8430.64	16.61	14.67	-0.016
1.228	31.184	1.737	1.627	32.142	13.339	0.415	0.100	2.717	0.998	591.1	0.999	0.998	0.432	8666.86	16.62	14.68	-0.009
1.261	32.034	1.785	1.672	32.127	13.372	0.416	0.100	2.721	1.000	591.5	1.000	1.000	0.431	8902.97	16.64	14.68	0.000
1.291	32.787	1.827	1.711	32.137	13.397	0.417	0.100	2.723	1.001	591.7	1.000	1.001	0.431	9112.35	16.64	14.69	0.004
1.296	32.907	1.833	1.717	32.140	13.437	0.418	0.099	2.727	1.002	592.0	1.001	1.002	0.430	9145.66	16.66	14.70	0.013
1.295	32.905	1.833	1.717	32.136	13.419	0.418	0.100	2.725	1.002	591.9	1.001	1.002	0.430	9145.31	16.65	14.69	0.009
1.296	32.909	1.833	1.717	32.136	13.448	0.418	0.099	2.728	1.003	592.1	1.001	1.003	0.430	9146.18	16.66	14.70	0.016
1.295	32.904	1.833	1.717	32.114	13.412	0.418	0.100	2.726	1.002	591.9	1.001	1.002	0.430	9145.04	16.65	14.69	0.010
1.296	32.906	1.833	1.717	32.114	13.433	0.418	0.099	2.728	1.003	592.1	1.001	1.003	0.430	9145.49	16.66	14.70	0.015
1.296	32.907	1.833	1.717	32.111	13.376	0.417	0.100	2.722	1.000	591.6	1.000	1.000	0.431	9145.73	16.64	14.69	0.002

Table 42. 20 Grit Plate Pitot Data

y (in)	y (mm)	y/δ_u	y/δ_M	P_{t1} (psia)	P_{t2} (psia)	P_{t2}/P_{t1}	P_s/P_{t2}	Mach	M/M_e	u (m/s)	u/u_e	ρ/ρ_e	ρ_w/ρ	y^+	u_{eff}^+	u^+	$(u-ue)/u^*$
0.016	0.396	0.022	0.022	32.359	2.702	0.083	0.514	1.024	0.379	318.9	0.541	0.522	0.835	114.31	8.13	7.89	-6.690
0.017	0.428	0.024	0.024	32.363	2.611	0.081	0.532	0.995	0.368	311.3	0.528	0.518	0.842	123.45	7.92	7.70	-6.879
0.034	0.871	0.049	0.048	32.356	2.828	0.087	0.491	1.062	0.393	328.7	0.558	0.529	0.824	251.25	8.39	8.13	-6.449
0.058	1.473	0.083	0.081	32.356	3.252	0.101	0.427	1.178	0.436	356.9	0.606	0.550	0.793	425.05	9.17	8.83	-5.751
0.084	2.130	0.121	0.117	32.355	3.459	0.107	0.401	1.229	0.455	368.8	0.626	0.560	0.779	614.71	9.50	9.12	-5.455
0.111	2.825	0.160	0.155	32.336	3.923	0.121	0.353	1.335	0.494	392.6	0.666	0.582	0.749	815.02	10.17	9.71	-4.866
0.140	3.554	0.201	0.195	32.329	4.188	0.130	0.331	1.392	0.515	404.6	0.687	0.594	0.734	1025.60	10.52	10.01	-4.570
0.170	4.312	0.244	0.237	32.333	4.549	0.141	0.305	1.465	0.542	419.5	0.712	0.611	0.714	1244.12	10.95	10.38	-4.202
0.200	5.089	0.288	0.280	32.324	5.358	0.166	0.259	1.615	0.598	448.2	0.761	0.648	0.673	1468.37	11.80	11.09	-3.491
0.232	5.883	0.333	0.323	32.331	6.022	0.186	0.230	1.727	0.640	468.0	0.794	0.677	0.644	1697.35	12.41	11.58	-3.002
0.263	6.686	0.379	0.368	32.316	6.494	0.201	0.213	1.804	0.668	480.5	0.815	0.698	0.624	1929.03	12.80	11.89	-2.692
0.295	7.503	0.425	0.412	32.318	6.300	0.195	0.220	1.773	0.656	475.5	0.807	0.690	0.632	2164.81	12.64	11.76	-2.817
0.328	8.326	0.471	0.458	32.304	7.068	0.219	0.196	1.892	0.700	494.3	0.839	0.724	0.602	2402.29	13.23	12.23	-2.352
0.360	9.155	0.518	0.503	32.294	7.476	0.231	0.185	1.952	0.723	503.3	0.854	0.742	0.588	2641.52	13.52	12.45	-2.130
0.393	9.992	0.566	0.549	32.295	8.645	0.268	0.160	2.114	0.783	525.7	0.892	0.792	0.550	2882.95	14.26	13.01	-1.573
0.427	10.839	0.614	0.596	32.300	8.766	0.271	0.158	2.130	0.789	527.8	0.896	0.797	0.547	3127.62	14.33	13.06	-1.522
0.460	11.687	0.662	0.643	32.291	9.449	0.293	0.147	2.219	0.822	539.0	0.915	0.827	0.527	3372.11	14.70	13.33	-1.245
0.494	12.537	0.710	0.689	32.275	10.095	0.313	0.137	2.300	0.852	548.7	0.931	0.855	0.510	3617.46	15.04	13.57	-1.006
0.527	13.384	0.758	0.736	32.273	11.053	0.342	0.125	2.415	0.894	561.4	0.953	0.895	0.487	3861.70	15.48	13.89	-0.690
0.560	14.234	0.806	0.783	32.274	10.896	0.338	0.127	2.396	0.887	559.5	0.949	0.888	0.491	4107.19	15.41	13.84	-0.739
0.593	15.073	0.853	0.829	32.270	12.213	0.378	0.113	2.546	0.943	575.0	0.976	0.944	0.462	4349.22	15.97	14.22	-0.355
0.627	15.918	0.901	0.875	32.263	12.645	0.392	0.109	2.594	0.960	579.5	0.983	0.961	0.453	4593.04	16.14	14.34	-0.242
0.660	16.760	0.949	0.921	32.259	12.941	0.401	0.107	2.626	0.972	582.5	0.988	0.973	0.448	4835.82	16.25	14.41	-0.169
0.693	17.602	0.997	0.968	32.249	12.992	0.403	0.106	2.632	0.974	583.0	0.989	0.976	0.447	5079.00	16.27	14.42	-0.155
0.726	18.446	1.044	1.014	32.231	13.559	0.421	0.102	2.693	0.997	588.6	0.999	0.999	0.436	5322.49	16.47	14.56	-0.018
0.759	19.282	1.092	1.060	32.231	13.497	0.419	0.102	2.686	0.994	588.0	0.998	0.997	0.437	5563.57	16.45	14.55	-0.033
0.792	20.120	1.139	1.106	32.226	13.570	0.421	0.102	2.694	0.997	588.7	0.999	1.000	0.436	5805.29	16.48	14.56	-0.016
0.825	20.961	1.187	1.152	32.223	13.684	0.425	0.101	2.706	1.002	589.8	1.001	1.005	0.434	6048.07	16.52	14.59	0.011
0.858	21.794	1.234	1.198	32.219	13.672	0.424	0.101	2.705	1.001	589.7	1.001	1.004	0.434	6288.29	16.51	14.59	0.008
0.891	22.640	1.282	1.245	32.217	13.641	0.423	0.101	2.702	1.000	589.4	1.000	1.003	0.435	6532.50	16.50	14.58	0.002
0.924	23.479	1.329	1.291	32.206	13.628	0.423	0.101	2.701	1.000	589.3	1.000	1.002	0.435	6774.71	16.50	14.58	-0.001
0.958	24.326	1.377	1.337	32.202	13.593	0.422	0.102	2.697	0.999	589.0	0.999	1.001	0.435	7018.99	16.49	14.57	-0.008
0.991	25.170	1.425	1.384	32.185	13.604	0.423	0.101	2.699	0.999	589.2	1.000	1.002	0.435	7262.56	16.49	14.58	-0.004
1.024	26.015	1.473	1.430	32.184	13.583	0.422	0.102	2.697	0.999	589.0	0.999	1.001	0.435	7506.48	16.49	14.57	-0.009
1.058	26.867	1.521	1.477	32.183	13.613	0.423	0.101	2.700	1.000	589.3	1.000	1.002	0.435	7752.25	16.50	14.58	-0.002
1.091	27.712	1.569	1.524	32.180	13.622	0.423	0.101	2.701	1.000	589.4	1.000	1.003	0.435	7995.89	16.50	14.58	0.001
1.124	28.557	1.617	1.570	32.170	13.656	0.424	0.101	2.705	1.002	589.7	1.001	1.004	0.434	8239.78	16.51	14.59	0.010
1.158	29.410	1.665	1.617	32.158	13.664	0.425	0.101	2.707	1.002	589.8	1.001	1.005	0.434	8485.87	16.52	14.59	0.012
1.191	30.256	1.713	1.663	32.163	13.655	0.425	0.101	2.706	1.002	589.6	1.000	1.004	0.434	8730.04	16.51	14.59	0.007
1.225	31.104	1.761	1.710	32.153	13.623	0.424	0.101	2.703	1.001	589.3	1.000	1.002	0.435	8974.68	16.50	14.58	-0.001
1.258	31.947	1.809	1.756	32.156	13.500	0.420	0.102	2.690	0.996	588.1	0.998	0.997	0.437	9218.03	16.45	14.55	-0.031
1.288	32.719	1.853	1.799	32.144	13.465	0.419	0.102	2.687	0.995	587.7	0.997	0.996	0.438	9440.75	16.44	14.54	-0.039
1.294	32.872	1.861	1.807	32.138	13.544	0.421	0.102	2.695	0.998	588.5	0.999	0.999	0.436	9484.94	16.47	14.56	-0.020
1.294	32.870	1.861	1.807	32.133	13.464	0.419	0.102	2.687	0.995	587.8	0.997	0.996	0.438	9484.15	16.44	14.54	-0.039
1.294	32.873	1.861	1.807	32.129	13.505	0.420	0.102	2.691	0.996	588.2	0.998	0.997	0.437	9485.11	16.46	14.55	-0.029
1.294	32.869	1.861	1.807	32.127	13.503	0.420	0.102	2.691	0.996	588.2	0.998	0.997	0.437	9484.05	16.46	14.55	-0.029
1.294	32.871	1.861	1.807	32.119	13.511	0.421	0.102	2.693	0.997	588.3	0.998	0.998	0.437	9484.54	16.46	14.55	-0.026
1.294	32.867	1.861	1.807	32.108	13.528	0.421	0.102	2.695	0.998	588.5	0.999	0.999	0.436	9483.48	16.47	14.56	-0.021

Table 43. Smooth Plate, x-y Plane, HWA Data

y (in)	y (mm)	y/δ	$(\rho u)_{rms}$	$(\rho v)_{rms}$	$(\rho u)'(\rho v)'$	θ_{xy}(deg)	P_{t1} (psia)	T_t (K)	Re_x	$(\rho u)_{bar}$ (kg/m^{2}s)	$(\rho v)_{bar}$ (kg/m^{2}s)	$(\rho u)_{bar}/(ru)_e$	$(\rho v)_{bar}/(ru)_e$
1.22E-01	3.10E+00	2.50E-01	1.05E-01	8.22E-02	-3.96E-03	-2.22E+00	3.47E+01	2.96E+02	2.56E+02	9.15E+01	-9.91E+00	5.55E-01	-6.01E-02
1.22E-01	3.10E+00	2.50E-01	1.04E-01	8.19E-02	-3.85E-03	-2.13E+00	3.47E+01	2.96E+02	2.54E+02	9.09E+01	-9.82E+00	5.51E-01	-5.95E-02
1.23E-01	3.13E+00	2.53E-01	1.04E-01	8.17E-02	-4.06E-03	-2.15E+00	3.47E+01	2.96E+02	2.54E+02	9.08E+01	-1.04E+01	5.50E-01	-6.29E-02
1.30E-01	3.29E+00	2.66E-01	1.06E-01	8.26E-02	-4.10E-03	-2.21E+00	3.47E+01	2.96E+02	2.56E+02	9.16E+01	-1.12E+01	5.55E-01	-6.76E-02
1.44E-01	3.65E+00	2.95E-01	1.10E-01	8.15E-02	-4.23E-03	-2.37E+00	3.47E+01	2.96E+02	2.65E+02	9.49E+01	-1.26E+01	5.75E-01	-7.61E-02
1.66E-01	4.21E+00	3.40E-01	1.12E-01	7.95E-02	-4.21E-03	-2.50E+00	3.47E+01	2.96E+02	2.76E+02	9.89E+01	-1.38E+01	5.99E-01	-8.39E-02
1.92E-01	4.87E+00	3.94E-01	1.14E-01	7.55E-02	-4.15E-03	-2.56E+00	3.47E+01	2.96E+02	2.89E+02	1.04E+02	-1.47E+01	6.28E-01	-8.90E-02
2.19E-01	5.57E+00	4.50E-01	1.18E-01	7.33E-02	-4.27E-03	-2.60E+00	3.47E+01	2.96E+02	3.03E+02	1.08E+02	-1.55E+01	6.57E-01	-9.40E-02
2.48E-01	6.29E+00	5.08E-01	1.21E-01	6.98E-02	-4.21E-03	-2.62E+00	3.47E+01	2.96E+02	3.16E+02	1.13E+02	-1.63E+01	6.86E-01	-9.90E-02
2.76E-01	7.01E+00	5.67E-01	1.22E-01	6.77E-02	-4.02E-03	-2.61E+00	3.47E+01	2.96E+02	3.28E+02	1.18E+02	-1.70E+01	7.13E-01	-1.03E-01
3.05E-01	7.75E+00	6.26E-01	1.21E-01	6.43E-02	-3.80E-03	-2.64E+00	3.47E+01	2.96E+02	3.42E+02	1.22E+02	-1.77E+01	7.41E-01	-1.07E-01
3.35E-01	8.50E+00	6.86E-01	1.17E-01	6.02E-02	-3.39E-03	-2.64E+00	3.47E+01	2.96E+02	3.57E+02	1.28E+02	-1.83E+01	7.74E-01	-1.11E-01
3.64E-01	9.25E+00	7.47E-01	1.15E-01	5.55E-02	-3.16E-03	-2.70E+00	3.47E+01	2.96E+02	3.73E+02	1.34E+02	-1.93E+01	8.10E-01	-1.17E-01
3.94E-01	1.00E+01	8.08E-01	1.09E-01	5.23E-02	-2.76E-03	-2.66E+00	3.47E+01	2.96E+02	3.84E+02	1.38E+02	-1.97E+01	8.34E-01	-1.19E-01
4.24E-01	1.08E+01	8.70E-01	1.00E-01	4.86E-02	-2.33E-03	-2.63E+00	3.47E+01	2.96E+02	3.97E+02	1.42E+02	-1.99E+01	8.62E-01	-1.20E-01
4.55E-01	1.15E+01	9.32E-01	8.96E-02	4.50E-02	-1.88E-03	-2.55E+00	3.47E+01	2.96E+02	4.09E+02	1.47E+02	-1.96E+01	8.88E-01	-1.19E-01
4.85E-01	1.23E+01	9.95E-01	7.13E-02	3.99E-02	-1.25E-03	-2.42E+00	3.47E+01	2.96E+02	4.25E+02	1.52E+02	-1.88E+01	9.22E-01	-1.14E-01
5.16E-01	1.31E+01	1.06E+00	5.88E-02	3.70E-02	-9.17E-04	-2.25E+00	3.47E+01	2.96E+02	4.34E+02	1.55E+02	-1.75E+01	9.41E-01	-1.06E-01
5.47E-01	1.39E+01	1.12E+00	4.78E-02	3.44E-02	-6.18E-04	-2.09E+00	3.47E+01	2.96E+02	4.41E+02	1.58E+02	-1.64E+01	9.56E-01	-9.93E-02
5.77E-01	1.47E+01	1.18E+00	4.27E-02	3.32E-02	-5.59E-04	-2.00E+00	3.47E+01	2.96E+02	4.44E+02	1.59E+02	-1.58E+01	9.63E-01	-9.55E-02
6.08E-01	1.54E+01	1.25E+00	3.97E-02	3.32E-02	-5.33E-04	-1.85E+00	3.47E+01	2.96E+02	4.46E+02	1.60E+02	-1.47E+01	9.68E-01	-8.91E-02
6.38E-01	1.62E+01	1.31E+00	3.55E-02	3.29E-02	-4.94E-04	-1.84E+00	3.47E+01	2.96E+02	4.50E+02	1.61E+02	-1.47E+01	9.76E-01	-8.88E-02
6.68E-01	1.70E+01	1.37E+00	3.25E-02	3.27E-02	-4.63E-04	-1.92E+00	3.47E+01	2.96E+02	4.53E+02	1.62E+02	-1.54E+01	9.83E-01	-9.31E-02
6.99E-01	1.77E+01	1.43E+00	2.83E-02	3.26E-02	-4.18E-04	-2.00E+00	3.47E+01	2.96E+02	4.56E+02	1.63E+02	-1.60E+01	9.90E-01	-9.70E-02
7.29E-01	1.85E+01	1.50E+00	2.63E-02	3.37E-02	-4.37E-04	-2.06E+00	3.47E+01	2.96E+02	4.58E+02	1.64E+02	-1.65E+01	9.94E-01	-9.98E-02
7.59E-01	1.93E+01	1.56E+00	2.72E-02	3.52E-02	-4.85E-04	-1.89E+00	3.47E+01	2.96E+02	4.58E+02	1.64E+02	-1.51E+01	9.95E-01	-9.17E-02
7.90E-01	2.01E+01	1.62E+00	2.85E-02	3.65E-02	-5.55E-04	-1.83E+00	3.47E+01	2.96E+02	4.59E+02	1.64E+02	-1.46E+01	9.96E-01	-8.86E-02
8.20E-01	2.08E+01	1.68E+00	3.00E-02	3.78E-02	-6.10E-04	-1.68E+00	3.47E+01	2.96E+02	4.58E+02	1.64E+02	-1.34E+01	9.95E-01	-8.10E-02
8.50E-01	2.16E+01	1.74E+00	3.29E-02	3.93E-02	-7.35E-04	-1.62E+00	3.47E+01	2.96E+02	4.58E+02	1.64E+02	-1.29E+01	9.94E-01	-7.82E-02
8.81E-01	2.24E+01	1.81E+00	3.49E-02	4.01E-02	-8.15E-04	-1.53E+00	3.47E+01	2.96E+02	4.57E+02	1.64E+02	-1.22E+01	9.92E-01	-7.41E-02
9.11E-01	2.31E+01	1.87E+00	3.59E-02	4.05E-02	-8.61E-04	-1.45E+00	3.47E+01	2.96E+02	4.57E+02	1.64E+02	-1.15E+01	9.92E-01	-6.99E-02
9.42E-01	2.39E+01	1.93E+00	3.45E-02	4.07E-02	-7.98E-04	-1.33E+00	3.47E+01	2.96E+02	4.57E+02	1.64E+02	-1.06E+01	9.92E-01	-6.42E-02
9.71E-01	2.47E+01	1.99E+00	3.28E-02	4.06E-02	-7.35E-04	-1.31E+00	3.46E+01	2.96E+02	4.57E+02	1.64E+02	-1.05E+01	9.93E-01	-6.34E-02
1.00E+00	2.54E+01	2.05E+00	3.06E-02	3.99E-02	-6.64E-04	-1.35E+00	3.46E+01	2.96E+02	4.58E+02	1.64E+02	-1.08E+01	9.93E-01	-6.54E-02
1.03E+00	2.62E+01	2.11E+00	2.96E-02	3.91E-02	-6.33E-04	-1.24E+00	3.46E+01	2.96E+02	4.58E+02	1.64E+02	-9.90E+00	9.94E-01	-6.00E-02
1.06E+00	2.70E+01	2.18E+00	2.83E-02	3.78E-02	-5.93E-04	-1.11E+00	3.46E+01	2.96E+02	4.58E+02	1.64E+02	-8.93E+00	9.95E-01	-5.41E-02
1.09E+00	2.78E+01	2.24E+00	2.74E-02	3.70E-02	-5.51E-04	-8.97E-01	3.46E+01	2.96E+02	4.58E+02	1.64E+02	-7.21E+00	9.95E-01	-4.37E-02
1.13E+00	2.86E+01	2.31E+00	2.62E-02	3.61E-02	-5.16E-04	-9.74E-01	3.46E+01	2.96E+02	4.59E+02	1.65E+02	-7.84E+00	9.97E-01	-4.75E-02
1.16E+00	2.93E+01	2.37E+00	2.52E-02	3.52E-02	-4.53E-04	-7.65E-01	3.46E+01	2.96E+02	4.60E+02	1.65E+02	-6.17E+00	9.99E-01	-3.74E-02
1.19E+00	3.01E+01	2.43E+00	2.43E-02	3.45E-02	-3.99E-04	-6.13E-01	3.46E+01	2.96E+02	4.61E+02	1.65E+02	-4.01E+00	1.00E+00	-2.43E-02
1.22E+00	3.09E+01	2.50E+00	2.32E-02	3.41E-02	-3.17E-04	-3.76E-01	3.46E+01	2.96E+02	4.61E+02	1.65E+02	-1.12E+00	1.00E+00	-6.80E-03
1.25E+00	3.16E+01	2.55E+00	2.31E-02	3.41E-02	-2.80E-04	-2.36E-01	3.46E+01	2.96E+02	4.62E+02	1.65E+02	0.00E+00	1.00E+00	0.00E+00

Table 44. 2D Plate, x-y Plane, HWA Data

y (in)	y (mm)	y/δ	$(\rho u)_{rms}$	$(\rho v)_{rms}$	$(\rho u)'(\rho v)'$	θ_{xy}(deg)	P_{t1} (psia)	T_t (K)	Re_x	$(\rho u)_{bar}$ (kg/m^{2}s)	$(\rho v)_{bar}$ (kg/m^{2}s)	$(\rho u)_{bar}/(\rho u)_e$	$(\rho v)_{bar}/(\rho u)_e$
2.12E-01	5.38E+00	3.21E-01	1.48E-01	1.15E-01	-6.30E-03	-6.14E-01	3.47E+01	2.96E+02	2.55E+02	9.12E+01	-2.71E+00	5.34E-01	-1.59E-02
2.12E-01	5.38E+00	3.21E-01	1.48E-01	1.13E-01	-6.01E-03	-4.98E-01	3.47E+01	2.96E+02	2.53E+02	9.06E+01	-2.25E+00	5.30E-01	-1.32E-02
2.13E-01	5.41E+00	3.23E-01	1.48E-01	1.13E-01	-5.92E-03	-4.63E-01	3.47E+01	2.96E+02	2.53E+02	9.05E+01	-2.18E+00	5.30E-01	-1.27E-02
2.20E-01	5.58E+00	3.33E-01	1.48E-01	1.13E-01	-5.91E-03	-5.57E-01	3.47E+01	2.96E+02	2.55E+02	9.12E+01	-2.71E+00	5.33E-01	-1.59E-02
2.35E-01	5.97E+00	3.56E-01	1.49E-01	1.13E-01	-6.13E-03	-7.08E-01	3.47E+01	2.96E+02	2.60E+02	9.32E+01	-3.57E+00	5.45E-01	-2.09E-02
2.59E-01	6.57E+00	3.92E-01	1.52E-01	1.13E-01	-6.36E-03	-8.64E-01	3.47E+01	2.96E+02	2.69E+02	9.62E+01	-4.53E+00	5.63E-01	-2.65E-02
2.86E-01	7.27E+00	4.34E-01	1.55E-01	1.12E-01	-6.80E-03	-1.11E+00	3.47E+01	2.96E+02	2.78E+02	9.96E+01	-6.00E+00	5.83E-01	-3.51E-02
3.15E-01	8.00E+00	4.77E-01	1.57E-01	1.11E-01	-6.88E-03	-1.31E+00	3.47E+01	2.96E+02	2.87E+02	1.03E+02	-7.50E+00	6.01E-01	-4.39E-02
3.44E-01	8.74E+00	5.21E-01	1.59E-01	1.08E-01	-7.12E-03	-1.60E+00	3.47E+01	2.96E+02	2.98E+02	1.07E+02	-9.54E+00	6.25E-01	-5.58E-02
3.74E-01	9.49E+00	5.66E-01	1.60E-01	1.04E-01	-6.97E-03	-1.76E+00	3.47E+01	2.96E+02	3.08E+02	1.10E+02	-1.10E+01	6.46E-01	-6.43E-02
4.03E-01	1.02E+01	6.11E-01	1.61E-01	9.88E-02	-7.08E-03	-2.02E+00	3.47E+01	2.96E+02	3.25E+02	1.16E+02	-1.31E+01	6.81E-01	-7.67E-02
4.33E-01	1.10E+01	6.56E-01	1.62E-01	9.49E-02	-6.68E-03	-2.18E+00	3.47E+01	2.96E+02	3.41E+02	1.22E+02	-1.46E+01	7.14E-01	-8.56E-02
4.63E-01	1.18E+01	7.01E-01	1.65E-01	9.00E-02	-6.49E-03	-2.30E+00	3.47E+01	2.96E+02	3.58E+02	1.28E+02	-1.58E+01	7.50E-01	-9.27E-02
4.93E-01	1.25E+01	7.47E-01	1.63E-01	8.50E-02	-5.82E-03	-2.20E+00	3.47E+01	2.96E+02	3.71E+02	1.33E+02	-1.57E+01	7.78E-01	-9.16E-02
5.23E-01	1.33E+01	7.93E-01	1.60E-01	7.95E-02	-5.25E-03	-2.05E+00	3.47E+01	2.96E+02	3.84E+02	1.38E+02	-1.52E+01	8.05E-01	-8.91E-02
5.54E-01	1.41E+01	8.39E-01	1.54E-01	7.46E-02	-4.53E-03	-1.81E+00	3.47E+01	2.96E+02	3.95E+02	1.41E+02	-1.40E+01	8.27E-01	-8.20E-02
5.84E-01	1.48E+01	8.84E-01	1.44E-01	6.88E-02	-3.83E-03	-1.67E+00	3.47E+01	2.96E+02	4.09E+02	1.47E+02	-1.32E+01	8.57E-01	-7.73E-02
6.14E-01	1.56E+01	9.30E-01	1.29E-01	6.15E-02	-2.93E-03	-1.55E+00	3.47E+01	2.96E+02	4.26E+02	1.53E+02	-1.24E+01	8.94E-01	-7.24E-02
6.44E-01	1.64E+01	9.76E-01	1.12E-01	5.54E-02	-2.14E-03	-1.53E+00	3.47E+01	2.96E+02	4.43E+02	1.59E+02	-1.24E+01	9.29E-01	-7.26E-02
6.74E-01	1.71E+01	1.02E+00	1.00E-01	5.17E-02	-1.67E-03	-1.49E+00	3.47E+01	2.96E+02	4.53E+02	1.62E+02	-1.23E+01	9.49E-01	-7.18E-02
7.04E-01	1.79E+01	1.07E+00	9.24E-02	5.02E-02	-1.43E-03	-1.53E+00	3.47E+01	2.96E+02	4.57E+02	1.64E+02	-1.28E+01	9.59E-01	-7.49E-02
7.35E-01	1.87E+01	1.11E+00	7.89E-02	4.71E-02	-1.18E-03	-1.72E+00	3.47E+01	2.96E+02	4.65E+02	1.67E+02	-1.44E+01	9.75E-01	-8.43E-02
7.65E-01	1.94E+01	1.16E+00	6.26E-02	4.41E-02	-9.19E-04	-1.86E+00	3.47E+01	2.96E+02	4.72E+02	1.69E+02	-1.55E+01	9.90E-01	-9.10E-02
7.95E-01	2.02E+01	1.20E+00	4.60E-02	4.10E-02	-7.21E-04	-1.97E+00	3.47E+01	2.96E+02	4.79E+02	1.71E+02	-1.64E+01	1.00E+00	-9.62E-02
8.25E-01	2.09E+01	1.25E+00	3.74E-02	4.01E-02	-6.11E-04	-1.84E+00	3.47E+01	2.96E+02	4.80E+02	1.72E+02	-1.53E+01	1.01E+00	-8.96E-02
8.54E-01	2.17E+01	1.29E+00	3.39E-02	3.96E-02	-5.94E-04	-1.81E+00	3.47E+01	2.96E+02	4.80E+02	1.72E+02	-1.51E+01	1.01E+00	-8.81E-02
8.84E-01	2.25E+01	1.34E+00	3.33E-02	3.98E-02	-6.06E-04	-1.67E+00	3.47E+01	2.96E+02	4.78E+02	1.71E+02	-1.38E+01	1.00E+00	-8.10E-02
9.14E-01	2.32E+01	1.39E+00	3.38E-02	4.02E-02	-6.63E-04	-1.52E+00	3.47E+01	2.96E+02	4.77E+02	1.71E+02	-1.26E+01	1.00E+00	-7.35E-02
9.45E-01	2.40E+01	1.43E+00	3.51E-02	4.13E-02	-7.26E-04	-1.29E+00	3.47E+01	2.96E+02	4.76E+02	1.70E+02	-1.07E+01	9.97E-01	-6.25E-02
9.75E-01	2.48E+01	1.48E+00	3.57E-02	4.19E-02	-7.66E-04	-1.17E+00	3.47E+01	2.96E+02	4.75E+02	1.70E+02	-9.70E+00	9.96E-01	-5.68E-02
1.00E+00	2.55E+01	1.52E+00	3.50E-02	4.21E-02	-7.37E-04	-1.08E+00	3.47E+01	2.96E+02	4.75E+02	1.70E+02	-8.91E+00	9.95E-01	-5.21E-02
1.04E+00	2.63E+01	1.57E+00	3.39E-02	4.21E-02	-6.99E-04	-9.25E-01	3.46E+01	2.96E+02	4.75E+02	1.70E+02	-7.67E+00	9.95E-01	-4.49E-02
1.07E+00	2.71E+01	1.61E+00	3.28E-02	4.18E-02	-6.53E-04	-8.02E-01	3.46E+01	2.96E+02	4.74E+02	1.70E+02	-6.66E+00	9.94E-01	-3.90E-02
1.10E+00	2.78E+01	1.66E+00	3.13E-02	4.07E-02	-6.05E-04	-7.94E-01	3.46E+01	2.96E+02	4.75E+02	1.70E+02	-6.60E+00	9.95E-01	-3.86E-02
1.13E+00	2.86E+01	1.70E+00	2.91E-02	3.86E-02	-5.19E-04	-7.53E-01	3.46E+01	2.96E+02	4.75E+02	1.70E+02	-6.26E+00	9.96E-01	-3.66E-02
1.16E+00	2.93E+01	1.75E+00	2.73E-02	3.74E-02	-4.52E-04	-6.04E-01	3.46E+01	2.96E+02	4.76E+02	1.70E+02	-5.03E+00	9.97E-01	-2.94E-02
1.19E+00	3.01E+01	1.80E+00	2.64E-02	3.65E-02	-4.08E-04	-3.72E-01	3.46E+01	2.96E+02	4.76E+02	1.71E+02	-3.10E+00	9.98E-01	-1.81E-02
1.22E+00	3.09E+01	1.84E+00	2.59E-02	3.62E-02	-3.65E-04	-1.85E-01	3.46E+01	2.96E+02	4.77E+02	1.71E+02	-1.54E+00	9.99E-01	-9.00E-03
1.24E+00	3.15E+01	1.88E+00	2.52E-02	3.55E-02	-3.04E-04	-5.11E-02	3.46E+01	2.96E+02	4.77E+02	1.71E+02	-4.25E-01	1.00E+00	-2.49E-03
1.26E+00	3.20E+01	1.91E+00	2.55E-02	3.59E-02	-2.79E-04	-1.03E-01	3.46E+01	2.96E+02	4.77E+02	1.71E+02	1.03E-01	1.00E+00	6.05E-04
1.27E+00	3.22E+01	1.92E+00	2.61E-02	3.65E-02	-2.84E-04	-9.17E-02	3.46E+01	2.96E+02	4.77E+02	1.71E+02	6.93E-03	1.00E+00	4.06E-05
1.27E+00	3.23E+01	1.92E+00	2.71E-02	3.76E-02	-2.96E-04	-1.18E-01	3.46E+01	2.96E+02	4.78E+02	1.71E+02	0.00E+00	1.00E+00	0.00E+00

Table 45. 3D Plate, x-y Plane, HWA Data

y (in)	y (mm)	y/δ	$(\rho u)_{rms}$	$(\rho v)_{rms}$	$(\rho u)'(\rho v)'$	θ_{xy} (deg)	P_{t1} (psia)	T_t (K)	Re_x	$(\rho u)_{bar}$ (kg/m^{2}s)	$(\rho v)_{bar}$ (kg/m^{2}s)	$(\rho u)_{bar}/(\rho u)_e$	$(\rho v)_{bar}/(\rho u)_e$
1.82E-01	4.62E+00	2.93E-01	1.44E-01	1.14E-01	-6.02E-03	-6.58E-01	3.50E+01	2.96E+02	2.51E+02	9.00E+01	-2.90E+00	5.24E-01	-1.68E-02
1.82E-01	4.62E+00	2.93E-01	1.44E-01	1.12E-01	-5.76E-03	-5.43E-01	3.49E+01	2.96E+02	2.50E+02	8.95E+01	-2.43E+00	5.20E-01	-1.42E-02
1.83E-01	4.66E+00	2.95E-01	1.43E-01	1.12E-01	-5.88E-03	-5.06E-01	3.49E+01	2.96E+02	2.50E+02	8.96E+01	-2.36E+00	5.21E-01	-1.37E-02
1.91E-01	4.84E+00	3.07E-01	1.44E-01	1.12E-01	-6.09E-03	-5.42E-01	3.49E+01	2.96E+02	2.52E+02	9.03E+01	-2.60E+00	5.25E-01	-1.51E-02
2.07E-01	5.25E+00	3.33E-01	1.46E-01	1.12E-01	-6.60E-03	-7.96E-01	3.49E+01	2.96E+02	2.59E+02	9.27E+01	-3.92E+00	5.39E-01	-2.28E-02
2.31E-01	5.85E+00	3.71E-01	1.46E-01	1.10E-01	-6.46E-03	-1.01E+00	3.49E+01	2.96E+02	2.66E+02	9.51E+01	-5.24E+00	5.53E-01	-3.05E-02
2.58E-01	6.56E+00	4.16E-01	1.45E-01	1.07E-01	-6.19E-03	-1.22E+00	3.49E+01	2.96E+02	2.74E+02	9.81E+01	-6.67E+00	5.70E-01	-3.88E-02
2.87E-01	7.28E+00	4.62E-01	1.46E-01	1.05E-01	-5.92E-03	-1.33E+00	3.49E+01	2.96E+02	2.82E+02	1.01E+02	-7.52E+00	5.87E-01	-4.38E-02
3.15E-01	8.01E+00	5.08E-01	1.48E-01	1.01E-01	-5.91E-03	-1.49E+00	3.49E+01	2.96E+02	2.94E+02	1.05E+02	-8.86E+00	6.13E-01	-5.15E-02
3.45E-01	8.75E+00	5.55E-01	1.52E-01	9.82E-02	-6.10E-03	-1.76E+00	3.49E+01	2.96E+02	3.11E+02	1.11E+02	-1.09E+01	6.48E-01	-6.37E-02
3.74E-01	9.50E+00	6.03E-01	1.55E-01	9.45E-02	-5.98E-03	-1.85E+00	3.49E+01	2.96E+02	3.24E+02	1.16E+02	-1.20E+01	6.76E-01	-7.00E-02
4.04E-01	1.03E+01	6.50E-01	1.55E-01	9.03E-02	-5.72E-03	-1.93E+00	3.49E+01	2.96E+02	3.39E+02	1.21E+02	-1.28E+01	7.05E-01	-7.45E-02
4.34E-01	1.10E+01	6.99E-01	1.56E-01	8.52E-02	-5.56E-03	-2.00E+00	3.49E+01	2.96E+02	3.55E+02	1.27E+02	-1.41E+01	7.39E-01	-8.17E-02
4.64E-01	1.18E+01	7.47E-01	1.55E-01	7.90E-02	-5.30E-03	-2.08E+00	3.49E+01	2.96E+02	3.73E+02	1.34E+02	-1.51E+01	7.76E-01	-8.80E-02
4.94E-01	1.26E+01	7.96E-01	1.52E-01	7.49E-02	-4.78E-03	-1.84E+00	3.49E+01	2.96E+02	3.81E+02	1.37E+02	-1.41E+01	7.94E-01	-8.19E-02
5.25E-01	1.33E+01	8.45E-01	1.41E-01	6.85E-02	-3.85E-03	-1.59E+00	3.49E+01	2.96E+02	4.00E+02	1.43E+02	-1.24E+01	8.32E-01	-7.21E-02
5.55E-01	1.41E+01	8.94E-01	1.26E-01	6.21E-02	-2.92E-03	-1.40E+00	3.49E+01	2.96E+02	4.17E+02	1.50E+02	-1.11E+01	8.69E-01	-6.48E-02
5.85E-01	1.49E+01	9.43E-01	1.09E-01	5.37E-02	-2.06E-03	-1.40E+00	3.49E+01	2.96E+02	4.41E+02	1.58E+02	-1.13E+01	9.18E-01	-6.60E-02
6.15E-01	1.56E+01	9.92E-01	9.72E-02	4.98E-02	-1.59E-03	-1.32E+00	3.49E+01	2.96E+02	4.49E+02	1.61E+02	-1.08E+01	9.34E-01	-6.28E-02
6.46E-01	1.64E+01	1.04E+00	8.22E-02	4.56E-02	-1.23E-03	-1.26E+00	3.49E+01	2.96E+02	4.58E+02	1.64E+02	-1.04E+01	9.54E-01	-6.05E-02
6.76E-01	1.72E+01	1.09E+00	6.98E-02	4.29E-02	-1.05E-03	-1.18E+00	3.49E+01	2.96E+02	4.64E+02	1.66E+02	-9.79E+00	9.66E-01	-5.69E-02
7.06E-01	1.79E+01	1.14E+00	5.57E-02	4.01E-02	-8.27E-04	-1.10E+00	3.49E+01	2.96E+02	4.69E+02	1.68E+02	-9.13E+00	9.77E-01	-5.31E-02
7.36E-01	1.87E+01	1.19E+00	4.73E-02	3.94E-02	-7.70E-04	-1.11E+00	3.49E+01	2.96E+02	4.72E+02	1.69E+02	-9.23E+00	9.83E-01	-5.37E-02
7.66E-01	1.94E+01	1.23E+00	4.02E-02	3.89E-02	-7.09E-04	-1.17E+00	3.49E+01	2.96E+02	4.74E+02	1.70E+02	-9.70E+00	9.87E-01	-5.64E-02
7.96E-01	2.02E+01	1.28E+00	3.54E-02	3.86E-02	-6.70E-04	-1.21E+00	3.49E+01	2.96E+02	4.75E+02	1.70E+02	-1.01E+01	9.89E-01	-5.86E-02
8.26E-01	2.10E+01	1.33E+00	3.29E-02	3.89E-02	-6.48E-04	-1.13E+00	3.49E+01	2.96E+02	4.75E+02	1.70E+02	-9.42E+00	9.90E-01	-5.48E-02
8.56E-01	2.17E+01	1.38E+00	3.24E-02	3.97E-02	-6.75E-04	-1.07E+00	3.49E+01	2.96E+02	4.76E+02	1.70E+02	-8.97E+00	9.91E-01	-5.21E-02
8.86E-01	2.25E+01	1.43E+00	3.32E-02	4.12E-02	-7.34E-04	-1.02E+00	3.48E+01	2.96E+02	4.77E+02	1.71E+02	-8.52E+00	9.93E-01	-4.95E-02
9.16E-01	2.33E+01	1.48E+00	3.37E-02	4.23E-02	-7.95E-04	-1.14E+00	3.48E+01	2.96E+02	4.78E+02	1.71E+02	-9.59E+00	9.96E-01	-5.58E-02
9.46E-01	2.40E+01	1.52E+00	3.32E-02	4.27E-02	-7.86E-04	-1.19E+00	3.48E+01	2.96E+02	4.79E+02	1.72E+02	-9.99E+00	9.98E-01	-5.81E-02
9.76E-01	2.48E+01	1.57E+00	3.29E-02	4.26E-02	-7.66E-04	-1.17E+00	3.48E+01	2.96E+02	4.80E+02	1.72E+02	-9.84E+00	1.00E+00	-5.72E-02
1.01E+00	2.55E+01	1.62E+00	3.25E-02	4.24E-02	-7.31E-04	-1.07E+00	3.48E+01	2.96E+02	4.81E+02	1.72E+02	-9.01E+00	1.00E+00	-5.24E-02
1.04E+00	2.63E+01	1.67E+00	3.23E-02	4.27E-02	-7.10E-04	-9.43E-01	3.48E+01	2.96E+02	4.82E+02	1.73E+02	-7.93E+00	1.00E+00	-4.61E-02
1.07E+00	2.71E+01	1.72E+00	3.15E-02	4.22E-02	-6.69E-04	-7.54E-01	3.48E+01	2.96E+02	4.82E+02	1.73E+02	-6.33E+00	1.00E+00	-3.68E-02
1.10E+00	2.78E+01	1.76E+00	2.99E-02	4.10E-02	-5.84E-04	-5.19E-01	3.48E+01	2.96E+02	4.82E+02	1.73E+02	-4.35E+00	1.00E+00	-2.53E-02
1.13E+00	2.86E+01	1.81E+00	2.82E-02	3.99E-02	-5.04E-04	-2.81E-01	3.48E+01	2.96E+02	4.82E+02	1.72E+02	-2.35E+00	1.00E+00	-1.37E-02
1.16E+00	2.93E+01	1.86E+00	2.69E-02	3.90E-02	-4.30E-04	-1.54E-01	3.48E+01	2.96E+02	4.81E+02	1.72E+02	-1.29E+00	1.00E+00	-7.51E-03
1.19E+00	3.01E+01	1.91E+00	2.61E-02	3.83E-02	-3.82E-04	-7.72E-02	3.48E+01	2.96E+02	4.80E+02	1.72E+02	-6.47E-01	1.00E+00	-3.76E-03
1.22E+00	3.09E+01	1.96E+00	2.54E-02	3.69E-02	-3.31E-04	-1.25E-01	3.48E+01	2.96E+02	4.80E+02	1.72E+02	-1.05E+00	1.00E+00	-6.08E-03
1.24E+00	3.15E+01	2.00E+00	2.49E-02	3.58E-02	-2.72E-04	-1.36E-01	3.48E+01	2.96E+02	4.80E+02	1.72E+02	-1.07E+00	1.00E+00	-6.23E-03
1.26E+00	3.20E+01	2.03E+00	2.48E-02	3.56E-02	-2.18E-04	-3.64E-02	3.48E+01	2.96E+02	4.80E+02	1.72E+02	-8.24E-01	1.00E+00	-4.79E-03
1.27E+00	3.22E+01	2.04E+00	2.52E-02	3.60E-02	-1.90E-04	9.01E-02	3.48E+01	2.96E+02	4.80E+02	1.72E+02	0.00E+00	1.00E+00	0.00E+00

Table 46. 80 Grit Plate, x-y Plane, HWA Data

y (in)	y (mm)	y/δ	$(\rho u)_{rms}$	$(\rho v)_{rms}$	$(\rho u)'(\rho v)'$	θ_{xy}(deg)	P_{t1} (psia)	T_t (K)	Re_x	$(\rho u)_{bar}$ (kg/m^{2}s)	$(\rho v)_{bar}$ (kg/m^{2}s)	$(\rho u)_{bar}/(\rho u)_e$	$(\rho v)_{bar}/(\rho u)_e$
2.12E-01	5.38E+00	3.67E-01	1.35E-01	1.07E-01	-6.52E-03	-1.52E+00	3.47E+01	2.96E+02	2.62E+02	9.39E+01	-7.14E+00	5.53E-01	-4.21E-02
2.12E-01	5.38E+00	3.67E-01	1.35E-01	1.06E-01	-6.64E-03	-1.65E+00	3.48E+01	2.96E+02	2.65E+02	9.48E+01	-7.95E+00	5.58E-01	-4.68E-02
2.13E-01	5.41E+00	3.69E-01	1.37E-01	1.06E-01	-6.75E-03	-1.80E+00	3.47E+01	2.96E+02	2.69E+02	9.63E+01	-8.82E+00	5.67E-01	-5.19E-02
2.20E-01	5.58E+00	3.80E-01	1.37E-01	1.05E-01	-6.63E-03	-1.81E+00	3.47E+01	2.96E+02	2.70E+02	9.67E+01	-9.17E+00	5.70E-01	-5.40E-02
2.35E-01	5.96E+00	4.06E-01	1.43E-01	1.04E-01	-6.67E-03	-1.83E+00	3.47E+01	2.96E+02	2.76E+02	9.87E+01	-9.76E+00	5.81E-01	-5.75E-02
2.58E-01	6.56E+00	4.47E-01	1.44E-01	1.01E-01	-6.40E-03	-1.83E+00	3.47E+01	2.96E+02	2.81E+02	1.01E+02	-1.02E+01	5.93E-01	-6.02E-02
2.86E-01	7.26E+00	4.95E-01	1.47E-01	9.88E-02	-5.96E-03	-1.79E+00	3.47E+01	2.96E+02	2.91E+02	1.04E+02	-1.05E+01	6.14E-01	-6.20E-02
3.15E-01	7.99E+00	5.44E-01	1.46E-01	9.40E-02	-5.29E-03	-1.84E+00	3.47E+01	2.96E+02	3.06E+02	1.10E+02	-1.11E+01	6.45E-01	-6.55E-02
3.44E-01	8.72E+00	5.94E-01	1.48E-01	9.04E-02	-5.13E-03	-1.88E+00	3.47E+01	2.96E+02	3.20E+02	1.15E+02	-1.19E+01	6.75E-01	-7.00E-02
3.73E-01	9.47E+00	6.45E-01	1.47E-01	8.52E-02	-5.03E-03	-1.99E+00	3.47E+01	2.96E+02	3.37E+02	1.21E+02	-1.32E+01	7.10E-01	-7.77E-02
4.02E-01	1.02E+01	6.96E-01	1.47E-01	8.24E-02	-4.85E-03	-1.96E+00	3.47E+01	2.96E+02	3.46E+02	1.24E+02	-1.36E+01	7.30E-01	-8.03E-02
4.32E-01	1.10E+01	7.48E-01	1.48E-01	7.69E-02	-4.65E-03	-2.02E+00	3.47E+01	2.96E+02	3.61E+02	1.29E+02	-1.47E+01	7.62E-01	-8.64E-02
4.62E-01	1.17E+01	8.00E-01	1.41E-01	7.00E-02	-4.10E-03	-2.05E+00	3.47E+01	2.96E+02	3.80E+02	1.36E+02	-1.53E+01	8.01E-01	-9.02E-02
4.93E-01	1.25E+01	8.53E-01	1.34E-01	6.31E-02	-3.45E-03	-1.96E+00	3.47E+01	2.96E+02	3.99E+02	1.43E+02	-1.50E+01	8.41E-01	-8.85E-02
5.23E-01	1.33E+01	9.05E-01	1.19E-01	5.73E-02	-2.63E-03	-1.79E+00	3.47E+01	2.96E+02	4.16E+02	1.49E+02	-1.39E+01	8.77E-01	-8.16E-02
5.53E-01	1.40E+01	9.57E-01	1.06E-01	5.34E-02	-2.09E-03	-1.65E+00	3.47E+01	2.96E+02	4.28E+02	1.53E+02	-1.29E+01	9.02E-01	-7.62E-02
5.83E-01	1.48E+01	1.01E+00	9.12E-02	4.92E-02	-1.58E-03	-1.52E+00	3.47E+01	2.96E+02	4.39E+02	1.57E+02	-1.20E+01	9.26E-01	-7.09E-02
6.13E-01	1.56E+01	1.06E+00	8.26E-02	4.67E-02	-1.35E-03	-1.43E+00	3.47E+01	2.96E+02	4.44E+02	1.59E+02	-1.14E+01	9.36E-01	-6.73E-02
6.44E-01	1.63E+01	1.11E+00	6.86E-02	4.36E-02	-1.12E-03	-1.38E+00	3.47E+01	2.96E+02	4.49E+02	1.61E+02	-1.11E+01	9.47E-01	-6.52E-02
6.74E-01	1.71E+01	1.17E+00	5.45E-02	4.08E-02	-9.30E-04	-1.42E+00	3.47E+01	2.96E+02	4.54E+02	1.63E+02	-1.15E+01	9.58E-01	-6.75E-02
7.04E-01	1.79E+01	1.22E+00	4.00E-02	3.84E-02	-6.92E-04	-1.36E+00	3.47E+01	2.96E+02	4.60E+02	1.65E+02	-1.10E+01	9.70E-01	-6.46E-02
7.34E-01	1.86E+01	1.27E+00	3.54E-02	3.79E-02	-6.45E-04	-1.19E+00	3.47E+01	2.96E+02	4.62E+02	1.65E+02	-9.59E+00	9.73E-01	-5.64E-02
7.64E-01	1.94E+01	1.32E+00	3.46E-02	3.82E-02	-6.19E-04	-1.00E+00	3.47E+01	2.96E+02	4.62E+02	1.65E+02	-8.09E+00	9.74E-01	-4.76E-02
7.94E-01	2.02E+01	1.37E+00	3.41E-02	3.88E-02	-6.14E-04	-9.25E-01	3.47E+01	2.96E+02	4.62E+02	1.65E+02	-7.48E+00	9.73E-01	-4.40E-02
8.24E-01	2.09E+01	1.43E+00	3.28E-02	3.91E-02	-5.91E-04	-8.05E-01	3.47E+01	2.96E+02	4.62E+02	1.66E+02	-6.50E+00	9.74E-01	-3.83E-02
8.54E-01	2.17E+01	1.48E+00	3.19E-02	3.92E-02	-5.82E-04	-7.67E-01	3.47E+01	2.96E+02	4.62E+02	1.66E+02	-6.19E+00	9.75E-01	-3.65E-02
8.84E-01	2.24E+01	1.53E+00	3.14E-02	3.93E-02	-5.90E-04	-6.46E-01	3.47E+01	2.96E+02	4.63E+02	1.66E+02	-5.23E+00	9.77E-01	-3.08E-02
9.14E-01	2.32E+01	1.58E+00	3.17E-02	4.01E-02	-6.18E-04	-5.93E-01	3.47E+01	2.96E+02	4.63E+02	1.66E+02	-4.81E+00	9.76E-01	-2.83E-02
9.44E-01	2.40E+01	1.63E+00	3.18E-02	4.10E-02	-6.23E-04	-4.24E-01	3.47E+01	2.96E+02	4.63E+02	1.66E+02	-3.46E+00	9.77E-01	-2.04E-02
9.74E-01	2.47E+01	1.69E+00	3.09E-02	4.06E-02	-5.88E-04	-3.37E-01	3.47E+01	2.96E+02	4.64E+02	1.66E+02	-2.76E+00	9.78E-01	-1.63E-02
1.00E+00	2.55E+01	1.74E+00	3.04E-02	4.04E-02	-5.61E-04	-3.53E-01	3.47E+01	2.96E+02	4.65E+02	1.67E+02	-2.91E+00	9.82E-01	-1.71E-02
1.03E+00	2.63E+01	1.79E+00	2.94E-02	3.96E-02	-5.26E-04	-5.29E-01	3.46E+01	2.96E+02	4.68E+02	1.68E+02	-4.37E+00	9.87E-01	-2.57E-02
1.07E+00	2.71E+01	1.84E+00	2.89E-02	4.03E-02	-5.34E-04	-6.01E-01	3.46E+01	2.96E+02	4.70E+02	1.68E+02	-4.97E+00	9.92E-01	-2.93E-02
1.10E+00	2.78E+01	1.90E+00	2.75E-02	3.94E-02	-5.03E-04	-5.67E-01	3.46E+01	2.96E+02	4.73E+02	1.69E+02	-4.69E+00	9.97E-01	-2.76E-02
1.13E+00	2.86E+01	1.95E+00	2.63E-02	3.81E-02	-4.43E-04	-3.70E-01	3.46E+01	2.96E+02	4.74E+02	1.70E+02	-3.06E+00	9.99E-01	-1.80E-02
1.16E+00	2.93E+01	2.00E+00	2.48E-02	3.65E-02	-3.55E-04	-2.06E-01	3.46E+01	2.96E+02	4.74E+02	1.70E+02	-1.70E+00	1.00E+00	-1.00E-02
1.19E+00	3.01E+01	2.05E+00	2.39E-02	3.60E-02	-2.78E-04	6.23E-04	3.46E+01	2.96E+02	4.74E+02	1.70E+02	4.39E-03	1.00E+00	2.58E-05
1.22E+00	3.09E+01	2.10E+00	2.33E-02	3.56E-02	-2.27E-04	7.98E-02	3.46E+01	2.96E+02	4.74E+02	1.70E+02	6.59E-01	1.00E+00	3.88E-03
1.24E+00	3.15E+01	2.15E+00	2.29E-02	3.47E-02	-1.81E-04	2.00E-02	3.46E+01	2.96E+02	4.74E+02	1.70E+02	1.65E-01	1.00E+00	9.71E-04
1.26E+00	3.20E+01	2.18E+00	2.31E-02	3.44E-02	-1.59E-04	-9.01E-02	3.46E+01	2.96E+02	4.74E+02	1.70E+02	-4.84E-01	1.00E+00	-2.85E-03
1.27E+00	3.22E+01	2.20E+00	2.32E-02	3.44E-02	-1.62E-04	-1.26E-01	3.46E+01	2.96E+02	4.74E+02	1.70E+02	-6.50E-01	9.99E-01	-3.83E-03
1.27E+00	3.23E+01	2.20E+00	2.35E-02	3.45E-02	-1.50E-04	3.74E-02	3.46E+01	2.96E+02	4.74E+02	1.70E+02	0.00E+00	1.00E+00	0.00E+00

Table 47. 36 Grit Plate, x-y Plane, HWA Data

y (in)	y (mm)	y/δ	$(\rho u)_{rms}$	$(\rho v)_{rms}$	$(\rho u)'(\rho v)'$	θ_{xy} (deg)	P_{t1} (psia)	T_{t1} (K)	Re_x	$(\rho u)_{bar}$ (kg/m^{2}s)	$(\rho v)_{bar}$ (kg/m^{2}s)	$(\rho u)_{bar}/(ru)_e$	$(\rho v)_{bar}/(ru)_e$
2.12E-01	5.38E+00	3.00E-01	1.64E-01	1.31E-01	-8.47E-03	-3.19E-01	3.48E+01	2.96E+02	2.55E+02	9.12E+01	-1.43E+00	5.33E-01	-8.38E-03
2.12E-01	5.38E+00	3.00E-01	1.61E-01	1.31E-01	-8.23E-03	-3.22E-01	3.48E+01	2.96E+02	2.54E+02	9.11E+01	-1.47E+00	5.33E-01	-8.62E-03
2.13E-01	5.42E+00	3.02E-01	1.60E-01	1.32E-01	-8.10E-03	-3.72E-01	3.48E+01	2.96E+02	2.55E+02	9.15E+01	-1.78E+00	5.35E-01	-1.04E-02
2.20E-01	5.59E+00	3.12E-01	1.59E-01	1.31E-01	-8.09E-03	-5.19E-01	3.48E+01	2.96E+02	2.58E+02	9.24E+01	-2.54E+00	5.40E-01	-1.48E-02
2.36E-01	5.99E+00	3.33E-01	1.59E-01	1.31E-01	-7.97E-03	-6.47E-01	3.48E+01	2.96E+02	2.61E+02	9.33E+01	-3.35E+00	5.46E-01	-1.96E-02
2.59E-01	6.59E+00	3.67E-01	1.62E-01	1.28E-01	-7.78E-03	-8.84E-01	3.48E+01	2.96E+02	2.68E+02	9.61E+01	-4.69E+00	5.62E-01	-2.74E-02
2.87E-01	7.29E+00	4.06E-01	1.64E-01	1.24E-01	-7.58E-03	-1.21E+00	3.48E+01	2.96E+02	2.79E+02	1.00E+02	-6.64E+00	5.85E-01	-3.88E-02
3.16E-01	8.03E+00	4.47E-01	1.68E-01	1.19E-01	-7.49E-03	-1.54E+00	3.48E+01	2.96E+02	2.93E+02	1.05E+02	-8.72E+00	6.14E-01	-5.10E-02
3.45E-01	8.77E+00	4.89E-01	1.68E-01	1.16E-01	-7.10E-03	-1.66E+00	3.48E+01	2.96E+02	3.02E+02	1.08E+02	-9.79E+00	6.32E-01	-5.73E-02
3.75E-01	9.52E+00	5.30E-01	1.71E-01	1.13E-01	-7.25E-03	-1.82E+00	3.48E+01	2.96E+02	3.12E+02	1.12E+02	-1.13E+01	6.52E-01	-6.58E-02
4.05E-01	1.03E+01	5.72E-01	1.72E-01	1.09E-01	-7.10E-03	-1.89E+00	3.48E+01	2.96E+02	3.22E+02	1.15E+02	-1.24E+01	6.74E-01	-7.25E-02
4.35E-01	1.10E+01	6.15E-01	1.74E-01	1.03E-01	-7.24E-03	-2.04E+00	3.48E+01	2.96E+02	3.38E+02	1.21E+02	-1.39E+01	7.07E-01	-8.12E-02
4.65E-01	1.18E+01	6.57E-01	1.71E-01	9.61E-02	-6.70E-03	-1.95E+00	3.48E+01	2.96E+02	3.54E+02	1.27E+02	-1.38E+01	7.41E-01	-8.08E-02
4.95E-01	1.26E+01	7.00E-01	1.67E-01	8.87E-02	-6.15E-03	-1.92E+00	3.48E+01	2.96E+02	3.75E+02	1.34E+02	-1.39E+01	7.86E-01	-8.13E-02
5.25E-01	1.33E+01	7.43E-01	1.63E-01	8.36E-02	-5.55E-03	-1.73E+00	3.47E+01	2.96E+02	3.90E+02	1.40E+02	-1.32E+01	8.17E-01	-7.72E-02
5.55E-01	1.41E+01	7.86E-01	1.55E-01	7.71E-02	-4.77E-03	-1.71E+00	3.47E+01	2.96E+02	4.07E+02	1.46E+02	-1.35E+01	8.53E-01	-7.88E-02
5.86E-01	1.49E+01	8.28E-01	1.47E-01	7.37E-02	-4.16E-03	-1.67E+00	3.47E+01	2.96E+02	4.16E+02	1.49E+02	-1.36E+01	8.71E-01	-7.96E-02
6.16E-01	1.56E+01	8.71E-01	1.28E-01	6.53E-02	-3.26E-03	-1.85E+00	3.47E+01	2.96E+02	4.38E+02	1.57E+02	-1.53E+01	9.18E-01	-8.93E-02
6.46E-01	1.64E+01	9.13E-01	1.09E-01	5.95E-02	-2.59E-03	-2.01E+00	3.47E+01	2.96E+02	4.53E+02	1.62E+02	-1.66E+01	9.49E-01	-9.73E-02
6.76E-01	1.72E+01	9.56E-01	8.69E-02	5.33E-02	-1.87E-03	-2.16E+00	3.47E+01	2.96E+02	4.67E+02	1.67E+02	-1.80E+01	9.79E-01	-1.05E-01
7.06E-01	1.79E+01	9.98E-01	7.24E-02	5.08E-02	-1.45E-03	-2.18E+00	3.47E+01	2.96E+02	4.72E+02	1.69E+02	-1.82E+01	9.88E-01	-1.06E-01
7.36E-01	1.87E+01	1.04E+00	6.52E-02	4.97E-02	-1.29E-03	-2.11E+00	3.47E+01	2.96E+02	4.74E+02	1.70E+02	-1.77E+01	9.93E-01	-1.04E-01
7.65E-01	1.94E+01	1.08E+00	5.73E-02	4.79E-02	-1.15E-03	-1.99E+00	3.47E+01	2.96E+02	4.78E+02	1.70E+02	-1.67E+01	9.97E-01	-9.76E-02
7.95E-01	2.02E+01	1.12E+00	5.27E-02	4.64E-02	-1.02E-03	-1.84E+00	3.47E+01	2.96E+02	4.78E+02	1.71E+02	-1.55E+01	1.00E+00	-9.05E-02
8.25E-01	2.09E+01	1.17E+00	4.64E-02	4.51E-02	-8.93E-04	-1.71E+00	3.47E+01	2.96E+02	4.80E+02	1.72E+02	-1.45E+01	1.01E+00	-8.45E-02
8.55E-01	2.17E+01	1.21E+00	4.38E-02	4.54E-02	-8.46E-04	-1.56E+00	3.47E+01	2.96E+02	4.82E+02	1.73E+02	-1.31E+01	1.01E+00	-7.66E-02
8.85E-01	2.25E+01	1.25E+00	4.20E-02	4.57E-02	-8.49E-04	-1.40E+00	3.47E+01	2.96E+02	4.83E+02	1.73E+02	-1.18E+01	1.01E+00	-6.91E-02
9.15E-01	2.32E+01	1.29E+00	3.85E-02	4.58E-02	-8.24E-04	-1.30E+00	3.47E+01	2.96E+02	4.84E+02	1.73E+02	-1.09E+01	1.01E+00	-6.37E-02
9.45E-01	2.40E+01	1.34E+00	3.74E-02	4.56E-02	-7.91E-04	-1.20E+00	3.47E+01	2.96E+02	4.83E+02	1.73E+02	-1.00E+01	1.01E+00	-5.86E-02
9.75E-01	2.48E+01	1.38E+00	3.59E-02	4.54E-02	-7.18E-04	-1.22E+00	3.47E+01	2.96E+02	4.82E+02	1.73E+02	-1.02E+01	1.01E+00	-5.95E-02
1.01E+00	2.55E+01	1.42E+00	3.49E-02	4.50E-02	-6.74E-04	-1.21E+00	3.47E+01	2.96E+02	4.81E+02	1.72E+02	-1.01E+01	1.01E+00	-5.89E-02
1.04E+00	2.63E+01	1.46E+00	3.39E-02	4.50E-02	-6.48E-04	-1.19E+00	3.47E+01	2.96E+02	4.80E+02	1.72E+02	-9.90E+00	1.01E+00	-5.79E-02
1.07E+00	2.71E+01	1.51E+00	3.30E-02	4.36E-02	-6.15E-04	-1.06E+00	3.47E+01	2.96E+02	4.79E+02	1.72E+02	-8.82E+00	1.00E+00	-5.16E-02
1.10E+00	2.78E+01	1.55E+00	3.16E-02	4.27E-02	-5.33E-04	-9.80E-01	3.47E+01	2.96E+02	4.78E+02	1.71E+02	-8.17E+00	1.00E+00	-4.78E-02
1.13E+00	2.86E+01	1.59E+00	3.04E-02	4.09E-02	-4.61E-04	-9.37E-01	3.47E+01	2.96E+02	4.78E+02	1.71E+02	-7.82E+00	1.00E+00	-4.57E-02
1.16E+00	2.93E+01	1.63E+00	2.91E-02	4.07E-02	-4.16E-04	-9.77E-01	3.47E+01	2.96E+02	4.78E+02	1.71E+02	-8.15E+00	1.00E+00	-4.76E-02
1.19E+00	3.01E+01	1.68E+00	2.84E-02	4.02E-02	-3.61E-04	-8.43E-01	3.47E+01	2.96E+02	4.78E+02	1.71E+02	-7.02E+00	1.00E+00	-4.11E-02
1.22E+00	3.09E+01	1.72E+00	2.79E-02	4.03E-02	-3.19E-04	-7.43E-01	3.47E+01	2.96E+02	4.78E+02	1.71E+02	-6.19E+00	1.00E+00	-3.62E-02
1.24E+00	3.15E+01	1.76E+00	2.75E-02	3.97E-02	-2.62E-04	-5.45E-01	3.47E+01	2.96E+02	4.78E+02	1.71E+02	-4.54E+00	1.00E+00	-2.65E-02
1.26E+00	3.20E+01	1.78E+00	2.73E-02	3.88E-02	-2.36E-04	-4.92E-01	3.47E+01	2.96E+02	4.77E+02	1.71E+02	-2.96E+00	9.99E-01	-1.73E-02
1.27E+00	3.22E+01	1.79E+00	2.74E-02	3.88E-02	-2.32E-04	-5.30E-01	3.46E+01	2.96E+02	4.77E+02	1.71E+02	-1.21E+00	9.99E-01	-7.09E-03
1.27E+00	3.23E+01	1.80E+00	2.73E-02	3.88E-02	-2.28E-04	-4.63E-01	3.46E+01	2.96E+02	4.77E+02	1.71E+02	0.00E+00	9.99E-01	0.00E+00

Table 48. 20 Grit Plate, x-y Plane, HWA Data

y (in)	y (mm)	y/δ	$(\rho u)_{rms}$	$(\rho v)_{rms}$	$(\rho u)'(\rho v)'$	θ_{xy}(deg)	P_{t1} (psia)	T_t (K)	Re_x	$(\rho u)_{bar}$ (kg/m^{2}s)	$(\rho v)_{bar}$ (kg/m^{2}s)	$(\rho u)_{bar}/(ru)_e$	$(\rho v)_{bar}/(ru)_e$
2.12E-01	5.38E+00	3.05E-01	1.75E-01	1.32E-01	-7.48E-03	-1.01E-01	3.47E+01	2.96E+02	2.52E+02	9.03E+01	-4.50E-01	5.11E-01	-2.55E-03
2.12E-01	5.38E+00	3.05E-01	1.75E-01	1.32E-01	-7.15E-03	-7.24E-02	3.47E+01	2.96E+02	2.51E+02	8.99E+01	-3.29E-01	5.09E-01	-1.87E-03
2.13E-01	5.41E+00	3.07E-01	1.76E-01	1.31E-01	-7.27E-03	-8.54E-02	3.47E+01	2.96E+02	2.52E+02	9.03E+01	-4.01E-01	5.11E-01	-2.27E-03
2.20E-01	5.59E+00	3.17E-01	1.76E-01	1.30E-01	-7.04E-03	-8.32E-02	3.47E+01	2.96E+02	2.55E+02	9.14E+01	-4.24E-01	5.18E-01	-2.40E-03
2.36E-01	5.99E+00	3.39E-01	1.74E-01	1.28E-01	-6.91E-03	-2.11E-01	3.47E+01	2.96E+02	2.60E+02	9.31E+01	-1.09E+00	5.27E-01	-6.17E-03
2.60E-01	6.60E+00	3.74E-01	1.74E-01	1.27E-01	-6.69E-03	-3.74E-01	3.47E+01	2.96E+02	2.68E+02	9.60E+01	-1.97E+00	5.44E-01	-1.12E-02
2.88E-01	7.31E+00	4.14E-01	1.77E-01	1.27E-01	-7.07E-03	-6.63E-01	3.47E+01	2.96E+02	2.79E+02	1.00E+02	-3.61E+00	5.66E-01	-2.04E-02
3.17E-01	8.04E+00	4.55E-01	1.80E-01	1.27E-01	-7.54E-03	-9.04E-01	3.47E+01	2.96E+02	2.90E+02	1.04E+02	-5.08E+00	5.88E-01	-2.88E-02
3.46E-01	8.78E+00	4.97E-01	1.79E-01	1.25E-01	-7.66E-03	-1.12E+00	3.47E+01	2.96E+02	2.99E+02	1.07E+02	-6.46E+00	6.07E-01	-3.66E-02
3.75E-01	9.52E+00	5.39E-01	1.79E-01	1.22E-01	-8.20E-03	-1.38E+00	3.47E+01	2.96E+02	3.08E+02	1.10E+02	-8.36E+00	6.25E-01	-4.73E-02
4.04E-01	1.03E+01	5.81E-01	1.78E-01	1.19E-01	-8.43E-03	-1.69E+00	3.47E+01	2.96E+02	3.20E+02	1.14E+02	-1.06E+01	6.48E-01	-6.03E-02
4.34E-01	1.10E+01	6.24E-01	1.81E-01	1.17E-01	-9.01E-03	-2.02E+00	3.47E+01	2.96E+02	3.31E+02	1.19E+02	-1.36E+01	6.72E-01	-7.68E-02
4.64E-01	1.18E+01	6.67E-01	1.81E-01	1.13E-01	-8.66E-03	-2.23E+00	3.47E+01	2.96E+02	3.46E+02	1.24E+02	-1.56E+01	7.01E-01	-8.85E-02
4.94E-01	1.26E+01	7.11E-01	1.82E-01	1.10E-01	-8.46E-03	-2.33E+00	3.47E+01	2.96E+02	3.58E+02	1.28E+02	-1.71E+01	7.26E-01	-9.69E-02
5.25E-01	1.33E+01	7.54E-01	1.79E-01	1.02E-01	-7.74E-03	-2.39E+00	3.46E+01	2.96E+02	3.83E+02	1.37E+02	-1.81E+01	7.76E-01	-1.02E-01
5.55E-01	1.41E+01	7.98E-01	1.75E-01	9.65E-02	-6.94E-03	-2.33E+00	3.46E+01	2.96E+02	4.00E+02	1.43E+02	-1.84E+01	8.11E-01	-1.04E-01
5.85E-01	1.49E+01	8.41E-01	1.71E-01	8.78E-02	-6.08E-03	-2.24E+00	3.46E+01	2.96E+02	4.20E+02	1.50E+02	-1.83E+01	8.51E-01	-1.04E-01
6.15E-01	1.56E+01	8.85E-01	1.60E-01	8.13E-02	-5.20E-03	-2.24E+00	3.46E+01	2.96E+02	4.34E+02	1.56E+02	-1.88E+01	8.81E-01	-1.06E-01
6.46E-01	1.64E+01	9.28E-01	1.50E-01	7.50E-02	-4.51E-03	-2.18E+00	3.46E+01	2.96E+02	4.52E+02	1.62E+02	-1.86E+01	9.17E-01	-1.05E-01
6.76E-01	1.72E+01	9.71E-01	1.33E-01	6.77E-02	-3.59E-03	-2.15E+00	3.46E+01	2.96E+02	4.70E+02	1.68E+02	-1.85E+01	9.54E-01	-1.04E-01
7.06E-01	1.79E+01	1.01E+00	1.20E-01	6.38E-02	-2.94E-03	-1.97E+00	3.46E+01	2.96E+02	4.80E+02	1.72E+02	-1.69E+01	9.72E-01	-9.59E-02
7.36E-01	1.87E+01	1.06E+00	1.05E-01	6.02E-02	-2.31E-03	-1.93E+00	3.46E+01	2.96E+02	4.87E+02	1.75E+02	-1.68E+01	9.88E-01	-9.49E-02
7.66E-01	1.94E+01	1.10E+00	9.24E-02	5.74E-02	-1.87E-03	-1.89E+00	3.46E+01	2.96E+02	4.91E+02	1.76E+02	-1.64E+01	9.96E-01	-9.30E-02
7.96E-01	2.02E+01	1.14E+00	8.43E-02	5.54E-02	-1.60E-03	-1.87E+00	3.46E+01	2.96E+02	4.94E+02	1.77E+02	-1.63E+01	1.00E+00	-9.23E-02
8.26E-01	2.10E+01	1.19E+00	7.20E-02	5.23E-02	-1.25E-03	-1.96E+00	3.46E+01	2.96E+02	4.96E+02	1.78E+02	-1.71E+01	1.01E+00	-9.68E-02
8.56E-01	2.17E+01	1.23E+00	6.38E-02	5.16E-02	-1.17E-03	-2.13E+00	3.46E+01	2.96E+02	4.98E+02	1.78E+02	-1.86E+01	1.01E+00	-1.05E-01
8.86E-01	2.25E+01	1.27E+00	5.17E-02	4.91E-02	-9.62E-04	-2.29E+00	3.46E+01	2.96E+02	4.99E+02	1.79E+02	-1.99E+01	1.01E+00	-1.13E-01
9.16E-01	2.33E+01	1.32E+00	4.75E-02	4.86E-02	-9.60E-04	-2.31E+00	3.46E+01	2.96E+02	5.00E+02	1.79E+02	-2.00E+01	1.01E+00	-1.13E-01
9.46E-01	2.40E+01	1.36E+00	4.21E-02	4.69E-02	-8.40E-04	-2.19E+00	3.46E+01	2.96E+02	4.99E+02	1.79E+02	-1.90E+01	1.01E+00	-1.07E-01
9.75E-01	2.48E+01	1.40E+00	4.00E-02	4.66E-02	-7.98E-04	-2.02E+00	3.46E+01	2.96E+02	4.99E+02	1.79E+02	-1.75E+01	1.01E+00	-9.93E-02
1.01E+00	2.55E+01	1.45E+00	3.83E-02	4.61E-02	-7.47E-04	-1.77E+00	3.46E+01	2.96E+02	4.98E+02	1.78E+02	-1.53E+01	1.01E+00	-8.68E-02
1.04E+00	2.63E+01	1.49E+00	3.66E-02	4.53E-02	-6.83E-04	-1.48E+00	3.46E+01	2.96E+02	4.97E+02	1.78E+02	-1.29E+01	1.01E+00	-7.29E-02
1.07E+00	2.71E+01	1.53E+00	3.54E-02	4.42E-02	-6.29E-04	-1.13E+00	3.46E+01	2.96E+02	4.97E+02	1.78E+02	-9.86E+00	1.01E+00	-5.58E-02
1.10E+00	2.79E+01	1.58E+00	3.46E-02	4.34E-02	-5.46E-04	-7.66E-01	3.46E+01	2.96E+02	4.97E+02	1.78E+02	-6.66E+00	1.01E+00	-3.77E-02
1.13E+00	2.87E+01	1.62E+00	3.40E-02	4.23E-02	-4.66E-04	-4.80E-01	3.46E+01	2.96E+02	4.98E+02	1.78E+02	-4.17E+00	1.01E+00	-2.36E-02
1.16E+00	2.95E+01	1.67E+00	3.36E-02	4.20E-02	-3.69E-04	-3.14E-01	3.46E+01	2.96E+02	4.99E+02	1.79E+02	-2.71E+00	1.01E+00	-1.54E-02
1.19E+00	3.02E+01	1.71E+00	3.32E-02	4.11E-02	-2.58E-04	-3.21E-01	3.46E+01	2.96E+02	4.98E+02	1.78E+02	-2.76E+00	1.01E+00	-1.56E-02
1.22E+00	3.10E+01	1.75E+00	3.30E-02	4.06E-02	-1.74E-04	-2.20E-01	3.46E+01	2.96E+02	4.97E+02	1.78E+02	-1.89E+00	1.01E+00	-1.07E-02
1.25E+00	3.17E+01	1.79E+00	3.28E-02	3.96E-02	-1.29E-04	-1.95E-01	3.46E+01	2.96E+02	4.95E+02	1.77E+02	-1.67E+00	1.00E+00	-9.46E-03
1.26E+00	3.21E+01	1.82E+00	3.28E-02	3.94E-02	-1.15E-04	-7.11E-02	3.46E+01	2.96E+02	4.93E+02	1.77E+02	-2.91E-01	1.00E+00	-1.65E-03
1.27E+00	3.23E+01	1.83E+00	3.25E-02	3.97E-02	-1.10E-04	-2.08E-01	3.46E+01	2.96E+02	4.91E+02	1.76E+02	-2.70E-01	9.95E-01	-1.53E-03
1.27E+00	3.23E+01	1.83E+00	3.29E-02	4.03E-02	-1.24E-04	-2.26E-01	3.46E+01	2.96E+02	4.90E+02	1.76E+02	0.00E+00	9.94E-01	0.00E+00

Table 49. Smooth Plate, x-z Plane, HWA Data

y (in)	y (mm)	y/δ	$(pu)_{rms}$	$(pw)_{rms}$	$(pu)'/(pw)'$	θ_{xz}(deg)	P_{t1} (psia)	T_t (K)	Re_x	$(pu)_{bar}$ (kg/m^{2}s)	$(pw)_{bar}$ (kg/m^{2}s)	$(pu)_{bar}/(ru)_e$	$(pw)_{bar}/(ru)_e$
1.06E-01	2.69E+00	2.17E-01	1.22E-01	9.26E-02	3.74E-03	3.56E+00	3.44E+01	2.95E+02	2.48E+02	8.86E+01	1.55E+01	5.47E-01	9.58E-02
1.06E-01	2.69E+00	2.17E-01	1.21E-01	9.23E-02	3.66E-03	3.57E+00	3.44E+01	2.95E+02	2.48E+02	8.84E+01	1.59E+01	5.46E-01	9.82E-02
1.08E-01	2.73E+00	2.21E-01	1.21E-01	9.15E-02	3.78E-03	3.62E+00	3.44E+01	2.95E+02	2.49E+02	8.90E+01	1.67E+01	5.50E-01	1.03E-01
1.14E-01	2.90E+00	2.34E-01	1.20E-01	9.11E-02	3.75E-03	3.63E+00	3.44E+01	2.95E+02	2.50E+02	8.91E+01	1.74E+01	5.51E-01	1.07E-01
1.28E-01	3.26E+00	2.63E-01	1.20E-01	8.94E-02	3.61E-03	3.48E+00	3.44E+01	2.95E+02	2.55E+02	9.09E+01	1.73E+01	5.62E-01	1.07E-01
1.50E-01	3.80E+00	3.07E-01	1.21E-01	8.58E-02	2.99E-03	3.18E+00	3.44E+01	2.94E+02	2.64E+02	9.43E+01	1.63E+01	5.83E-01	1.01E-01
1.74E-01	4.43E+00	3.58E-01	1.21E-01	8.20E-02	2.34E-03	2.87E+00	3.44E+01	2.94E+02	2.74E+02	9.78E+01	1.52E+01	6.04E-01	9.41E-02
2.01E-01	5.10E+00	4.12E-01	1.25E-01	7.85E-02	1.71E-03	2.57E+00	3.44E+01	2.94E+02	2.85E+02	1.02E+02	1.42E+01	6.28E-01	8.80E-02
2.28E-01	5.79E+00	4.68E-01	1.27E-01	7.58E-02	1.42E-03	2.44E+00	3.44E+01	2.94E+02	2.95E+02	1.05E+02	1.42E+01	6.50E-01	8.79E-02
2.56E-01	6.51E+00	5.26E-01	1.27E-01	7.25E-02	1.22E-03	2.22E+00	3.44E+01	2.94E+02	3.05E+02	1.09E+02	1.37E+01	6.73E-01	8.44E-02
2.85E-01	7.24E+00	5.85E-01	1.25E-01	6.82E-02	9.41E-04	2.06E+00	3.44E+01	2.94E+02	3.19E+02	1.14E+02	1.33E+01	7.03E-01	8.22E-02
3.15E-01	7.99E+00	6.45E-01	1.26E-01	6.46E-02	6.83E-04	1.91E+00	3.44E+01	2.94E+02	3.35E+02	1.20E+02	1.27E+01	7.39E-01	7.84E-02
3.44E-01	8.74E+00	7.06E-01	1.24E-01	6.13E-02	3.15E-04	1.78E+00	3.44E+01	2.94E+02	3.54E+02	1.26E+02	1.22E+01	7.79E-01	7.56E-02
3.74E-01	9.51E+00	7.68E-01	1.17E-01	5.72E-02	-1.68E-04	1.48E+00	3.44E+01	2.94E+02	3.71E+02	1.32E+02	1.03E+01	8.18E-01	6.38E-02
4.05E-01	1.03E+01	8.31E-01	1.09E-01	5.40E-02	-5.06E-04	1.13E+00	3.44E+01	2.94E+02	3.81E+02	1.36E+02	8.18E+00	8.40E-01	5.06E-02
4.36E-01	1.11E+01	8.94E-01	1.01E-01	5.04E-02	-7.25E-04	7.51E-01	3.44E+01	2.94E+02	3.95E+02	1.41E+02	5.52E+00	8.71E-01	3.41E-02
4.67E-01	1.18E+01	9.57E-01	9.20E-02	4.79E-02	-5.61E-04	8.19E-01	3.44E+01	2.94E+02	4.03E+02	1.44E+02	6.19E+00	8.89E-01	3.83E-02
4.98E-01	1.26E+01	1.02E+00	7.73E-02	4.43E-02	-3.67E-04	7.05E-01	3.44E+01	2.94E+02	4.16E+02	1.49E+02	5.40E+00	9.18E-01	3.34E-02
5.29E-01	1.34E+01	1.09E+00	6.73E-02	4.22E-02	-5.88E-05	5.97E-01	3.43E+01	2.94E+02	4.23E+02	1.51E+02	4.59E+00	9.32E-01	2.84E-02
5.60E-01	1.42E+01	1.15E+00	5.60E-02	3.98E-02	2.39E-04	2.75E-01	3.43E+01	2.94E+02	4.31E+02	1.54E+02	2.12E+00	9.50E-01	1.31E-02
5.92E-01	1.50E+01	1.21E+00	5.00E-02	3.84E-02	4.92E-04	4.72E-02	3.43E+01	2.94E+02	4.36E+02	1.56E+02	3.58E-01	9.62E-01	2.21E-03
6.23E-01	1.58E+01	1.28E+00	4.40E-02	3.74E-02	7.45E-04	-6.52E-02	3.43E+01	2.94E+02	4.42E+02	1.58E+02	-5.06E-01	9.74E-01	-3.13E-03
6.54E-01	1.66E+01	1.34E+00	4.34E-02	3.75E-02	8.29E-04	-3.52E-01	3.43E+01	2.94E+02	4.43E+02	1.58E+02	-2.73E+00	9.77E-01	-1.69E-02
6.85E-01	1.74E+01	1.40E+00	4.37E-02	3.80E-02	8.52E-04	-4.10E-01	3.43E+01	2.94E+02	4.44E+02	1.58E+02	-3.18E+00	9.78E-01	-1.97E-02
7.16E-01	1.82E+01	1.47E+00	4.41E-02	3.86E-02	8.55E-04	-5.50E-01	3.43E+01	2.94E+02	4.44E+02	1.58E+02	-4.26E+00	9.78E-01	-2.63E-02
7.47E-01	1.90E+01	1.53E+00	4.45E-02	3.93E-02	8.88E-04	-4.80E-01	3.43E+01	2.94E+02	4.44E+02	1.58E+02	-3.71E+00	9.79E-01	-2.29E-02
7.78E-01	1.98E+01	1.60E+00	4.41E-02	3.99E-02	9.06E-04	-5.86E-01	3.43E+01	2.94E+02	4.44E+02	1.58E+02	-4.52E+00	9.78E-01	-2.79E-02
8.09E-01	2.05E+01	1.66E+00	4.37E-02	4.01E-02	9.14E-04	-5.78E-01	3.43E+01	2.94E+02	4.43E+02	1.58E+02	-4.45E+00	9.77E-01	-2.75E-02
8.40E-01	2.13E+01	1.72E+00	4.30E-02	3.98E-02	8.61E-04	-6.12E-01	3.43E+01	2.93E+02	4.43E+02	1.58E+02	-4.70E+00	9.76E-01	-2.91E-02
8.71E-01	2.21E+01	1.79E+00	4.25E-02	3.94E-02	8.23E-04	-5.89E-01	3.43E+01	2.93E+02	4.42E+02	1.58E+02	-4.53E+00	9.74E-01	-2.80E-02
9.02E-01	2.29E+01	1.85E+00	4.20E-02	3.89E-02	7.94E-04	-5.36E-01	3.43E+01	2.93E+02	4.41E+02	1.57E+02	-4.13E+00	9.73E-01	-2.55E-02
9.33E-01	2.37E+01	1.91E+00	4.15E-02	3.84E-02	7.84E-04	-4.40E-01	3.43E+01	2.93E+02	4.41E+02	1.57E+02	-3.40E+00	9.72E-01	-2.10E-02
9.63E-01	2.45E+01	1.98E+00	4.18E-02	3.81E-02	8.03E-04	-3.28E-01	3.43E+01	2.93E+02	4.41E+02	1.57E+02	-2.54E+00	9.73E-01	-1.57E-02
9.94E-01	2.53E+01	2.04E+00	4.21E-02	3.80E-02	8.27E-04	-2.99E-01	3.43E+01	2.93E+02	4.42E+02	1.58E+02	-2.33E+00	9.74E-01	-1.44E-02
1.02E+00	2.60E+01	2.10E+00	4.32E-02	3.86E-02	8.61E-04	-2.77E-01	3.43E+01	2.93E+02	4.43E+02	1.58E+02	-2.17E+00	9.76E-01	-1.34E-02
1.06E+00	2.68E+01	2.17E+00	4.38E-02	3.89E-02	8.91E-04	-2.18E-01	3.43E+01	2.93E+02	4.44E+02	1.58E+02	-1.71E+00	9.78E-01	-1.06E-02
1.09E+00	2.76E+01	2.23E+00	4.46E-02	3.91E-02	9.32E-04	-2.90E-02	3.43E+01	2.93E+02	4.46E+02	1.59E+02	-2.22E-01	9.82E-01	-1.37E-03
1.12E+00	2.84E+01	2.30E+00	4.49E-02	3.87E-02	9.56E-04	-4.52E-02	3.43E+01	2.93E+02	4.47E+02	1.60E+02	-3.65E-01	9.86E-01	-2.26E-03
1.15E+00	2.92E+01	2.36E+00	4.50E-02	3.80E-02	9.88E-04	4.70E-03	3.43E+01	2.93E+02	4.51E+02	1.61E+02	3.37E-02	9.93E-01	2.08E-04
1.18E+00	3.00E+01	2.42E+00	4.46E-02	3.71E-02	9.86E-04	-4.34E-02	3.43E+01	2.93E+02	4.54E+02	1.62E+02	-4.56E-01	1.00E+00	-2.82E-03
1.21E+00	3.08E+01	2.49E+00	4.38E-02	3.67E-02	9.84E-04	-1.20E-03	3.43E+01	2.93E+02	4.57E+02	1.63E+02	2.59E-01	1.01E+00	1.60E-03
1.24E+00	0.00E+00	2.54E+00	4.31E-02	3.63E-02	9.45E-04	-1.26E-01	3.43E+01	2.93E+02	4.59E+02	1.64E+02	0.00E+00	1.01E+00	0.00E+00

Table 50. 2D Plate, x-z Plane, HWA Data

y (in)	y (mm)	y/δ	$(pu)_{rms}$	$(\rho w)_{rms}$	$(pu)'/(pw)'$	θ_{xz} (deg)	P_{t1} (psia)	T_{t1} (K)	Re_x	$(\rho u)_{bar}$ (kg/m^{2}s)	$(\rho w)_{bar}$ (kg/m^{2}s)	$(pu)_{bar}/(ru)_e$	$(pw)_{bar}/(ru)_e$
1.96E-01	4.98E+00	2.97E-01	2.08E-01	1.54E-01	1.81E-02	4.62E+00	3.50E+01	2.95E+02	2.54E+02	9.06E+01	2.06E+01	5.24E-01	1.19E-01
1.96E-01	4.98E+00	2.97E-01	2.08E-01	1.55E-01	1.87E-02	4.70E+00	3.50E+01	2.95E+02	2.52E+02	9.00E+01	2.13E+01	5.21E-01	1.23E-01
1.98E-01	5.02E+00	3.00E-01	2.07E-01	1.55E-01	1.82E-02	4.64E+00	3.50E+01	2.95E+02	2.54E+02	9.06E+01	2.17E+01	5.24E-01	1.26E-01
2.06E-01	5.22E+00	3.11E-01	2.05E-01	1.54E-01	1.75E-02	4.49E+00	3.50E+01	2.94E+02	2.56E+02	9.15E+01	2.16E+01	5.30E-01	1.25E-01
2.22E-01	5.63E+00	3.36E-01	2.01E-01	1.50E-01	1.62E-02	4.35E+00	3.50E+01	2.94E+02	2.60E+02	9.28E+01	2.14E+01	5.37E-01	1.24E-01
2.45E-01	6.23E+00	3.72E-01	1.97E-01	1.44E-01	1.41E-02	4.06E+00	3.50E+01	2.94E+02	2.68E+02	9.58E+01	2.06E+01	5.55E-01	1.19E-01
2.73E-01	6.92E+00	4.13E-01	1.91E-01	1.38E-01	1.24E-02	3.87E+00	3.50E+01	2.94E+02	2.76E+02	9.85E+01	2.05E+01	5.70E-01	1.19E-01
3.01E-01	7.64E+00	4.56E-01	1.87E-01	1.33E-01	1.07E-02	3.61E+00	3.50E+01	2.94E+02	2.82E+02	1.01E+02	2.00E+01	5.84E-01	1.16E-01
3.30E-01	8.37E+00	4.99E-01	1.84E-01	1.26E-01	9.15E-03	3.43E+00	3.50E+01	2.94E+02	2.92E+02	1.04E+02	2.00E+01	6.03E-01	1.16E-01
3.59E-01	9.11E+00	5.43E-01	1.82E-01	1.18E-01	7.22E-03	3.18E+00	3.50E+01	2.94E+02	3.05E+02	1.09E+02	1.91E+01	6.31E-01	1.10E-01
3.88E-01	9.86E+00	5.88E-01	1.79E-01	1.11E-01	5.70E-03	2.90E+00	3.50E+01	2.94E+02	3.18E+02	1.14E+02	1.82E+01	6.57E-01	1.05E-01
4.18E-01	1.06E+01	6.33E-01	1.77E-01	1.04E-01	4.15E-03	2.61E+00	3.50E+01	2.94E+02	3.36E+02	1.20E+02	1.67E+01	6.94E-01	9.65E-02
4.48E-01	1.14E+01	6.79E-01	1.76E-01	9.94E-02	3.40E-03	2.47E+00	3.50E+01	2.94E+02	3.45E+02	1.23E+02	1.67E+01	7.14E-01	9.64E-02
4.78E-01	1.21E+01	7.25E-01	1.75E-01	9.25E-02	2.25E-03	2.29E+00	3.50E+01	2.94E+02	3.58E+02	1.28E+02	1.64E+01	7.40E-01	9.49E-02
5.09E-01	1.29E+01	7.71E-01	1.74E-01	8.94E-02	1.88E-03	2.19E+00	3.49E+01	2.94E+02	3.66E+02	1.31E+02	1.63E+01	7.58E-01	9.44E-02
5.40E-01	1.37E+01	8.18E-01	1.67E-01	8.25E-02	9.83E-04	1.95E+00	3.49E+01	2.94E+02	3.86E+02	1.38E+02	1.52E+01	7.99E-01	8.77E-02
5.71E-01	1.45E+01	8.64E-01	1.57E-01	7.51E-02	-1.96E-04	1.64E+00	3.49E+01	2.94E+02	4.11E+02	1.47E+02	1.31E+01	8.49E-01	7.56E-02
6.01E-01	1.53E+01	9.11E-01	1.45E-01	6.92E-02	-7.60E-04	1.48E+00	3.49E+01	2.94E+02	4.29E+02	1.53E+02	1.20E+01	8.86E-01	6.97E-02
6.32E-01	1.61E+01	9.58E-01	1.27E-01	6.32E-02	-9.26E-04	1.05E+00	3.49E+01	2.94E+02	4.46E+02	1.59E+02	8.64E+00	9.23E-01	5.00E-02
6.63E-01	1.68E+01	1.00E+00	1.15E-01	5.91E-02	-7.56E-04	7.77E-01	3.49E+01	2.94E+02	4.57E+02	1.63E+02	6.43E+00	9.46E-01	3.72E-02
6.93E-01	1.76E+01	1.05E+00	1.02E-01	5.57E-02	-6.11E-04	5.14E-01	3.49E+01	2.94E+02	4.68E+02	1.67E+02	4.35E+00	9.67E-01	2.52E-02
7.24E-01	1.84E+01	1.10E+00	9.21E-02	5.36E-02	-2.76E-04	4.83E-01	3.49E+01	2.94E+02	4.73E+02	1.69E+02	4.10E+00	9.79E-01	2.37E-02
7.54E-01	1.92E+01	1.14E+00	8.10E-02	5.15E-02	1.30E-05	4.02E-01	3.49E+01	2.94E+02	4.79E+02	1.71E+02	3.42E+00	9.91E-01	1.98E-02
7.85E-01	1.99E+01	1.19E+00	7.08E-02	4.96E-02	2.04E-04	1.25E-01	3.49E+01	2.94E+02	4.84E+02	1.73E+02	1.06E+00	1.00E+00	6.17E-03
8.15E-01	2.07E+01	1.24E+00	6.55E-02	4.79E-02	3.56E-04	-8.85E-02	3.49E+01	2.94E+02	4.87E+02	1.74E+02	-7.55E-01	1.01E+00	-4.37E-03
8.46E-01	2.15E+01	1.28E+00	5.62E-02	4.56E-02	5.81E-04	-3.05E-01	3.49E+01	2.94E+02	4.90E+02	1.75E+02	-2.60E+00	1.01E+00	-1.50E-02
8.76E-01	2.23E+01	1.33E+00	4.87E-02	4.30E-02	7.47E-04	-3.96E-01	3.49E+01	2.94E+02	4.91E+02	1.75E+02	-3.37E+00	1.02E+00	-1.95E-02
9.07E-01	2.30E+01	1.37E+00	4.52E-02	4.13E-02	7.49E-04	-4.84E-01	3.49E+01	2.94E+02	4.91E+02	1.75E+02	-4.11E+00	1.01E+00	-2.38E-02
9.37E-01	2.38E+01	1.42E+00	4.43E-02	4.06E-02	7.44E-04	-5.07E-01	3.49E+01	2.94E+02	4.89E+02	1.75E+02	-4.29E+00	1.01E+00	-2.48E-02
9.67E-01	2.46E+01	1.47E+00	4.28E-02	4.01E-02	7.96E-04	-5.63E-01	3.49E+01	2.94E+02	4.87E+02	1.74E+02	-4.75E+00	1.01E+00	-2.75E-02
9.96E-01	2.53E+01	1.51E+00	4.30E-02	4.04E-02	8.46E-04	-5.76E-01	3.49E+01	2.94E+02	4.86E+02	1.74E+02	-4.85E+00	1.00E+00	-2.81E-02
1.03E+00	2.60E+01	1.55E+00	4.36E-02	4.06E-02	9.06E-04	-6.14E-01	3.49E+01	2.94E+02	4.85E+02	1.73E+02	-5.17E+00	1.00E+00	-2.99E-02
1.06E+00	2.68E+01	1.60E+00	4.43E-02	4.07E-02	9.55E-04	-6.17E-01	3.49E+01	2.94E+02	4.84E+02	1.73E+02	-5.19E+00	1.00E+00	-3.01E-02
1.09E+00	2.77E+01	1.65E+00	4.46E-02	4.07E-02	9.85E-04	-5.97E-01	3.49E+01	2.94E+02	4.83E+02	1.73E+02	-5.03E+00	1.00E+00	-2.91E-02
1.12E+00	2.85E+01	1.70E+00	4.54E-02	4.07E-02	1.04E-03	-4.72E-01	3.49E+01	2.94E+02	4.83E+02	1.73E+02	-3.98E+00	9.99E-01	-2.30E-02
1.16E+00	2.93E+01	1.75E+00	4.56E-02	4.05E-02	1.08E-03	-3.94E-01	3.49E+01	2.94E+02	4.83E+02	1.72E+02	-3.32E+00	9.98E-01	-1.92E-02
1.19E+00	3.01E+01	1.80E+00	4.62E-02	4.05E-02	1.12E-03	-4.05E-01	3.49E+01	2.94E+02	4.83E+02	1.72E+02	-3.42E+00	9.98E-01	-1.98E-02
1.22E+00	3.09E+01	1.84E+00	4.63E-02	4.02E-02	1.14E-03	-4.23E-01	3.49E+01	2.94E+02	4.83E+02	1.73E+02	-3.57E+00	9.99E-01	-2.07E-02
1.24E+00	3.15E+01	1.88E+00	4.67E-02	4.05E-02	1.17E-03	-4.44E-01	3.48E+01	2.94E+02	4.83E+02	1.73E+02	-3.75E+00	9.99E-01	-2.17E-02
1.26E+00	3.19E+01	1.90E+00	4.72E-02	4.13E-02	1.22E-03	-4.82E-01	3.48E+01	2.93E+02	4.84E+02	1.73E+02	-2.22E+00	1.00E+00	-1.29E-02
1.26E+00	3.20E+01	1.91E+00	4.73E-02	4.17E-02	1.22E-03	-5.69E-01	3.48E+01	2.93E+02	4.84E+02	1.73E+02	-1.17E+00	1.00E+00	-6.79E-03
1.26E+00	0.00E+00	1.91E+00	4.73E-02	4.21E-02	1.23E-03	-5.42E-01	3.48E+01	2.93E+02	4.84E+02	1.73E+02	0.00E+00	1.00E+00	0.00E+00

Table 51. 3D Plate, x-z Plane, HWA Data

y (in)	y (mm)	y/δ	$(\rho u)_{rms}$	$(\rho w)_{rms}$	$(\rho u)'(\rho w)'$	θ_{xz} (deg)	P_{t1} (psia)	T_t (K)	Re_x	$(\rho u)_{bar}$ (kg/m^{2}s)	$(\rho w)_{bar}$ (kg/m^{2}s)	$(\rho u)_{bar}/(ru)_e$	$(\rho w)_{bar}/(ru)_e$
1.66E-01	4.22E+00	2.67E-01	1.87E-01	1.42E-01	1.41E-02	4.36E+00	3.49E+01	2.95E+02	2.49E+02	8.87E+01	1.92E+01	5.21E-01	1.13E-01
1.66E-01	4.22E+00	2.67E-01	1.89E-01	1.44E-01	1.51E-02	4.50E+00	3.49E+01	2.95E+02	2.48E+02	8.85E+01	2.03E+01	5.20E-01	1.19E-01
1.67E-01	4.25E+00	2.69E-01	1.89E-01	1.44E-01	1.50E-02	4.46E+00	3.49E+01	2.95E+02	2.49E+02	8.87E+01	2.08E+01	5.21E-01	1.22E-01
1.74E-01	4.41E+00	2.80E-01	1.87E-01	1.42E-01	1.45E-02	4.35E+00	3.49E+01	2.95E+02	2.52E+02	9.00E+01	2.10E+01	5.29E-01	1.24E-01
1.88E-01	4.78E+00	3.03E-01	1.80E-01	1.35E-01	1.23E-02	4.11E+00	3.49E+01	2.95E+02	2.59E+02	9.24E+01	2.06E+01	5.42E-01	1.21E-01
2.10E-01	5.34E+00	3.39E-01	1.75E-01	1.27E-01	1.00E-02	3.82E+00	3.49E+01	2.95E+02	2.68E+02	9.55E+01	2.00E+01	5.61E-01	1.17E-01
2.37E-01	6.02E+00	3.82E-01	1.71E-01	1.19E-01	7.88E-03	3.48E+00	3.48E+01	2.95E+02	2.77E+02	9.90E+01	1.86E+01	5.81E-01	1.09E-01
2.65E-01	6.72E+00	4.26E-01	1.71E-01	1.13E-01	6.36E-03	3.20E+00	3.48E+01	2.95E+02	2.88E+02	1.03E+02	1.75E+01	6.03E-01	1.03E-01
2.93E-01	7.45E+00	4.72E-01	1.69E-01	1.08E-01	5.07E-03	3.01E+00	3.48E+01	2.95E+02	3.00E+02	1.07E+02	1.72E+01	6.29E-01	1.01E-01
3.22E-01	8.18E+00	5.19E-01	1.67E-01	1.05E-01	4.53E-03	2.89E+00	3.48E+01	2.95E+02	3.07E+02	1.10E+02	1.74E+01	6.43E-01	1.02E-01
3.52E-01	8.93E+00	5.66E-01	1.63E-01	1.00E-01	3.95E-03	2.68E+00	3.48E+01	2.95E+02	3.14E+02	1.12E+02	1.72E+01	6.58E-01	1.01E-01
3.81E-01	9.68E+00	6.14E-01	1.63E-01	9.52E-02	3.20E-03	2.49E+00	3.48E+01	2.95E+02	3.27E+02	1.17E+02	1.66E+01	6.86E-01	9.74E-02
4.11E-01	1.04E+01	6.62E-01	1.63E-01	8.81E-02	2.23E-03	2.34E+00	3.48E+01	2.95E+02	3.47E+02	1.24E+02	1.63E+01	7.27E-01	9.58E-02
4.41E-01	1.12E+01	7.11E-01	1.63E-01	8.12E-02	1.32E-03	2.15E+00	3.48E+01	2.95E+02	3.69E+02	1.32E+02	1.55E+01	7.73E-01	9.09E-02
4.72E-01	1.20E+01	7.61E-01	1.59E-01	7.65E-02	8.67E-04	2.09E+00	3.48E+01	2.95E+02	3.82E+02	1.36E+02	1.58E+01	8.00E-01	9.30E-02
5.03E-01	1.28E+01	8.10E-01	1.52E-01	7.04E-02	5.35E-05	1.71E+00	3.48E+01	2.95E+02	4.01E+02	1.43E+02	1.32E+01	8.40E-01	7.76E-02
5.34E-01	1.36E+01	8.60E-01	1.44E-01	6.64E-02	-5.17E-04	1.35E+00	3.48E+01	2.95E+02	4.14E+02	1.48E+02	1.07E+01	8.68E-01	6.28E-02
5.64E-01	1.43E+01	9.09E-01	1.24E-01	6.01E-02	-9.51E-04	7.02E-01	3.48E+01	2.95E+02	4.34E+02	1.55E+02	5.59E+00	9.10E-01	3.28E-02
5.95E-01	1.51E+01	9.59E-01	1.08E-01	5.66E-02	-7.43E-04	3.68E-01	3.48E+01	2.95E+02	4.45E+02	1.59E+02	2.93E+00	9.33E-01	1.72E-02
6.26E-01	1.59E+01	1.01E+00	9.49E-02	5.44E-02	-3.77E-04	2.62E-01	3.48E+01	2.95E+02	4.55E+02	1.62E+02	2.16E+00	9.53E-01	1.27E-02
6.57E-01	1.67E+01	1.06E+00	8.57E-02	5.28E-02	-9.28E-05	2.75E-01	3.48E+01	2.95E+02	4.59E+02	1.64E+02	2.27E+00	9.62E-01	1.33E-02
6.87E-01	1.75E+01	1.11E+00	7.56E-02	5.08E-02	2.48E-04	2.23E-01	3.48E+01	2.95E+02	4.64E+02	1.65E+02	1.84E+00	9.72E-01	1.08E-02
7.18E-01	1.82E+01	1.16E+00	5.84E-02	4.61E-02	6.08E-04	-6.27E-02	3.48E+01	2.95E+02	4.71E+02	1.68E+02	-5.30E-01	9.87E-01	-3.11E-03
7.48E-01	1.90E+01	1.21E+00	5.37E-02	4.50E-02	7.83E-04	-2.19E-01	3.48E+01	2.95E+02	4.73E+02	1.69E+02	-1.83E+00	9.92E-01	-1.07E-02
7.79E-01	1.98E+01	1.25E+00	5.03E-02	4.38E-02	9.72E-04	-1.79E-01	3.48E+01	2.95E+02	4.75E+02	1.70E+02	-1.49E+00	9.96E-01	-8.75E-03
8.09E-01	2.06E+01	1.30E+00	4.99E-02	4.39E-02	9.90E-04	-1.23E-02	3.48E+01	2.95E+02	4.76E+02	1.70E+02	-9.76E-02	9.98E-01	-5.73E-04
8.40E-01	2.13E+01	1.35E+00	4.73E-02	4.35E-02	1.05E-03	6.86E-02	3.48E+01	2.95E+02	4.79E+02	1.71E+02	5.79E-01	1.00E+00	3.40E-03
8.70E-01	2.21E+01	1.40E+00	4.59E-02	4.30E-02	9.91E-04	3.04E-02	3.47E+01	2.95E+02	4.80E+02	1.71E+02	2.57E-01	1.01E+00	1.51E-03
9.01E-01	2.29E+01	1.45E+00	4.48E-02	4.25E-02	9.79E-04	3.83E-03	3.47E+01	2.94E+02	4.82E+02	1.72E+02	3.25E-02	1.01E+00	1.91E-04
9.31E-01	2.37E+01	1.50E+00	4.34E-02	4.11E-02	9.07E-04	-4.44E-02	3.47E+01	2.94E+02	4.83E+02	1.72E+02	-3.73E-01	1.01E+00	-2.19E-03
9.62E-01	2.44E+01	1.55E+00	4.37E-02	4.05E-02	9.01E-04	-1.14E-01	3.47E+01	2.94E+02	4.83E+02	1.72E+02	-9.54E-01	1.01E+00	-5.60E-03
9.93E-01	2.52E+01	1.60E+00	4.36E-02	3.99E-02	8.91E-04	-2.55E-01	3.47E+01	2.94E+02	4.83E+02	1.72E+02	-2.13E+00	1.01E+00	-1.25E-02
1.02E+00	2.60E+01	1.65E+00	4.40E-02	3.96E-02	9.30E-04	-2.96E-01	3.47E+01	2.94E+02	4.83E+02	1.72E+02	-2.47E+00	1.01E+00	-1.45E-02
1.06E+00	2.68E+01	1.70E+00	4.46E-02	3.92E-02	9.61E-04	-3.31E-01	3.47E+01	2.94E+02	4.81E+02	1.72E+02	-2.76E+00	1.01E+00	-1.62E-02
1.09E+00	2.76E+01	1.75E+00	4.52E-02	3.95E-02	1.02E-03	-2.21E-01	3.47E+01	2.94E+02	4.80E+02	1.71E+02	-1.84E+00	1.00E+00	-1.08E-02
1.12E+00	2.83E+01	1.80E+00	4.63E-02	4.01E-02	1.08E-03	-2.30E-01	3.47E+01	2.94E+02	4.79E+02	1.71E+02	-1.91E+00	1.00E+00	-1.12E-02
1.15E+00	2.91E+01	1.84E+00	4.66E-02	4.04E-02	1.12E-03	-2.12E-01	3.47E+01	2.94E+02	4.78E+02	1.71E+02	-1.77E+00	1.00E+00	-1.04E-02
1.18E+00	2.98E+01	1.89E+00	4.66E-02	4.00E-02	1.11E-03	-3.13E-01	3.47E+01	2.94E+02	4.77E+02	1.70E+02	-2.61E+00	1.00E+00	-1.53E-02
1.21E+00	3.06E+01	1.94E+00	4.60E-02	3.95E-02	1.11E-03	-4.13E-01	3.47E+01	2.94E+02	4.77E+02	1.70E+02	-3.44E+00	1.00E+00	-2.02E-02
1.23E+00	3.13E+01	1.99E+00	4.57E-02	3.95E-02	1.11E-03	-4.25E-01	3.47E+01	2.94E+02	4.77E+02	1.70E+02	-2.62E+00	1.00E+00	-1.54E-02
1.25E+00	3.18E+01	2.02E+00	4.59E-02	3.98E-02	1.14E-03	-4.08E-01	3.47E+01	2.94E+02	4.77E+02	1.70E+02	-1.61E+00	1.00E+00	-9.45E-03
1.26E+00	0.00E+00	2.03E+00	4.57E-02	3.97E-02	1.14E-03	-3.07E-01	3.47E+01	2.94E+02	4.77E+02	1.70E+02	0.00E+00	1.00E+00	0.00E+00

Table 52. 80 Grit Plate, x-z Plane, HWA Data

y (in)	y (mm)	y/δ	$(\rho u)_{rms}$	$(\rho w)_{rms}$	$(\rho u)'(\rho w)'$	θ_{xz} (deg)	P_{t1} (psia)	T_t (K)	Re_x	$(\rho u)_{bar}$ (kg/m^{2}s)	$(\rho w)_{bar}$ (kg/m^{2}s)	$(\rho u)_{bar}/(ru)_e$	$(\rho w)_{bar}/(ru)_e$
1.96E-01	4.98E+00	3.39E-01	1.68E-01	1.25E-01	8.10E-03	3.09E+00	3.48E+01	2.95E+02	2.76E+02	9.86E+01	1.48E+01	5.77E-01	8.65E-02
1.96E-01	4.98E+00	3.39E-01	1.68E-01	1.25E-01	8.44E-03	3.12E+00	3.48E+01	2.94E+02	2.75E+02	9.84E+01	1.52E+01	5.76E-01	8.87E-02
1.98E-01	5.04E+00	3.43E-01	1.70E-01	1.27E-01	9.02E-03	3.19E+00	3.48E+01	2.94E+02	2.72E+02	9.73E+01	1.60E+01	5.70E-01	9.38E-02
2.07E-01	5.25E+00	3.58E-01	1.72E-01	1.25E-01	8.98E-03	3.13E+00	3.48E+01	2.94E+02	2.74E+02	9.80E+01	1.62E+01	5.73E-01	9.50E-02
2.24E-01	5.69E+00	3.87E-01	1.70E-01	1.22E-01	8.29E-03	2.99E+00	3.48E+01	2.94E+02	2.78E+02	9.94E+01	1.60E+01	5.82E-01	9.37E-02
2.48E-01	6.29E+00	4.29E-01	1.69E-01	1.17E-01	6.90E-03	2.76E+00	3.48E+01	2.94E+02	2.87E+02	1.03E+02	1.55E+01	6.01E-01	9.05E-02
2.76E-01	7.00E+00	4.77E-01	1.64E-01	1.11E-01	5.54E-03	2.60E+00	3.48E+01	2.94E+02	2.97E+02	1.06E+02	1.52E+01	6.21E-01	8.91E-02
3.04E-01	7.72E+00	5.26E-01	1.60E-01	1.05E-01	4.19E-03	2.48E+00	3.48E+01	2.94E+02	3.07E+02	1.10E+02	1.53E+01	6.42E-01	8.97E-02
3.33E-01	8.45E+00	5.76E-01	1.58E-01	9.70E-02	3.23E-03	2.33E+00	3.48E+01	2.94E+02	3.21E+02	1.15E+02	1.51E+01	6.71E-01	8.86E-02
3.62E-01	9.19E+00	6.26E-01	1.58E-01	9.00E-02	2.14E-03	2.11E+00	3.48E+01	2.94E+02	3.35E+02	1.20E+02	1.43E+01	7.01E-01	8.40E-02
3.91E-01	9.94E+00	6.77E-01	1.58E-01	8.34E-02	1.31E-03	1.91E+00	3.48E+01	2.94E+02	3.55E+02	1.27E+02	1.34E+01	7.42E-01	7.87E-02
4.21E-01	1.07E+01	7.29E-01	1.56E-01	7.76E-02	2.43E-04	1.63E+00	3.47E+01	2.94E+02	3.74E+02	1.34E+02	1.17E+01	7.82E-01	6.88E-02
4.51E-01	1.15E+01	7.81E-01	1.51E-01	7.25E-02	-3.18E-04	1.42E+00	3.47E+01	2.94E+02	3.92E+02	1.40E+02	1.04E+01	8.21E-01	6.07E-02
4.82E-01	1.22E+01	8.34E-01	1.44E-01	6.77E-02	-7.99E-04	1.19E+00	3.47E+01	2.94E+02	4.06E+02	1.45E+02	8.87E+00	8.49E-01	5.19E-02
5.13E-01	1.30E+01	8.87E-01	1.38E-01	6.51E-02	-8.38E-04	1.05E+00	3.47E+01	2.94E+02	4.15E+02	1.48E+02	8.04E+00	8.67E-01	4.71E-02
5.43E-01	1.38E+01	9.40E-01	1.30E-01	6.25E-02	-9.12E-04	9.14E-01	3.47E+01	2.94E+02	4.21E+02	1.51E+02	7.13E+00	8.81E-01	4.17E-02
5.74E-01	1.46E+01	9.93E-01	1.21E-01	5.99E-02	-9.03E-04	7.41E-01	3.47E+01	2.94E+02	4.29E+02	1.53E+02	5.90E+00	8.96E-01	3.45E-02
6.05E-01	1.54E+01	1.05E+00	1.09E-01	5.72E-02	-6.39E-04	7.20E-01	3.47E+01	2.94E+02	4.37E+02	1.56E+02	5.85E+00	9.13E-01	3.42E-02
6.35E-01	1.61E+01	1.10E+00	9.19E-02	5.33E-02	-2.24E-04	6.04E-01	3.47E+01	2.94E+02	4.47E+02	1.60E+02	4.93E+00	9.36E-01	2.89E-02
6.66E-01	1.69E+01	1.15E+00	7.20E-02	4.84E-02	3.24E-04	3.40E-01	3.47E+01	2.94E+02	4.58E+02	1.64E+02	2.77E+00	9.57E-01	1.62E-02
6.96E-01	1.77E+01	1.21E+00	5.88E-02	4.49E-02	5.96E-04	7.45E-02	3.47E+01	2.94E+02	4.66E+02	1.66E+02	6.08E-01	9.74E-01	3.56E-03
7.27E-01	1.85E+01	1.26E+00	5.15E-02	4.29E-02	7.96E-04	-1.92E-01	3.47E+01	2.94E+02	4.69E+02	1.67E+02	-1.58E+00	9.80E-01	-9.25E-03
7.58E-01	1.92E+01	1.31E+00	4.97E-02	4.27E-02	8.47E-04	-1.88E-01	3.47E+01	2.94E+02	4.69E+02	1.68E+02	-1.55E+00	9.82E-01	-9.08E-03
7.88E-01	2.00E+01	1.36E+00	4.58E-02	4.21E-02	9.01E-04	-2.26E-01	3.47E+01	2.94E+02	4.71E+02	1.68E+02	-1.86E+00	9.84E-01	-1.09E-02
8.19E-01	2.08E+01	1.42E+00	4.49E-02	4.24E-02	9.35E-04	-2.43E-01	3.47E+01	2.94E+02	4.72E+02	1.68E+02	-2.00E+00	9.86E-01	-1.17E-02
8.49E-01	2.16E+01	1.47E+00	4.43E-02	4.25E-02	9.31E-04	-2.88E-01	3.47E+01	2.94E+02	4.72E+02	1.68E+02	-2.36E+00	9.86E-01	-1.38E-02
8.79E-01	2.23E+01	1.52E+00	4.33E-02	4.22E-02	9.56E-04	-3.57E-01	3.47E+01	2.94E+02	4.72E+02	1.69E+02	-2.93E+00	9.87E-01	-1.72E-02
9.10E-01	2.31E+01	1.57E+00	4.27E-02	4.13E-02	9.22E-04	-3.39E-01	3.47E+01	2.94E+02	4.71E+02	1.68E+02	-2.79E+00	9.85E-01	-1.63E-02
9.40E-01	2.39E+01	1.63E+00	4.23E-02	4.07E-02	9.16E-04	-3.83E-01	3.47E+01	2.94E+02	4.71E+02	1.68E+02	-3.16E+00	9.84E-01	-1.85E-02
9.70E-01	2.46E+01	1.68E+00	4.21E-02	4.00E-02	8.90E-04	-3.94E-01	3.47E+01	2.94E+02	4.71E+02	1.68E+02	-3.25E+00	9.84E-01	-1.90E-02
1.00E+00	2.54E+01	1.73E+00	4.23E-02	3.98E-02	9.16E-04	-3.53E-01	3.47E+01	2.94E+02	4.71E+02	1.68E+02	-2.92E+00	9.85E-01	-1.71E-02
1.03E+00	2.62E+01	1.78E+00	4.31E-02	3.99E-02	9.64E-04	-2.04E-01	3.47E+01	2.94E+02	4.72E+02	1.69E+02	-1.69E+00	9.88E-01	-9.89E-03
1.06E+00	2.69E+01	1.83E+00	4.45E-02	4.06E-02	1.07E-03	-8.64E-02	3.47E+01	2.94E+02	4.73E+02	1.69E+02	-7.15E-01	9.90E-01	-4.19E-03
1.09E+00	2.77E+01	1.89E+00	4.55E-02	4.12E-02	1.12E-03	-5.57E-02	3.47E+01	2.94E+02	4.75E+02	1.70E+02	-4.64E-01	9.92E-01	-2.71E-03
1.12E+00	2.84E+01	1.94E+00	4.68E-02	4.18E-02	1.21E-03	-8.18E-02	3.47E+01	2.94E+02	4.76E+02	1.70E+02	-6.81E-01	9.95E-01	-3.99E-03
1.15E+00	2.93E+01	2.00E+00	4.71E-02	4.17E-02	1.23E-03	-1.62E-01	3.47E+01	2.94E+02	4.76E+02	1.70E+02	-1.35E+00	9.96E-01	-7.89E-03
1.19E+00	3.01E+01	2.05E+00	4.73E-02	4.17E-02	1.28E-03	-1.22E-01	3.47E+01	2.94E+02	4.77E+02	1.70E+02	-1.02E+00	9.98E-01	-5.97E-03
1.22E+00	3.09E+01	2.11E+00	4.66E-02	4.09E-02	1.25E-03	-1.51E-01	3.47E+01	2.94E+02	4.77E+02	1.71E+02	-1.26E+00	9.98E-01	-7.40E-03
1.24E+00	3.15E+01	2.15E+00	4.63E-02	4.05E-02	1.24E-03	-2.46E-01	3.47E+01	2.94E+02	4.78E+02	1.71E+02	-2.05E+00	9.99E-01	-1.20E-02
1.25E+00	3.18E+01	2.17E+00	4.65E-02	4.05E-02	1.23E-03	-2.80E-01	3.46E+01	2.94E+02	4.78E+02	1.71E+02	-1.87E+00	1.00E+00	-1.09E-02
1.26E+00	3.20E+01	2.18E+00	4.65E-02	4.08E-02	1.24E-03	-3.71E-01	3.46E+01	2.94E+02	4.79E+02	1.71E+02	-1.20E+00	1.00E+00	-7.03E-03
1.26E+00	0.00E+00	2.18E+00	4.72E-02	4.15E-02	1.27E-03	-4.36E-01	3.46E+01	2.94E+02	4.79E+02	1.71E+02	0.00E+00	1.00E+00	0.00E+00

Table 53. 36 Grit Plate, x-z Plane, HWA Data

y (in)	y (mm)	y/δ	$(\rho u)_{rms}$	$(\rho w)_{rms}$	$(\rho u)'(\rho w)'$	θ_{xz} (deg)	P_{t1} (psia)	$\bar{T}_t$ (K)	Re_x	$(\rho u)_{bar}$ (kg/m^{2}s)	$(\rho w)_{bar}$ (kg/m^{2}s)	$(\rho u)_{bar}/(\rho u)_e$	$(\rho w)_{bar}/(\rho u)_e$
1.96E-01	4.98E+00	2.77E-01	2.11E-01	1.62E-01	1.97E-02	4.03E+00	3.48E+01	2.95E+02	2.70E+02	9.63E+01	1.89E+01	5.58E-01	1.10E-01
1.96E-01	4.98E+00	2.77E-01	2.13E-01	1.62E-01	1.99E-02	3.97E+00	3.48E+01	2.95E+02	2.70E+02	9.63E+01	1.90E+01	5.58E-01	1.10E-01
1.98E-01	5.02E+00	2.80E-01	2.09E-01	1.60E-01	1.89E-02	3.94E+00	3.48E+01	2.95E+02	2.70E+02	9.64E+01	1.92E+01	5.58E-01	1.12E-01
2.06E-01	5.22E+00	2.91E-01	2.06E-01	1.58E-01	1.86E-02	3.97E+00	3.48E+01	2.95E+02	2.70E+02	9.63E+01	2.02E+01	5.58E-01	1.17E-01
2.22E-01	5.65E+00	3.15E-01	2.02E-01	1.55E-01	1.74E-02	3.94E+00	3.48E+01	2.95E+02	2.74E+02	9.77E+01	2.09E+01	5.66E-01	1.21E-01
2.47E-01	6.27E+00	3.49E-01	2.01E-01	1.52E-01	1.63E-02	3.84E+00	3.48E+01	2.95E+02	2.80E+02	1.00E+02	2.12E+01	5.80E-01	1.23E-01
2.75E-01	6.98E+00	3.89E-01	1.97E-01	1.46E-01	1.41E-02	3.52E+00	3.48E+01	2.95E+02	2.91E+02	1.04E+02	2.02E+01	6.02E-01	1.17E-01
3.04E-01	7.71E+00	4.29E-01	1.94E-01	1.37E-01	1.16E-02	3.33E+00	3.48E+01	2.95E+02	3.04E+02	1.09E+02	1.97E+01	6.29E-01	1.14E-01
3.33E-01	8.45E+00	4.71E-01	1.90E-01	1.29E-01	9.47E-03	3.14E+00	3.48E+01	2.95E+02	3.17E+02	1.13E+02	1.94E+01	6.56E-01	1.12E-01
3.62E-01	9.20E+00	5.13E-01	1.87E-01	1.21E-01	7.88E-03	3.05E+00	3.48E+01	2.95E+02	3.30E+02	1.18E+02	1.94E+01	6.83E-01	1.13E-01
3.92E-01	9.96E+00	5.55E-01	1.83E-01	1.15E-01	6.71E-03	2.86E+00	3.48E+01	2.95E+02	3.40E+02	1.21E+02	1.92E+01	7.03E-01	1.11E-01
4.22E-01	1.07E+01	5.97E-01	1.80E-01	1.08E-01	5.23E-03	2.64E+00	3.48E+01	2.95E+02	3.54E+02	1.26E+02	1.84E+01	7.32E-01	1.07E-01
4.53E-01	1.15E+01	6.40E-01	1.80E-01	1.02E-01	4.18E-03	2.51E+00	3.48E+01	2.94E+02	3.66E+02	1.31E+02	1.84E+01	7.57E-01	1.06E-01
4.83E-01	1.23E+01	6.83E-01	1.76E-01	9.31E-02	2.89E-03	2.37E+00	3.48E+01	2.94E+02	3.85E+02	1.38E+02	1.78E+01	7.97E-01	1.03E-01
5.14E-01	1.30E+01	7.27E-01	1.72E-01	8.68E-02	2.18E-03	2.22E+00	3.48E+01	2.94E+02	4.01E+02	1.43E+02	1.71E+01	8.30E-01	9.89E-02
5.44E-01	1.38E+01	7.70E-01	1.64E-01	7.96E-02	1.28E-03	1.96E+00	3.48E+01	2.94E+02	4.19E+02	1.50E+02	1.54E+01	8.67E-01	8.93E-02
5.75E-01	1.46E+01	8.13E-01	1.54E-01	7.56E-02	8.45E-04	1.68E+00	3.48E+01	2.94E+02	4.31E+02	1.54E+02	1.36E+01	8.91E-01	7.87E-02
6.05E-01	1.54E+01	8.56E-01	1.42E-01	7.17E-02	2.05E-04	1.30E+00	3.48E+01	2.94E+02	4.43E+02	1.58E+02	1.07E+01	9.16E-01	6.17E-02
6.35E-01	1.61E+01	8.99E-01	1.29E-01	6.77E-02	-1.01E-04	9.37E-01	3.48E+01	2.94E+02	4.53E+02	1.62E+02	7.79E+00	9.37E-01	4.51E-02
6.66E-01	1.69E+01	9.42E-01	1.12E-01	6.31E-02	-2.27E-04	6.05E-01	3.48E+01	2.94E+02	4.64E+02	1.66E+02	5.05E+00	9.60E-01	2.92E-02
6.96E-01	1.77E+01	9.85E-01	9.69E-02	5.88E-02	5.35E-05	3.43E-01	3.48E+01	2.94E+02	4.71E+02	1.68E+02	2.87E+00	9.75E-01	1.67E-02
7.26E-01	1.84E+01	1.03E+00	8.28E-02	5.57E-02	3.32E-04	9.38E-02	3.48E+01	2.94E+02	4.77E+02	1.70E+02	7.80E-01	9.87E-01	4.52E-03
7.57E-01	1.92E+01	1.07E+00	7.39E-02	5.30E-02	5.11E-04	1.00E-01	3.48E+01	2.94E+02	4.79E+02	1.71E+02	8.51E-01	9.92E-01	4.93E-03
7.87E-01	2.00E+01	1.11E+00	6.42E-02	5.03E-02	6.88E-04	6.08E-02	3.48E+01	2.94E+02	4.83E+02	1.73E+02	5.19E-01	1.00E+00	3.01E-03
8.17E-01	2.07E+01	1.16E+00	5.69E-02	4.80E-02	8.43E-04	5.16E-02	3.48E+01	2.94E+02	4.86E+02	1.74E+02	4.41E-01	1.01E+00	2.56E-03
8.47E-01	2.15E+01	1.20E+00	5.20E-02	4.65E-02	9.44E-04	-1.06E-01	3.48E+01	2.94E+02	4.89E+02	1.75E+02	-9.11E-01	1.01E+00	-5.28E-03
8.77E-01	2.23E+01	1.24E+00	4.88E-02	4.56E-02	1.00E-03	-2.13E-01	3.48E+01	2.94E+02	4.90E+02	1.75E+02	-1.82E+00	1.02E+00	-1.05E-02
9.08E-01	2.31E+01	1.28E+00	4.68E-02	4.45E-02	1.01E-03	-3.34E-01	3.48E+01	2.94E+02	4.91E+02	1.75E+02	-2.84E+00	1.02E+00	-1.64E-02
9.38E-01	2.38E+01	1.33E+00	4.58E-02	4.37E-02	1.01E-03	-4.63E-01	3.48E+01	2.94E+02	4.91E+02	1.75E+02	-3.92E+00	1.02E+00	-2.27E-02
9.68E-01	2.46E+01	1.37E+00	4.59E-02	4.38E-02	1.02E-03	-6.11E-01	3.48E+01	2.94E+02	4.89E+02	1.75E+02	-5.16E+00	1.01E+00	-2.99E-02
9.97E-01	2.53E+01	1.41E+00	4.67E-02	4.42E-02	1.09E-03	-6.26E-01	3.48E+01	2.94E+02	4.88E+02	1.74E+02	-5.28E+00	1.01E+00	-3.06E-02
1.03E+00	2.61E+01	1.45E+00	4.78E-02	4.43E-02	1.18E-03	-6.11E-01	3.48E+01	2.94E+02	4.86E+02	1.74E+02	-5.15E+00	1.01E+00	-2.98E-02
1.06E+00	2.69E+01	1.50E+00	4.93E-02	4.47E-02	1.30E-03	-4.29E-01	3.47E+01	2.94E+02	4.84E+02	1.73E+02	-3.61E+00	1.00E+00	-2.09E-02
1.09E+00	2.77E+01	1.54E+00	5.03E-02	4.47E-02	1.38E-03	-3.63E-01	3.47E+01	2.94E+02	4.83E+02	1.73E+02	-3.05E+00	1.00E+00	-1.77E-02
1.12E+00	2.85E+01	1.59E+00	5.07E-02	4.49E-02	1.44E-03	-3.09E-01	3.47E+01	2.94E+02	4.82E+02	1.72E+02	-2.60E+00	9.99E-01	-1.51E-02
1.16E+00	2.93E+01	1.63E+00	5.06E-02	4.48E-02	1.45E-03	-3.74E-01	3.47E+01	2.94E+02	4.82E+02	1.72E+02	-3.15E+00	9.98E-01	-1.83E-02
1.19E+00	3.01E+01	1.68E+00	5.11E-02	4.50E-02	1.49E-03	-3.40E-01	3.47E+01	2.94E+02	4.82E+02	1.72E+02	-2.87E+00	9.98E-01	-1.66E-02
1.21E+00	3.08E+01	1.72E+00	5.07E-02	4.45E-02	1.46E-03	-4.33E-01	3.47E+01	2.94E+02	4.82E+02	1.72E+02	-3.65E+00	9.98E-01	-2.12E-02
1.24E+00	3.15E+01	1.75E+00	5.01E-02	4.44E-02	1.44E-03	-3.63E-01	3.47E+01	2.94E+02	4.83E+02	1.72E+02	-3.07E+00	9.99E-01	-1.78E-02
1.25E+00	3.18E+01	1.77E+00	4.92E-02	4.40E-02	1.39E-03	-3.95E-01	3.47E+01	2.94E+02	4.84E+02	1.73E+02	-2.29E+00	1.00E+00	-1.33E-02
1.26E+00	3.20E+01	1.78E+00	4.96E-02	4.45E-02	1.44E-03	-3.80E-01	3.47E+01	2.94E+02	4.84E+02	1.73E+02	-7.24E-01	1.00E+00	-4.19E-03
0.00E+00	0.00E+00	0.00E+00	0.00E+00	0.00E+00	0.00E+00	0.00E+00	0.00E+00	0.00E+00	0.00E+00	0.00E+00	0.00E+00	0.00E+00	0.00E+00

Table 54. 20 Grit Plate, x-z Plane, HWA Data

y (in)	y (mm)	y/δ	$(pu)_{rms}$	$(\rho w)_{rms}$	(pu)'(pw)'	θ_{xz} (deg)	P_{t1} (psia)	T_t (K)	Re_x	$(pu)_{bar}$ (kg/m^{2}s)	$(\rho w)_{bar}$ (kg/m^{2}s)	$(pu)_{bar}/(ru)_e$	$(\rho w)_{bar}/(ru)_e$
1.96E-01	4.98E+00	2.82E-01	2.41E-01	1.80E-01	2.74E-02	4.62E+00	3.48E+01	2.95E+02	2.58E+02	9.22E+01	2.11E+01	5.16E-01	1.18E-01
1.96E-01	4.98E+00	2.82E-01	2.40E-01	1.82E-01	2.73E-02	4.61E+00	3.48E+01	2.95E+02	2.59E+02	9.25E+01	2.14E+01	5.17E-01	1.19E-01
1.98E-01	5.02E+00	2.84E-01	2.41E-01	1.83E-01	2.71E-02	4.55E+00	3.48E+01	2.95E+02	2.59E+02	9.27E+01	2.16E+01	5.18E-01	1.21E-01
2.06E-01	5.22E+00	2.96E-01	2.42E-01	1.84E-01	2.74E-02	4.59E+00	3.48E+01	2.95E+02	2.61E+02	9.34E+01	2.25E+01	5.22E-01	1.26E-01
2.23E-01	5.65E+00	3.20E-01	2.38E-01	1.81E-01	2.62E-02	4.44E+00	3.48E+01	2.95E+02	2.66E+02	9.49E+01	2.24E+01	5.31E-01	1.25E-01
2.47E-01	6.27E+00	3.55E-01	2.32E-01	1.78E-01	2.46E-02	4.30E+00	3.48E+01	2.95E+02	2.72E+02	9.73E+01	2.26E+01	5.44E-01	1.26E-01
2.75E-01	6.97E+00	3.95E-01	2.22E-01	1.71E-01	2.08E-02	3.95E+00	3.48E+01	2.94E+02	2.81E+02	1.00E+02	2.14E+01	5.61E-01	1.20E-01
3.03E-01	7.69E+00	4.35E-01	2.14E-01	1.63E-01	1.75E-02	3.69E+00	3.48E+01	2.94E+02	2.89E+02	1.03E+02	2.07E+01	5.77E-01	1.16E-01
3.32E-01	8.42E+00	4.77E-01	2.08E-01	1.53E-01	1.41E-02	3.43E+00	3.48E+01	2.94E+02	3.01E+02	1.08E+02	1.98E+01	6.02E-01	1.11E-01
3.61E-01	9.17E+00	5.19E-01	2.03E-01	1.44E-01	1.18E-02	3.27E+00	3.48E+01	2.94E+02	3.12E+02	1.11E+02	1.96E+01	6.23E-01	1.10E-01
3.91E-01	9.93E+00	5.62E-01	2.02E-01	1.38E-01	1.04E-02	3.21E+00	3.48E+01	2.94E+02	3.23E+02	1.15E+02	2.05E+01	6.45E-01	1.15E-01
4.21E-01	1.07E+01	6.05E-01	2.01E-01	1.32E-01	9.16E-03	3.19E+00	3.48E+01	2.94E+02	3.32E+02	1.19E+02	2.16E+01	6.63E-01	1.21E-01
4.51E-01	1.15E+01	6.49E-01	2.00E-01	1.27E-01	8.31E-03	3.14E+00	3.48E+01	2.94E+02	3.45E+02	1.23E+02	2.23E+01	6.89E-01	1.25E-01
4.82E-01	1.22E+01	6.92E-01	1.96E-01	1.15E-01	6.21E-03	3.01E+00	3.48E+01	2.94E+02	3.66E+02	1.31E+02	2.24E+01	7.31E-01	1.25E-01
5.12E-01	1.30E+01	7.37E-01	1.92E-01	1.06E-01	4.65E-03	2.84E+00	3.48E+01	2.94E+02	3.88E+02	1.39E+02	2.18E+01	7.76E-01	1.22E-01
5.43E-01	1.38E+01	7.81E-01	1.88E-01	9.70E-02	3.55E-03	2.75E+00	3.48E+01	2.94E+02	4.06E+02	1.45E+02	2.17E+01	8.12E-01	1.21E-01
5.74E-01	1.46E+01	8.25E-01	1.79E-01	9.01E-02	2.52E-03	2.50E+00	3.48E+01	2.94E+02	4.26E+02	1.52E+02	2.00E+01	8.52E-01	1.12E-01
6.04E-01	1.53E+01	8.69E-01	1.70E-01	8.45E-02	1.99E-03	2.41E+00	3.48E+01	2.94E+02	4.40E+02	1.57E+02	1.99E+01	8.79E-01	1.12E-01
6.35E-01	1.61E+01	9.12E-01	1.64E-01	8.07E-02	1.29E-03	2.28E+00	3.48E+01	2.94E+02	4.52E+02	1.62E+02	1.95E+01	9.04E-01	1.09E-01
6.65E-01	1.69E+01	9.56E-01	1.56E-01	7.74E-02	1.05E-03	2.08E+00	3.48E+01	2.94E+02	4.61E+02	1.65E+02	1.80E+01	9.21E-01	1.01E-01
6.95E-01	1.77E+01	1.00E+00	1.40E-01	7.22E-02	4.70E-04	1.68E+00	3.48E+01	2.94E+02	4.74E+02	1.69E+02	1.46E+01	9.48E-01	8.19E-02
7.26E-01	1.84E+01	1.04E+00	1.22E-01	6.70E-02	-3.48E-05	1.22E+00	3.48E+01	2.94E+02	4.90E+02	1.75E+02	1.07E+01	9.79E-01	6.00E-02
7.56E-01	1.92E+01	1.09E+00	1.08E-01	6.37E-02	-2.55E-05	9.23E-01	3.48E+01	2.94E+02	4.97E+02	1.77E+02	8.17E+00	9.93E-01	4.57E-02
7.86E-01	2.00E+01	1.13E+00	9.84E-02	6.20E-02	1.41E-04	7.81E-01	3.47E+01	2.94E+02	5.01E+02	1.79E+02	6.93E+00	1.00E+00	3.88E-02
8.17E-01	2.07E+01	1.17E+00	8.49E-02	5.85E-02	4.44E-04	6.00E-01	3.47E+01	2.94E+02	5.05E+02	1.80E+02	5.31E+00	1.01E+00	2.97E-02
8.47E-01	2.15E+01	1.22E+00	7.27E-02	5.59E-02	7.49E-04	4.85E-01	3.47E+01	2.94E+02	5.08E+02	1.81E+02	4.28E+00	1.01E+00	2.39E-02
8.77E-01	2.23E+01	1.26E+00	6.22E-02	5.22E-02	9.37E-04	2.49E-01	3.47E+01	2.94E+02	5.08E+02	1.82E+02	2.20E+00	1.02E+00	1.23E-02
9.08E-01	2.31E+01	1.31E+00	5.74E-02	5.01E-02	1.02E-03	1.71E-01	3.47E+01	2.94E+02	5.07E+02	1.81E+02	1.51E+00	1.01E+00	8.42E-03
9.38E-01	2.38E+01	1.35E+00	5.43E-02	4.82E-02	1.05E-03	9.23E-02	3.47E+01	2.94E+02	5.05E+02	1.81E+02	8.11E-01	1.01E+00	4.54E-03
9.68E-01	2.46E+01	1.39E+00	5.32E-02	4.74E-02	1.15E-03	1.66E-01	3.47E+01	2.94E+02	5.04E+02	1.80E+02	1.46E+00	1.01E+00	8.15E-03
9.99E-01	2.54E+01	1.44E+00	5.18E-02	4.67E-02	1.23E-03	2.42E-01	3.47E+01	2.94E+02	5.04E+02	1.80E+02	2.14E+00	1.01E+00	1.20E-02
1.03E+00	2.61E+01	1.48E+00	5.19E-02	4.69E-02	1.32E-03	3.22E-01	3.47E+01	2.94E+02	5.05E+02	1.80E+02	2.84E+00	1.01E+00	1.59E-02
1.06E+00	2.69E+01	1.52E+00	5.25E-02	4.67E-02	1.40E-03	3.39E-01	3.47E+01	2.94E+02	5.05E+02	1.80E+02	2.99E+00	1.01E+00	1.67E-02
1.09E+00	2.77E+01	1.57E+00	5.39E-02	4.74E-02	1.52E-03	3.08E-01	3.47E+01	2.94E+02	5.05E+02	1.81E+02	2.71E+00	1.01E+00	1.51E-02
1.12E+00	2.84E+01	1.61E+00	5.48E-02	4.78E-02	1.62E-03	3.05E-01	3.47E+01	2.94E+02	5.05E+02	1.80E+02	2.67E+00	1.01E+00	1.49E-02
1.15E+00	2.92E+01	1.65E+00	5.51E-02	4.83E-02	1.66E-03	3.29E-01	3.47E+01	2.94E+02	5.05E+02	1.80E+02	2.87E+00	1.01E+00	1.61E-02
1.18E+00	3.00E+01	1.70E+00	5.51E-02	4.78E-02	1.64E-03	1.69E-01	3.47E+01	2.94E+02	5.03E+02	1.80E+02	1.47E+00	1.01E+00	8.23E-03
1.21E+00	3.08E+01	1.74E+00	5.45E-02	4.69E-02	1.56E-03	2.71E-02	3.47E+01	2.94E+02	5.02E+02	1.79E+02	2.35E-01	1.00E+00	1.32E-03
1.24E+00	3.15E+01	1.78E+00	5.48E-02	4.68E-02	1.57E-03	-1.36E-01	3.47E+01	2.94E+02	5.00E+02	1.79E+02	-1.18E+00	1.00E+00	-6.63E-03
1.25E+00	3.18E+01	1.80E+00	5.41E-02	4.68E-02	1.55E-03	-4.76E-02	3.47E+01	2.94E+02	5.00E+02	1.79E+02	-5.96E-01	9.99E-01	-3.34E-03
1.26E+00	3.20E+01	1.81E+00	5.44E-02	4.71E-02	1.58E-03	-5.28E-02	3.47E+01	2.94E+02	4.99E+02	1.78E+02	-2.12E-01	9.98E-01	-1.19E-03
0.00E+00	0.00E+00	0.00E+00	0.00E+00	0.00E+00	0.00E+00	0.00E+00	0.00E+00	0.00E+00	0.00E+00	0.00E+00	0.00E+00	0.00E+00	0.00E+00

Table 55. Smooth Plate LDV Data

y (mm)	y/δ	y/δ_M	ρ (kg/m^3)	ρ/ρ_e	M	M/Me	M'	u (m/s)	u/u_e	u'/u_e		y/δ	$-\rho v'v'/\rho u_{bar}$
2.0	0.197	0.180	0.168	0.697	1.911	0.682	0.265	500.4	0.830	0.080		0.250	0.0027
2.5	0.246	0.225	0.173	0.716	1.977	0.705	0.268	510.2	0.847	0.076		0.250	0.0025
3.0	0.295	0.270	0.176	0.729	2.023	0.721	0.268	516.7	0.857	0.073		0.253	0.0028
3.8	0.374	0.342	0.184	0.761	2.125	0.758	0.270	530.6	0.881	0.067		0.266	0.0028
4.6	0.453	0.414	0.191	0.791	2.221	0.792	0.282	542.9	0.901	0.064		0.295	0.0030
5.7	0.561	0.513	0.202	0.834	2.351	0.838	0.271	558.2	0.926	0.055		0.340	0.0031
7.0	0.689	0.630	0.214	0.884	2.495	0.890	0.258	573.8	0.952	0.046		0.394	0.0032
8.6	0.846	0.775	0.225	0.932	2.625	0.936	0.210	586.6	0.973	0.034		0.450	0.0033
10.7	1.053	0.964	0.239	0.987	2.771	0.988	0.113	599.8	0.995	0.016		0.508	0.0034
13.2	1.299	1.189	0.241	0.998	2.799	0.998	0.079	602.2	0.999	0.011		0.567	0.0033
16.3	1.604	1.468	0.242	1.000	2.804	1.000	0.065	602.6	1.000	0.009		0.626	0.0032
												0.686	0.0029
y (mm)	Sk_u	Fl_u	γ_u	v (m/s)	v'/u_e	Sk_v	Fl_v	$-uv'/u_e^2$	$-pu'v'/\tau_w$	u+	y+	0.747	0.0028
2.0	-0.295	2.83	1.059	-0.961	0.042	0.112	3.55	0.0014	0.7972	19.4	331.5	0.808	0.0025
2.5	-0.351	2.85	1.054	-0.352	0.041	0.298	3.75	0.0013	0.8023	19.7	414.4	0.870	0.0021
3.0	-0.422	2.92	1.026	0.231	0.039	0.194	3.75	0.0012	0.7489	20.0	497.3	0.933	0.0017
3.8	-0.497	2.98	1.007	0.268	0.036	0.277	4.18	0.0010	0.6819	20.5	629.9	0.995	0.0011
4.6	-0.633	3.11	0.965	3.161	0.034	0.241	5.05	0.0009	0.7181	21.0	762.5	1.058	0.0009
5.7	-0.849	3.56	0.843	3.959	0.030	0.417	4.84	0.0007	0.5831	21.6	944.9	1.121	0.0006
7.0	-1.269	4.87	0.616	3.191	0.026	0.236	7.98	0.0005	0.4310	22.2	1160.4	1.184	0.0005
8.6	-1.736	6.93	0.433	7.557	0.022	-0.358	14.45	0.0002	0.2470	22.7	1425.6	1.246	0.0005
10.7	-2.415	15.12	0.198	7.092	0.016	-0.468	29.33	0.0001	0.0689	23.2	1773.7	1.309	0.0005
13.2	-4.290	76.76	0.039	4.056	0.013	-3.456	57.18	0.0000	0.0176	23.3	2188.2	1.371	0.0004
16.3	-4.920	98.33	0.031	2.176	0.011	-1.950	39.49	0.0000	0.0011	23.3	2702.1	1.433	0.0004
												1.496	0.0004
												1.558	0.0005

Table 56. 2D Plate LDV Data

y (mm)	y/δ	y/δ_M	ρ (kg/m^3)	ρ/ρ_e	M	M/Me	M'	u (m/s)	u/u_e	u'/u_e		y/δ	$-\rho\overline{v'v'}/\rho u_{tau}^2$
2.0	0.104	0.091	0.152	0.546	1.144	0.427	0.256	348.8	0.591	0.179		0.321	0.0038
2.6	0.135	0.119	0.156	0.560	1.218	0.455	0.280	366.8	0.621	0.178		0.321	0.0035
3.3	0.171	0.150	0.166	0.598	1.398	0.522	0.268	406.5	0.688	0.138		0.323	0.0034
4.3	0.223	0.196	0.175	0.631	1.538	0.574	0.252	434.8	0.736	0.111		0.333	0.0034
5.6	0.291	0.255	0.183	0.659	1.648	0.615	0.285	455.3	0.771	0.112		0.356	0.0037
7.2	0.374	0.328	0.193	0.693	1.775	0.663	0.308	477.4	0.808	0.107		0.392	0.0040
9.3	0.483	0.424	0.210	0.756	1.988	0.742	0.338	510.4	0.864	0.095		0.434	0.0047
12.0	0.624	0.547	0.233	0.839	2.243	0.838	0.314	544.5	0.922	0.070		0.477	0.0050
15.5	0.805	0.707	0.260	0.936	2.513	0.938	0.203	574.6	0.973	0.036		0.521	0.0055
20.1	1.044	0.917	0.274	0.985	2.639	0.985	0.079	586.9	0.994	0.012		0.566	0.0056
25.9	1.346	1.181	0.278	1.000	2.678	1.000	0.061	590.5	1.000	0.009		0.611	0.0060
												0.656	0.0058
y (mm)	Sk_u	Fl_u	γ_u	v (m/s)	v'/u_e	Sk_v	Fl_v	$-\overline{u'v'}/u_e^2$	$-\overline{puv'}/\tau_w$	u+	y+	0.701	0.0058
2.0	0.356	2.31	1.301	-11.426	0.089	-0.094	3.17	0.0055	0.5685	8.9	530.1	0.747	0.0053
2.6	0.141	2.18	1.376	-7.488	0.082	0.020	3.25	0.0055	0.6489	9.4	689.1	0.793	0.0049
3.3	-0.034	2.44	1.228	-10.205	0.077	0.063	3.12	0.0035	0.5407	10.4	874.6	0.839	0.0043
4.3	0.223	2.33	1.289	-11.654	0.068	0.132	3.43	0.0024	0.4478	11.1	1139.6	0.884	0.0036
5.6	-0.037	2.33	1.290	-9.324	0.067	0.259	3.40	0.0025	0.5348	11.6	1484.2	0.930	0.0028
7.2	-0.294	2.54	1.180	-5.092	0.061	0.301	3.44	0.0025	0.6056	12.2	1908.2	0.976	0.0020
9.3	-0.664	3.10	0.968	-0.952	0.052	0.508	3.99	0.0019	0.5723	13.0	2464.8	1.021	0.0016
12.0	-1.176	4.56	0.658	0.754	0.039	0.660	4.88	0.0010	0.3746	13.9	3180.4	1.067	0.0014
15.5	-2.368	11.55	0.260	5.476	0.025	0.692	9.81	0.0003	0.1404	14.7	4108.0	1.113	0.0012
20.1	-1.266	13.86	0.216	7.065	0.014	0.388	13.72	0.0000	0.0182	15.0	5327.2	1.158	0.0009
25.9	-6.385	177.61	0.017	7.507	0.012	-2.996	71.64	0.0000	0.0028	15.1	6864.4	1.204	0.0007
												1.249	0.0006
												1.294	0.0006
												1.340	0.0006

Table 57. 3D Plate LDV Data

y (mm)	y/δ	y/δ_M	ρ (kg/m^3)	ρ/ρ_e	M	M/Me	M'	u (m/s)	u/u_e	u'/u_e		y/δ	$-\rho\overline{v'v'}/\rho u_{bar}$
2.0	0.138	0.118	0.152	0.562	1.241	0.461	0.277	373.0	0.629	0.171		0.293	0.0028
2.6	0.180	0.153	0.159	0.585	1.354	0.503	0.296	398.2	0.671	0.161		0.293	0.0026
3.3	0.228	0.194	0.165	0.609	1.462	0.543	0.288	420.8	0.710	0.138		0.295	0.0027
4.2	0.290	0.247	0.174	0.641	1.593	0.592	0.291	446.4	0.753	0.121		0.307	0.0031
5.3	0.366	0.312	0.185	0.682	1.748	0.650	0.294	474.1	0.799	0.105		0.333	0.0038
6.8	0.470	0.400	0.197	0.727	1.905	0.708	0.312	499.4	0.842	0.095		0.371	0.0041
8.7	0.601	0.512	0.215	0.791	2.113	0.785	0.321	529.0	0.892	0.080		0.416	0.0040
11.1	0.767	0.654	0.238	0.878	2.367	0.879	0.296	560.2	0.945	0.059		0.462	0.0039
14.1	0.974	0.830	0.262	0.965	2.602	0.967	0.195	584.6	0.986	0.032		0.508	0.0040
18.0	1.244	1.060	0.271	0.998	2.687	0.998	0.082	592.6	0.999	0.012		0.555	0.0044
23.0	1.589	1.354	0.271	1.000	2.691	1.000	0.064	593.1	1.000	0.010		0.603	0.0045
												0.650	0.0044
y (mm)	Sk_u	Fl_u	γ_u	v (m/s)	v'/u_e	Sk_v	Fl_v	$-\overline{u'v'}/u_e^2$	$-\rho\overline{u'v'}/\tau_w$	u+	y+	0.699	0.0045
2.0	0.093	2.28	1.313	-7.147	0.079	-0.004	3.16	0.0061	0.7415	9.7	529.3	0.747	0.0044
2.6	-0.165	2.39	1.255	-6.244	0.074	0.097	3.17	0.0052	0.7550	10.3	688.1	0.796	0.0041
3.3	-0.197	2.51	1.193	-7.195	0.070	0.175	3.17	0.0039	0.6571	10.9	873.4	0.845	0.0033
4.2	-0.205	2.57	1.169	-6.260	0.064	0.232	3.33	0.0032	0.6366	11.6	1111.6	0.894	0.0025
5.3	-0.245	2.53	1.186	-5.867	0.059	0.253	3.41	0.0024	0.5755	12.3	1402.7	0.943	0.0018
6.8	-0.477	2.97	1.012	-2.992	0.053	0.337	3.60	0.0020	0.5634	13.0	1799.7	0.992	0.0014
8.7	-0.750	3.40	0.883	1.232	0.044	0.551	4.19	0.0015	0.5254	13.7	2302.5	1.040	0.0011
11.1	-1.257	4.85	0.618	5.445	0.033	0.745	5.43	0.0008	0.3253	14.5	2937.7	1.088	0.0009
14.1	-2.281	11.39	0.263	8.036	0.024	0.505	11.66	0.0002	0.1145	15.2	3731.7	1.137	0.0007
18.0	-1.613	17.67	0.170	4.098	0.015	-1.455	36.83	0.0000	0.0124	15.4	4763.8	1.185	0.0007
23.0	-3.232	53.49	0.056	1.392	0.011	-1.329	63.03	0.0000	0.0002	15.4	6087.1	1.233	0.0007
												1.282	0.0006
												1.330	0.0006
												1.379	0.0007

Table 58. 80 Grit Plate LDV Data

y (mm)	y/δ	y/δ_M	ρ (kg/m^3)	ρ/ρ_e	M	M/Me	M'	u (m/s)	u/u_e	u'/u_e		y/δ	$-\rho\overline{v'v'}/\rho u_{tau}^2$
2.0	0.147	0.126	0.161	0.580	1.312	0.490	0.288	389.8	0.658	0.164		0.367	0.0041
2.5	0.184	0.157	0.167	0.604	1.418	0.530	0.275	412.7	0.697	0.138		0.367	0.0042
3.3	0.243	0.207	0.174	0.629	1.528	0.571	0.285	434.7	0.734	0.127		0.369	0.0043
4.1	0.302	0.257	0.182	0.658	1.640	0.613	0.287	455.9	0.769	0.114		0.380	0.0043
5.2	0.383	0.327	0.193	0.698	1.788	0.668	0.294	481.5	0.813	0.100		0.406	0.0044
6.6	0.486	0.414	0.203	0.732	1.906	0.712	0.304	500.3	0.844	0.093		0.447	0.0043
8.3	0.611	0.521	0.219	0.790	2.092	0.782	0.312	527.1	0.890	0.080		0.495	0.0041
10.6	0.781	0.666	0.243	0.876	2.347	0.877	0.295	558.7	0.943	0.060		0.544	0.0036
13.4	0.987	0.841	0.269	0.970	2.599	0.971	0.189	585.2	0.988	0.031		0.595	0.0037
17.0	1.252	1.067	0.276	0.998	2.669	0.998	0.088	591.9	0.999	0.014		0.645	0.0037
21.6	1.591	1.356	0.277	1.000	2.675	1.000	0.055	592.5	1.000	0.008		0.696	0.0037
												0.748	0.0037
y (mm)	Sk_u	Fl_u	γ_u	v (m/s)	v'/u_e	Sk_v	Fl_v	$-u'v'/u_e^2$	$-\rho u'v'/\tau_w$	u+	y+	0.800	0.0034
2.0	-0.128	2.30	1.307	-5.196	0.071	0.050	3.20	0.0051	0.8576	11.0	476.1	0.853	0.0029
2.5	-0.203	2.50	1.199	-6.141	0.066	0.144	3.29	0.0035	0.6944	11.7	595.1	0.905	0.0022
3.3	-0.313	2.71	1.106	-4.878	0.065	0.138	3.39	0.0032	0.7355	12.3	785.6	0.957	0.0018
4.1	-0.275	2.70	1.110	-4.676	0.061	0.194	3.31	0.0029	0.7664	12.9	976.0	1.009	0.0014
5.2	-0.316	2.64	1.135	-4.755	0.055	0.242	3.39	0.0024	0.7315	13.6	1237.9	1.062	0.0012
6.6	-0.511	3.06	0.982	-1.965	0.050	0.343	3.66	0.0019	0.6635	14.2	1571.1	1.114	0.0010
8.3	-0.754	3.47	0.863	1.154	0.043	0.522	4.00	0.0014	0.5956	14.9	1975.8	1.166	0.0008
10.6	-1.233	4.61	0.651	4.420	0.034	0.757	5.67	0.0008	0.4213	15.8	2523.3	1.218	0.0006
13.4	-2.192	10.37	0.289	8.141	0.023	0.624	10.90	0.0002	0.1392	16.6	3189.9	1.269	0.0006
17.0	-2.468	24.07	0.125	3.477	0.015	-0.387	17.39	0.0000	0.0100	16.8	4046.9	1.321	0.0006
21.6	0.027	3.76	0.797	1.183	0.013	-5.184	82.68	0.0000	0.0000	16.8	5141.9	1.373	0.0006
												1.425	0.0006
												1.477	0.0006
												1.529	0.0006

Table 59. 36 Grit Plate LDV Data

y (mm)	y/δ	y/δ_M	ρ (kg/m^3)	ρ/ρ_e	M	M/Me	M'	u (m/s)	u/u_e	u'/u_e		y/δ	$-\rho v'/\rho u_{bar}$
2.0	0.110	0.093	0.156	0.543	1.099	0.415	0.280	338.3	0.573	0.206		0.300	0.0050
2.6	0.143	0.121	0.161	0.562	1.198	0.452	0.296	362.3	0.613	0.193		0.300	0.0047
3.3	0.182	0.153	0.167	0.583	1.303	0.492	0.295	386.6	0.655	0.170		0.302	0.0046
4.3	0.237	0.200	0.177	0.617	1.458	0.550	0.303	419.5	0.710	0.146		0.312	0.0048
5.6	0.309	0.260	0.189	0.659	1.626	0.614	0.305	451.9	0.765	0.123		0.333	0.0049
7.3	0.402	0.339	0.203	0.706	1.800	0.679	0.309	482.3	0.817	0.104		0.367	0.0050
9.4	0.518	0.437	0.218	0.761	1.986	0.750	0.323	511.1	0.865	0.091		0.406	0.0052
12.1	0.667	0.562	0.245	0.854	2.273	0.858	0.290	548.9	0.929	0.063		0.447	0.0053
15.7	0.865	0.729	0.272	0.948	2.532	0.956	0.174	577.4	0.978	0.030		0.489	0.0051
20.3	1.119	0.943	0.281	0.980	2.617	0.987	0.076	585.7	0.992	0.012		0.530	0.0055
26.3	1.450	1.221	0.285	0.993	2.650	1.000	0.061	588.8	0.997	0.010		0.572	0.0056
31.8	1.753	1.477	0.287	1.000	2.669	1.007	0.063	590.5	1.000	0.010		0.615	0.0060
												0.657	0.0058
y (mm)	Sk_u	Fl_u	γ_u	v (m/s)	v/u_e	Sk_v	Fl_v	$-uv'/u_e^2$	$-\rho uv'/\tau_w$	u+	y+	0.700	0.0054
2.0	-0.084	2.18	1.377	-5.228	0.093	0.005	3.16	0.0077	0.7147	8.4	555.9	0.743	0.0049
2.6	-0.055	2.18	1.379	-6.223	0.091	0.052	3.18	0.0071	0.7780	9.0	722.6	0.786	0.0043
3.3	-0.081	2.26	1.325	-7.362	0.084	0.069	3.06	0.0057	0.7468	9.6	917.2	0.829	0.0038
4.3	-0.183	2.39	1.254	-9.863	0.078	0.129	3.19	0.0044	0.7164	10.4	1195.1	0.871	0.0031
5.6	-0.247	2.53	1.187	-10.311	0.070	0.235	3.29	0.0034	0.6742	11.2	1556.4	0.913	0.0024
7.3	-0.390	2.64	1.136	-8.126	0.060	0.377	3.60	0.0024	0.5782	12.0	2028.9	0.956	0.0017
9.4	-0.676	3.15	0.953	-3.104	0.052	0.589	4.14	0.0018	0.5401	12.7	2612.5	0.998	0.0013
12.1	-1.356	5.41	0.554	1.253	0.038	0.683	5.67	0.0009	0.3396	13.6	3362.9	1.041	0.0012
15.7	-2.543	14.73	0.204	4.616	0.024	0.673	8.96	0.0002	0.0989	14.3	4363.4	1.083	0.0011
20.3	-1.864	33.93	0.088	2.642	0.015	-1.709	31.25	0.0000	0.0118	14.5	5641.9	1.125	0.0010
26.3	-2.297	48.44	0.062	8.084	0.011	-3.178	55.42	0.0000	-0.0005	14.6	7309.5	1.167	0.0009
31.8	-3.775	76.24	0.039	9.934	0.010	-1.560	27.34	0.0000	0.0016	14.7	8838.1	1.209	0.0008
												1.252	0.0008
												1.294	0.0008

Table 60. 20 Grit Plate LDV Data

y (mm)	y/δ	y/δ_M	ρ (kg/m^3)	ρ/ρ_e	M	M/Me	M*	u (m/s)	u/u_e	u'/u_e		y/δ	$-\rho\overline{v'v'}/\rho u_{tau}^2$
2.0	0.102	0.082	0.157	0.553	1.185	0.445	0.287	359.9	0.609	0.190		0.305	0.0046
2.6	0.133	0.107	0.160	0.562	1.233	0.463	0.302	371.1	0.628	0.189		0.305	0.0043
3.4	0.174	0.140	0.166	0.586	1.348	0.507	0.307	397.1	0.672	0.168		0.307	0.0044
4.5	0.230	0.185	0.176	0.619	1.491	0.560	0.309	427.1	0.722	0.144		0.317	0.0042
5.8	0.296	0.239	0.185	0.652	1.626	0.611	0.307	453.1	0.766	0.124		0.339	0.0042
7.6	0.388	0.313	0.200	0.705	1.821	0.684	0.313	486.8	0.823	0.104		0.374	0.0042
10.0	0.511	0.411	0.217	0.764	2.015	0.757	0.322	516.5	0.873	0.088		0.414	0.0047
13.1	0.669	0.539	0.244	0.858	2.298	0.864	0.278	553.4	0.936	0.059		0.455	0.0054
17.1	0.873	0.703	0.267	0.940	2.523	0.948	0.156	578.0	0.977	0.027		0.497	0.0057
22.4	1.144	0.921	0.278	0.978	2.624	0.986	0.078	587.9	0.994	0.013		0.539	0.0066
29.2	1.491	1.201	0.282	0.992	2.661	1.000	0.060	591.3	1.000	0.009		0.581	0.0071
31.8	1.624	1.308	0.284	1.000	2.680	1.007	0.058	593.1	1.003	0.009		0.624	0.0081
												0.667	0.0081
y (mm)	Sk_u	Fl_u	γ_u	v (m/s)	v'/u_e	Sk_v	Fl_v	$-\overline{u'v'}/u_e^2$	$-\rho\overline{u'v'}/\tau_w$	u+	y+	0.711	0.0080
2.0	-0.071	2.23	1.342	-16.361	0.091	-0.032	3.01	0.0076	0.7694	8.9	577.1	0.754	0.0074
2.6	-0.175	2.22	1.352	-13.299	0.094	0.110	3.17	0.0077	0.8498	9.2	750.2	0.798	0.0067
3.4	-0.181	2.33	1.286	-14.222	0.088	0.144	3.08	0.0061	0.7997	9.8	981.0	0.841	0.0059
4.5	-0.243	2.44	1.228	-14.829	0.079	0.208	3.14	0.0044	0.7060	10.6	1298.4	0.885	0.0051
5.8	-0.270	2.55	1.177	-13.334	0.070	0.217	3.24	0.0029	0.5553	11.2	1673.5	0.928	0.0044
7.6	-0.408	2.71	1.106	-11.422	0.063	0.360	3.63	0.0025	0.5836	12.0	2192.9	0.971	0.0035
10.0	-0.748	3.42	0.878	-7.010	0.053	0.549	3.95	0.0019	0.5407	12.8	2885.4	1.015	0.0029
13.1	-1.356	5.42	0.553	0.865	0.036	0.645	5.13	0.0006	0.2135	13.7	3779.9	1.058	0.0023
17.1	-2.001	10.45	0.287	7.132	0.024	1.142	9.02	0.0001	0.0388	14.3	4934.0	1.101	0.0018
22.4	-3.774	78.12	0.038	9.945	0.015	-1.712	37.87	0.0000	0.0114	14.5	6463.3	1.144	0.0016
29.2	-3.981	83.33	0.036	12.919	0.014	-4.650	70.99	0.0000	0.0027	14.6	8425.3	1.187	0.0012
31.8	-2.326	49.84	0.060	11.610	0.013	-3.811	57.30	0.0000	0.0073	14.7	9175.5	1.230	0.0012
												1.273	0.0009

Figures

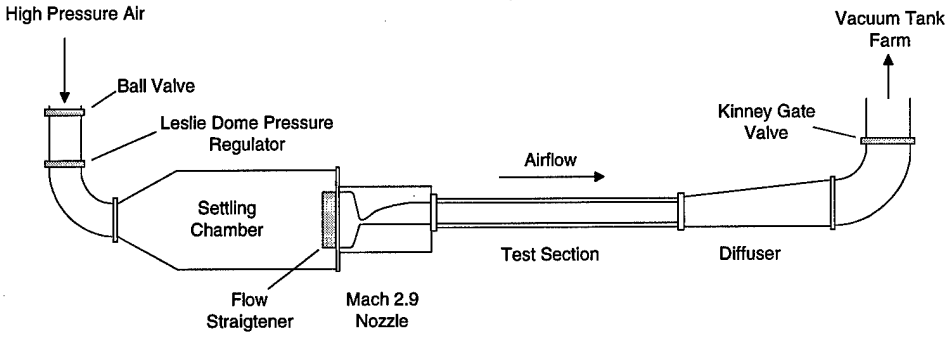

Figure 1. AFIT Mach 2.9 Wind Tunnel Schematic

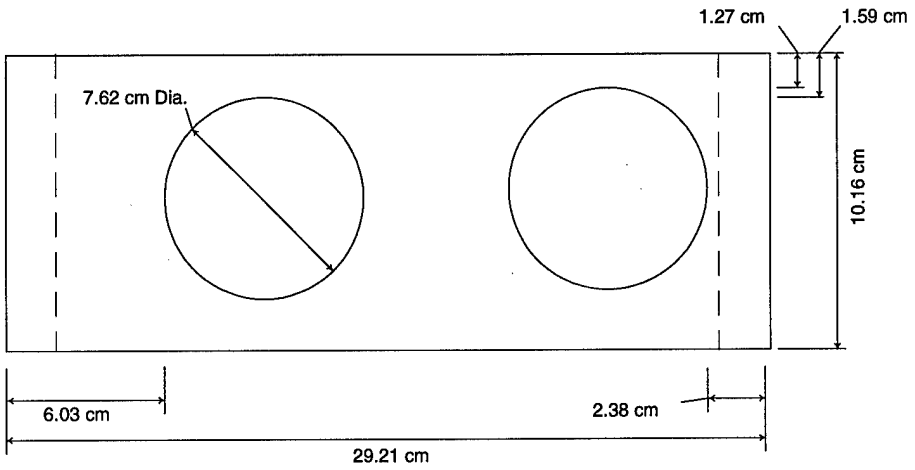

Figure 2. Tunnel Side Wall Optical Window Placement

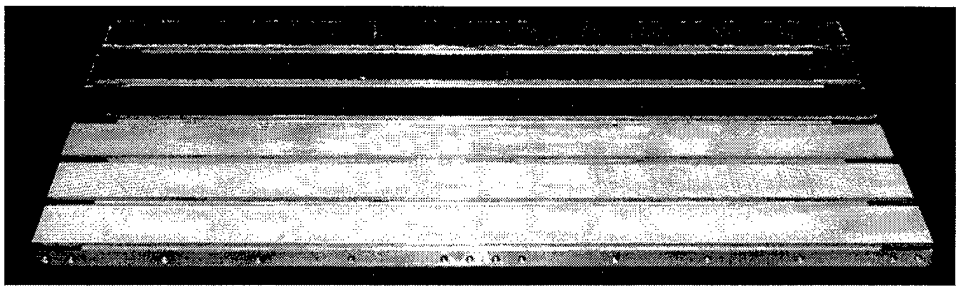

Figure 3. Six Test Section Floor Plates

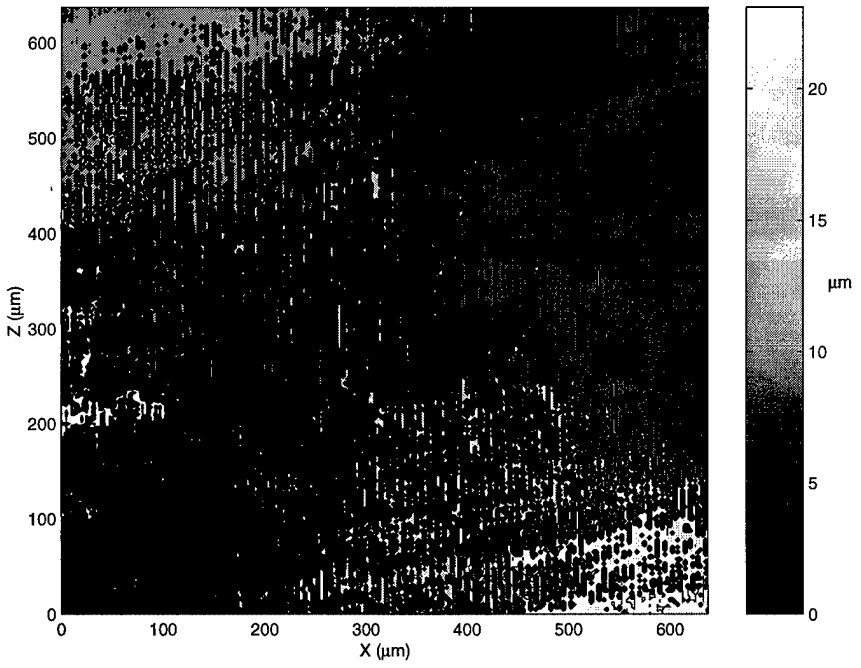

Figure 4. Smooth Plate, Surface Topography

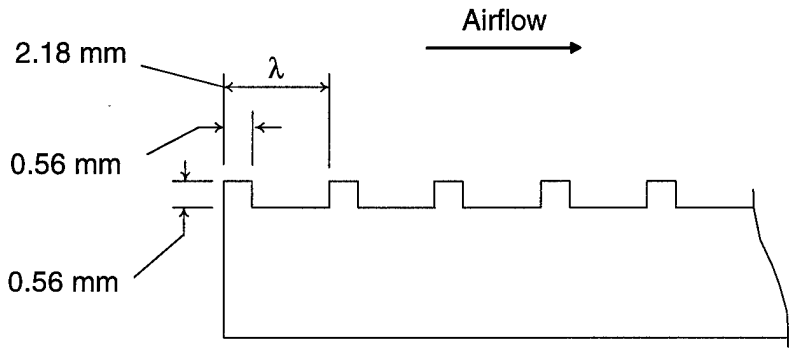

Figure 5. 2D Plate, Surface Roughness Profile

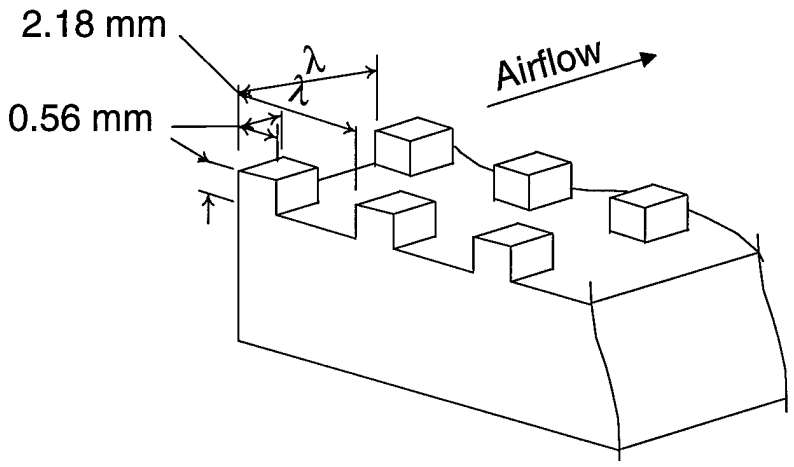

Figure 6. 3D Plate, Surface Roughness Profile

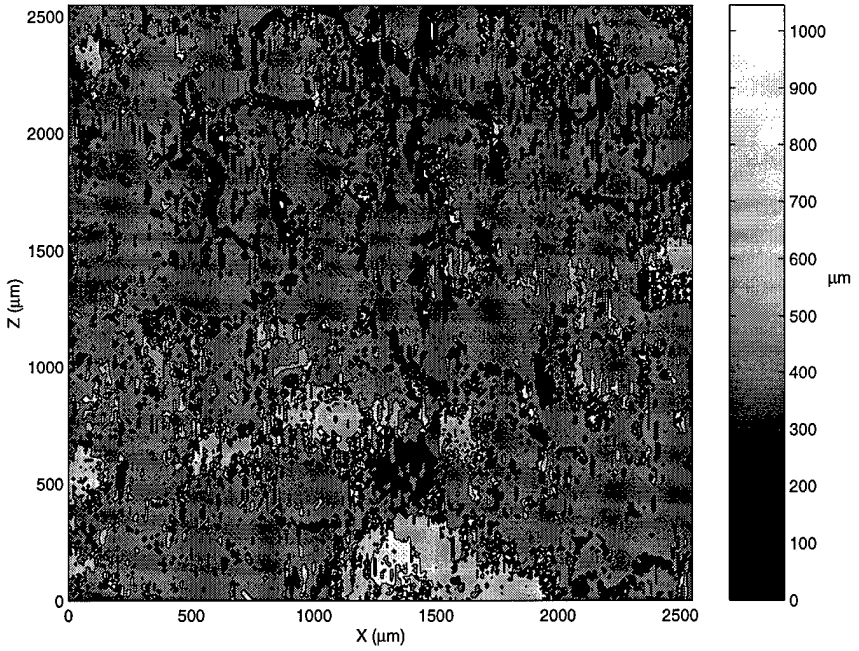

Figure 7. 80 Grit Plate, Surface Topography

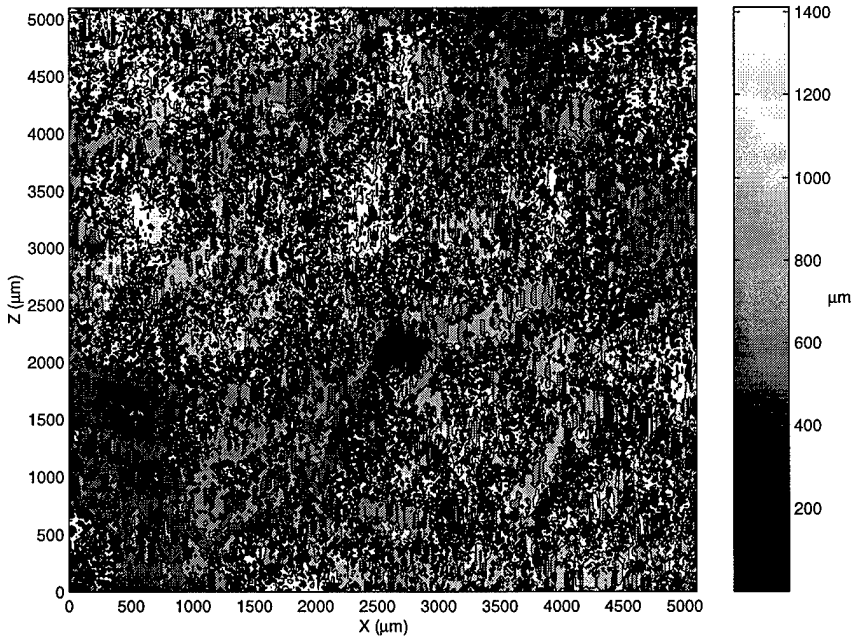

Figure 8. 36 Grit Plate, Surface Topography

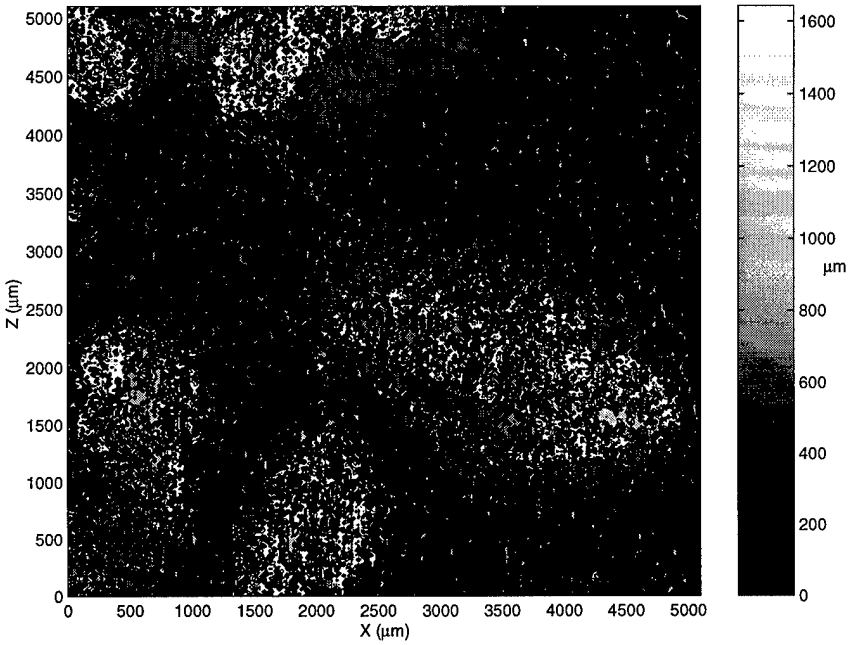

Figure 9. 20 Grit Plate, Surface Topography

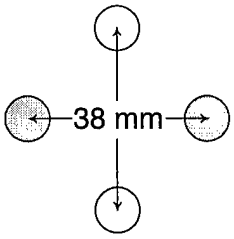

Figure 10. Transmitter Face Laser Beam Spacing

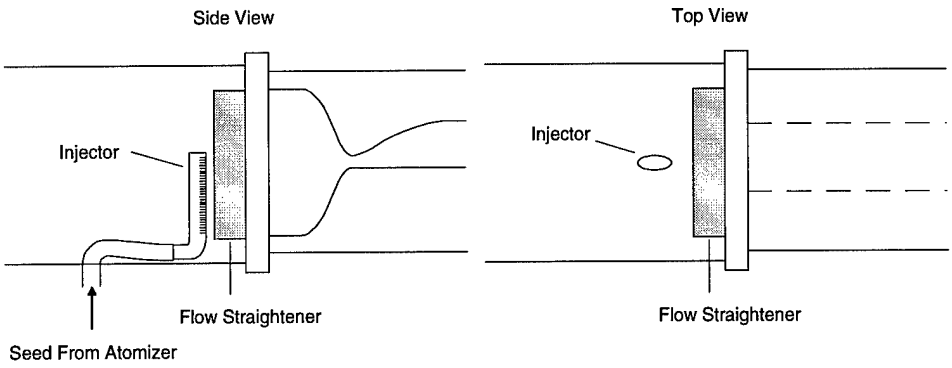

Figure 11. LDV Olive Oil Injector

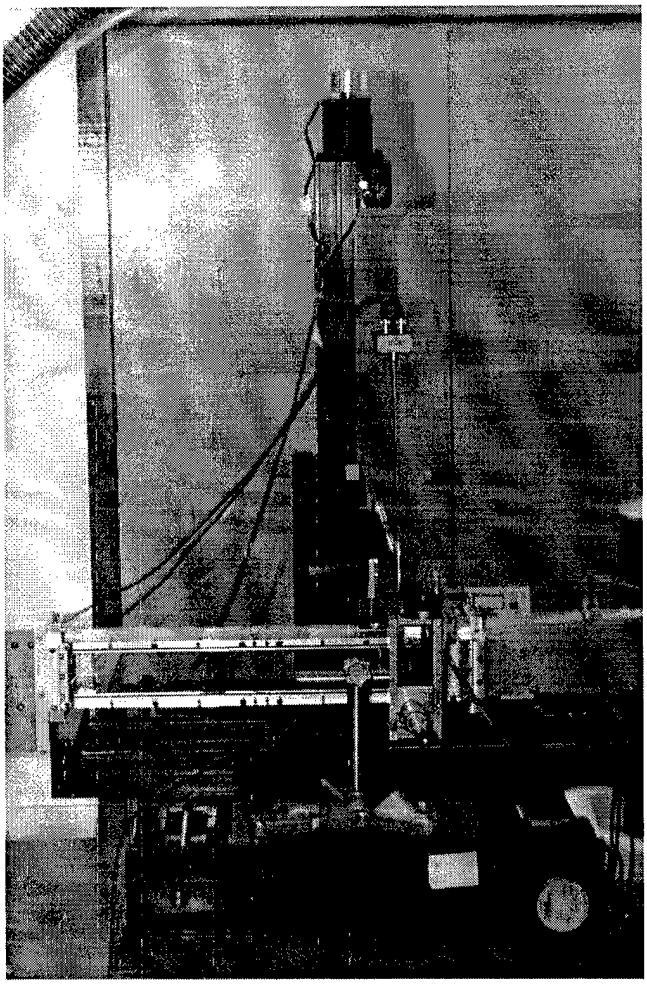

Figure 12. Cross-Film Probe and Traverse Setup

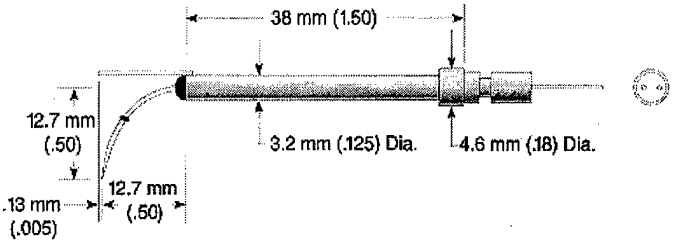

Figure 13. TSI 1218-20 Normal-Film Probe

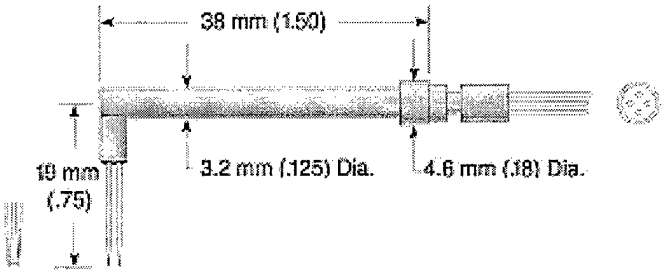

Figure 14. TSI 1246AD-20 Parallel-Film Probe

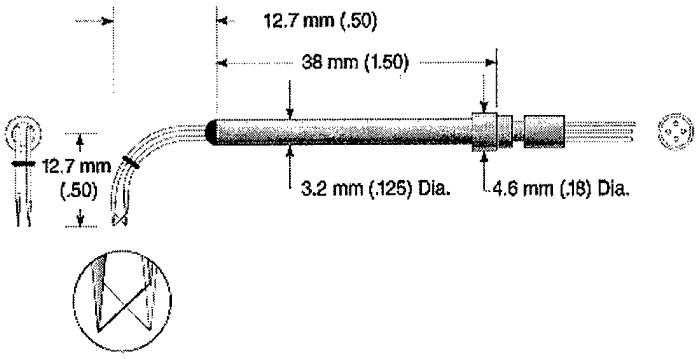

Figure 15. TSI 1243-20 u-v Cross-Film Probe

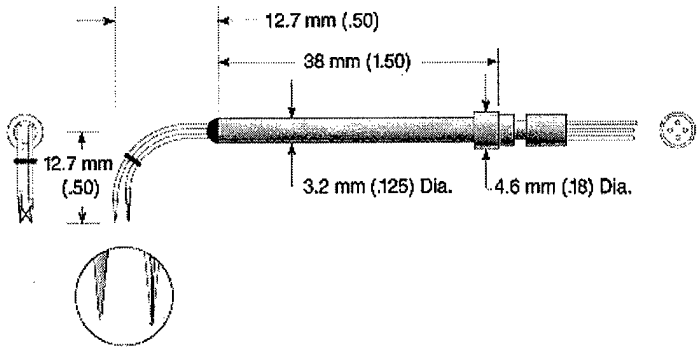

Figure 16. TSI 1243AN-20 u-w Cross-Film Probe

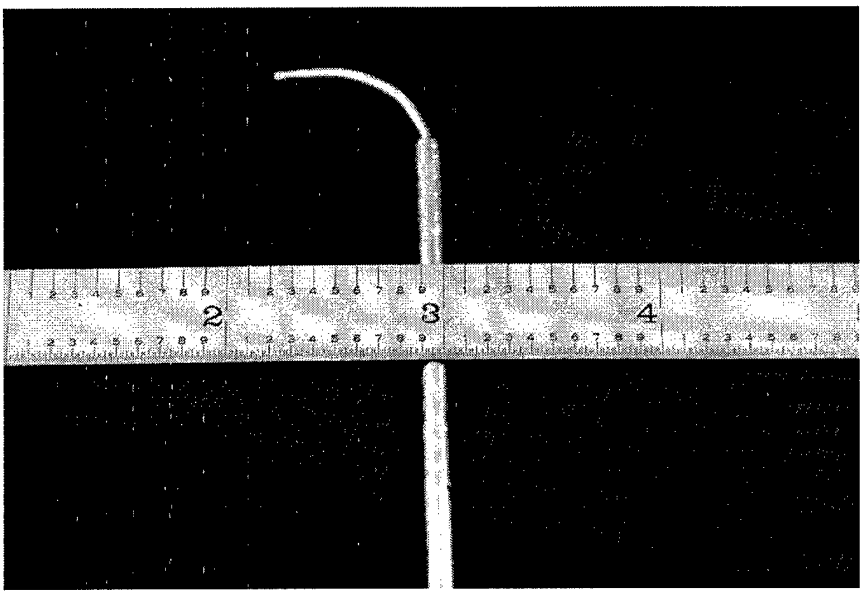

Figure 17. Pitot Pressure Probe

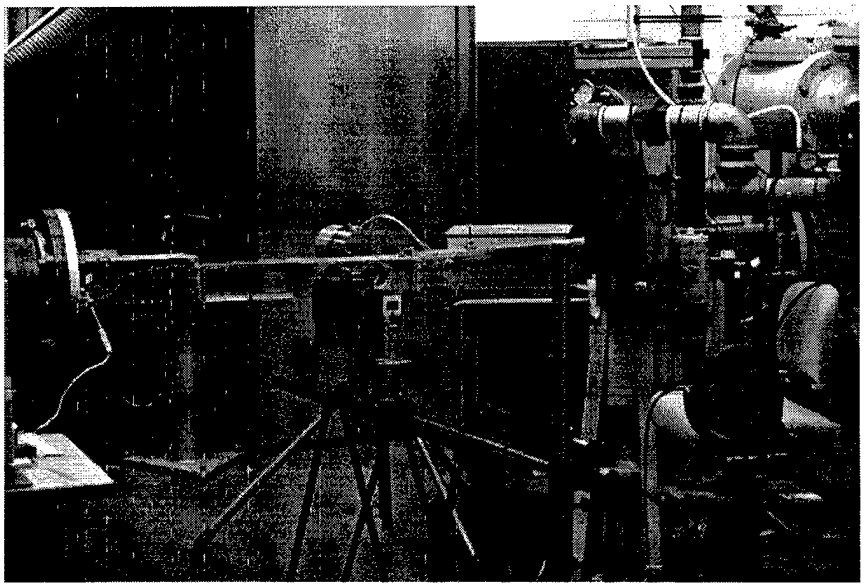

Figure 18. Color Schlieren Setup

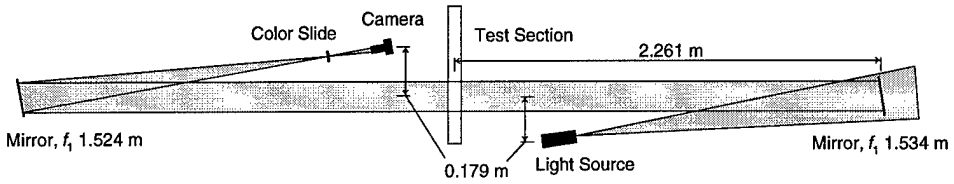

Figure 19. Color Schlieren Schematic

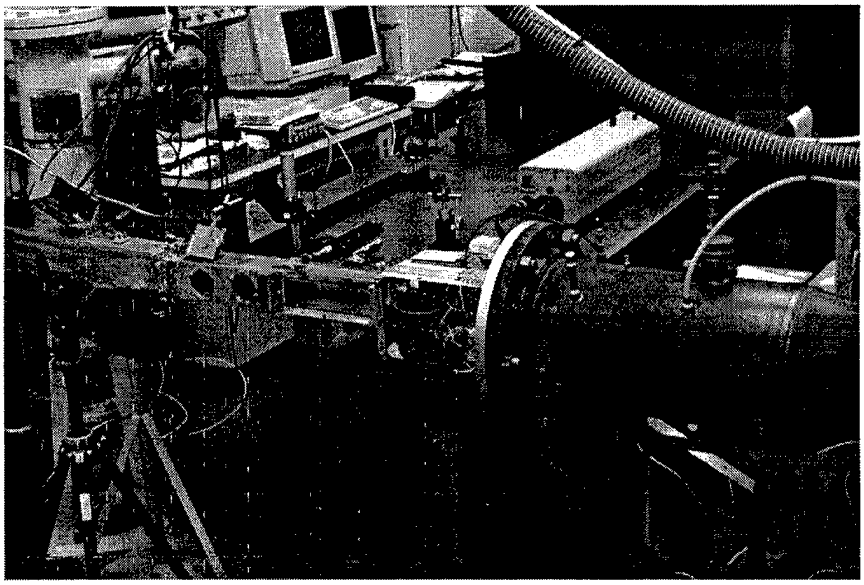

Figure 20. Laser Sheet Imaging Setup

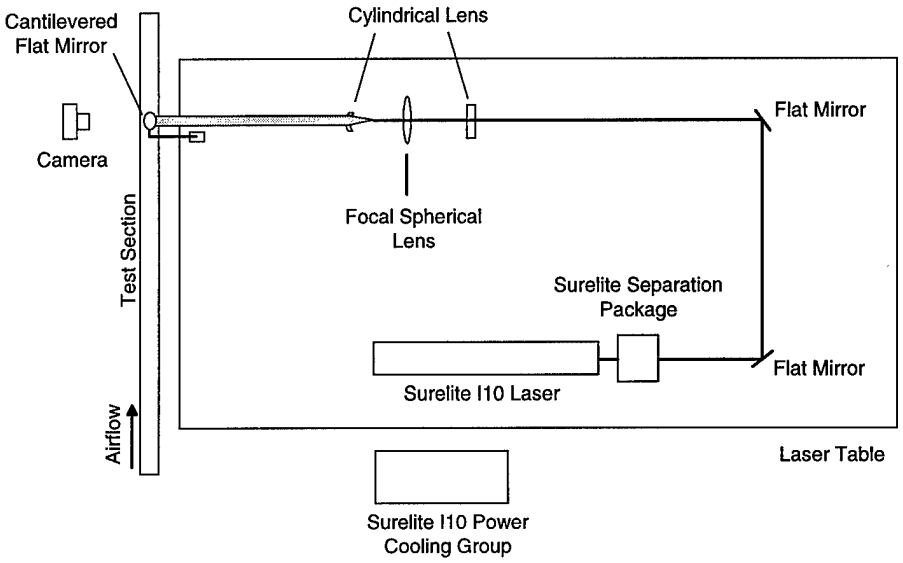

Figure 21. Laser Sheet Imaging Schematic

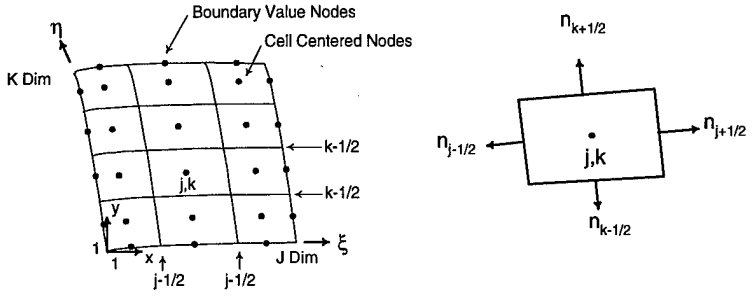

Figure 22. Discretization Grid of the Navier-Stokes Equations

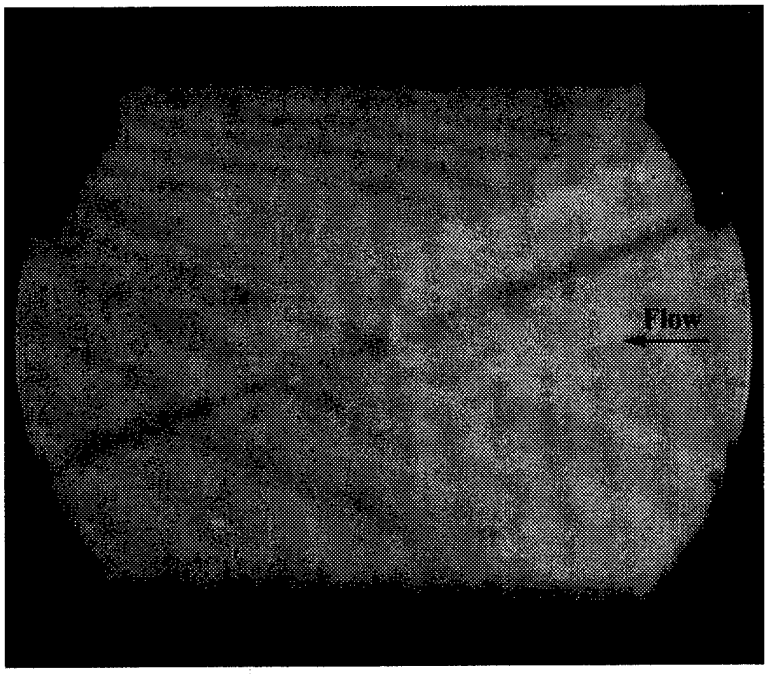

Figure 23. Smooth Plate Schlieren at Nozzle Exit, Horizontal Knife Edge

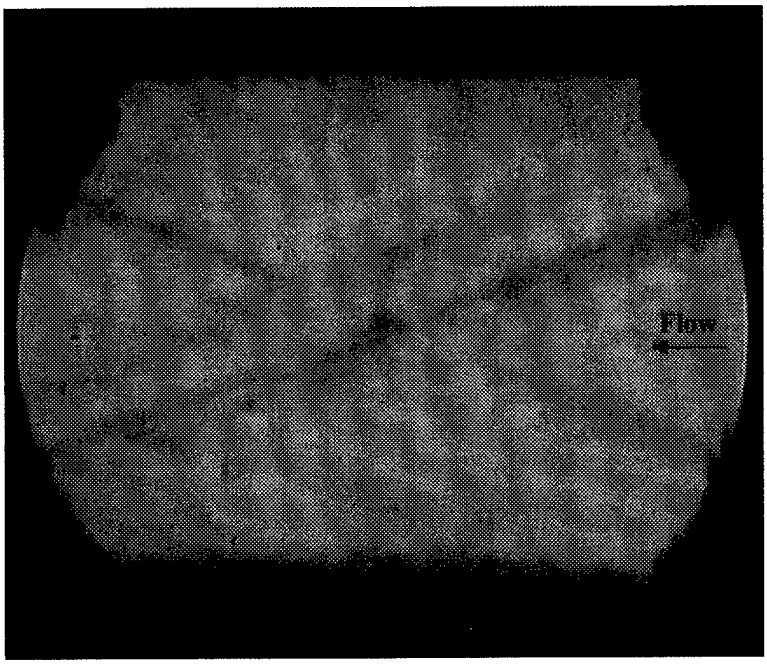

Figure 24. 2D Plate Schlieren at Nozzle Exit, Horizontal Knife Edge

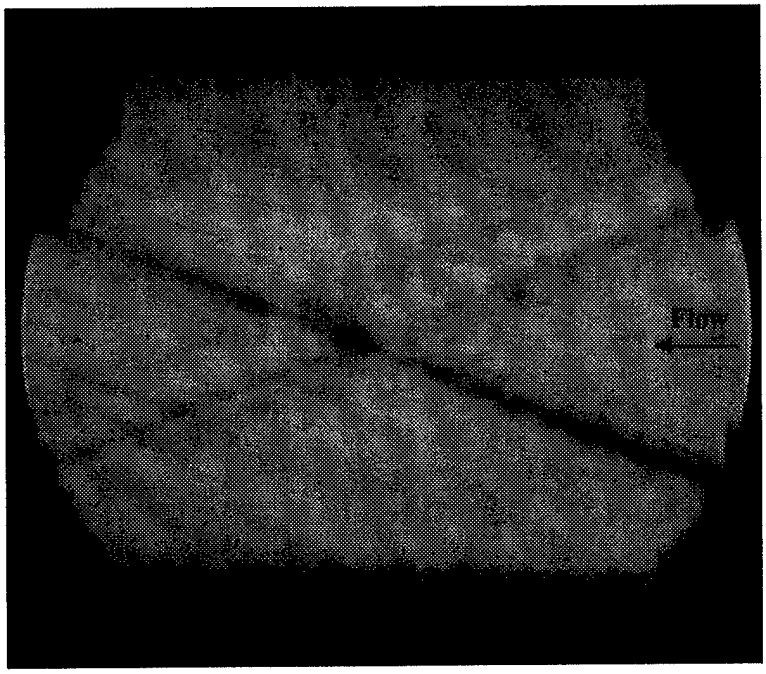

Figure 25. 3D Plate Schlieren at Nozzle Exit, Horizontal Knife Edge

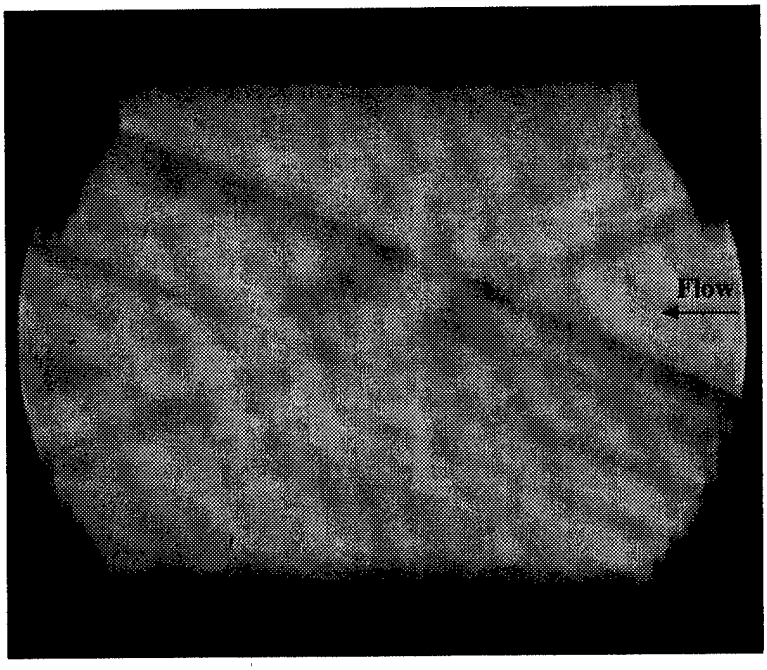

Figure 26. 80 Grit Plate Schlieren at Nozzle Exit, Horizontal Knife Edge

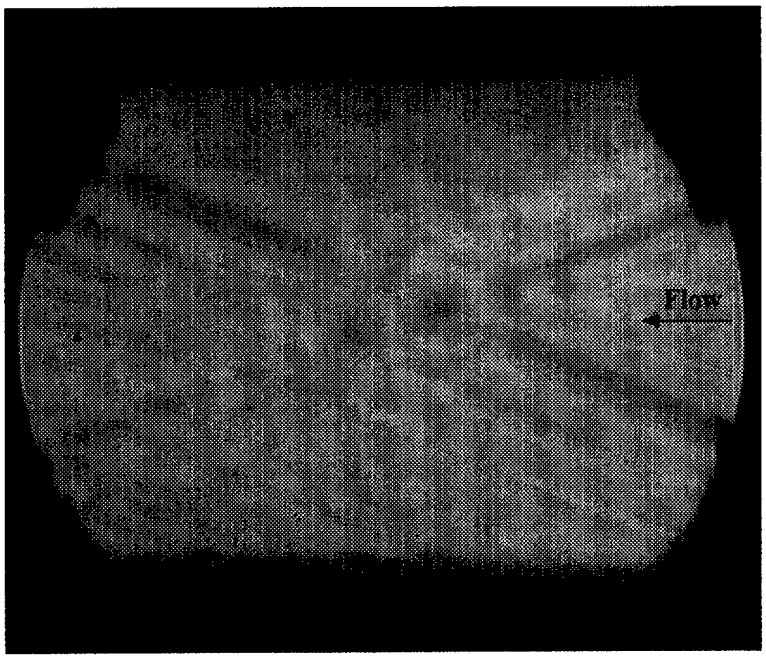

Figure 27. 36 Grit Plate Schlieren at Nozzle Exit, Horizontal Knife Edge

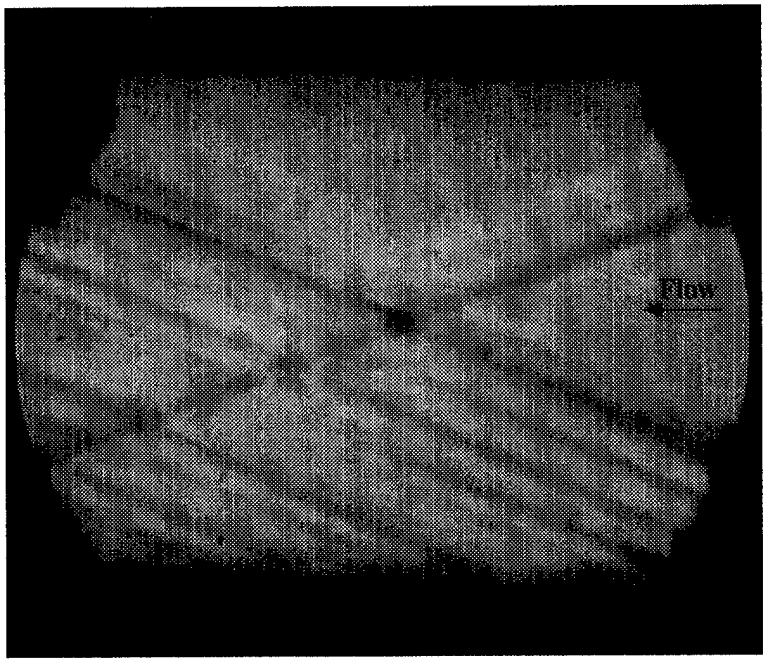

Figure 28. 20 Grit Plate Schlieren at Nozzle Exit, Horizontal Knife Edge

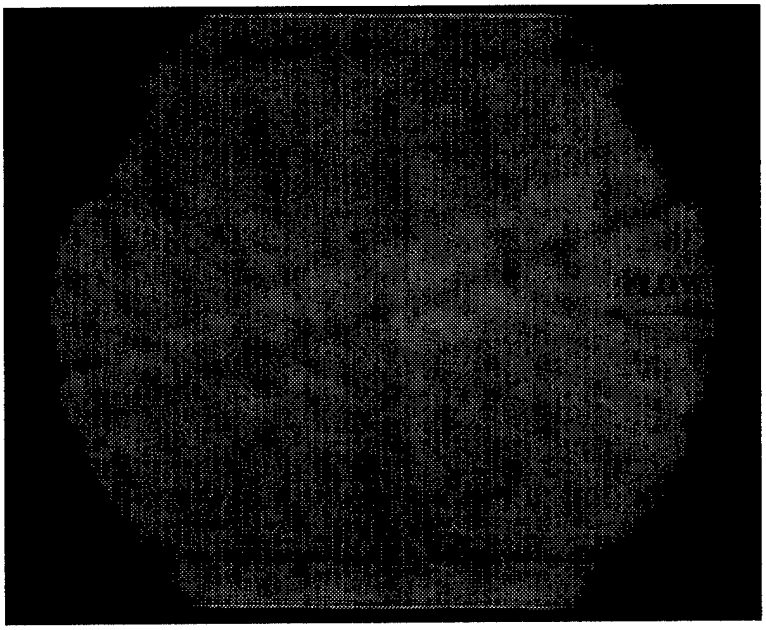

Figure 29. Smooth Plate Schlieren at Nozzle Exit, Vertical Knife Edge

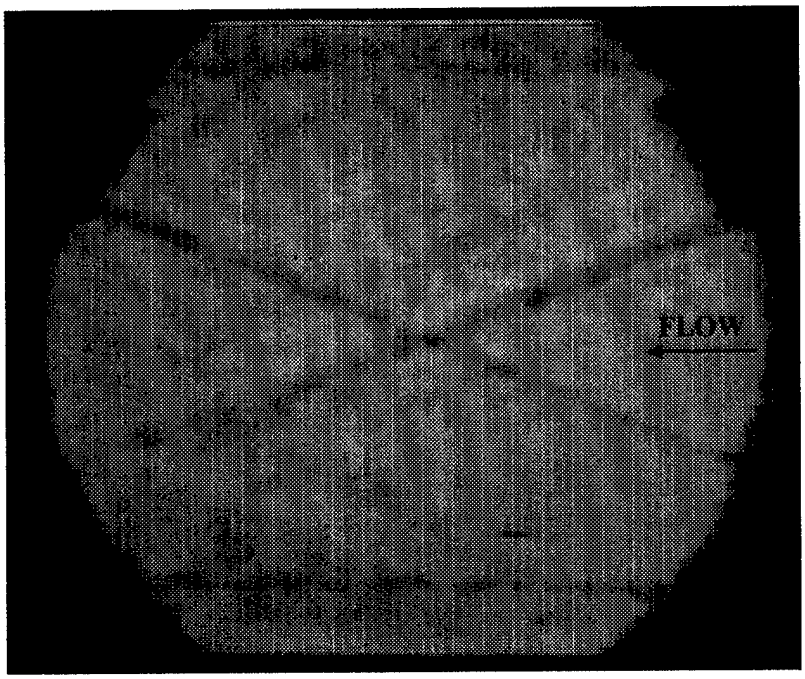

Figure 30. 2D Plate Schlieren at Nozzle Exit, Vertical Knife Edge

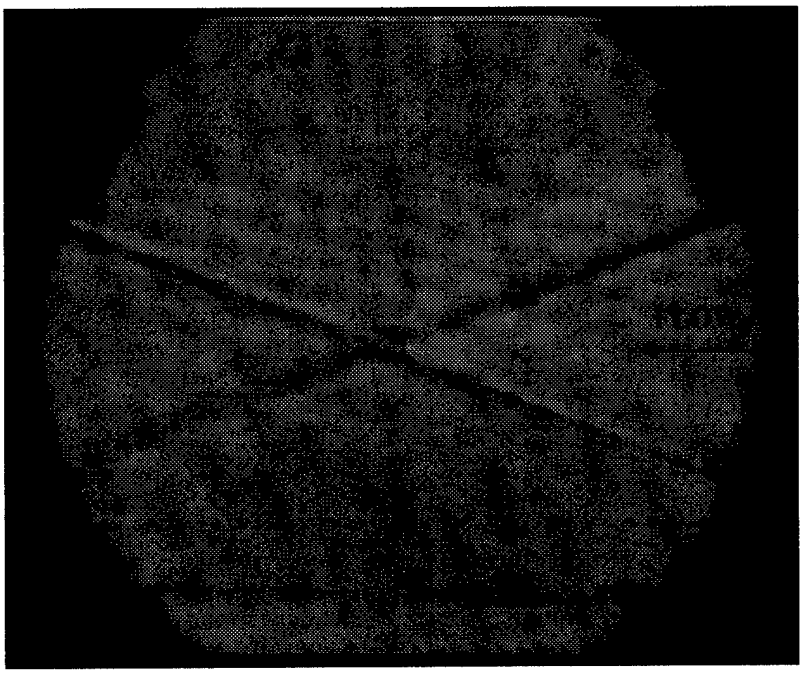

Figure 31. 3D Plate Schlieren at Nozzle Exit, Vertical Knife Edge

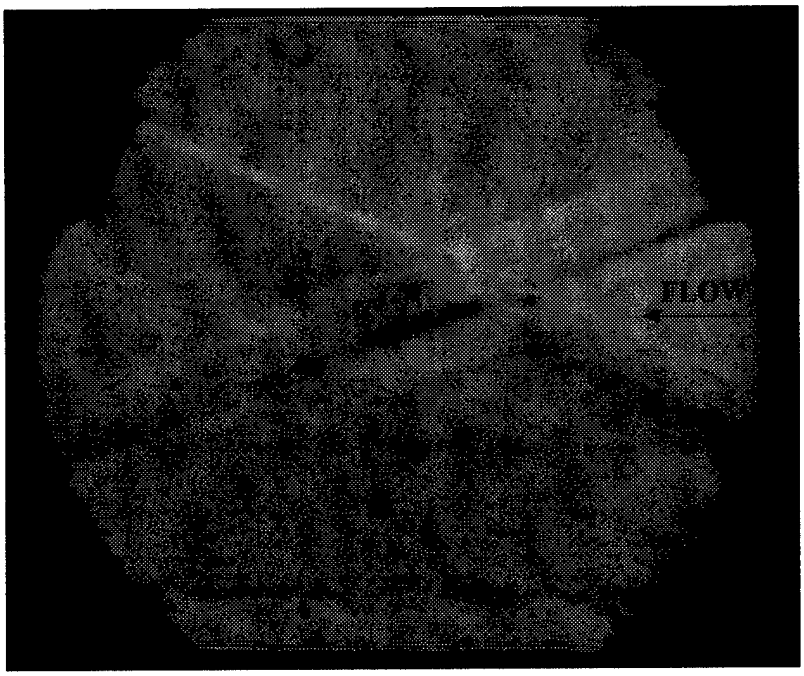

Figure 32. 80 Grit Plate Schlieren at Nozzle Exit, Vertical Knife Edge

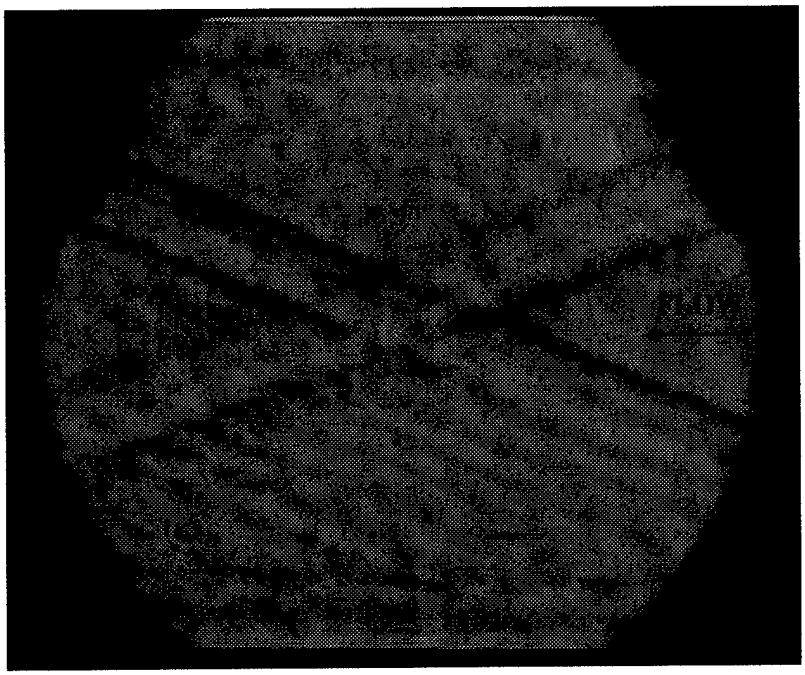

Figure 33. 36 Grit Plate Schlieren at Nozzle Exit, Vertical Knife Edge

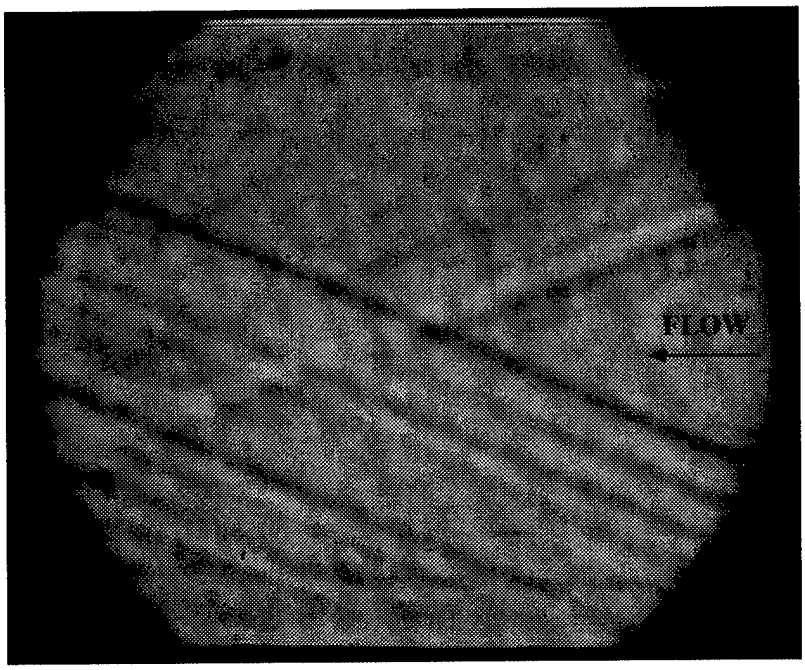

Figure 34. 20 Grit Plate Schlieren at Nozzle Exit, Vertical Knife Edge

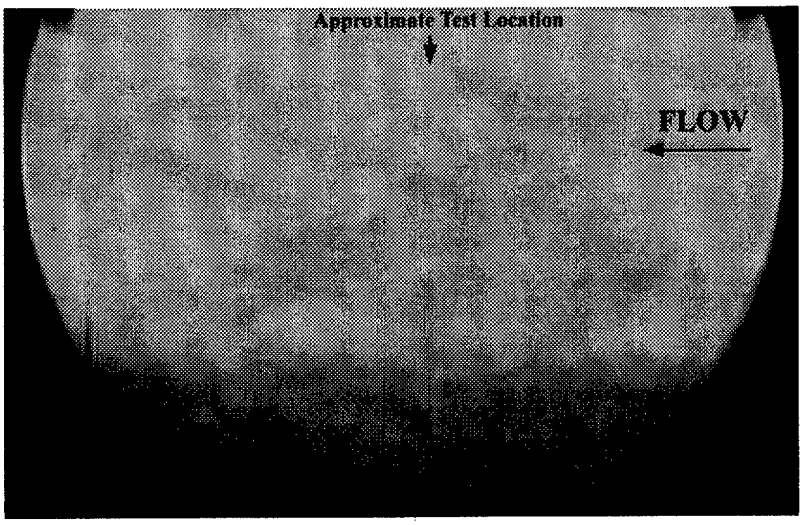

Figure 35. Smooth Plate Schlieren at Test Location, Horizontal Knife Edge

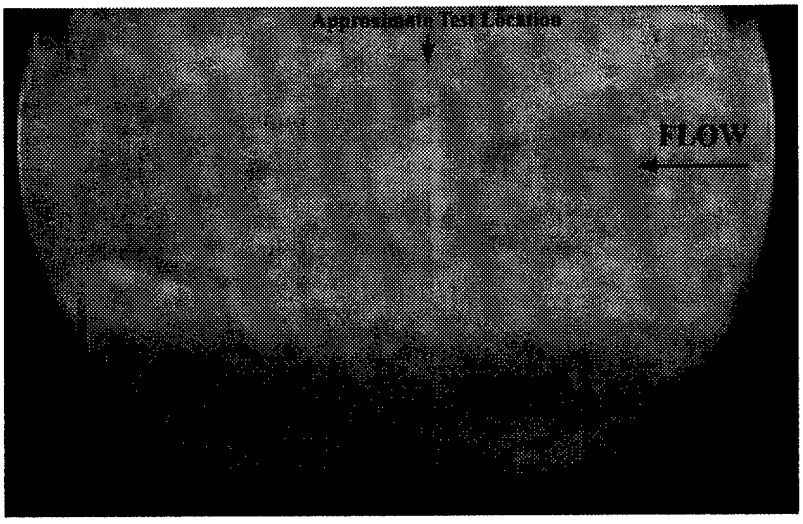

Figure 36. 2D Plate Schlieren at Test Location, Horizontal Knife Edge

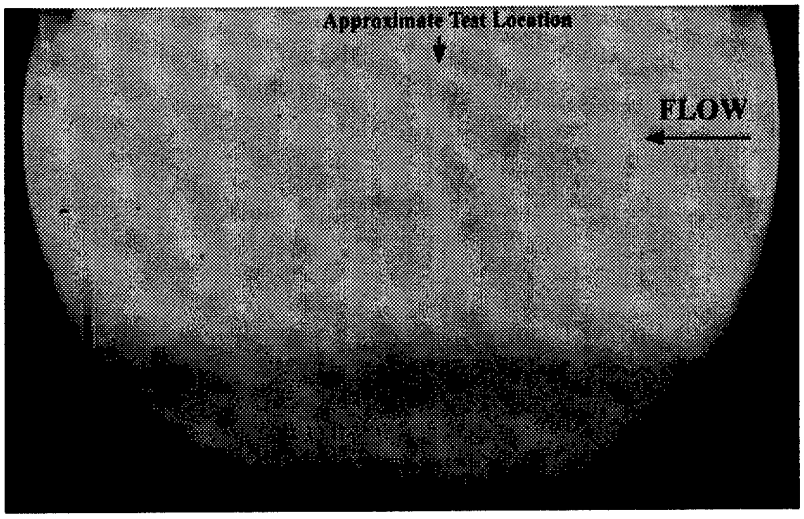

Figure 37. 3D Plate Schlieren at Test Location, Horizontal Knife Edge

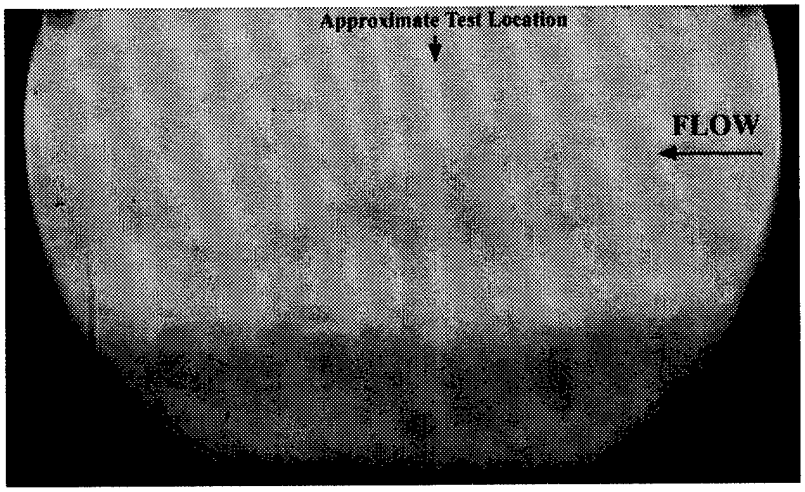

Figure 38. 80 Grit Plate Schlieren at Test Location, Horizontal Knife Edge

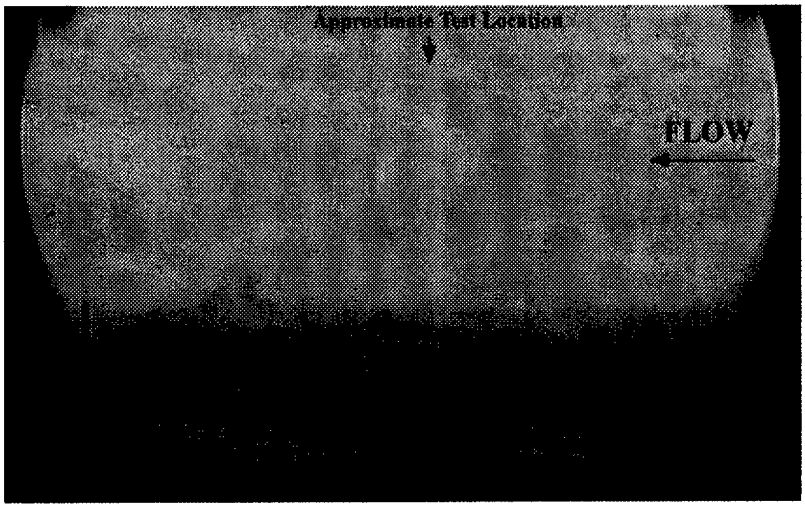

Figure 39. 36 Grit Plate Schlieren at Test Location, Horizontal Knife Edge

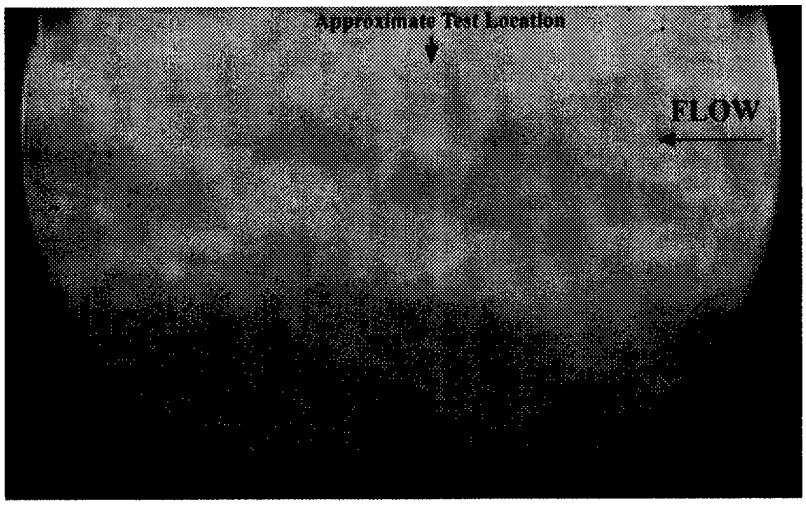

Figure 40. 20 Grit Plate Schlieren at Test Location, Horizontal Knife Edge

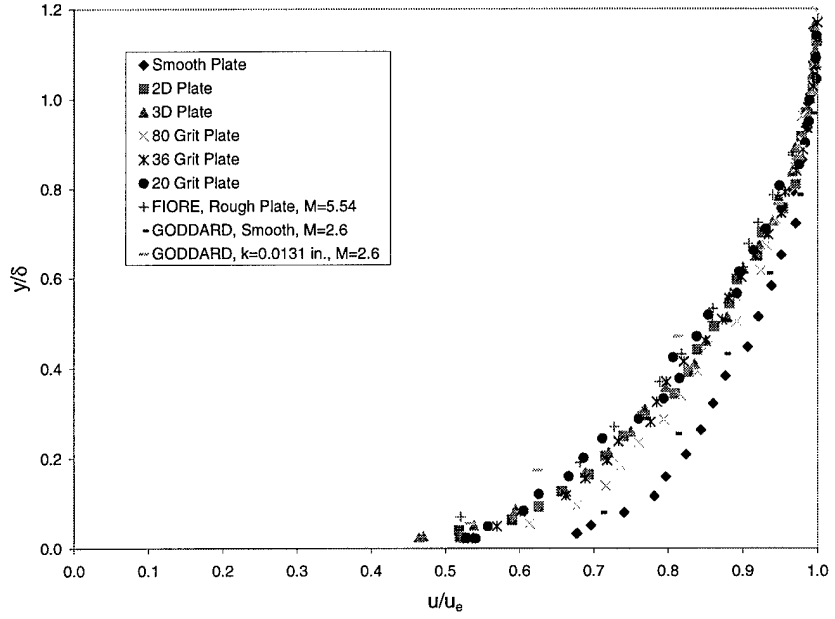

Figure 41. Pitot Probe Velocity Profiles

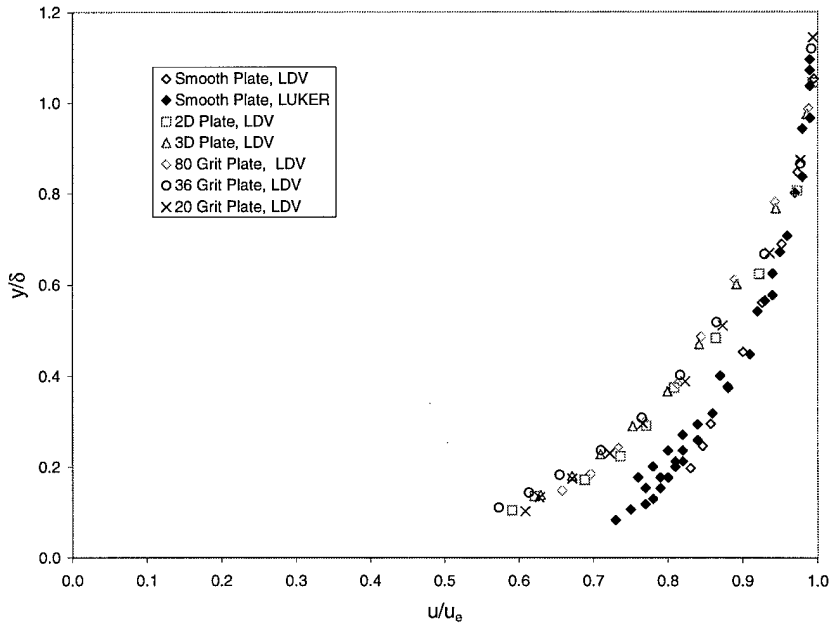

Figure 42. LDV Velocity Profiles

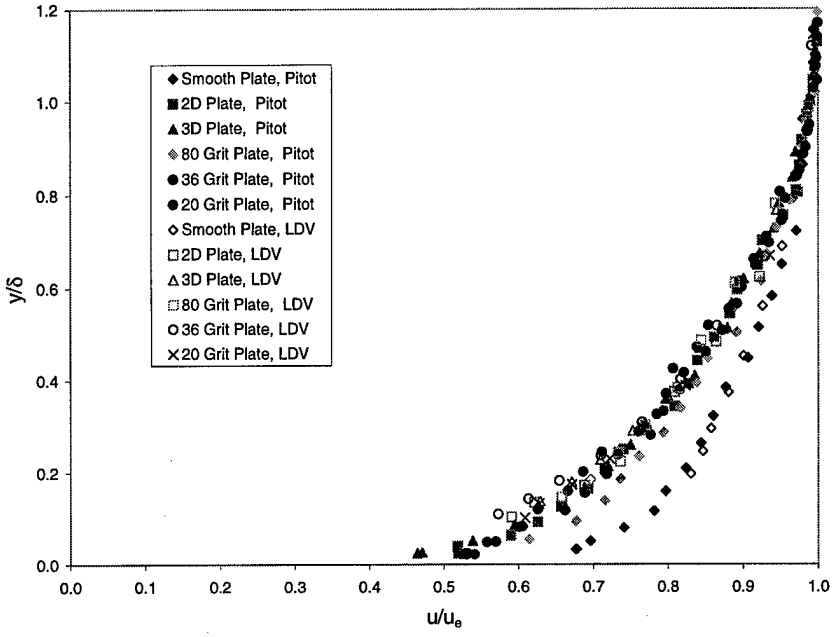

Figure 43. Pitot and LDV Velocity Profiles

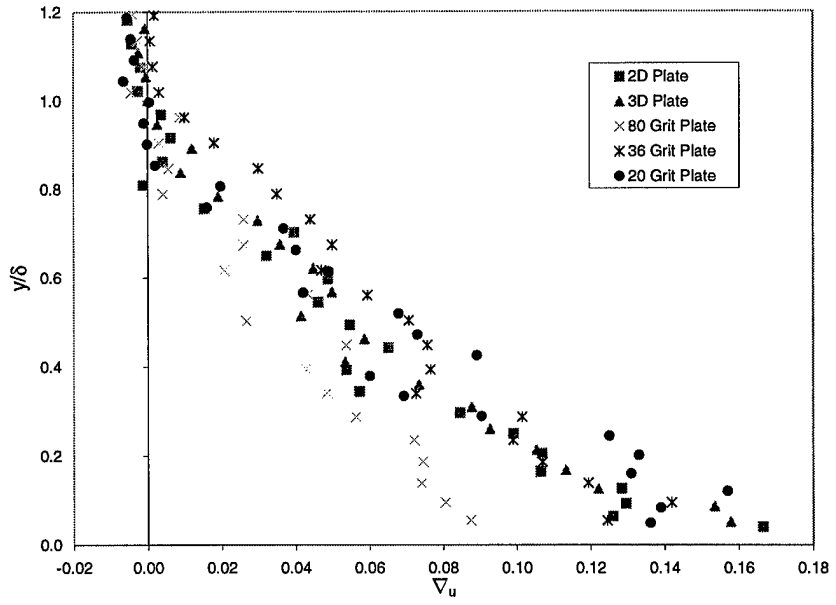

Figure 44. Pitot Rough Surface Velocity Profiles Relative to Smooth Plate

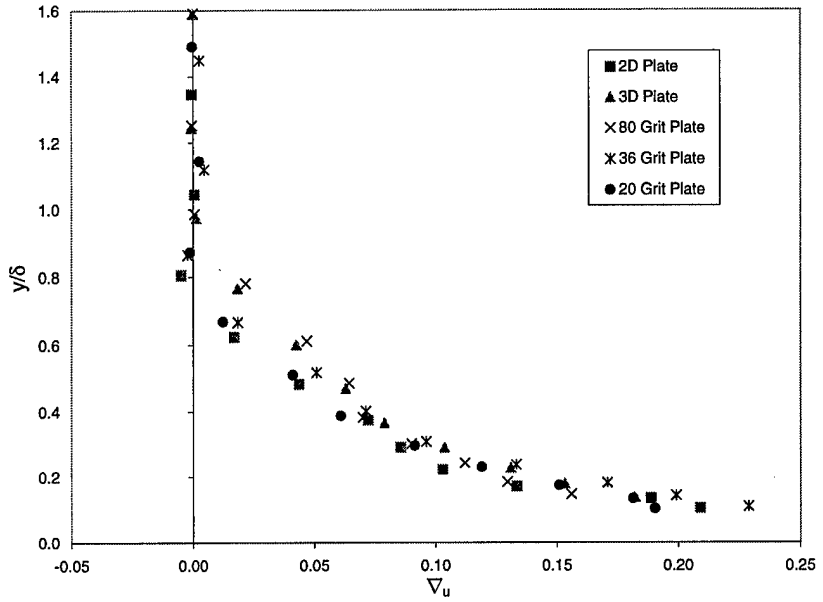

Figure 45. LDV Rough Surface Velocity Profiles Relative to Smooth Plate

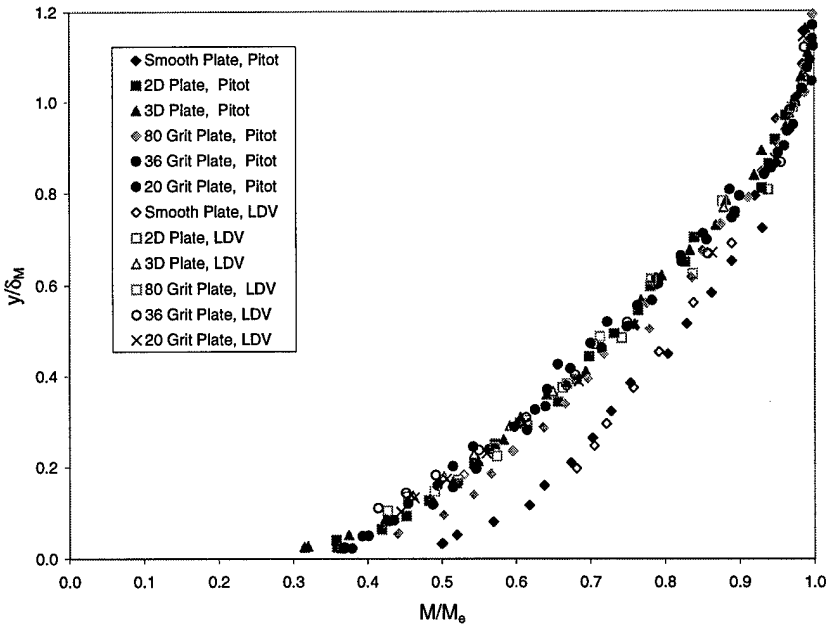

Figure 46. Pitot and LDV Mach Profiles

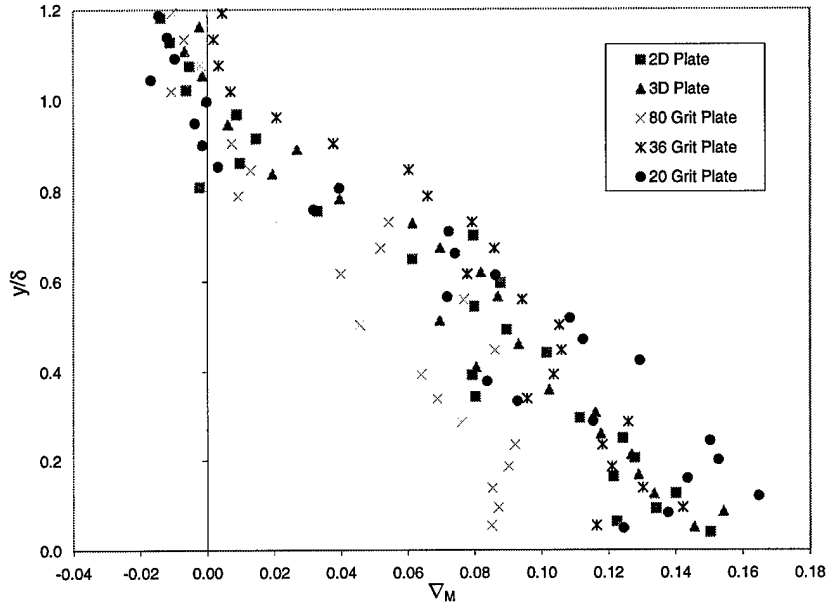

Figure 47. Pitot Rough Surface Mach Profiles Relative to Smooth Plate

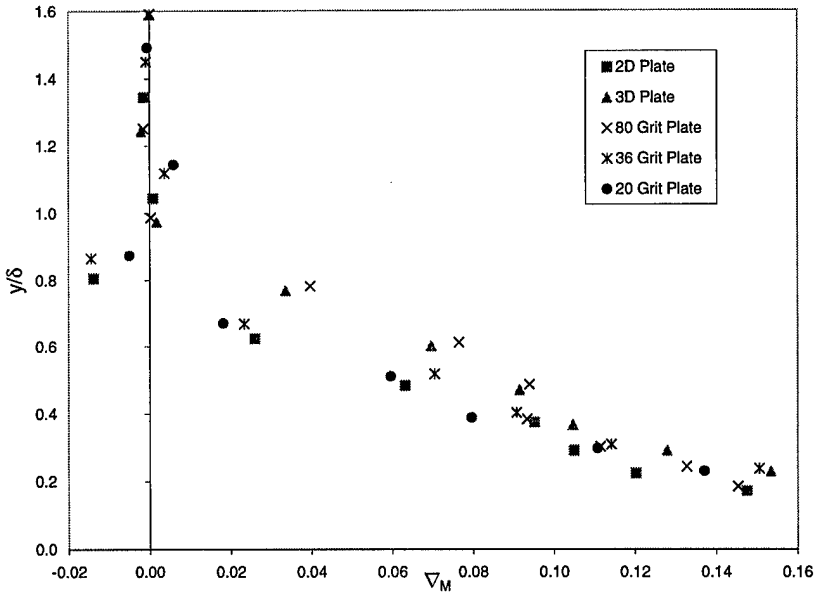

Figure 48. LDV Rough Surface Mach Profiles Relative to Smooth Plate

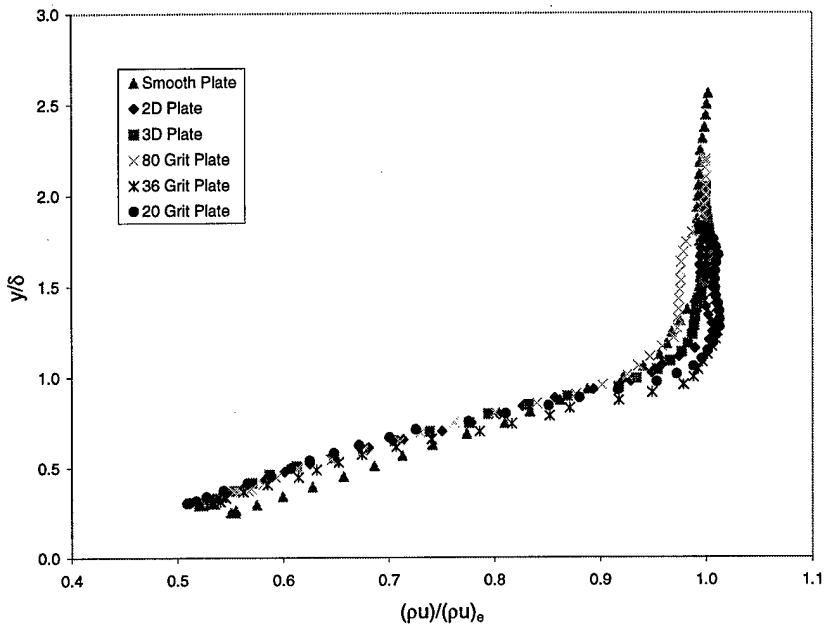

Figure 49. x-y Plane, Cross-Film, $(\rho u)_{bar}$ Profiles

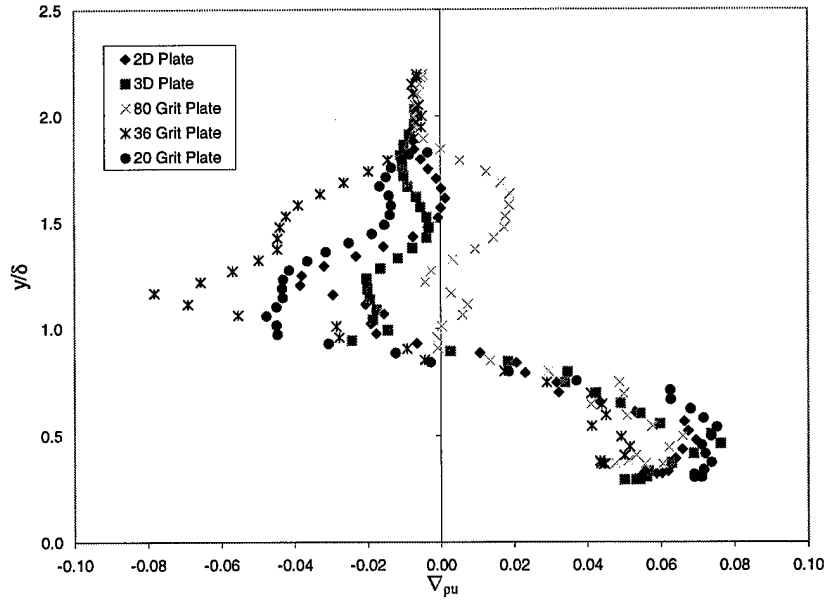

Figure 50. x-y Plane, Cross-Film, Rough Surface $(\rho u)_{bar}$ Profiles Relative to Smooth Plate

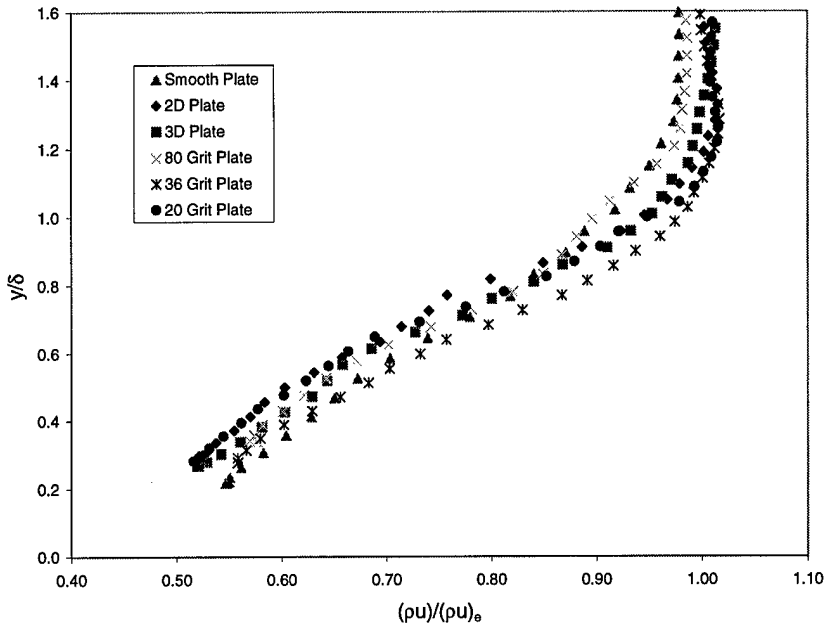

Figure 51. x-z Plane, Cross-Film, $(\rho u)_{bar}$ Profiles

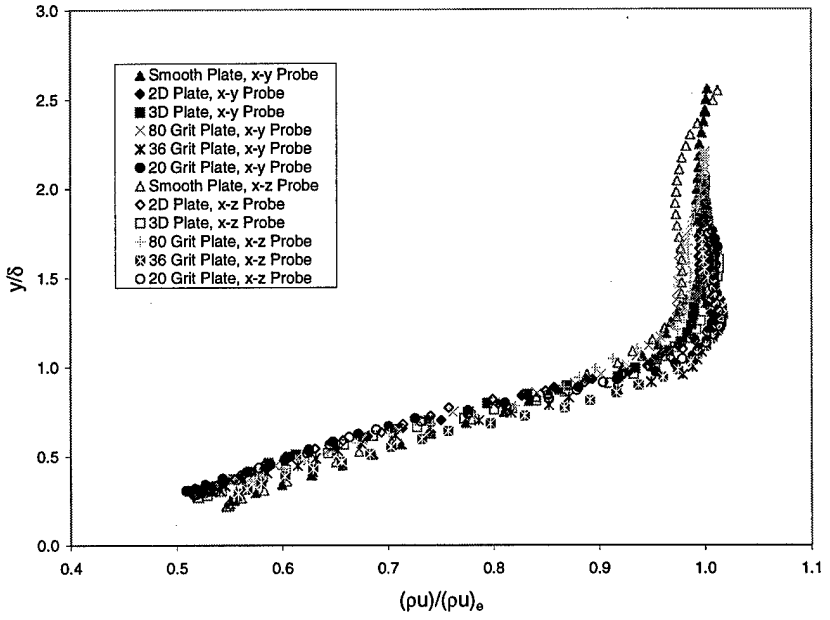

Figure 52. Combined Cross-film $(\rho u)_{bar}$ Profiles

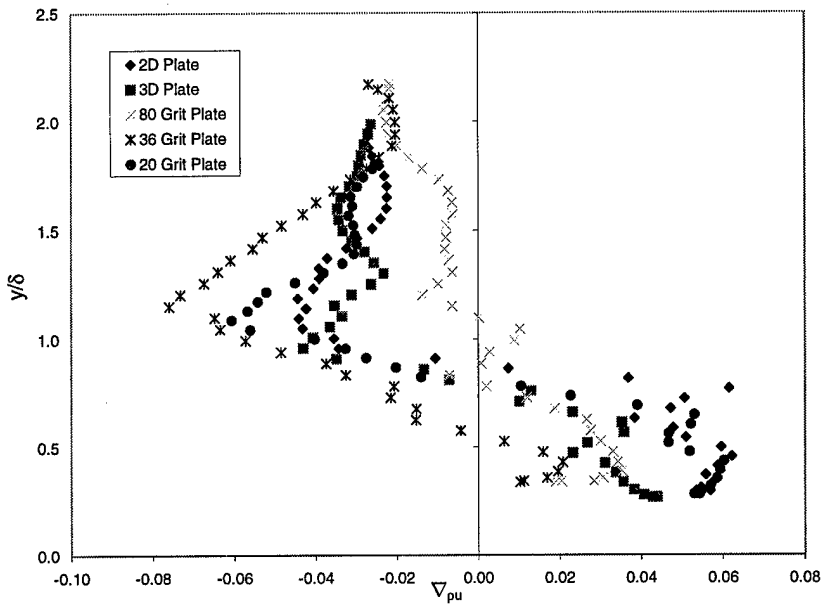

Figure 53. x-z Plane, Cross-Film, Rough Surface $(\rho u)_{bar}$ Profiles Relative to Smooth Plate

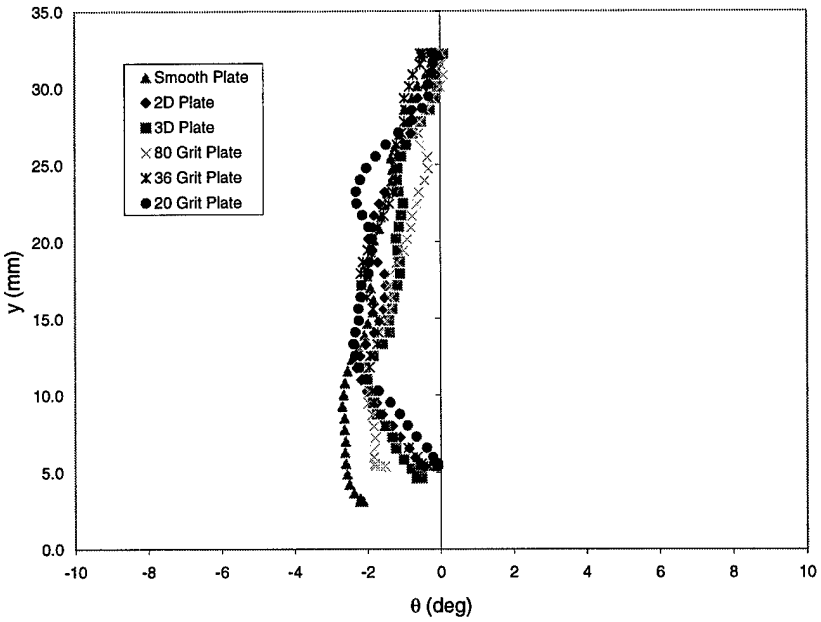

Figure 54. x-y Plane, Cross-Film, Mean Flow Angle

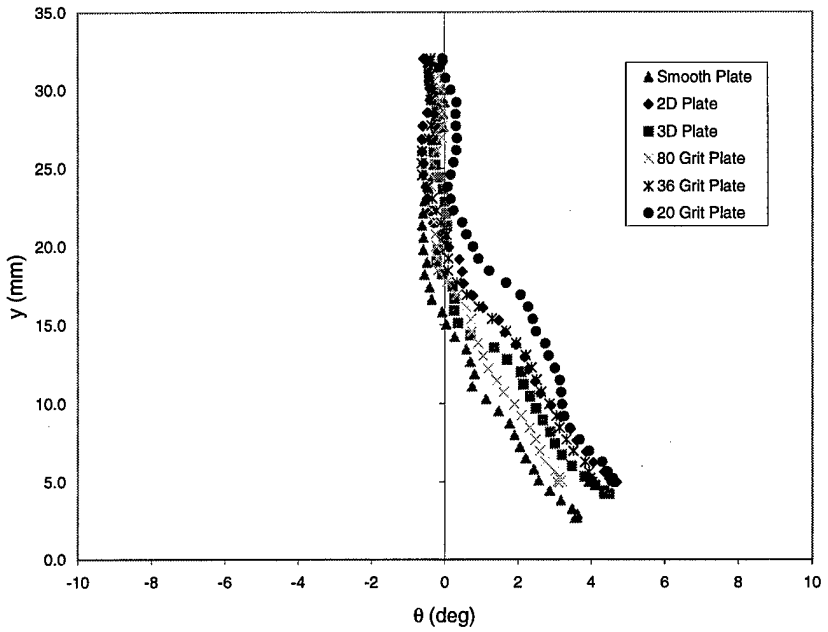

Figure 55. *x-z* Plane, Cross-Film, Mean Flow Angle

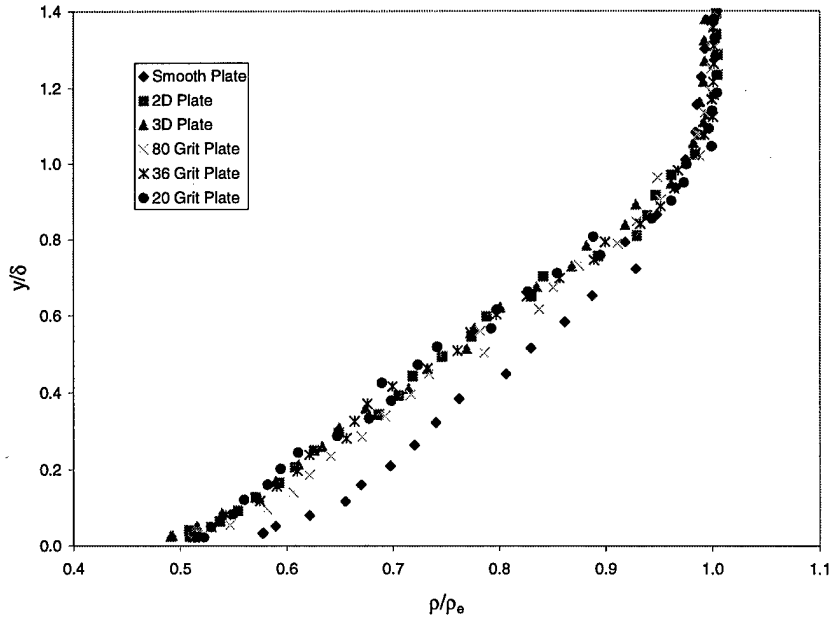

Figure 56. Pitot Probe Density Profiles, Crocco-Busemann Method

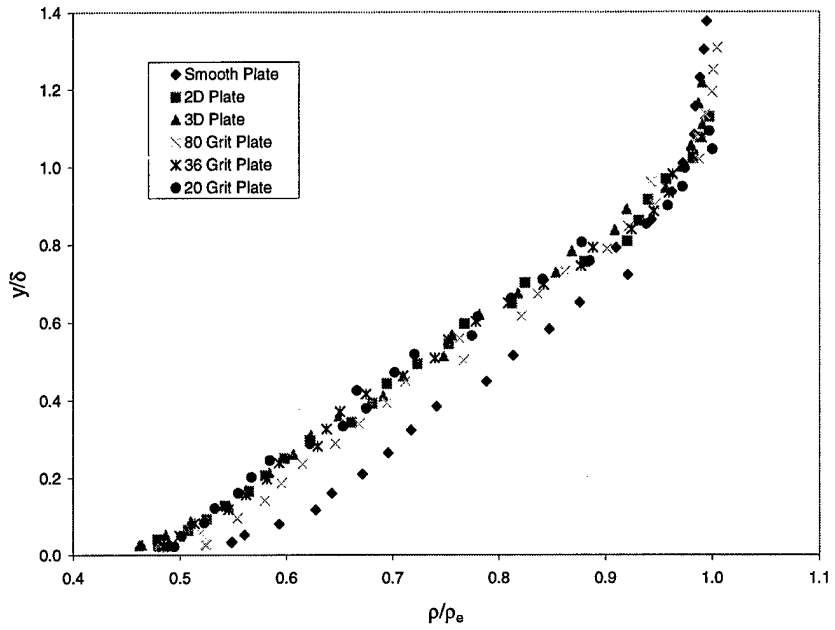

Figure 57. Pitot Probe Density Profiles, Isentropic Method

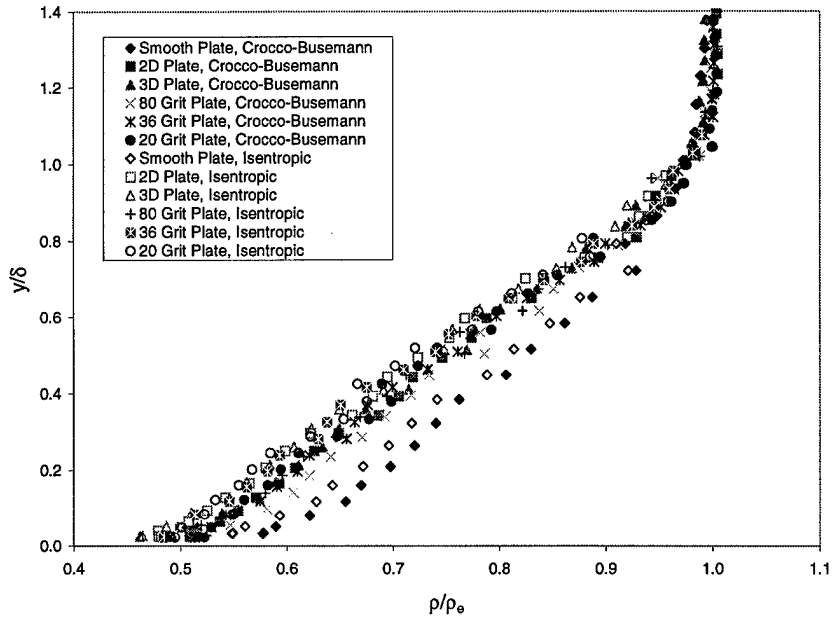

Figure 58. Pitot Probe Density Profiles, Combined Methods

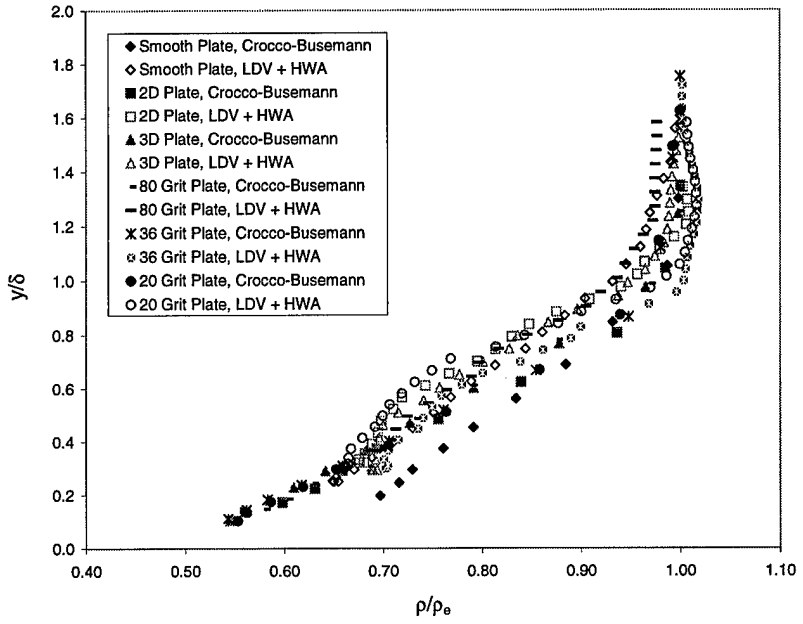

Figure 59. Density Profiles, Combined LDV and HWA

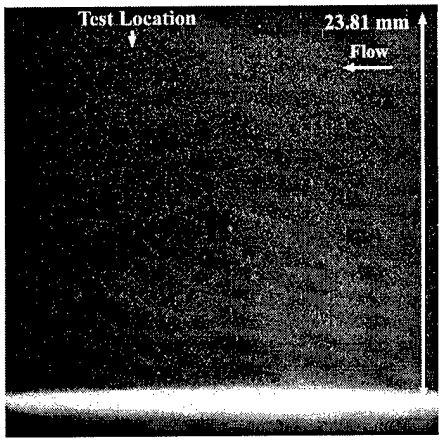

Figure 60. Smooth Plate Laser Sheet Image

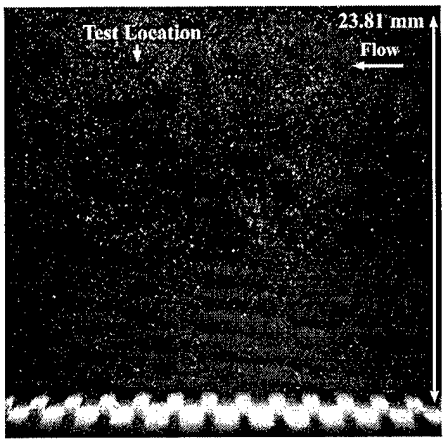

Figure 61. 2D Plate Laser Sheet Image

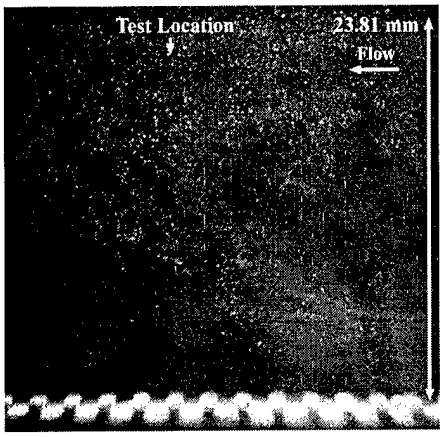

Figure 62. 3D Plate Laser Sheet Image

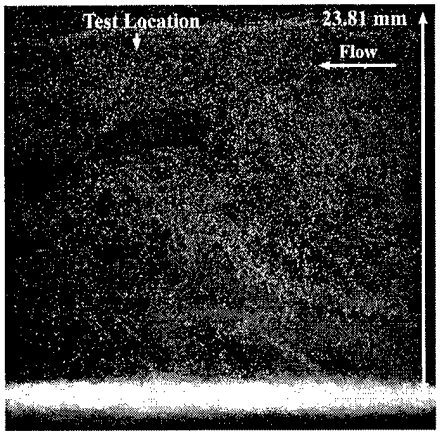

Figure 63. 80 Grit Plate Laser Sheet Image

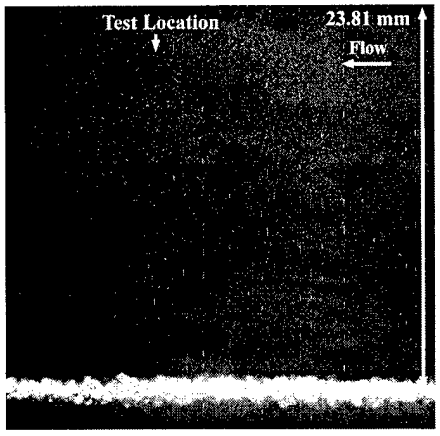

Figure 64. 36 Grit Plate Laser Sheet Image

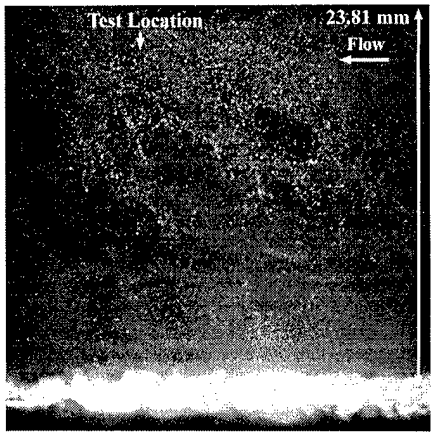

Figure 65. 20 Grit Plate Laser Sheet Image

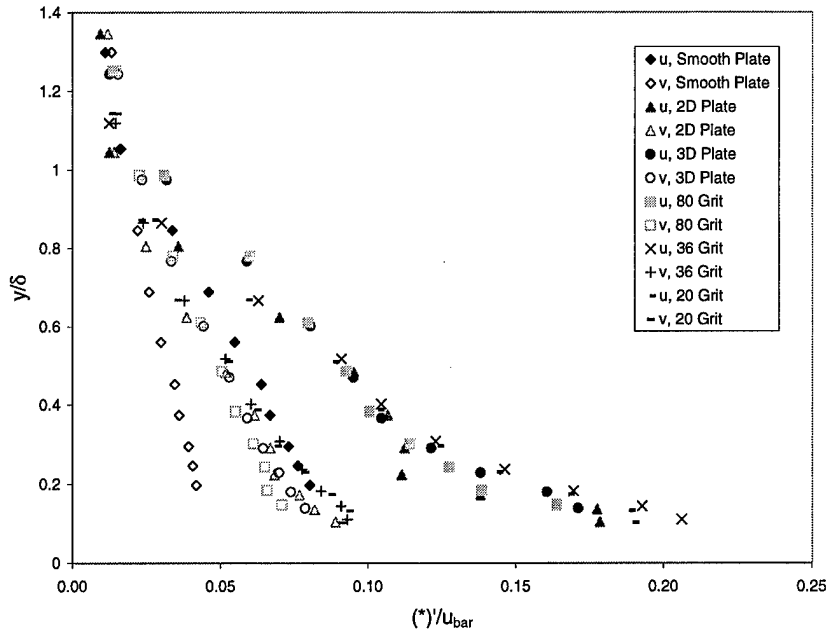

Figure 66. Turbulence Intensity

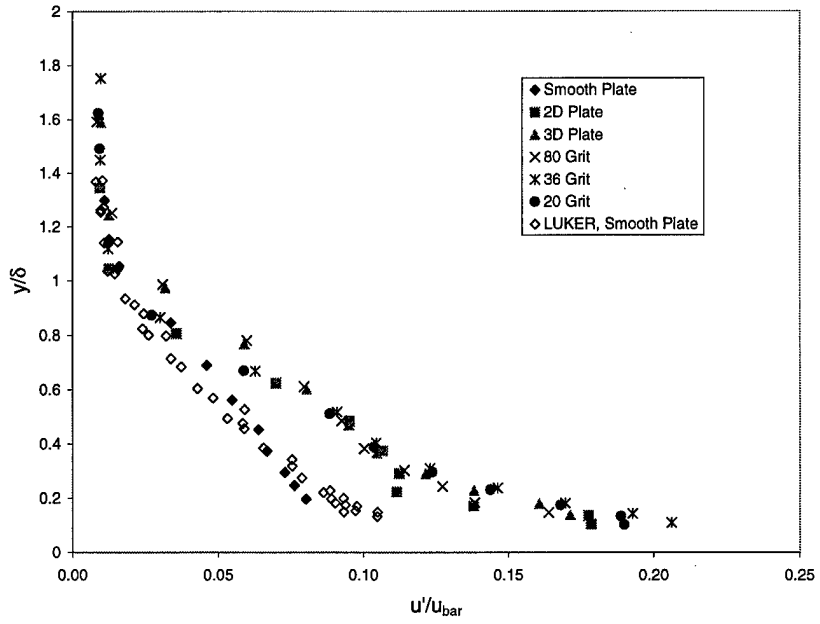

Figure 67. u-Turbulence Intensity

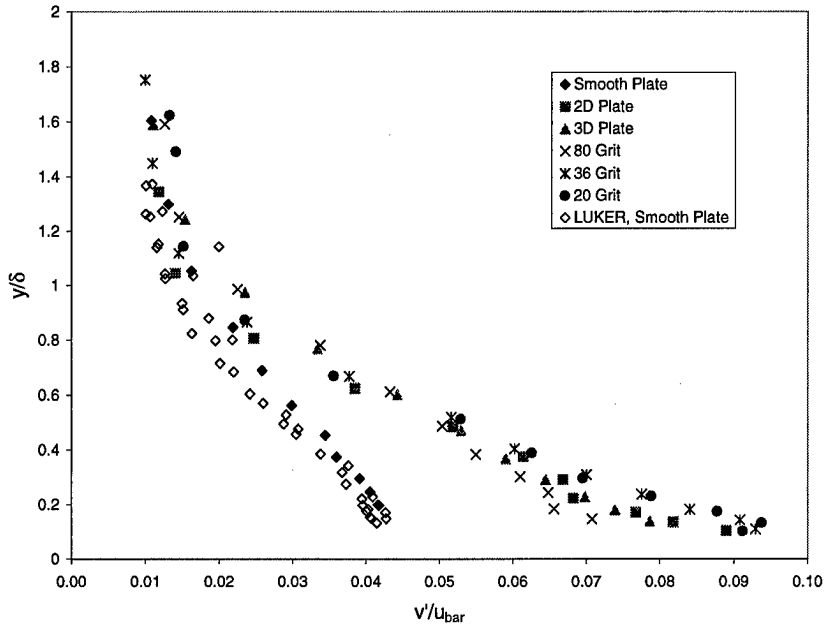

Figure 68. v-Turbulence Intensity

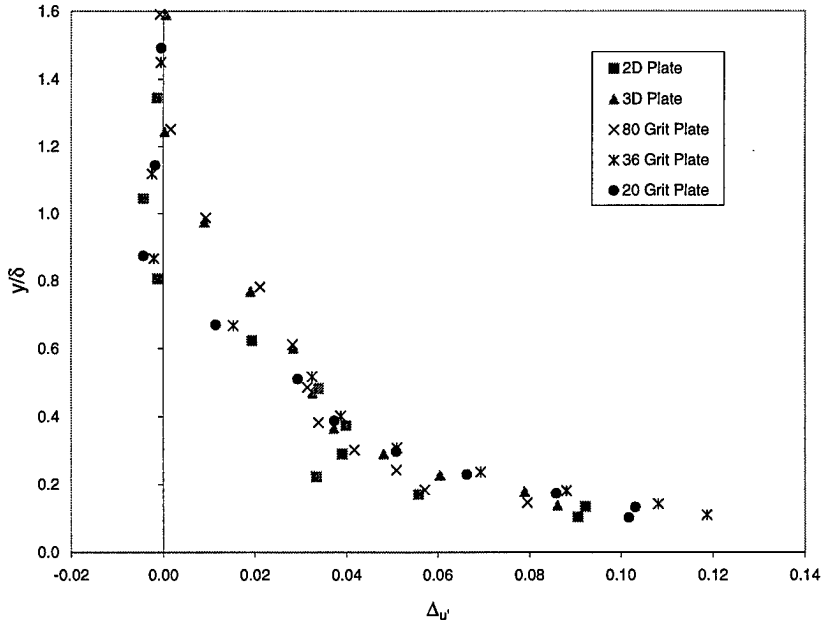

Figure 69. u-Turbulence Intensity Relative to Smooth Plate

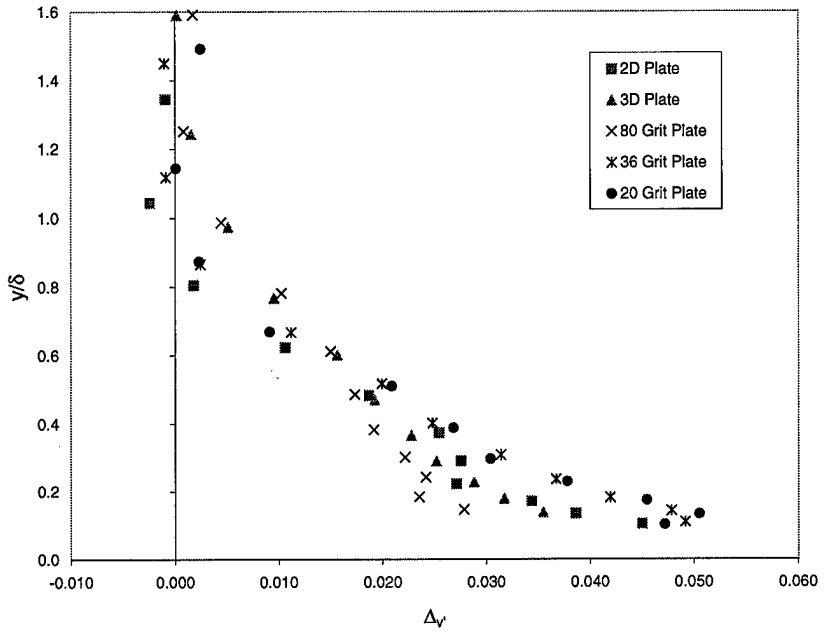

Figure 70. v-Turbulence Intensity Relative to Smooth Plate

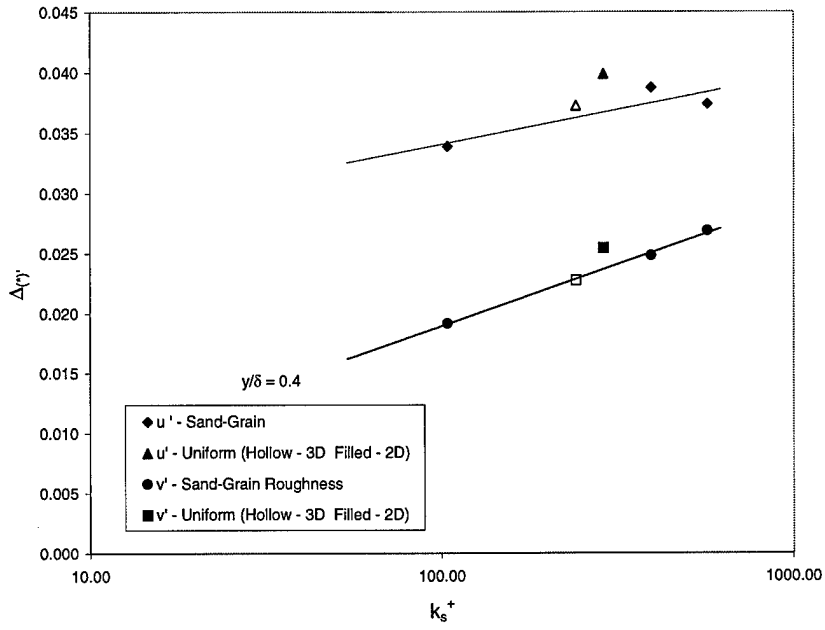

Figure 71. u- and v-Turbulence Intensity Versus Roughness Reynolds Number

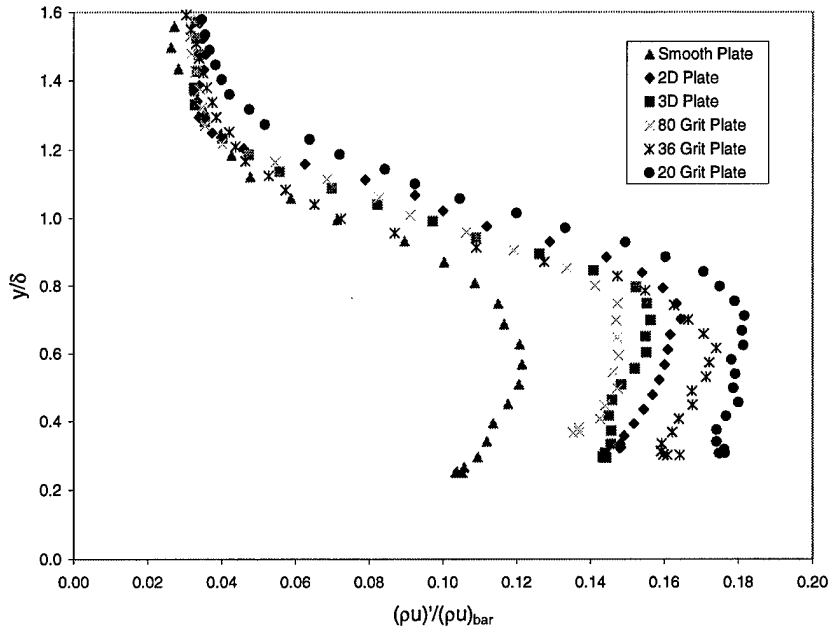

Figure 72. ρu-Turbulence Intensity

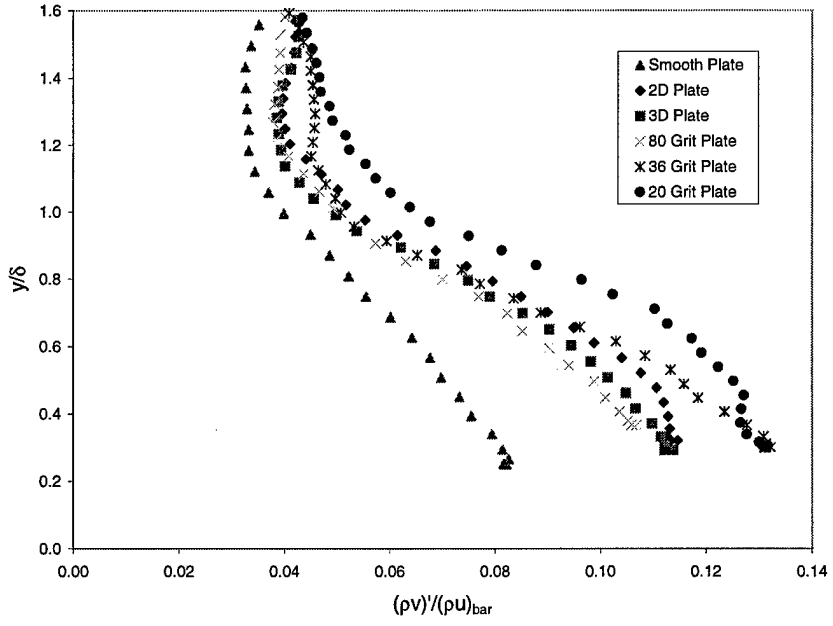

Figure 73. ρv-Turbulence Intensity

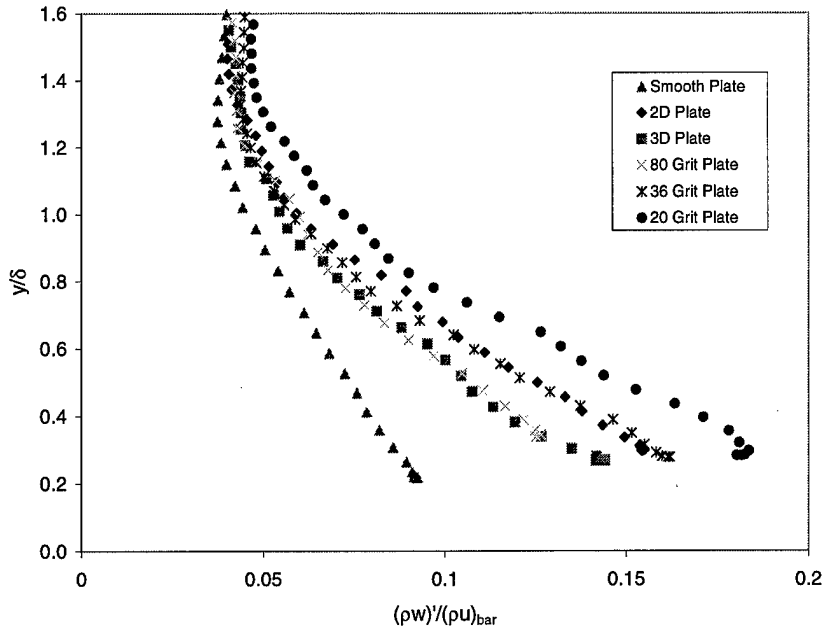

Figure 74. ρw-Turbulence Intensity

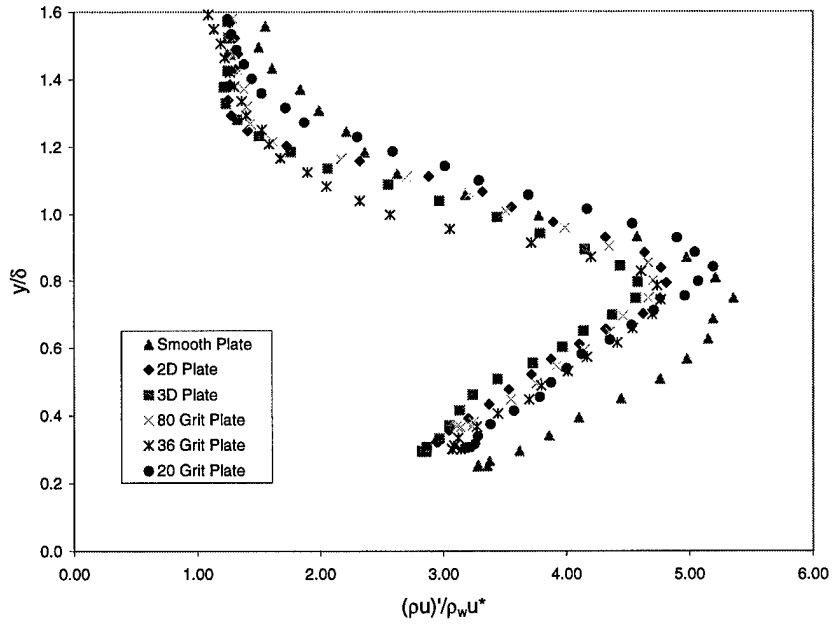

Figure 75. ρu-Turbulence Intensity Scaled by Wall Density and Friction Velocity

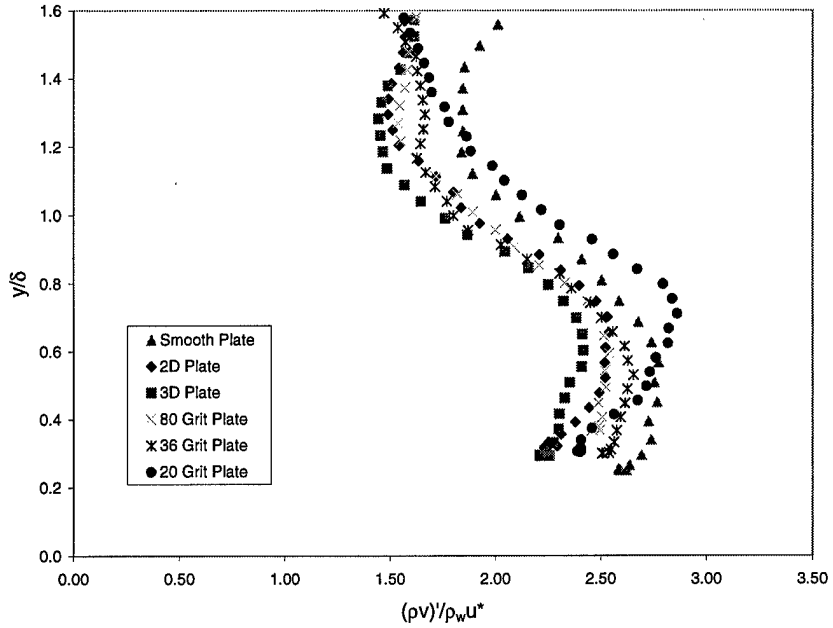

Figure 76. ρv-Turbulence Intensity Scaled by Wall Density and Friction Velocity

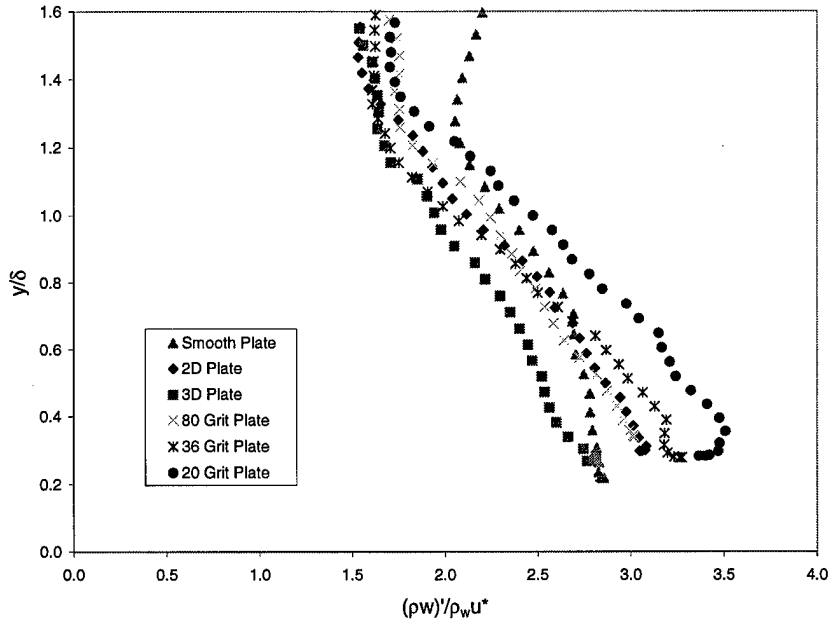

Figure 77. ρw-Turbulence Intensity Scaled by Wall Density and Friction Velocity

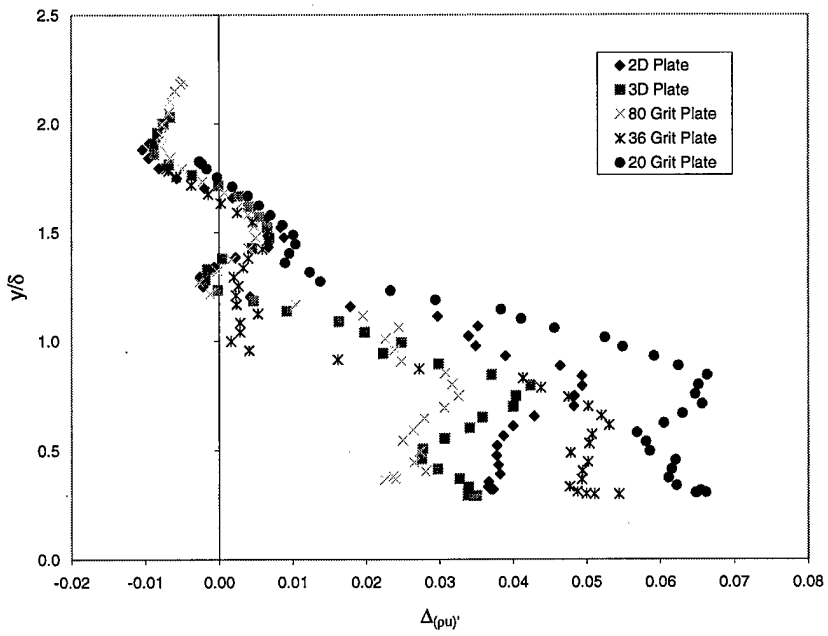

Figure 78. ρu-Turbulence Intensity Relative to Smooth Plate

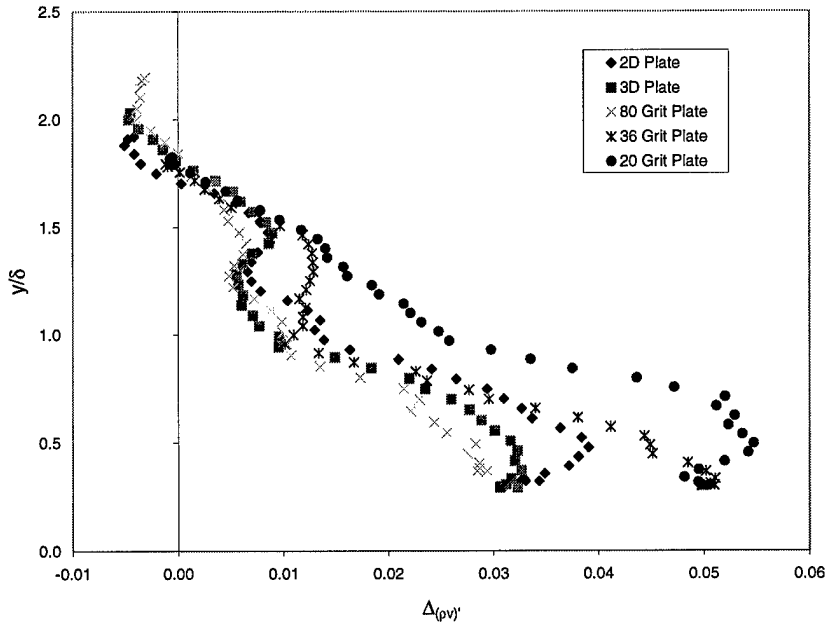

Figure 79. ρv-Turbulence Intensity Relative to Smooth Plate

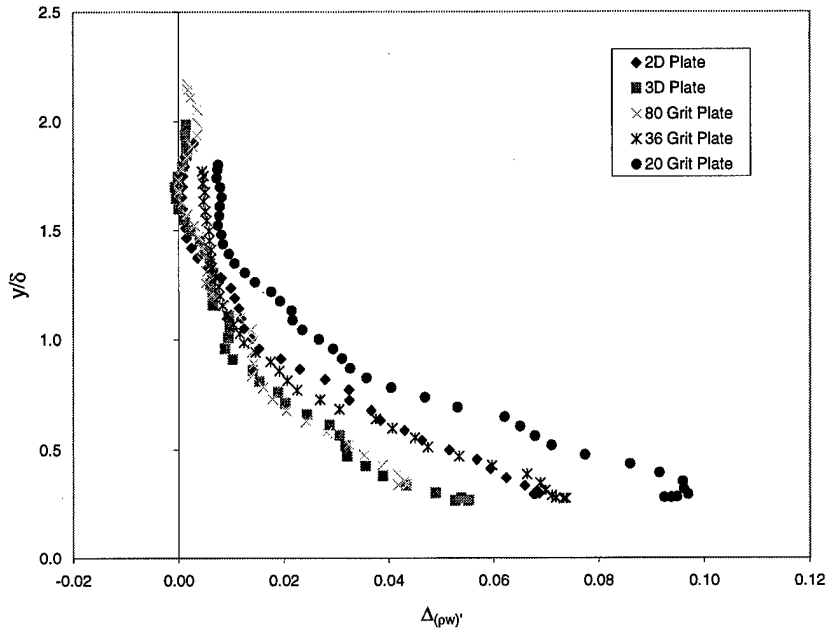

Figure 80. ρw-Turbulence Intensity Relative to Smooth Plate

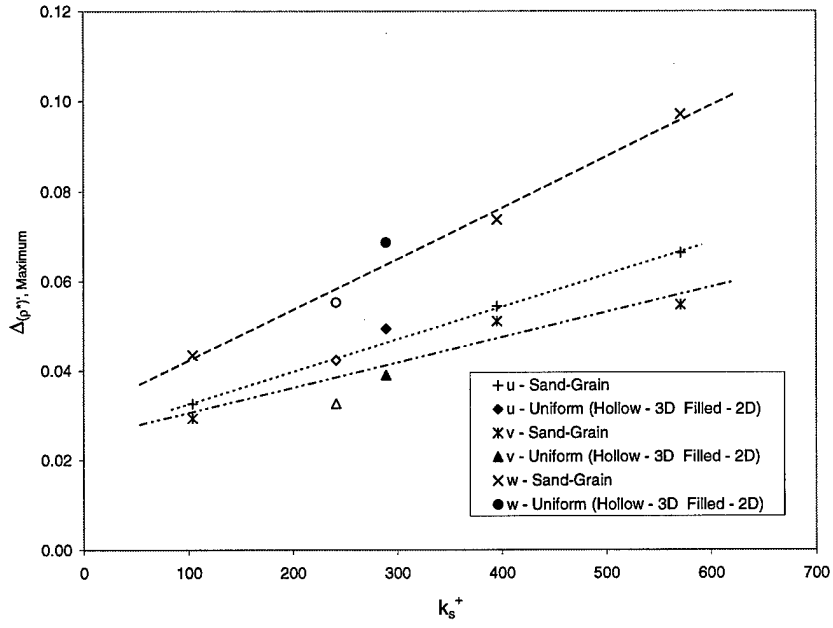

Figure 81. Mass Flux Turbulence Intensity Versus Roughness Reynolds Number

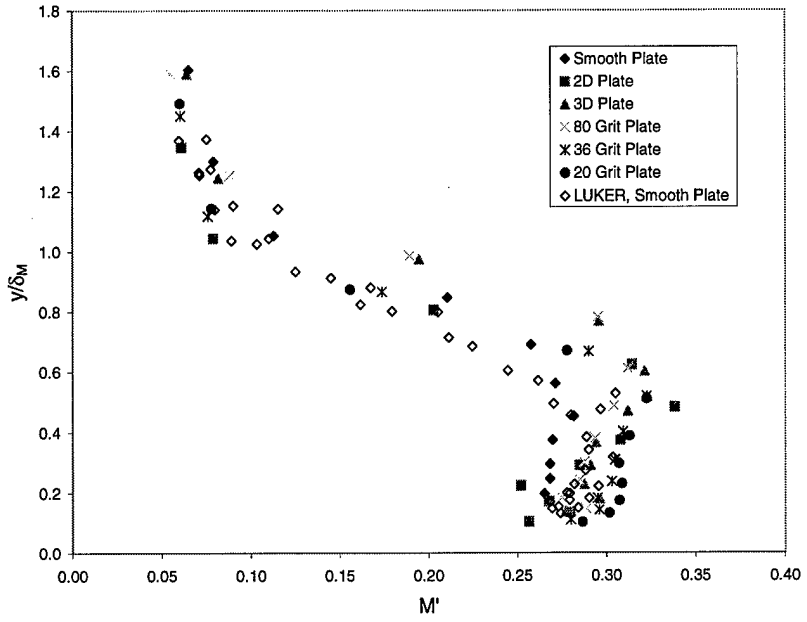

Figure 82. Fluctuating Mach Number

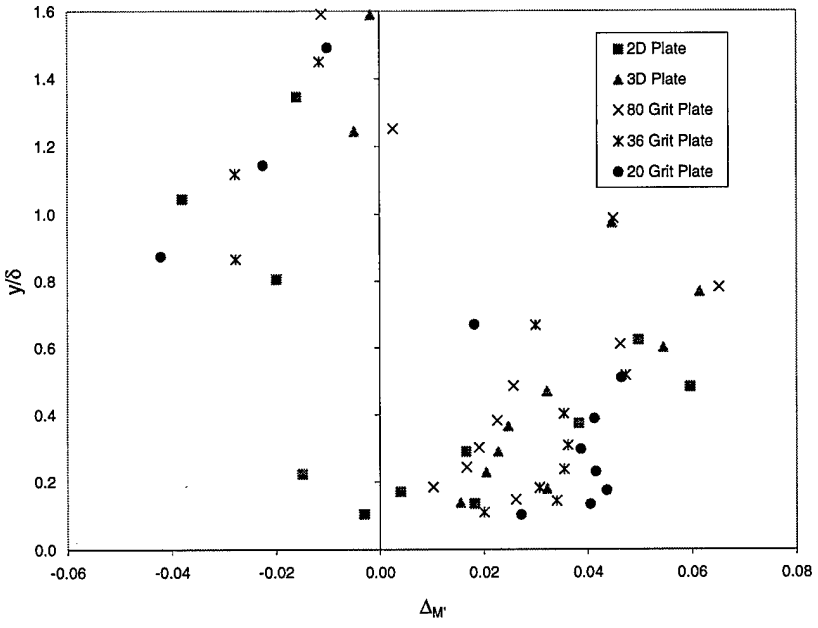

Figure 83. Fluctuating Mach Number Relative to Smooth Plate

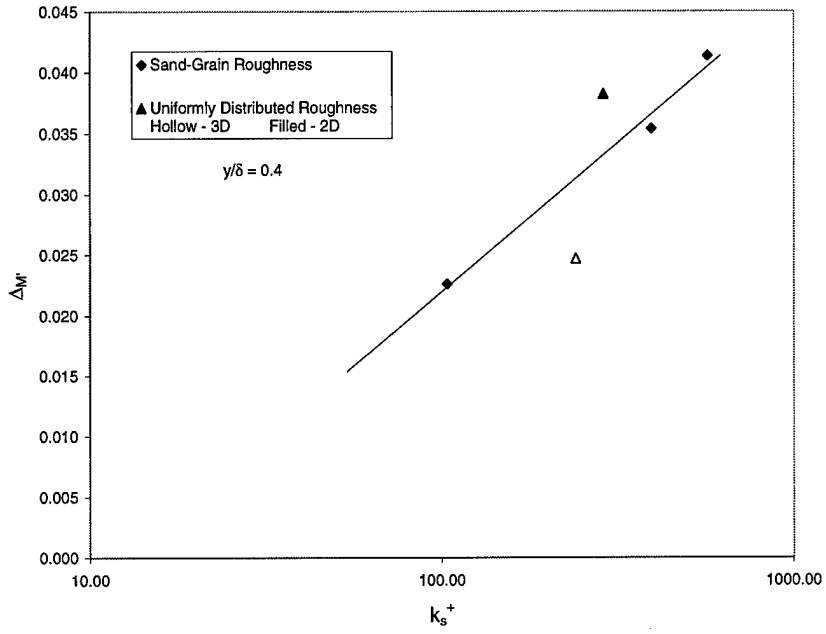

Figure 84. Fluctuating Mach Number Versus Roughness Reynolds Number

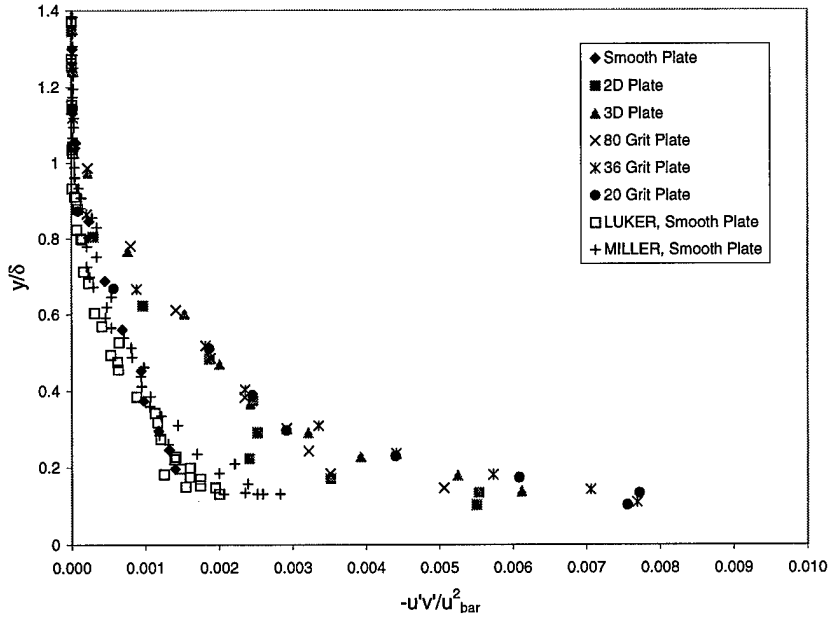

Figure 85. Incompressible Reynolds Shear Stress Scaled by Local Mean Velocity

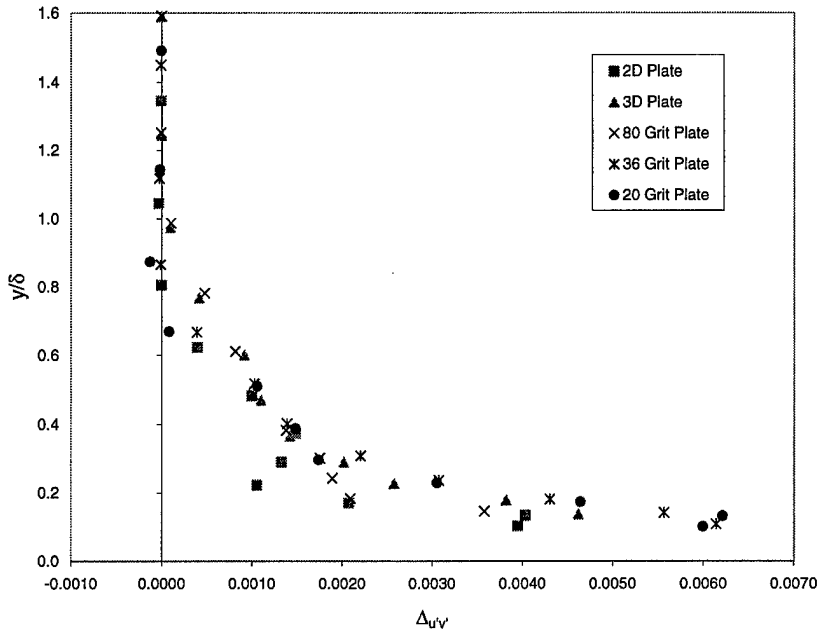

Figure 86. Kinematic Reynolds Shear Stress Relative to Smooth Plate

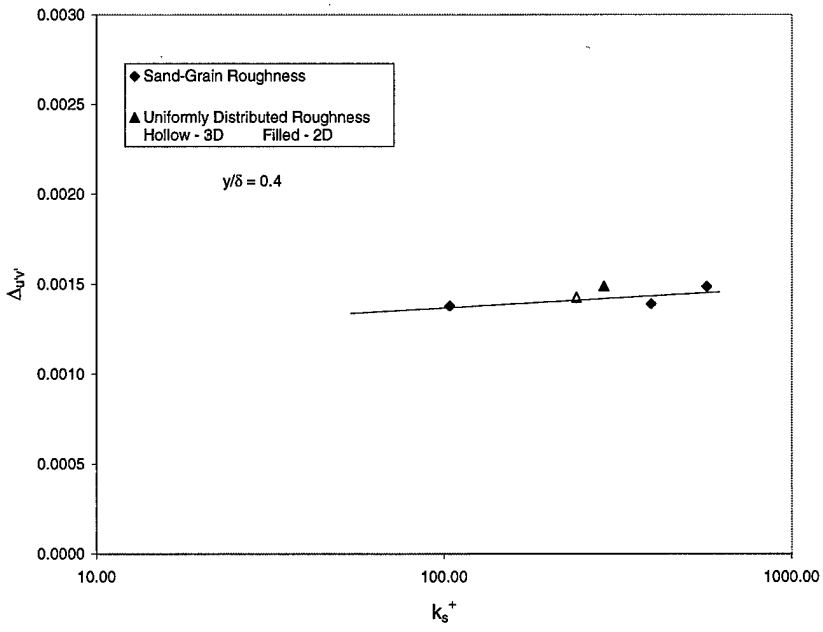

Figure 87. Kinematic Reynolds Shear Stress Versus Roughness Reynolds Number

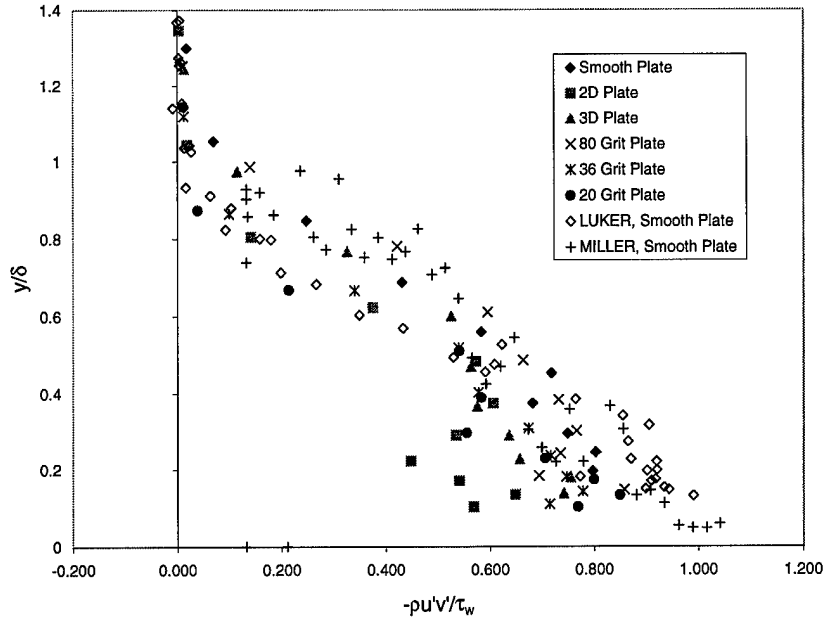

Figure 88. Kinematic Reynolds Shear Stress Scaled by Wall Shear Stress

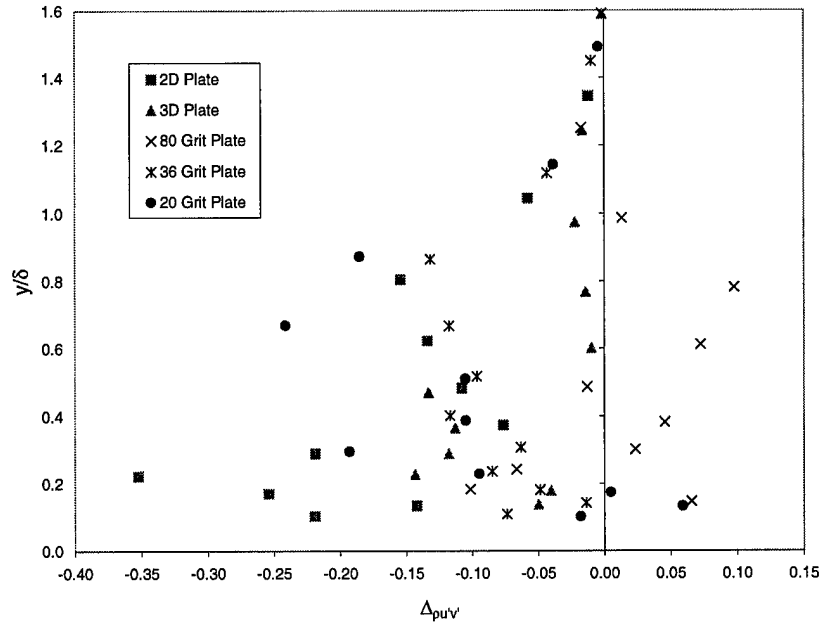

Figure 89. Kinematic Reynolds Shear Stress Relative to Smooth Plate

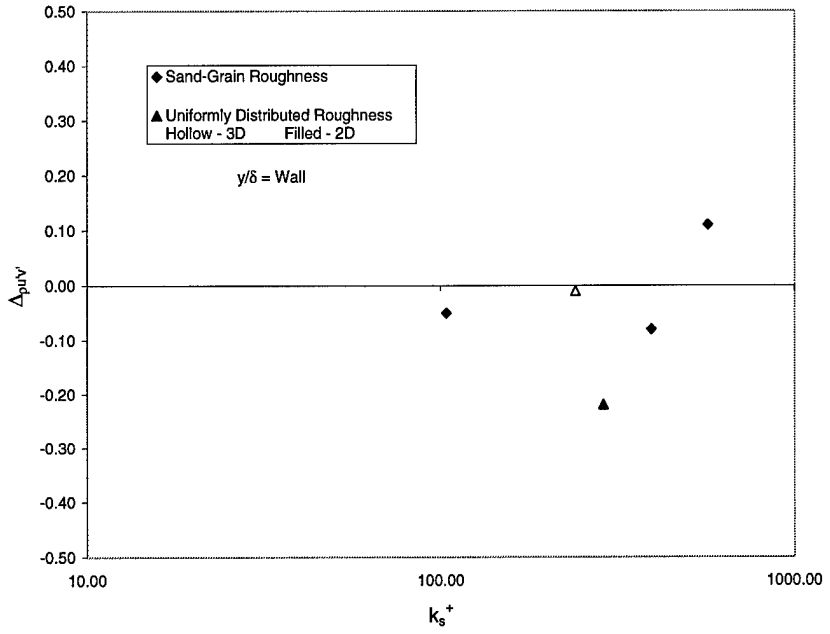

Figure 90. Kinematic Reynolds Shear Stress Versus Roughness Reynolds Number

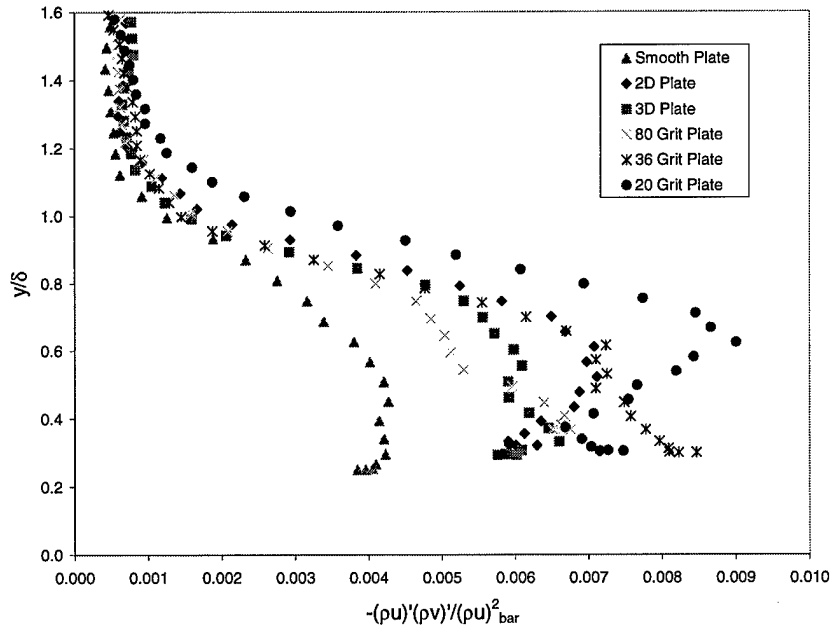

Figure 91. x-y Plane, Cross-Film, Mass Flux Shear Stress

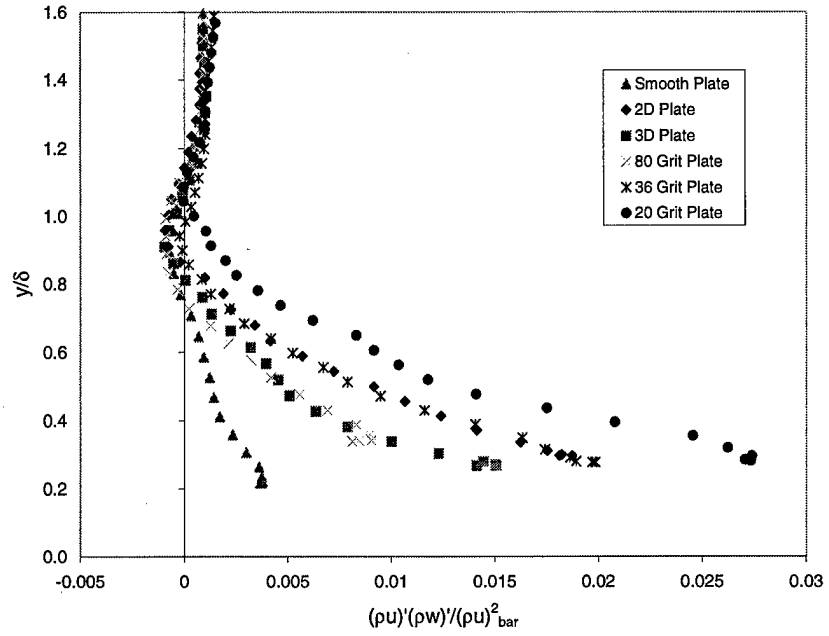

Figure 92. x-z Plane, Cross-Film, Mass Flux Shear Stress

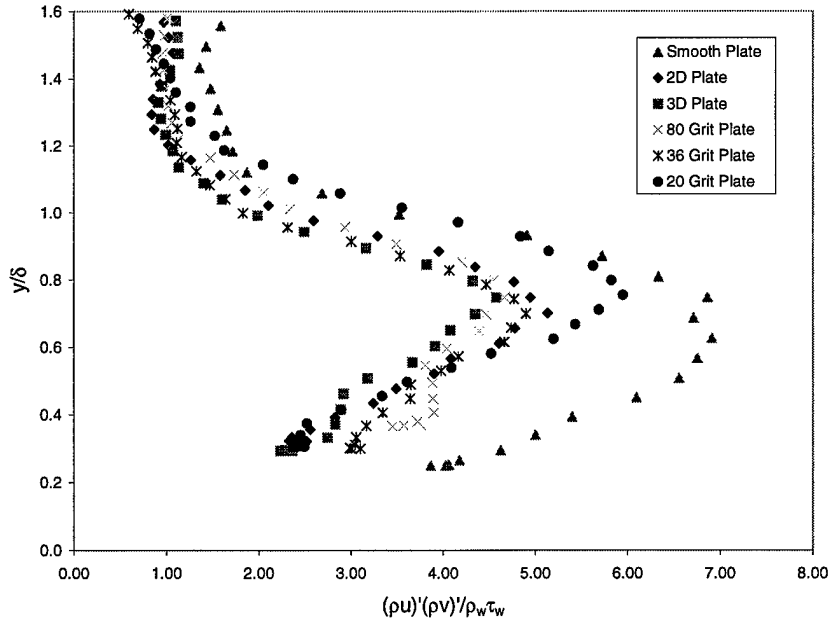

Figure 93. x-y Plane, Cross-Film, Mass Flux Shear Stress Scaled by Wall Density and Shear Stress

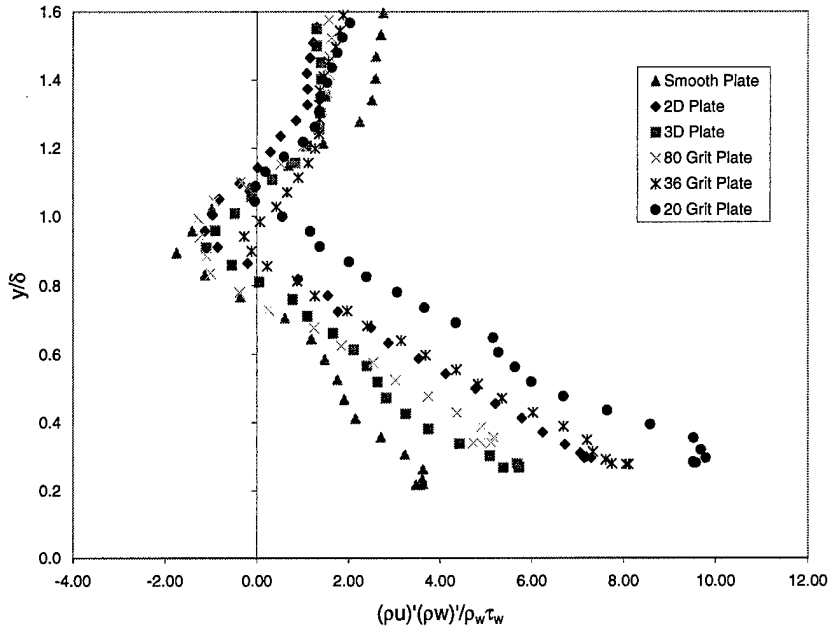

Figure 94. x-z Plane, Cross-Film, Mass Flux Shear Stress Scaled by Wall Density and Shear Stress

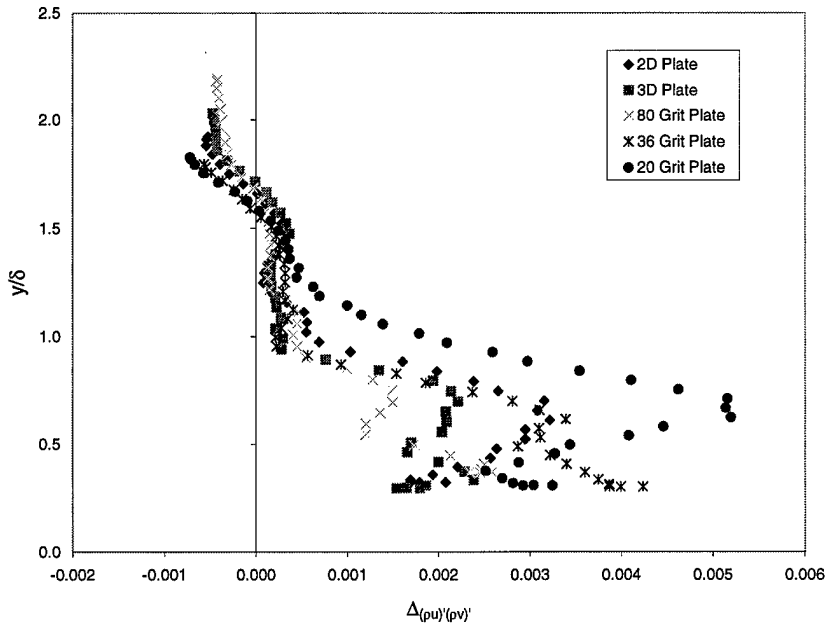

Figure 95. x-y Plane, Cross-Film, Mass Flux Shear Stress Relative to Smooth Plate

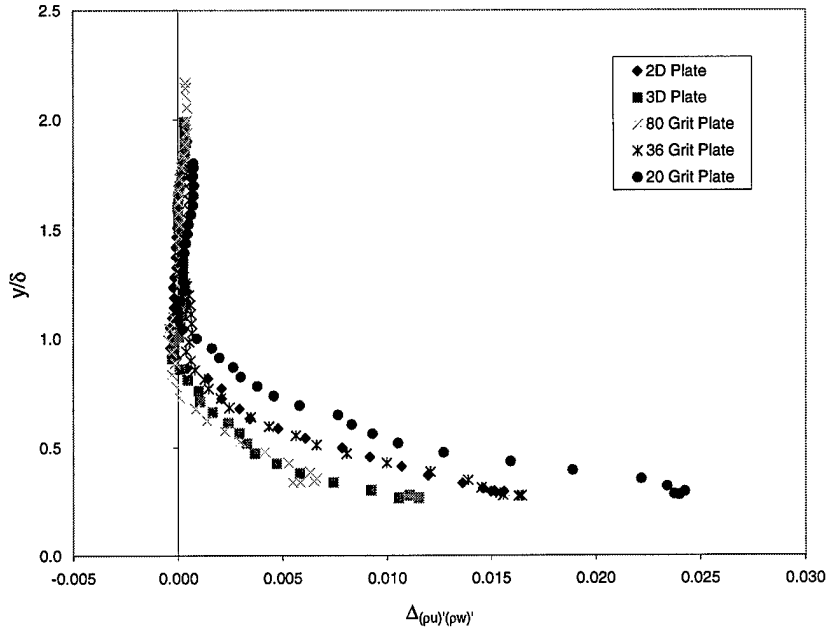

Figure 96. x-z Plane, Cross-Film, Mass Flux Shear Stress Relative to Smooth Plate

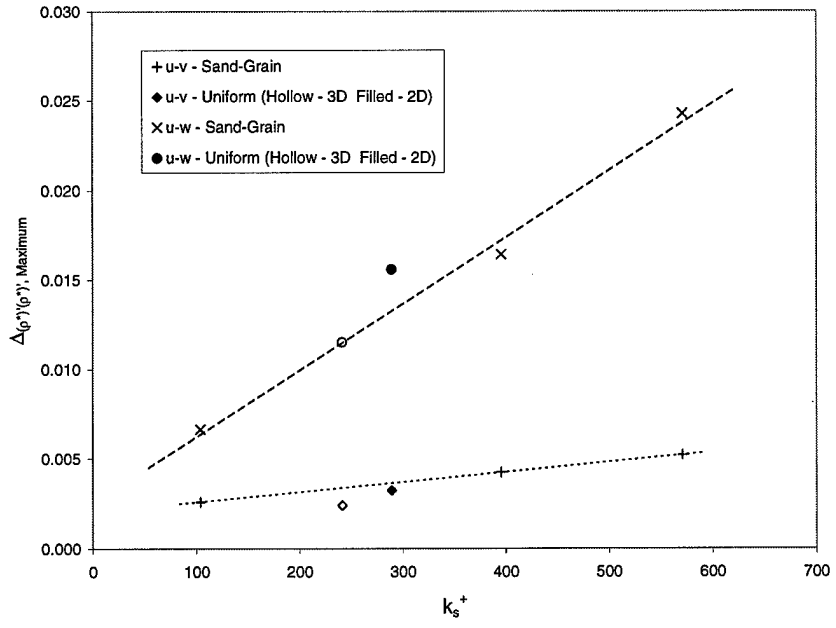

Figure 97. Cross-Film, Mass Flux Shear Stress Versus Roughness Reynolds Number

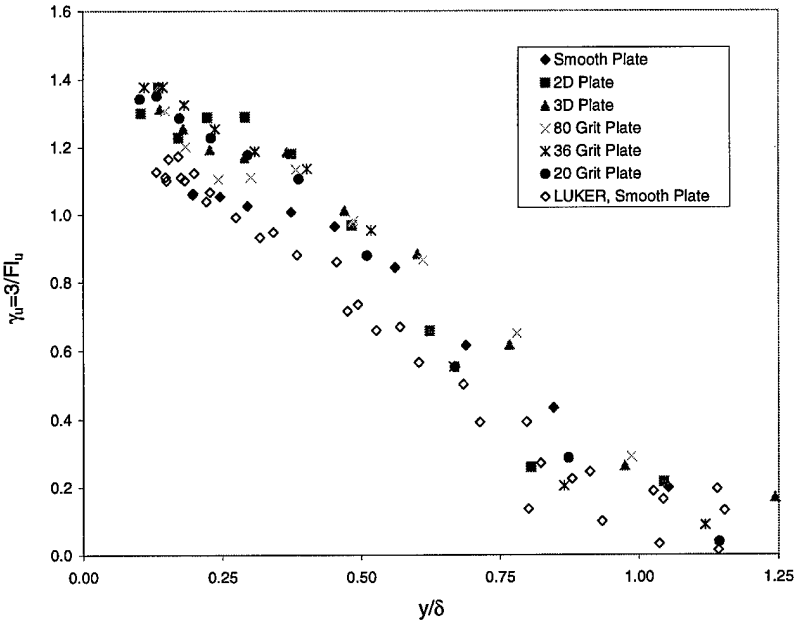

Figure 98. Intermittency Function

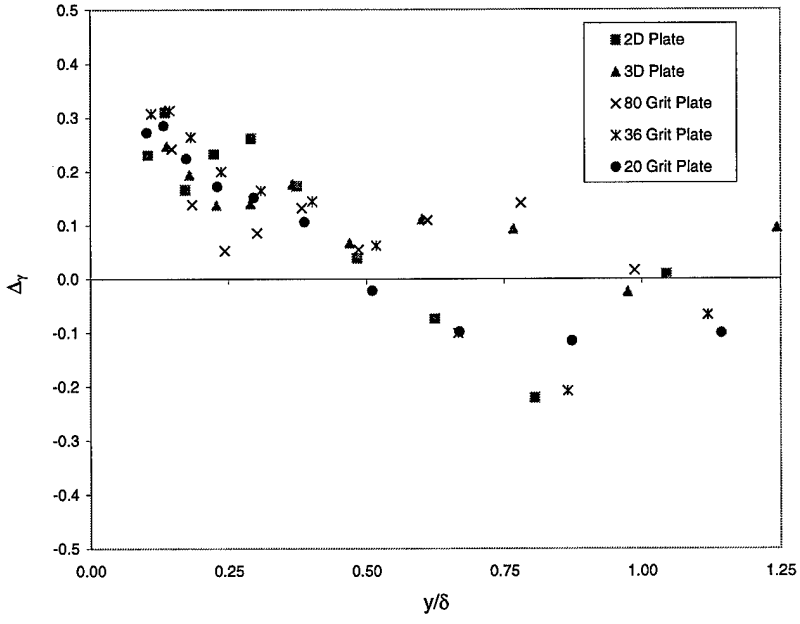

Figure 99. Intermittency Function Relative to Smooth Plate

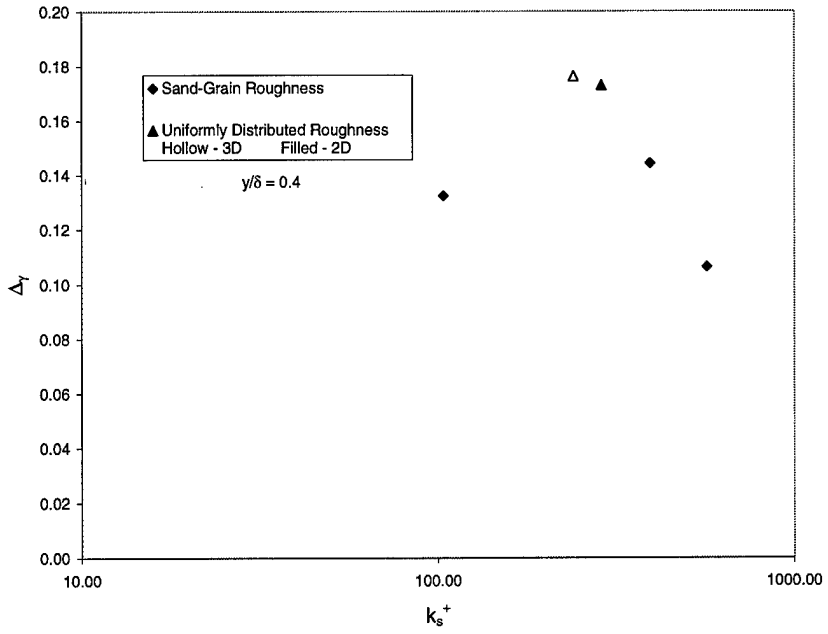

Figure 100. Intermittency Versus Roughness Reynolds Number

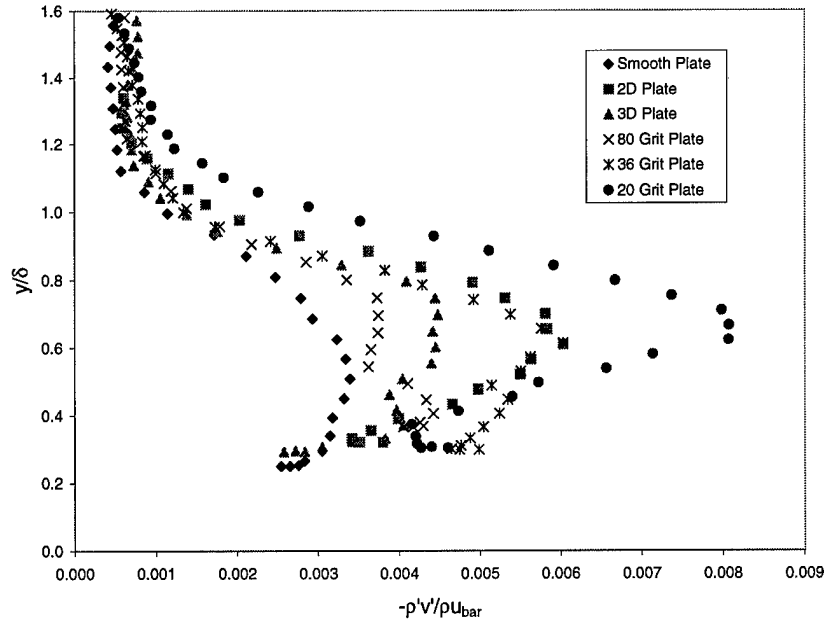

Figure 101. Second Order Density - Velocity Correlation

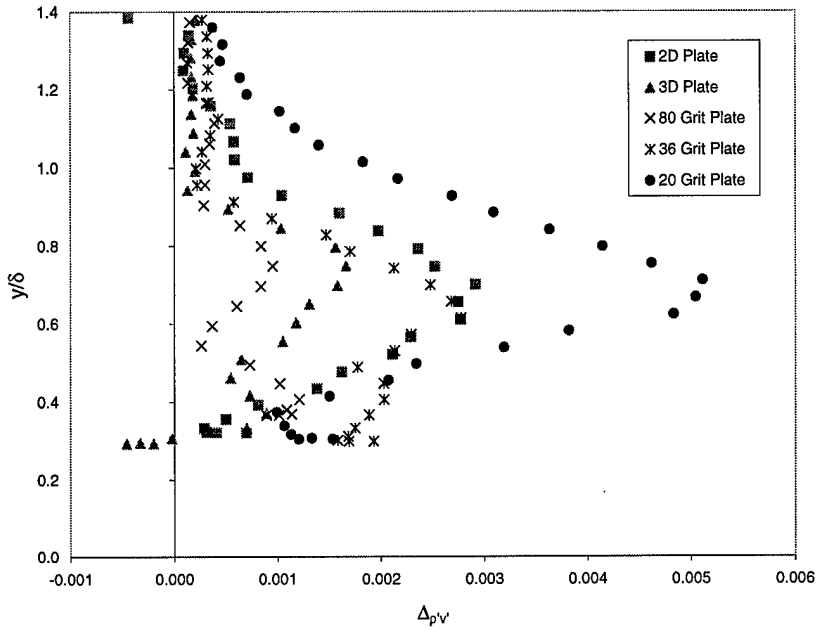

Figure 102. Second Order Density - Velocity Correlation Relative to Smooth Plate

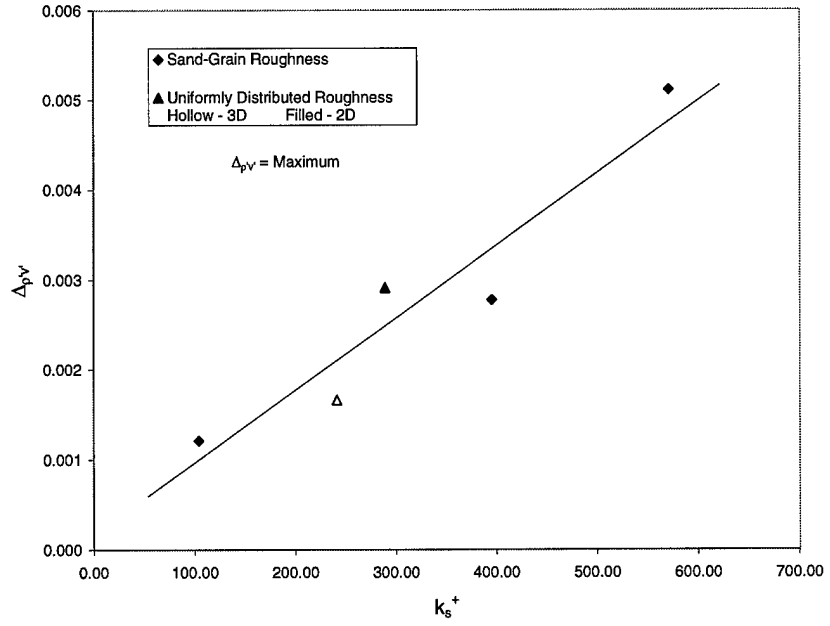

Figure 103. Density - Velocity Correlation Versus Roughness Reynolds Number

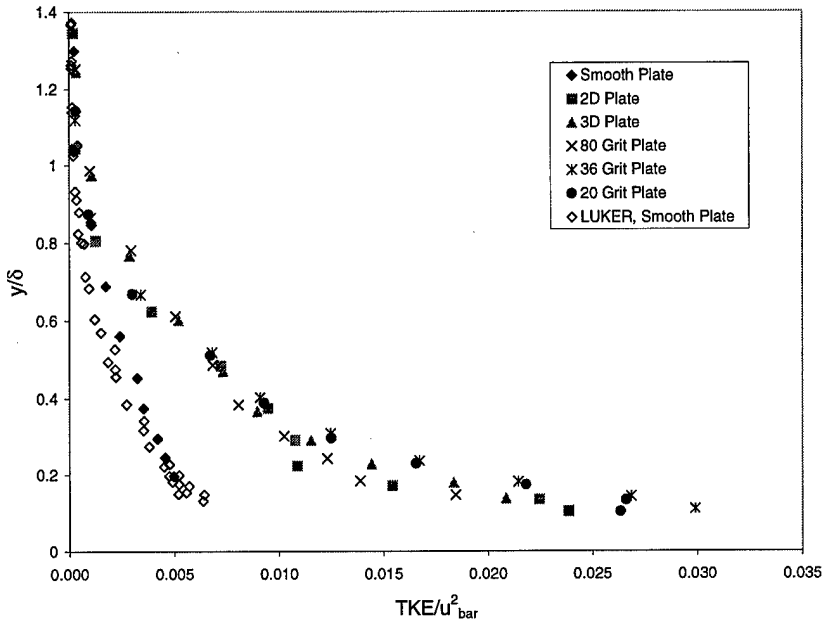

Figure 104. Turbulent Kinetic Energy

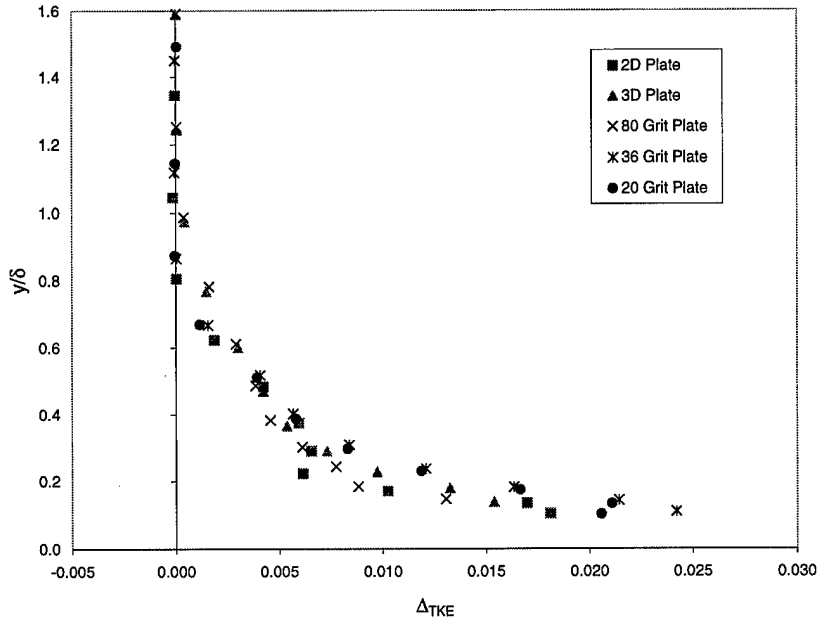

Figure 105. Turbulent Kinetic Energy Relative to Smooth Plate

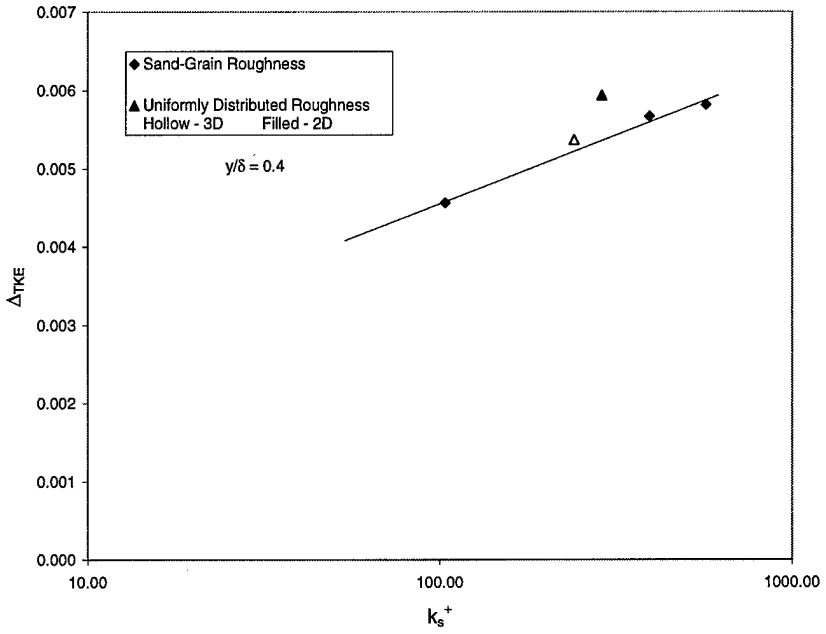

Figure 106. Turbulent Kinetic Energy Versus Roughness Reynolds Number

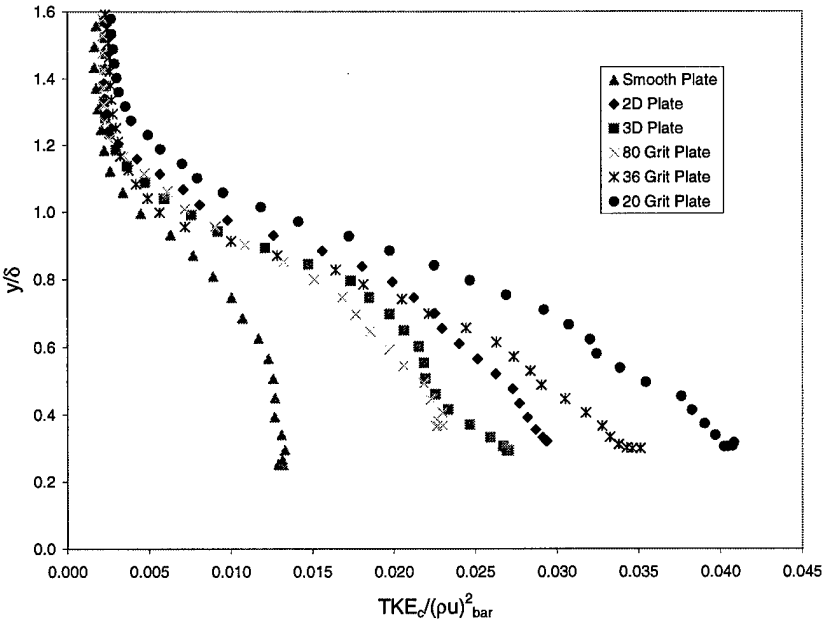

Figure 107. Compressible Turbulent Kinetic Energy

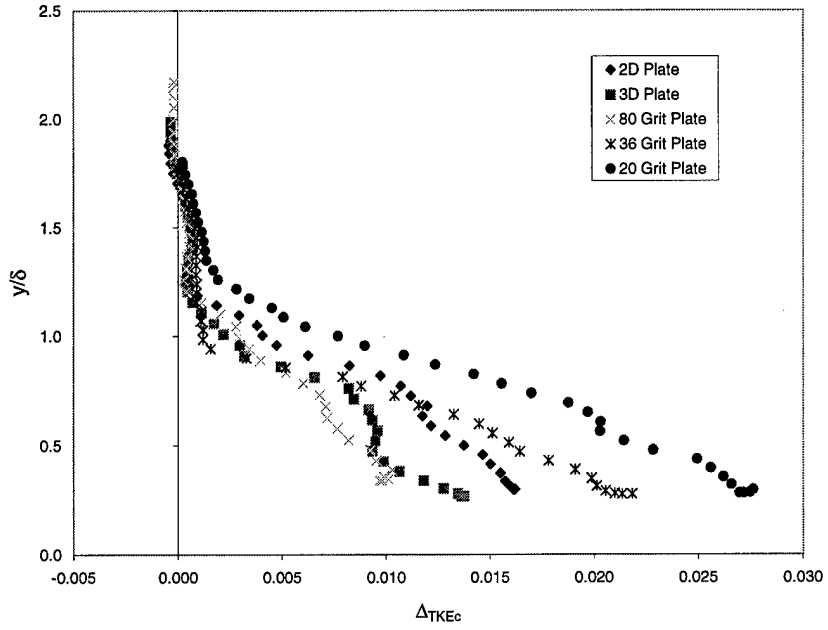

Figure 108. Compressible Turbulent Kinetic Energy Relative to Smooth Plate

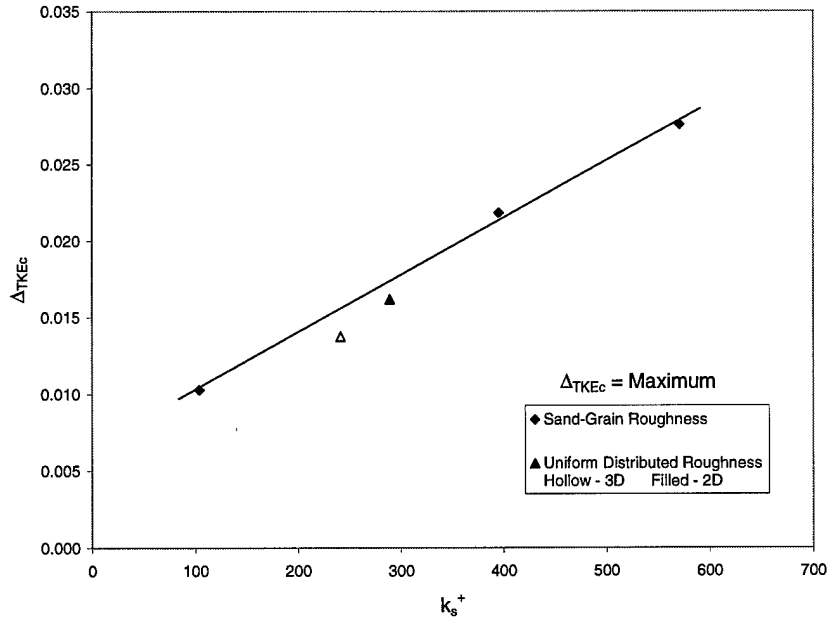

Figure 109. Compressible Turbulent Kinetic Energy Versus Roughness Reynolds Number

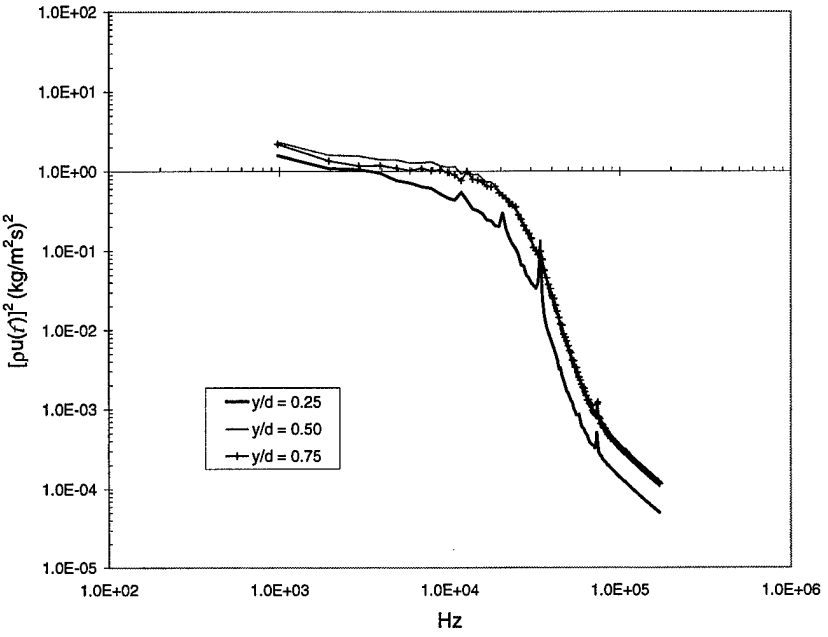

Figure 110. Smooth Plate Power Spectra

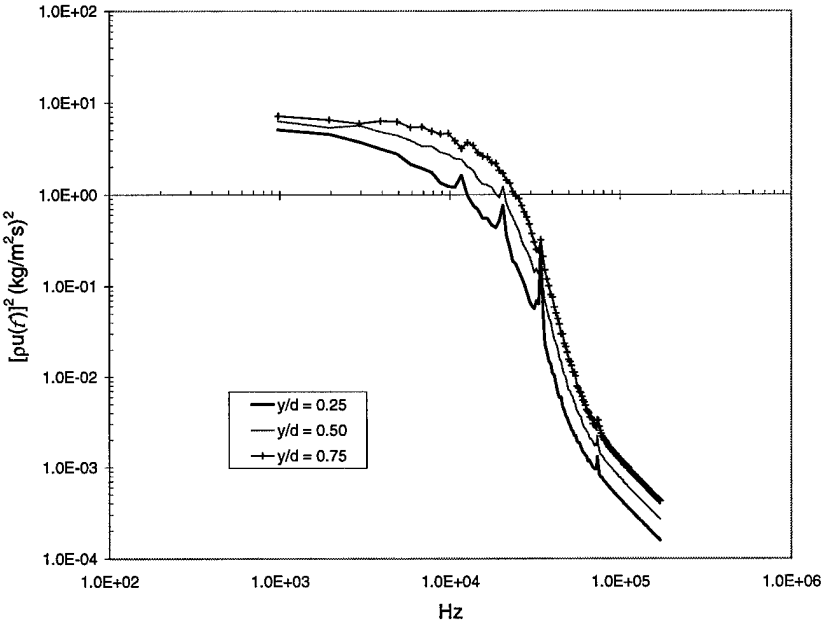

Figure 111. 2D Plate Power Spectra

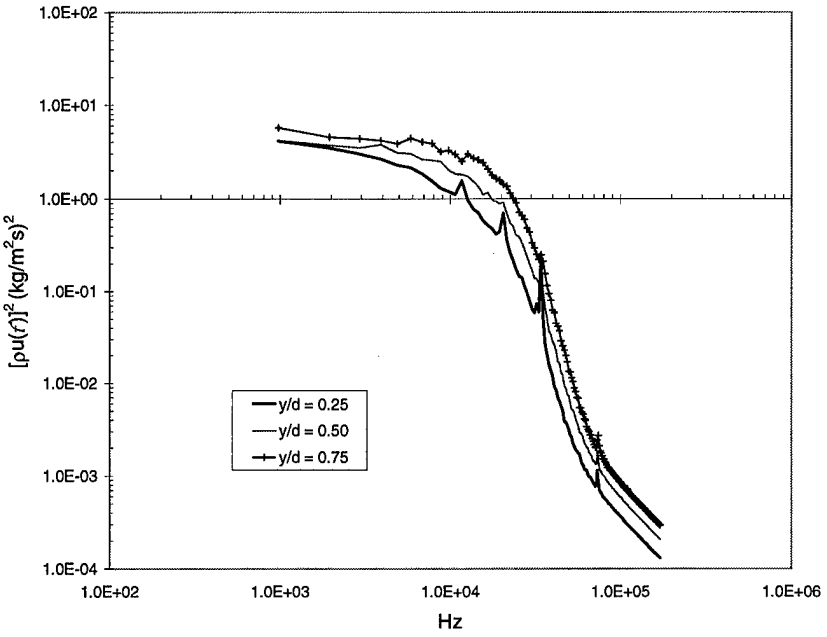

Figure 112. 3D Plate Power Spectra

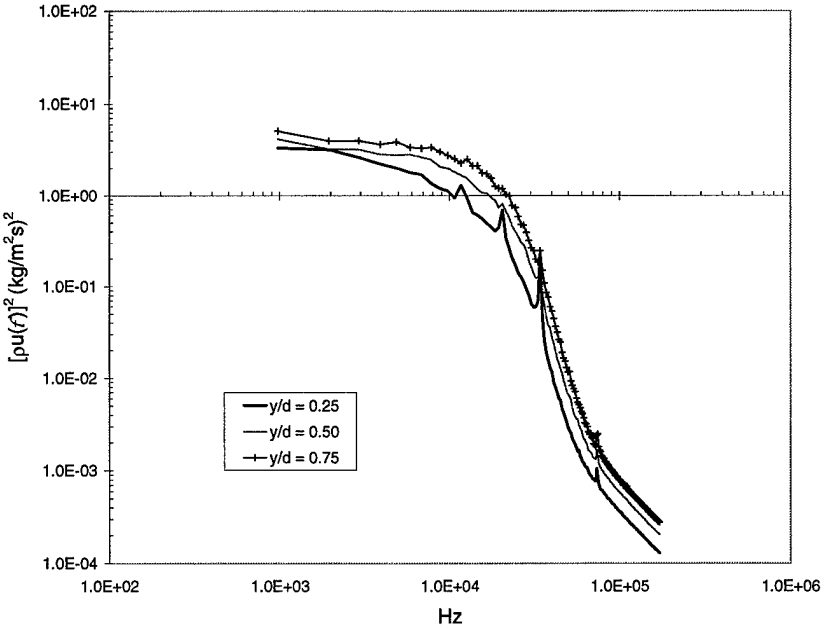

Figure 113. 80 Grit Plate Power Spectra

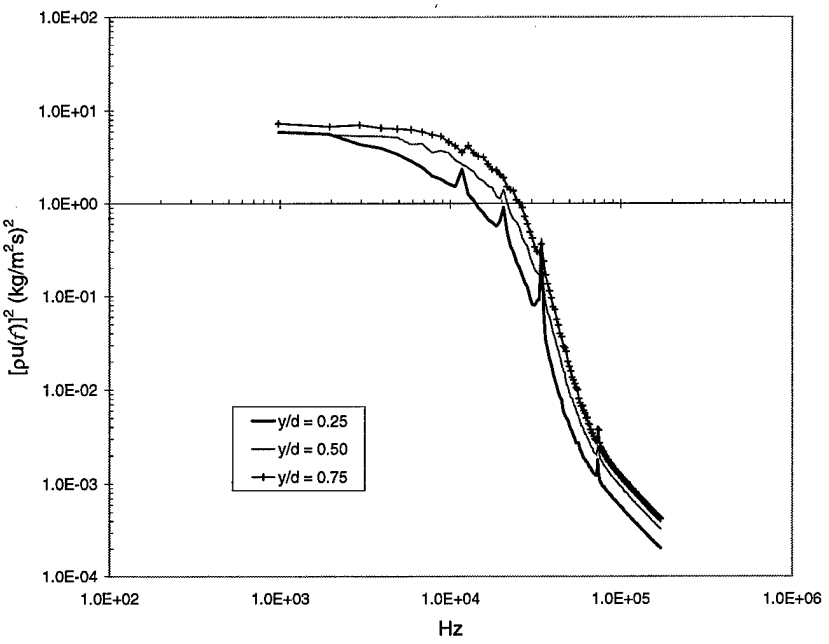

Figure 114. 36 Grit Plate Power Spectra

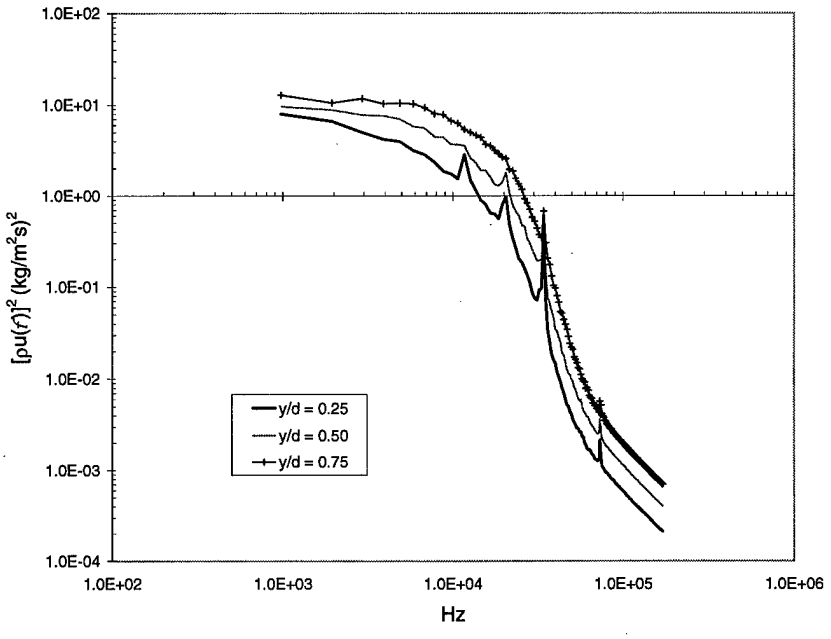

Figure 115. 20 Grit Plate Power Spectra

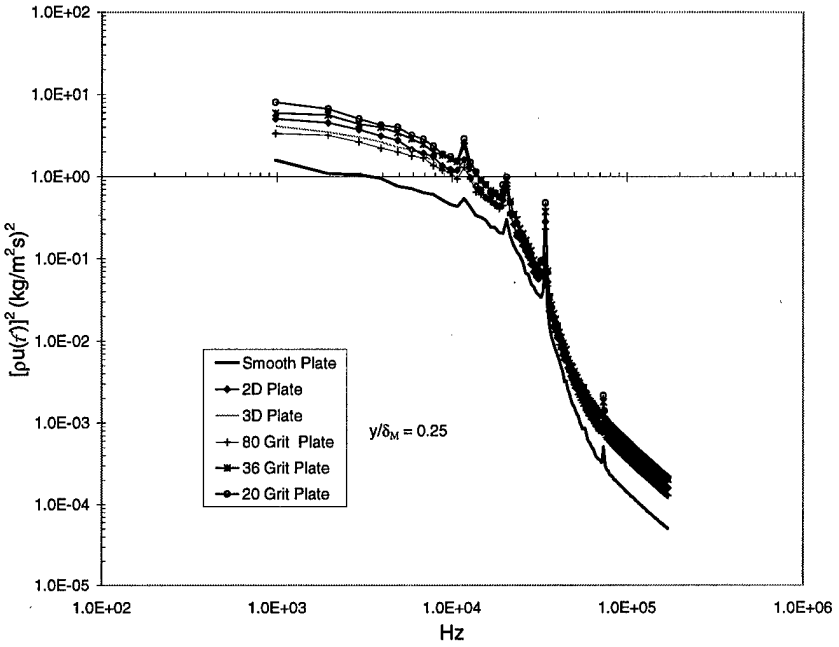

Figure 116. Power Spectra, $y/\delta_M = 0.25$

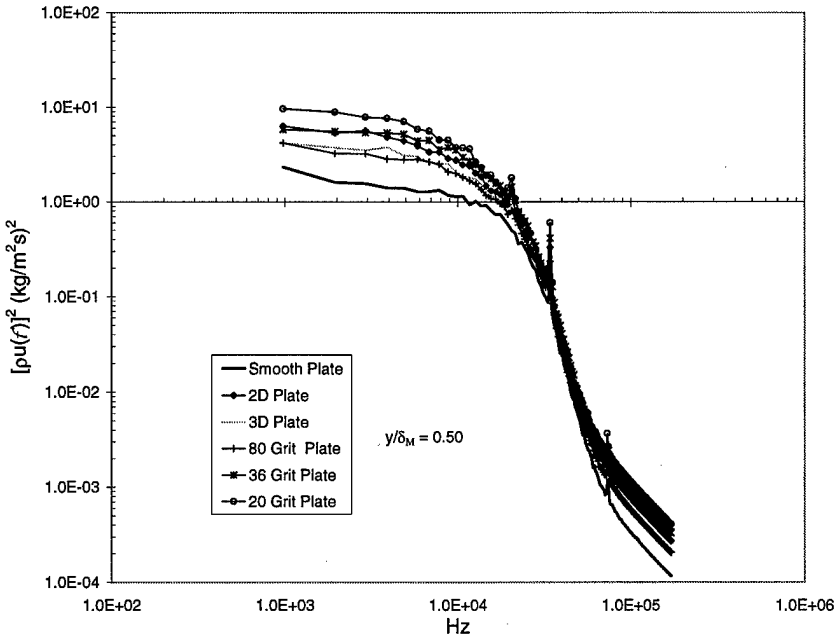

Figure 117. Power Spectra, $y/\delta_M = 0.50$

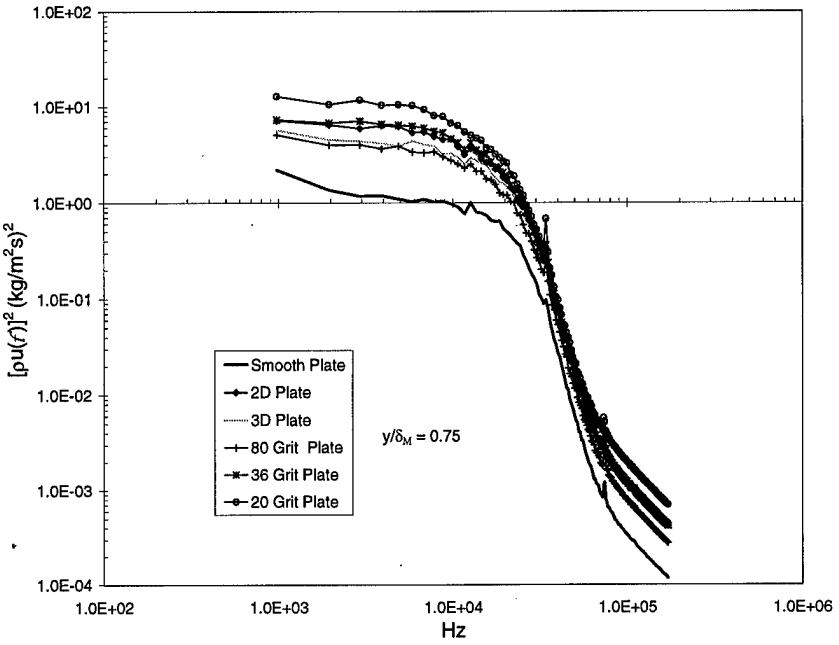

Figure 118. Power Spectra, $y/\delta_M = 0.75$

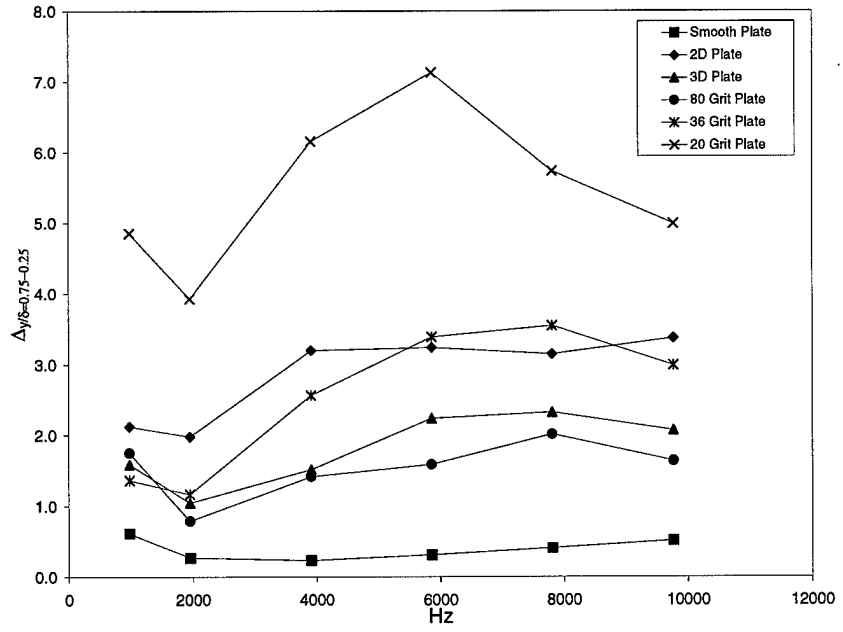

Figure 119. Power Spectra Difference, $\left(\frac{y}{\delta}\right)_{0.75} - \left(\frac{y}{\delta}\right)_{0.25}$

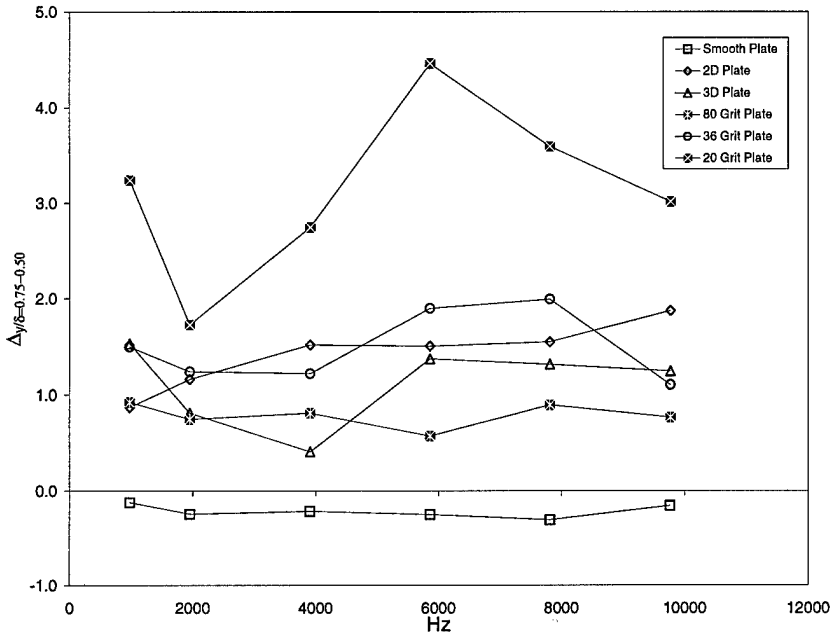

Figure 120. Power Spectra Difference, $\left(\frac{y}{\delta}\right)_{0.75} - \left(\frac{y}{\delta}\right)_{0.50}$

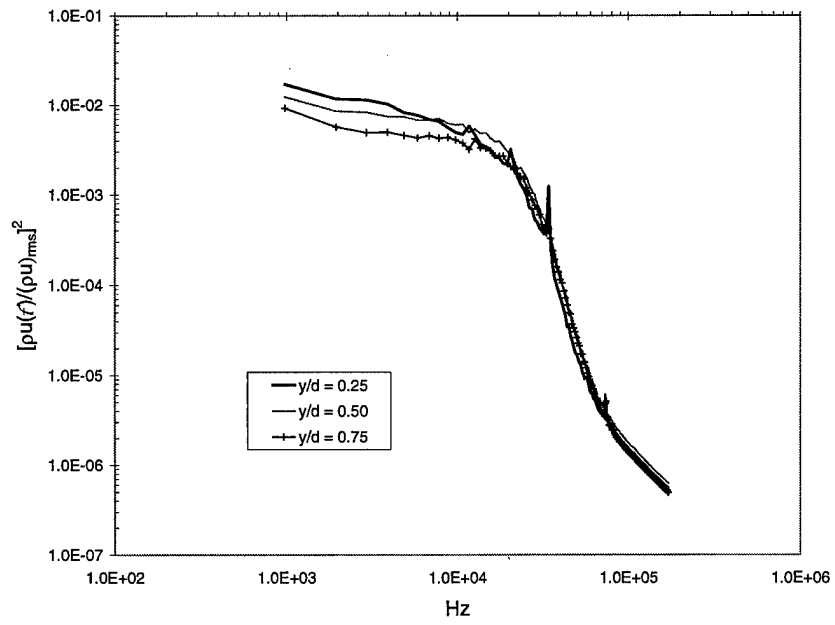

Figure 121. Smooth Plate Power Spectra

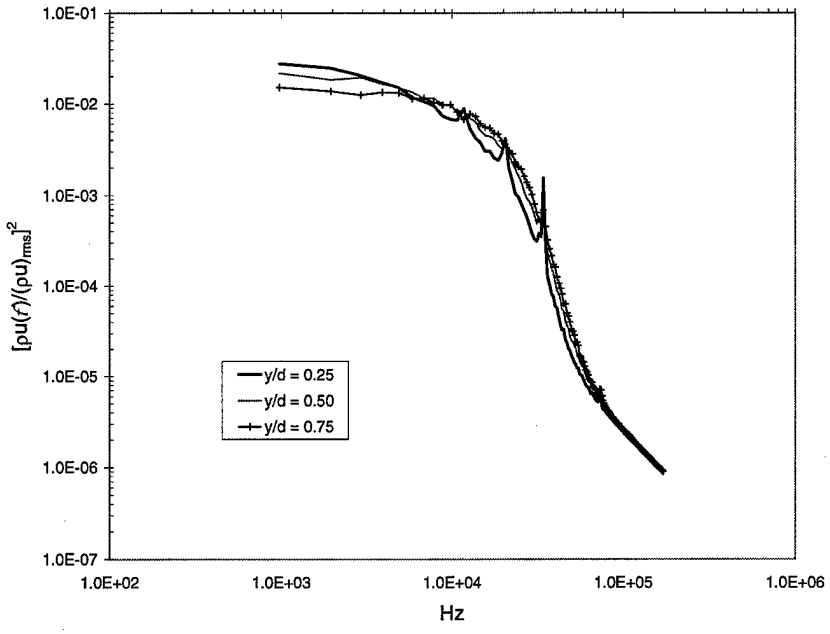

Figure 122. 2D Plate Power Spectra

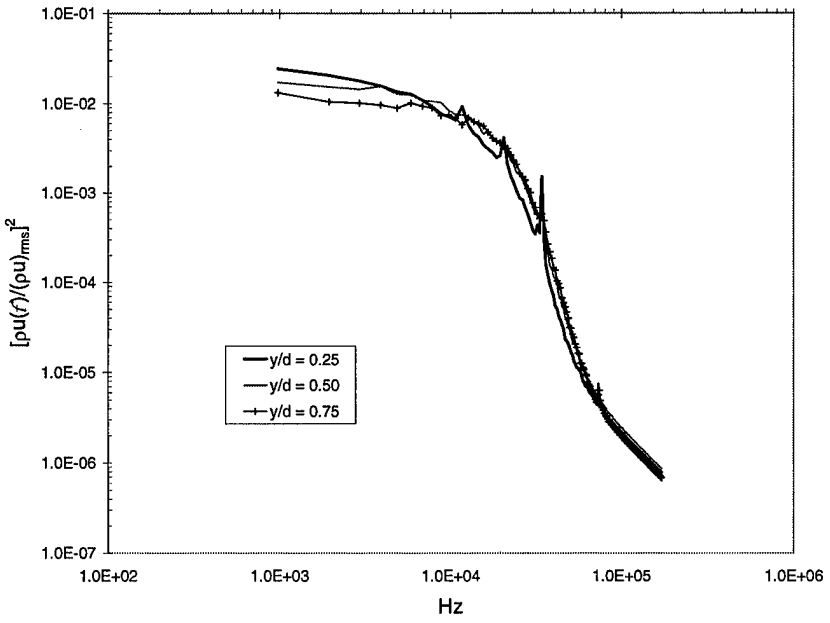

Figure 123. 3D Plate Power Spectra

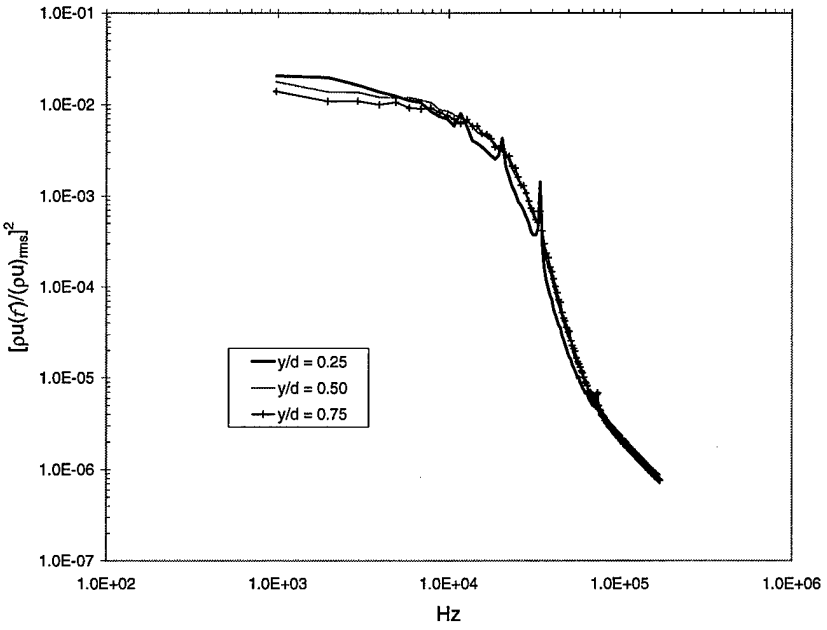

Figure 124. 80 Grit Plate Power Spectra

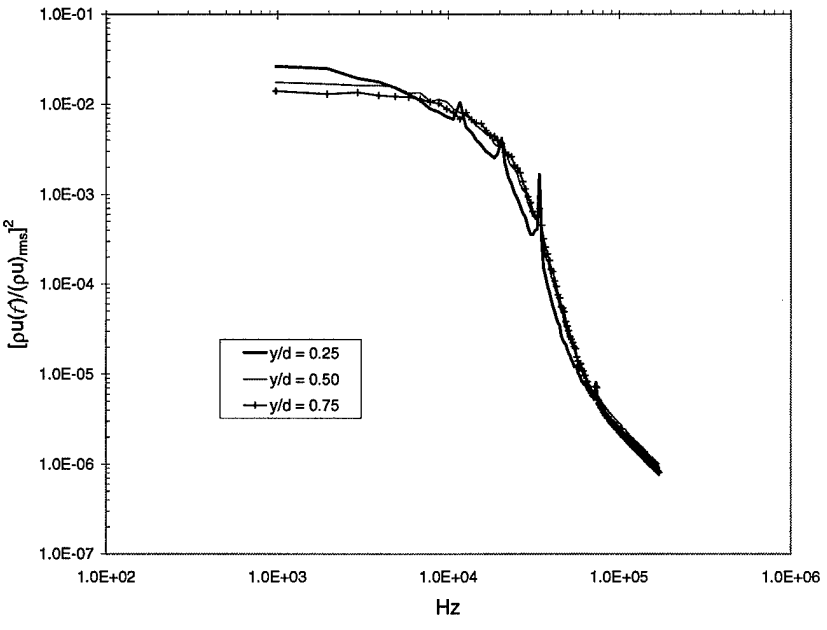

Figure 125. 36 Grit Plate Power Spectra

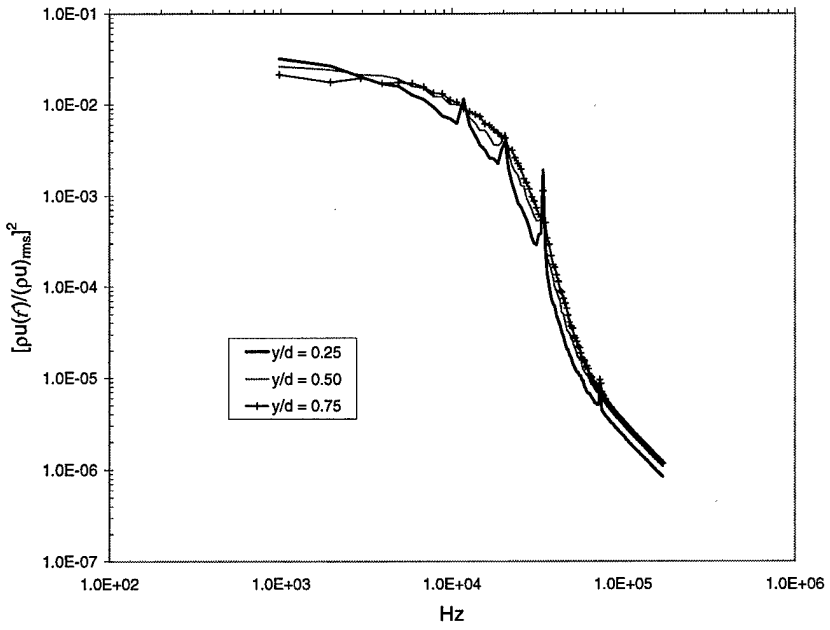

Figure 126. 20 Grit Plate Power Spectra

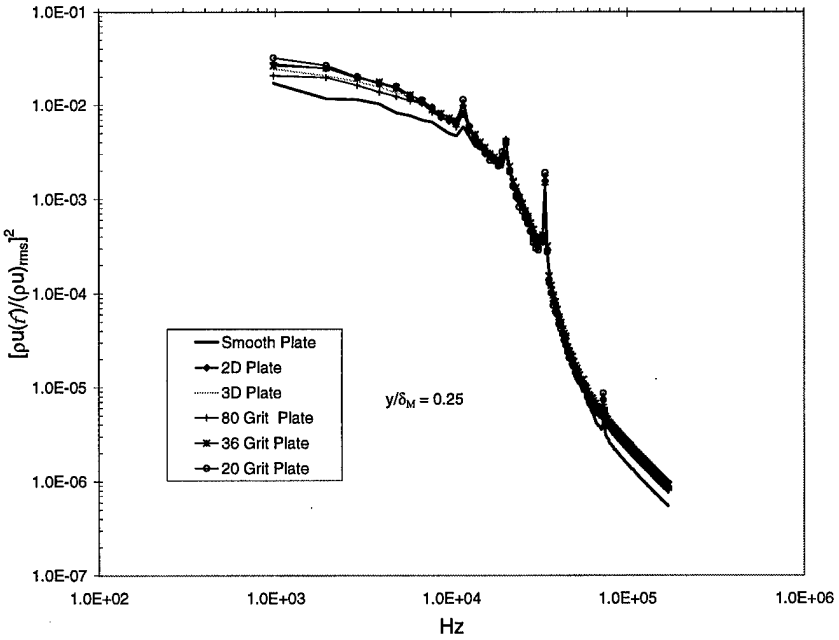

Figure 127. Power Spectra, $y/\delta_M = 0.25$

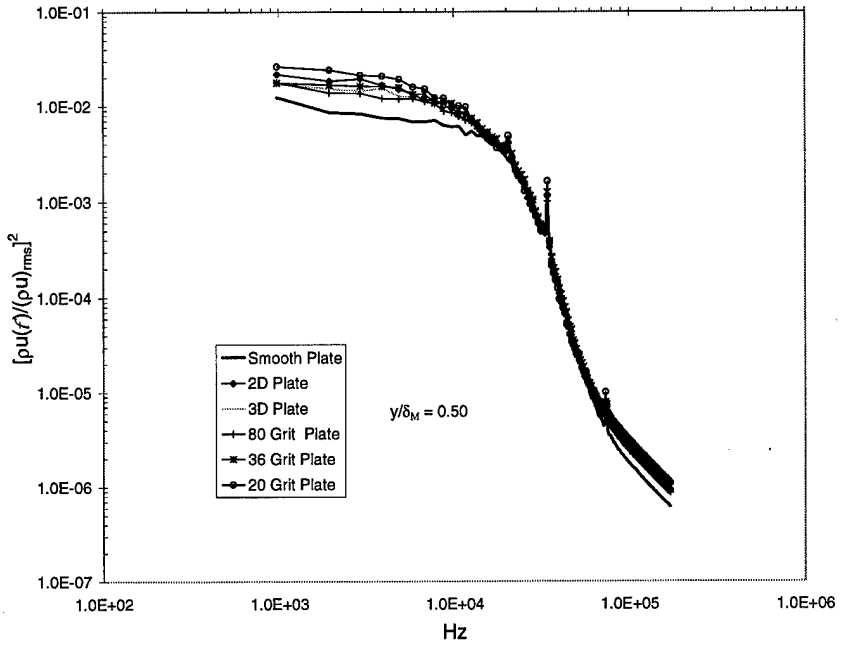

Figure 128. Power Spectra, $y/\delta_M = 0.50$

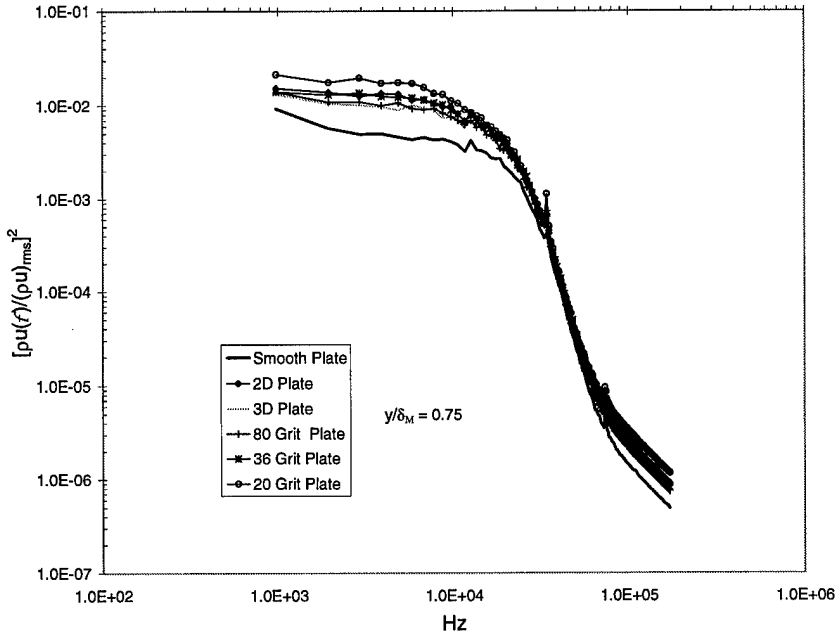

Figure 129. Power Spectra, $y/\delta_M = 0.75$

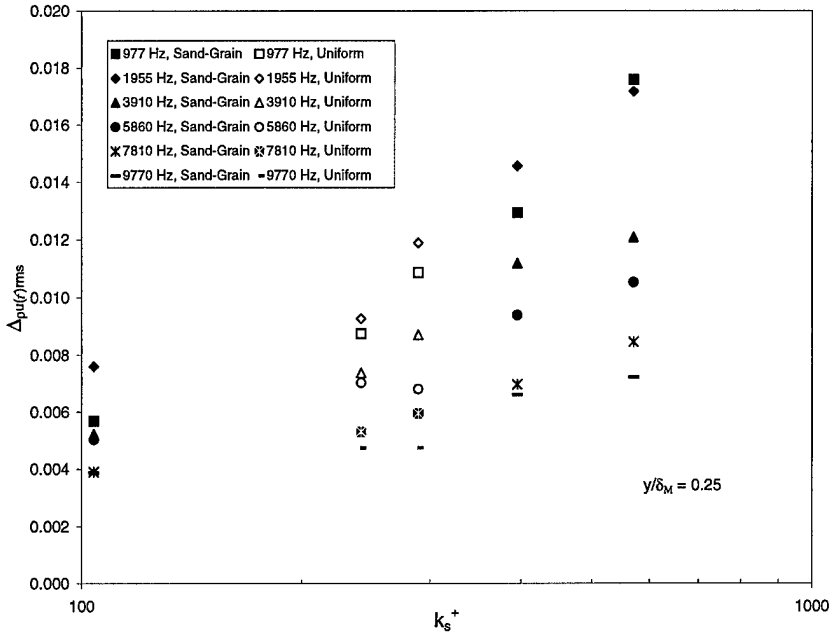

Figure 130. Power Spectra Versus Roughness Reynolds Number, $y/\delta_M = 0.25$

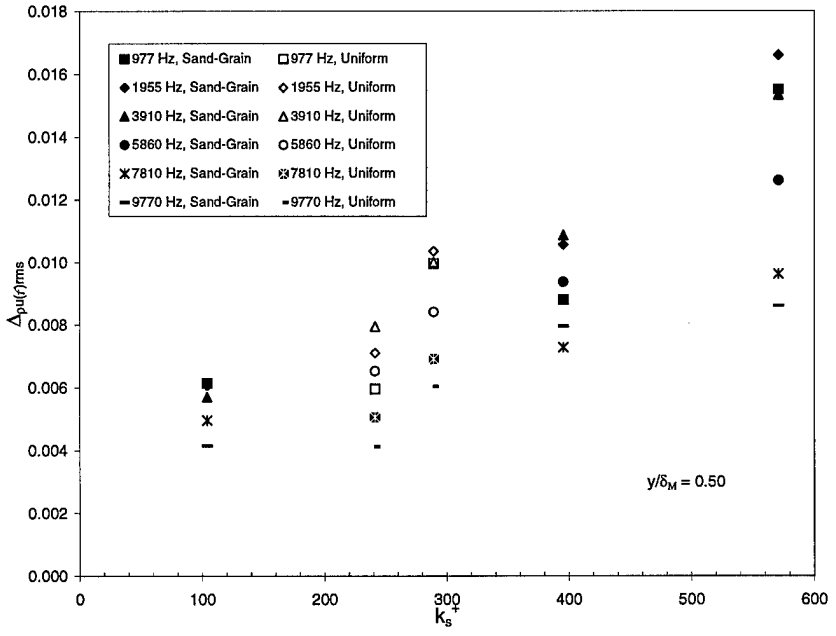

Figure 131. Power Spectra Versus Roughness Reynolds Number, $y/\delta_M = 0.50$

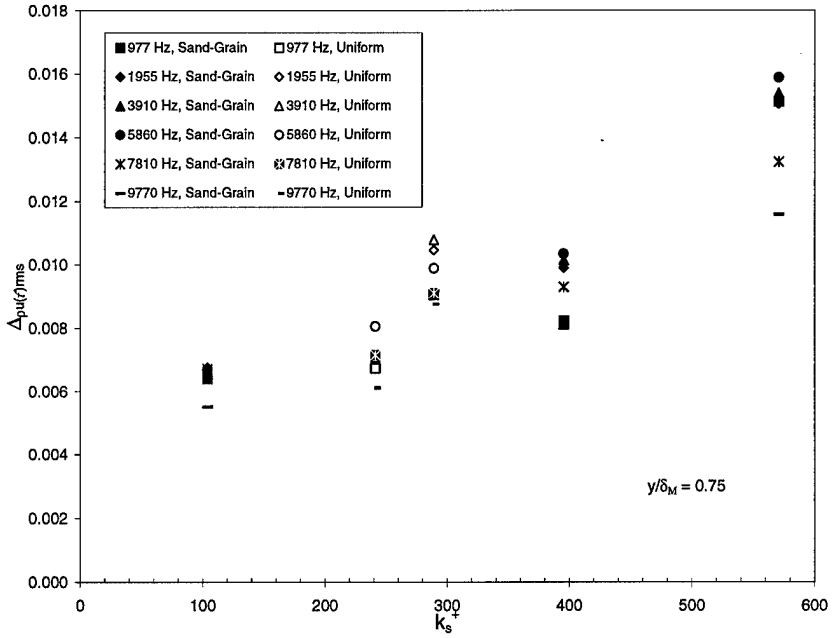

Figure 132. Power Spectra Versus Roughness Reynolds Number, $y/\delta_M = 0.75$

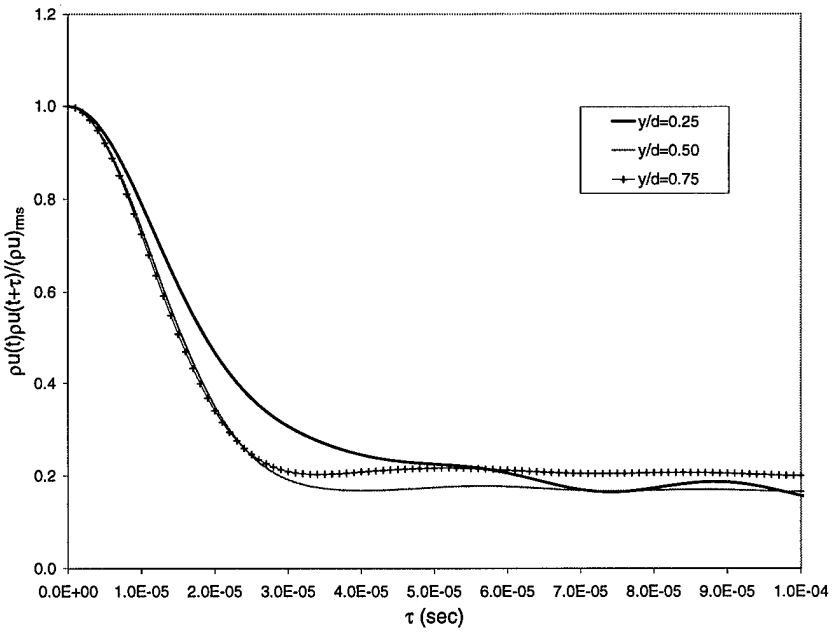

Figure 133. Smooth Plate Normal-Film Autocorrelation

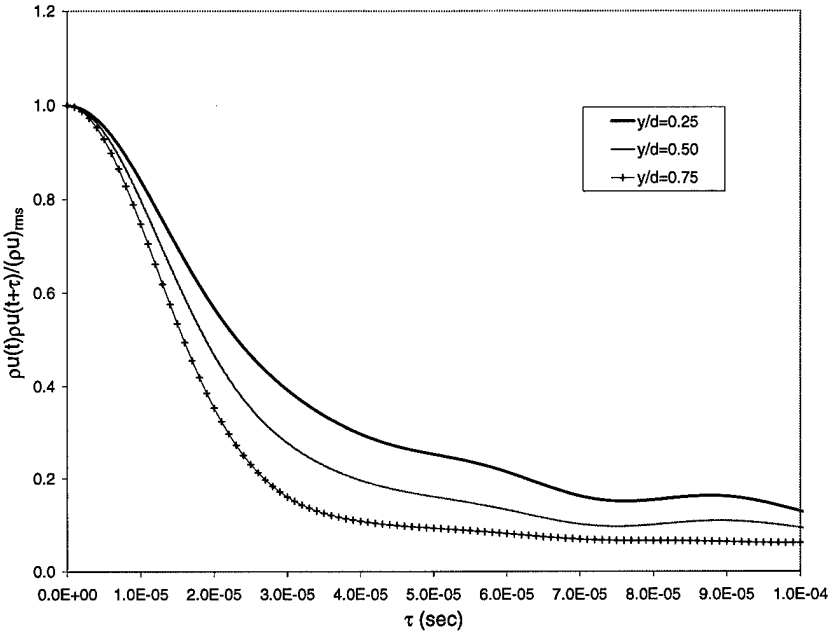

Figure 134. 2D Plate Normal-Film Autocorrelation

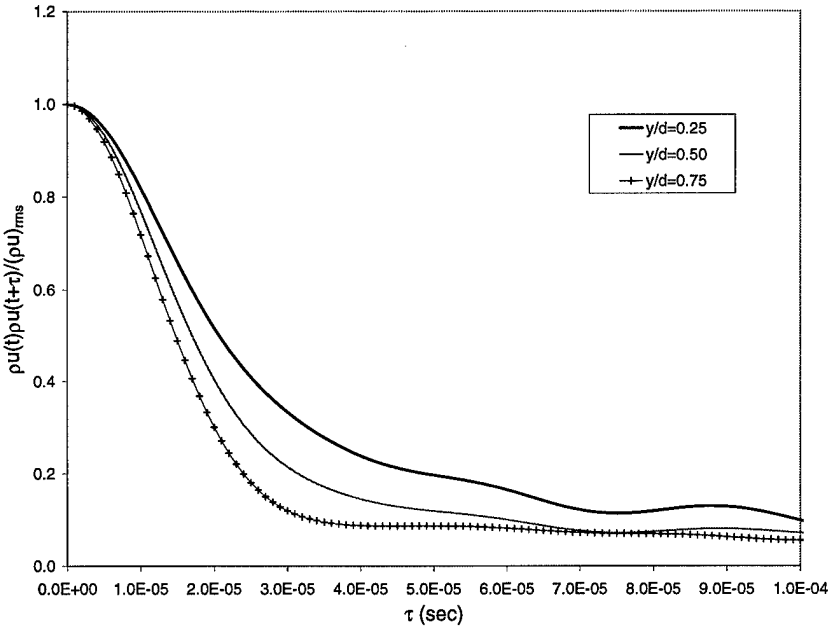

Figure 135. 3D Plate Normal-Film Autocorrelation

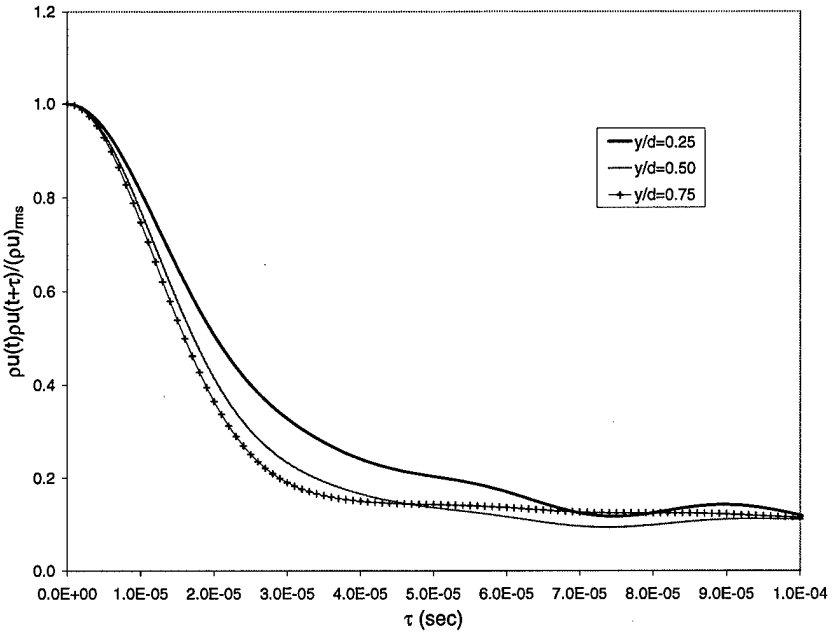

Figure 136. 80 Grit Plate Normal-Film Autocorrelation

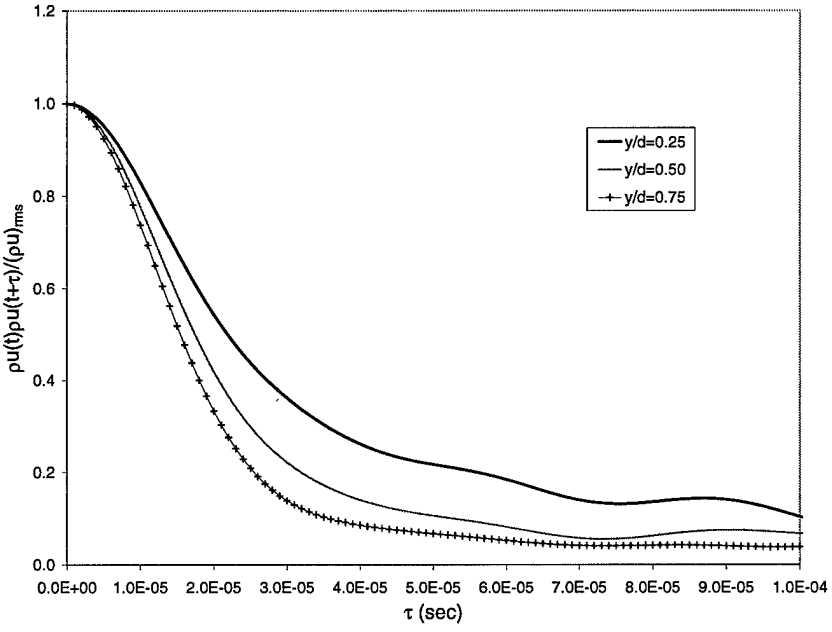

Figure 137. 36 Grit Plate Normal-Film Autocorrelation

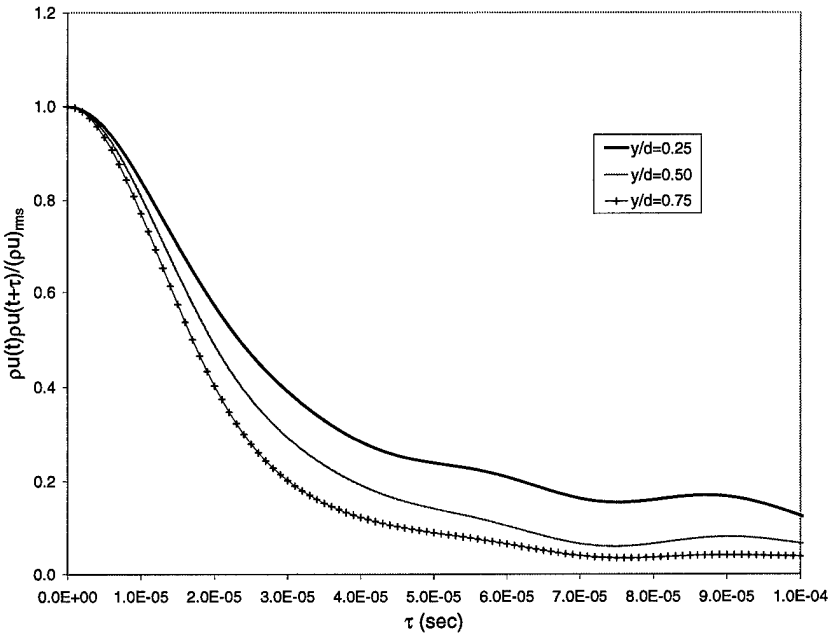

Figure 138. 20 Grit Plate Normal-Film Autocorrelation

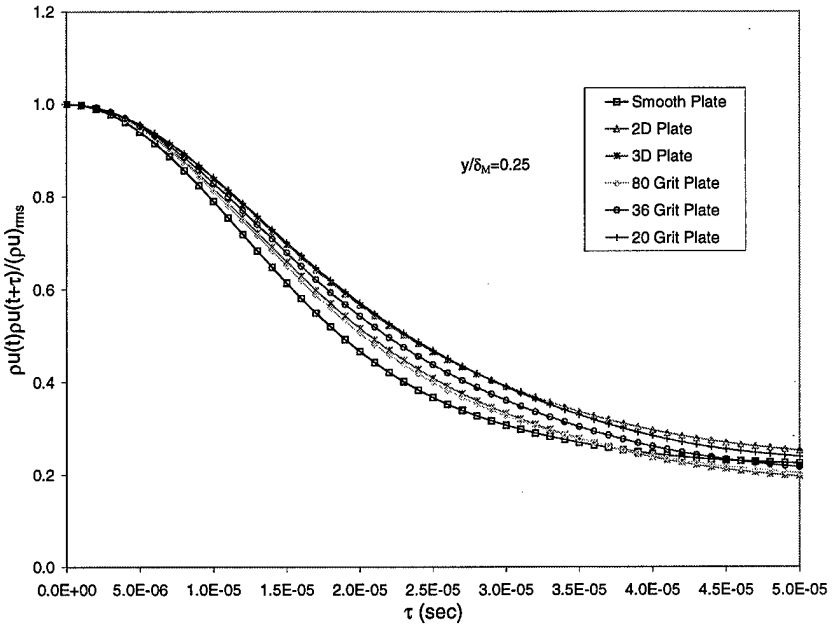

Figure 139. Normal-Film Autocorrelation, $y/\delta_M = 0.25$

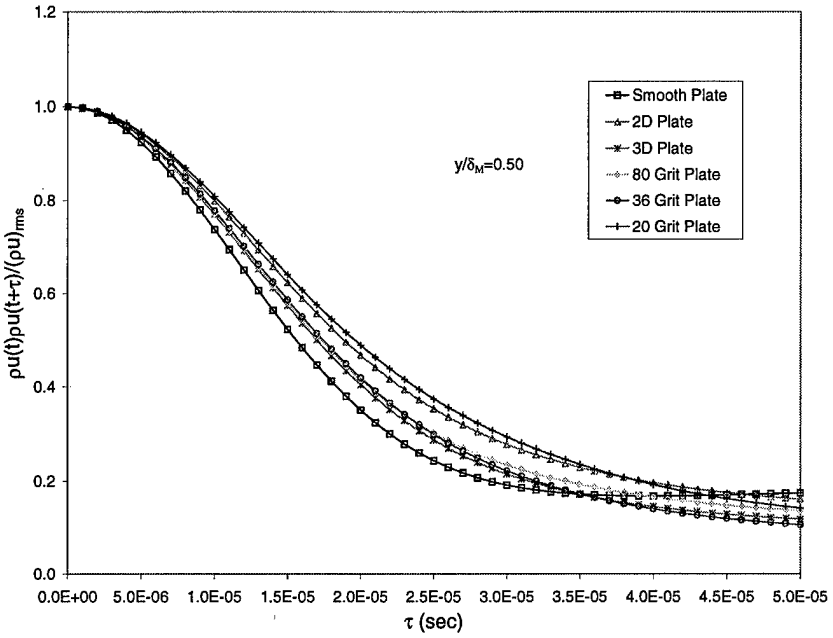

Figure 140. Normal-Film Autocorrelation, $y/\delta_M = 0.50$

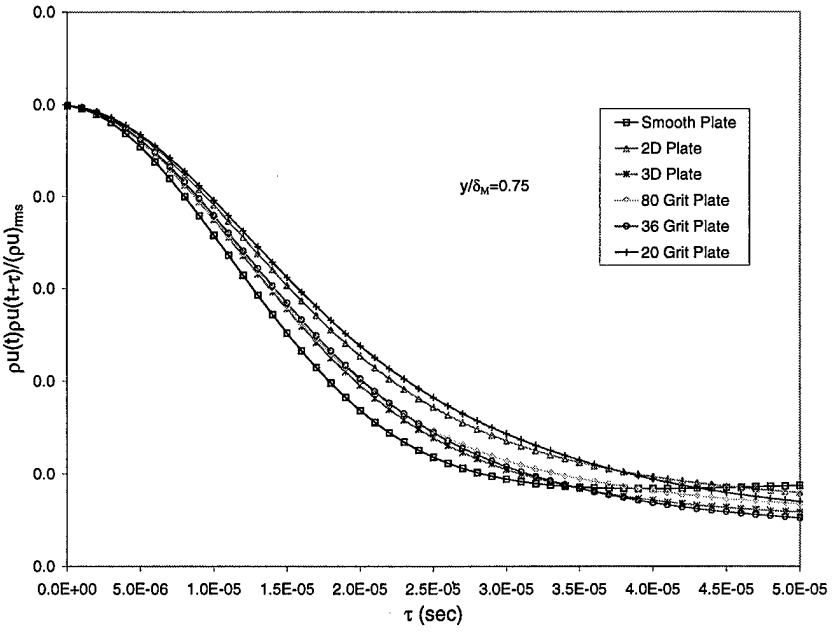

Figure 141. Normal-Film Autocorrelation, $y/\delta_M = 0.75$

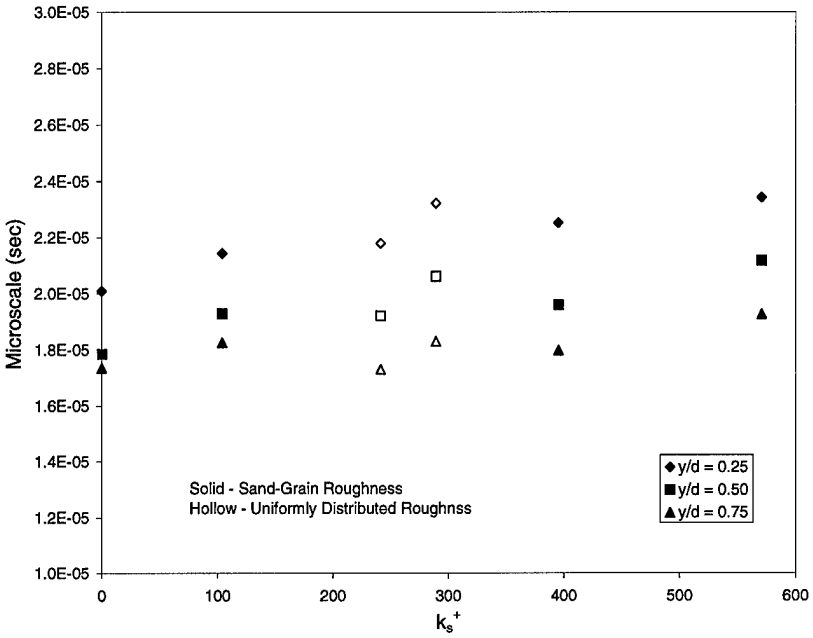

Figure 142. Microscale

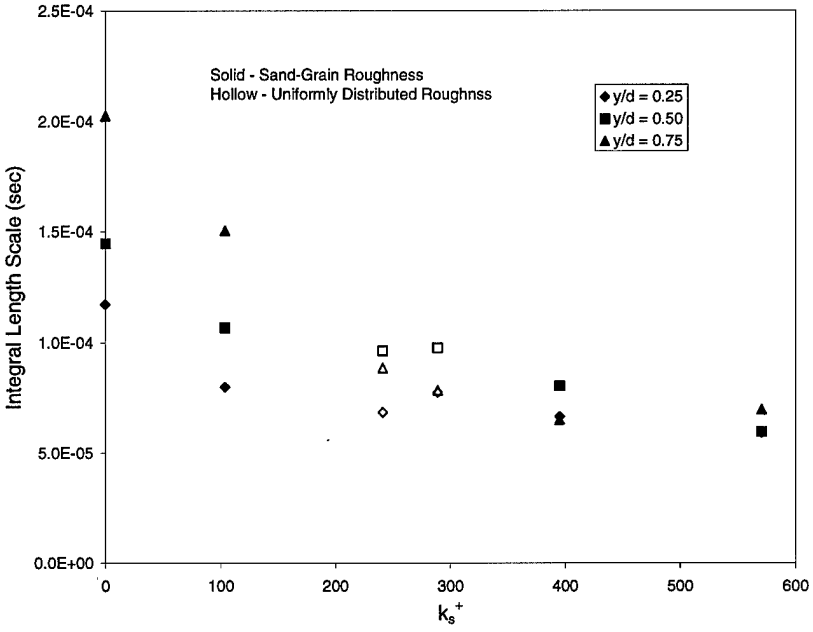

Figure 143. Integral Length Scale

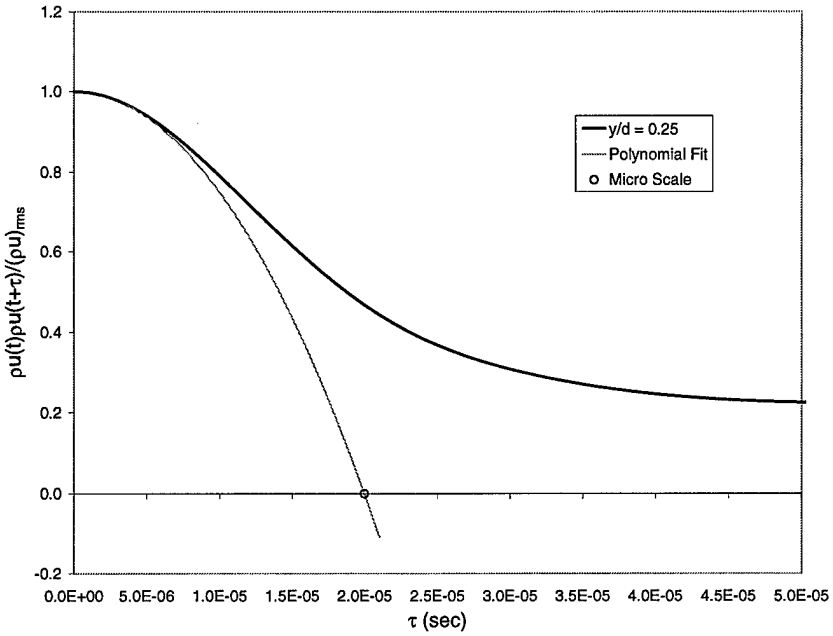

Figure 144. Smooth Plate Osculating Parabola Fit

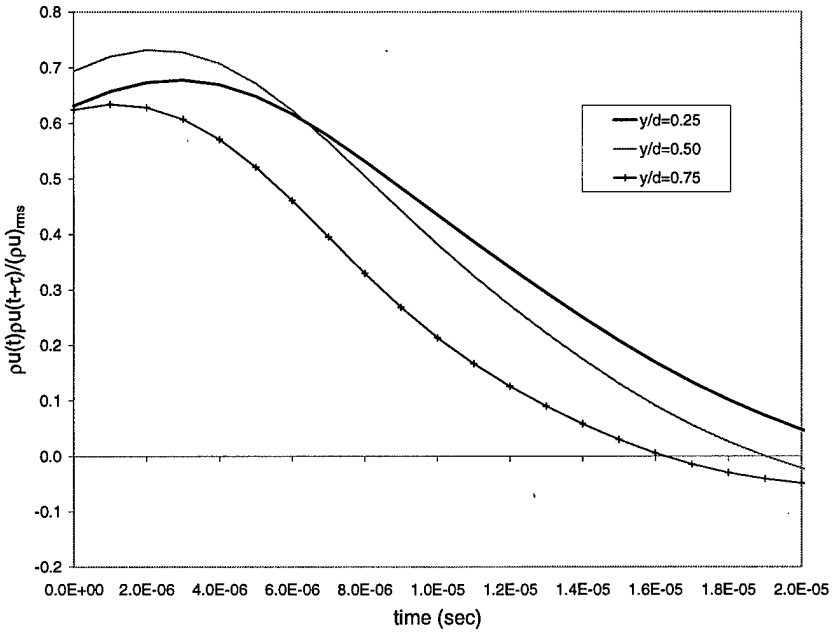

Figure 145. Smooth Plate Parallel-Film Cross-Correlation

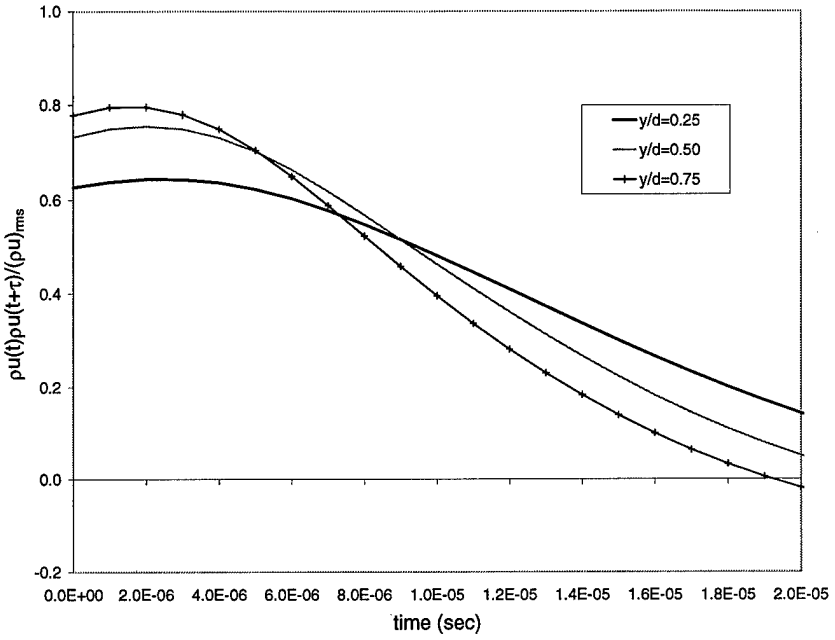

Figure 146. 2D Plate Parallel-Film Cross-Correlation

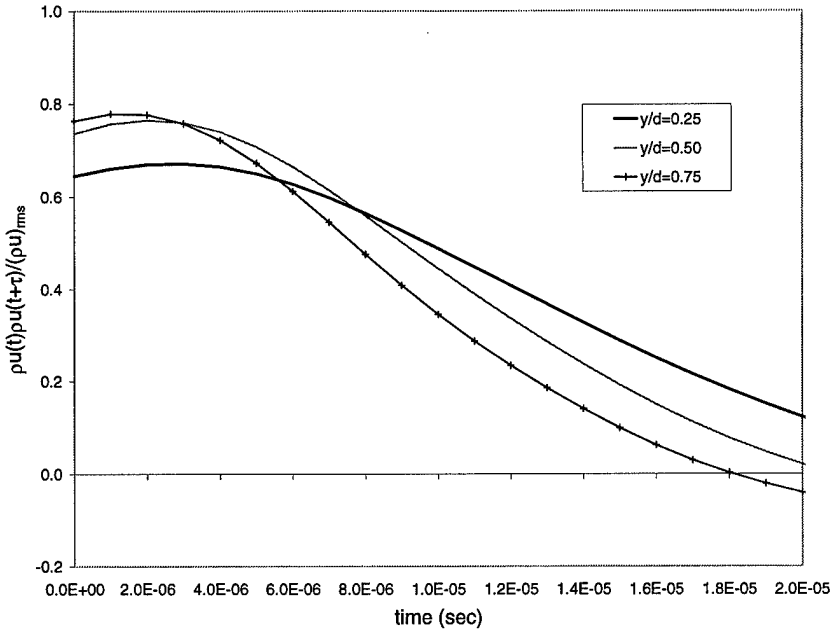

Figure 147. 3D Plate Parallel-Film Cross-Correlation

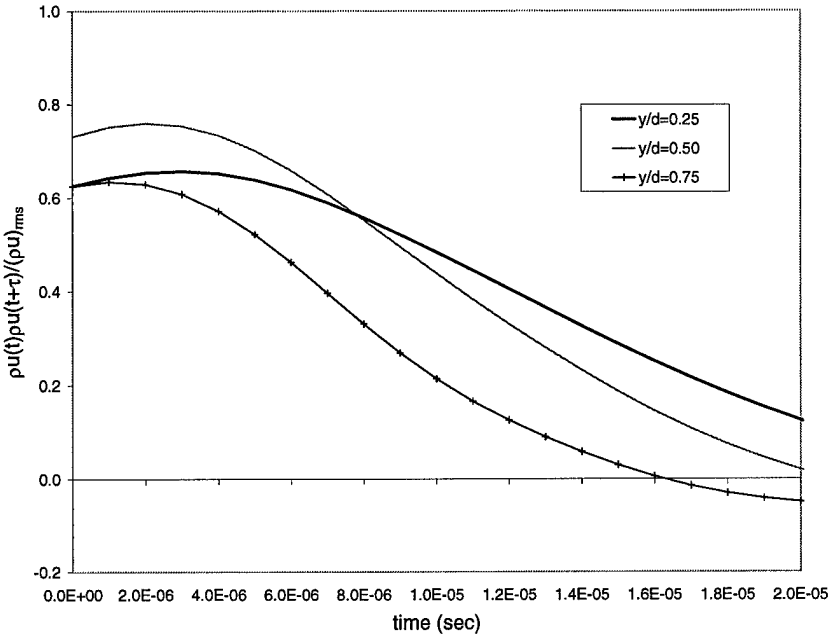

Figure 148. 80 Grit Plate Parallel-Film Cross-Correlation

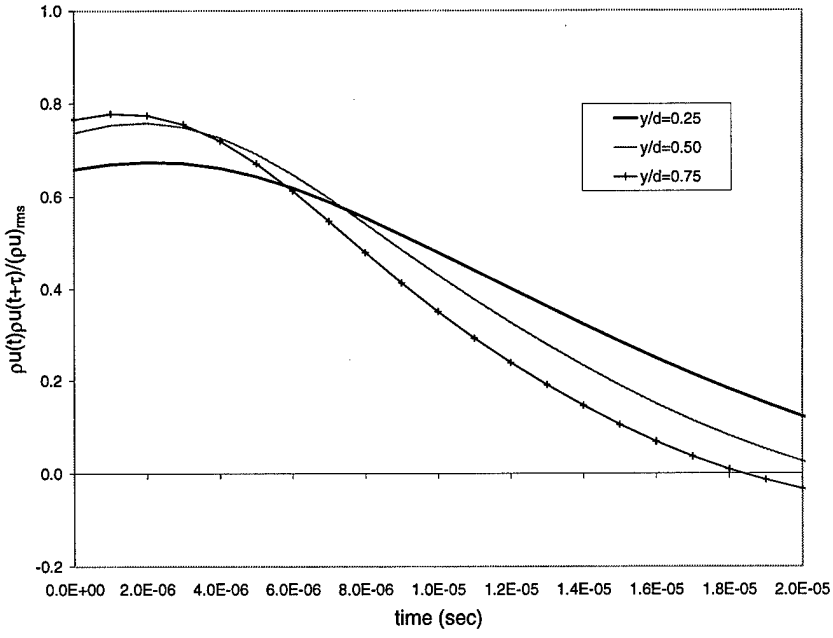

Figure 149. 36 Grit Plate Parallel-Film Cross-Correlation

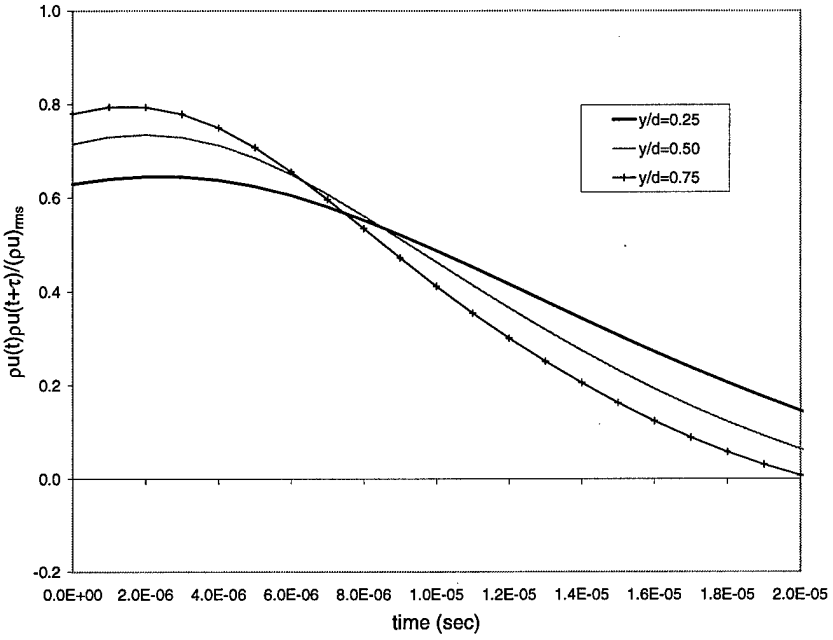

Figure 150. 20 Grit Plate Parallel-Film Cross-Correlation

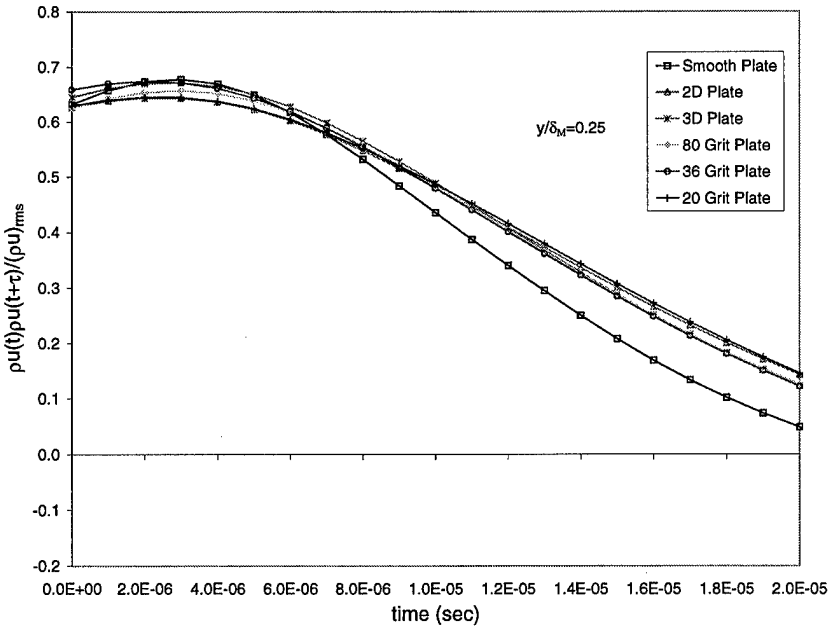

Figure 151. Parallel-Film Cross-Correlation, $y/\delta_M = 0.25$

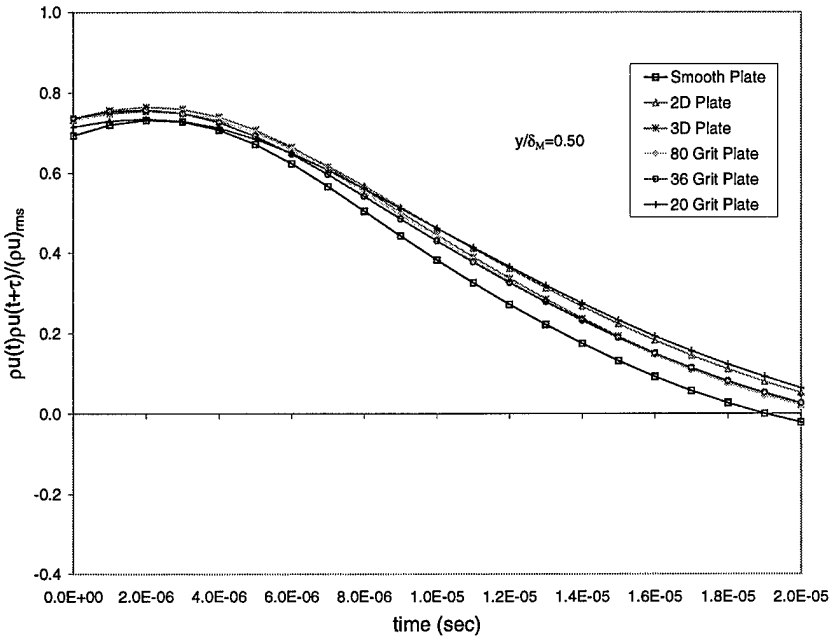

Figure 152. Parallel-Film Cross-Correlation, $y/\delta_M = 0.50$

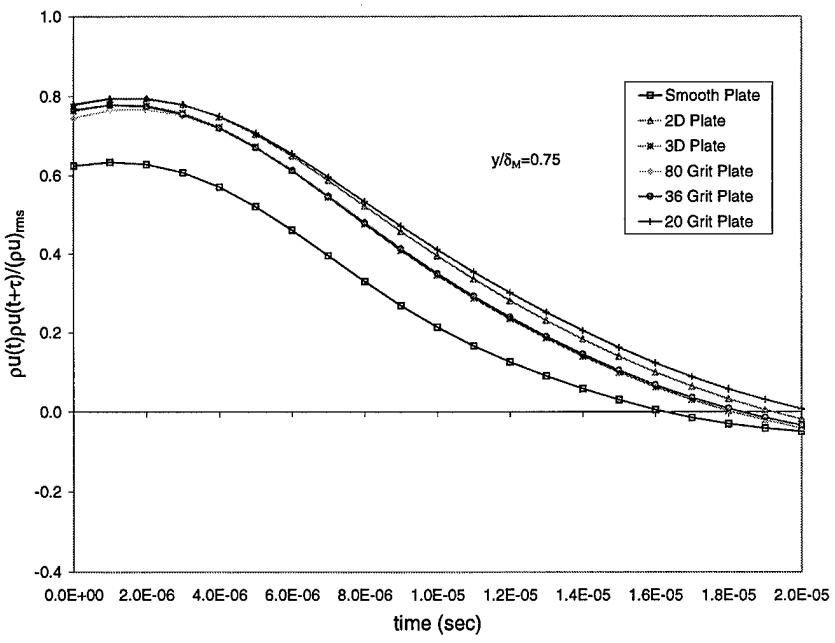

Figure 153. Parallel-Film Cross-Correlation, $y/\delta_M = 0.75$

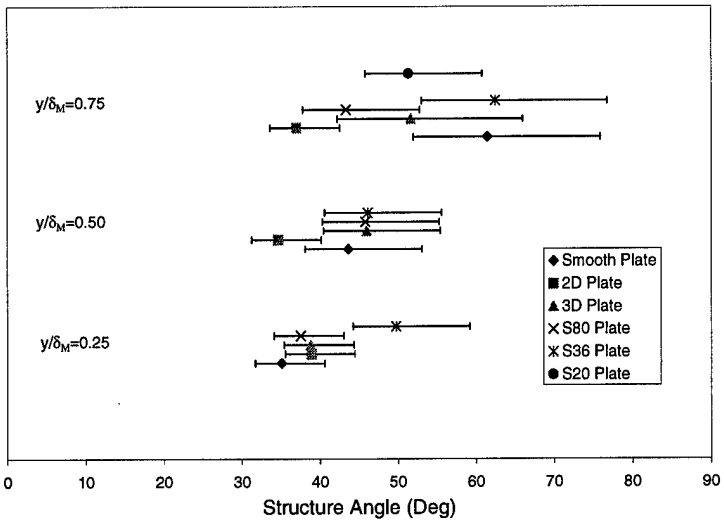

Figure 154. Structure Angle

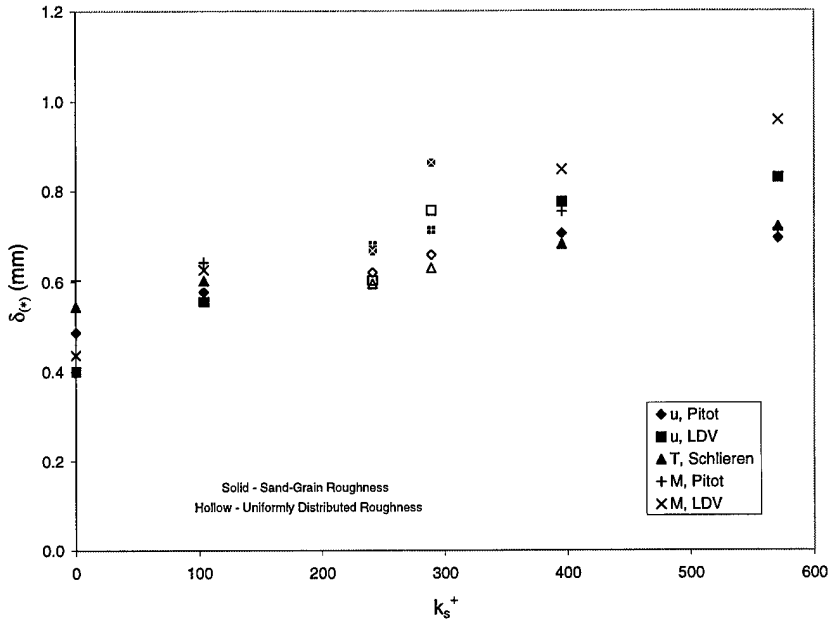

Figure 155. Boundary Layer Thickness Versus Roughness Reynolds Number

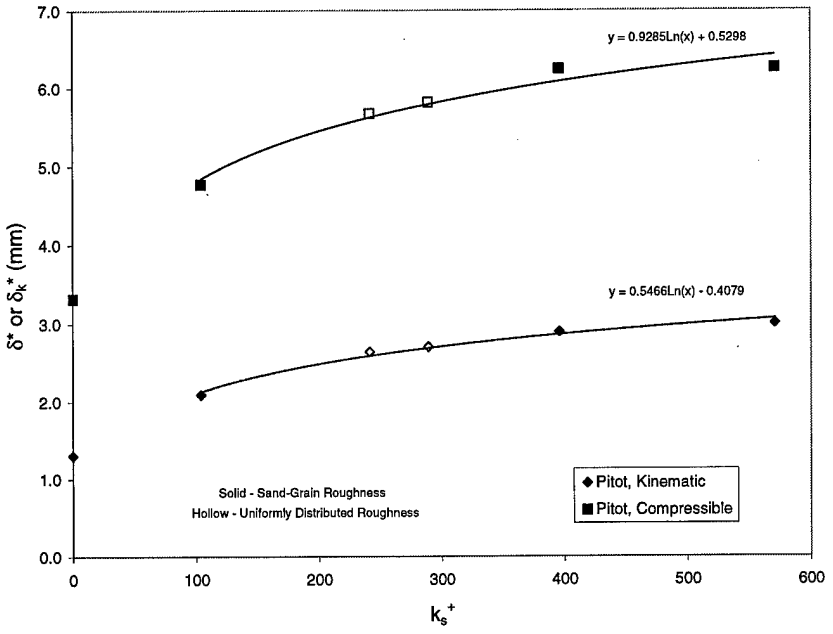

Figure 156. Displacement Thickness Versus Roughness Reynolds Number

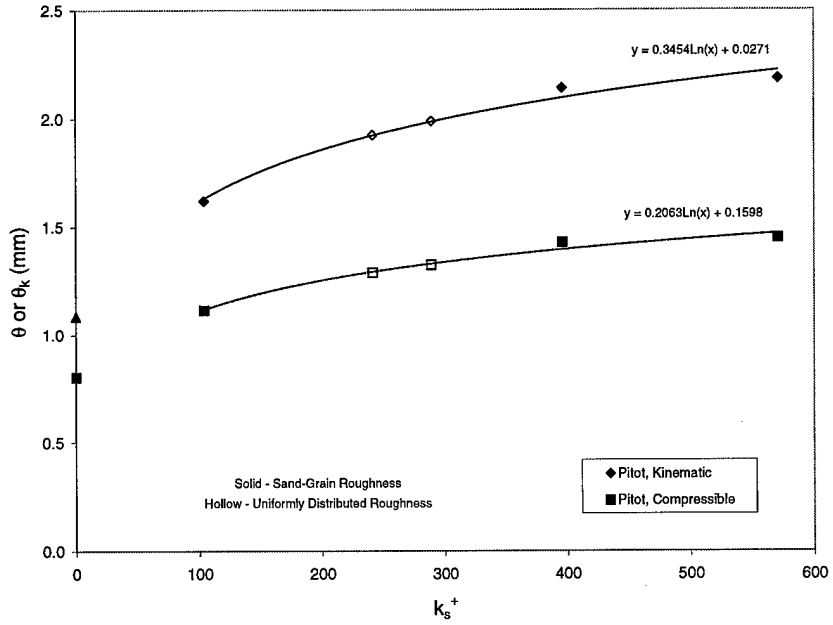

Figure 157. Momentum Thickness Versus Roughness Reynolds Number

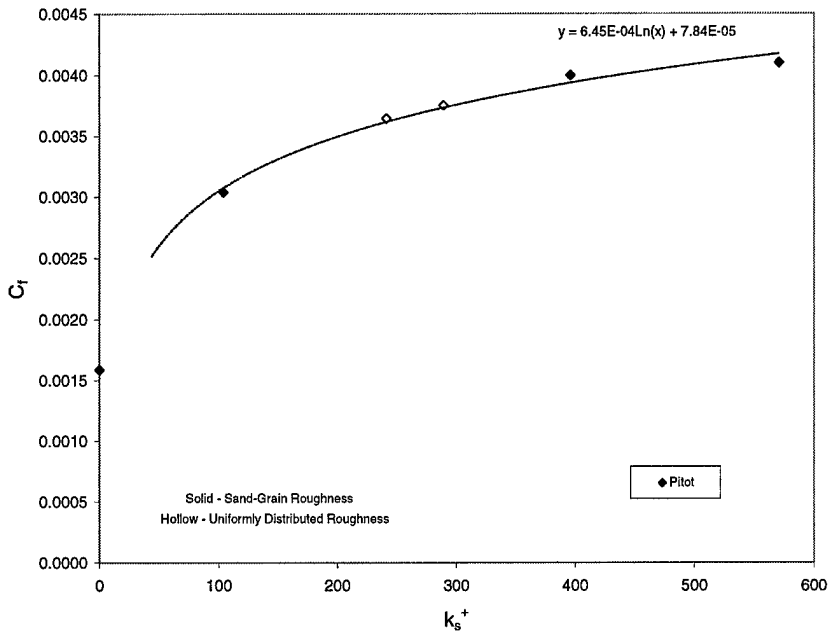

Figure 158. Skin Friction Coefficient Versus Roughness Reynolds Number

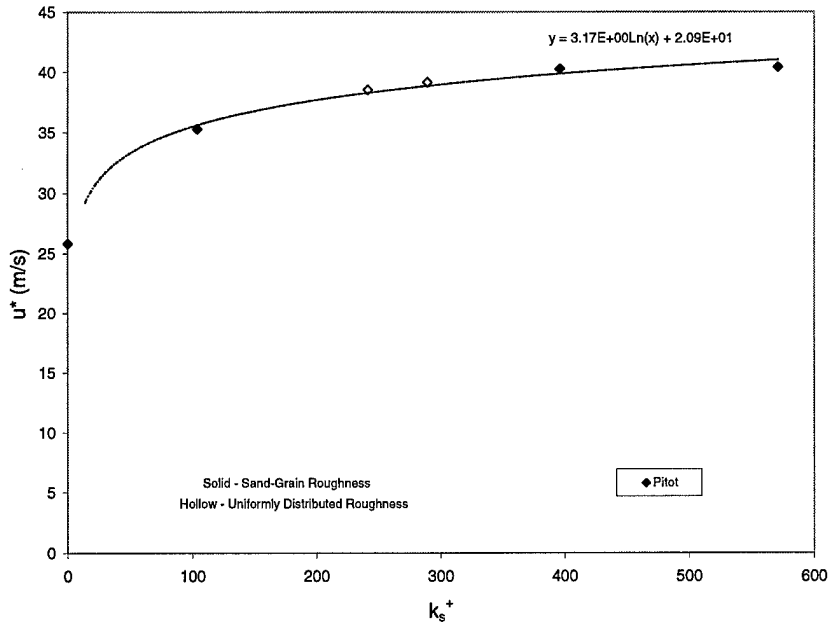

Figure 159. Friction Velocity Versus Roughness Reynolds Number

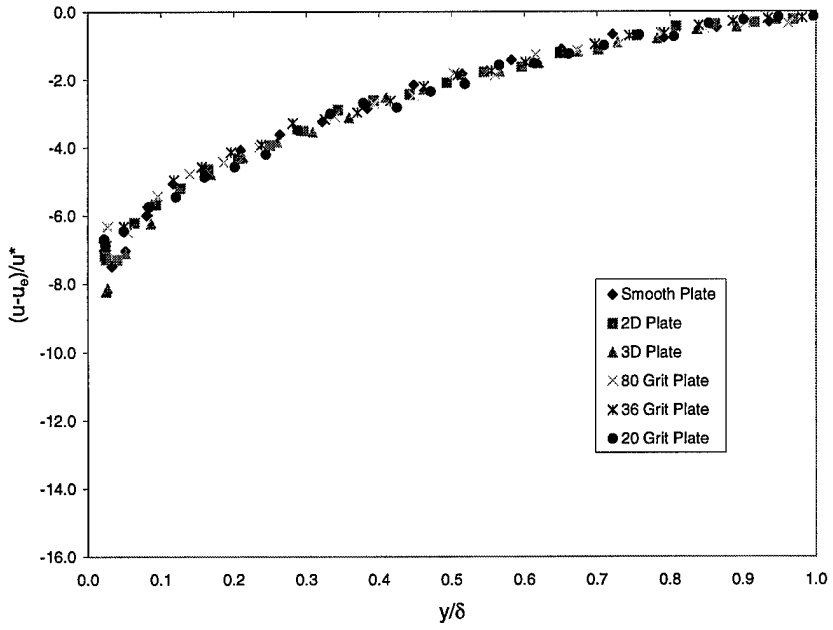

Figure 160. Velcocity Defect, Pitot Data

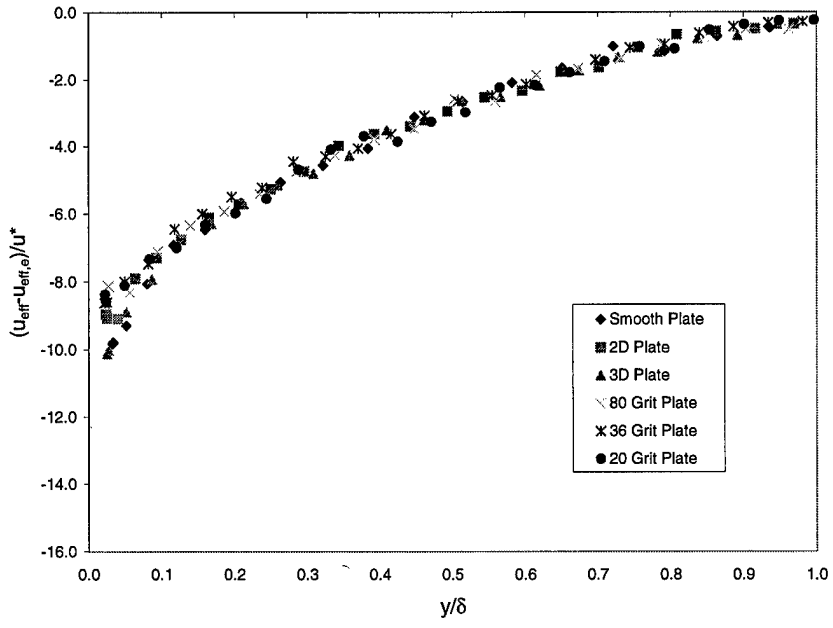

Figure 161. Effective Velocity Defect, Pitot Data

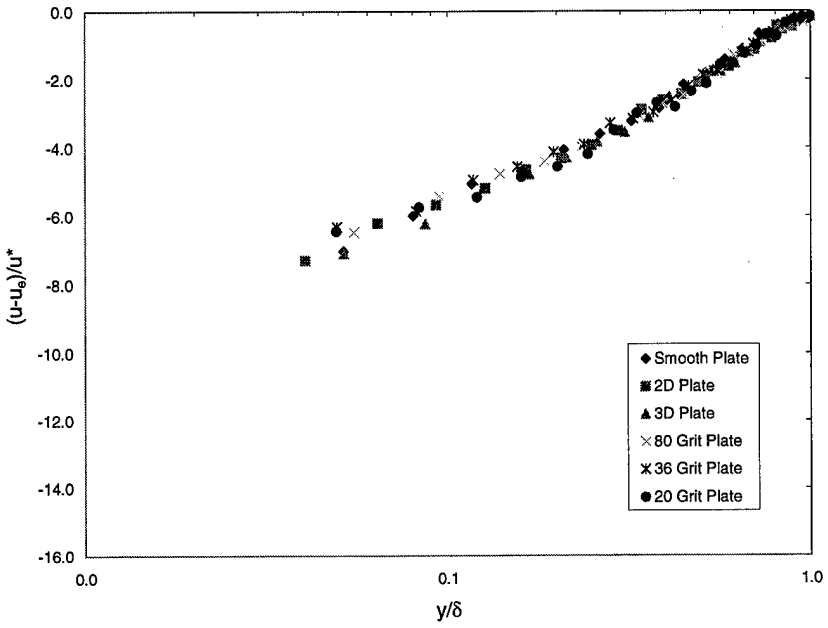

Figure 162. Velocity Defect, LDV Data

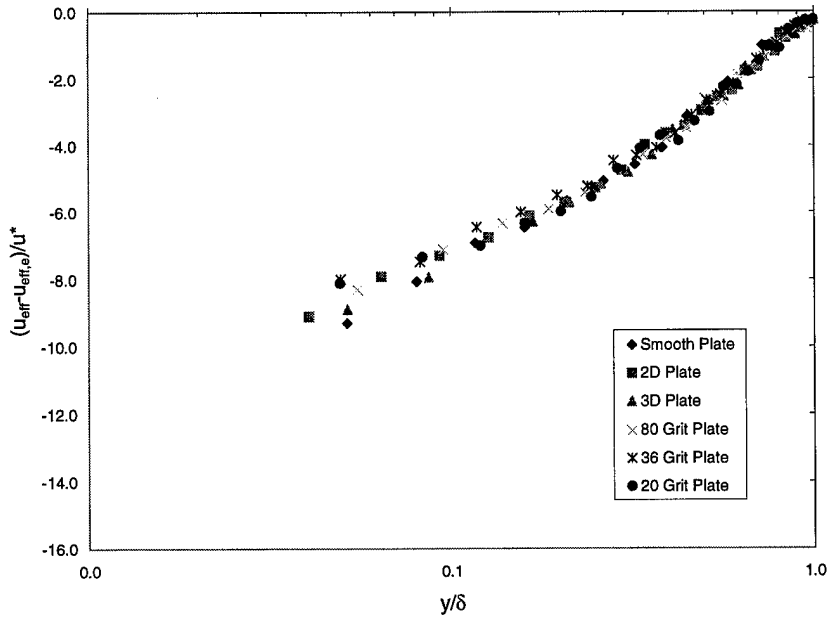

Figure 163. Effective Velocity Defect, LDV Data

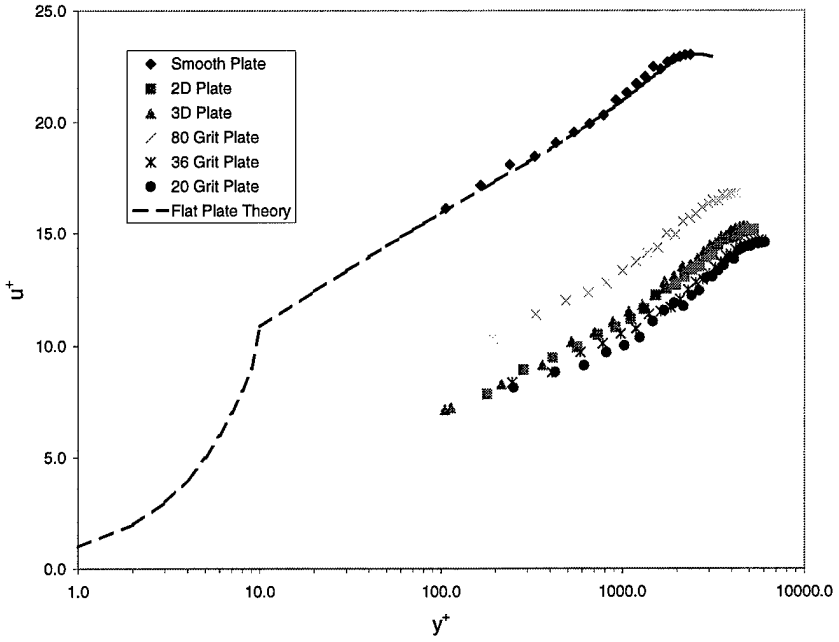

Figure 164. Van Driest Velocity Profile, Pitot Data

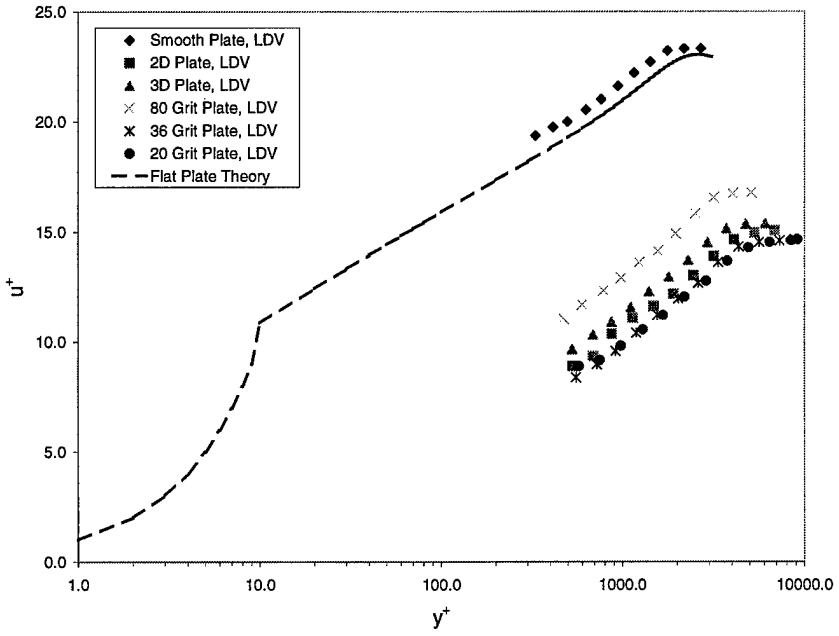

Figure 165. Van Driest Velocity Profile, LDV Data

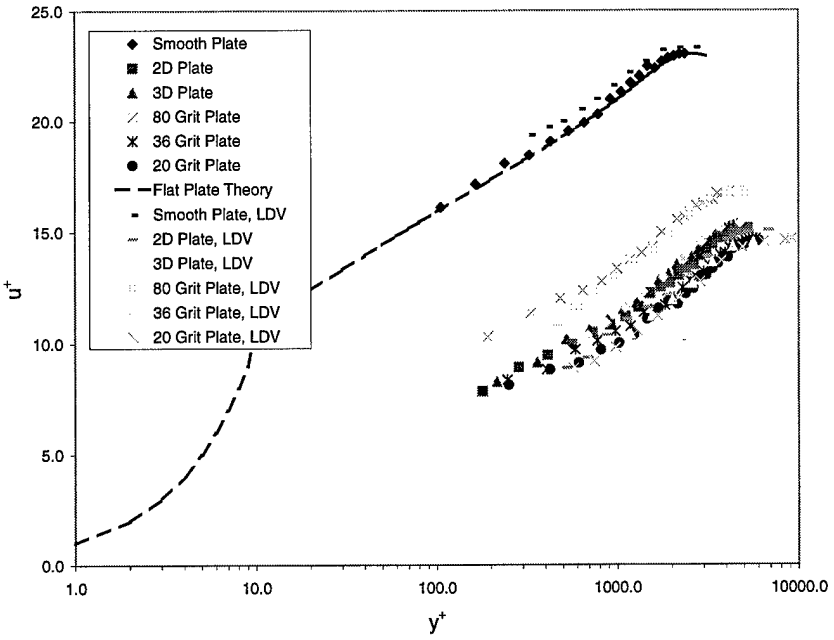

Figure 166. Van Driest Velocity Profile, Pitot and LDV Data

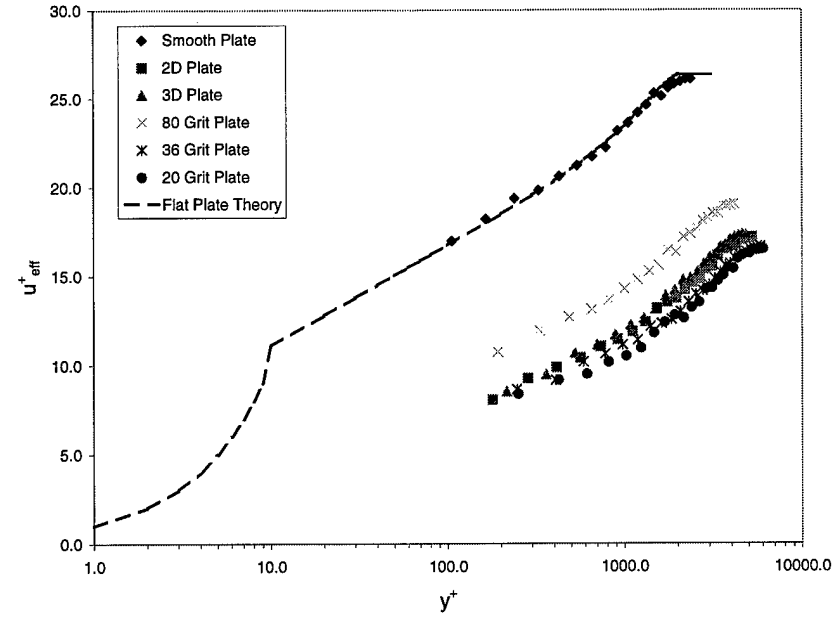

Figure 167. Van Driest Effective Velocity Profile, Pitot Data

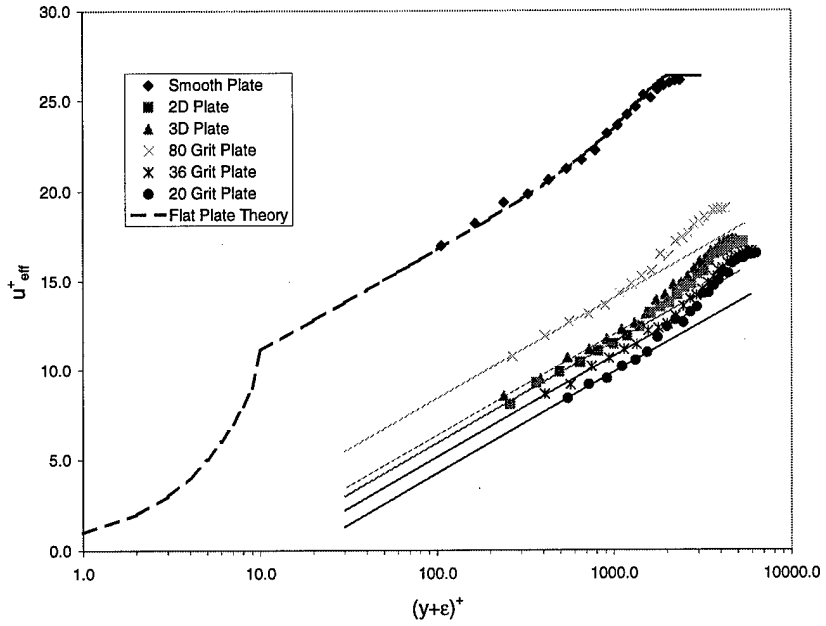

Figure 168. Van Driest Effective Velocity Profile

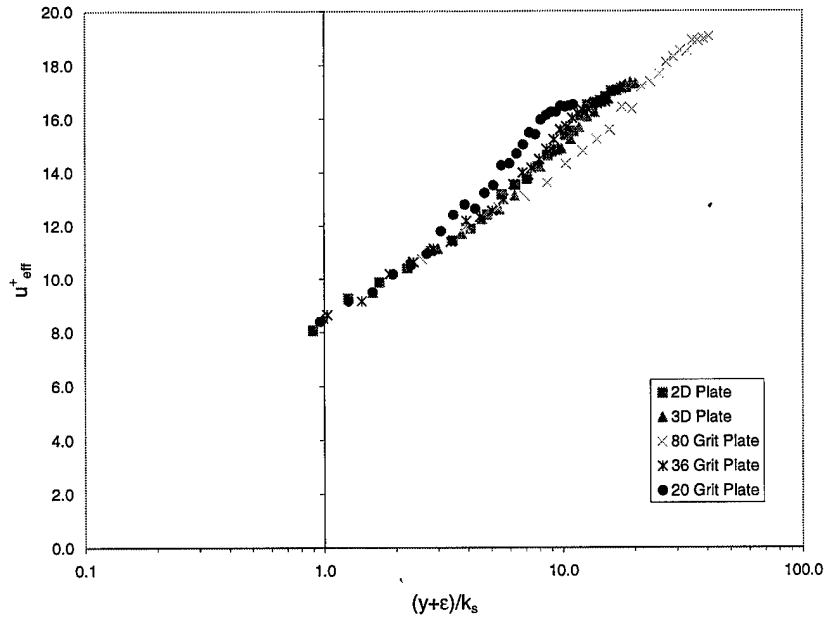

Figure 169. Full Rough Flow Van Driest Velocity Profile

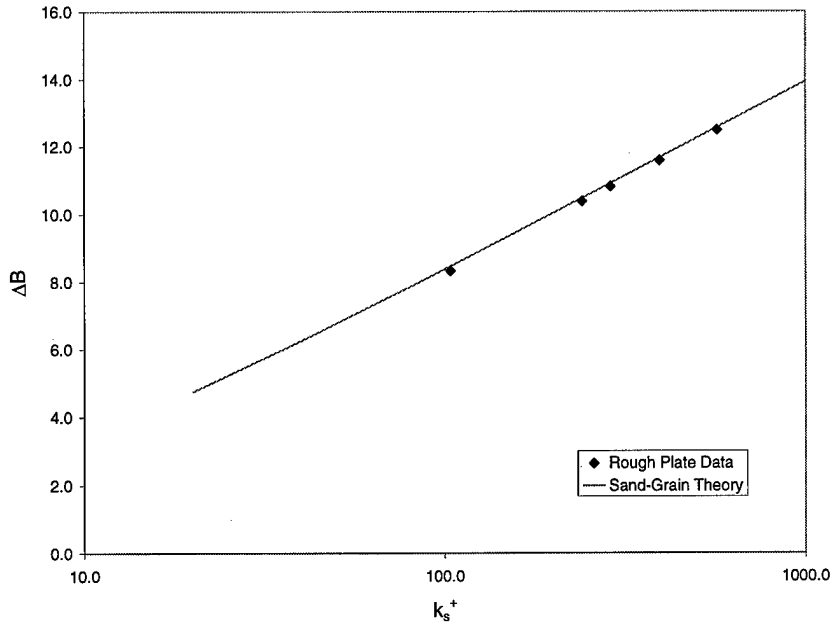

Figure 170. Profile Shift

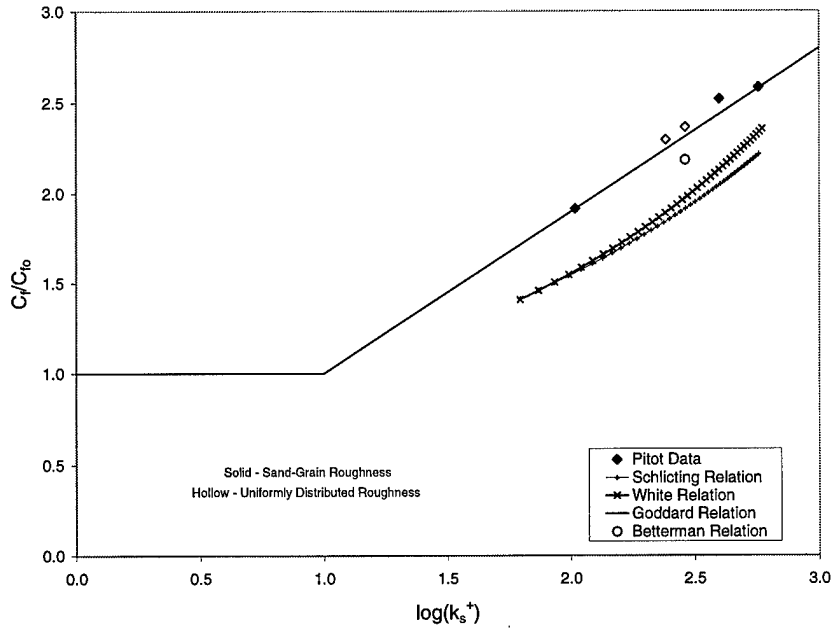

Figure 171. Rough Wall Skin Friction Ratio Correlation

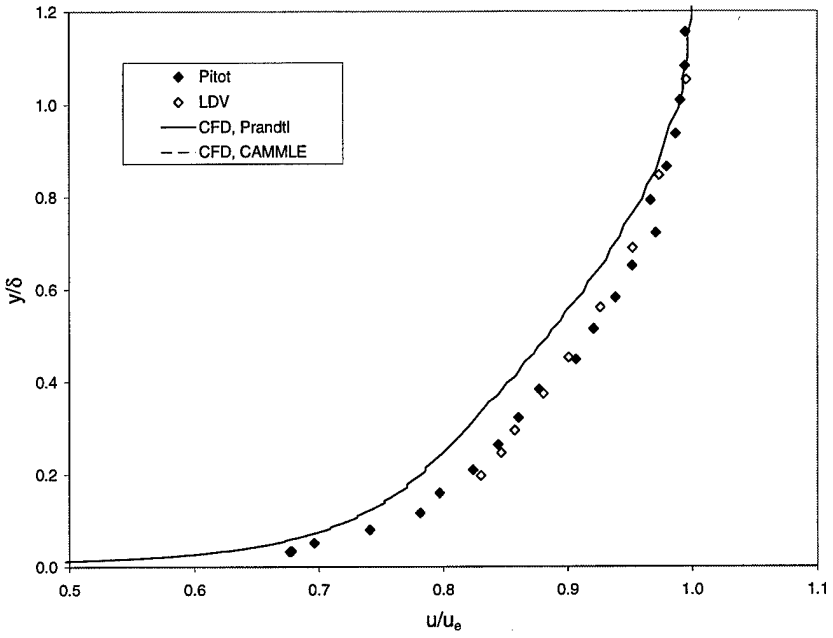

Figure 172. Smooth Plate Velocity Profiles

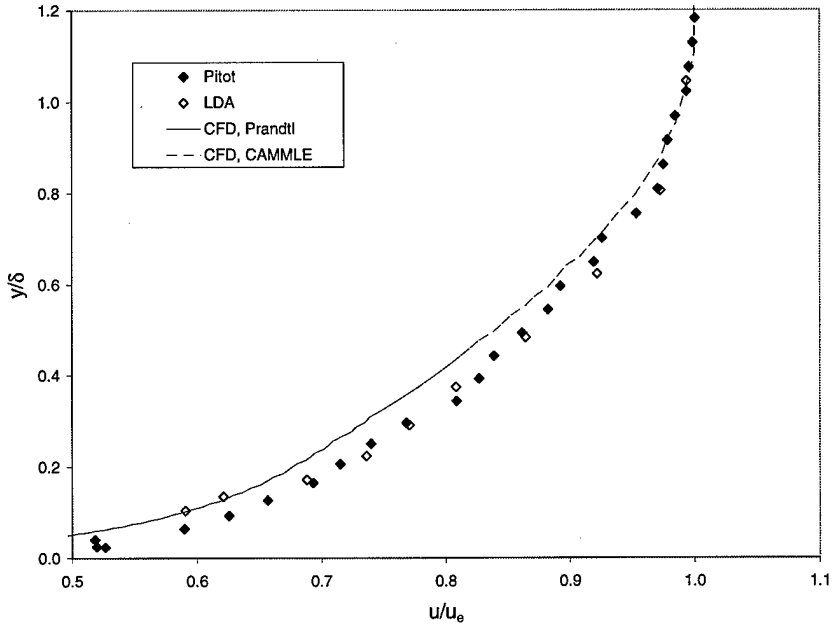

Figure 173. 2D Plate Velocity Profiles

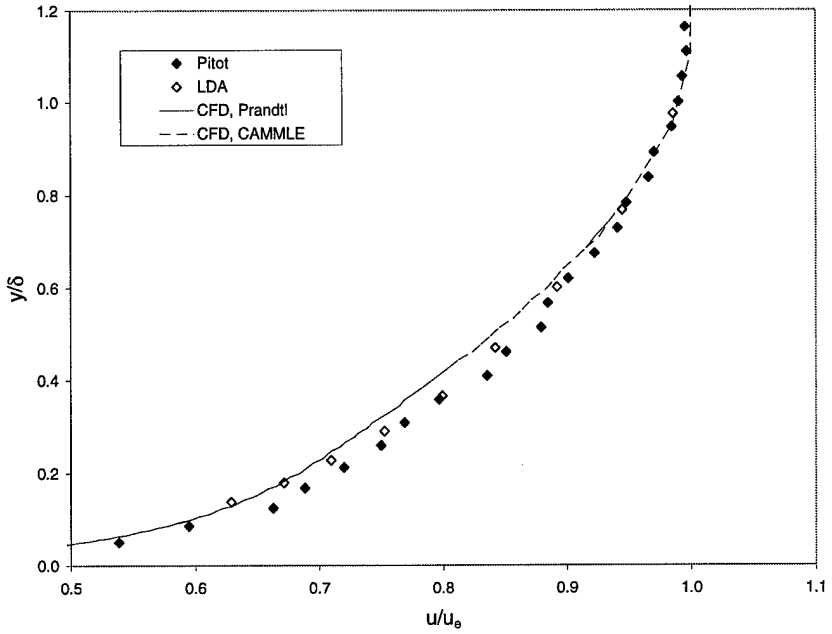

Figure 174. 3D Plate Velocity Profiles

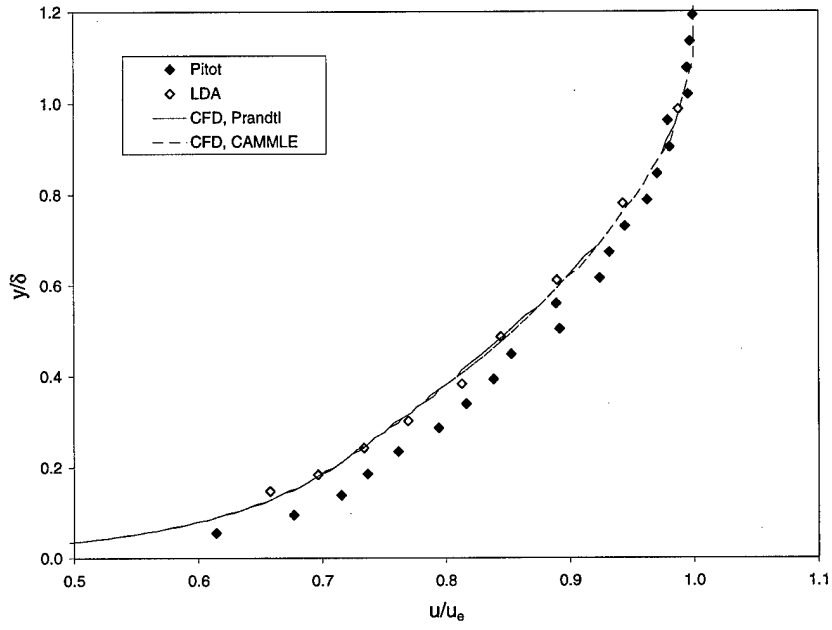

Figure 175. 80 Grit Plate Velocity Profiles

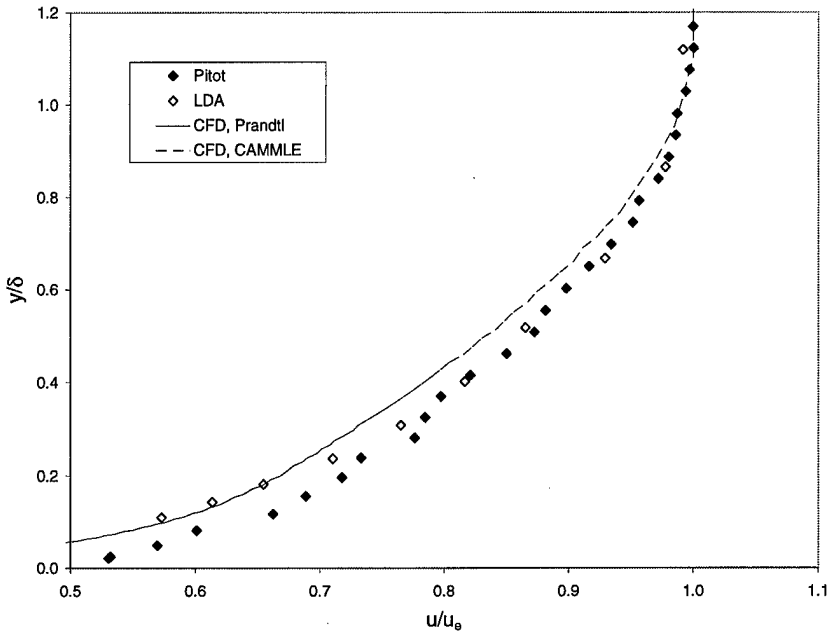

Figure 176. 36 Grit Plate Velocity Profiles

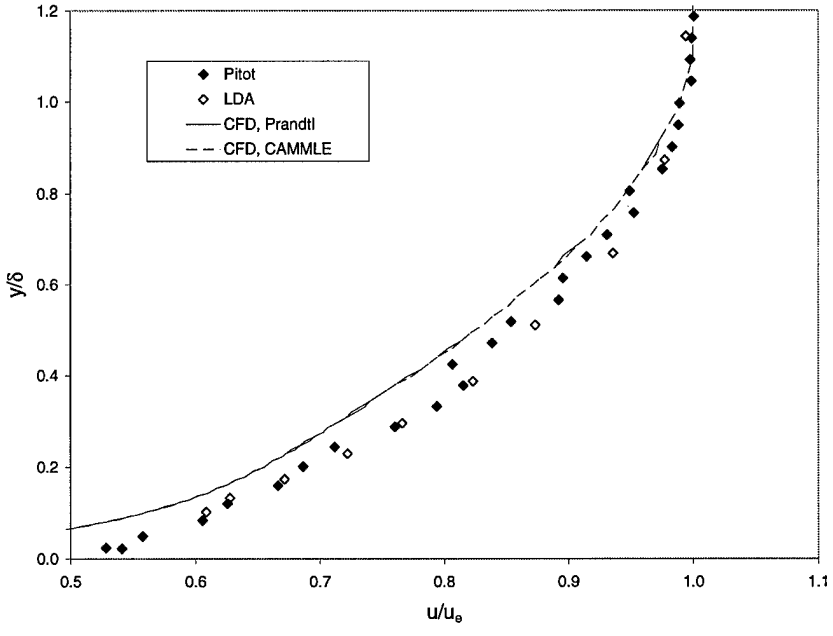

Figure 177. 20 Grit Plate Velocity Profiles

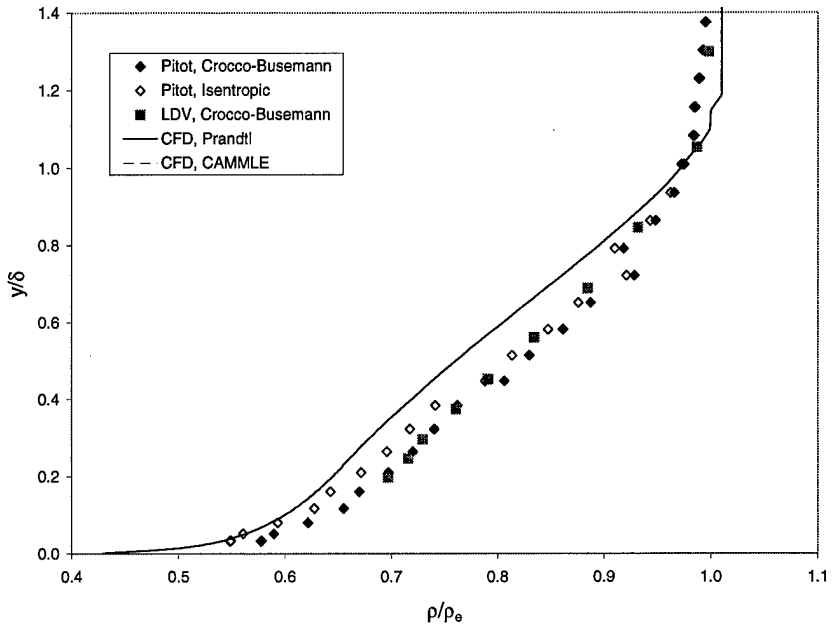

Figure 178. Smooth Plate Density Profiles

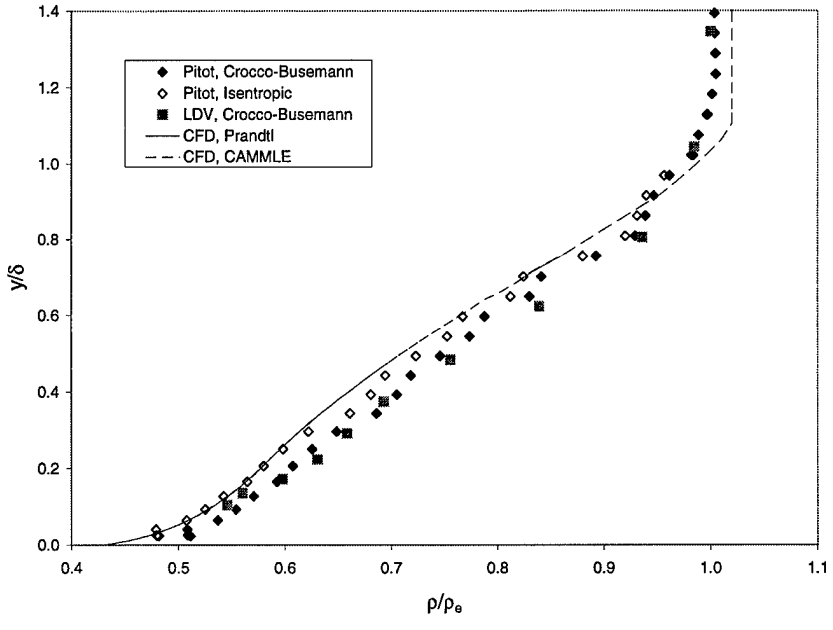

Figure 179. 2D Plate Density Profiles

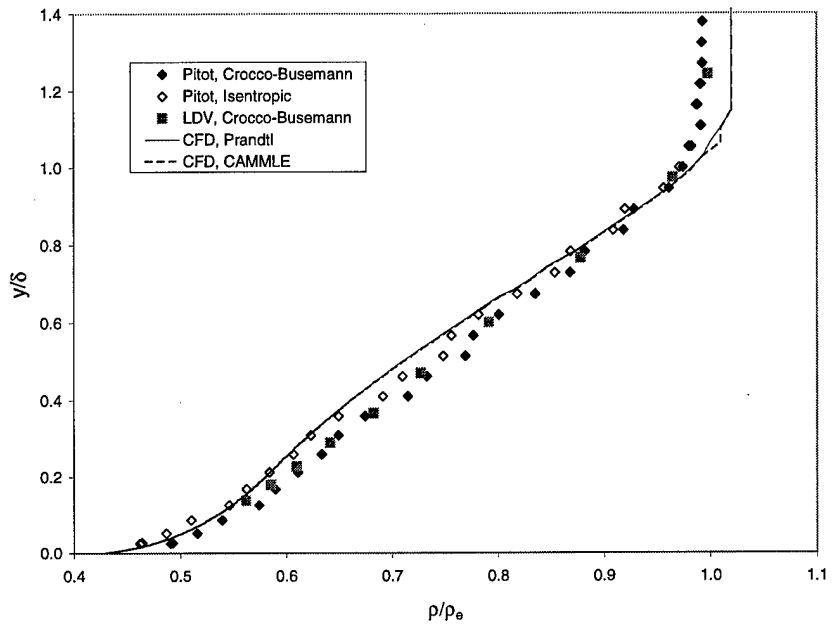

Figure 180. 3D Plate Density Profiles

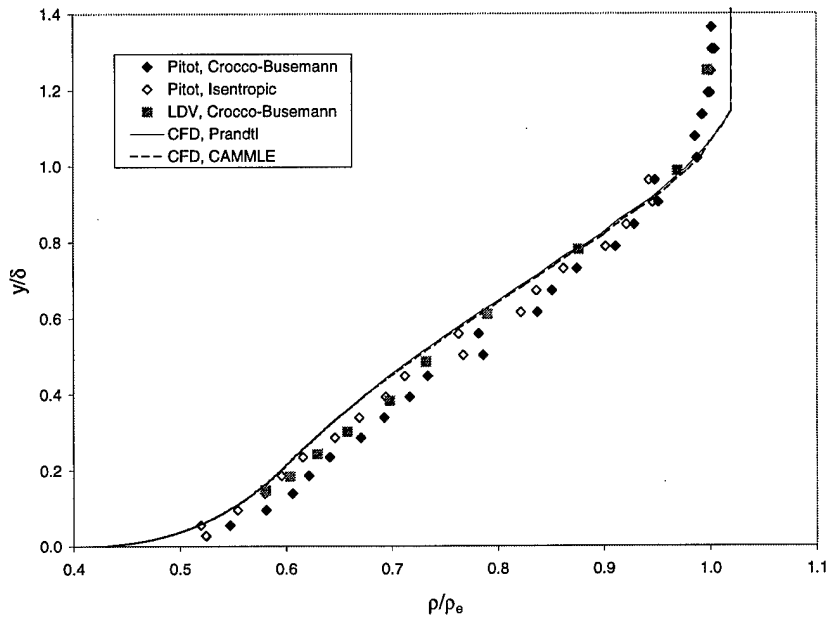

Figure 181. 80 Grit Plate Density Profiles

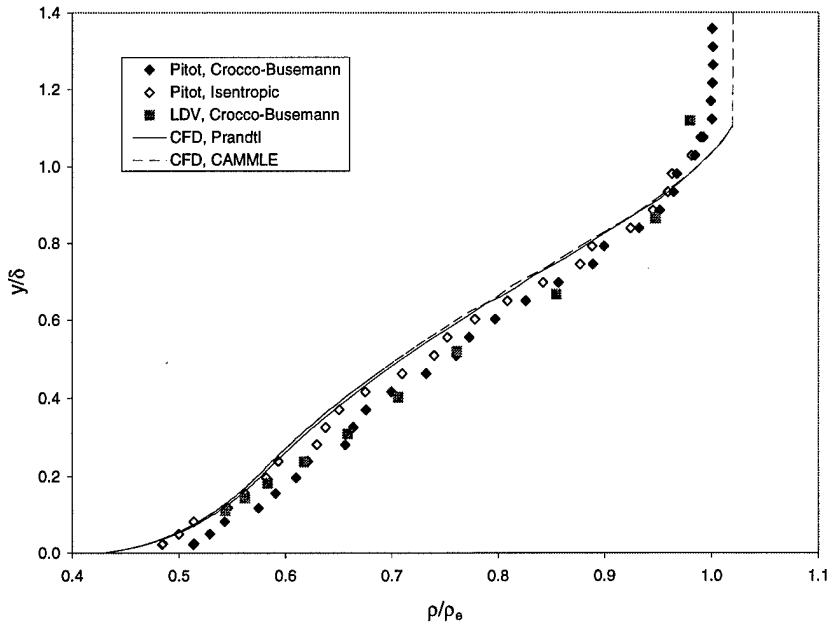

Figure 182. 36 Grit Plate Density Profiles

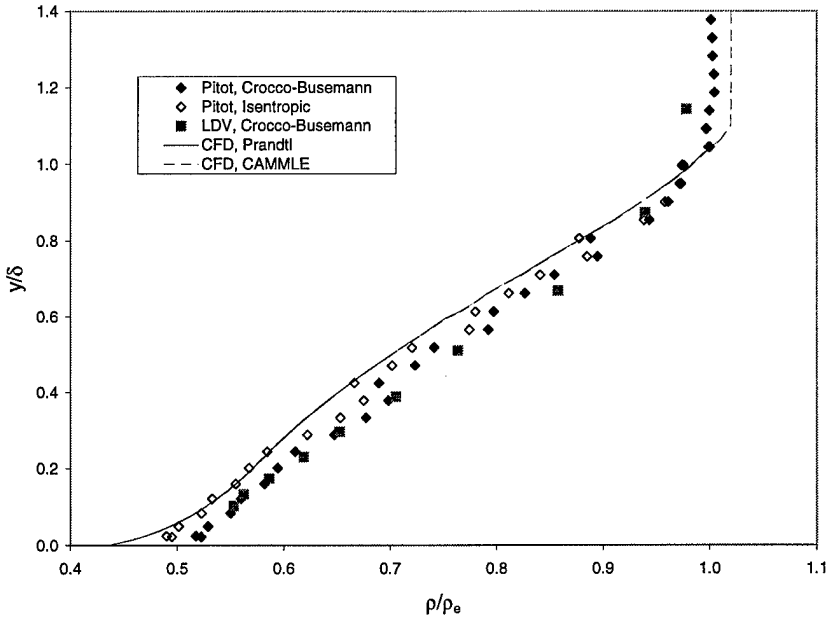

Figure 183. 20 Grit Plate Density Profiles

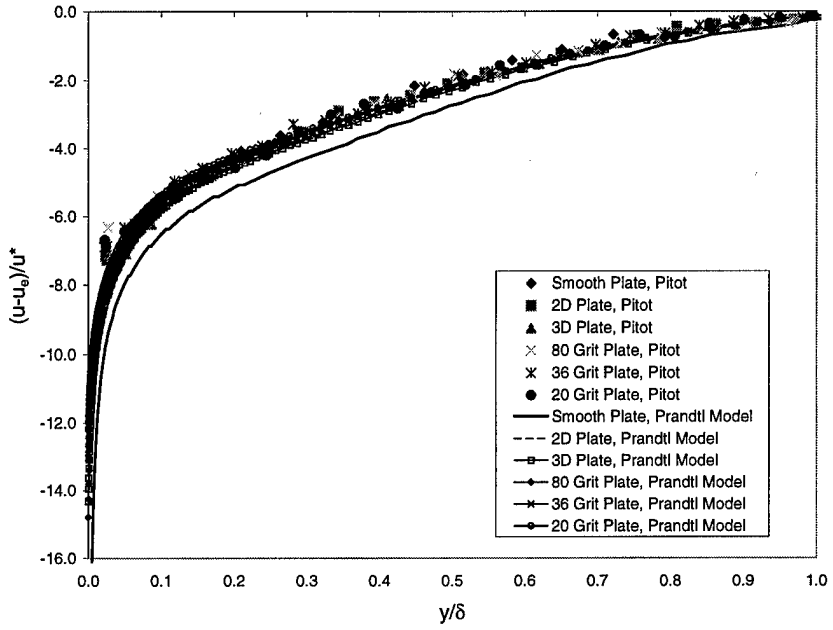

Figure 184. Prandtl Turbulence Model Velocity Defect

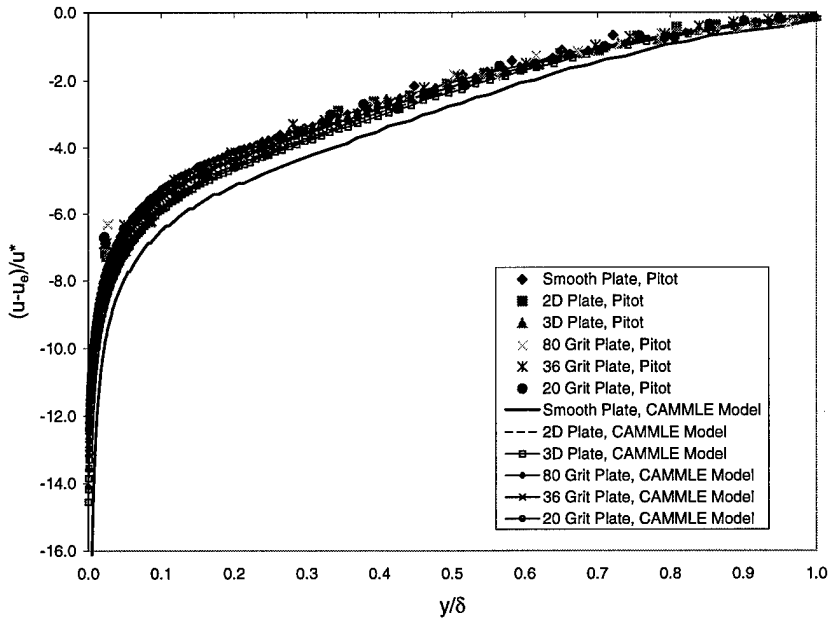

Figure 185. CAMMLE Turbulence Model Velocity Defect

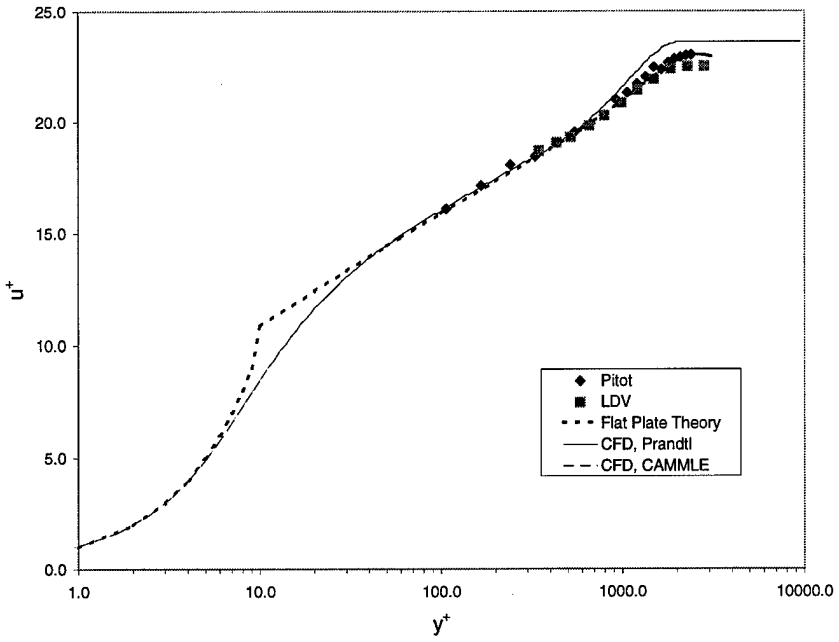

Figure 186. Smooth Plate Van Driest Velocity Profile

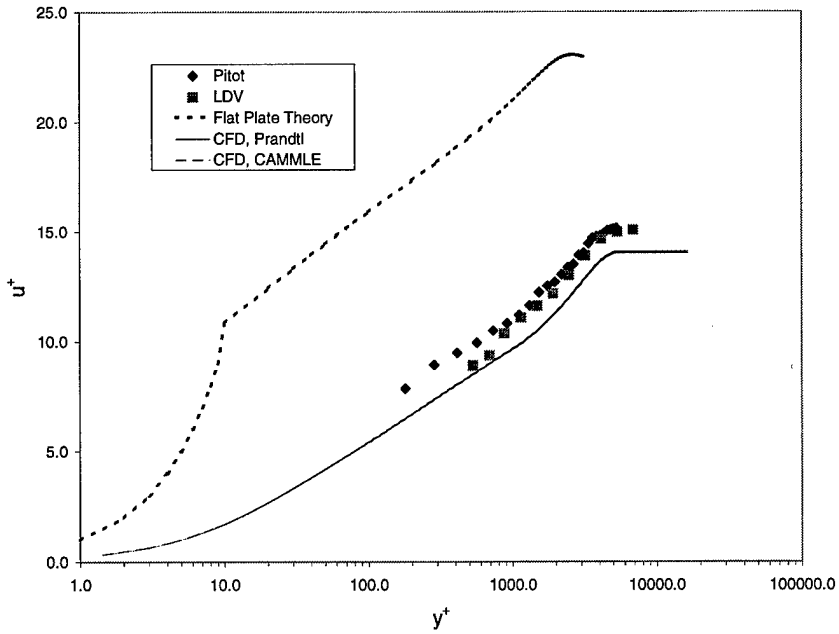

Figure 187. 2D Plate Van Driest Velocity Profile

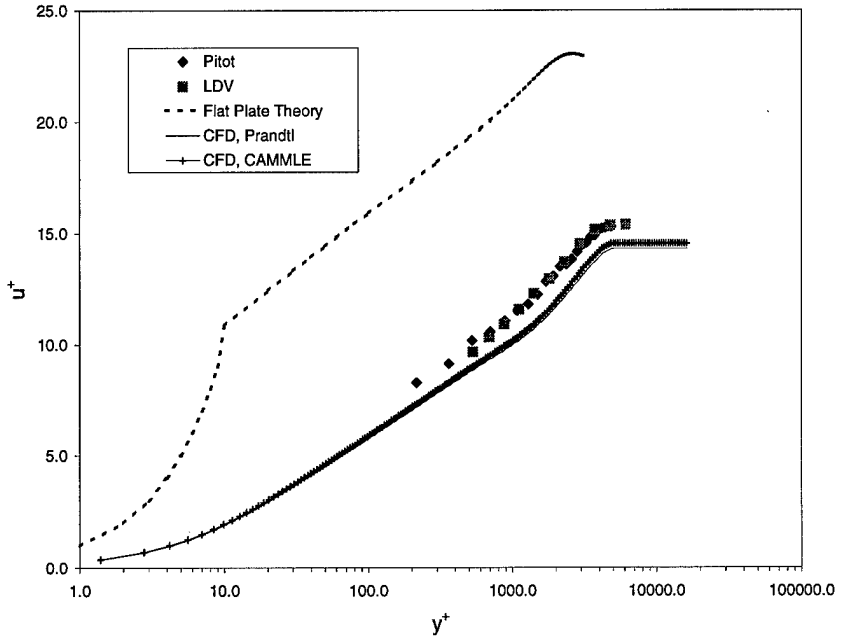

Figure 188. 3D Plate Van Driest Velocity Profile

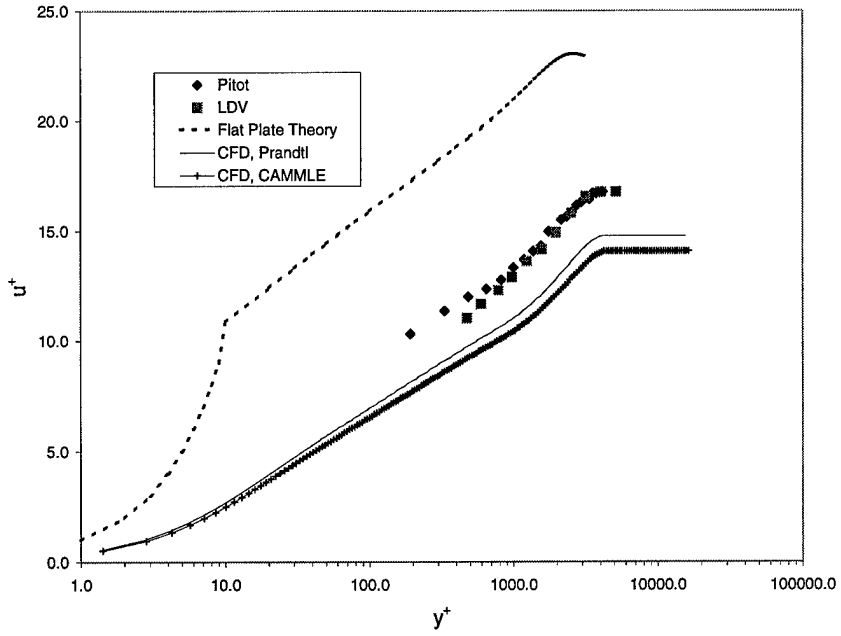

Figure 189. 80 Grit Plate Van Driest Velocity Profile

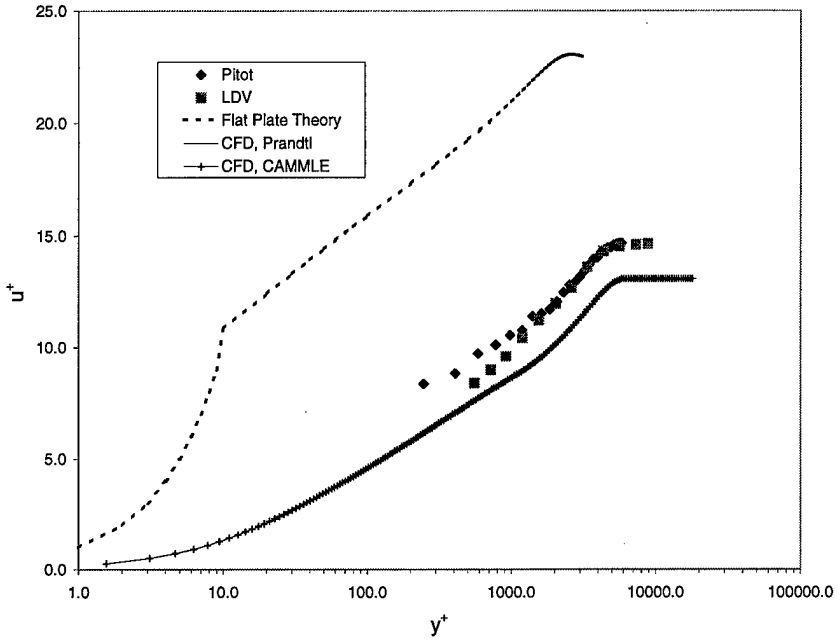

Figure 190. 36 Grit Plate Van Driest Velocity Profile

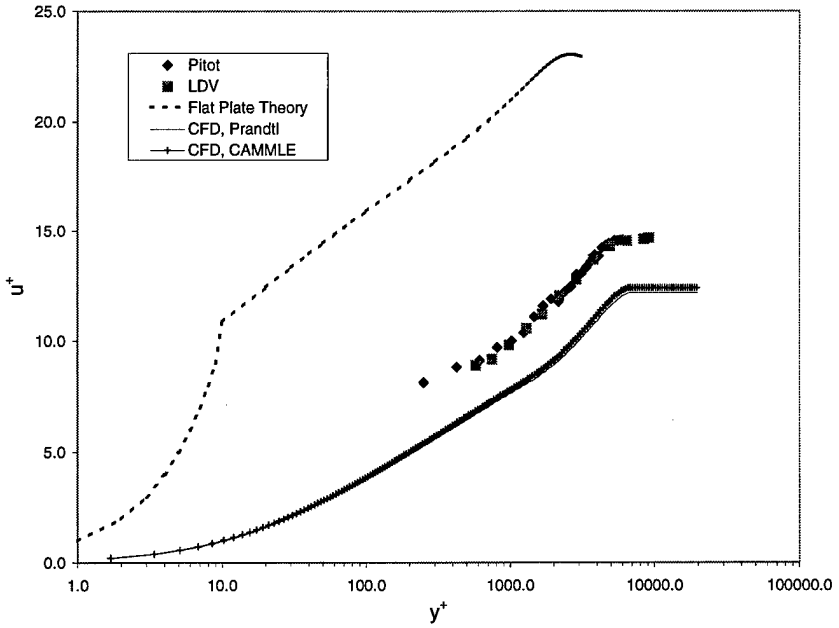

Figure 191. 20 Grit Plate Van Driest Velocity Profile

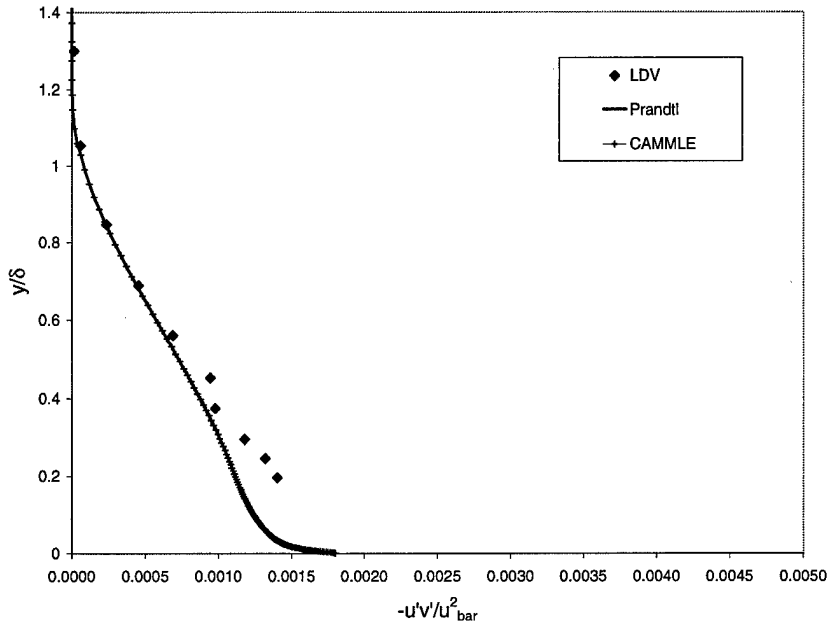

Figure 192. Smooth Plate Incompressible Reynolds Shear Stress

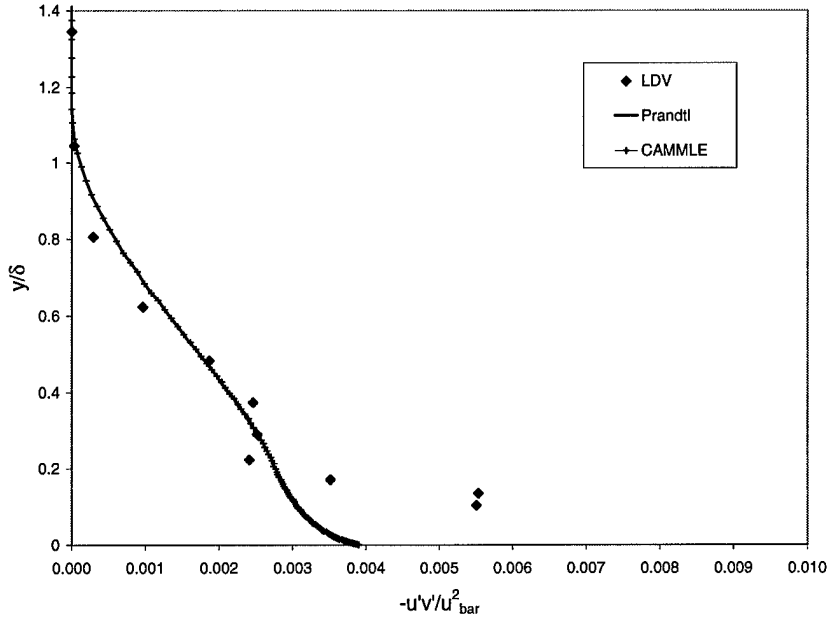

Figure 193. 2D Plate Incompressible Reynolds Shear Stress

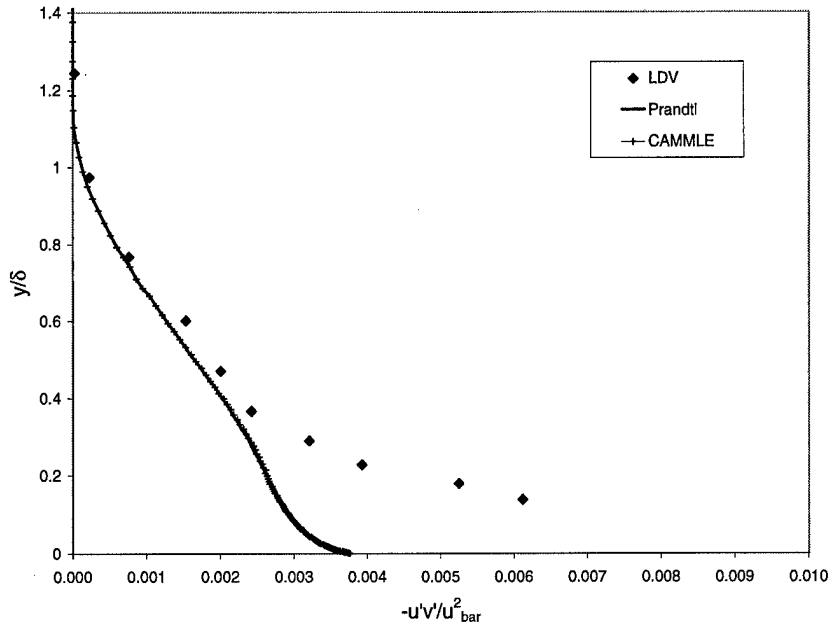

Figure 194. 3D Plate Incompressible Reynolds Shear Stress

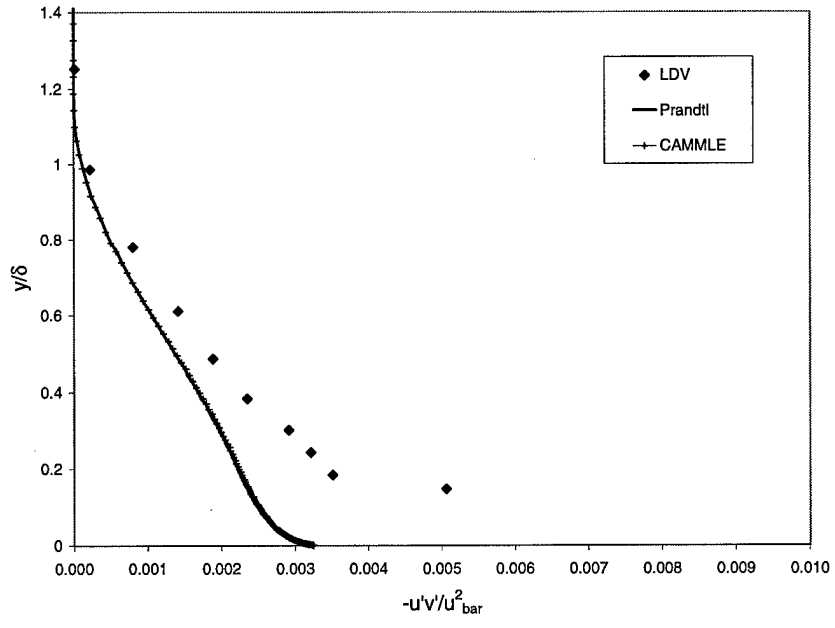

Figure 195. 80 Grit Plate Incompressible Reynolds Shear Stress

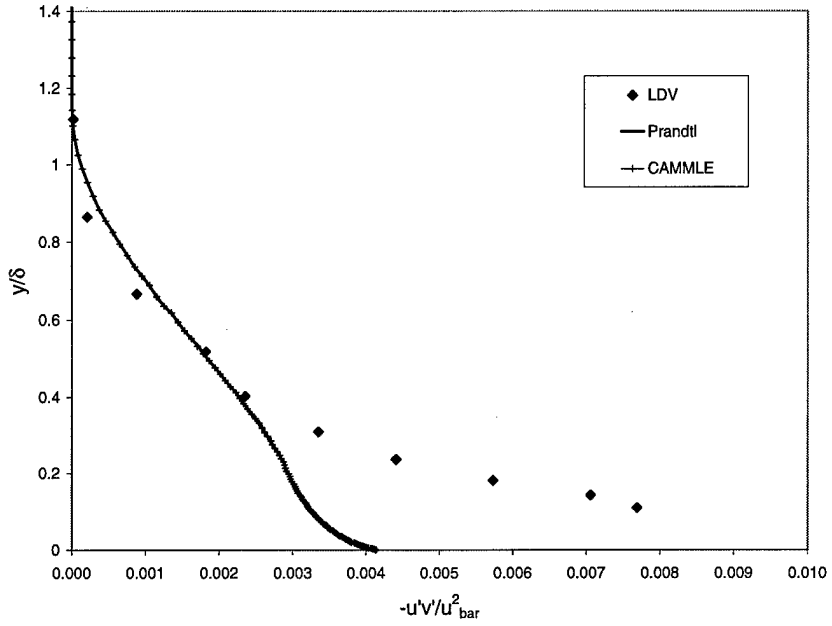

Figure 196. 36 Grit Plate Incompressible Reynolds Shear Stress

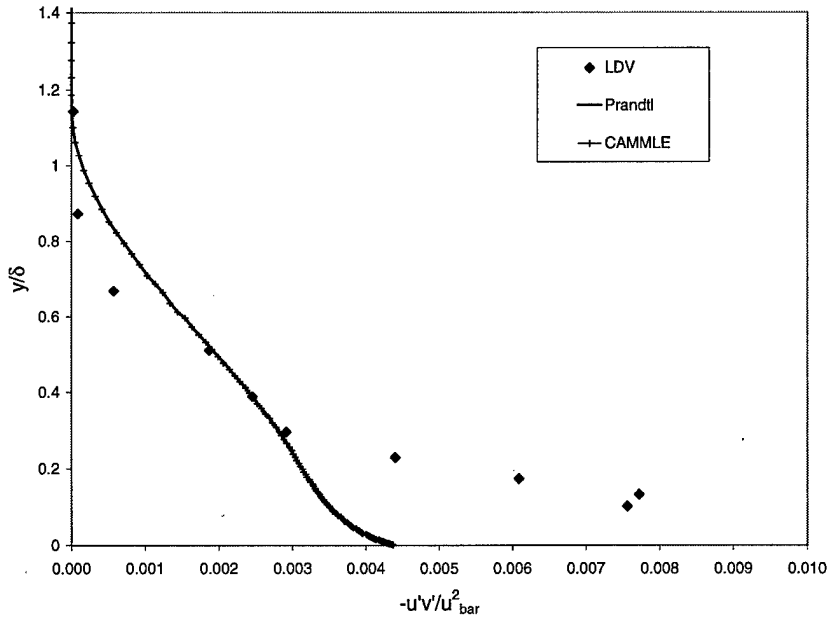

Figure 197. 20 Grit Plate Incompressible Reynolds Shear Stress

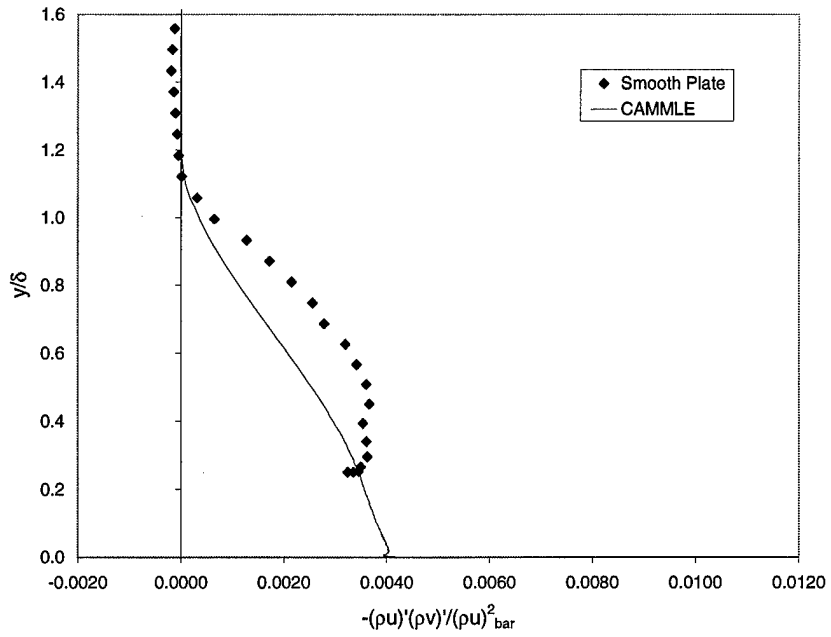

Figure 198. Smooth Plate Compressible Reynolds Shear Stress

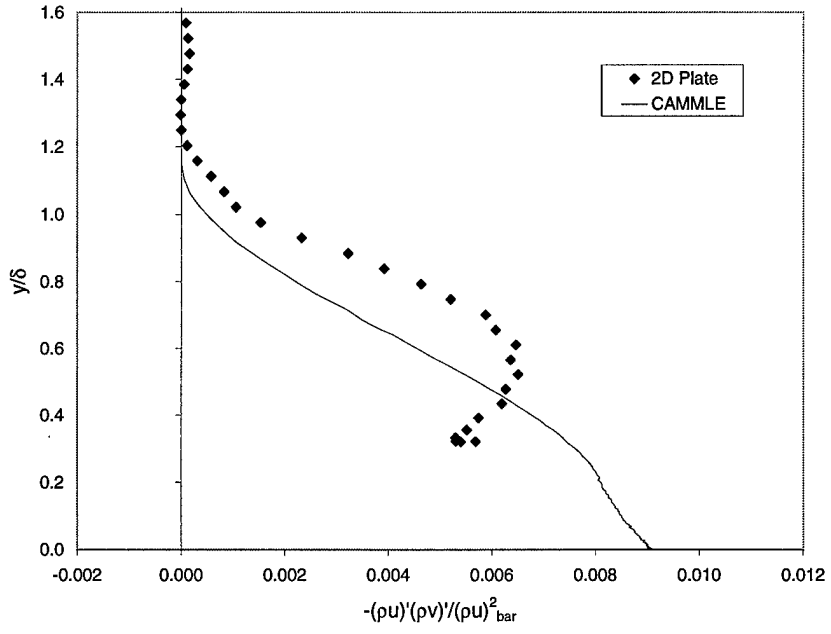

Figure 199. 2D Plate Compressible Reynolds Shear Stress

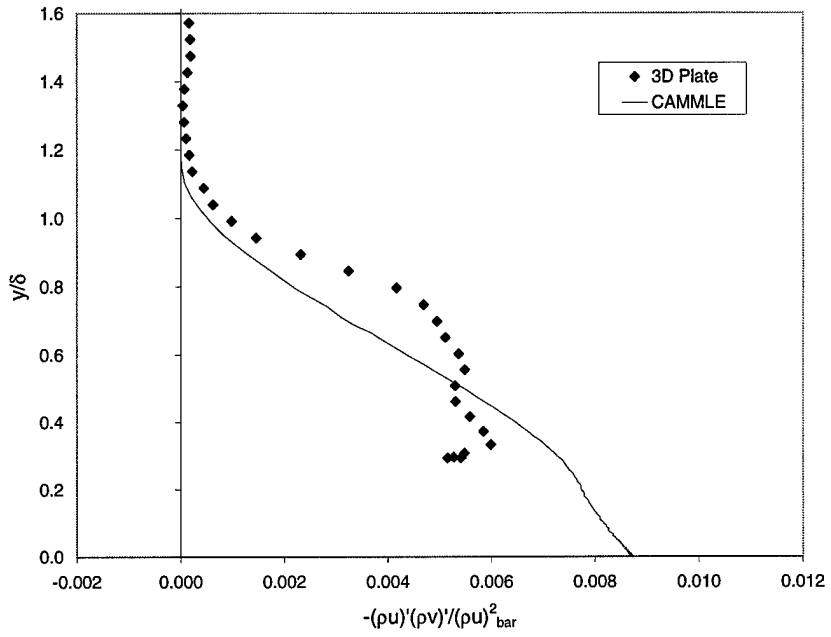

Figure 200. 3D Plate Compressible Reynolds Shear Stress

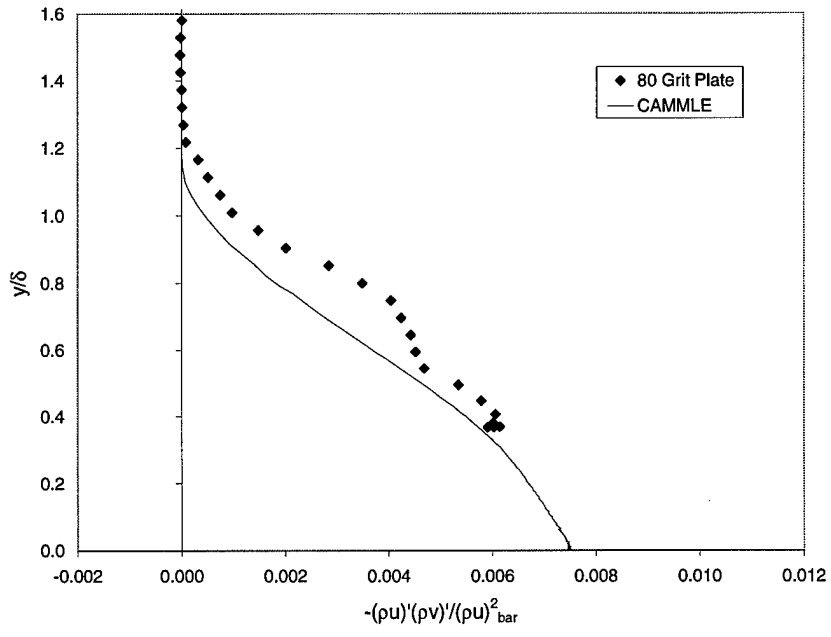

Figure 201. 80 Grit Plate Compressible Reynolds Shear Stress

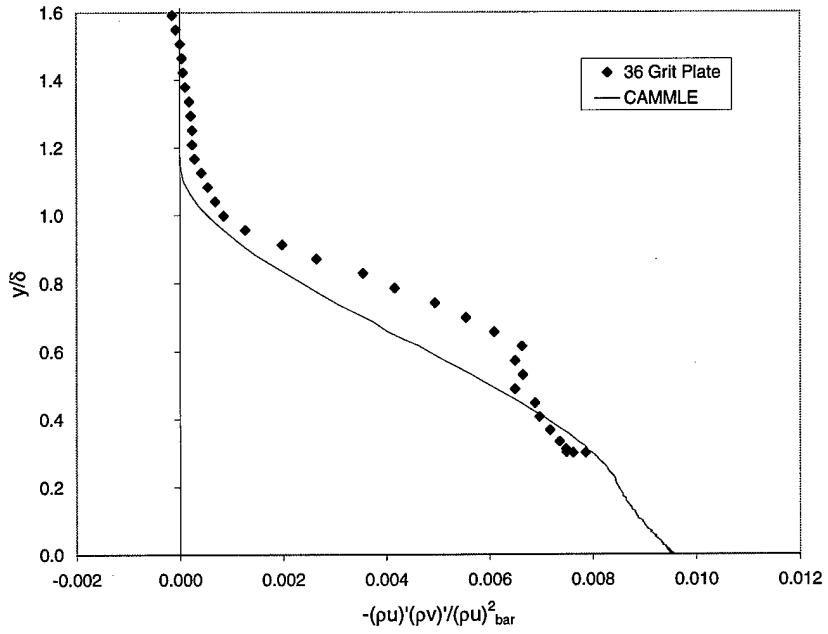

Figure 202. 36 Grit Plate Compressible Reynolds Shear Stress

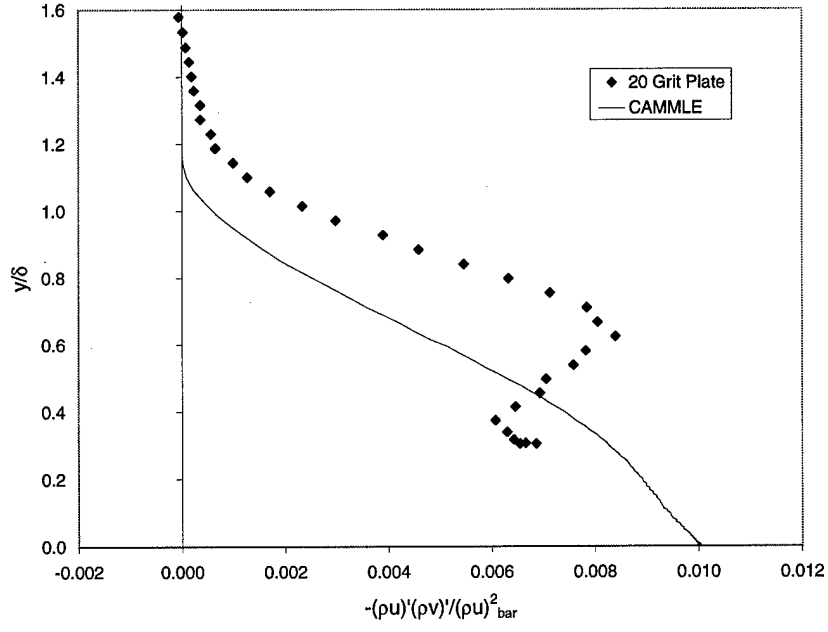

Figure 203. 20 Grit Plate Compressible Reynolds Shear Stress

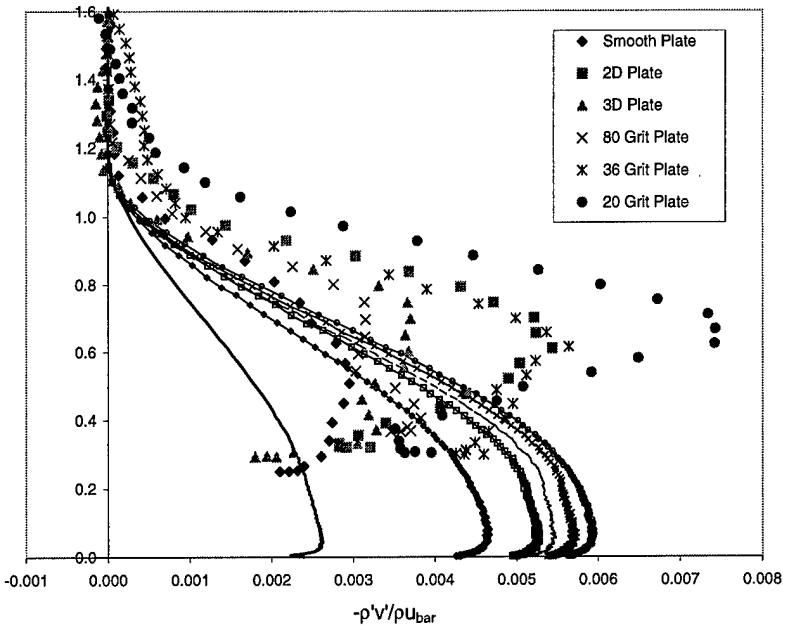

Figure 204. Second Order Density - Velocity Correlation

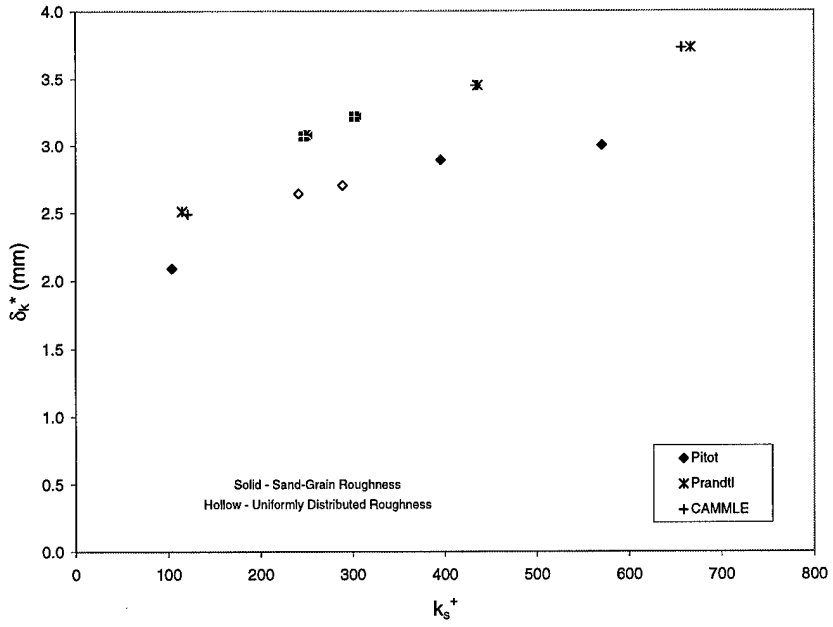

Figure 205. Displacement Thickness Versus Roughness Reynolds Number

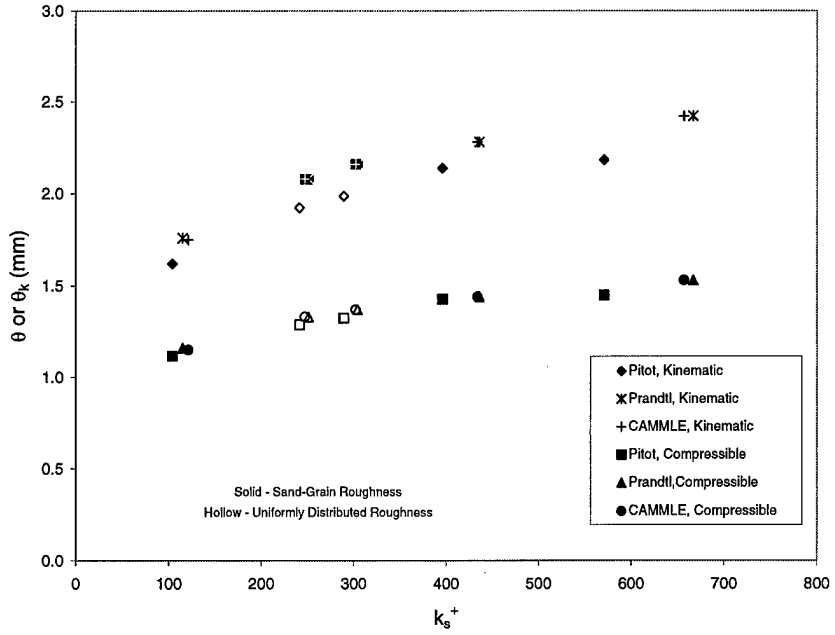

Figure 206. Momentum Thickness Versus Roughness Reynolds Number

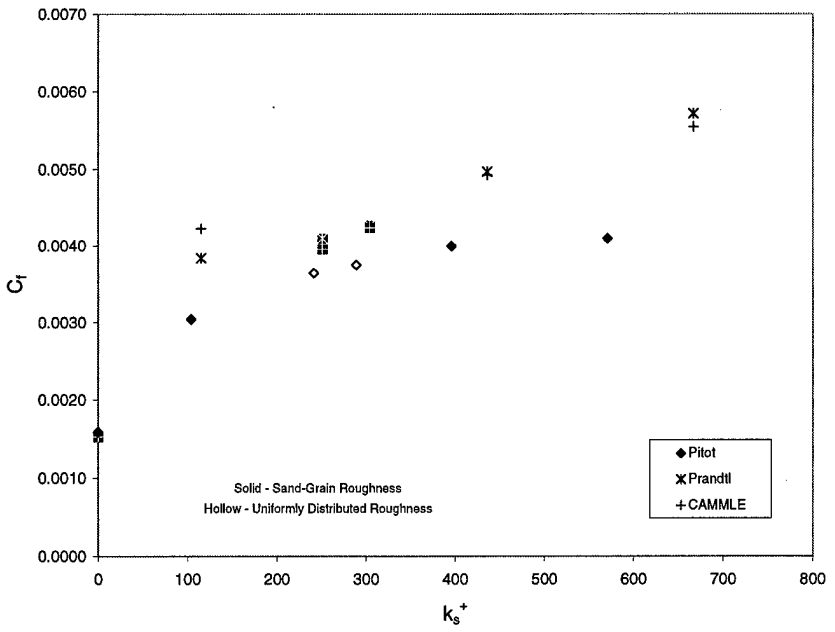

Figure 207. Skin Friction Coefficient Versus Roughness Reynolds Number

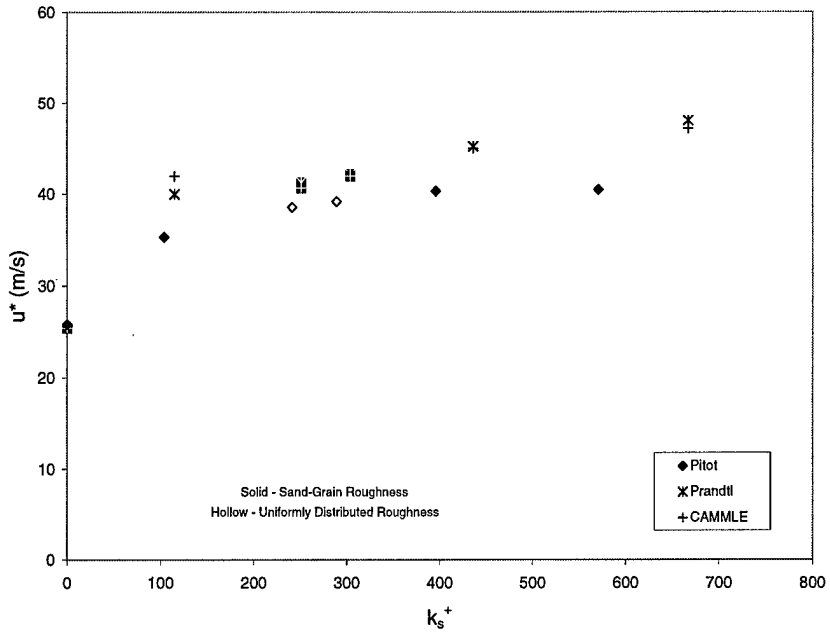

Figure 208. Friction Velocity Versus Roughness Reynolds Number

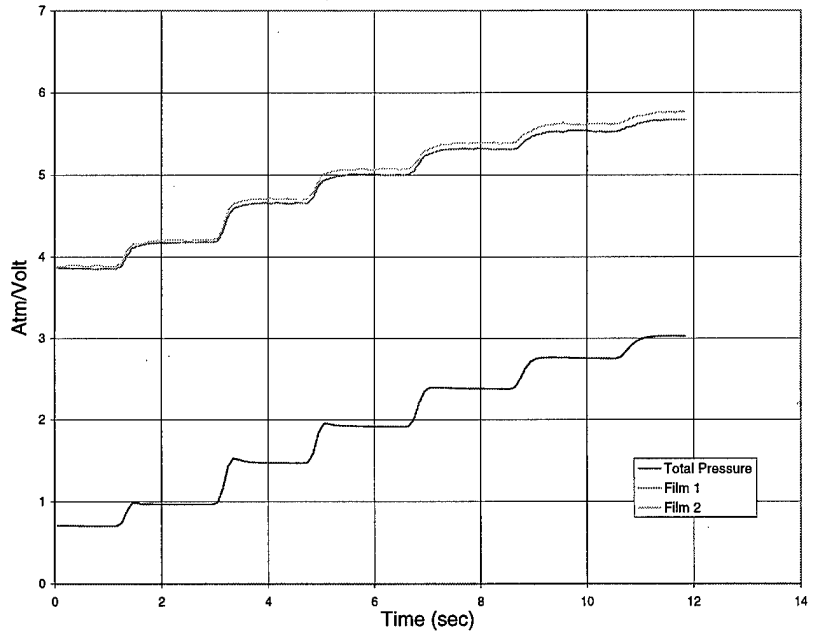

Figure 209. Smooth Plate, x-y Plane, Cross-Film Calibration Data

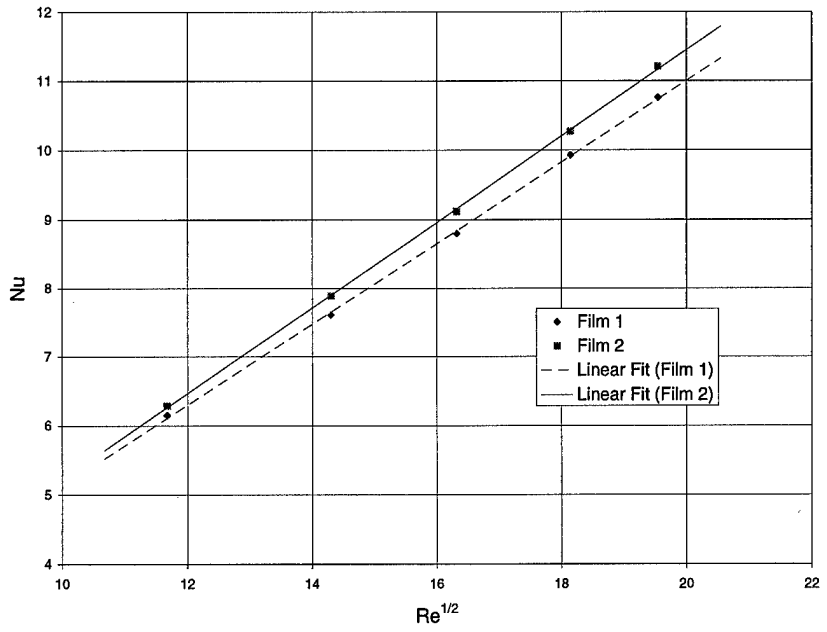

Figure 210. Smooth Plate, x-y Plane, Cross-Film Calibration

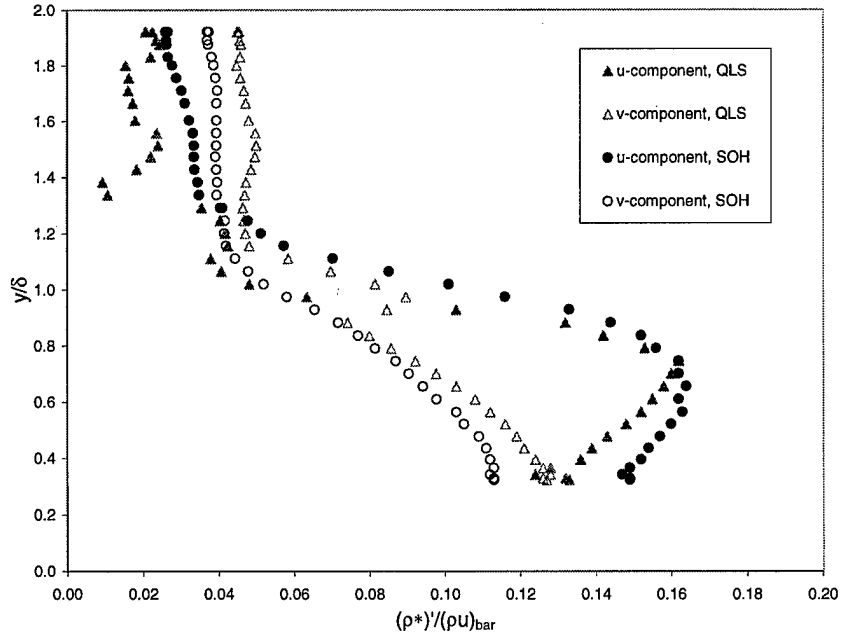

Figure 211. 2D Plate, Mutiple Overheat, ρu-Turbulence Intensity

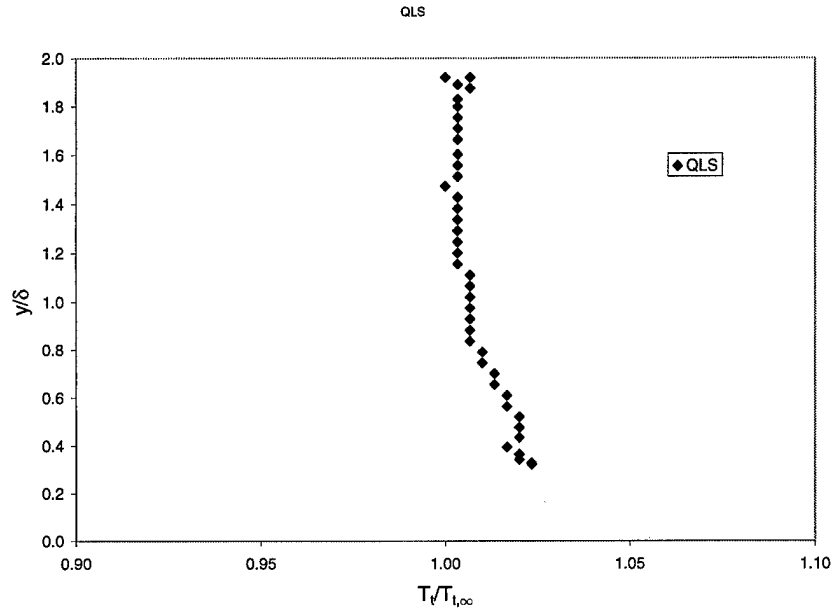

Figure 212. 2D Plate, Multiple Overheat, Total Temperature Profile

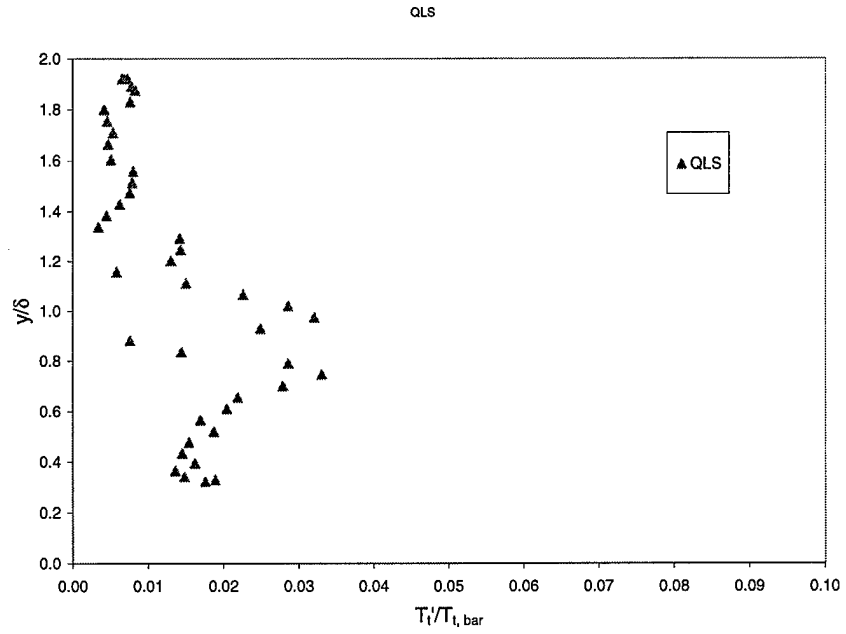

Figure 213. 2D Plate, Mutiple Overheat, T_t-Turbulence Intensity

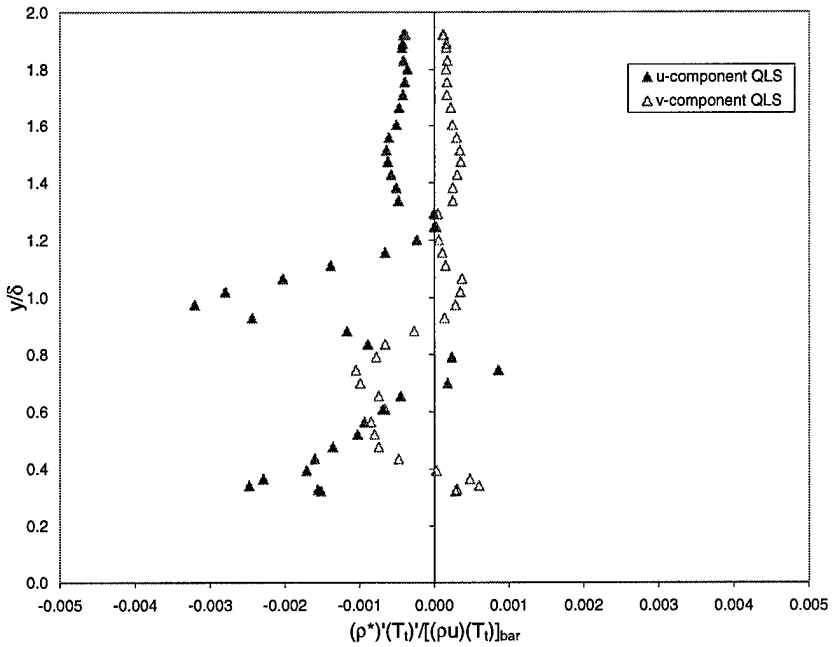

Figure 214. 2D Plate, Multiple Overheat, Second Order, Mass Flux - Total Temperature Correlation

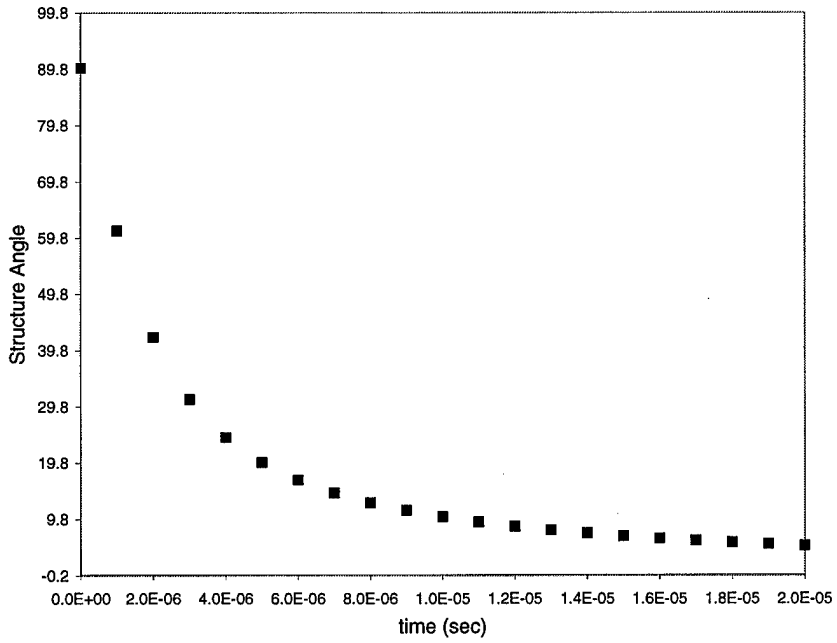

Figure 215. Flow Structure Angle Versus Cross-Correlation Peak Time Lag

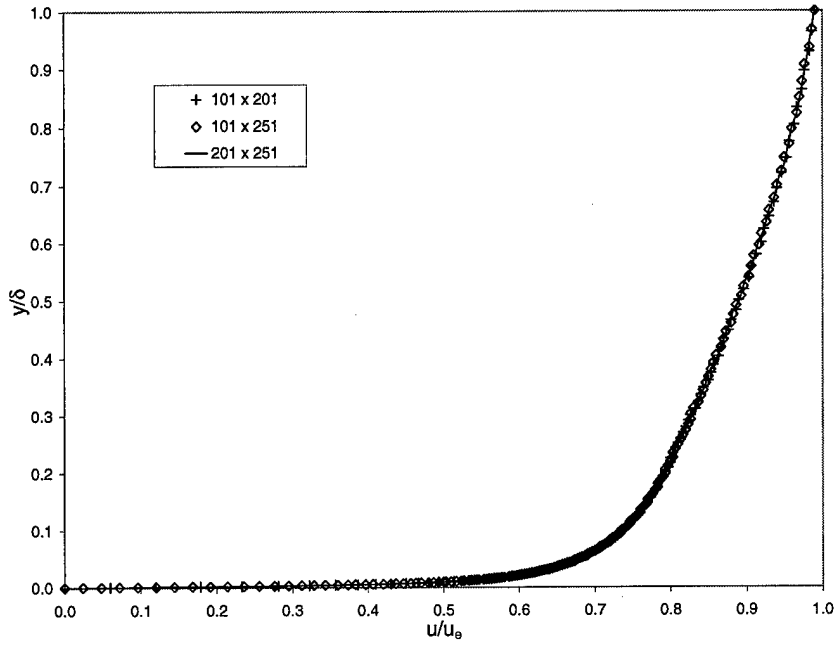

Figure 216. Grid Resolution Velocity Profiles

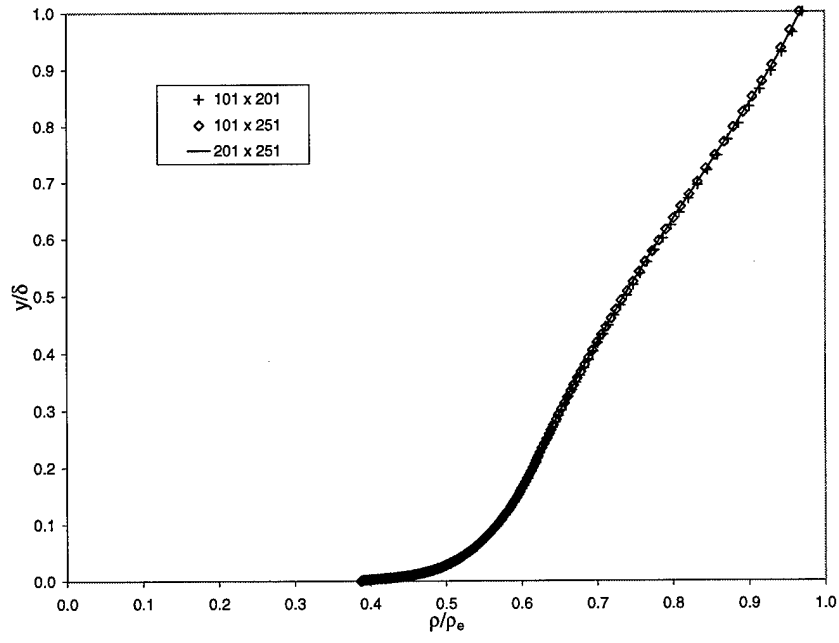

Figure 217. Grid Resolution Density Profiles

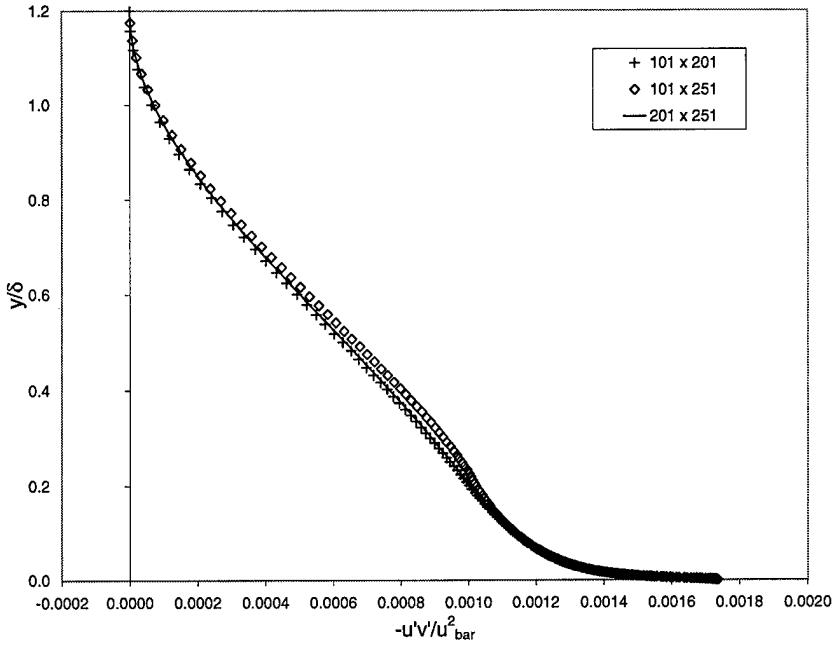

Figure 218. Grid Resolution Kinematic Reynolds Shear Stress Profiles

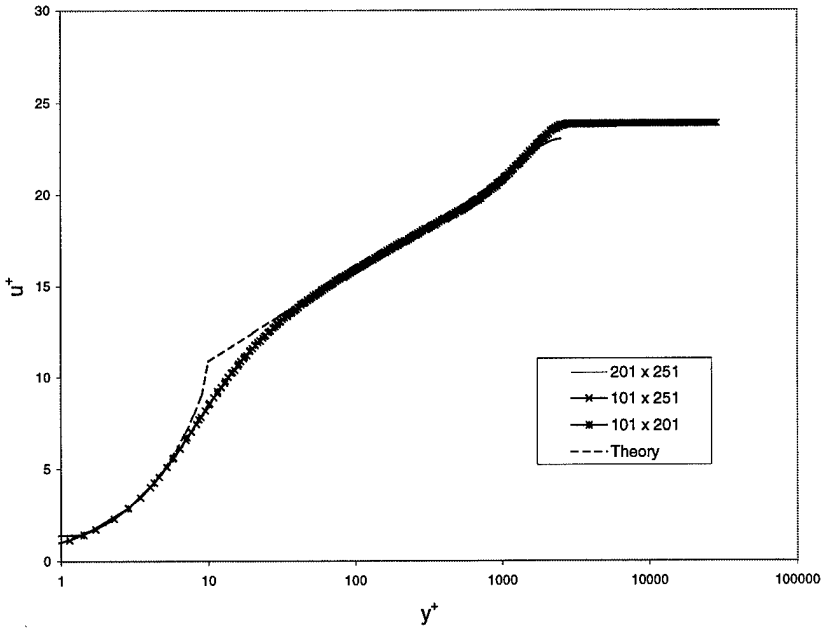

Figure 219. Turbulence Model Validation Van Driest Velocity Profiles

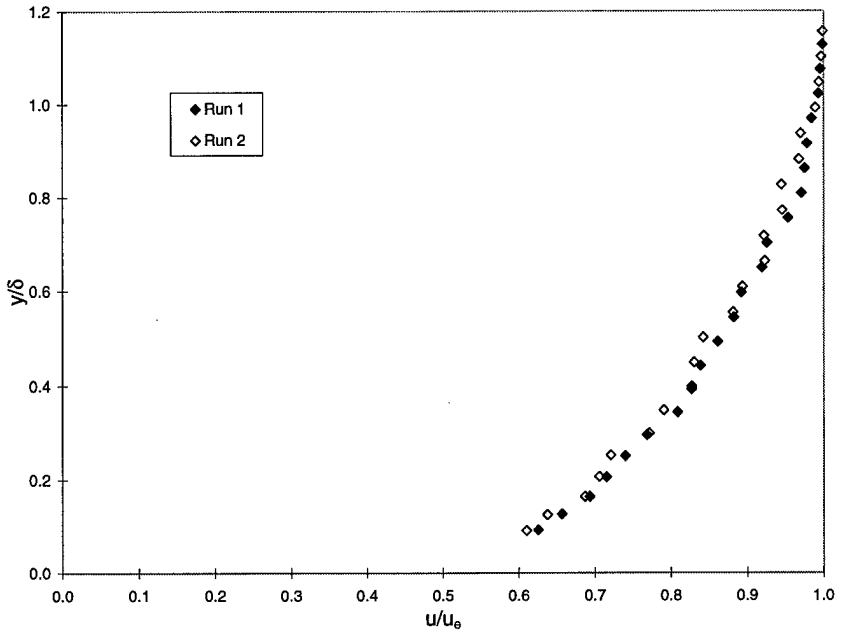

Figure 220. 2D Plate Pitot Probe Velocity Profiles

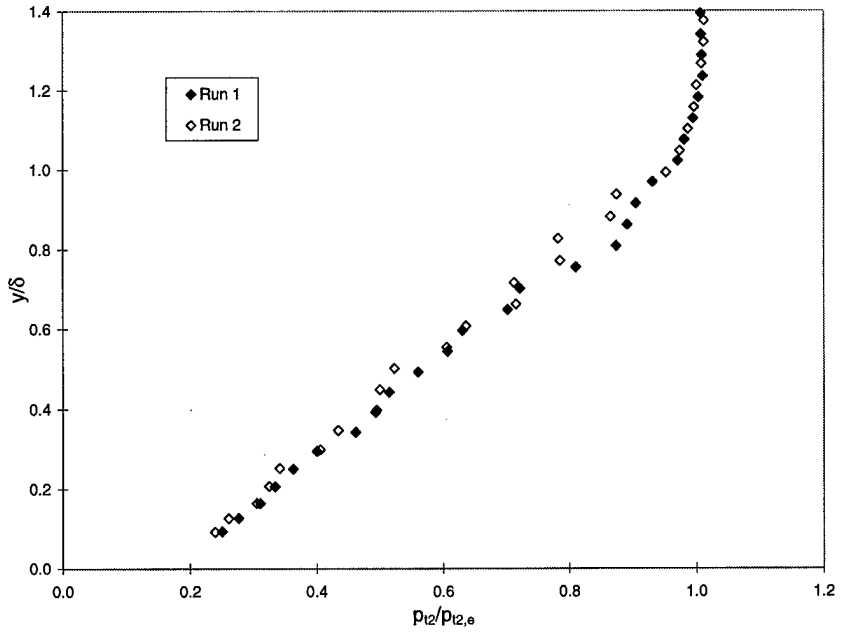

Figure 221. 2D Plate Pitot Probe P_{t2} Profiles

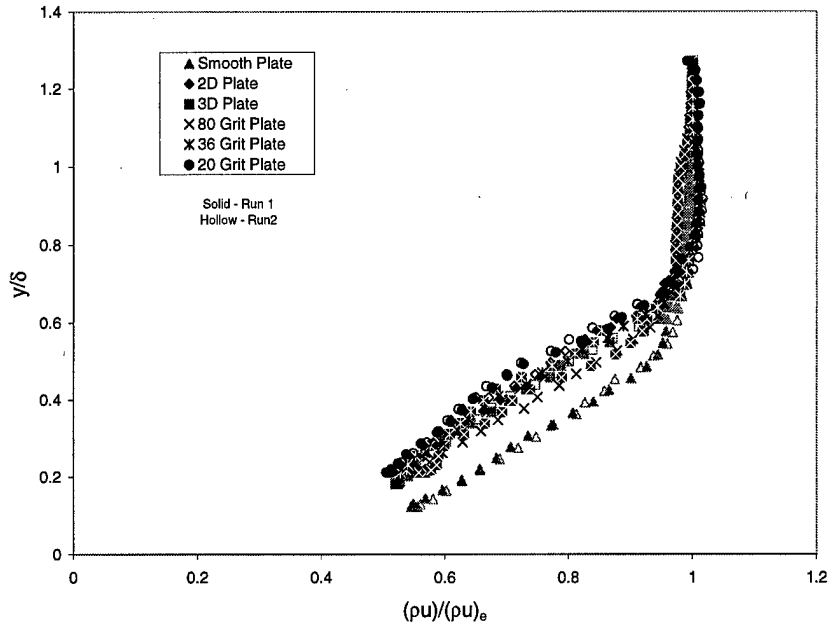

Figure 222. x-y Plane, Cross-Film, $(\rho u)_{bar}$ Profiles

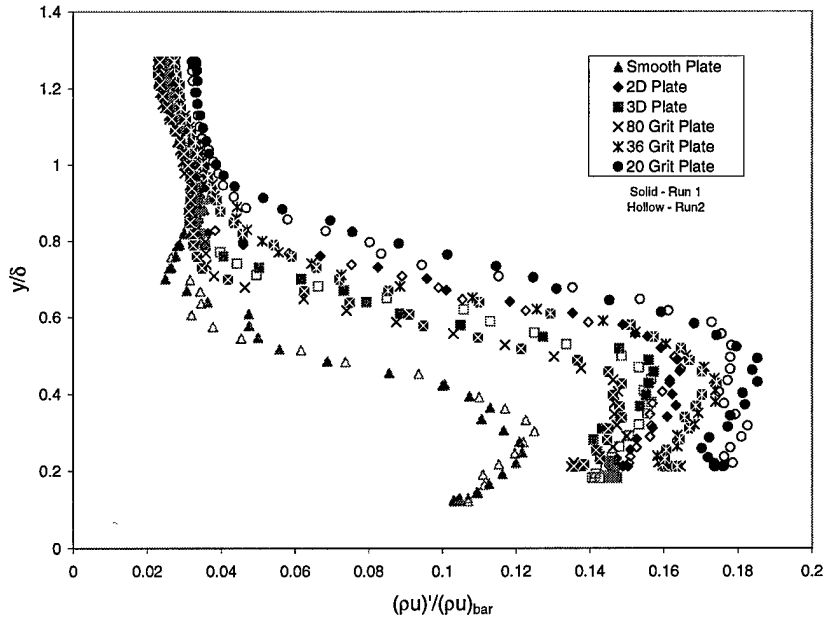

Figure 223. ρu-Turbulence Intensity

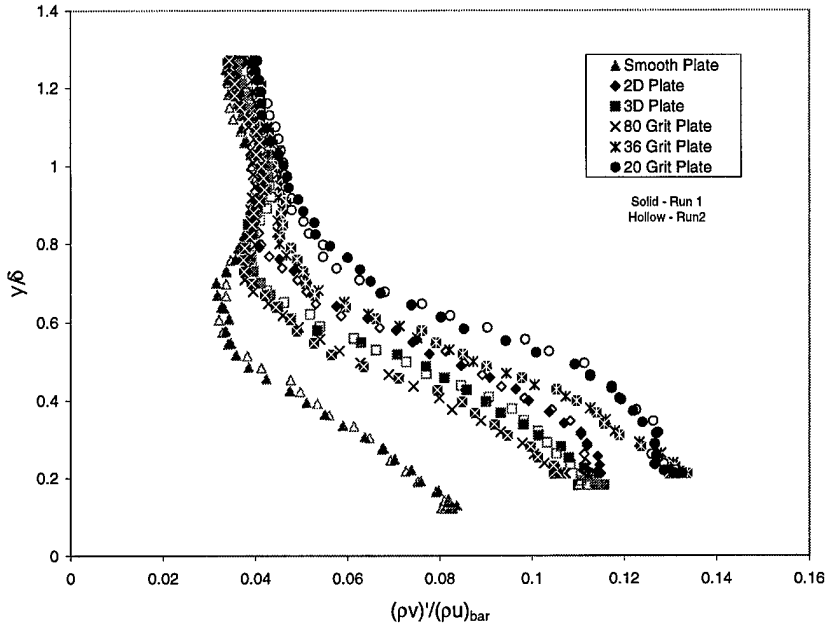

Figure 224. ρv-Turbulence Intensity

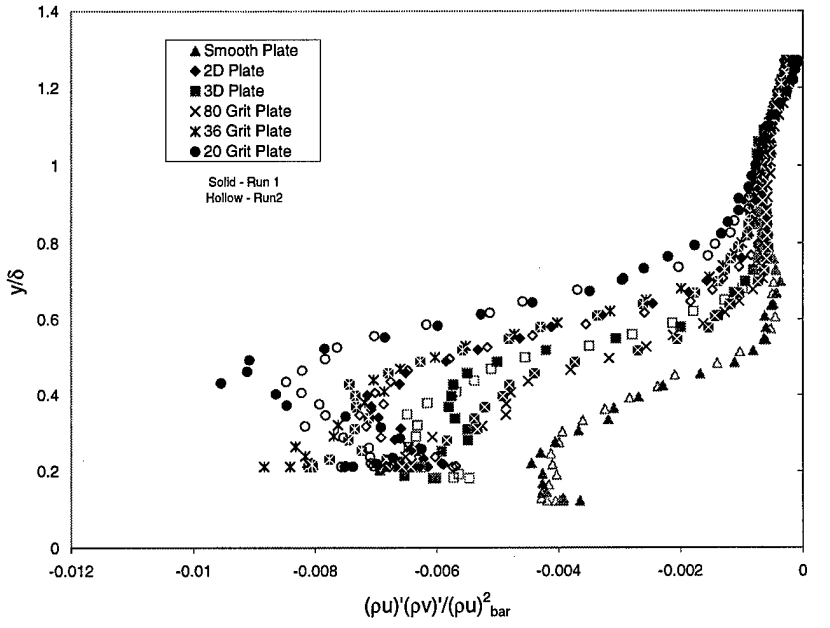

Figure 225. x-y Plane, Cross-Film, Mass Flux Shear Stress

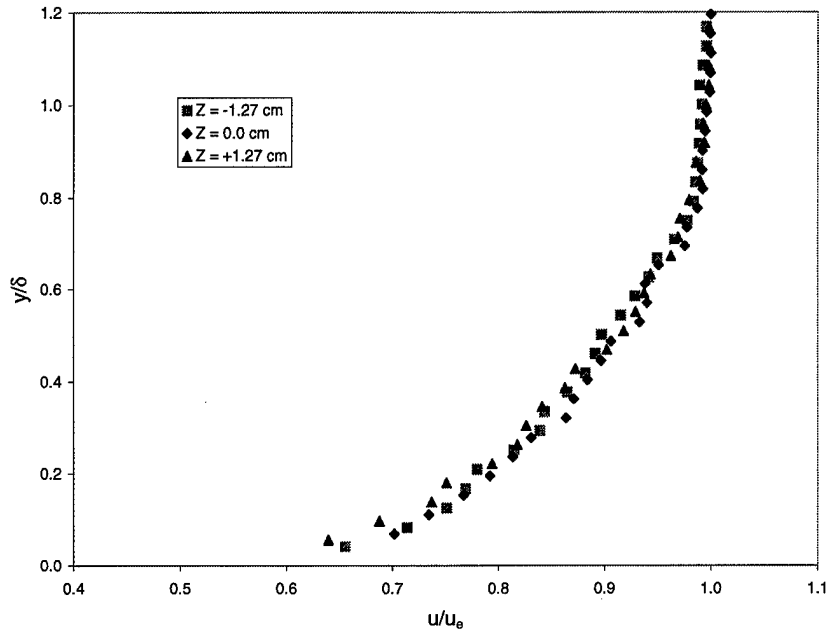

Figure 226. Velocity Comparison for Two-Dimensionality Check

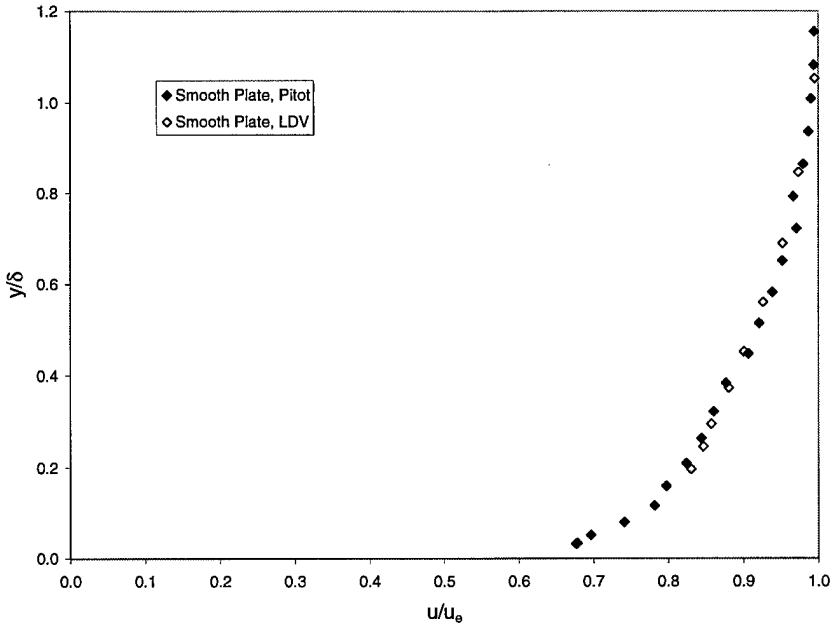

Figure 227. Smooth Plate Velocity Profiles

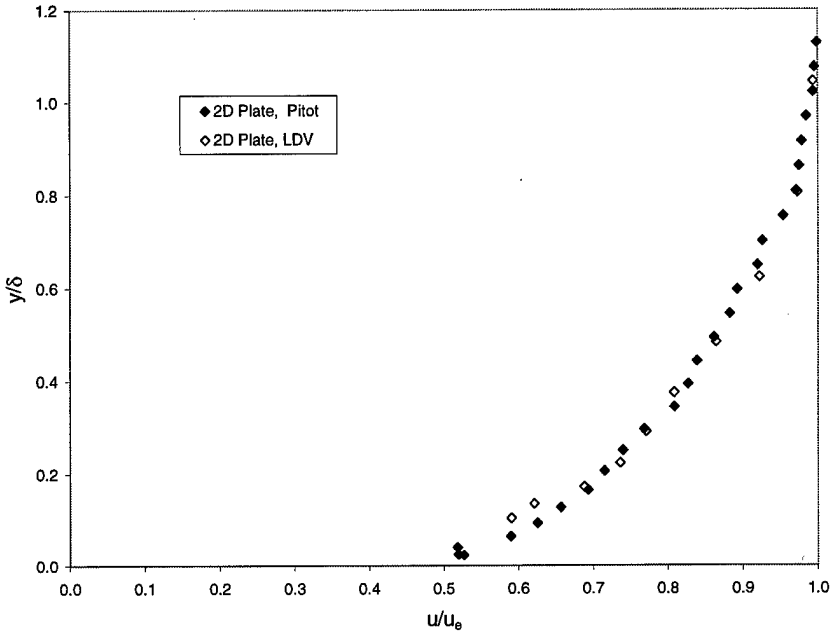

Figure 228. 2D Plate Velocity Profiles

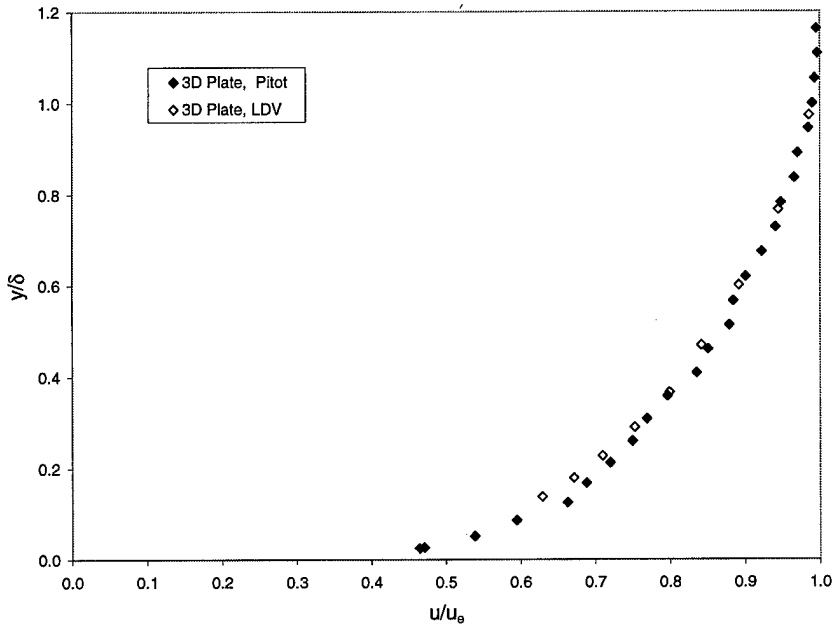

Figure 229. 3D Plate Velocity Profiles

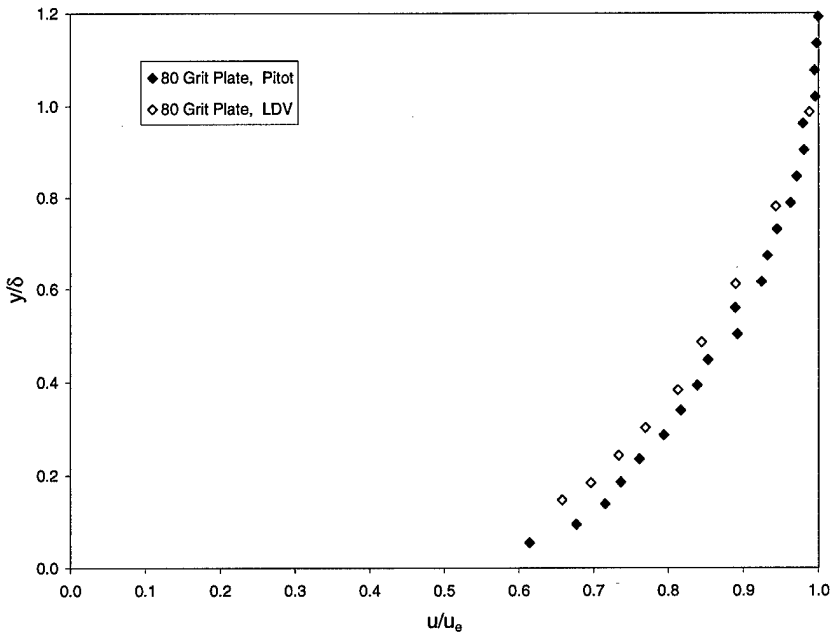

Figure 230. 80 Grit Plate Velocity Profiles

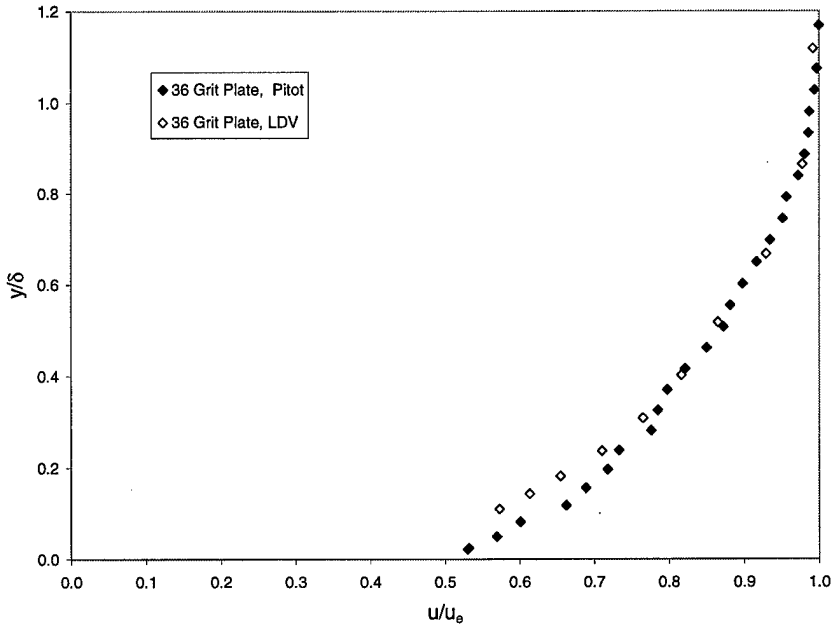

Figure 231. 36 Grit Plate Velocity Profiles

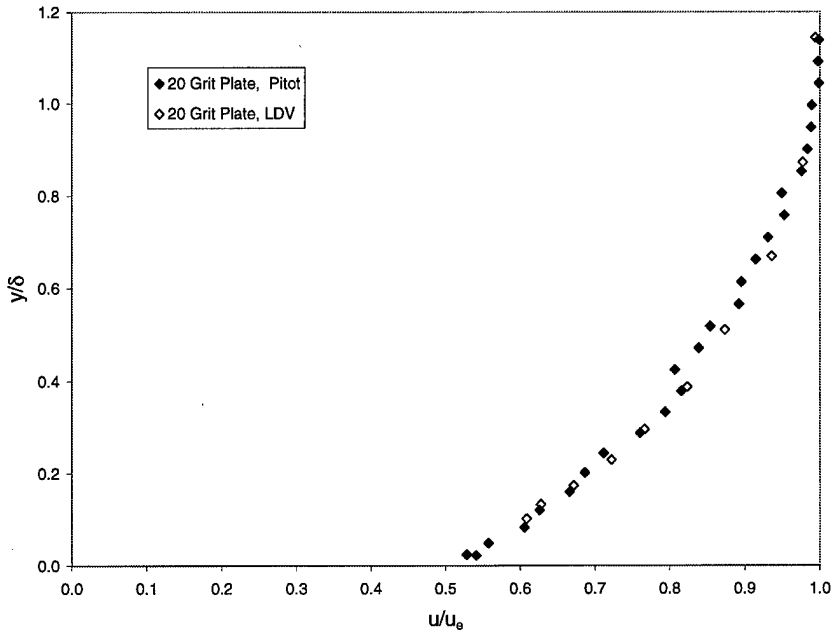

Figure 232. 20 Grit Plate Velocity Profiles

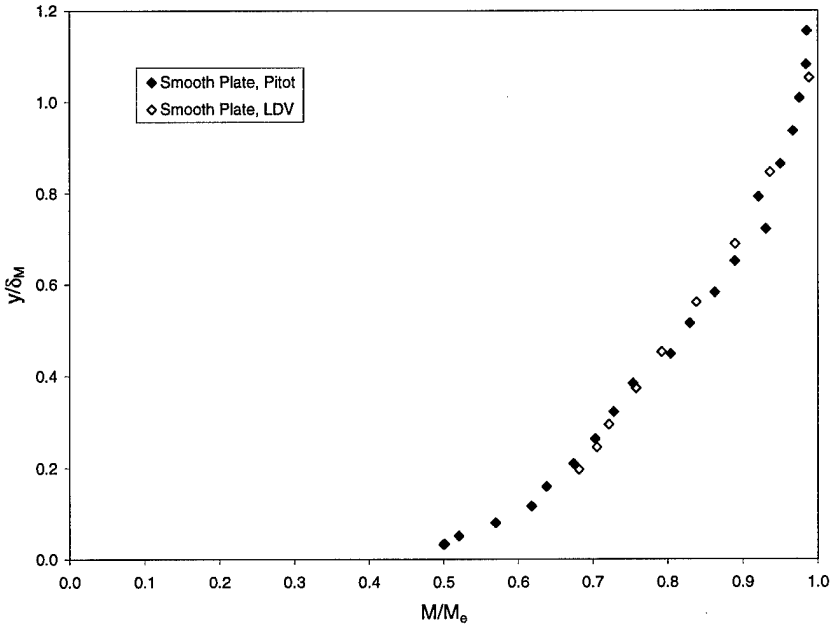

Figure 233. Smooth Plate Mach Profiles

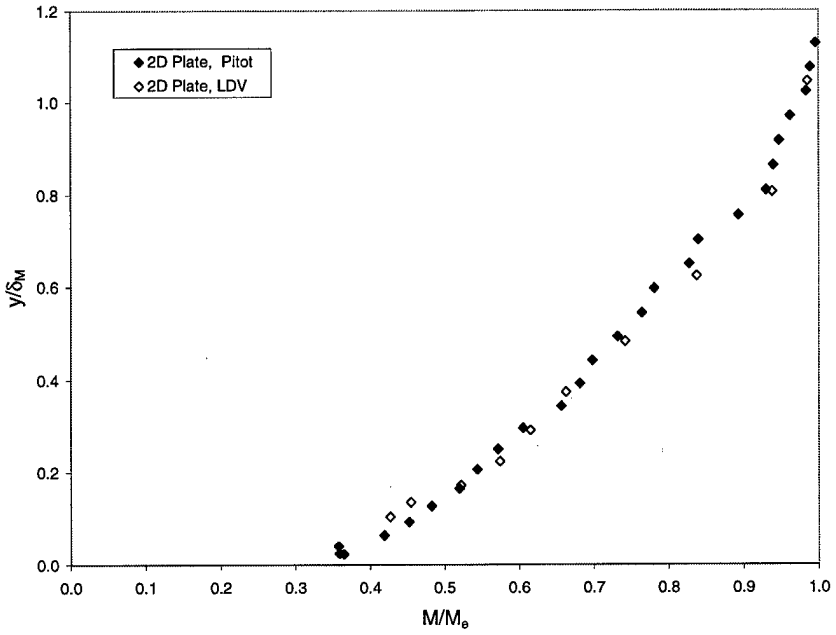

Figure 234. 2D Plate Mach Profiles

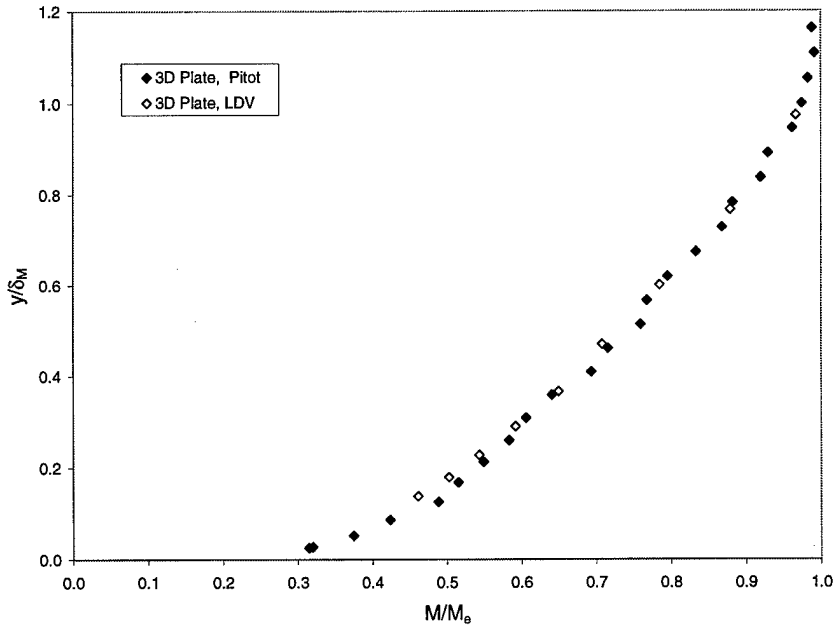

Figure 235. 3D Plate Mach Profiles

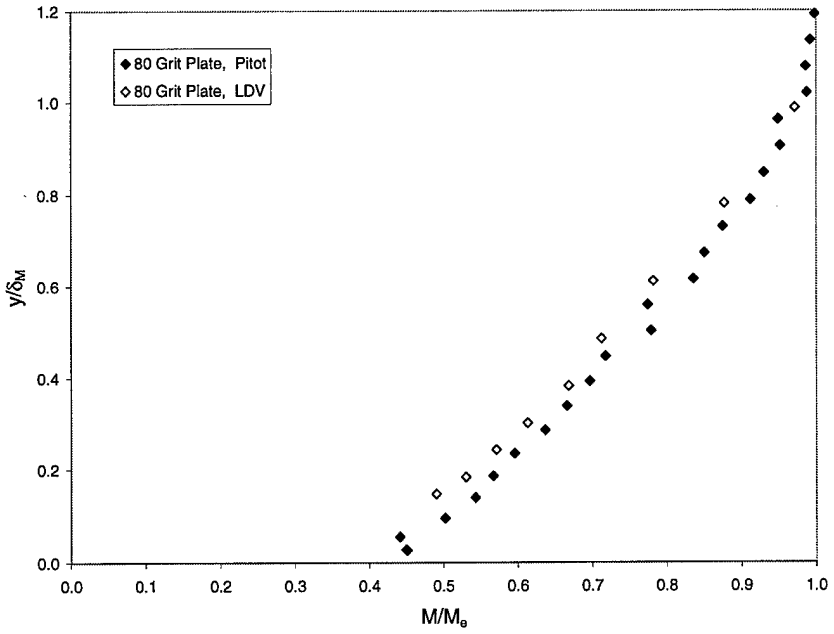

Figure 236. 80 Grit Plate Mach Profiles

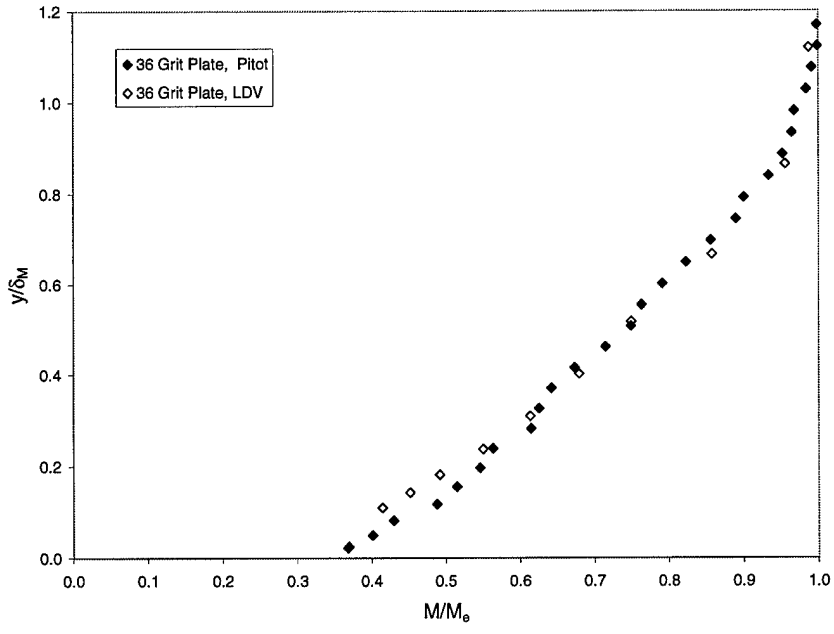

Figure 237. 36 Grit Plate Mach Profiles

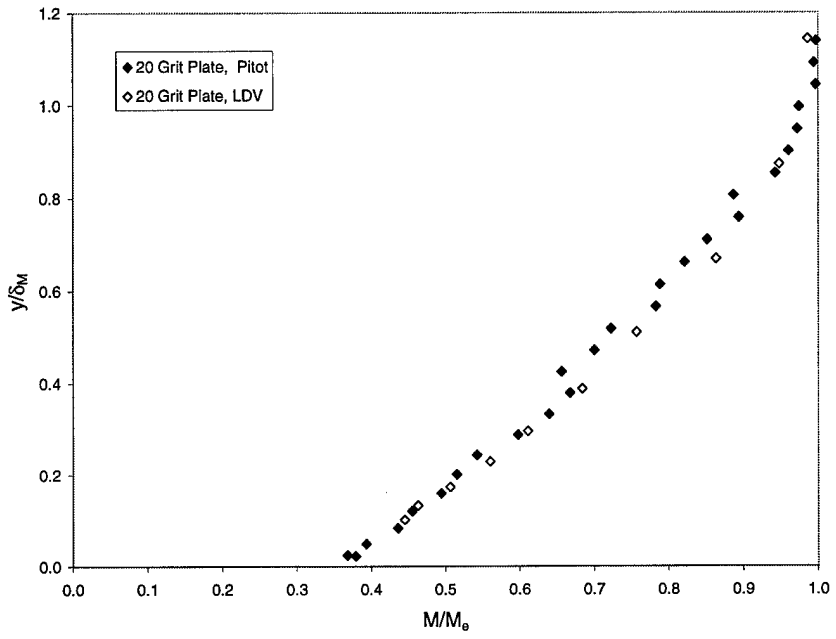

Figure 238. 20 Grit Plate Mach Profiles

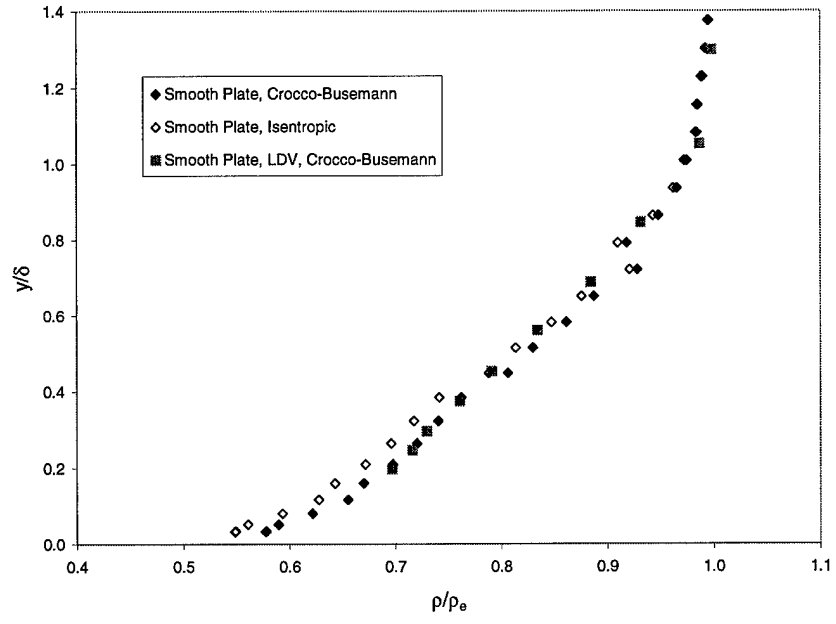

Figure 239. Pitot and LDV Smooth Plate Density Profiles

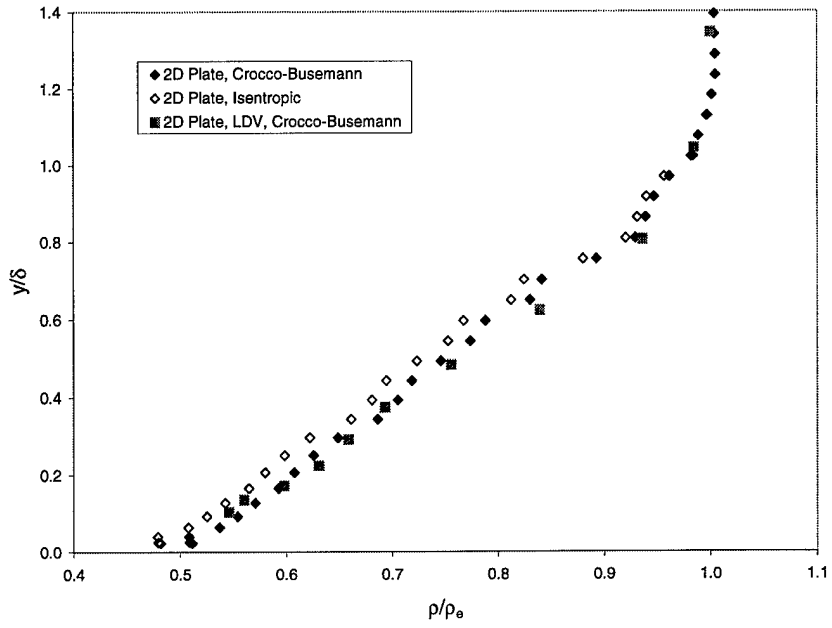

Figure 240. Pitot and LDV 2D Plate Density Profiles

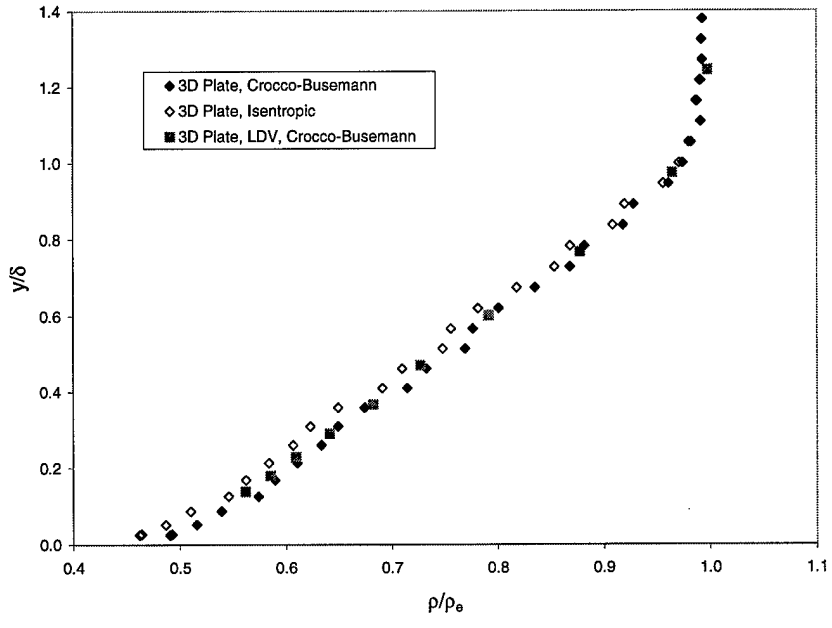

Figure 241. Pitot and LDV 3D Plate Density Profiles

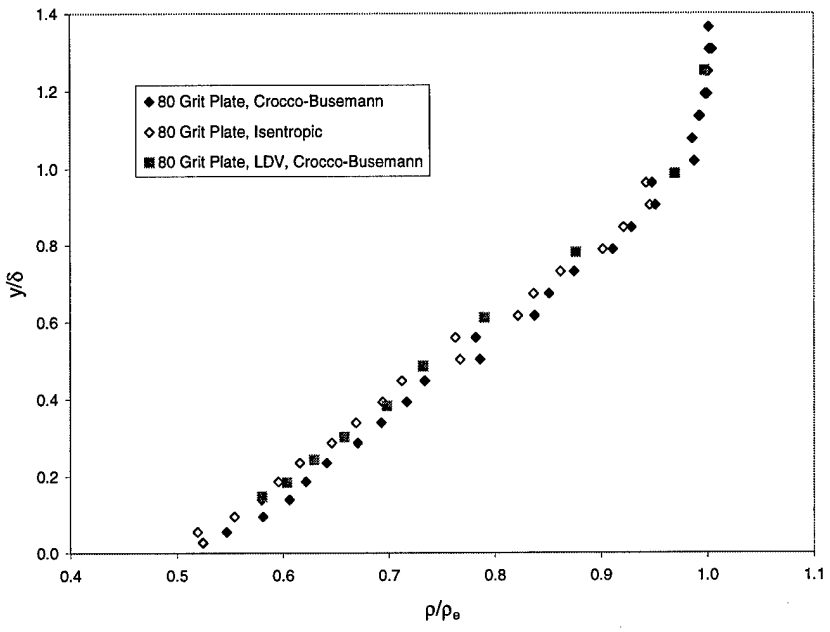

Figure 242. Pitot and LDV 80 Grit Plate Density Profiles

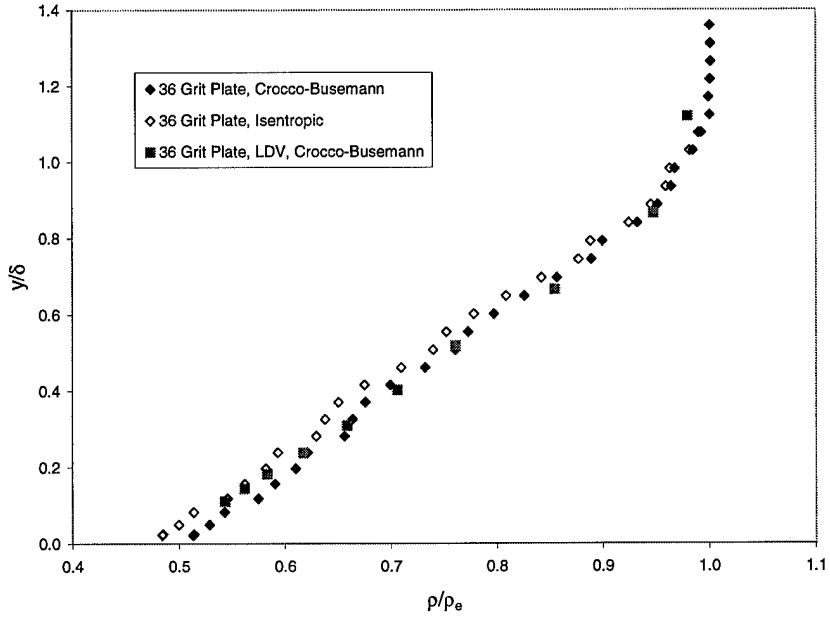

Figure 243. Pitot and LDV 36 Grit Plate Density Profiles

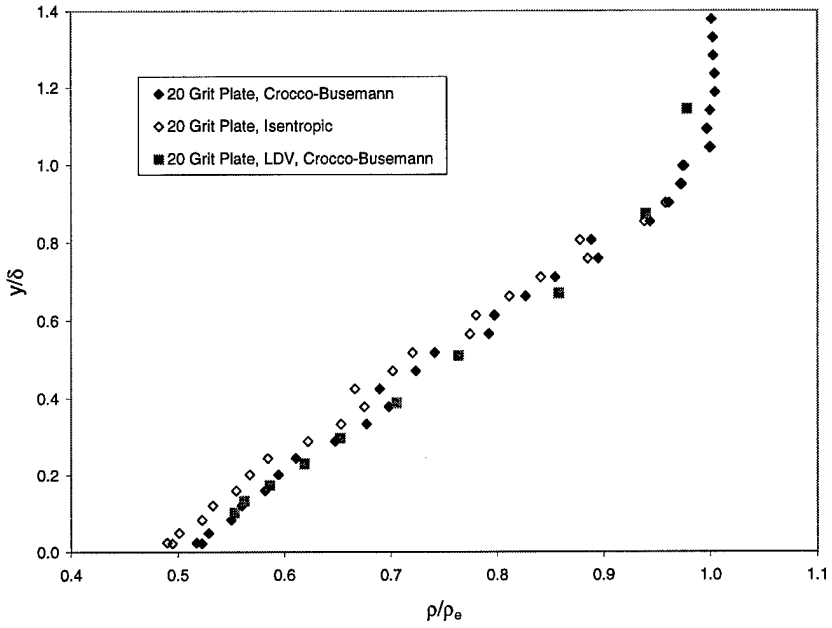

Figure 244. Pitot and LDV 20 Grit Plate Density Profiles

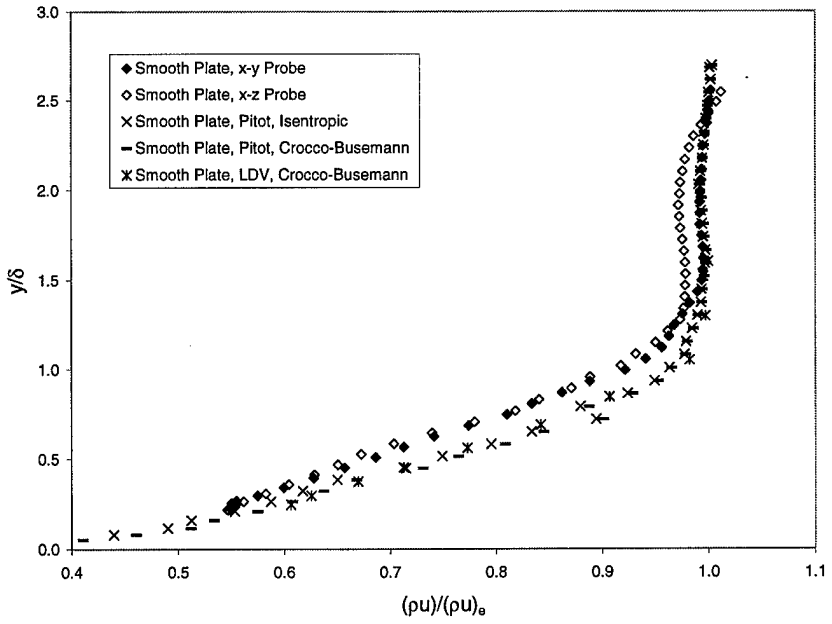

Figure 245. Smooth Plate $(\rho u)_{bar}$ Profiles

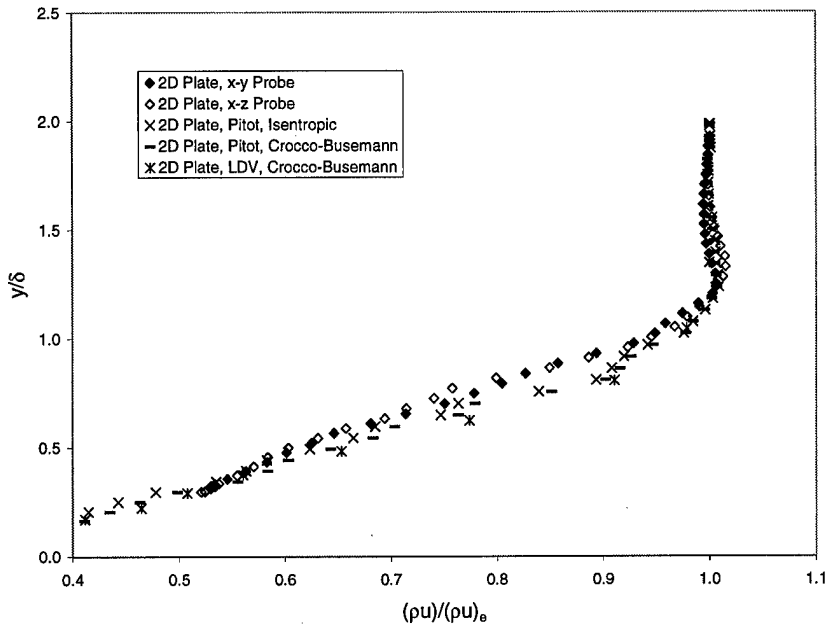

Figure 246. 2D Plate $(\rho u)_{bar}$ Profiles

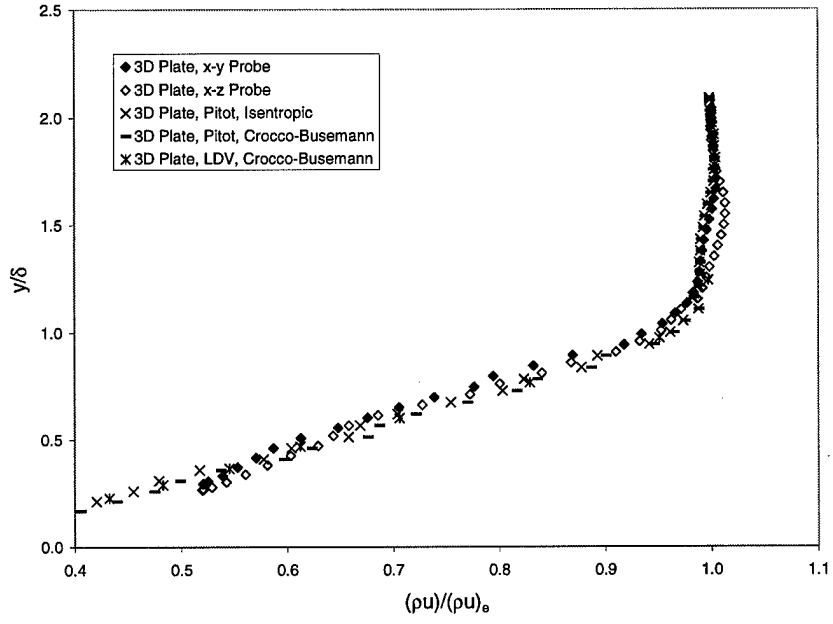

Figure 247. 3D Plate $(\rho u)_{bar}$ Profiles

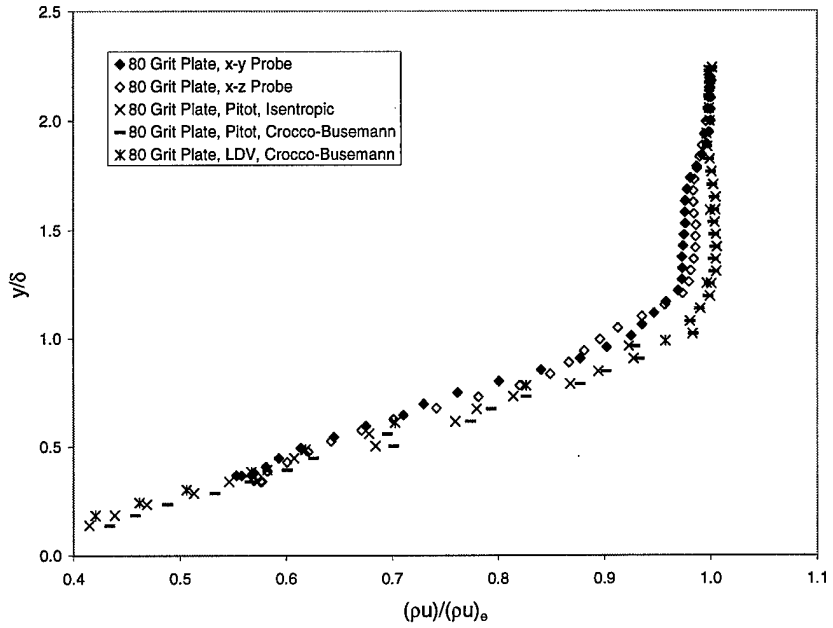

Figure 248. 80 Grit Plate $(\rho u)_{bar}$ Profiles

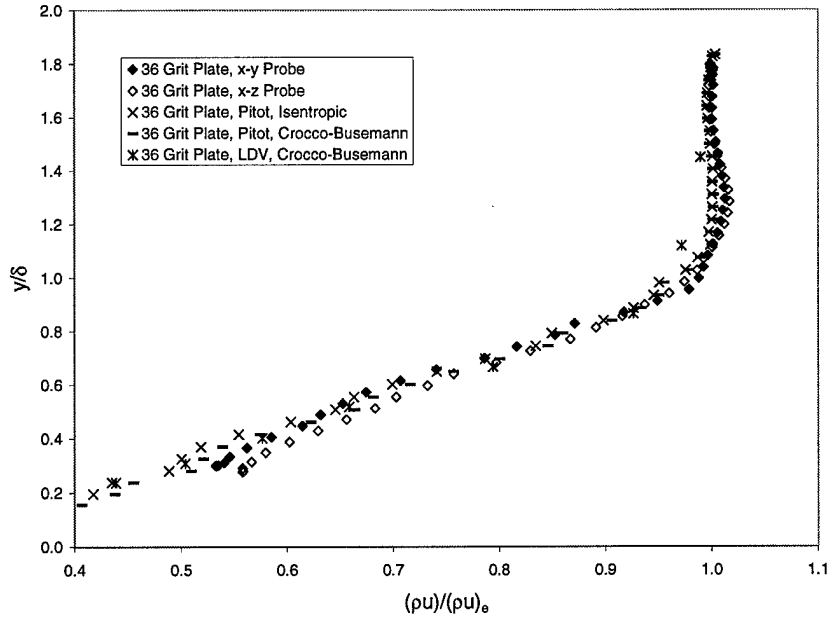

Figure 249. 36 Grit Plate $(\rho u)_{bar}$ Profiles

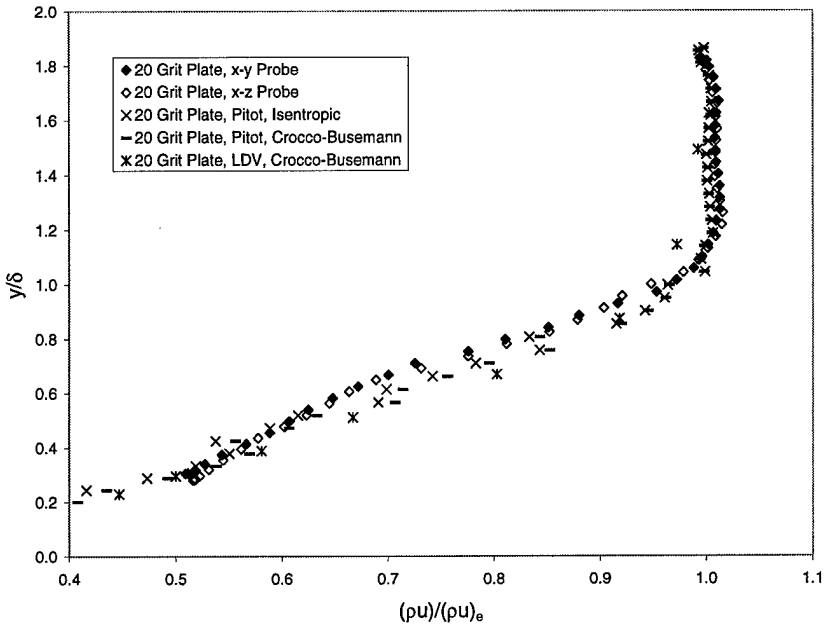

Figure 250. 20 Grit Plate $(\rho u)_{bar}$ Profiles

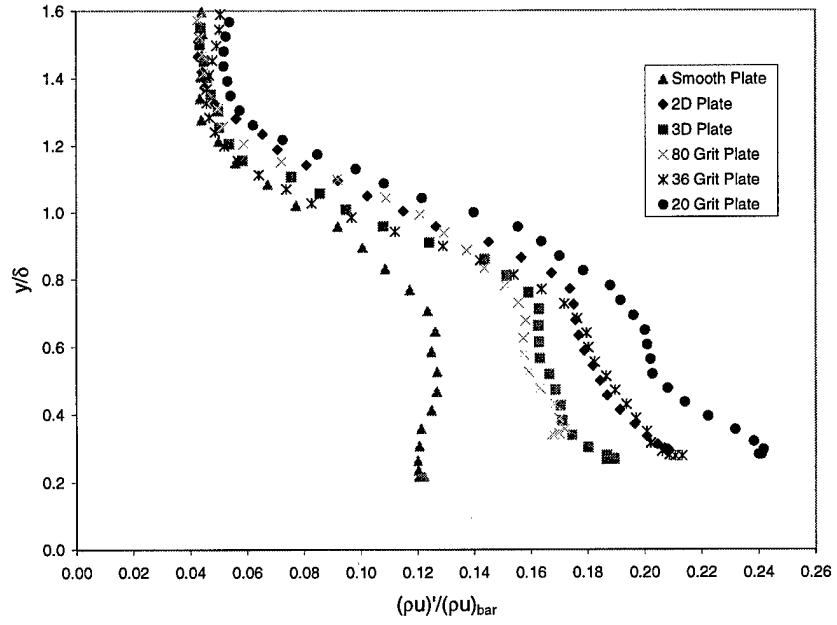

Figure 251. x-z Plane, Cross-Film, ρu-Turbulence Intensity

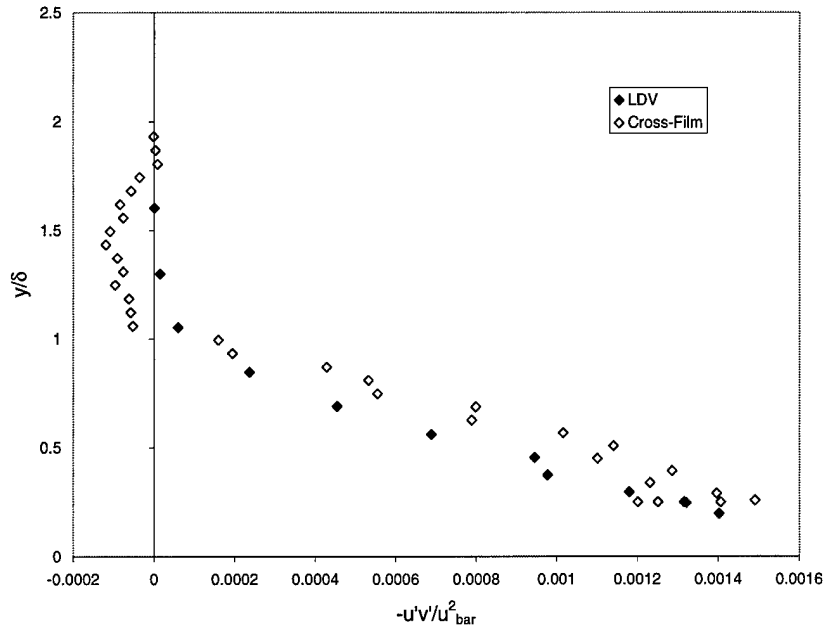

Figure 252. Smooth Plate Incompressible Reynolds Shear Stress

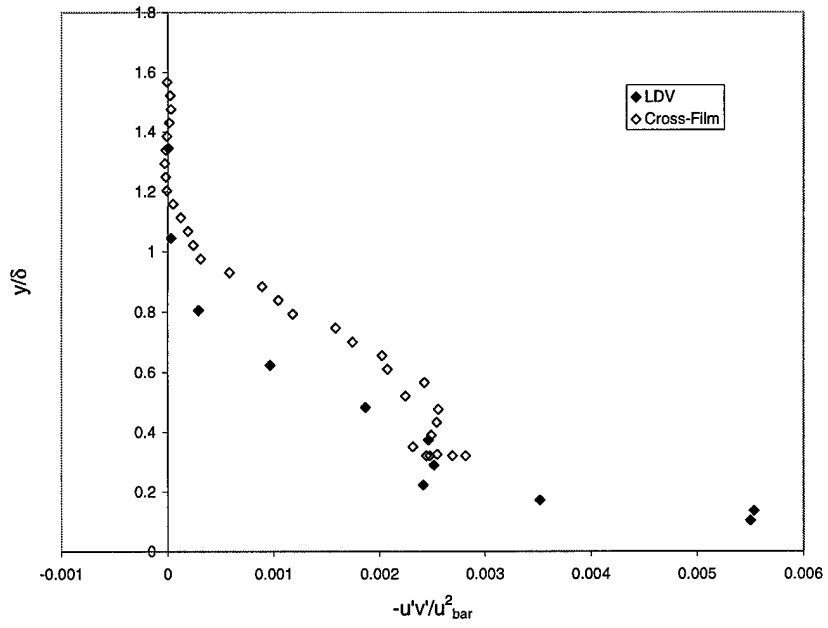

Figure 253. 2D Plate Incompressible Reynolds Shear Stress

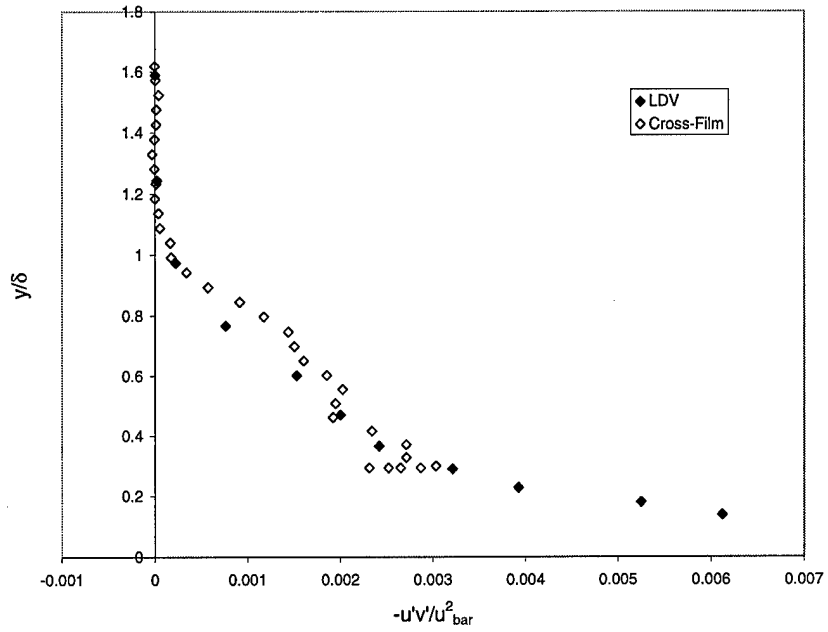

Figure 254. 3D Plate Incompressible Reynolds Shear Stress

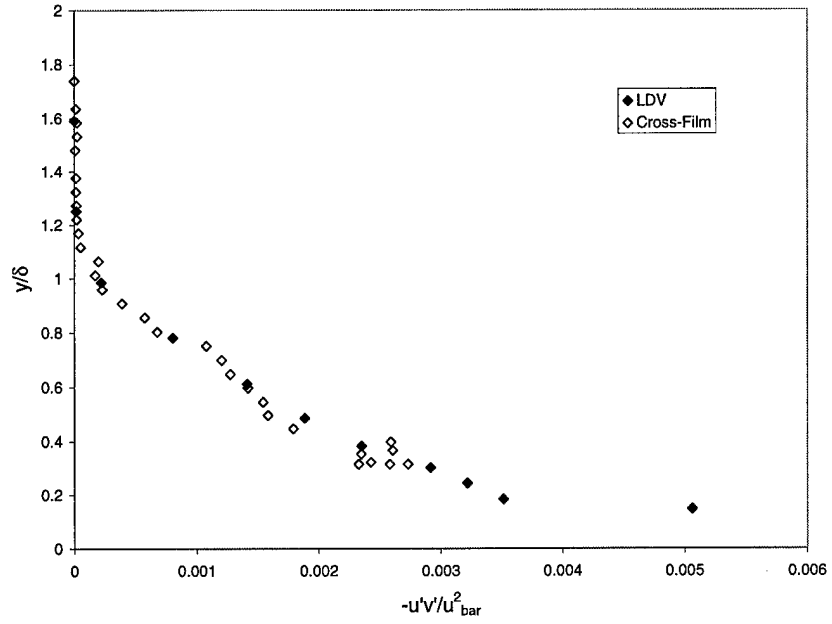

Figure 255. 80 Grit Plate Incompressible Reynolds Shear Stress

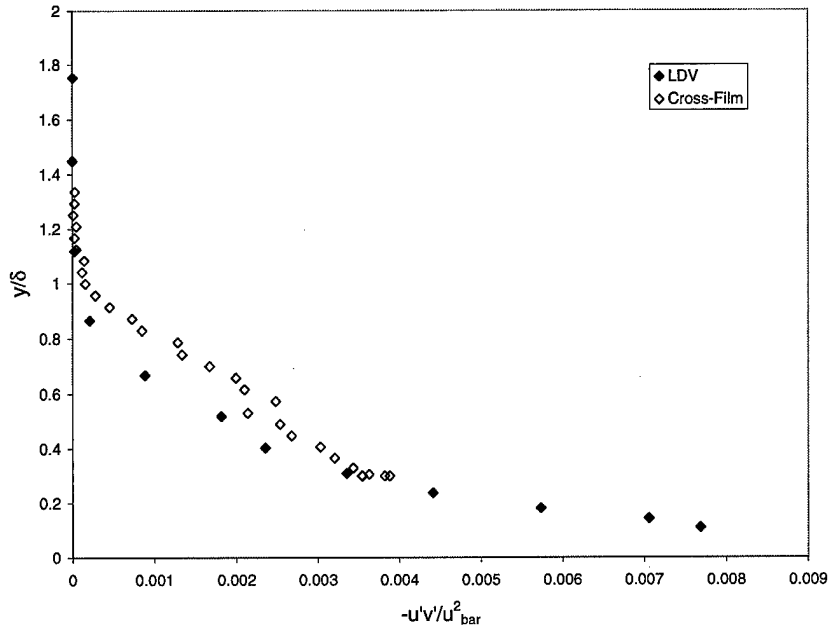

Figure 256. 36 Grit Plate Incompressible Reynolds Shear Stress

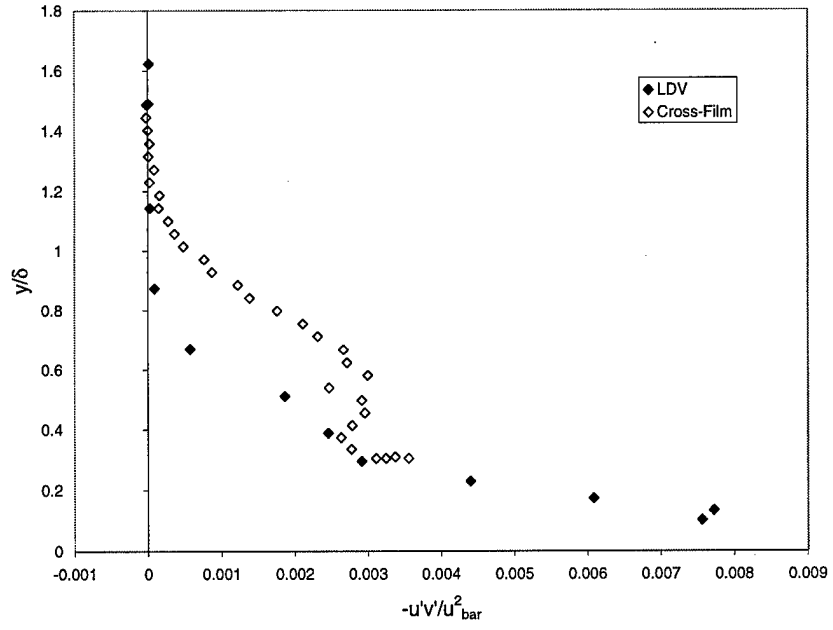

Figure 257. 20 Grit Plate Incompressible Reynolds Shear Stress

Vita

Captain Robert M. Latin was born on 25 August 1963 in Harrisburg, Pennsylvania. He graduated from Lower Dauphin High School in 1981 and joined the United States Air Force in 1982. He graduated with honors from the technical school at Lowry AFB, CO and began his Air Force career as an F-4E radar technician. In 1986, he entered the Air Force Airman Education and Commissioning Program (AECP) and went to the Ohio State University. He graduated Summa Cum Laude, earning a Bachelor of Science in Aeronautical and Astronautical Engineering and was commissioned a Second Lieutenant in the United States Air Force on 28 September 1989. Captain Latin began his graduate studies in the spring of 1993 when he entered the Air Force Institute of Technology (AFIT) in the Systems Engineering program. He earned a Master of Science in Systems Engineering in 1994 and began pursuing a Doctor of Philosophy in Aeronautical Engineering at AFIT. His follow-on assignment is at the Air Force Office of Scientific Research (AFOSR) at Bolling AFB, DC.

Permanent Address: FA 43 RD 3
Harrisburg, PA 17112

REPORT DOCUMENTATION PAGE

Form Approved
OMB No. 0704-0188

1. AGENCY USE ONLY (Leave blank)	2. REPORT DATE	3. REPORT TYPE AND DATES COVERED
	March 1998	Dissertation

4. TITLE AND SUBTITLE

The Influence of Surface Roughness on Supersonic High Reynolds Number Turbulent Boundary Layer Flow

5. FUNDING NUMBERS

6. AUTHOR(S)

Captain Robert M. Latin

7. PERFORMING ORGANIZATION NAME(S) AND ADDRESS(ES)

Air Force Institute of Technology, WPAFB OH 45433-7655

8. PERFORMING ORGANIZATION REPORT NUMBER

AFIT/DS/ENY/98M-02

9. SPONSORING / MONITORING AGENCY NAME(S) AND ADDRESS(ES)

Dr. Mark Glauser
AFOSR/NA
110 Duncan Ave, Suite B115
Bolling AFB, D.C. 20332

Drs. Diane Glawe and Mark Gruber
AFRL/PRSS
Bldg 18 1950 5th Street
WPAFB, OH 45433

10. SPONSORING / MONITORING AGENCY REPORT NUMBER

11. SUPPLEMENTARY NOTES

Dissertation advisor
Dr. Rodney D. W. Bowersox

12a. DISTRIBUTION / AVAILABILITY STATEMENT

Approved For Public Release;
Distribution Unlimited

12b. DISTRIBUTION CODE

13. ABSTRACT *(Maximum 200 words)*

A comprehensive study of rough-wall high-speed ($M = 2.9$) high Reynolds number ($Re/m = 1.9 \cdot 10^7$) turbulent boundary layer flow was performed consisting of experimental, analytical, and numerical methods. Six wall topologies consisting of a smooth and five rough surfaces were studied. The experimental measurement techniques included a Pitot pressure probe, laser Doppler velocimetry, hot-wire anemometry, color schlieren and laser sheet imaging. Mean measurements included velocity, Mach number, density, and mass flux. Turbulent measurements included velocity and mass flux turbulence intensities, kinematic and compressible Reynolds shear stresses, and the traverse apparent mass flux. Kinematic turbulent flow statistical properties were found to scale by local mean quantities and displayed a weak dependence on surface roughness. Turbulent flow statistical properties with the explicit appearance of density did not scale by local mean quantities, and had a strong linear dependence on roughness. Surface roughness also had a significant effect on the flow structure size and energy spectra. A theoretical analysis was performed and a new integral method for the estimation of skin friction was developed. A numerical study was performed which used a parabolized Navier-Stokes solver with two algebraic turbulence models and the Rotta model for surface roughness. A new method for the estimation of momentum loss improved the numerical flow predictability. The algebraic turbulence models predicted qualitatively correct profile shapes.

14. SUBJECT TERMS

Turbulence, Compressible, Boundary Layers, Surface Roughness, Supersonic, Hot-Wire Anemometry, Laser Doppler Velocimetry, Color Schlieren, Laser Sheet Imaging

15. NUMBER OF PAGES

361

16. PRICE CODE

17. SECURITY CLASSIFICATION OF REPORT	18. SECURITY CLASSIFICATION OF THIS PAGE	19. SECURITY CLASSIFICATION OF ABSTRACT	20. LIMITATION OF ABSTRACT
UNCLASSIFIED	UNCLASSIFIED	UNCLASSIFIED	UL